

University of Southampton Research Repository ePrints Soton

Copyright © and Moral Rights for this thesis are retained by the author and/or other copyright owners. A copy can be downloaded for personal non-commercial research or study, without prior permission or charge. This thesis cannot be reproduced or quoted extensively from without first obtaining permission in writing from the copyright holder/s. The content must not be changed in any way or sold commercially in any format or medium without the formal permission of the copyright holders.

When referring to this work, full bibliographic details including the author, title, awarding institution and date of the thesis must be given e.g.

AUTHOR (year of submission) "Full thesis title", University of Southampton, name of the University School or Department, PhD Thesis, pagination

UNIVERSITY OF SOUTHAMPTON

FACULTY OF NATURAL AND ENVIRONMENTAL SCIENCES

School of Ocean and Earth Science

The geological controls on the Von Damm Vent Field

by

Matthew Ronald Stephen Hodgkinson

Thesis for the degree of Doctor of Philosophy

December 2015

ABSTRACT

FACULTY OF NATURAL AND ENVIRONMENTAL SCIENCES

SCHOOL OF OCEAN AND EARTH SCIENCE

Thesis for the Doctor of Philosophy

THE GEOLOGICAL CONTROLS ON THE VON DAMM VENT FIELD

Matthew Ronald Stephen Hodgkinson

Hydrothermal systems at mid-ocean ridges (MOR) are of scientific interest due to their role in oceanic crustal heat loss, global geochemical cycles, and the evolution of chemosynthetic life. Hydrothermal circulation at MOR is usually characterised by high-temperature (up to 400°C), low pH (~3) vent fluids with high concentrations of dissolved base metals and H₂S. The driver of this hydrothermal circulation is magmatic heat, and results in the formation of massive sulphide deposits. Hydrothermal vent fields were originally thought to be sparse at slow spreading ridges due to the low magma supply. However, the emergence of low angle detachment faulting at ridges with spreading rates of < 75 mm yr⁻¹, indicated that tectonic controls are of equal importance to magmatic activity in generating hydrothermal circulation at slow-spreading MOR. These oceanic core complexes (OCC) expose lower crustal and upper mantle rocks along the flanks, and result in a greater geochemical diversity of hydrothermal deposit at slow spreading MOR. This thesis describes the geological setting, mineralogy and geochemistry of the Von Damm Vent Field (VDVF), which is hosted atop the Mt. Dent OCC at a seawater depth of 2300 metres.

The VDVF was discovered in 2010, and is located in the Caribbean on the ultraslow spreading Mid-Cayman Rise. It is hosted in a gabbro-peridotite basement, 13 km away from the axial rift. The mineralogy is predominantly talc (Mg₃Si₄O₁₀(OH)₂), with accessory microcrystalline silica and sulphides. The talc has a botryoidal and banded habit, textures that are indicative of precipitation from a hydrothermal fluid. Trace element geochemistry indicates a strong, positive europium anomaly in the talc, characteristic of high-temperature vent fluids. ⁸⁷Sr/⁸⁶Sr_{talc} ranges from 0.70613-0.70913, in between the value of the end-member vent fluid (0.70291) and seawater (0.70917). Hydrothermal vent fluids have low metal concentrations, intermediate pH (5.8) and high concentrations of chloride (667 mmol kg⁻¹) relative to seawater, and are generated by interaction with the mafic-ultramafic basement at low water-rock ratios. The calculated heat flux of 487±101 MW is comparable to some of the largest hydrothermal vent fields known. This heat and volume flux from the VDVF may represent a previously unrecognised, significant mode of off-axis crustal cooling, and has implications for global geochemical cycles.

Table of contents

Table of contents	i
List of figures	vii
List of tables	xiii
Declaration of authorship	xv
Acknowledgements	xvii
List of symbols and abbreviations	xix
CHAPTER ONE – Introduction and previous work	1
1.1. Introduction	1
1.1.1. Rationale	1
1.2. The Mid-Cayman Rise	2
1.2.1. Hydrothermal vent fields on the Mid-Cayman Rise	2
1.3. Aims and objectives	4
1.4. Diversity of seafloor spreading: rift morphology and crustal generation	5
1.4.1. Fast-intermediate spreading mid-ocean ridges	5
1.4.2. Medium - ultraslow spreading mid-ocean ridges	7
1.5. Diversity of hydrothermal venting	9
1.5.1. Common interactions in basalt hosted systems	10
1.5.2. Alteration of host rock	10
1.5.3. Chimney formation	12
1.5.4. Massive sulphide formation	13
1.5.5. Variations with host rock	14
1.5.6. Longevity of hydrothermal venting	17
1.5.7. Serpentinisation at slow-spreading ridges	18
1.6. Heat and chemical fluxes from mid-ocean ridges	19
1.6.1. Calculation of heat fluxes from individual vent fields	20
1.6.2. Global heat and chemical fluxes	22
1.6.3. Geophysical methods	22
1.6.4. Geochemical methods	23
1.6.5. Uncertainties in calculating global fluxes	25

CHAPTER TWO – Methods.....	29
2.1. Introduction.....	29
2.1.1. Ship tracks.....	31
2.1.2. ROV and submersible tracks.....	31
2.2. Sample recovery.....	37
2.2.1. Sample locations.....	39
2.3. Geophysical surveys and processing	41
2.4. Petrography.....	43
2.4.1. Petrographic microscopy.....	43
2.4.2. Scanning electron microscopy	43
2.4.3. X-Ray diffraction	44
2.5. Geochemistry	45
2.5.1. X-Ray fluorescence.....	45
2.5.2. Inductively-coupled plasma mass spectroscopy	46
2.5.3. Inductively coupled plasma atomic emission spectroscopy	48
2.5.4. Stable isotopes.....	50
2.5.5. Hydrothermal vent fluids.....	51
2.5.6. Strontium isotopes.....	52
2.6. Heat flux calculation.....	53
2.7. Thermodynamic modelling.....	54
 CHAPTER THREE – Regional Setting of the Mid-Cayman Rise.....	 55
3.1. Evolution and present day tectonics of the Caribbean Plate.....	55
3.1.1. Boundaries of the Caribbean Plate.....	56
3.1.2. Major geological features of the Caribbean Sea	59
3.2. History and evolution of the Cayman Trough.....	60
3.2.1. History of the Cayman Trough and opening of the Mid-Cayman Rise.....	60
3.3. Geological setting of the Mid-Cayman Rise.....	62
3.3.1. Oceanic core complexes on the Mid-Cayman Rise	64
3.3.2. Northern segment of the Mid-Cayman Rise	67
3.3.3. Southern segment of the Mid Cayman Rise.....	71
3.4. The Mount Dent oceanic core complex.....	75
3.4.1. Submersible observations and samples from previous investigations to Mt. Dent	77

3.4.2. Dredged samples.....	78
3.4.3. Primary phases and common alteration minerals in altered mafic rocks.	80
3.4.4. Altered ultramafics	90
3.4.5. Accessory minerals.....	90
3.4.6. Textures and mineral relationships.....	91
3.4.7. Origin of Mt.Dent:deformation and metamorphic history	96

CHAPTER FOUR – Local setting of the Von Damm Vent Field 99

4.1. Situation on the flanks of the Mid-Cayman Rise	99
4.2. Setting of the VDVF.....	102
4.3. Host rocks in the vicinity of the VDVF.....	107
4.3.1. Appearance at outcrop scale.....	107
4.3.2. Common primary igneous minerals.....	108
4.3.3. Common replacement minerals	116
4.3.4. Accessory minerals.....	119
4.3.5. Textures and summary of alteration	123
4.3.6. Whole rock geochemistry of basement rocks	126
4.3.7. Origin of basement lithologies	131
4.4. Active chimneys.....	132
4.4.1. Venting styles at the VDVF	132
4.4.2. Petrography of the active chimneys	133
4.5. Active mounds.....	143
4.5.1. Main cone	143
4.5.2. North and south spurs	149
4.6. Inactive mounds.....	151
4.6.1. Mystic Mountain area	151
4.6.2. Other hydrothermally inactive areas.....	151
4.7. Whole rock geochemistry.....	154
4.8. Summary of the local setting of the Von Damm Vent Field	155

CHAPTER FIVE – Talc precipitation at the Von Damm Vent Field..... 161

5.1. Von Damm Vent Field hydrothermal fluids.....	161
5.1.1. Vent fluid pH	163

5.1.2. Vent fluid chlorinity	166
5.1.3. Cations	169
5.2. Rare earth elements.....	172
5.2.1. Hydrothermal precipitates.....	172
5.2.2. Precipitation of talc from a hydrothermal fluid.....	174
5.3. Strontium isotopes.....	183
5.3.1. Host rocks and dredged samples	183
5.3.2. VDVF fluids.....	185
5.3.3. Talc separates.....	186
5.4. Stable isotopes	187
5.4.1. $\delta^{18}\text{O}$ results	188
5.4.2. Fractionation equations for talc and quartz.....	189
5.4.3. Temperatures of formation	190
5.4.4. Talc-quartz mineral pairs and calculation of fluid ratios.....	192
5.4.5. Hydrogen isotopes.....	193
5.5. Thermodynamic modelling.....	195
5.5.1. Simple mixing models.....	196
5.5.2. Chimneys on the main cone.....	198
5.5.3. Conductive cooling	200
5.5.4. pH at the VDVF.....	201
5.6. Summary of talc precipitation at the VDVF.....	202

CHAPTER SIX – Importance of the Von Damm Vent Field 205

6.1. Talc occurrences at seafloor spreading centres.....	205
6.1.1. Sediment-related talc	207
6.1.2. Talc and similar clays in other active hydrothermal deposits.....	209
6.1.3. Extinct hydrothermal talc deposits.....	210
6.1.4. Hydrothermal talc occurrences at oceanic core complexes	210
6.2. Extinct hydrothermal deposits located downslope of the VDVF	211
6.3. Extinct hydrothermal deposits with similar tectonic settings to the VDVF ...	215
6.3.1 St Paul Fracture Zone.....	215
6.3.2. Southwest Indian Ridge.....	218
6.3.3. Whole rock geochemistry.....	221
6.3.4. Rare earth element geochemistry	222

6.4. Heat flux from the VDFV	229
6.4.1. Assumptions and errors.....	229
6.4.2. Hydrothermal heat flux	230
6.4.3. Comparison to other measurements.....	231
6.4.4. Heat source at the VDFV	231
6.5. Global implications of VDFV-type vents.....	235
6.5.1. Summary of current knowledge of mid-ocean ridge heat and chemical fluxes	235
6.5.2. Occurrence of oceanic core complexes and VDFV-type vents.....	235
6.5.3. Heat loss at oceanic core complexes and VDFV-type vents	236
6.5.4. Chemical fluxes from the VDFV	238
Summary and Conclusions	241
7.1. Summary of the VDFV.....	241
7.1.1. Mt. Dent	241
7.1.2. Local geological setting.....	241
7.1.3. Talc precipitation.....	242
7.2. Scope for further work.....	243
7.2.1. Understanding the processes of heat extraction at OCC's	243
7.2.2. Discovery of VDFV-type vents	243
7.3. Concluding remarks.....	244
Appendix A.....	245
A.1. XRD	245
A.1.1. Bulk	245
A.1.2. Clays.....	245
A.2. Preparation of whole rock samples for XRF.....	246
A.3. Preparation of talc separates and whole rock samples for trace element analysis	246
A.4. Preparation and procedure of samples for strontium isotope analysis	247
A.5. Preparation of samples for stable isotope analysis	249
A.6. Hydrothermal fluids	250
A.7. Heat flux calculations.....	252
Appendix B	255
List of references	245

List of Figures

Figure 1.1: Map showing the location of the MCR	3
Figure 1.2: Characteristics of fast spreading ridges	7
Figure 1.3: Characteristics of slow-spreading ridges.....	8
Figure 1.4: Schematic of a hydrothermal circulation cell.....	11
Figure 1.5: Schematic of a hydrothermal vent system	14
Figure 1.6: Schematic of an oceanic core complex	15
Figure 1.7: Location of global hydrothermal vent fields.....	21
Figure 2.1: Map of the world showing the locations of samples analysed.....	30
Figure 2.2: Cruise track of JC044.....	32
Figure 2.3: Cruise track of JC082.....	33
Figure 2.4: Navigation tracks for HyBIS dives 27-29 during cruise JC044.....	34
Figure 2.5: Navigation track for Isis dive 197	35
Figure 2.6: Navigation tracks for Isis dives 198-202 during cruise JC082.....	36
Figure 2.7: Navigation tracks for Isis dives 198-202 during cruise JC082 for the active VDVF.....	37
Figure 2.8: Location map of samples recovered from the regional VDVF.....	38
Figure 2.9: Location map of samples from the main VDVF cone.....	39
Figure 3.1: Regional tectonic map of the Caribbean	58
Figure 3.2: Schematic map showing the history of the Cayman Trough, present day tectonics and opening of the Mid-Cayman Rise.....	63
Figure 3.3: Bathymetry of the MCR showing lithologies recovered.....	65
Figure 3.4: Bathymetry and interpretive geology of the MCR.....	66
Figure 3.5: Side scan sonar of the MCR	68
Figure 3.6: Side scan sonar and interpretive tectonics of the northern segment of the MCR.....	70
Figure 3.7: Side scan sonar of the basin tectonic ridge south of Mt. Dent on the southern segment of the MCR.....	72
Figure 3.8: Side scan sonar of the AVR and Mt. Hudson on the southern segment of the MCR.....	74
Figure 3.9: E-W cross section showing the topographic profile of Mt. Dent.....	75
Figure 3.10: Side scan sonar of Mt. Dent	76

Figure 3.11: Scans of hand specimen fresh faces.....	79
Figure 3.12: X-Ray diffraction (XRD) of dredged samples.....	81
Figure 3.13: XRD of dredged samples.....	82
Figure 3.14: Remnant plagioclase and clinopyroxene in dredged samples.....	83
Figure 3.15: Chlorite occurrences in dredged samples.....	84
Figure 3.16: SEM images of common minerals within the groundmass.....	85
Figure 3.17: Amphiboles present in dredged samples.....	87
Figure 3.18: Groundmass within dredged samples.....	88
Figure 3.19: Chemistry of hornblende and pargasite.....	88
Figure 3.20: Talc and prehnite forms within dredged samples.....	89
Figure 3.21: Serpentine occurrences within dredged samples.....	92
Figure 3.22: Deformation textures.....	95
Figure 3.23: Schematic showing the evolution of the alteration assemblage within Mt. Dent.....	97
Figure 4.1: Map of Mt. Dent showing the location of the VDFV.....	100
Figure 4.2: Geological map of the region surrounding the VDFV.....	101
Figure 4.3: Geological map of the VDFV.....	103
Figure 4.4: Rubble and sediment contacts.....	104
Figure 4.5: ROV images of the regional VDFV.....	106
Figure 4.6: Rose diagrams showing the orientations of linear features at the regional VDFV.....	107
Figure 4.7: Scans of hand specimens.....	109
Figure 4.8: XRD plots of VDFV host rocks.....	110
Figure 4.9: XRD plots of VDFV host rocks.....	111
Figure 4.10: Feldspar forms in VDFV host rocks.....	115
Figure 4.11: Remnant pyroxene and olivine in VDFV host rocks.....	117
Figure 4.12: Groundmass in altered dykes.....	118
Figure 4.13: Chlorite replacement of plagioclase in VDFV host rock.....	120
Figure 4.14: Actinolite-tremolite forms in VDFV gabbros.....	121
Figure 4.15: Hornblende in VDFV host rocks and amphibole occurrences in ultramafics	122
Figure 4.16: Composition of hornblende in VDFV host rocks.....	122
Figure 4.17: Mineralogy of serpentinised ultramafics.....	124
Figure 4.18: Accessory minerals in VDFV host rocks.....	126

Figure 4.19: Deformation textures in VDVF host rocks	126
Figure 4.20: Na _{8,0} values plotted against depth	128
Figure 4.21: REE of host rocks.	129
Figure 4.22: ROV images of venting styles at the main cone.	133
Figure 4.23: ROV images of venting styles on the north and south spurs	134
Figure 4.24: Scans of fresh faces of active chimneys	135
Figure 4.25: XRD of hydrothermal precipitates.	136
Figure 4.26: XRD of clay separates from the VDVF	137
Figure 4.27: Precipitation textures observed in open pore spaces of active chimneys	138
Figure 4.28: Common textures in less porous chimney areas.	139
Figure 4.29: Sulphide textures in VDVF chimneys.	141
Figure 4.30: Microcrystalline silica in VDVF precipitates	142
Figure 4.31: ROV images of the active and inactive mounds.	144
Figure 4.32: Scans of hand specimens of massive and brecciated talc	145
Figure 4.33: Textures observed in clastic talc	146
Figure 4.34: Fine grained and banded talc.	147
Figure 4.35: Microcrystalline silica and talc overprinting textures.	148
Figure 4.36: Sulphides in mound material from the main cone.	149
Figure 4.37: Talc textures in from the north and south spurs	150
Figure 4.38: Scans of fresh faces of samples from inactive samples.	152
Figure 4.39: Textures and mineralogy of inactive precipitates from Mystic Mountain	153
Figure 4.40: Mineralogy and textures of inactive samples	154
Figure 5.1: Shimmering fluid venting at the top of the VDVF	161
Figure 5.2: Plots of VDVF fluid projected to zero magnesium.	165
Figure 5.3: Phase diagram of seawater	167
Figure 5.4: Chondrite normalised REE patterns for active chimneys at the VDVF ..	177
Figure 5.5: Chondrite normalised REE patterns for active mounds at the VDVF. ...	178
Figure 5.6: Chondrite normalised REE patterns for inactive mounds in the vicinity of the VDVF	179
Figure 5.7: La _(N) /Sm _(N) and Dy _(N) /Yb _(N) ratios(where (N)=chondrite normalised) of hydrothermal precipitates	180

Figure 5.8: Eu/Eu* and Ce/Ce* anomalies of active and inactive hydrothermal precipitates.	181
Figure 5.9: REE profiles of hydrothermal fluids from selected vent fields	182
Figure 5.10: Distribution of $^{87}\text{Sr}/^{86}\text{Sr}$ and end-member fluid ratio.	186
Figure 5.11: Stable isotope fractionation factors	189
Figure 5.12: $\delta^{18}\text{O}_{\text{fluid}}$ of co-existing talc and quartz mineral pairs.	192
Figure 5.13: $\delta^{18}\text{O}_{\text{fluid}}$ versus temperature of 4 pure talc separates from the chimneys at the top of the main cone.	193
Figure 5.14: δD and $\delta^{18}\text{O}$ of talc and serpentine in oceanic environments.	195
Figure 5.15: Saturation indices for talc, quartz, anhydrite and brucite on mixing with ambient seawater at 4°C	197
Figure 5.16: Mineral saturation indices in mixed fluids in chimneys from the main cone.	199
Figure 5.17: Stability boundaries of talc, quartz and brucite.	200
Figure 5.18: Conductive cooling mixing regimes for seawater heated up to 150°C and 100°C.	201
Figure 5.19: Talc saturation on mixing VDVF fluids with seawater at pH values ranging from 3 to 7.	202
 Figure 6.1: Map detailing the location of samples from other seafloor spreading centres.	 206
Figure 6.2: XRD of bulk powders from Mt. Dent.	212
Figure 6.3: Transmitted light, reflected light and scanning electron microscope (SEM) images of samples from Mt. Dent	213
Figure 6.4: XRD of clay separates from the MCR.	214
Figure 6.5: XRD of bulk powder from the SPFZ	216
Figure 6.6: SEM images of accessory minerals and groundmass	217
Figure 6.7: XRD of clay separates from the SPFZ	217
Figure 6.8: XRD of bulk powders from the SWIR	218
Figure 6.9: Transmitted light and SEM images of samples from the SWIR.	219
Figure 6.10: XRD of clay separates from the SWIR	220
Figure 6.11: Chondrite normalised REE patterns in samples from the MCR, the St. Paul fracture zone and the SWIR	224
Figure 6.12: Chondrite normalised REE plots from other talc deposits	226
Figure 6.13: REE ratios and anomalies for other talc occurrences.	228

Figure A.1: velocity flow measurements at the main hole.....	253
--	-----

List of Tables

Table 1.1: End-member vent fluid concentrations from a range of hydrothermal fields.	16
Table 1.2: Summary of heat fluxes based on various geophysical methods	26
Table 1.3: Summary of heat and chemical fluxes based on geochemical methods.....	26
Table 2.1: Dates and locations of cruises that collected the samples	29
Table 2.2: Depths, latitudes and longitudes of samples from the MCR recovered by ROV or submersible	41
Table 2.3: Latitudes and longitudes of samples recovered by dredging from the MCR, SWIR and the SPFZ.....	41
Table 2.4: Accuracy and precision of international geological reference material, standard BRR-1	44
Table 2.5: List of mineral standards used in calibrating the EDS spectra.	45
Table 2.6: Accuracy and precision for XRF analysis.	47
Table 2.7: Precision of reference materials used in ICP-MS analysis	48
Table 2.8: Accuracy of standards used in ICP-MS.....	49
Table 2.9: Precision of multi-element standards used in ICP-AES	50
Table 3.1: Energy dispersive spectra (EDS) analysis	93
Table 3.2: Cr#, Mg# and empirical formulae	94
Table 4.1: EDS analysis of minerals within VDFV host rocks.....	113
Table 4.2: An content, Mg#, Cr#, Fo content and empirical formulae	114
Table 4.3: Major and trace elements in host rocks recovered from within 1 km of the VDFV.....	130
Table 4.4: Eu anomalies, Ce anomalies, La _N /Sm _N ratios and Dy _N /Yb _N ratios in host rock samples and basalt glass from the AVR.....	131
Table 4.5: List of active vent structures at the VDFV	132
Table 4.6: Major and trace elements of hydrothermal precipitates from the VDFV and the surrounding inactive mounds.....	156-159
Table 5.1: Measured concentrations in VDFV fluid samples	162

Table 5.2: Extrapolated end-members for the VDVf compared to other hydrothermal vent fields.....	171
Table 5.3: REE concentrations in VDVf samples.....	175
Table 5.4: Eu anomalies, Ce anomalies, La/Sm ratios and Dy/Yb ratios in VDVf samples.....	176
Table 5.5: Strontium concentration and $^{87}\text{Sr}/^{86}\text{Sr}$ isotope ratios in host rocks, fluids and hydrothermal precipitates.....	184
Table 5.6: $\delta^{18}\text{O}$ and δD of talc and $\delta^{18}\text{O}$ of quartz separates from the VDVf and surrounding inactive mounds.....	188
Table 6.1: Summary of other occurrences of talc at MOR's.....	208
Table 6.2: Major element concentrations derived by X-Ray fluorescence.....	221
Table 6.3: Trace element concentrations in samples from the MCR, the SPFZ and the SWIR.....	222
Table 6.4: REE concentrations in samples from the MCR, the SPFZ and the SWIR..	225
Table 6.5: Estimated heat flux at the VDVf.....	230
Table A.1: Concentrations of dissolved elements within the water phase of hydrothermal fluid.....	250
Table A.2: Concentrations of elements within the solid phases that precipitated within the fluid sample bottles.....	251
Table A.3: Weighted concentrations of dissolved elements from both solid and water phases.....	251
Table A.4: Variations in the velocities of entrained particles.....	252

Declaration of authorship

I, declare that this thesis and the work presented in it are my own and has been generated by me as the result of my own original research.

The geological controls on the Von Damm Vent Field

I confirm that:

1. This work was done wholly or mainly while in candidature for a research degree at this University;
2. Where any part of this thesis has previously been submitted for a degree or any other qualification at this University or any other institution, this has been clearly stated;
3. Where I have consulted the published work of others, this is always clearly attributed;
4. Where I have quoted from the work of others, the source is always given. With the exception of such quotations, this thesis is entirely my own work;
5. I have acknowledged all main sources of help;
6. Where the thesis is based on work done by myself jointly with others, I have made clear exactly what was done by others and what I have contributed myself;
7. Parts of this work have been published, as:

Hodgkinson, M.R.S., Webber, A.P., Roberts S., Mills, R.A., Connelly, D.P. and Murton, B.J., 2015, Talc-dominated hydrothermal deposits reveal a new class of hydrothermal, *Nature Communications*, (*in press*.)

Signed:

Date:

Acknowledgements

This thesis would not have been possible without the help of many people. A huge amount of thanks goes towards my supervisors, Bramley Murton and Steve Roberts, firstly for giving me the opportunity to work on this project, and then for their enthusiasm and expertise during the last four years. I would like to thank Damon Teagle, for his advice and input during my panel chair meetings. Alex Webber is owed a huge amount of thanks for providing advice in many different sections of this project.

The data involved in this project would not have been provided without the help of many people involved in the lab work. I would like to thank Matt Cooper for his help and patience in all the sample preparation, instrument techniques and data analysis. Agnes Michalik and Catriona Menzies were also of huge help with during the clean lab work. Bob Jones and John Ford were incredibly helpful and kind (especially in the first few months of settling in), and for producing polished thin sections and help with sample preparation. Richard Pearce and Suzie Maclachlan are thanked for helping with sample preparation and running the SEMs. Ross Williams and Richard both helped hugely with the XRD analysis. I would like to thank Adrian Boyce, Alison McDonald, Julie Dougans and Terry Donnelly at the SUERC facility for help with the stable isotope analysis. I would like to thank InterRidge for the student fellowship to give me the opportunity to study abroad. Frieder Klein is owed a lot of thanks for providing samples from the WHOI archive, help with applying for the InterRidge fellowship, and his expertise and knowledge during the visit. Also, I would like to acknowledge the help of Doug Connelly and Rachel Mills for thought provoking discussions throughout the duration of my PhD, particularly with their advice concerning the vent fluid chemistry. The cruise teams during JC82, and the ISIS ROV team, for their help with making ship time so enjoyable, and for sample collection. My friends have made the past four years in Southampton incredibly enjoyable, for both advice and distractions when they have been needed. A special thanks goes my officemates past and present – Rhiannon, Lavinia, Lissie, Sophia and Ally, and my housemates James and Paris.

To Jen, and my family, thank you for all your support for the duration of the last four years.

List of symbols and common abbreviations

MOR	Mid-Ocean Ridge
MAR	Mid-Atlantic ridge
SWIR	Southwest Indian Ridge
MCR	Mid-Cayman Rise
BVF	Beebe Vent Field
VDVF	Von Damm Vent Field
Mt. Dent	Mount Dent
OCC	Oceanic core complex
ROV	Remotely operated vehicle
REE	Rare earth element
TAG	Trans-Atlantic Geotraverse
mmol kg ⁻¹	Millimoles per kilogram
μmol kg ⁻¹	Micromoles per kilogram
⁸⁷ Sr/ ⁸⁶ Sr	Strontium isotope ratio
MORB	Mid-ocean ridge basalt
³ He/ ⁴ He	Helium isotope ratio
NOCS	National Oceanography Centre, Southampton
SUERC	Scottish Universities Environmental Research Centre
WHOI	Woods Hole Oceanographic Institute
SPFZ	St. Paul Fracture Zone
kHz	Kilohertz
SVP	Sound velocity profile
AUV	Autonomous underwater vehicle
CTD	Conductivity temperature depth
E _h	Oxidation potential
SEM	Scanning electron microscope
XRD	X-Ray diffraction
EDS	Energy dispersive X-Ray analysis
%RSD	Relative standard deviation
wt. %	Weight percent
ICP-MS	Inductively couple plasma mass spectroscopy

HF	Hydrofluoric acid
HNO ₃	Nitric acid
ICP-AES	Inductively coupled plasma atomic emissions spectroscopy
δ ¹⁸ O	Oxygen isotope ratio relative to SMOW
SMOW	Standard Mean Ocean Water
‰	per mil
δD	Hydrogen isotope ratio relative to SMOW
H ₂ S	Hydrogen sulphide
HCl	Hydrochloric acid
TIMS	Thermal ionisation mass spectrometry
σ	Standard deviation
GWB	Geochemist's Workbench
log K	Stability constant
Q/K	Mineral saturation index
ODP	Ocean Drilling Program
Ma	Million years
CLIP	Caribbean Large Igneous Province
MCSC	Mid-Cayman Spreading Centre
AVR	Axial volcanic ridge
PPL	Plane-polarised light
XPL	Cross-polarised light
ΣREE	Total rare earth elements
Eu/Eu*	Europium anomaly
Ce/Ce*	Cerium anomaly
N-MORB	Normal mid-ocean ridge basalt
D-MORB	Depleted mid-ocean ridge basalt
E-MORB	Enriched mid-ocean ridge basalt
LREE	Light rare earth element
Å	Angstrom
mmol kg ⁻¹	Millimoles per kilogram
HREE	Heavy rare earth element
MREE	Middle rare earth element
MW	Megawatts

Chapter One – Introduction and Previous Work

This chapter discusses the rationale of the thesis, and the motivations, aims and objectives of the study. It places the work in the context of the current state of knowledge about seafloor spreading ridges, specifically focusing on the known diversity of hydrothermal vent fields, and the influence of hydrothermal circulation on global heat fluxes and ocean chemical cycles.

1.1. Introduction

1.1.1. Rationale

The discovery of hydrothermal vents on the Galapagos Rift in 1977 (Corliss et al., 1979) led to intense scientific research based on the role of hydrothermal circulation on crustal heat loss, oceanic chemical budgets, and the evolution of chemosynthetic life (Wolery and Sleep, 1976; Edmond et al., 1979a; Francheteau et al., 1979; Rona et al., 1986; Elderfield and Shultz, 1996). High-temperature hydrothermal circulation at fast spreading mid-ocean ridges (MOR) is typically associated with young volcanic systems (Von Damm et al., 1995). Magmatic activity is the dominant control on hydrothermal activity where it is predominantly hosted by mafic rocks (Detrick et al., 1987; Collier and Sinha, 1990). In contrast, at medium-slow spreading MOR's, a greater diversity of high-temperature circulation is observed, as host rocks include both mafic and ultramafic lithologies. Here, hydrothermal activity is localised both by magmatism and faulting (Canales et al., 2007; McCaig et al., 2007; Rona, 2010). In addition, the discovery of the Lost City hydrothermal field in 2000, located at 30°N on the Mid-Atlantic Ridge, 15 km away from the volcanic axis (MAR) (Kelley et al., 2001), provided an indication that hydrothermal circulation may be driven by the exothermic serpentinisation reaction, and the residual heat of the oceanic crust (Allen and Seyfried Jr, 2004; Lowell, 2010).

Hydrothermal systems were originally thought to be scarce and have large separation at ultraslow spreading ridges; due to the reduced magma supply in comparison to faster spreading ridges (Baker et al., 1996). The first indication of hydrothermal activity on ultraslow spreading ridges was the discovery of particulate plumes over

the Southwest Indian Ridge (SWIR) in 1997 (German et al., 1998). This has been followed by subsequent discoveries on the Gakkel Ridge (Edmonds et al., 2003) and the Mid-Cayman Rise (MCR; Connelly et al., 2012). As a result, a new paradigm has arisen challenging the hypothesis that hydrothermal activity is directly proportional to spreading rate. The emerging evidence is, with decreasing spreading rate, tectonic factors such as deep normal faults and long-lived detachment faults are of equal importance to enabling hydrothermal circulation as the presence of active magmatic systems e.g. (McCaig et al., 2007). Thus, at spreading rates of $<75 \text{ mm yr}^{-1}$, the relationship between vent field distribution and spreading rate is not a linear, as initially proposed (Baker et al., 1996; Baker and German, 2004), but increases as deep residual crustal heat fluxes are focused by fault systems.

1.2. The Mid-Cayman Rise

The MCR is classed as an ultraslow spreading MOR due to its full spreading rate of 15 mm yr^{-1} (Leroy et al., 2000) and is the world's deepest seafloor spreading centre. The extreme depth and low crustal thickness identifies the MCR as an end-member in terms of its low melt production and hence makes it an important end-member of the oceanic spreading ridge system (Stroup and Fox, 1981; Langmuir et al., 1992).

1.2.1. Hydrothermal vent fields on the Mid-Cayman Rise

Following the detection of neutrally buoyant plumes in 2009 (German et al., 2010a), two contrasting vent fields were discovered on the MCR in 2010 (Figure 1.1; Murton et al., 2011; Connelly et al., 2012). The Beebe Vent Field (BVF) is a basalt-hosted, black smoker system that is situated at 5000 m seawater depth, making it the deepest hydrothermal vent field currently known (Connelly et al., 2012). A second hydrothermal system is situated at a seawater depth of 2300 m, and is called the Von Damm Vent Field (VDVF; Connelly et al., 2012). The VDVF is hosted in gabbro and serpentinite on the upper-slopes of Mount Dent (Mt. Dent), an oceanic core complex (OCC; Connelly et al., 2012). The contrasting venting styles at the MCR, located within $\sim 20 \text{ km}$ of each other, provide a unique opportunity to study the effects of host lithology, geological setting and depth on the composition of hydrothermal fluids, and the resulting seafloor deposits.

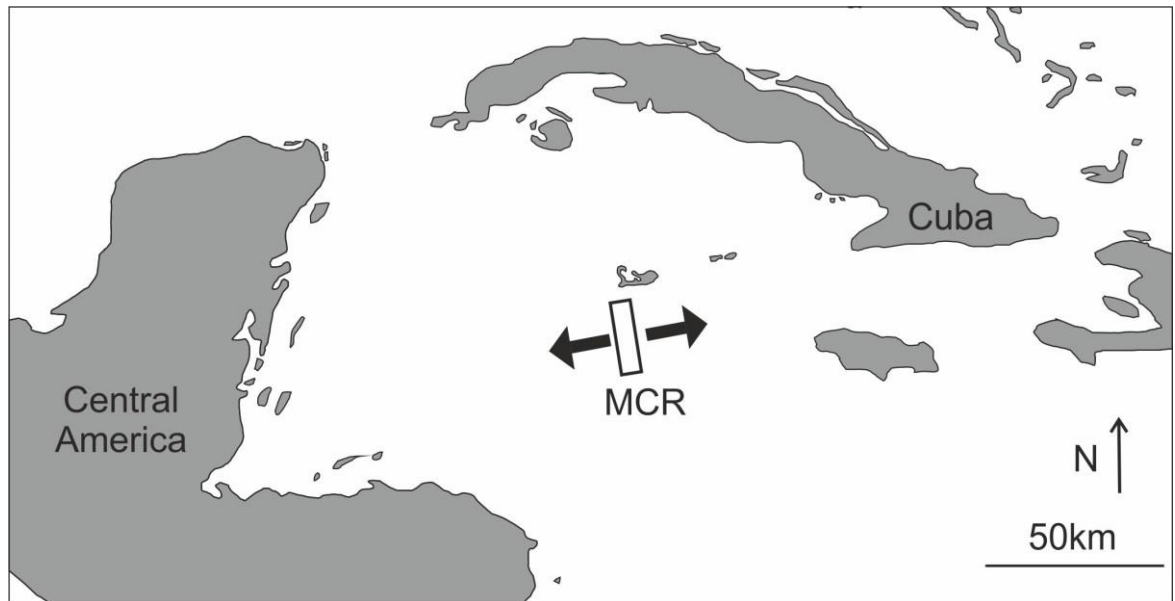


Figure 1.1: Map showing the location of the MCR

The BVF is situated at almost twice the depth of most seafloor hydrothermal systems. Hydrothermal fluids at this pressure have the potential to be transported as supercritical fluids up to shallow crustal levels, or even vented (Ryabchikov, 1981; Koschinsky et al., 2008). Given the enhanced capacity of supercritical fluids to mobilise base metals, hydrothermal systems such as the BVF could concentrate metals in proximity to the seafloor at higher grades than in conventional black smoker massive sulphides (Ryabchikov, 1981).

In contrast, the VDVF is hosted within a gabbro and peridotite basement forming an OCC, making it an ideal site to investigate the effects of basement lithology on vent fluid composition and mineralisation. OCC's are located at ridges with ultraslow to medium ($<75 \text{ mm yr}^{-1}$) spreading rates, and are associated with low magma flux (Harper, 1985; Tucholke et al., 1998). Deeply penetrating detachment faults at these settings provide pathways for hydrothermal fluids ascending from depth in the crust (McCaig et al., 2007). Of additional interest is the role OCC's play in the heat budget for slow spreading ridges and their potential to involve lower crustal and upper mantle lithologies in hydrothermal circulation and alteration (McCaig et al., 2007). The VDVF could be classed as a new type of hydrothermal system due to its unusual mineralogy, chemistry and geological setting. The active site comprises a series of three conical mounds, up to 80 m tall, made predominantly of talc: a magnesium silicate mineral ($\text{Mg}_3\text{Si}_4\text{O}_{10}(\text{OH})_2$). The importance of the VDVF is highlighted by its

unusual mineralogy, tectonic setting, and implications for off-axis heat flux and ocean water chemistry, thus it was chosen as the study site for this project.

1.3. Aims and objectives

To understand the processes of formation of the VDVF, and explore its wider implications, new data from two research cruises to the VDVF (*JC044* in 2010 and *JC082* in 2013) are examined in relation to the current state of knowledge of hydrothermal systems. Rock and fluid samples, recovered during the two surveys, are the subject of a variety of laboratory studies including mineralogy and geochemistry.

Previous sampling of the MCR during the 1970s and 1980s have been compiled with geophysical data from two *RRS James Cook* cruises, with the aim of producing geological/tectonic maps of the MCR, and the setting of the VDVF. These new data include ROV footage of the seafloor obtained from dives of the ROV's *HyBIS* and *Isis*, including an assessment of the degree of hydrothermal activity. From these, structural and geological maps have been compiled to identify active hydrothermal structures, areas of diffuse flow, host rock outcrop, hydrothermally active and inactive mounds, fault structures, pock marks and areas of pelagic sediment cover.

Petrology of the active chimneys, active and inactive mounds and host rock was determined using hand specimens, binocular microscopy, transmitted light microscopy, reflected light microscopy, scanning electron microscopy and X-Ray diffraction. X-Ray fluorescence, inductively coupled plasma mass spectrometry, inductively coupled plasma atomic emission spectroscopy and isotope ratio mass spectrometry were used to characterise the major and trace element geochemistry of the hydrothermal precipitates, in order to determine their conditions of formation.

An assessment and interpretation of end-member vent fluids is based on compositional data, and is used here to understand the processes controlling the mineralogy and geochemistry of the VDVF. These data are used with mineral stability diagrams derived from the fluid chemistry, and modelled in the thermodynamic-based modelling software 'Geochemist's Workbench' to explore talc stability at the conditions of hydrothermal venting at the VDVF.

Finally, the VDVF and similar hydrothermal systems are placed in the wider context in terms of their implications for global heat fluxes and geochemical budgets. The VDVF is also compared to known active and inactive hydrothermal vents fields, in terms of its hydrothermal fluids, mineralogy and setting.

1.4. Diversity of seafloor spreading: rift morphology and crustal generation

MOR form a network of spreading centres ~60,000 km in length that extends around the globe, and which is responsible for up to 80% of global volcanism (Parsons, 1981). Consequently, understanding the processes occurring at MOR is important due to their role in forming new crust and cooling of the Earth. MOR spreading rate greatly influences the morphology, crustal structure, tectonics, hydrothermal vent field distribution and lithologies exposed on the seafloor (Macdonald, 1982; Rona, 2010). In the following section, MOR morphology is divided into two sections, one describing ridges with fast to intermediate ($>60 \text{ mm yr}^{-1}$) spreading rates, and another describing ridges with intermediate to ultraslow spreading rates ($<60 \text{ mm yr}^{-1}$).

1.4.1. Fast-intermediate spreading mid-ocean ridges

Fast spreading MOR are characterised by smooth axial rises and ridge crests that are bathymetrically higher than the surrounding seafloor (Figure 1.2; Phipps Morgan et al., 1987; Perfit and Chadwick, 1998). Neovolcanic zones are generally <250 metres wide and reflect a process of focussing melt towards the central axis of the spreading centre. Occasionally, axial summit troughs or axial summit calderas, several tens of metres wide, form along the centre of volcanic axis and are thought to result from dykes rising from underlying axial magma chambers (Figure 1.2; Detrick et al., 1987; Collier and Sinha, 1990; Haymon et al., 1991). The high melt flux results in a symmetrical pattern of crustal accretion with small throw faults and lobate sheet flows generating smooth topography (Bonatti and Harrison, 1988; Perfit and Chadwick, 1998). On average the magmatic crust is usually 6-7 km thick and varies by $<10\%$ along entire ridges, provided they are free from the influence of mantle hot-spots (Figure 1.2; White et al., 1992). In contrast to slow spreading MOR, faulting in

close proximity to fast spreading ridge axes is characterised by low throw, short length and high density, indicative of shallow-rooted fault systems reflecting steeper geothermal gradients (Carbotte and Macdonald, 1990).

Two contrasting models for the development of the lower oceanic crust are proposed at ridges where melt supply is dominant. In one scenario, described as the “*Gabbro Glacier*” model, melt is supplied from the mantle into a shallow melt lens and crystal mush zone located in the upper crust (Phipps Morgan and Chen, 1993; Quick and Denlinger, 1993). Cumulative crystallisation, settling and subsidence of the floor of the magma chamber results in outward and downward flow of material through the bottom of the melt zone. This results in the creation of the lower crustal cumulate or plutonic section via relatively shallow level processes, and the slow accumulation of magmatic material beneath the ridge axis (Henstock et al., 1993; Quick and Denlinger, 1993). An alternative theory, described as the “*Sheeted Sill*” model, proposes that melt exists at varying levels in the middle and lower crust, and new crust is generated by both sills and dykes intruding parallel to the spreading direction, without the requirement for any downward subsidence of a ‘crystal mush’ (Kelemen et al., 1997; MacLeod and Yaouancq, 2000).

The two models have very different thermal implications: the Sheeted Sill model requires the extraction of heat from close to the spreading axis throughout the whole depth of the crust, and cooling rates in the lower crust of up to five times that of the Gabbro Glacier model (Coogan et al., 2002; VanTongeren et al., 2008). Estimates of cooling rates from the Oman ophiolite, based on crystal diffusion, give contrasting results depending on the different crustal section sampled. While one section indicates a rapid change in cooling rates in the upper crust, supporting the Gabbro Glacier model (Coogan et al., 2002; Coogan, 2007), the other section shows no significant change and supports the Sheeted Sill model (VanTongeren et al., 2008). It is possible that both processes may apply, depending on the location within a spreading segment. The geophysical evidence for both shallow melt lenses and deeper sills at the East Pacific Rise also indicates that a combination of both processes is likely, with mantle upwelling yielding melts to the crust with crystallisation and downward subsidence of crystal mush together with sill and dyke intrusion

throughout the lower crust (Boudier et al., 1996; Wanless and Shaw, 2012; Marjanovic et al., 2014).

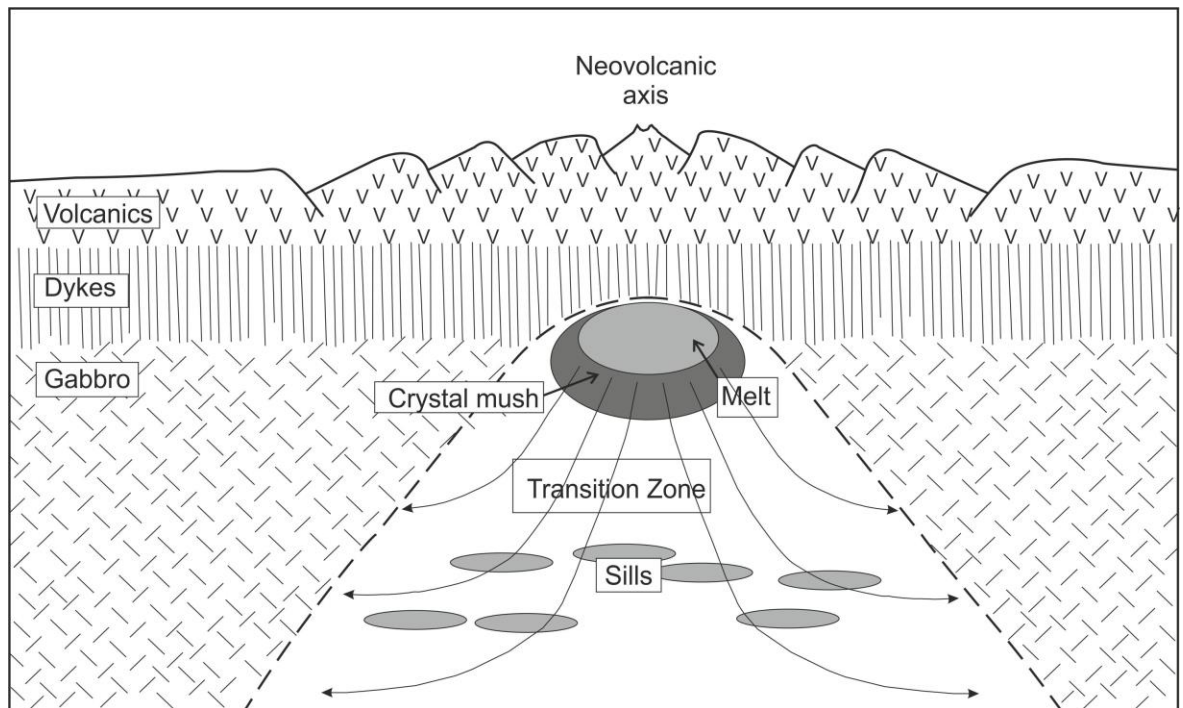


Figure 1.2: Characteristics of fast spreading ridges; the dashed line represents the brittle-ductile transition. The solid lines indicate the downward flow of crystal mush in a Gabbro Glacier model, along with sill intrusion into the lower crust (after: Detrick et al., 1987; Phipps Morgan et al., 1987; Collier and Sinha, 1990; Haymon et al., 1991; Quick and Denlinger, 1993; MacLeod and Yaouancq, 2000; Marjanovic et al., 2014)

1.4.2. Medium - ultraslow spreading mid-ocean ridges

Spreading centres classified as medium-ultraslow spreading make up approximately 80% of the total length of the global MOR (Murton and Rona, 2015). Tectonic spreading at slow spreading MOR develops a lithologically diverse seafloor with a rugged and undulating topography (White and Stroup, 1979; Murton et al., 1999; Murton and Rona 2015). Melt lenses appear to be less common here than at fast spreading ridges, resulting in deep rift axes and a fault-bounded axial valley.

Axial valley floors are dominated by pillow lavas and hummocky volcanic flows, and are up to 20 km across and several hundred metres deep (Phipps Morgan et al., 1987; Smith and Cann, 1993; Shaw and Lin, 1996; Dick et al., 2003). Volcanic activity is focused at axial volcanic ridges that range in dimension, but are usually 100 to 300 m

high, 10 to 30 km long and 2 to 5 km wide. Volcanic features are comprised of small hummocks, volcanoes and lavas, which rise above the floor of the axial valleys e.g. (Smith and Cann, 1993). Crustal thickness is far more variable at slow spreading ridges, with some ultraslow spreading ridges reported as having magmatic crust as thin as 2 km due to low melt fractions (Figure 1.3; White et al., 2001). Magmatic crustal accretion is focused at segment centres, meaning crustal thickness is highly variable along axis and thins substantially at the segment ends (Lin and Morgan, 1992; Cannat, 1996; Magde and Sparks, 1997; Gràcia and Escartin, 1999). Slow spreading MOR's are characteristically segmented by large transform faults, giving ridge axes that run orthogonal to the spreading direction (Vogt et al., 1979).

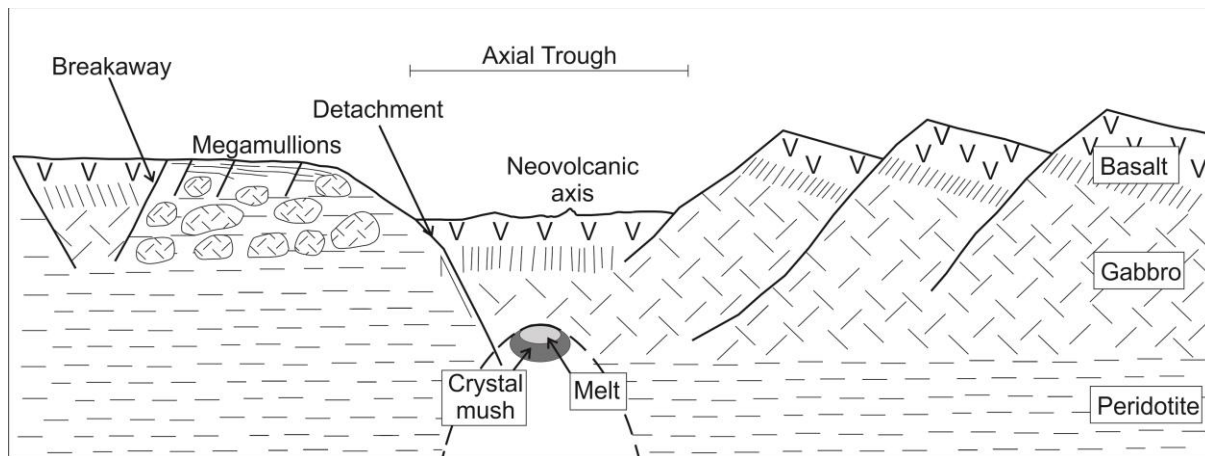


Figure 1.3: Characteristics of slow-spreading ridges. Displays the smaller, deep-seated magma chamber at the ridge axis, a deep axial valley, and the presence of asymmetrical spreading in the form of OCC's (White and Stroup, 1979; Cann et al., 1997; Tucholke et al., 1998; Blackman et al., 2002; Escartin et al., 2008; MacLeod et al., 2009)

At slow spreading rates, asymmetric, tectonically-dominated spreading is common (Figure 1.3; Vogt et al., 1979; Buck et al., 2005; Singh et al., 2006). In the late 1990s and early 2000s, corrugated megamullions on the flanks of the Mid-Atlantic Ridge were recognised (Cann et al., 1997; Blackman et al., 1998; Tucholke et al., 1998) and hypothesised to result from similar tectonic processes to low-angle detachments fault exposing terrestrial metamorphic complexes e.g. (Dewey, 1988). These OCC's are now known to occur at MOR with spreading rates of up to 75 mm yr^{-1} (Tucholke et al., 2008; Escartin, 2008), and expose upper mantle and lower crustal rocks at the seafloor e.g. (Eggler et al., 1973; Blackman et al., 2002).

OCC's intimate as steep normal faults along the ridge axis that shallow out by a combination of fault weakening, strain localisation, and seawater ingress to allow hydrothermal alteration of the lower crust and upper mantle (Cannat et al., 1992; Escartin et al., 2001; Boschi et al., 2006). Hydrothermal alteration of these lithologies produces minerals such as talc, tremolite and serpentine, which enables further slip along the same low-angle fault surface (Escartin et al., 2001). Although magmatism is reduced, it is not completely restricted at OCC's, as a small volume is required to power the hydrothermal circulation that alters the fault surface (Buck et al., 2005; Escartin et al., 2008). Tectonic displacement and extension thins the crust, which allows seawater ingress and alteration of the lower crust and serpentinisation of the upper mantle (Cann et al., 1997; Wilson et al., 2013). The formation of talc reduces fault-plane friction focusing strain on a single fault plane enhancing the formation of long-lived detachment faults. Slip along these OCC detachment faults is thought to be halted either by the injection of magma into the OCC footwall (MacLeod et al., 2009), by a complete drop in magmatic activity, or the cessation of asymmetric spreading (Buck et al., 2005; Tucholke et al., 2008).

1.5. Diversity of hydrothermal venting

Hydrothermal systems form at oceanic spreading centres when seawater percolates downward through faults and fractures in the oceanic crust. At high-temperature systems, the fluid is heated up to $\sim 400^{\circ}\text{C}$, while water-rock interactions reduces its pH, and leaches metals from the surrounding host rock (Bischoff and Pitzer, 1985; Alt, 1995; Von Damm, 1995). The resultant vent fluid is volatile rich and highly buoyant causing it to rapidly ascend where it vents at the seafloor (Alt, 1995).

MOR contain 65% of known hydrothermal systems, with the remainder located at back-arc ridges (22%) and at volcanic arcs (12%) (Beaulieu, 2010; Hannington et al., 2011). Host lithologies consist of sediments, volcanic, plutonic or mantle rocks (Alt et al., 1995; Tivey, 2007).

1.5.1. Common water-rock interactions in basalt hosted systems

While hydrothermal systems have common characteristics, there are significant variations in host rock, seawater depth, temperature and pressure that lead to changes in fluid chemistry and mineral deposit composition.

Seawater reacts with host lithologies during its path through the crust (Humphris and Thompson, 1978; Edmond et al., 1979b), which alters the composition of the circulating fluid and rock. Magnesium is quantitatively removed from seawater and sequestered into clays (at temperatures below 200°C) and into chlorite (at temperatures above 200°C), leading it to be a useful tracer in deriving end-member fluid compositions e.g. (Andrews, 1977; Humphris and Thompson, 1978; Von Damm 1995). Calcium levels increase in the fluid from the albitisation of plagioclase (Bischoff and Seyfried, 1978). As the fluid reaches the base of the reaction cell at around 2-3 km depth, base metals and sulphur are stripped out of the host due to the high temperatures and acidic pH (Seewald and Seyfried Jr, 1990). Volatiles such as ³He, CO₂, CH₄ and H₂ are also added to the fluid in various amounts, either from the magmatic source, or from fluid-rock interactions (Lupton et al., 1980; Alt, 1995). Physical conditions within the reaction zone mean that the fluid commonly crosses the two-phase boundary (Bischoff and Pitzer, 1985), and sometimes supercritical conditions are reached (Bischoff and Rosenbauer, 1988; Koschinsky et al., 2008). The resultant hot and buoyant hydrothermal fluid rises to the seafloor, where it forms stockwork feeder zones and alters the host rock below the active mound (Alt, 1995; Humphris et al., 1998). The hydrothermal fluids vent either in focused chimneys, or as diffuse flow areas distributed throughout a texturally and mineralogically zoned mound (Alt, 1995; Knott et al., 1998; Zierenberg et al., 1998).

1.5.2. Alteration of host rock

The high-temperature (up to 400°C) and low pH (2-4) of the hydrothermal fluid leads to alteration of the host rock in the stockwork zone below the seafloor. At shallow depths (<300m) and low temperatures (30-60°C), the main reactions that occur are the precipitation of Fe-oxyhydroxides on basalt rims, and the fixation of alkalis (Li, K, Rb, Cs and B; Andrews, 1977; Seyfried and Bischoff, 1979; Böhlke et al., 1980). Nontronite and saponite, along with other smectite clays, form on the rims of basaltic

pillow lavas, replacing glass and in fractures (Figure 1.4; Honnorez et al., 1983; Alt et al., 1992), with the Fe and Mg composition dependent on the degree of oxidation and water/rock ratios (Andrews, 1977). Goethite and hematite rims develop on sulphide and olivine crystals (Böhlke et al., 1981; Honnorez et al., 1983; Alt and Honnorez, 1984). Occasionally, potassium feldspar forms in the upper volcanics, and carbonate and zeolite form in diffuse, lower temperature, off-axis areas depending on the pH (Böhlke et al., 1980). Mg in the primary host rock is not increased in large concentrations as, at these temperatures, a majority of the magnesium that is removed from seawater precipitates as minerals forming veins and infilling pore spaces (Teagle et al., 1996).

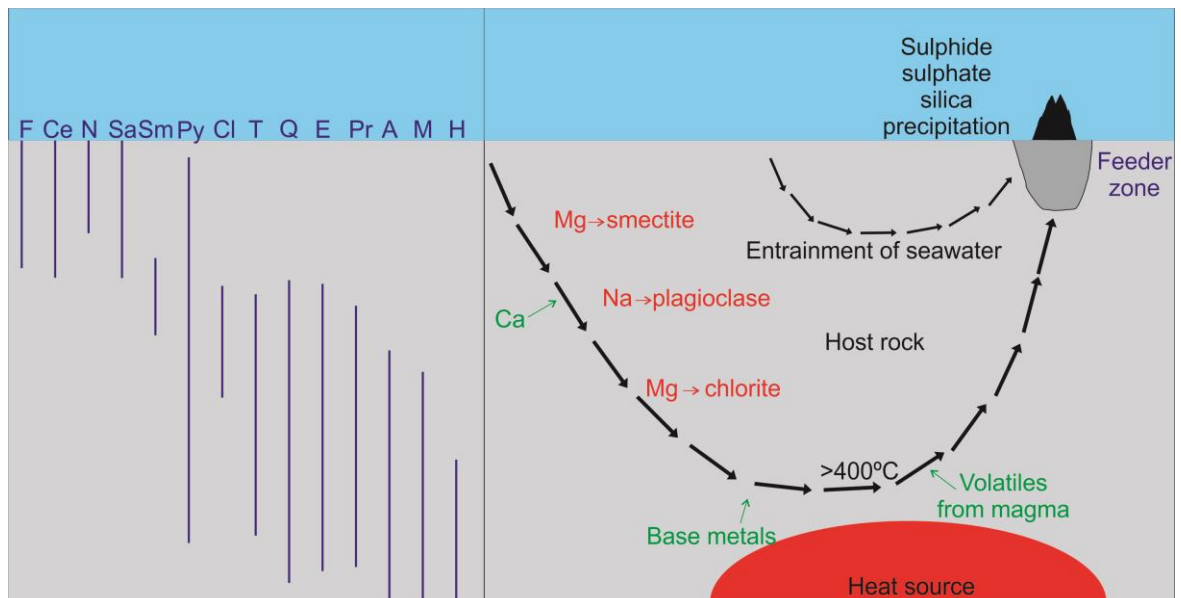


Figure 1.4: Schematic of a hydrothermal circulation cell. The left hand panel shows some of the common minerals and their relative depths of occurrence. Mineral abbreviations: A = actinolite; Ce = celadonite; Cl = chlorite; E = epidote; F = Fe-oxyhydroxides; H = hornblende; M = magnetite; N = Nontronite; Pr = prehnite; Py = pyrite; Q = quartz; Sa = saponite; Sm = smectite; T = talc. Right hand panel shows a schematic of a hydrothermal circulation cell (Wolery and Sleep, 1976; Andrews, 1977; Mottl and Holland, 1978; Lupton et al., 1980; Craig and Lupton, 1981; Anderson et al., 1982; Alt and Honnorez, 1984; Adamson, 1985; Alt, 1995; Humphris et al., 1995; Humphris et al., 1998; Knott et al., 1998; Alt et al., 2010).

At temperatures of up to 200°C, basaltic pillows are altered to saponite-smectite-chlorite, with rare quartz and pyrite, and calcite/saponite amygdals (Mottl and Holland, 1978; Alt et al., 1986). Albite and chlorite replacement of plagioclase begins

at the top of the sheeted dyke complex, commonly in the cores of phenocrysts, and olivine and clinopyroxene are replaced by chlorite, actinolite and other amphibole phases (Figure 1.4; Alt et al., 1986). Permeability exerts a strong control on the degree of fixation of Mg and alteration of the host rock. For example, olivine is commonly seen to alter to chlorite, but in areas of low permeability, the formation of secondary talc is prevalent (Alt, 1995). This is due to the lack of SiO₂ and Al from the alteration of primary igneous minerals in basalt, which means that simple hydration of olivine occurs instead (Alt, 1995).

As temperatures rise above 200°C, anorthite is altered to albite/oligoclase, quartz, prehnite and epidote following Si, Na and Al fixation, and pyroxene is converted to actinolite/chlorite (Humphris and Thompson, 1978; Teagle and Alt, 2004). As temperature increases to greenschist facies conditions, amphibole (hornblende ± actinolite) becomes dominant over chlorite in the replacement of pyroxene (Alt et al., 2010). Olivine is altered to chlorite, and then further to paragonite and quartz, with minor clays, pyrite and quartz (Figure 1.4; Alt et al., 1986; Honnorez et al., 1998).

1.5.3. Chimney formation

Variations in fluid composition mean that a wide range of minerals can be stable on mixing with seawater; however a number of sulphide and sulphate minerals are common in most hydrothermal deposits e.g. (Tivey, 2007). Anhydrite precipitates as high concentrations of calcium in the vent fluid mix and react rapidly with seawater-derived sulphate (Haymon, 1983). This reaction leads to the formation of a fragile, highly porous scaffold-like framework of anhydrite into which later stage minerals precipitate (Haymon, 1983). High temperature hydrothermal chimneys have slightly different mineralogies depending on the precise vent temperature and composition, but the mechanism of growth is similar (Turner and Campbell, 1987; Tivey, 1995; Gamo et al., 1997). Initially, few sulphides form but are instantly oxidised on exposure to seawater. As the volume and thickness of anhydrite walls increase, fine grained pyrrhotite and sphalerite begin to precipitate on the inner chimney walls (Haymon, 1983). Chimneys grow both parallel and perpendicular to the seafloor, with anhydrite steadily replaced from the inside out by sulphide (Haymon, 1983). If the vent fluids reach 350°C, copper sulphides start to precipitate on the innermost

chimney walls, forming a layer of massive, fine grained chalcopyrite, with bornite, cubanite and/or pyrrhotite (Haymon, 1983; Oudin and Constantinou, 1984). In the central section, chimneys can consist almost of entirely pyrite and sphalerite, with rare Cu-Fe sulphides; anhydrite that initially precipitated in this layer is completely replaced (Haymon, 1983). The outer layer contains sulphide, oxide, sulphate and silica, with anhydrite still providing the matrix into which later stage minerals precipitate; the amount of oxide/sulphate depends on the thickness of the chimney and the dissolved oxygen levels in seawater (Haymon, 1983; Berkenbosch et al., 2012).

1.5.4. Massive sulphide formation

At the onset of hydrothermal activity, colloform pyrite forms from diffuse flow at a temperature range of 250-300°C (Knott et al., 1998). Chimneys grow as fluid is channelled into pore space and eventually become unstable and collapse onto the seafloor, contributing to the observed brecciated texture (Lydon, 1989; Knott et al., 1998). This brecciated chimney rubble eventually coalesces to form a steep-sided sulphide mound or seafloor massive sulphide deposit (Figure 1.5). As temperatures rise above 300°C, the sulphide rubble apron on the seafloor develops further from repeated growth and collapse of chimneys, giving rise to a permeable mass into which secondary iron and copper sulphides precipitate (Lydon, 1989). Copper bearing phases such as chalcopyrite and bornite replace original, lower temperature sulphides such as sphalerite and pyrite (Ohmoto, 1996). At periods of rapid/hotter fluid flux, pyrite, sphalerite and chalcopyrite grow into open pore space towards the surface of the hydrothermal mound at temperatures around 350°C (Knott et al., 1998). Previous chimney material is extensively reworked in the centre of the mound, destroying primary colloform and botryoidal textures (Knott et al., 1998). Copper and zinc sulphides are oxidised rapidly after chimney collapse, with the centre of the mound forming a brecciated pyrite lens with varying levels of anhydrite and quartz (Knott et al., 1998). Mixing of dissolved Ca^{2+} cations in the vent fluid with SO_4^{2-} derived from circulating seawater precipitates anhydrite at temperatures above 150°C in the central part of hydrothermal mounds (Knott et al., 1998; Teagle et al., 1998a). Continued precipitation and dissolution of sulphate by fluctuating temperature conditions displaces massive sulphide and causes internal expansion

and fracturing towards the outer margins of the mound (Humphris et al., 1995; Knott et al., 1998).

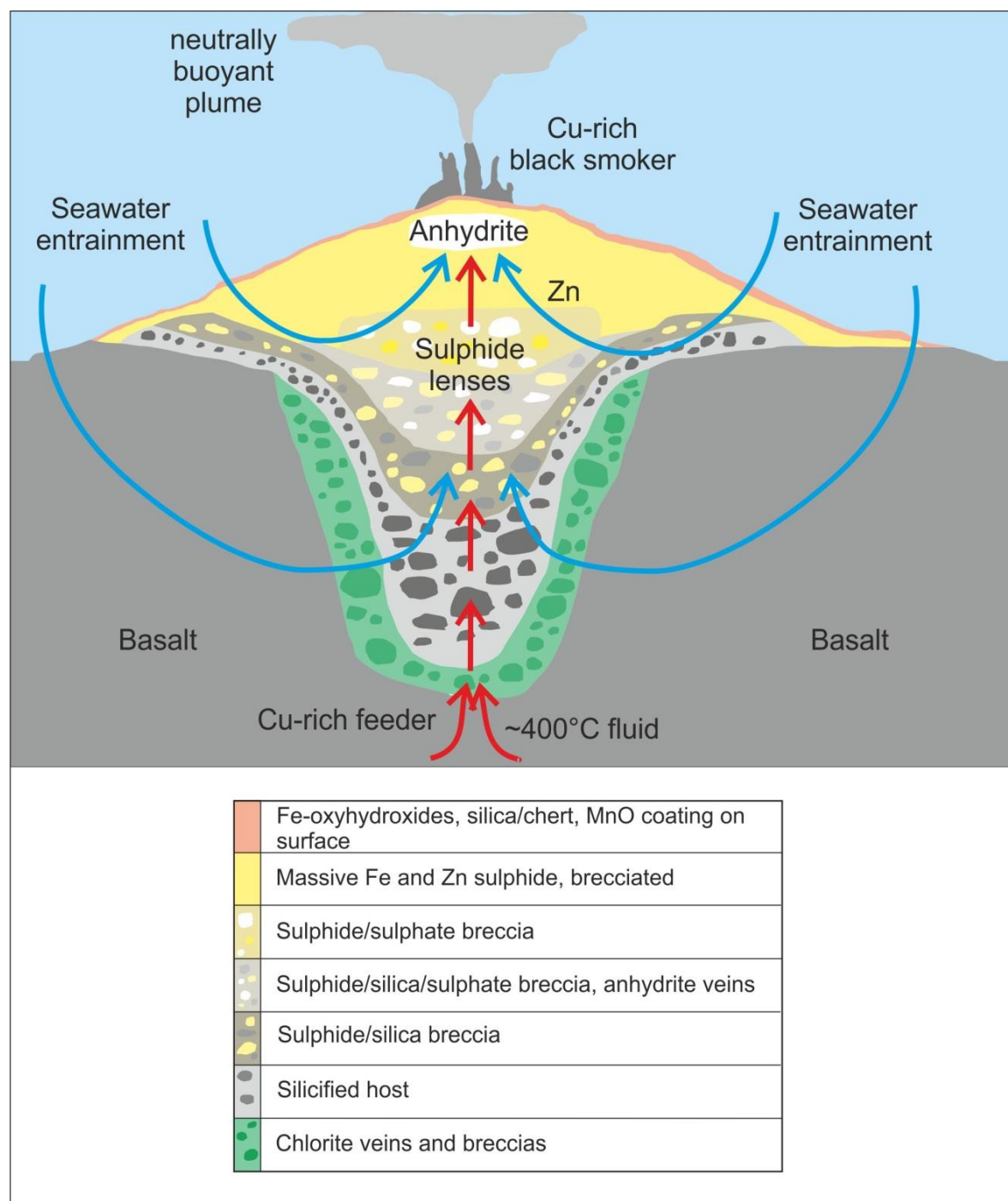


Figure 1.5: Schematic of a hydrothermal vent system. The key at the bottom indicates the stratigraphy through a large, basalt hosted hydrothermal mound (Humphris et al., 1995; Knott et al., 1998; You and Bickle, 1998; Zierenberg et al., 1998; Tivey, 2007)

1.5.5. Variations with host rock

Although the majority of known hydrothermal vent fields are hosted in basalt, slight changes occur due to differences in host rock mineralogy and sediment thickness e.g. (Alt, 1995). For example, typically, lower (<2.5) pH fluids are generated in dacite hosted systems such as the PACMANUS field, due to volatile addition of HF, SO₂ and HCl from more silicic magmas (Fouquet et al., 1991). The increased acidity of the fluids aids the addition of metals such as Ag, As, Cu, Zn, Pb, Ba, Mn and Si (Table 1.1) that generally occur at higher concentrations than in basalt hosted systems (Fouquet et al., 1993; Gamo et al., 1997).

Magmatically-driven, ultramafic-hosted systems (Figure 1.6) differ in their volatile content from basalt-hosted systems, as the oxidation of Fe²⁺ to Fe³⁺ produces higher concentrations of CH₄ and H₂ (Janecky and Seyfried Jr, 1986; Berndt et al., 1996; Wetzell and Shock, 2000), but lower concentrations of H₂S (Charlou et al., 2002). REE, Cu, Fe, Mn and Pb concentrations are also elevated (Table 1.1) as the lower pH, formed by the hydration of orthopyroxene (Reactions 1-3), leads to greater stability of REE-chloride and metal-chloride complexes (Charlou et al., 2002; Douville et al., 2002; Schmidt et al., 2007).

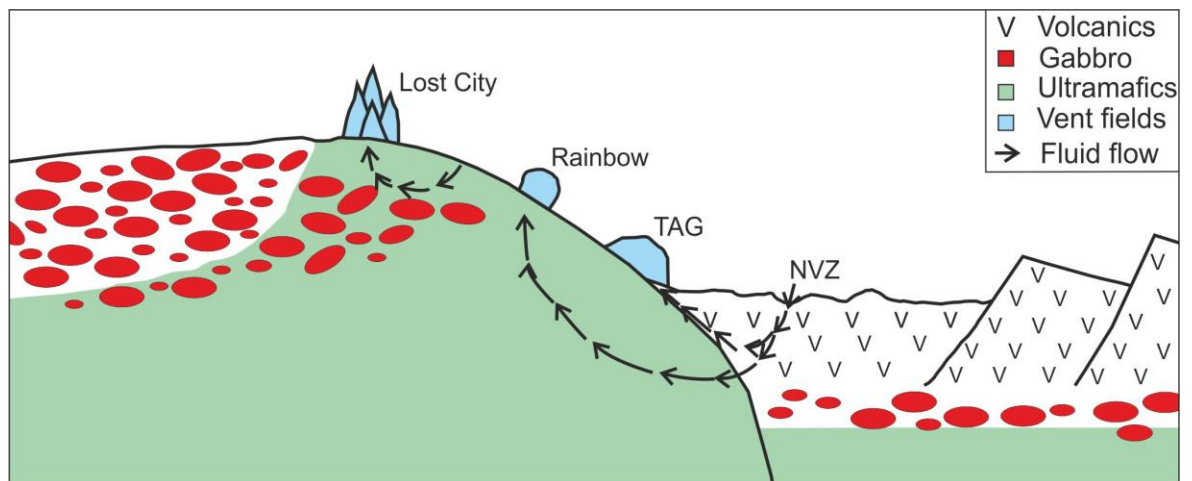


Figure 1.6: Schematic of an oceanic core complex showing the tectonic setting of selected hydrothermal systems on the MAR (Blackman et al., 1998; McCaig et al., 2007; McCaig et al., 2010)

Vent Field	TAG	9-21°N	Broken Spur	Guaymas Basin	Escanaba	Rainbow	Logatchev	Lost City	PACMANUS	Vai Lili
Ridge name	MAR	EPR	MAR	Gulf of California	Gorda Ridge	MAR	MAR	MAR	Manus basin	Lau
Setting	MOR	MOR	MOR	MOR	MOR	MOR	MOR	MOR	back-arc	back-arc
Host	B	B	B	S	S	UM	UM	UM	D/R	BA/RD
T (°C)	290-369	273-405	356-364	264-315	108-218	362-365	350-353	40-91	241-358	334
pH at 25°C	3-3.8	2.6-5.1	n.d.	5.9	5.4	2.7-3.1	3.3-3.9	9-9.8	2.3-2.7	2
Cl mmol	636-659	41.6-760	469	580-637	632-668	745-756	515-551	541-549	414-731	650-800
Si mmol	21-22	3.7-21.9	n.d.	12-13.8	5.6-5.9	6.4-7.1	8.2-8.6	0.02-0.07	12.2-23.9	14
Ca mmol	26-31	2.1-54.8	11.8-12.8	27.7-41.5	32-33.4	66.6	28-29	21.0-27.4	3.59-27.1	28-41
Na mmol	549-584	242-449	419-422	472-513	536-560	553	438-455	479-494	326-541	520-615
K mmol	16.6-20	1.56-25	18.1-19.6	40.1-49.2	33.2-40.4	20.2-20.4	22-24	10.5	52.4-96.8	55-80
Fe mmol	1.64-5.59	0.687-12.5	1.68-2.16	0.008-1.8	0.01-0.06	23.6-25.0	2.4-2.5	<0.01	1.22-14.6	1.2-2.9
Mn mmol	0.67-1.0	0.07-2.93	0.25-0.26	0.13-0.24	0.01-31.1	2.2-2.35	0.33-0.34	n.d.	2.39-4.71	5.8-7.1
Ba µmol	19	0.27-95	12.9-21.3	15-54	4.4	59-79	n.d.	n.d.	16-92	20-60
Li µmol	360-410	27-920	100-104	720-1076	1110-1286	327-345	245-252	43-46	627-1320	580-745
Zn µmol	36-46	75-121	41-88	0.1-40	11	115-185	29-36	n.d.	115-231	1200-3100
Cu µmol	83-150	45-162	28.3-68.6	0.02-1.1	3.2	121-162	27-44	n.d.	35.6-39.1	15-35
Sr µmol	99-103	8-387	43-48	158-226	192-209	200	127-138	88-105	7-176	105-135
Rb µmol	9.1-9.4	26-33	13-13.6	56-85	80-105	36.7-37.1	27-28	2.8	51.6-94.5	60-75
B µmol	297-416	429-465	468-473	1570-1370	1710-2160	n.d.	335	n.d.	1-2	770-870
Cd nmol	66	17-180	75-102	0-46	115	105-178	32-63	n.d.	n.d.	700-1500
Mo nmol	5	n.d.	n.d.	n.d.	n.d.	1.3-3.2	1-4	n.d.	n.d.	n.d.
Ag nmol	51	24-26	n.d.	0-230	n.d.	46-49	11-17	n.d.	n.d.	n.d.
As nmol	n.d.	30-452	n.d.	283-1074	n.d.	n.d.	n.d.	n.d.	n.d.	6000-11000
Pb nmol	110	9-359	221-376	20-652	1560	135-169	86-138	n.d.	7027-7082	3800-7000
CH ₄ mmol	0.15	0.06-0.09	0.06	12.2-16.7	1.9-16.5	2.5	3.5	1.03-1.98	14-51	3.6-4.5
H ₂ S mmol	2.5-3.5	2.9-26	9.3	3.95-6.00	1.1-5.98	1.2	2.5	0.06	2.8-20.8	1.3-13.1
H ₂ mmol	0.15-0.37	0.23-1.7	0.43	n.d.	0.03	16	19	0.25-10.8	8.4-127	0.035-0.5

Table 1.1: End-member vent fluid concentrations from a range of hydrothermal vent fields. Abbreviations for host lithologies: B=basalt, S=sediment, UM=ultramafic, D=dacite, R=rhyolite, BA=basaltic andesite, RD=rhyolitic dacite (Edmond, 1981; Edmond et al., 1982; Lilley et al., 1983; Von Damm et al., 1985; Spivack and Edmond, 1987; Welhan and Lupton, 1987; Bowers et al., 1988; Campbell et al., 1988a; Campbell

et al., 1988b; Welhan, 1988; Von Damm, 1990; Charlou et al., 1991; Fouquet et al., 1991; Chan et al., 1993; Charlou and Donval, 1993; Campbell et al., 1994; Edmond et al., 1995; Ishibashi and Urabe, 1995; James et al., 1995; Charlou et al., 1996; Edmonds et al., 1996; Gamo et al., 1996; James and Elderfield, 1996; Douville et al., 1999; James et al., 1999; Kelley et al., 2001; Charlou et al., 2002; Douville et al., 2002; Ishibashi et al., 2002; Von Damm et al., 2003; Von Damm, 2004; Von Damm et al., 2005; Ludwig et al., 2006; Proskurowski et al., 2006; Schmidt et al., 2007; Craddock et al., 2010; Reeves et al., 2011; McDermott, 2015; Seyfried Jr et al., 2015).

1.5.6. Longevity of hydrothermal venting

The longevity of active venting at hydrothermal systems is highly dependent on the spreading rate e.g. (Hannington et al., 2005). The methods used to indicate the history of activity at hydrothermal systems include $^{238}\text{U}/^{230}\text{Th}$ dating (Lalou et al., 1998), energy balances between heat outputs and magma cooling (James and Elderfield, 1996; Humphris and Cann, 2000), ^{210}Pb dating (Kadko et al., 1985) and $^{228}\text{Th}/^{228}\text{Ra}$ dating (Stakes and Moore, 1991).

At faster spreading ridges, radiometric dating of sulphides indicate that sustained venting only occurs, at most, for periods of a few 10s of years in the same location (Koski et al., 1994a). Comparatively smaller sulphide mounds and closer spacing between individual fields reflects semi- continuous magma lenses along the ridge axes that in turn is consistent with a higher magma supply rate at these ridges (Stakes and Moore, 1991; Koski et al., 1994a; Baker and German, 2004).

At slower spreading ridges, venting is thought to remain in the same location for longer, building larger sulphide deposits, but is far more episodic. Estimates for the length of time it would take to form the amount of anhydrite in the TAG mound range between 200 and 2000 years (James and Elderfield, 1996; Mills et al., 1998). Radiometric dating of sulphides indicates high temperature activity was likely to have commenced at approximately ~ 50 ka, with pulses at 20 ka and then every 2-5 ka years until the present day (Lalou et al., 1995; Lalou et al., 1998, You and Bickle, 1998). The discrepancy in ages exists as continued anhydrite precipitation over short periods of time is thought to be followed by brecciation and dissolution during long

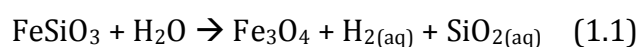
hiatuses in hydrothermal activity (Honnorez et al., 1998; Knott et al., 1998).. This indicates that mound formation occurs in pulses of high temperature activity at the same site, but not continuously (Lalou et al., 1998; Mills et al., 1998).

Similar timescales are recorded for vents at the Middle Valley hydrothermal sites, located at the northern end of the intermediate-spreading Juan de Fuca Ridge, the magma supply is thought to be very low at the northern-most end of the ridge segment (Davis and Villinger, 1992). Here, hydrothermal activity commenced at 125 ka, and the strong structural controls imposed by the basement are as important in fixing the location of the vent field as is the magmatic heat source (Davis and Villinger, 1992).

1.5.7. Serpentinisation at slow-spreading ridges

Hydrothermal alteration of peridotites is an important process at slow and ultraslow spreading ridges where the upper mantle is exposed at the seafloor by tectonic extension (Christie et al., 1998; Tucholke et al., 1998; Escartin et al., 2008).

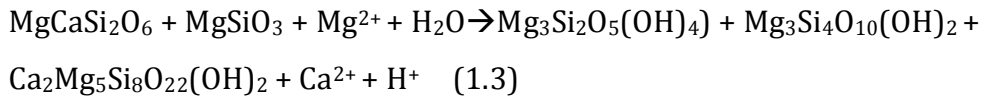
Serpentinisation leads to changes in the rheology, mineralogy, seismic structure and magnetic susceptibility of the oceanic crust (Barnes et al., 1967; Miyashiro et al., 1969; de Wit and Stern, 1976; Escartin et al., 2001; Seyfried Jr et al., 2007). The alteration of peridotite is a multi-stage process, and the resulting mineral assemblage is a function of pH, temperature, pressure, oxidation state of Fe and the activity of aqueous H₂ and SiO₂ (Bach et al., 2004; Bach et al., 2006; Seyfried Jr et al., 2007; Klein and Bach, 2009). The most important of these mineralogical changes are the alteration of olivine and pyroxene to serpentine, brucite and magnetite (Miyashiro et al., 1969). The potential range in mineral chemistry of protoliths results in a large range of possible geochemical interactions; the main and most common ones are shown below (reactions 1.1-1.7; Bach et al., 2004; Bach et al., 2006; Douville et al., 2002).



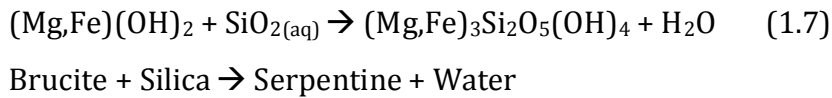
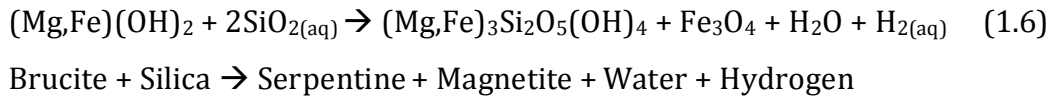
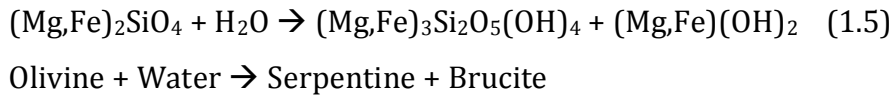
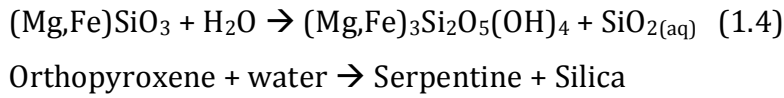
Orthopyroxene (Fe-rich) + Water → Magnetite + Hydrogen + Silica



Enstatite + Water + Magnesium → Serpentine + Hydrogen



Diopside + Enstatite + Magnesium + Water → Serpentine + Talc + Tremolite + Calcium + Hydrogen



1.6. Heat and chemical fluxes from mid-ocean ridges

Of the ~60,000km of global MOR length, less than one third has been explored using conductivity, temperature, depth (CTD) profiles to search for active hydrothermal vent fields (Beaulieu et al., 2012). To date there are currently >300 known active vent fields (Figure 1.7). Hydrothermal inputs contribute approximately one-third of the heat loss from the oceanic crust, and are of considerable significance in oceanic geochemical cycles (Elderfield and Shultz, 1996).

Generally, the relationship between hydrothermal plume incidence (a proxy for the spatial frequency of hydrothermal activity) and MOR spreading rate shows a proportional increase (Baker and German, 2004; Beaulieu et al., 2012). However, the occurrence of detachment faulting at MOR with slow to medium spreading rates perturbs this trend, especially in terms of inferred magma budget (McCaig et al., 2007).

1.6.1. Calculation of heat fluxes from individual vent fields

Two different methods are used to calculate the heat flux from individual hydrothermal vent fields. Point source measurements are based on individual areas of focussed flow, whereas integrated measurements sample neutrally buoyant plumes to determine their physical and chemical characteristics (Baker, 2007). Uncertainties associated with calculated heat flux means that out of the >300 high temperature vent fields known, less than 30 have an existing heat flux, and in some cases, the errors are equal to the calculated value (German et al., 2010b). Generally, point-source measurements underestimate the flux as they discount diffuse flow, whereas plume models make the assumptions that heat flux is directly proportional to the source of the end-member fluid (McDougall, 1990). The associated errors and minimal sample set leads to large errors and ranges in estimates of the total hydrothermal heat flux from the oceanic crust (Baker, 2007). For example, when considering direct measurement from active sites, the estimates from the same vent field can vary by factors of >10 (Elderfield and Shultz, 1996; James and Elderfield, 1996; Goto et al., 2003).

The spacing of vent fields at slow-spreading ridges is approximately one site per 100 km, but at faster spreading ridges this value is more difficult to quantify (Baker and German, 2004). This is because the boundaries of individual vent fields on fast spreading ridges are not well constrained (Baker, 2007). An alternative mechanism is calculating the heat flux per unit area of ridge based on magma replenishment rates, as opposed to deriving a value per vent field (Lowell et al., 2013). However, this still involves the quantification of parameters such as individual vent field heat output and magma chamber volumes, which are difficult to quantify accurately (Lowell et al., 2013). Heat/energy fluxes can also be calculated as a function of the hydrothermal fluid volume flux, and the difference in elemental concentration between the end-member fluid and seawater. Energy balances of base metals indicate the activity that forms the mounds at hydrothermal systems is episodic (Humphris and Cann, 2000). Hydrothermal activity generally occurs over a period of 100s-1000s of years, and is then followed 1000s-10,000s years of inactivity (James and Elderfield, 1996; Humphris and Cann, 2000).

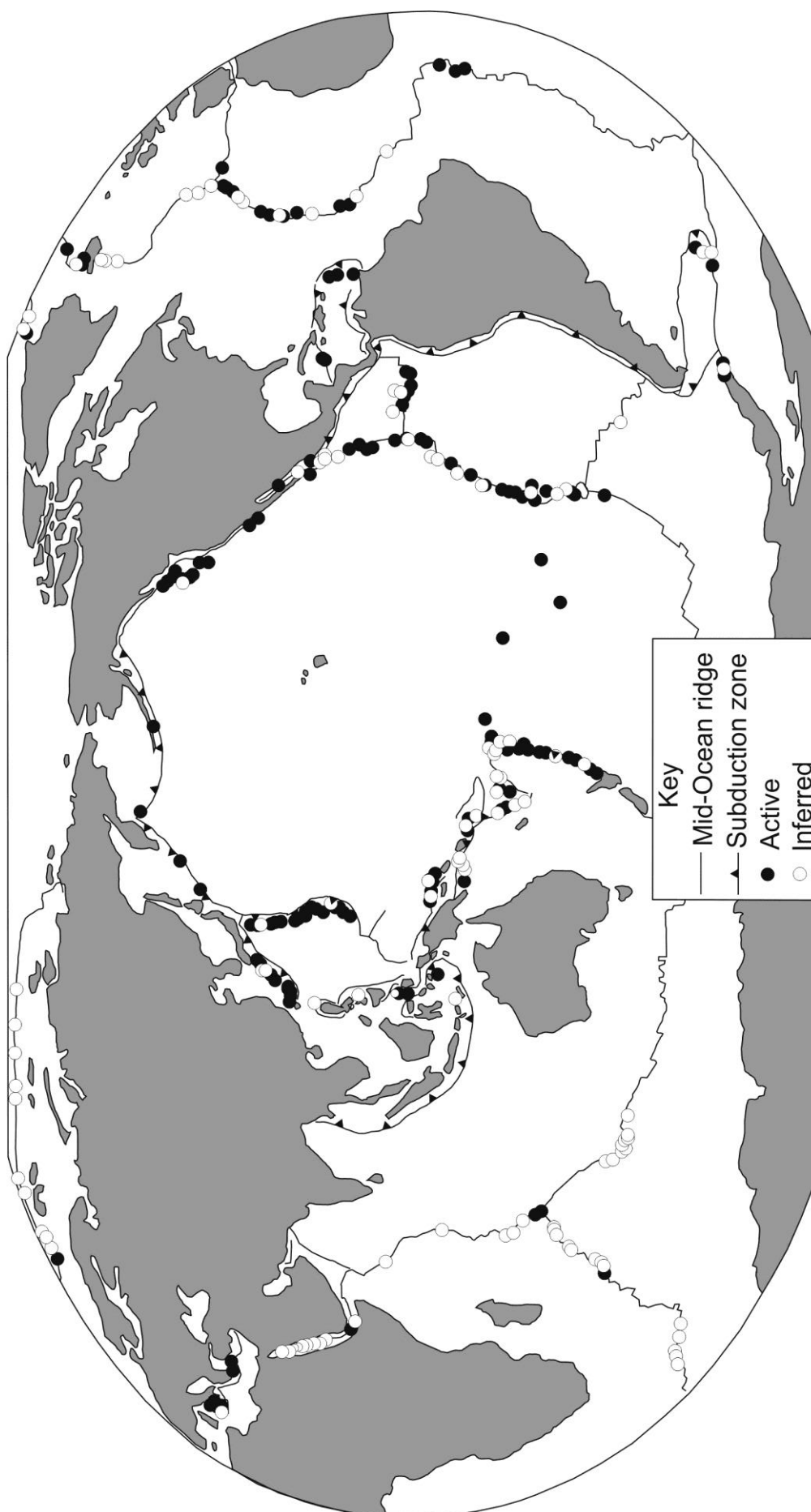


Figure 1.7: Location of global hydrothermal vent fields

1.6.2. Global heat and chemical fluxes

The total heat lost from oceanic crust generated by seafloor spreading ridges is calculated to be ~ 32 TW, which is almost 75% of the total for the Earth (Pollack et al., 1993; Kadko et al., 1994). One of the reasons why accurately calculating the global fluid flux is considered to be important is that hydrothermal circulation is far more efficient at removing heat from the oceanic crust than conduction. Furthermore, the chemical interaction between seawater and ocean crust has a major effect on the global cycling of elements such as magnesium, strontium and calcium (Phipps Morgan and Chen, 1993; Elderfield and Shultz, 1996). Various geochemical and geophysical traces have been used to estimate the global heat lost from oceanic crust and the proportion contributed by hydrothermal heat loss (Elderfield and Shultz, 1996; Mottl, 2003). This section features a comparison of the main ways, and a summary of the uncertainties associated with each method.

1.6.3. Geophysical methods

A majority of the heat lost at MOR axes is dissipated by convective hydrothermal circulation (Mottl, 2003). Of this heat, the majority is derived from a combination of latent heat of crystallisation and the specific heat of magma as it cools from $\sim 1250^{\circ}\text{C}$ (Kadko et al., 1995). The estimate for the global MOR axial heat flux in crust < 0.1 Ma is 1.5-2.1 TW (Mottl, 2003). These calculations included weighting the result for the length of slow spreading ridges compared to fast spreading ridges. This weighting is applied because the shallower melt lenses present at fast spreading ridges constrain hydrothermal circulation to shallower depths in the crust than at slower spreading ridges (Mottl, 2003).

Another geophysical method includes calculating a global heat flow anomaly by estimating the total heat flux from the oceanic crust. This is done by fitting a conductive heat flow function to the results of depth and heat flow measurements at different ages of ocean floor (Stein and Stein, 1994; Stein et al., 1995). The convective hydrothermal component of heat loss is then calculated by subtracting the observed heat flow from the predicted model (Stein and Stein, 1994). In this way, 7 to 11 TW of the total oceanic heat is thought to be dissipated by hydrothermal heat loss, with

~30% of this occurring in crust younger than 1 Ma. Although previous estimates overestimated the global 'missing heat' (Stein and Stein, 1994) more recent models give a near axial (0-1 Ma crust) hydrothermal flux of 2.4-3.2 TW (Mottl, 2003), resulting in a hydrothermal heat flux of ~50 MW per km of ridge length.

The subsequent calculation of the water flux is a function of the temperature difference, the heat capacity of seawater (influenced by salinity, temperature and pressure) and the estimated hydrothermal heat flux (Bischoff and Rosenbauer, 1984; Bischoff and Rosenbauer, 1985). Depending on the balance between diffuse and high-temperature flow, water fluxes for the axial component can vary between $3\text{--}6 \times 10^{13} \text{ kg yr}^{-1}$ (assumes all heat loss is via 350°C vent fluid) or up to $560 \times 10^{13} \text{ kg yr}^{-1}$ (assuming 90% diffuse flow; Elderfield and Shultz, 1996; James and Elderfield, 1996; Murton et al., 1999).

1.6.4. Geochemical methods

The hydrothermal heat flux can also be estimated by assuming a steady state mass-balance in the oceanic strontium cycle (Palmer and Edmond, 1989). This method is a useful tracer as the inputs, (rivers, benthic fluxes and hydrothermal circulation) are thought to be reasonably well constrained in terms of isotopic ratio and, for some, in mass flux (Palmer and Edmond, 1989). End-member strontium concentrations in hydrothermal fluids range between 40-400 $\mu\text{mol kg}^{-1}$, but are broadly similar to the seawater concentration, and have $^{87}\text{Sr}/^{86}\text{Sr}$ ratios close to that of mid-ocean ridge basalt 'MORB' (Sun et al., 1979; Von Damm, 1995). Balancing the ratio between river input and high temperature hydrothermal flux requires $>10^{14} \text{ kg yr}^{-1}$ of hydrothermal fluid, however isotope ratios in ophiolites and drill cores suggest that the actual figure is $0.5\text{--}3 \times 10^{13} \text{ kg yr}^{-1}$ (Davis et al., 2003). This either suggests a significant contribution of off-axis, low temperature flow, or discrepancy existing from errors in the inputs (Butterfield et al., 2001). This may be due to variations in the degree of weathering and uplift of marine carbonates and pelagic diagenesis, and temporal variability in the strontium isotope ratio from continental runoff (Vance et al., 2009). Also, although the river input is the best estimate to date, it is difficult to accurately constrain river catchment areas and fluxes from those in inaccessible areas (Palmer and Edmond, 1989).

Excess primordial ^3He from hydrothermal plume sources can be used to estimate the heat flux as hydrothermal plumes have $^3\text{He}/^4\text{He}$ ratios up to an order of magnitude greater than the atmosphere (Lupton et al., 1980). The ^3He /heat ratio can be calculated using the global flux of ^3He to the oceans ($540\text{-}1080\text{ mol yr}^{-1}$) and the geophysical estimate for the global oceanic crust production (Lupton et al., 1980). The estimate is simplified as there is no detectable ^3He anomaly at the ridge flank, meaning all of the excess ^3He is produced from high temperature venting, giving a water flux equivalent of $0.9\text{-}5.4 \times 10^{13}\text{ kg yr}^{-1}$ (Lupton et al., 1989). This large range is due to the variable ^3He /heat ratios in plumes following outgassing of fresh lava, difficulties in getting ratios from sediment hosted systems, and the spatial variability of $^3\text{He}/^4\text{He}$ ratios (Lupton et al., 1989; Elderfield and Shultz, 1996). Theoretical calculations, based on the $^3\text{He}/^4\text{He}$ ratio of the mantle and the assumption that all ^4He is derived from a radiogenic source, give an axial water flux of $0.9 \times 10^{13}\text{ kg yr}^{-1}$ (Lupton et al., 1989). The lower bound of the practical estimate and the theoretical estimate from ^3He correlate well to the axial estimates from geophysical methods (Elderfield and Shultz, 1996; Mottl, 2003).

The oceanic magnesium budget was originally thought to be a useful tracer due to its behaviour in hydrothermal solutions and seawater. This is because, Mg is completely removed from seawater during high-temperature hydrothermal circulation, vent fluids show conservative mixing with seawater, and Mg is has well constrained sources and sinks including biogenic carbonates, clays and basalt alteration (Drever, 1974). As a result, the remaining difference (equivalent to $4.4\text{-}4.8 \times 10^{12}\text{ mol yr}^{-1}$) is thought to be a result of sequestration by MOR axial hydrothermal fluids (Drever, 1974; Elderfield and Shultz, 1996). This gives an axial water flux of $8\text{-}9 \times 10^{13}\text{ kg yr}^{-1}$, assuming a steady state for magnesium concentrations in seawater (53 mmol kg^{-1}) and axial hydrothermal circulation as the main sink. As magnesium is sequestered into the oceanic crust at low temperature ($<45^\circ\text{C}$), complete fixation can occur with very low associated heat flux (Mottl and Wheat, 1994). This leads to great uncertainty with using magnesium, due to the lack of an accurate ridge flank flux estimate (Elderfield and Shultz, 1996).

Another estimate of global hydrothermal circulation is derived from the lithium cycle. The inputs into the global lithium cycle are: continental runoff, pore waters and

hydrothermal vents, whilst low temperature alteration and marine sediments are the main sinks (Chan et al., 1993). Lithium is enriched in hydrothermal fluids compared to seawater, but behaves differently in water/rock reactions at differing temperatures (Seyfried et al., 1984). At higher temperatures ($>250^{\circ}\text{C}$), lithium is stripped from the host rock and enriched in the fluid, but at temperatures of $<150^{\circ}\text{C}$, Li is sequestered into the crust (Seyfried et al., 1984). Profiles through the oceanic crust enable a more quantitative method of estimating the Li budget, and the degree of removal from seawater into the crust from low temperature alteration (Chan et al., 2002). An estimate for the global flux of lithium into the oceans gives a high temperature water flux of $0.4\text{-}3.6 \times 10^{13} \text{ kg yr}^{-1}$ (Chan et al., 2002). The heat flux is in agreement with axial estimates from geophysical methods, but the fluid flux is below the accepted value, indicating some diffuse flow from the ridge flanks (Chan et al., 2002).

1.6.5. Uncertainties in calculating global fluxes

A summary of the estimates of fluid and heat fluxes are shown in Tables 1.2 and 1.3. The main cause of error in geochemical studies is the uncertainty of the true depth of hydrothermal circulation at the ridge axis and flanks (Gillis, 1995). This is crucial in determining whether all of the magmatic heat at the ridge axis is accessible to high temperature circulation. The presence of melt lenses at fast spreading ridges e.g. (Detrick et al., 1987) suggests hydrothermal circulation will not penetrate much deeper than $\sim 1.5 \text{ km}$. Slower spreading MOR's have rare melt lenses, and only within segment centres (Singh et al., 2006). The absence of a steady-state melt lens at slow spreading MOR's means that the potential depth of hydrothermal circulation is unconstrained. Further sources of uncertainty are the amount of heat removed by conduction across the brittle-ductile transition zone, and whether there is a significant degree of intermediate temperature hydrothermal circulation (Chen and Phipps Morgan, 1996; Teagle et al., 1998b).

Furthermore, many estimates were made prior to the discovery of off-axis hydrothermal fields (e.g. Lost City), and before the emergence discovery of OCC's as potentially significant pathways for hydrothermal circulation (McCaig et al., 2007). Also, mass balance models based on elemental concentrations and isotopic characteristics of rocks recovered in drill cores have to consider that core recovery at

these sites can be <30% e.g. (Bach et al., 2003). This loss of recovery is potentially important as the majority of alteration (e.g. Mg, Li sequestration) that affects the upper crust occurs in veins and fractures, phases that are the most likely to not be recovered during drilling. The location of study sites affects mass balance calculations as mineral assemblages are also a function of the age of the crust (Staudigel and Hart, 1985; Nielsen et al., 2006).

Type	Axial flux	Flanks flux	Water flux (high T)	Water flux (low T)
	10^{12} W	10^{12} W	10^{13} Kg	10^{13} Kg
Axial heat	1.5-2.1	-	3-6	280-560
Heat flow	2.1-3.1	5.0-7.4	1.5-4.5	370-1100
Hydrothermal models	1-5.5	-	-	-

Table 1.2: Summary of heat fluxes based on various geophysical methods (Kadko et al., 1994; Stein and Stein, 1994; Elderfield and Shultz, 1996; Butterfield et al., 2001; Mottl, 2003).

		Strontium	$^3\text{He}/\text{heat}$	Mg	Li	Tl
Heat flux	10^{12} W	10	1-18	9-10	2	0.08-1.42
Water flux (high T)	10^{13} Kg	15	1-15	8-9	0.4-2.6	0.17-2.93

Table 1.3: Summary of heat and chemical fluxes based on geochemical methods (Lupton et al., 1989; Palmer and Edmond, 1989; Chan et al., 1992; Chan et al., 1993; Elderfield and Shultz, 1996; Teagle et al., 1998; Chan et al., 2002; Davis et al., 2003; Nielsen et al., 2006).

For both geochemical and geophysical methods, the main discrepancies are the relative importance of low temperature, diffuse flow versus high temperature, on-axis venting, and the amount of ridge flank hydrothermal activity (Lister, 1982; Mottl, 2003). Diffuse flow is a characteristic of many vent fields, and low temperature vents occur extensively along the ridge axis e.g. (Corliss et al., 1979; Cooper et al., 2000). The key factor is whether these are simply diluted black smoker fluids, or whether they represent low temperature, shallow hydrothermal circulation cells (Elderfield and Shultz, 1996). The range of estimates for the degree of diffuse flow at individual vent sites is between 5-90%, although a more widely accepted value of ~25% is generally used (Kadko et al., 1994; Elderfield and Shultz, 1996; Veirs et al., 2006).

In order to determine fluxes from the oceanic crust more accurately, the importance of MOR flank hydrothermal inputs needs to be established, along with better constraints on the depth of hydrothermal circulation. The characterisation of ridge flank hydrothermal activity is thus highly important in order to enhance the current knowledge of off-axis venting styles and their contribution to oceanic cycles.

Chapter Two – Methods

This chapter describes the geochemical methods employed for analysing samples from the Von Damm Vent Field (VDVF). Most analyses were conducted at the National Oceanography Centre, Southampton (NOCS). The stable isotope data was collected at the Scottish Universities Environmental Research Centre (SUERC), University of Glasgow, and some additional preparation of samples was conducted at the Woods Hole Oceanographic Institute (WHOI). The vent fluids were geochemically analysed by Matthew Cooper, Jeff Hawkes and Rachel Mills.

2.1. Introduction

Samples from the VDVF were obtained during *RRS James Cook* cruises *JC044* and *JC082* to the Mid-Cayman Rise (MCR) in March-April 2010 and February-March 2013 using the *HyBIS* and *Isis* remotely operated vehicles (ROV; Figure 2.1, Table 2.1).

Ship	Cruise number	Start port	Date	Destination port	Date
RRS James Cook	44	Port of Spain, Trinidad	25/03/2010	Montego Bay, Jamaica	22/04/2010
RRS James Cook	82	Montego Bay, Jamaica	06/02/2013	St John's Antigua	28/02/2013
R/V Chain	35	Recife, Brazil	06/03/1963	Recife, Brazil	26/03/1963
R/V Knorr	162	Port Louis, Mauritius	30/03/2001	Port Louis, Mauritius	01/05/2001
R/V Lulu	83-8	Georgetown, Grand Cayman	17/02/1976	Georgetown, Grand Cayman	22/02/1976

Table 2.1: Dates and locations of cruises that collected the samples analysed.

Other samples, are from the Southwest Indian Ridge (SWIR) and St. Paul Fracture Zone (SPFZ), and were obtained during dredging on *R/V Chain Cruise 35* and *R/V Knorr Cruise 162-9* (Figure 2.1; Table 2.1). Further samples from the MCR were obtained by *DSV Alvin* on *R/V Lulu Cruise 83-8* (Figure 2.1; Table 2.1). The samples were subject to petrographic studies, analysis of whole rock major and trace elements, rare earth elements on talc separates, and stable and radiogenic isotope ratio analyses.

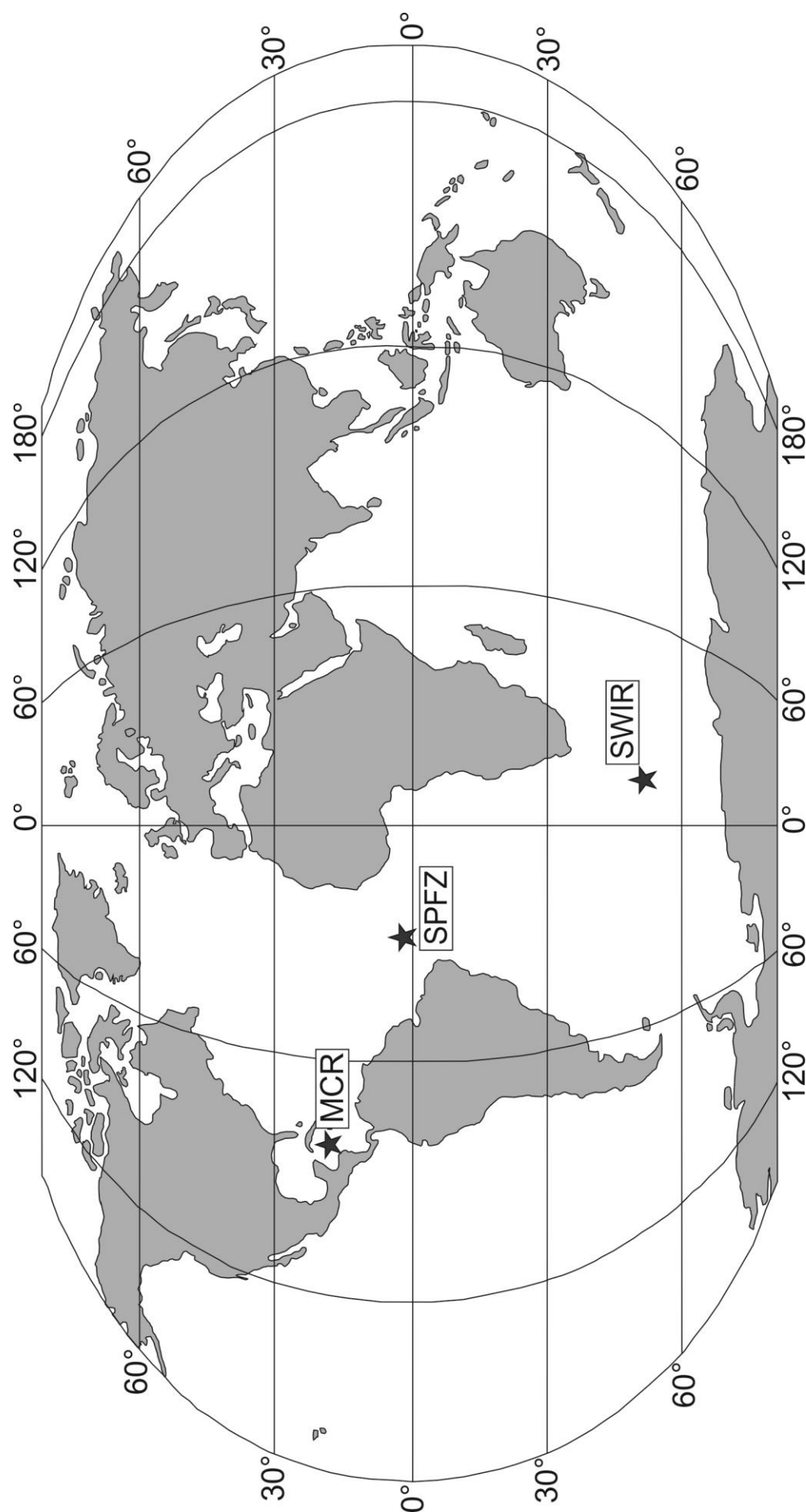


Figure 2.1: Map of the world showing the locations of samples analysed. Abbreviations; MCR – Mid-Cayman Rise, SWIR – Southwest Indian Ridge; SPFZ – St. Paul Fracture Zone.

2.1.1. Ship tracks

The two known MCR hydrothermal vent fields were discovered on cruise *JC044* (Connelly et al., 2012), which departed from Port of Spain, Trinidad and arrived at Montego Bay, Jamaica (Table 2.1). Three sites of potential hydrothermal plumes were studied (Figure 2.2). Following the discovery of two active hydrothermal vent fields, a second cruise was planned for early 2013. Cruise *JC082* departed from Montego Bay, Jamaica and finished at St John's, Antigua with the aim of returning to the previously located vent fields (Figure 2.3) for more extensive sampling.

Although access to the samples from the WHOI archive was allowed, there was no access to any geophysical data from those cruises to the SWIR and SPFZ, so the navigation tracks for these samples are absent from this thesis. However bathymetric maps, cruise tracks, submersible dive tracks and dredge tracks associated with the studies can be found in Stroup and Fox (1981), Thompson (1981) and Bach et al. (2002), and the dredge latitudes and longitudes are included in section 2.2.

2.1.2. ROV and submersible tracks

During cruise *JC044*, the VDVF was surveyed by the ROV *HyBIS* on dives 27-29 and samples were collected during dive 28 (Figure 2.4). The bathymetry data for the high-resolution bathymetric map of the VDVF was collected by the ROV *Isis* during dive 197 during cruise *JC082* (Figure 2.5). Samples were collected from five additional dives (198-202; Figure 2.6-2.7). Samples from the SWIR and St Paul Fracture Zones were collected during dredges 43 and 11 on cruises *Chain 35* and *Knorr 162-9* respectively.

Navigation for *HyBIS* was determined by the *Sonardyne* ultra-short baseline (USBL) acoustic navigation system mounted on a spar on the *RRS James Cook*, with a 10kHz transponder on the ROV. The *Isis* ROV was navigated by both USBL and doppler velocity log (DVL). The USBL navigation data were used following smoothing, as there were gaps in the DVL from instrument failure, and USBL gives a position in a reference frame relative to the ship's GPS-derived, absolute position. Typical errors in USBL position at 5000 m water depth were ± 15 -20m.

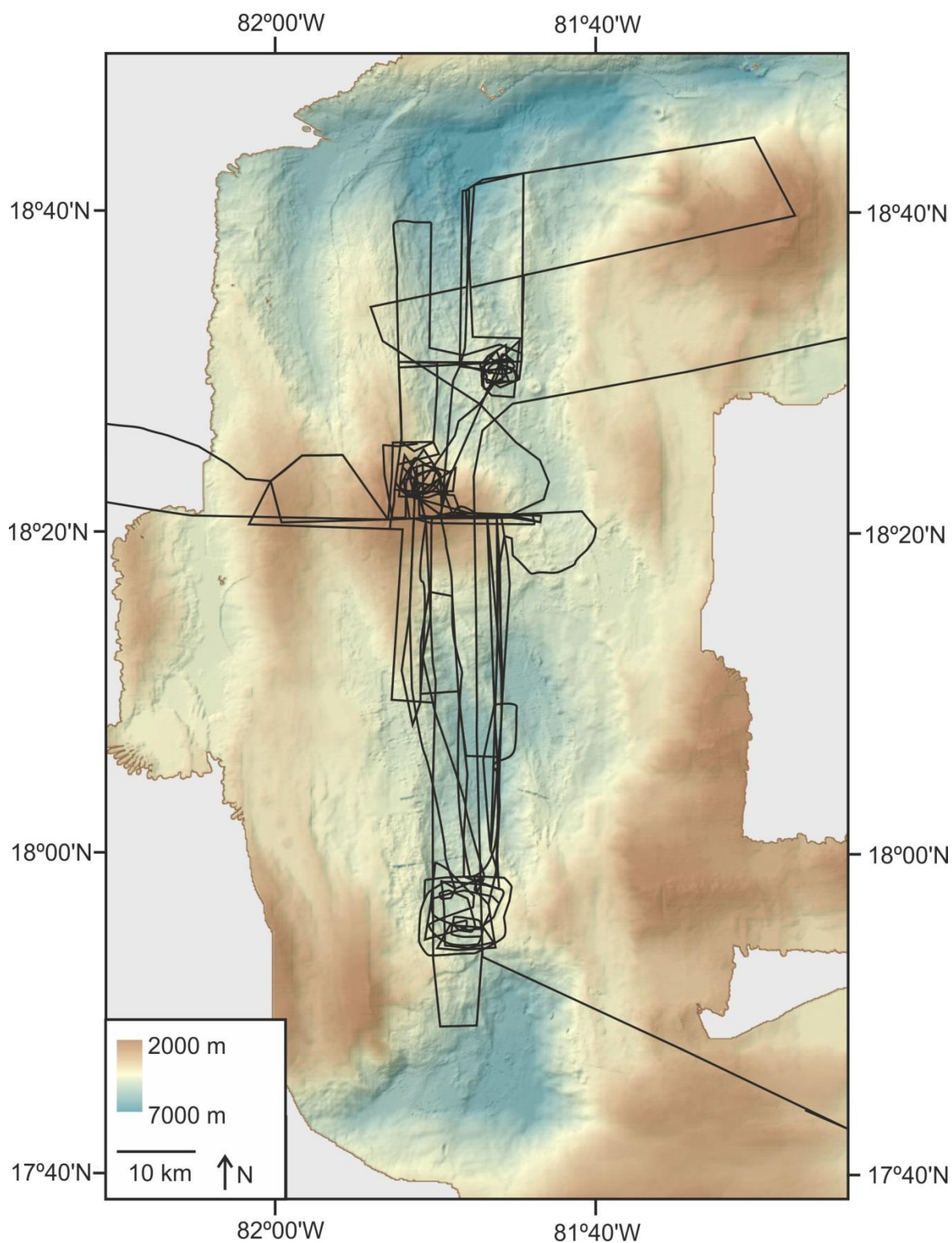


Figure 2.2: Cruise track of JC044. The background bathymetry is a composite map generated from the two surveys conducted using the James Cook's swath system on JC044 and JC082.

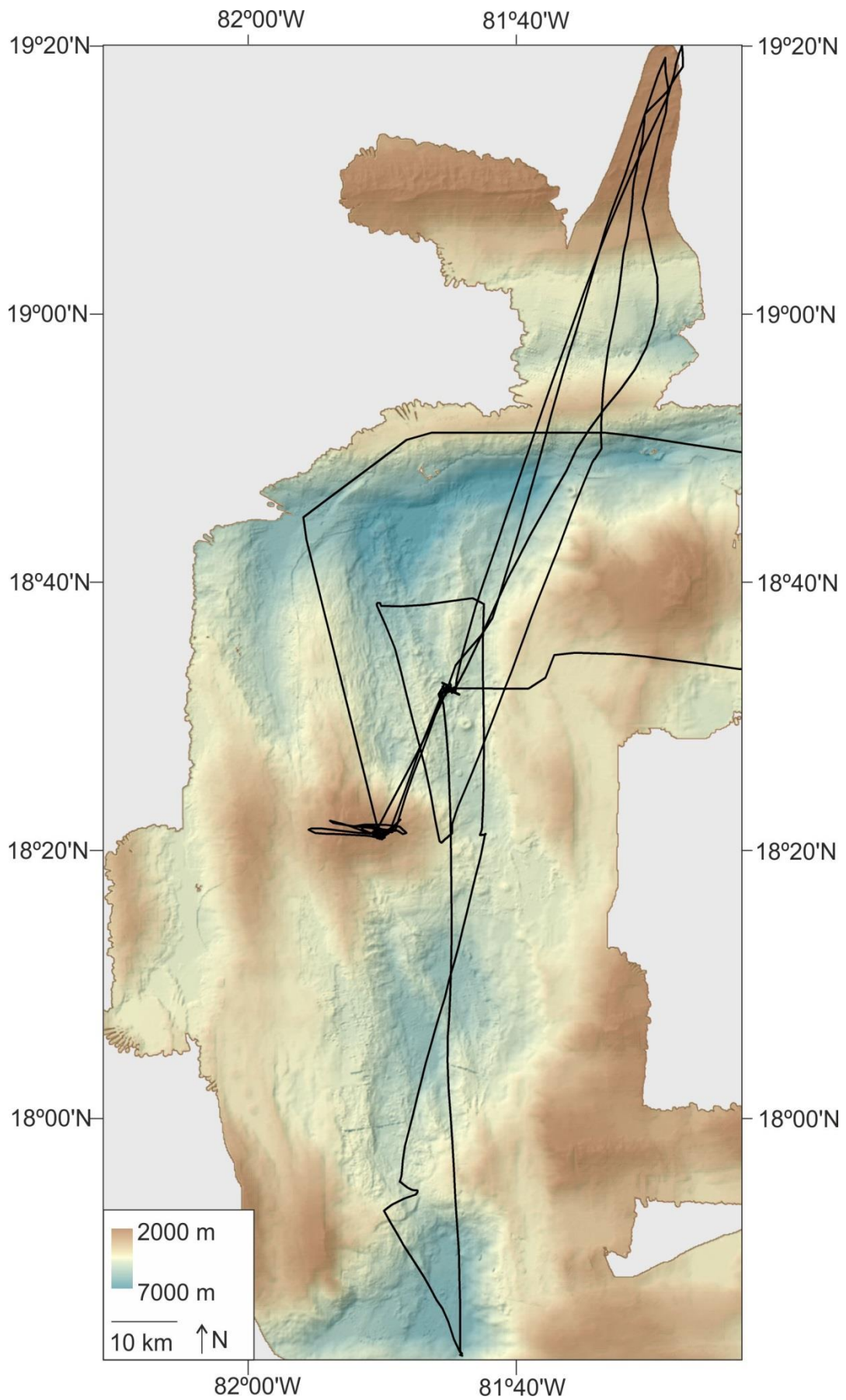


Figure 2.3: Cruise track of JC082, using the same basemap as Figure 2.2.

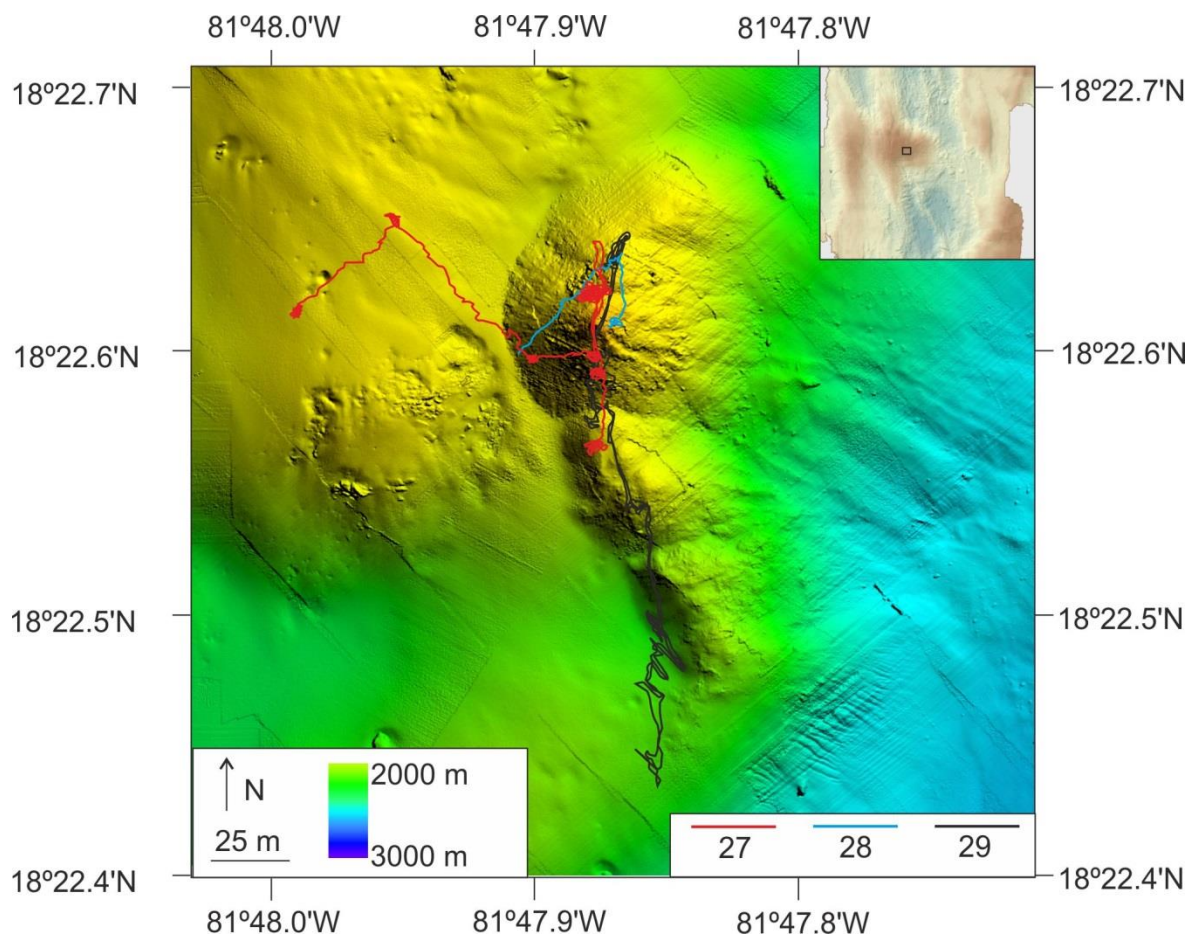


Figure 2.4: Navigation tracks for HyBIS dives 27-29 during cruise JC044. Basemap is from the swath survey conducted by the Isis ROV during cruise JC082. Inset shows the location of the VDVf on the MCR.

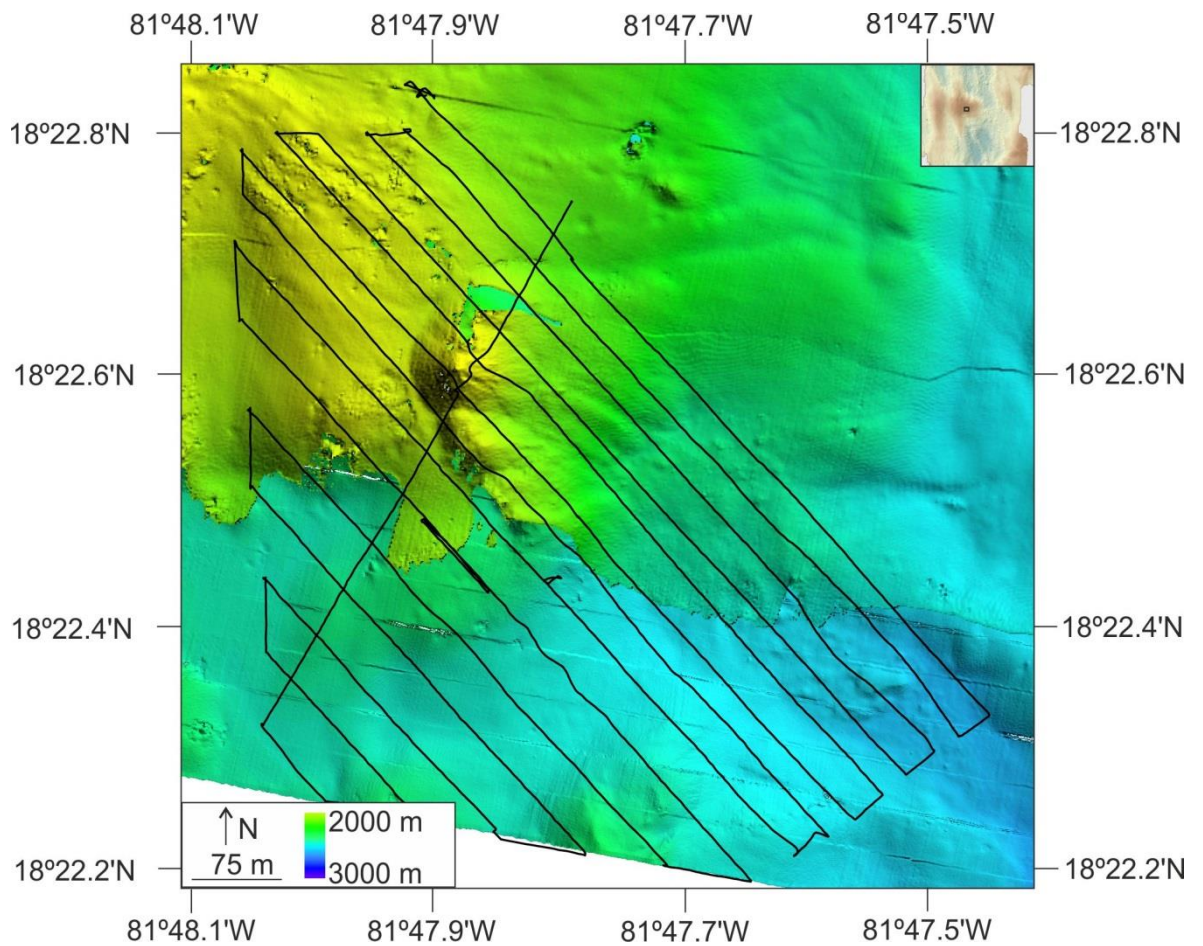


Figure 2.5: Navigation track for Isis dive 197. This shows the path taken whilst conducting the swath survey on cruise JC082. The basemap is from Autosub 6000 missions 33 and 34 conducted during cruise JC044. Inset shows the location of the VDVF on the MCR.

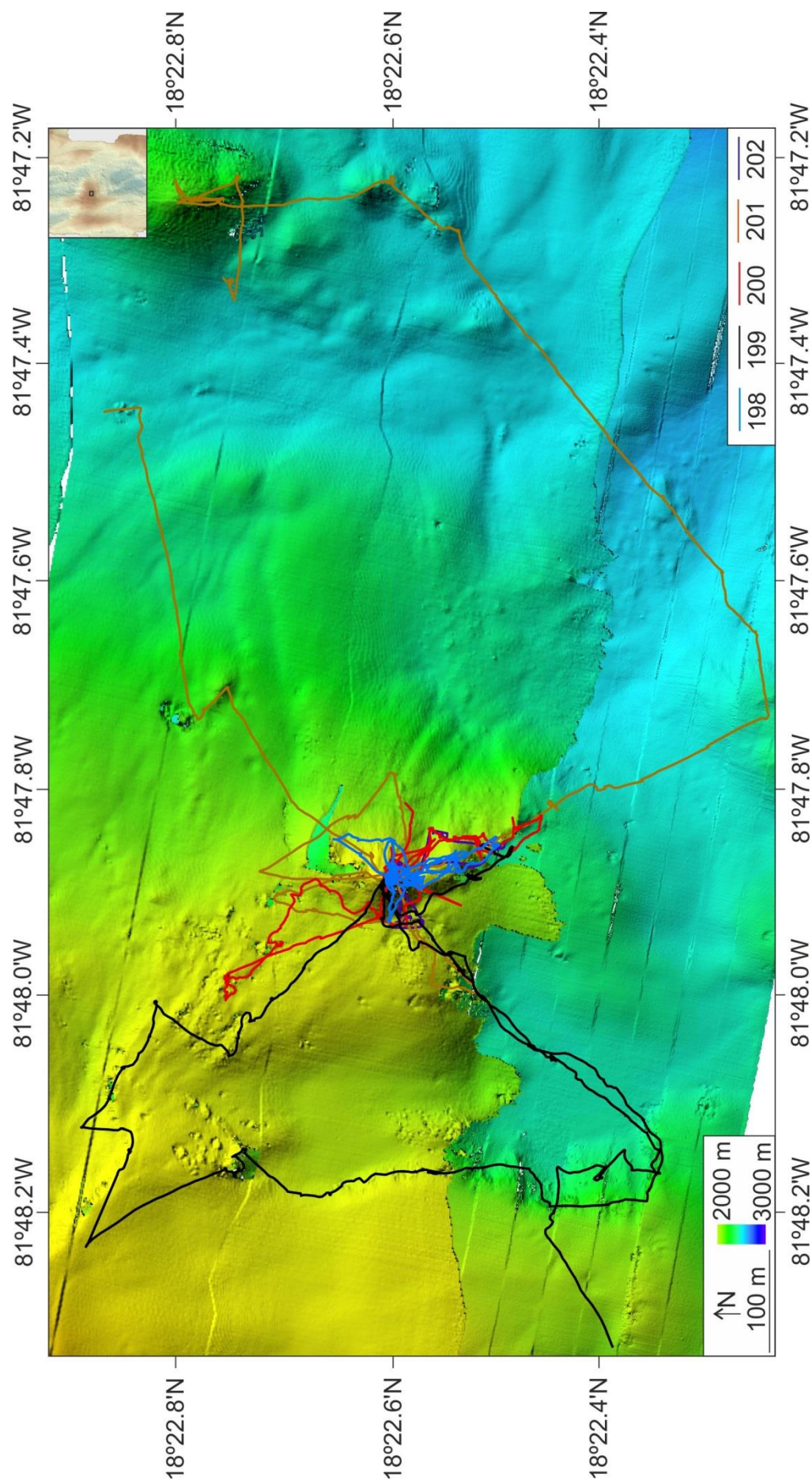


Figure 2.6: Navigation tracks for Isis dives 198-202 during cruise JC082 for the whole study site. The basemap is the same as for Figure. Inset shows the location of the VDVf on the MCR.

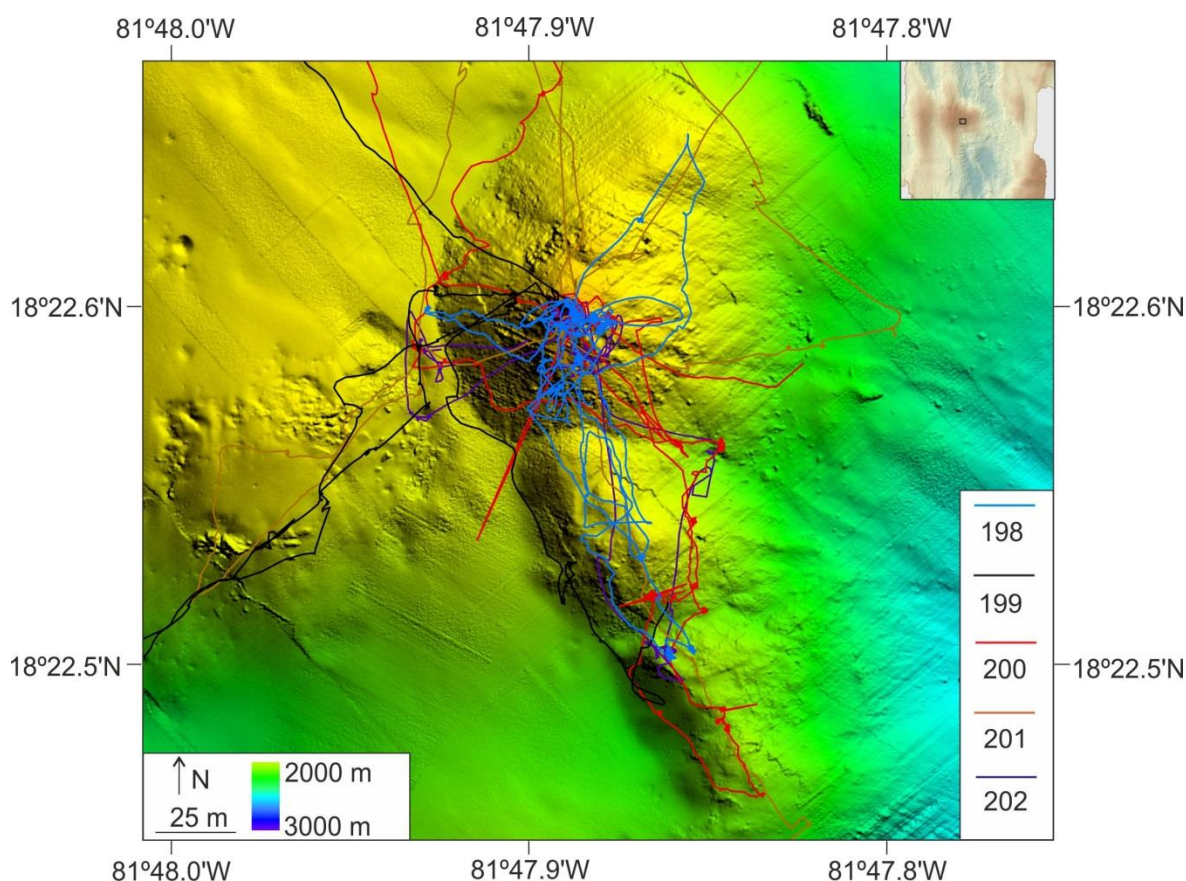


Figure 2.7: Navigation tracks for Isis dives 198-202 during cruise JC082 for the active VDVF. Basemap is from survey data collected by the Isis ROV during cruise JC082. Inset shows the location of the VDVF on the MCR.

2.2. Sample recovery

The *HyBIS* ROV features a clam-grab mechanism that allows it to sample *in-situ* hydrothermal material. The samples collected at the VDVF by *HyBIS* are from two different localities, one site at the top of the main cone, and the other site at the rubble apron on the eastern margin of the active site (Figure 2.8). The *Isis* ROV features two fully functional manipulator arms that allow for multiple samples during a single dive. The samples recovered during JC044 include three grabs from the top of the main 1 m-diameter orifice on the western side of the spire, 3 pieces of talus material grabbed from the base of the main mound, 1 dredge sample of altered host rock, and 1 grab sample of the spire material. The samples recovered by *Isis* during JC082 total 53, including active chimneys, mound talus from the three different cones at the active site, outcrops of inactive talc mounds in the vicinity and basement material.

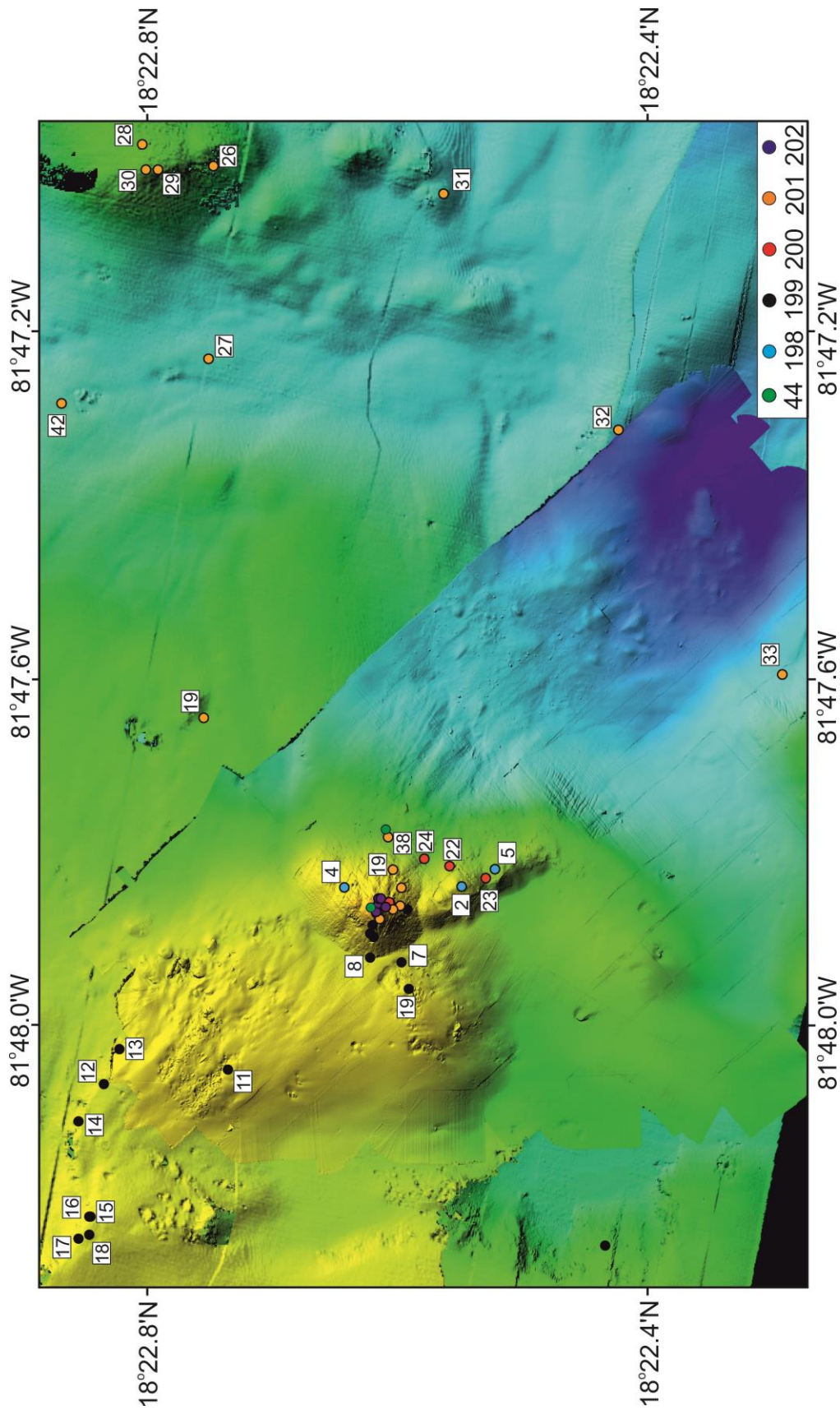


Figure 2.8: Location map of samples recovered from the regional VDF. The background map is a composite of the Autosub and Isis ROV surveys. The numbers represent the samples recovered by the Isis and HyBis ROV. The colours for numbers 198-202 correspond to the Isis dive number during cruise JC082, and the green dots represent the two sample localities for JC044.

2.2.1. Sample locations

The locations of the samples taken during the *JC044* and *JC082* cruises are shown in Table 2.2, Table 2.3, and Figure 2.8. Although no detailed bathymetry is available for the SWIR samples and SPFZ samples, the sample station positions are shown in Table.

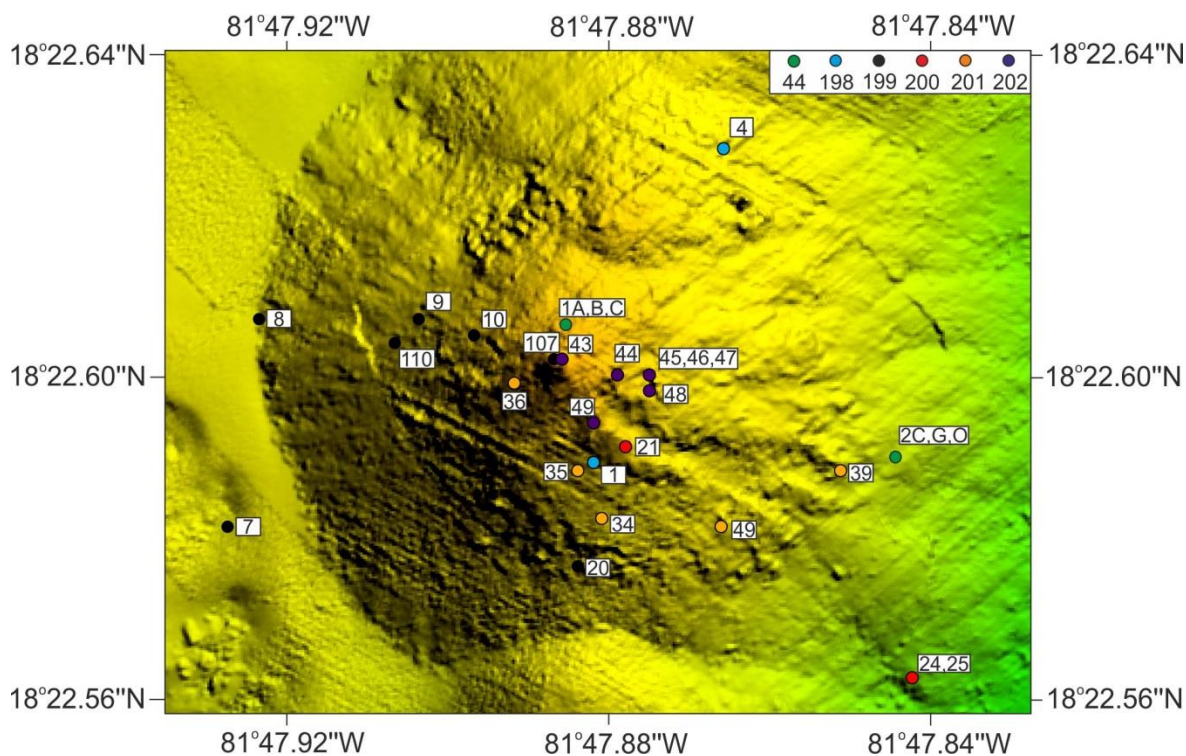


Figure 2.9: Location map of samples from the main VDVF cone. The numbers represent the samples recovered by the Isis and HyBis ROV's. The colours either correspond to the Isis dive number (198-202) during cruise *JC082*, or the sample locations for HyBis during *JC044* (green circles).

Cruise Number	Sample Name	Vehicle	Latitude	Longitude	Depth (metres)
JC044	JC44-1A	HyBIS	18°22.606'N	81°47.887'W	2290
JC044	JC44-1B	HyBIS	18°22.606'N	81°47.887'W	2290
JC044	JC44-1C	HyBIS	18°22.606'N	81°47.887'W	2290
JC044	JC44-2C	HyBIS	18°22.555'N	81°47.883'W	2337
JC044	JC44-2G	HyBIS	18°22.555'N	81°47.883'W	2337
JC044	JC44-2O	HyBIS	18°22.555'N	81°47.883'W	2337
JC082	JC82-198-01	Isis	18°22.588'N	81°47.884'W	2310
JC082	JC82-198-02	Isis	18°22.530'N	81°47.867'W	2349
JC082	JC82-198-03	Isis	18°22.530'N	81°47.867'W	2349
JC082	JC82-198-04	Isis	18°22.627'N	81°47.867'W	2349
JC082	JC82-198-05	Isis	18°22.502'N	81°47.853'W	2320
JC082	JC82-199-06	Isis	18°22.411'N	81°48.165'W	2391
JC082	JC82-199-07	Isis	18°22.580'N	81°47.930'W	2349
JC082	JC82-199-08	Isis	18°22.606'N	81°47.926'W	2346
JC082	JC82-199-09	Isis	18°22.606'N	81°47.906'W	2346
JC082	JC82-199-10	Isis	18°22.604'N	81°47.899'W	2321
JC082	JC82-199-11	Isis	18°22.724'N	81°48.019'W	2321
JC082	JC82-199-12	Isis	18°22.827'N	81°48.031'W	2321
JC082	JC82-199-13	Isis	18°22.814'N	81°48.002'W	2286
JC082	JC82-199-14	Isis	18°22.848'N	81°48.062'W	2329
JC082	JC82-199-15	Isis	18°22.838'N	81°48.141'W	2327
JC082	JC82-199-16	Isis	18°22.839'N	81°48.141'W	2339
JC082	JC82-199-17	Isis	18°22.848'N	81°48.159'W	2332
JC082	JC82-199-18	Isis	18°22.839'N	81°48.156'W	2295
JC082	JC82-199-19	Isis	18°22.574'N	81°47.952'W	2295
JC082	JC82-199-20	Isis	18°22.575'N	81°47.886'W	2283
JC082	JC82-199-110	Isis	18°22.603'N	81°47.909'W	2319
JC082	JC82-199-107	Isis	18°22.601'N	81°47.889'W	2295
JC082	JC82-199-108	Isis	18°22.601'N	81°47.889'W	2295
JC082	JC82-199-109	Isis	18°22.601'N	81°47.889'W	2295
JC082	JC82-200-21	Isis	18°22.590'N	81°47.880'W	2295
JC082	JC82-200-22	Isis	18°22.540'N	81°47.850'W	2367
JC082	JC82-200-23	Isis	18°22.510'N	81°47.860'W	2362
JC082	JC82-200-24	Isis	18°22.561'N	81°47.844'W	2379
JC082	JC82-200-25	Isis	18°22.561'N	81°47.844'W	2379
JC082	JC82-201-26	Isis	18°22.736'N	81°47.269'W	2482
JC082	JC82-201-27	Isis	18°22.740'N	81°47.429'W	2435
JC082	JC82-201-28	Isis	18°22.795'N	81°47.251'W	2426
JC082	JC82-201-29	Isis	18°22.782'N	81°47.272'W	2415
JC082	JC82-201-30	Isis	18°22.792'N	81°47.272'W	2528
JC082	JC82-201-31	Isis	18°22.545'N	81°47.292'W	2513
JC082	JC82-201-32	Isis	18°22.400'N	81°47.488'W	2516
JC082	JC82-201-33	Isis	18°22.264'N	81°47.691'W	2469
JC082	JC82-201-34	Isis	18°22.581'N	81°47.883'W	2318
JC082	JC82-201-35	Isis	18°22.587'N	81°47.886'W	2308
JC082	JC82-201-36	Isis	18°22.598'N	81°47.894'W	2292
JC082	JC82-201-37	Isis	18°22.598'N	81°47.894'W	2291
JC082	JC82-201-38	Isis	18°22.591'N	81°47.826'W	2397
JC082	JC82-201-39	Isis	18°22.587'N	81°47.853'W	2347

JC082	JC82-201-40	Isis	18°22.580'N	81°47.868'W	2330
JC082	JC82-201-41	Isis	18°22.744'N	81°47.727'W	2418
JC082	JC82-201-42	Isis	18°22.862'N	81°47.466'W	2408
JC082	JC82-202-43	Isis	18°22.601'N	81°47.888'W	2294
JC082	JC82-202-44	Isis	18°22.599'N	81°47.881'W	2299
JC082	JC82-202-45	Isis	18°22.599'N	81°47.877'W	2307
JC082	JC82-202-46	Isis	18°22.599'N	81°47.877'W	2307
JC082	JC82-202-47	Isis	18°22.599'N	81°47.877'W	2307
JC082	JC82-202-48	Isis	18°22.597'N	81°47.877'W	2307
JC082	JC82-202-49	Isis	18°22.593'N	81°47.884'W	2300
LU83-8	ALV-622-3-1	Alvin	18°22.763'N	81°46.879'W	2500
LU83-8	ALV-622-3-1(a)	Alvin	18°22.763'N	81°46.879'W	2500
LU83-8	ALV-624-6-1	Alvin	18°21.561'N	81°44.998'W	3400

Table 2.2: Depths, latitudes and longitudes of samples from the MCR recovered by ROV or submersible.

Sample Numbers	Start		Finish	
	Latitude	Longitude	Latitude	Longitude
JC44-3A	18°23.2'N	81°43.5'W	18°23.2'N	81°43.5'W
JC82-D1- 102,103,104,105,106	18°22.015'N	81°43.364'W	18°22.293'N	81°43.063'W
KN162-9-43- 3,4,11,19,27,72,79	52°38.700'S	12°31.560'E	52°40.740'S	12°31.380'E
CH35-11-4,12	01°24.5'S	29°12.0'W	01°20.0'S	29°17.5'W

Table 2.3: Latitudes and longitudes of samples recovered by dredging from the MCR, SWIR and the SPFZ

2.3. Geophysical surveys and processing

Regional bathymetry of the MCR was obtained by an EM120 multibeam echosounder mounted on the hull of the *RRS James Cook* operating at a frequency of 12 kHz and a survey speed of ~9 knots. The data were gridded at 100 m with a ~3x3 m footprint. Sound velocity profiles (SVP), heave, pitch and roll of the ship was recorded to allow for later corrections.

High-resolution bathymetry was obtained by the *Autosub6000* autonomous underwater vehicle (AUV). This vehicle carried an EM2000, 200kHz multibeam echosounder that produced maps from ~100 m above the seafloor with a swath width of ~350 m. The maps have an approximate resolution of 1x1 m. The

Autosub6000 also features a Seabird Dual conductivity temperature depth (CTD) system with an attached E_h sensor to detect changes in oxidation potential, which proved crucial when locating the VDVF. A total of seven missions were made over Mount Dent, with two (missions 33 and 34) providing detailed bathymetric maps of the VDVF.

The *Isis* ROV features a RESON Seabat 7125 multibeam echosounder system operating at frequencies of 200 and 400 kHz with 512 beams. Survey data were acquired using the PDS2000 software system. Each survey was acquired at a height of 25 or 35 m above the seafloor at a speed of ~ 0.3 knots. The survey lines were occupied at a spacing of between 50 and 75 m, with a total of 16 lines, including one crossline, and one repeated line during the VDVF survey. The data were cleaned, processed and gridded with a ~ 20 cm resolution (Figure 2.5) generating a highly detailed map of the VDVF.

Regional sidescan sonar data were collected by the Towed Ocean Bottom Instrument (TOBI) operating at a frequency of 30 kHz with a 6 km swath width at 10-12 metre resolution. The vehicle features depth, altitude and gyro sensors and operates at a distance of between 200-400 m above the seafloor. The data were obtained by four N-S trending tracks over the northern half of the MCR, one E-W trending track over Mt. Dent, and two N-S tracks over the southern half of the MCR.

All of the sonar data obtained during *JC044* and *JC082* were initially processed by Dr Tim Le Bas using the CARIS HIPS, CARIS SIPS and PRISM software packages. These data products were then processed into an ArcMAP project and displayed at UTM Zone 17 using the WGS84 datum projection, for investigation into the regional and local settings of the VDVF.

2.4. Petrography

Polished thin sections were prepared by John Ford and Bob Jones to a wafer width of 30 μm and analysed using transmitted light microscopy, reflected light microscopy, scanning electron microscopy (SEM) and X-Ray diffraction (XRD).

2.4.1. Petrographic microscopy

Hand specimens were analysed using a hand lens and under an Olympus SZH binocular microscope and photomicrographs acquired using a Nikon D70s SLR digital camera. These were processed using the Dinolite and the digiCamControl software packages. Polished thin sections were analysed using the Meiji MX9430 and Olympus BH-2 microscopes, with an attached Olympus TGH power supply for reflected light.

2.4.2. Scanning electron microscopy

SEM analysis was conducted using a Hitachi TM1000 Tabletop Microscope and a LEO 1450-VP Microscope. Samples for the table-top microscope were cut to a maximum of 1 cm in thickness and mounted onto the sample chamber using aluminium mounts, conductive carbon strips and *blu-tac* at an angle of 45° to allow for maximum secondary electron detection. The Hitachi system features a SWIFT ED energy dispersive X-Ray analysis (EDS) system for quantitative elemental analysis and data were processed using the TM-1000 software package with an acceleration voltage of 15 kV. Thin sections for the LEO SEM were carbon coated and analysed at an acceleration voltage of 20 kV. Images were processed using the Zeiss' Smart SEM software and two different EDS systems were used; the Princeton Gamma-Tech (PGT) EDS detector and the x-act 10 mm SDD detector. The data was processed using the X-Rays integrated software control system (IMIX) and the AztecEnergy software packages. To maintain consistent quantitative data, the beam was consistently focused onto a Faraday Cup detector to accurately measure the current and adjust the voltage accordingly. The specimen current to 0.7 nA (Faraday Cup) and the working distance was set to 19 mm. Spectra was collected to a total of 300,000 counts (usually ~200 seconds). The accuracy and precision of EDS analyses was checked by repeated runs of basalt standard BRR-1 (Table 2.4). The quantitative methods used to calculate

accuracy and precision for all analytical methods were relative error and RSD (relative standard deviation; Equations 2.1 and 2.2), and both are expressed as percentages relative to the mean. Relative error and RSD ranges between 0.3-9% and 0.4-4.6% respectively, except in TiO₂ and MnO, which have low concentrations in the standard so small variations are exaggerated in the relative error. Mineral standards for calibration were acquired from Micro-Analysis Consultants Ltd, Cambridge, UK and the British Museum of Natural History (BMNH; Table 2.5).

$$\text{Relative error} = \left[\frac{(\text{accepted} - \text{mean})}{\text{mean}} \right] * 100 \quad (2.1)$$

$$\text{Relative standard deviation} = \left[\frac{\text{standard deviation}}{\text{mean}} \right] * 100 \quad (2.2)$$

Oxide	Mean (%)	Accepted (%)	Relative error (%)	R.S.D. (%)
Na ₂ O	2.07	2.24	8.07	3.30
MgO	8.43	9.05	7.33	1.20
Al ₂ O ₃	14.50	14.45	-0.34	0.92
SiO ₂	49.85	48.54	-2.62	0.47
CaO	12.04	11.59	-3.70	1.31
TiO ₂	1.18	0.95	-19.52	4.52
MnO	0.07	0.22	222.67	163.66
Fe ₂ O ₃	11.72	12.68	8.20	3.45

Table 2.4: Accuracy and precision of international geological reference material, standard BRR-1, for quantified SEM-acquired EDS spectral analysis (n=22). Relative error and RSD are expressed as a percentage of the mean, which is expressed in wt. %.

2.4.3. X-Ray diffraction

XRD analyses were conducted on representative aliquots of material, picked from whole-rock samples. The samples were first compressed in a fly press and then crushed by hand using an agate pestle and mortar to prevent any deformation of the crystal lattice. Samples were analysed using a Philips X'Pert pro XRD machine using a copper X-Ray tube and mineral identification was done using the X'Pert and Crystal Impact Match! Software packages. The powders were scanned under Cu K α radiation from 2° to 76° 2 θ at steps of 0.02° at 1 second per step. The accelerating voltage was 35 kV and the source current 40 mA. The samples showing clay interlayering were

crushed further using an agate pestle and mortar and analysed as air dried, glycolated, randomly-orientated and orientated glass mounts.

Standard	Element(s)	Supplied by:
MgO	Mg	Micro-Analysis Consultants Ltd, Cambridge, UK
Quartz	Si, O	Micro-Analysis Consultants Ltd, Cambridge, UK
Pyrite	Fe, S	Micro-Analysis Consultants Ltd, Cambridge, UK
Mendipite	Pb, Cl	BMNH
Wollastonite	Ca	Micro-Analysis Consultants Ltd, Cambridge, UK
Al ₂ O ₃	Al	Micro-Analysis Consultants Ltd, Cambridge, UK
K-Feldspar	K	Micro-Analysis Consultants Ltd, Cambridge, UK
TiO ₂	Ti	Micro-Analysis Consultants Ltd, Cambridge, UK
Cu metal	Cu	BMNH
Zn metal	Zn	BMNH
U metal	U	BMNH
NiO ₂	Ni	Micro-Analysis Consultants Ltd, Cambridge, UK
Arsenopyrite	As	BMNH
Apatite	P	Micro-Analysis Consultants Ltd, Cambridge, UK
Rhodonite	Mn	Micro-Analysis Consultants Ltd, Cambridge, UK
Jadeite	Na	Micro-Analysis Consultants Ltd, Cambridge, UK
Cr metal	Cr	Oxford Polytechnic
Sb metal	Sb	BMNH

Table 2.5: List of mineral standards used in calibrating the EDS spectra on the SEM.

2.5. Geochemistry

This section will describe the calibration and the equipment used to obtain geochemical datasets from the VDVF. However, for detailed step by step methods for wet chemistry, digestion processes and lab procedures please refer to the appendices.

2.5.1. X-Ray fluorescence

Representative sub-samples were selected for whole rock geochemical analyses after the hand specimens were examined. The samples were analysed in a MagiX Pro X-Ray fluorescence spectrometer equipped with a PW2540 VRC sample changer. The calibration was done using standards BHVO-2, SiO₂ (an internal pure quartz bead), GSP-2, JP-1, JR-1, BE-N, NIM-G and NIM-S. Accuracy and precision was determined by analysis of standards UB-N, BIR-1 and OPY-1 (n.b. OPY-1 was only ran once and so is not included as a measure of precision; Table 2.6). RSD and relative error ranged between 0-10% (except for MnO) and 0-10% (for elements with a concentration <1.5

wt.%) respectively.. The data was processed using the PANalytical SuperQ software package. This software includes the correction of results by inputting the correction coefficients for alpha radiation and multidimensional regression for matrix effects.

2.5.2. Inductively-coupled plasma mass spectroscopy

Trace element (rare earth elements, Ba, Cs, Nb, Rb, Sc, Sr, Zr, Y) analysis was conducted on pure talc and representative whole rock powders by inductively coupled plasma mass spectroscopy (ICP-MS). Pure talc sub-samples were handpicked from the whole rock samples, and were digested using a combination of HF/HNO₃ (please see the appendices for a detailed step by step method) under clean lab conditions. Samples were run on a Thermo Fisher Scientific X-Series 2 inductively couple mass spectrometer and processed using the QTegra Intelligent Data Solution Software (ISDS).

For each ICP-MS analytical run, the drift of the plasma and sensitivity of the machine was monitored using an internal tuning solution (i.e. a standard that was re-run repeatedly throughout the analyses) and in between each sample analysis, the machine was washed with ~3% HNO₃ until acceptably low background levels of counts were restored. Each sample was run for a total of 3 cycles.

The international geological reference materials used as standards for calibration were BIR-1, JB1a, JGB1, JB-3 and BHVO-2 as well as a calibration blank. Non-calibration blanks were analysed alongside real samples to check for contamination. Each sample, standard and blank contained an indium (5 ppb), rhenium (5 ppb) and beryllium (20 ppb) spike to correct for the drift in instrument and detector sensitivity. RSD is expressed as a percentage of the mean and generally ranges between 0.2-6% (depending on the element) and relative error generally ranges between 0.01-10% (Tables 2.7-2.8).

	UB-N				BIR-1				OPY-1		
	Mean (wt.%)	Accepted (wt. %)	Relative error (%)	R.S.D. (%)	Mean (wt.%)	Accepted (wt. %)	Relative error (%)	R.S.D. (%)	Mean (wt.%)	Accepted (wt. %)	Relative error (%)
SiO ₂	39.34	39.43	0.23	0.17	50.38	47.50	-5.72	1.84	43.10	44.30	2.79
TiO ₂	0.10	0.08	-18.37	0.45	1.17	1.04	-11.11	9.52	0.36	0.39	7.38
Al ₂ O ₃	2.84	2.90	2.04	0.18	14.75	15.50	5.08	2.05	7.92	8.12	2.56
Fe ₂ O ₃	8.27	8.34	0.88	0.18	10.90	10.40	-4.59	2.18	11.87	11.86	-0.07
MnO	0.12	0.12	-3.69	0.19	0.22	0.19	-13.64	35.57	0.18	0.18	-3.51
MgO	35.02	35.21	0.54	0.22	8.68	9.40	8.29	5.66	20.94	21.10	0.75
CaO	1.22	1.20	-1.64	0.29	12.29	13.30	8.22	3.79	7.64	7.79	1.91
K ₂ O	0.02	0.02	11.11	1.30	N.D.	N.D.	N.D.	N.D.	0.05	0.05	8.70
Na ₂ O	0.17	0.11	-33.73	0.64	2.31	1.85	-19.91	7.48	1.09	0.11	-89.92
P ₂ O ₅	0.01	0.004	-55.56	4.38	N.D.	N.D.	N.D.	N.D.	0.03	0.03	-3.70

Table 2.6: Accuracy and precision for XRF analysis on international reference materials ($n=10$). Relative error and RSD are expressed as percentages of the mean.

Element	JA-2	Bas-206	BRR-1	BIR-1	JGB-1	BHVO-2	JB-1a	JB3	Average
	R.S.D. (%)	R.S.D. (%)	R.S.D. (%)	R.S.D. (%)	R.S.D. (%)	R.S.D. (%)	R.S.D. (%)	R.S.D. (%)	R.S.D. (%)
Rb	0.57	2.31	4.10	7.79	1.53	1.86	1.50	1.30	2.62
Sr	0.64	1.87	1.97	2.35	1.25	0.99	1.30	0.99	1.42
Y	0.92	1.27	0.54	0.51	1.16	1.19	1.36	1.00	0.99
Zr	5.45	5.71	11.04	8.05	31.83	10.15	3.67	7.60	10.44
Nb	1.65	1.07	2.86	4.51	1.29	3.59	0.92	3.28	2.40
Cs	0.68	4.86	36.43	30.78	1.11	4.49	1.46	1.32	10.14
Ba	0.79	1.15	16.52	1.17	2.06	1.83	1.14	1.39	3.26
La	0.88	0.49	1.25	1.67	1.68	1.83	0.89	1.16	1.23
Ce	0.97	0.91	0.91	0.50	1.73	1.45	0.55	0.91	0.99
Pr	0.56	0.33	0.93	0.76	0.90	0.91	0.47	0.69	0.69
Nd	0.44	0.57	0.76	0.52	1.05	0.66	0.54	0.67	0.65
Sm	1.80	1.19	1.74	0.57	0.91	0.74	1.24	0.66	1.11
Eu	0.46	0.91	1.59	0.52	1.04	0.55	0.74	0.86	0.83
Gd	0.97	0.66	1.33	0.46	1.19	0.73	1.14	1.39	0.98
Tb	0.51	0.62	1.23	0.45	0.58	0.51	0.98	0.67	0.69
Dy	0.72	0.56	0.86	0.43	0.67	0.34	0.91	0.99	0.68
Ho	0.86	0.62	1.02	0.21	0.93	0.90	0.69	0.75	0.75
Er	0.78	0.61	1.45	0.39	0.68	0.67	0.86	0.80	0.78
Tm	0.88	0.67	1.67	0.76	2.51	2.49	0.50	2.15	1.45
Yb	1.40	0.50	1.45	0.27	1.14	0.50	0.89	0.68	0.85
Lu	1.02	0.77	0.98	0.43	2.20	2.47	1.90	1.03	1.35

Table 2.7: Precision of reference materials used in ICP-MS analysis expressed as %RSD as a function of the mean from 6 different analyses.

2.5.3. Inductively-coupled plasma atomic emission spectroscopy

Inductively coupled plasma atomic emission spectroscopy (ICP-AES) was conducted to analyse base metals and metalloids (including As, Cd, Co, Cr, Cu, Mn, Mo, Ni, Pb, Sb, Se, Sn, Ti, V, Zn). Some samples displayed concentrations below the detection limit. Thus, samples were analysed using both ICP-MS and ICP-AES, and both machines were calibrated by the use of the same multi-element synthetic standards. The synthetic standards used were from PanAnalytical solutions, using aliquots with a starting concentration of ~1000 ppm. The approximate concentrations of the multi-element synthetic standards used for the calibration of the ICP-MS were 50 ppb, 10 ppb, 5 ppb, 2 ppb, 1 ppb, 0.5 ppb and 0.1 ppb, along with single element standards. All samples, standards and blanks included the same In, Re and Be spike, used for earlier trace elements analysis and for internal mass fractionation/response corrections.

	JA-2			BIR-1			JGB-1			BHVO-2			JB-1a		
	Mean (ppb)	Accepted (ppb)	Relative error (%)	Mean (ppb)	Accepted (ppb)	Relative error (%)	Mean (ppb)	Accepted (ppb)	Relative error (%)	Mean (ppb)	Accepted (ppb)	Relative error (%)	Mean (ppb)	Accepted (ppb)	Relative error (%)
Rb	77598	71000	-8.50	233	200	-14.08	6131	6870	12.06	9760	9110	-6.66	41228	39000	-5.40
Sr	247600	250000	0.97	106954	109000	1.91	324994	321000	-1.23	392884	396000	0.79	443723	444000	0.06
Y	17631	18100	2.66	16054	15600	-2.83	9868	10400	5.39	26730	26000	-2.73	23376	24000	2.67
Zr	120521	112000	-7.07	15685	14000	-10.74	36392	33500	-7.95	169414	172000	1.53	142707	142000	-0.50
Nb	9101	9000	-1.11	551	550	-0.27	2213	2800	26.55	17508	18100	3.38	27422	28000	2.11
Cs	5232	4900	-6.35	5	7	40.51	217	260	20.08	101	100	-1.43	1318	1200	-8.92
Ba	325368	315000	-3.19	6445	7140	10.79	6134	6300	2.70	130841	131000	0.12	511344	489000	-4.37
La	16297	16100	-1.21	599	615	2.75	3432	3600	4.90	15177	15200	0.15	37995	38000	0.01
Ce	34057	33700	-1.05	1871	1920	2.64	8138	8170	0.39	37506	37500	-0.02	67149	66000	-1.71
Pr	3859	3700	-4.12	375	370	-1.40	1137	1140	0.28	5369	5350	-0.35	7199	7200	0.02
Nd	14642	14200	-3.02	2384	2380	-0.18	5198	5470	5.24	24272	24500	0.94	26236	26300	0.24
Sm	3153	3100	-1.68	1090	1120	2.79	1425	1490	4.54	6035	6070	0.57	5066	5100	0.67
Eu	905	910	0.55	525	530	0.98	606	620	2.29	2045	2070	1.24	1477	1460	-1.17
Gd	3075	3000	-2.45	1875	1870	-0.25	1641	1630	-0.66	6192	6240	0.78	4704	4700	-0.09
Tb	484	480	-0.73	365	360	-1.31	273	290	6.31	923	920	-0.37	706	720	1.96
Dy	2933	2900	-1.12	2529	2510	-0.74	1711	1560	-8.84	5184	5310	2.43	4095	4100	0.11
Ho	604	610	1.01	566	560	-1.10	354	330	-6.84	962	980	1.92	805	830	3.08
Er	1717	1700	-1.00	1674	1660	-0.86	990	1040	5.00	2447	2540	3.82	2193	2200	0.31
Tm	258	260	0.83	252	250	-0.97	141	150	6.05	329	330	0.33	322	300	-6.69
Yb	1718	1680	-2.21	1680	1650	-1.80	944	970	2.75	1988	2000	0.58	2079	2160	3.89
Lu	260	250	-3.71	254	250	-1.51	140	150	7.23	280	274	-2.15	311	310	-0.22

Table 2.8: Accuracy of standards used in ICP-MS. Relative error is expressed as a comparison between the mean obtained during 6 different analyses and the accepted values for their international reference materials.

Cations for both fluid and whole rock samples were analysed by ICP-AES. Samples were analysed using a ThermoScientific iCAP 600 Series ICP-AES with an ASX 250 Autosampler, and processed using the QTegra ISDS software. Detection limits for elements are much higher for ICP-AES than ICP-MS and thus higher concentration daughter solutions were analysed. The approximate concentrations of the standards used for calibration were 50,000 ppb, 10,000 ppb, 1000 ppb, 500 ppb, 100 ppb, 50 ppb, 10 ppb, 5 ppb and 2 ppb, as well as procedural and calibration blanks (Table 2.9)

	MES 1 R.S.D. (%)	MES 2 R.S.D. (%)	MES 3 R.S.D. (%)	MES 4 R.S.D. (%)	Average R.S.D. (%)
Cr	3.00	1.74	1.34	0.55	1.66
Mn	0.67	0.33	0.44	0.31	0.44
Co	0.53	0.45	0.20	0.56	0.43
Ni	1.92	0.80	0.31	0.64	0.92
Cu	1.08	1.07	0.33	0.21	0.67
Zn	3.21	1.53	0.62	0.67	1.51
As	3.20	0.49	0.32	0.60	1.15
Se	10.64	4.52	1.23	0.72	4.28
Mo	0.83	1.30	0.51	0.41	0.76
Cd	1.58	0.82	0.46	0.22	0.77
Sb	0.88	0.54	0.21	0.50	0.53
Pb	0.21	0.52	0.43	0.27	0.36

Table 2.9: Precision of multi-element standards used in ICP-AES, reported as %RSD relative to the mean. MES = multi-element standard.

2.5.4. Stable isotopes

Stable isotope analysis was conducted on pure talc and quartz mineral separates, handpicked under a binocular microscope.

Oxygen isotope analysis was conducted using the laser fluorination technique of Sharp (1990) and the SUERC isotope facility (see appendices for details). The gas was analysed using a VG Isotech Sira 10 mass spectrometer and was calibrated using quartz standards SES ($\delta^{18}\text{O} = 10.2$) and TOR1 ($\delta^{18}\text{O} = 9.6$), garnet standards UWG2 ($\delta^{18}\text{O} = 5.8$) and GP147 ($\delta^{18}\text{O} = 7.25$), olivine standard SCX0 ($\delta^{18}\text{O} = 5.2$) and agate standard JJB8 ($\delta^{18}\text{O} = 30.3$). Changes in the stability of the mass spectrometer were checked by running a known internal reference gas. The raw $^{18}\text{O}/^{16}\text{O}$ values for the

standards were used to obtain a $\delta^{18}\text{O}$ ratio relative to Standard Mean Ocean Water (SMOW; Craig, 1961)). Standard error for the calibration lines ranges between 0.1-0.4‰ and reproducibility for the standards is up to 0.6‰.

Hydrogen isotopes were conducted using the method of Donnelly et al. (2001), also at the SUERC facility. The samples were analysed using a VG-Micromass 602 mass spectrometer and the δD reported relative to SMOW (Craig, 1961). Two internal standards, snow melt ($\delta\text{D} = -123.6$) and seawater ($\delta\text{D} = -6$), and international standards GISP ($\delta\text{D} = -189$) were used to provide a calibration line. Standard error is 1.9‰ and standards have a reproducibility of ~ 2.5 ‰.

2.5.5. *Hydrothermal vent fluids*

In situ sampling of end-member fluids using the ROV was difficult as the chimneys at the VDVF do not form tall, narrow chimneys such as those at conventional black smoker sites. The fluid conduits are instead relatively wide (see section on vent chimneys in Chapter 4) and thus sampling a pure end-member without significant seawater entrainment is difficult. Fluid vent temperatures were obtained using a high-temperature inductively coupled link (ICL) probe and sampled using titanium gas tight syringes that were developed at the University of Toulouse (Seewald et al., 2002). Sub-samples were taken off for analysis of anions (Dionex ICS 2500 Ion Chromatograph), pH (ion specific electrodes), H_2S (iodimetric titration), and cations (ICP-AES and ICP-MS). Analysis was conducted by Jeff Hawkes and Matt Cooper on *JC082* and at NOCS. The data were assessed by Rachel Mills using the protocols of the Mottl (2012) database and those that contained an Mg value exceeding that of seawater, or had Mg/Si ratios that did not fall on the correlation, were eliminated as this indicated entrainment of talc while sampling.

Before the fluids were analysed for cations, small amounts (up to 1.6 g) of the samples precipitated in the titanium syringes. The dregs were digested in HF/HNO_3 , following a similar protocol the talcs, although aqua regia was used instead of 6M HCl. The concentrations were determined in both the fluid and dreg phases, which gave a total amount of each element, eventually giving an overall concentration for the whole sample. For the precise weighting of concentrations, please see the appendices.

2.5.6. Strontium isotopes

Strontium isotope analysis was conducted on vent fluids, host rocks and talc.

Analyses were made on aliquots of mineral samples, already digested for trace element analysis, following which Sr concentrations were derived to determine the mass of sample needed for analyses. These masses were: 200 ng for the talc samples, and 1 µg for the fluids and host rock. In the initial method, talc samples were ran only through Eichron's Sr-spec resin. However, due to the large volume of solution required (up to 15 ml) to obtain the required mass of strontium, the concentrations of residual magnesium were found to be too high and the columns became flooded by excess Mg.

After the initial failed run, the dissolved talc was rerun through cation columns in AG50-X8 200-400 resin first, followed by Sr-spec, and then loaded onto rhenium filaments. The host rock and fluid samples were ran only through Sr-spec resin and loaded onto tantalum filaments. For a detailed step-by step method, the column procedures and a table for the proportion of the solid and water phases for the fluids, please see the appendices.

The solid mineral samples were analysed for $^{87}\text{Sr}/^{86}\text{Sr}$ using a ThermoFisher Triton Plus Multicollector Thermal Ionisation Mass Spectrometer (TIMS). This system has seven Faraday Cup detectors to allow for high precision data collection. The samples were heated up steadily to remove any potential contaminants and were eventually run at a current of 2600-2800 mA. A total of 300 cycles were acquired for each sample with at least 270 ratios obtained for each sample at an ^{88}Sr beam ion beam between 1.6 and 2.8 V. The obtained ratios were normalised to an $^{86}\text{Sr}/^{88}\text{Sr}$ value of 0.1194 to correct for mass bias on the mass spectrometer and subsequent fractionation of ^{86}Sr and ^{88}Sr (Steiger and Jäger, 1977). External reproducibility of the data was checked against international reference material NBS987, analysed every 10/11 unknown samples. The analysis of NBS987 averaged 0.710250 ($2\sigma = 0.000011$; $n=6$), and is within error of the accepted value of 0.710248.

2.6. Heat flux calculation

Focused hydrothermal flow rates were calculated from high-definition video footage of the vertical velocity of particles entrained within venting hydrothermal fluid. Individual particles entrained in the exiting vent fluid were filmed over a rise height of ~ 1 m and their velocity calculated from frame to frame. The distance travelled by the particles was measured against two parallel laser beams separated by a constant distance of 10 cm and shone through the rising vent fluid. The fluid exit velocities at each vent orifice were determined by measuring multiple particles over 1 to 2 m of rise height in the upflowing fluid. Different particles entrained in the up-flow zone from each orifice displayed only slight variation in their velocities (see appendices), indicating that the flow rates are relatively uniform for fluids exiting each vent orifice. The velocity of a number of particles was thus calculated over a period of several minutes and a mean velocity derived for the vent fluid. Equation 2.3 shows the relationship used to calculate the heat flux.

$$Q = \delta T.C.M. \quad (2.3)$$

Where: Q = Heat flux (Watts), δT = difference in temperature ($^{\circ}\text{C}$) between mean temperature of venting hydrothermal fluid and ambient bottom water (4°C), C = specific thermal capacity of seawater at 200 bar and 215°C (i.e. $4500 \text{ J Kg}^{-1} \text{ K}^{-1}$) and M = mass flux (kg s^{-1}). The equation to calculate the mass flux was $M = A.V.\rho$; where: A = area of vent orifice (m^2), V = mean vertical flow rate (m s^{-1}) and ρ = density of seawater at 215°C .

The calculated error in the velocities is derived from the variation in particle velocity. This method models the vent orifices as circles, and makes the assumptions that the fluid is emanating from the vent at a constant velocity across its diameter, the temperature is uniform across the vent orifice, and the particle velocities recorded were representative of the flow velocity. For a diagram and video showing the particle velocities, please see the appendices.

2.7. Thermodynamic modelling

Thermodynamic modelling was carried out using the Geochemist's Workbench (GWB; (Bethke, 1996). A thermodynamic database was created using DBCreate (Kong et al., 2013), at the pressure and temperature conditions of the VDVF. This database creator uses SUPCRT92, a program that calculates stability constants ($\log K$) at the specified temperature and pressure. In case of the VDVF, the full temperature range used was 4-300°C, and the pressure was 230 bar. The thermodynamic properties for aqueous and mineral phases are taken from the 2006 revision of the SUPCRT database (Johnson et al., 1992).

The inputs into the modelling are the VDVF end-member fluid chemistry, calculated by extrapolating to zero Mg. End-member fluid and seawater mixing was simulated using the React program in GWB, which calculates the mineral saturation index based on the physical and chemical inputs into the system and the thermodynamic properties, calculated by DBCreate and SUPCRT92. The mineral saturation index is expressed as $\log (Q/K)$; where Q = ion activity coefficient in the solution calculated by inputting the geochemical data, and K = the solubility equilibrium constant. This is calculated at each step of the mixing reaction, and where $\log (Q/K)$ is >1 , the mineral is supersaturated and will precipitate, and when $\log (Q/K) <1$, the mineral is undersaturated and thus remains in solution. This data can then be plotted to display the saturation index of minerals throughout the mixing regime.

The mineral stability diagram was constructed using the Spec8 program in GWB. The thermodynamic stability boundaries for minerals at the temperatures of venting on the VDVF were calculated using the SUPCRT database. The Mg and Si activity of the fluid at difference stages of mixing (0.1-96%) between the VDVF end-member and seawater was calculated using the geochemical data of the hydrothermal fluids and seawater. These were then plotted on a magnesium and silica activity diagram to display the saturation states of quartz, brucite and talc, with respect to the mixing regime between the end-member fluid and seawater.

Chapter Three – Regional Setting of the Mid-Cayman Rise

This chapter describes the current geology of the Caribbean, the geological history of the Mid-Cayman Rise (MCR) and the Cayman Trough, and summarises the regional setting of the Von Damm Vent Field (VDVF). This will be done by reviewing the available literature on the geological evolution of the Caribbean, the Cayman Trough and the MCR, and by incorporating previously recovered samples and remotely operated vehicle (ROV)/submersible observations with the new geophysical surveys and sampling obtained as part of this study.

3.1. Evolution and present day tectonics of the Caribbean Plate

The Caribbean Plate is a major tectonic plate that separates the North American and South American plates. It is currently moving eastwards at a rate of 20 mm yr⁻¹ relative to the North American Plate (DeMets et al., 2007). The evolution of the Caribbean plate has been the subject of intense debate over many decades, especially the origin of the thickened oceanic crust in the central Caribbean (Pindell and Barrett, 1990; Meschede and Frisch, 1998; James, 2006; James, 2009; Pindell and Kennan, 2009; Pindell et al., 2012; van Benthem et al., 2013; Nerlich et al., 2014). The Caribbean Sea comprises several basins and bathymetric highs, delineated and interpreted using bathymetric studies and seismic surveys e.g. (Burke et al., 1978; van Benthem et al., 2013), in concert with the geochemistry of volcanic material recovered from Ocean Drilling Program (ODP) drill cores, dredged basement rocks, and onshore mapping and geochronology of terrestrial regions in Central and South America and the Caribbean Islands (Leroy et al., 2000; James, 2006; Boschman et al., 2014).

The geological and tectonic diversity of the Caribbean Plate margins are difficult to interpret, but the prevailing model is that the Caribbean Plate originated in the Pacific and migrated east relative to the South American and North American Plates e.g. (Pindell and Barrett, 1990). The production of the oceanic crust that currently forms the Caribbean Plate commenced at ~143 Ma (Mattinson et al., 2008), and subduction

of the North and South America Plates beneath the Caribbean Plate commenced soon after in a now extinct volcanic arc called ‘The Great Arc of the Caribbean’ (Burke, 1988). This narrative is supported by the record of oceanic spreading in the Cayman Trough (Leroy et al., 2000), and seismic imaging of at least 1000 km of subducted slab deep within the mantle under the eastern margin of the Caribbean Plate (van Benthem et al., 2013). Geochemical data suggests the plateau in the Caribbean is oceanic in origin, and rocks recovered in dredged rocks indicate a large igneous province origin (Neill et al., 2011).

3.1.1. Boundaries of the Caribbean Plate

The plate boundaries surrounding the Caribbean are complex and bounded by tectonically variable structures (Boschman et al., 2014). The north west section of the Caribbean features four sinistral strike slip faults including the Montagua, Polochic, Jocotan and Baja Verpaz shear zones, and are known collectively as the Montagua Fault Zone (Figure 3.1; Boschman et al., 2014; Ratschbacher et al., 2009). All four faults appear to have been active over the past 20 Ma (Rogers et al., 2007), but the only fault where recent movement has been detected is the Montagua Fault, which has been active for 3 Ma and is considered as a current plate boundary (Donnelly et al., 1990). The north west plate boundary occurs predominantly in continental crust in Guatemala and Belize, but towards the east, left-lateral strike slip movement along the Swan Island and Oriente fracture zones occurs mainly in oceanic crust that was formed by seafloor spreading at the MCR over the past ~49 Ma (Rosencrantz, 1994; Leroy et al., 2000). The deep pull-apart basin forming the Cayman Trough formed as a result of E-W strike slip motion along the plate boundary. The Gonave Microplate is located on the eastern section of the Cayman Trough and separates the northern margin of the Caribbean plate from the North American plate (Mann et al., 1995; DeMets and Wiggins-Grandison, 2007). To the east of the Cayman Trough are two large strike slip fault zones, the Oriente-Septentrional and Walton-Enriquillo Fault Zones (Boschman et al., 2014). These two faults systems carry the continuation of the relative motion of the Caribbean and North American plates, and a majority of the deformation is taken up in the North Hispaniola Deformed Belt (Mann et al., 1984; Pindell and Barrett, 1990). In the north-east corner of the Caribbean plate, strike slip motion continues along the Puerto Rico Trench (Figure 3.1; Boschman et al., 2014)

for >200km until its eastern margin intersects the Lesser Antilles trench (van Benthem et al., 2013).

The eastern boundary of the Caribbean is defined by subduction of Atlantic oceanic crust under the Caribbean Plate, which commenced at around 38 Ma (Briden et al., 1979). This forms the Lesser Antilles Arcs and the Barbados accretionary prism (Figure 3.1; Boschman et al., 2014).

The southern boundary of the Caribbean Plate is highly complicated and features areas of arc-continent collision (Levander et al., 2006; Escalona and Mann, 2011). The southern boundary is around 100 km wide at its eastern margin, and 600 km at its western boundary where it includes several minor tectonic blocks, including the Panama and Bonaire blocks (Figure 3.1; Audemard et al., 2005; Audemard, 2009). Similar to the northern boundary of the Caribbean Plate, movement between the South American and Caribbean Plates is dominantly strike slip. The main section of the southern plate boundary is defined by the South Caribbean Deformation Belt, which features thrust zones and several east-west trending foreland basins e.g. (Levander et al., 2006; Figure 3.1) that formed during past subduction of the South American Plate under the Caribbean Plate. Present movement is generally accommodated on oblique strike-slip faults within the Santa Marta-Bucaramanga and the Bocono-San Sebastian Fault Zones, as the Caribbean Plate moves east relative to the South American Plate (DeMets, 2001; Kennan and Pindell, 2009). The southwestern boundary of the Caribbean Plate is defined by both thrust and strike-slip faulting in continental crust along the Panama Deformed Belt and the Panama-Choco Block (Pindell and Kennan, 2009; Montes et al., 2012). This boundary developed during subduction of the Caribbean Plate under the South American Plate, and the subsequent accretion of the of the Panama-Choco block to the Caribbean Plate (Figure 3.1; Montes et al., 2012).

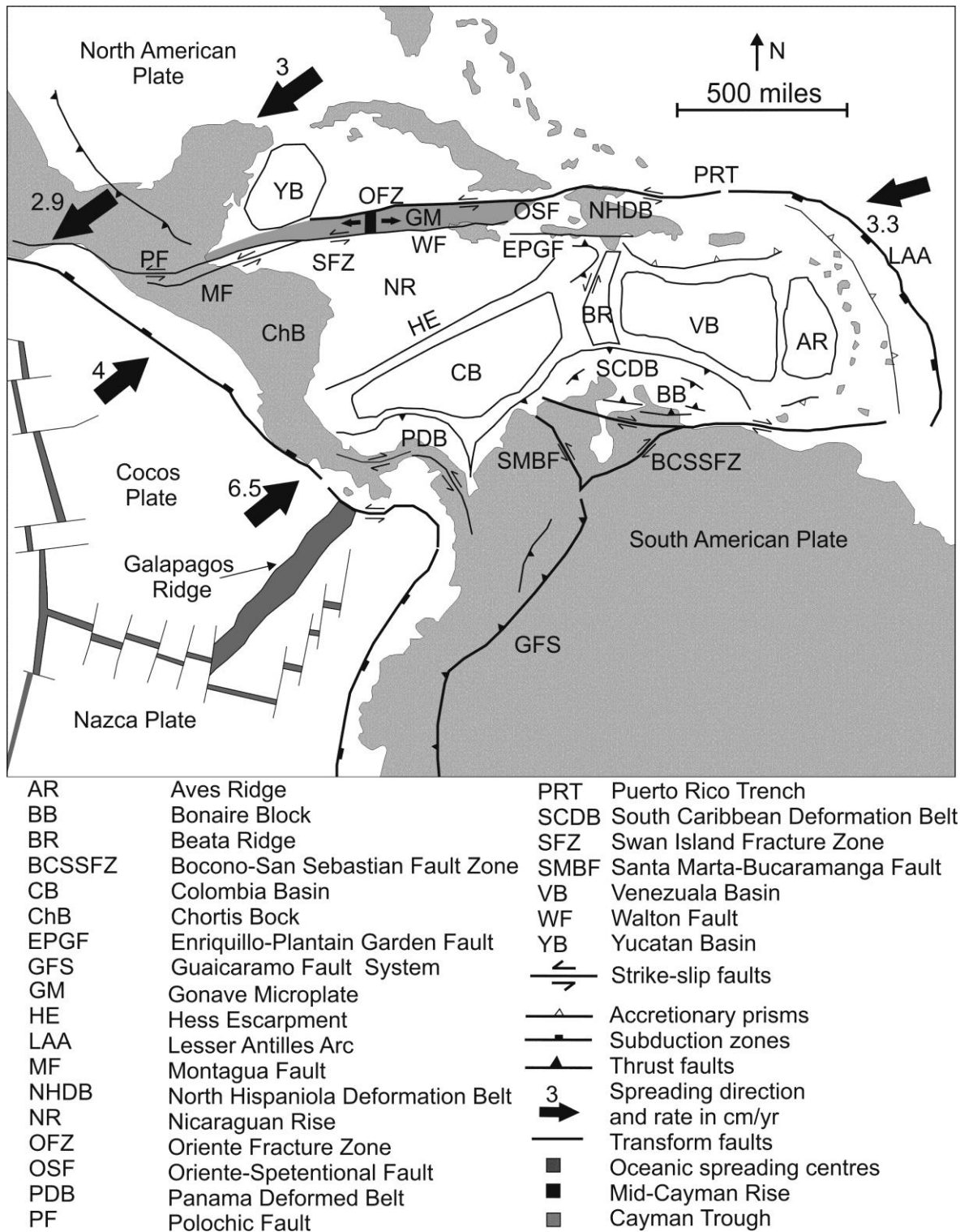


Figure 3.1: Regional tectonic map of the Caribbean showing the major features of the Caribbean region. Modified after: Jordan, 1975; Donnelly et al., 1990; Lewis et al., 1990; Pindell and Barrett, 1990; Rosencrantz, 1990; Venable, 1994; Gordon et al., 1997; Meschede and Frisch, 1998; Sinton et al., 1998; Marshall et al., 2000; Audemard et al., 2005; Giunta and Beccaluva, 2006; Levander et al., 2006; Pindell et al., 2006; DeMets and Wiggins-Grandison, 2007; Mann et al., 2007b; Rogers and Mann, 2007; Rogers et al.,

2007; Pindell and Kennan, 2009; Authemayou et al., 2011; Escalona and Mann, 2011; Neill et al., 2011; Montes et al., 2012; Pindell et al., 2012; Boschman et al., 2014.

The western margin of the Caribbean plate is defined by the Central America trench, and eastward subduction of the Cocos Plate along the west coast of Central America from Mexico down to Costa Rica and Panama (Figure 3.1; Jordan, 1975).

In summary, the E-W trending margins of the Caribbean Plate are defined by strike slip faulting, and continental and oceanic pull-apart basins. The two N-S trending margins of the Caribbean Plate feature active subduction zones, and consist of arc-related magmatism and deep oceanic trenches.

3.1.2. Major geological features of the Caribbean Sea

The basement in the Caribbean Sea is composed almost entirely of oceanic crust, including the Caribbean Large Igneous Province (CLIP; Perfit, 1977; Burke, 1988; Neill et al., 2011), while the only area of inferred continental crust is located at the northern Nicaraguan Rise (Lewis et al., 2011). The CLIP is the main geological feature in the south and central Caribbean region, and features oceanic crust up to 20 km in places (Burke et al., 1978). The CLIP has a total area of 6×10^5 km² (Burke, 1988), and extends from the Nicaragua Rise to the north, to the South Caribbean Deformed Belt in the south (Kerr et al., 1997; Lewis et al., 2011). The basement underlying the Venezuelan and Colombia Basins, and the Beata Ridge is all proposed to be comprised of the CLIP lithologies (Donnelly et al., 1973; Sinton et al., 1998). Estimates for the timing and emplacement of the CLIP vary, as radiometric dating indicates that the units comprising the oceanic crust of the Caribbean range in age from 69-139 Ma (Hauff et al., 2000; Hoernle et al., 2002; Kerr and Tarney, 2005; Whattam and Stern, 2015), however the CLIP was extruded during a much shorter time span of 3 Ma, at 91-88 Ma (Sinton et al., 1998).

The Nicaraguan Rise is located in the NW corner of the Caribbean (Figure 3.1) and is a large oceanic plateau that is divided into northern and southern sections, which have contrasting lithologies and origins (Lewis et al., 1990; Lewis et al., 2011). The southern Nicaraguan Rise consists of thickened oceanic crust and is part of the CLIP

(Donnelly et al., 1973), whereas the northern Nicaragua Rise consists of island arc and continental crust material (Lewis et al., 2011). The two different sections were brought together during the Late Cretaceous by strike slip motion along the 1000 km-long Hess Escarpment, which is now inactive except for its southern tip (Bowland, 1993; Mauffret and Leroy, 1997; Mann et al., 2007a). The Aves Ridge (Figure 3.1) is an extinct island arc formed during the eastern migration of the Great Caribbean Arc between 88-59 Ma (Neill et al., 2011). Despite its proximity to the Venezuela Basin and other regions in the central Caribbean, it is not thought to be related to the CLIP (Boschman et al., 2014).

The Yucatan Basin (Figure 3.1), is one of few areas in the Caribbean where the oceanic crust is not > 10 km thick (Burke et al., 1978). The western side is a deep, now inactive, pull-apart basin formed during the Eocene, and the eastern section consists of highly undulating oceanic crust of Late Cretaceous origin (Rosencrantz, 1990).

3.2. History and evolution of the Cayman Trough

The Cayman Trough is located in the north west of the Caribbean and is a sinistral pull-apart basin (Rosencrantz, 1994). It is a seismically active depression that extends 1600 km from the Windward Passage to the Gulf of Honduras, and is bound to the north by the Cayman Ridge and the Nicaraguan Plateau to the south (Perfit and Heezen, 1978). The Cayman Trough developed during the past ~49 Ma by strike-slip motion along the Swan Island, Walton and Oriente Faults (Rosencrantz and Sclater, 1986).

3.2.1. History of the Cayman Trough and opening of the Mid-Cayman Rise

Various geophysical studies, including acoustics, seismic, heat flow, gravity and magnetic have been conducted on the Cayman Trough in the past four decades (Macdonald and Holcombe, 1978; Rosencrantz and Sclater, 1986; Rosencrantz et al., 1988; Jacobs et al., 1989; Ramana et al., 1995; Leroy et al., 1996; ten Brink et al., 2002). Detection and interpretation of magnetic anomalies within the Cayman

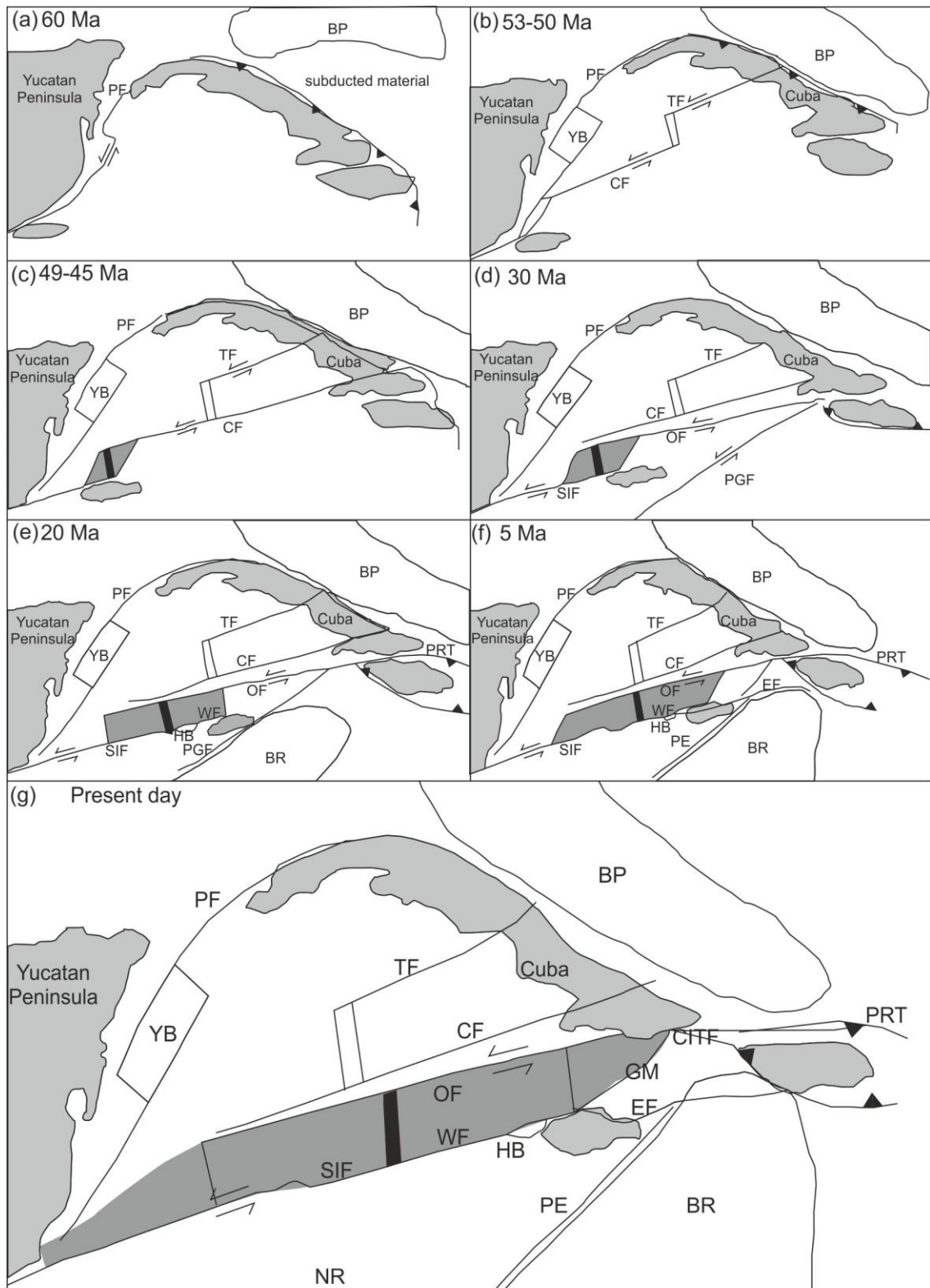
Trough are important, as this basin is the only quantitative measurement of relative motion within the Caribbean Plate since the Eocene (Boschman et al., 2014).


The interpretation of (Leroy et al., 2000) is the accepted geological model for the development of the Cayman Trough and is summarised here and in Figure 3.2. Subduction of the North American Plate under the Caribbean Plate is documented in the late Cretaceous (Fourcade et al., 1994), and at ~70 Ma strike-slip motion along the Yucatan Peninsula on the Pinar Fault commenced (Rosencrantz, 1990). This subduction continued until initial collision of the thickened Bahamas Platform crust in northern Cuba halted the eastward progression of the Caribbean Arc (Gordon et al., 1997). At ~60 Ma (Figure 3.2a) the Yucatan pull-apart basin opened up along the sinistral Pinar Fault, orientated along the coast of the Yucatan Peninsula (Rosencrantz, 1990). Seven million years later (Figure 3.2b), collision between Cuba and the Bahamas Platform restricted the progression of the Caribbean Arc and obducted oceanic crust onto north and west Cuba (Wadge et al., 1984; Goncalves et al., 2000). To accommodate the relative plate motions of the North American and Caribbean Plates, the Trocha/Cauto deformation front formed with sinistral strike-slip motion along two faults to the west of central Cuba (Figure 3.2b; Leroy et al., 1996; Leroy et al., 2000), causing segmentation of the volcanic arc across central Cuba along the Trocha Fault (Leroy et al., 2000). As the southern end of Cuba collided with the Bahamas, strike slip deformation moved further south, leading to the opening of the MCR in the Early Eocene at 49 Ma, (Figure 3.2c; Perfit and Heezen, 1978; Rosencrantz and Sclater, 1986; Leroy et al., 2000). At approximately 30 Ma, the plate boundary moved south, moving strike slip motion to the Oriente Fault and halting it along the Cauto Fault (Leroy et al., 2000). This progression initiated movement along the Swan Island fracture zone, causing the MCR to migrate 20 km to the west (Figure 3.2d; Rosencrantz et al., 1988). Subduction of the eastern Caribbean Plate began underneath Hispaniola as strike slip movement commenced along the Pedro-Gonave Fault in the Oligocene (Leroy et al., 2000). From 26-20 Ma (Figure 3.2e) the spreading rate decreased, and the Swan Island Fault moved south of the Swan Islands (Leroy et al., 1996). The MCR slowly moves southwards, segmenting in two, and extending to its present day length of 110 km (Rosencrantz, 1994). The Walton Fault, the eastern side of the Swan Island Fault, becomes active at 20 Ma, and leads to the formation of the Hendrix pull-apart basin (Leroy et al., 1996). At 5 Ma,

(Figure 3.f) movement ceased on the Pedro-Gonave Fault and transferred south onto the Enriquillo Fault forming the Pedro Escarpment and the Gonave rise (Leroy et al., 2000). The Beata Ridge then collided with the Enriquillo Fault and movement was transferred up to the Puerto-Rico Bahama Trough and the Cibao-Ile de la Tortue Fault. The Enriquillo Fault propagated further east across the Beata Ridge to its present day position forming the Gonave Microplate (Figure 3.2g; Rosencrantz and Mann, 1991).

3.3. Geological setting of the Mid-Cayman Rise

The MCR forms a segmented, 110 km long spreading centre with an average seawater depth of 5500 m at the axial volcanic ridge (AVR), and a full range of between 5000 m to 6500 m (Holcombe et al., 1973). The MCR is on average around 1000 m deeper than the seafloor of the Cayman Trough outside the axial valley (Holcombe et al., 1973). The MCR is classified as an ultra-slow spreading MOR due to its current full spreading rate of 15 mm yr⁻¹ (Hayman et al., 2011). The oceanic crust is only 2-3 km thick within 50 km of the spreading axis of the MCR, making it some of the thinnest in the world (Perfit and Heezen, 1978; ten Brink et al., 2002). The MCR was first hypothesised to be a spreading centre from studies of earthquake focal mechanisms (Molnar and Sykes, 1969) with confirmation following seismic reflection, bathymetric and magnetic surveys (Holcombe et al., 1973). The seafloor of the MCR and the surrounding Cayman Trough were extensively sampled (Figure 3.3), and new geophysical data collected between 1970 and 2000 (Eggler et al., 1973; Perfit, 1977; Rosencrantz and Sclater, 1986; Elthon, 1987; Rosencrantz et al., 1988; Rosencrantz and Mann, 1991; Ramana et al., 1995; ten Brink et al., 2002). The MCR was re-visited towards the start of the 2010s to search for hydrothermal venting, when the Beebe and Von Damm Vent Fields were discovered (Figure 3.3; German et al., 2010; Connelly et al., 2012).




 300 km
 (for diagrams a-f)
 100 km
 (diagram g)

BP	Bahamas Platform	OF	Oriente Fault
BR	Beata Ridge	PE	Pedro Escarpment
CF	Cauto Fault	PGF	Pedro-Gonave Fault
CITF	Cibao-Ile de la Tortue Fault	PF	Pinar Fault
EF	Enriquillo Fault	PRT	Puerto Rico Trench
GM	Gonave Microplate	SIF	Swan Island Fault
HB	Hendrix Basin	TF	Trocha Fault
NR	Nicaraguan Rise	WF	Walton Fault
■	Cayman Trough	YB	Yucatan Basin
■	Mid-Cayman Rise		

Figure 3.2: (On previous page) schematic map showing the history of the Cayman Trough, the present day tectonics, and the opening of the Mid-Cayman Rise. Constructed using the figures and data from Rosencrantz et al., 1988; Rosencrantz, 1994; Leroy et al., 1996; Leroy et al., 2000.

3.3.1. Oceanic core complexes on the Mid-Cayman Rise

The ultra-slow spreading rate of the MCR, its elevated $\text{Na}_{(8.0)}$ chemistry of lavas and its deep axial valley suggests low melt fractions, and that a large proportion of the spreading is from tectonic extension rather than magmatic processes (Klein and Langmuir, 1987; Hayman et al., 2011). At medium to ultra-slow spreading ridges, oceanic core complexes (OCC's) can accommodate 50% or more of the plate separation under reduced magma supply conditions (Buck et al., 2005; Escartin et al., 2008).

The geophysical surveys at the MCR indicate three topographically higher areas on its flanks (Figures 3.3-3.5) which are interpreted as OCC's (Hayman et al., 2011; Cheadle et al., 2012). These have been termed, from north to south, Mount Emms, Mount Dent and Mount Hudson (Cheadle et al., 2012). Dredged rocks from the OCC's on the flanks of the MCR (Eggler et al., 1973; Perfit, 1977; Perfit and Heezen, 1978), include variably serpentinitised peridotites and gabbros, consistent with the exposure of lower oceanic crust and upper mantle (Figure 3.3; Eggler et al., 1973; Elthon, 1987), while basalt has also been recovered from Mt. Dent (Hayman et al., 2011; Marr et al., 2014).

OCC's can eventually intersect the volcanic axis where the toe of the detachment fault (known as the termination zone), will be rifted away from the rest of the massif (MacLeod et al., 2009). Mt. Emms has been extinct for ~ 2 Ma, and has undergone extensive normal faulting, whereas Mt. Hudson was terminated within the last ~ 1 Ma, and underwent initial rifting at 0.5 Ma (Cheadle et al., 2012). This rifting at Mt. Hudson is post-dated by basaltic lava flows (confirmed by ROV operations) on top of the toe (Cheadle et al., 2012), indicating the presence of a developing AVR.

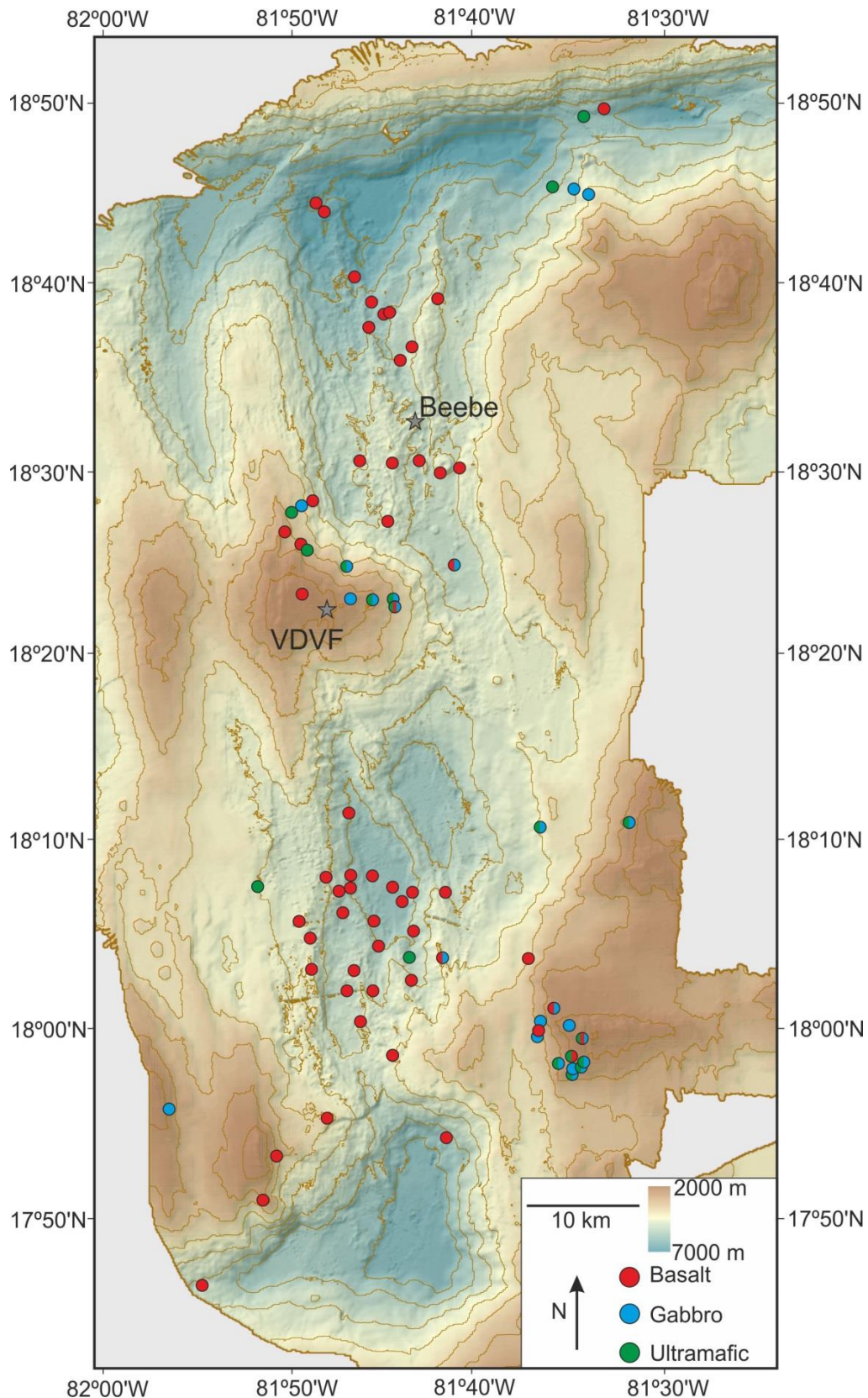


Figure 3.3: Bathymetry of the MCR obtained during JC044 and JC082 showing lithologies sampled from dredging, ROV and submersible recovered from previous expeditions, and the locations of the Von Damm and Beebe vent fields (grey stars; Ballard et al., 1979; White and Stroup, 1979; Stroup and Fox, 1981; Hayman et al., 2011).

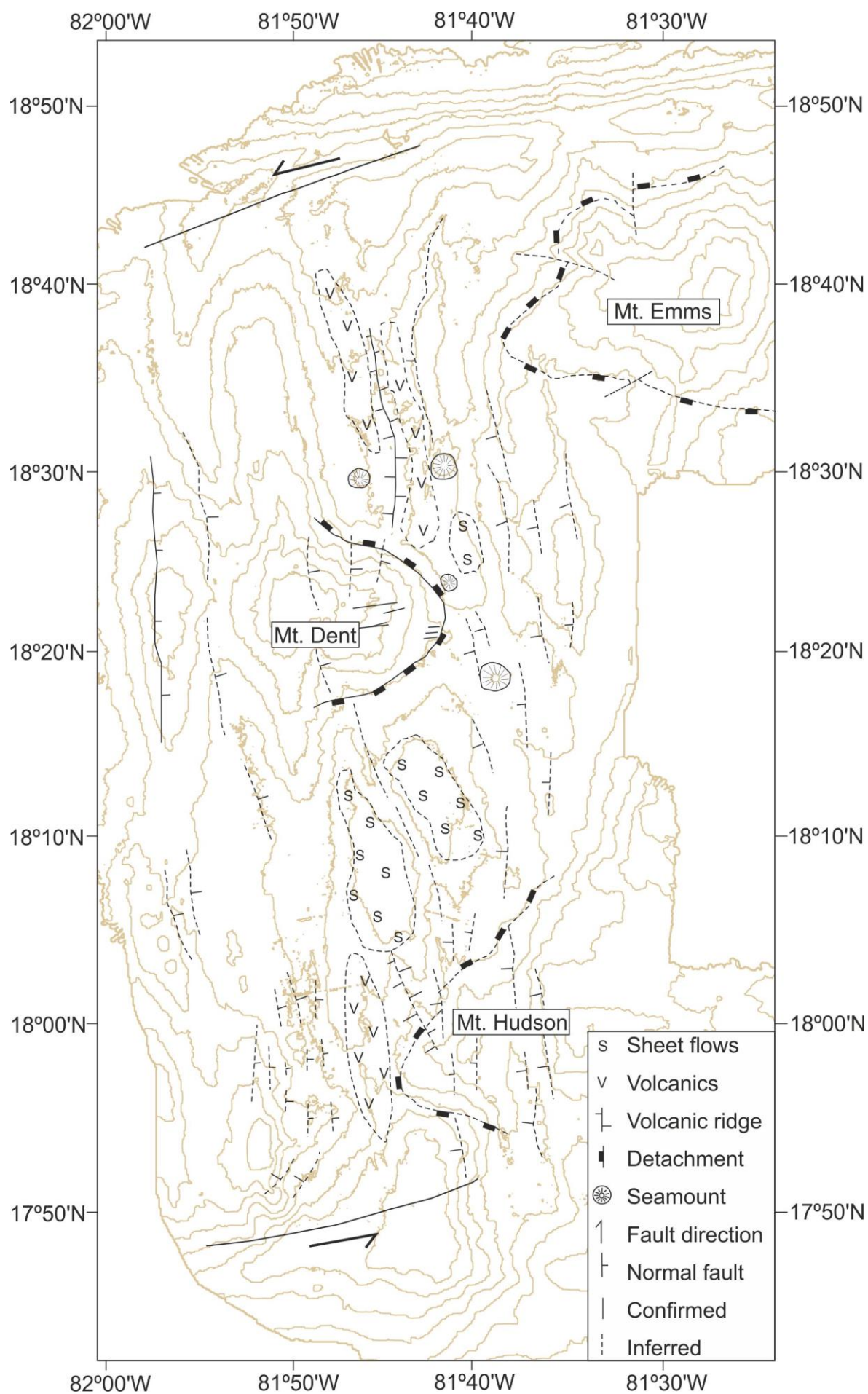


Figure 3.4: (On previous page) bathymetry and interpretive tectonics of the MCR showing contours at 500 metre spacing. Names of the OCC's are after Cheadle et al., 2012. The MCR is segmented into two by the Mt. Dent OCC. The northern segment is characterised by pillow basalts, a few seamounts, and the Mt. Emms OCC. The northern half of the southern segment features deep basins interpreted as sheet flows, with a ridge of tectonic origin. The southern half is more similar to the northern segment, and is dominated by hummocky pillow basalts and a young AVR (Hayman et al., 2011; Searle, 2012).

3.3.2. Northern segment of the Mid-Cayman Rise

Previous studies and recovered samples: The eastern flank of the northern segment on the Mid-Cayman Rise is dominated by the extinct Mt. Emms OCC (Cheadle et al., 2012), which, at its shallowest point 30 km off axis from the AVR, peaks at a depth of ~1700 m. Dredged samples recovered from this region consist predominantly of gabbros with minor ultramafics (Figure 3.3; Hayman et al., 2011). The gabbros commonly show recrystallisation textures within plagioclase, and occasionally display kink banding within twins. Olivine within recovered gabbros and peridotite is extensively replaced by serpentine (Hayman et al., 2011).

Rocks dredged from the rift axis of the northern segment consist of fresh and weathered basalt and have a range of compositions (Elthon et al., 1995). The basalts from the AVR commonly show plagioclase phenocrysts, and no glassy outer layer. Pillow basalts and fragments recovered from seamounts show thin glassy margins, with plagioclase and minor olivine phenocrysts (Ballard et al., 1979; Hayman et al., 2011). The hummocky volcanics comprise pillows and fragments, plagioclase-phyric (up to 6% phenocrysts), vesicular basalts, with occasional glassy rims and Mn coatings (Ballard et al., 1979). Two samples recovered from the top of the faulted ridge to the east of the AVR have a brecciated texture (Ballard et al., 1979; Hayman et al., 2011).

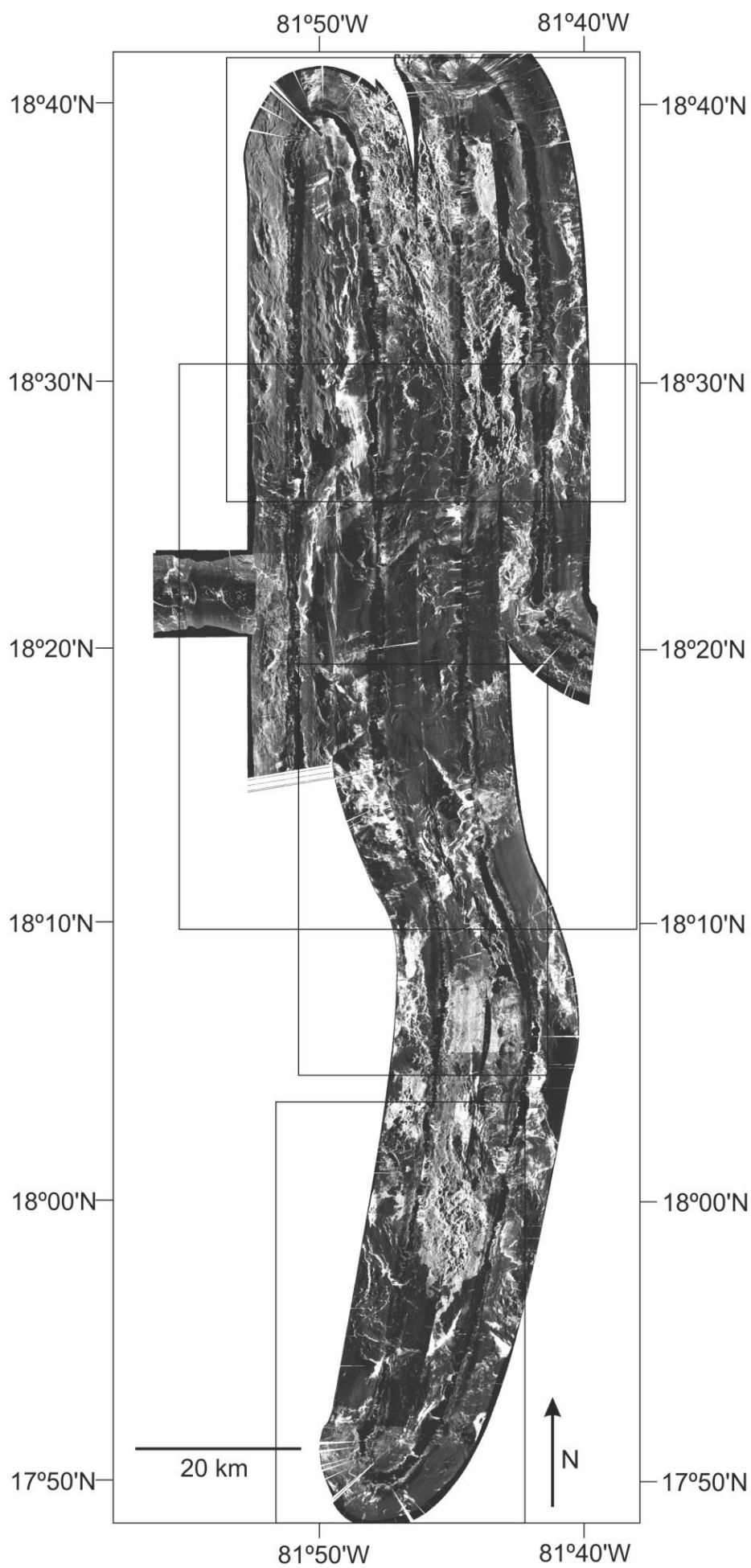


Figure 3.5: (On previous page) sidescan sonar of the MCR (white = high=backscatter) obtained by the towed-ocean bottom instrument (TOBI) during cruise JC044. Rectangles indicate areas for Figures 3.6-3.8, and Figure 3.10. In summary, from 18°40'N to 18°25'N the axial valley is dominated by a hummocky texture, indicating pillowed basalts. 18°25'N to 18°15'N indicates the area of Mt. Dent, and further south to 18°05'N are deep oceanic basins interpreted to be sheet flows. The southern end of the MCR is similar to the northern end, with pillow basalts and other volcanics defining a young AVR. Areas of low backscatter reflectance are inferred to be sediment covered, and are not marked on the oblique views shown in Figures 3.6-3.8 and Figure 3.10.

Sidescan and bathymetric data of the northern segment: The northern end of the MCR features an intersection with the Oriente Fault, where the seafloor is at >6700 m depth. The rift axis forming the northern segment of the MCR ranges between 13 and 18 km in width. Two prominent linear topographic highs are located within the northern segment and strike NNW-SSE. The eastern ridge rises to a depth of approximately 4700 m and is up to 3 km wide (Figure 3.6). The western ridge is the AVR of the northern segment along the MCR. This ridge is situated at a minimum depth of 4500 m, slightly shallower than the eastern ridge, and is up to 5 km wide.

A highly undulating and rugged topography, and a hummocky texture in the sidescan data across the AVR and the surrounding seafloor indicate the presence of basaltic pillow lavas situated to the east and west. The Beebe Vent Field is hosted on the eastern flank of the AVR, along a NE-SW volcanic spur (Webber et al., 2015). Progression of the AVR to the south is truncated by the intersection of the Mt. Dent OCC. The ridge to the east of the AVR was initially believed to be another volcanic ridge, but there is little evidence for any volcanic activity (Searle, 2012). Furthermore, the backscatter image reveals a smooth topography and minor amounts of striations along the west flank, which is far steeper than the eastern flank. This suggests that this linear, bathymetric feature is the edge of a faulted block, and not formed from volcanic activity.

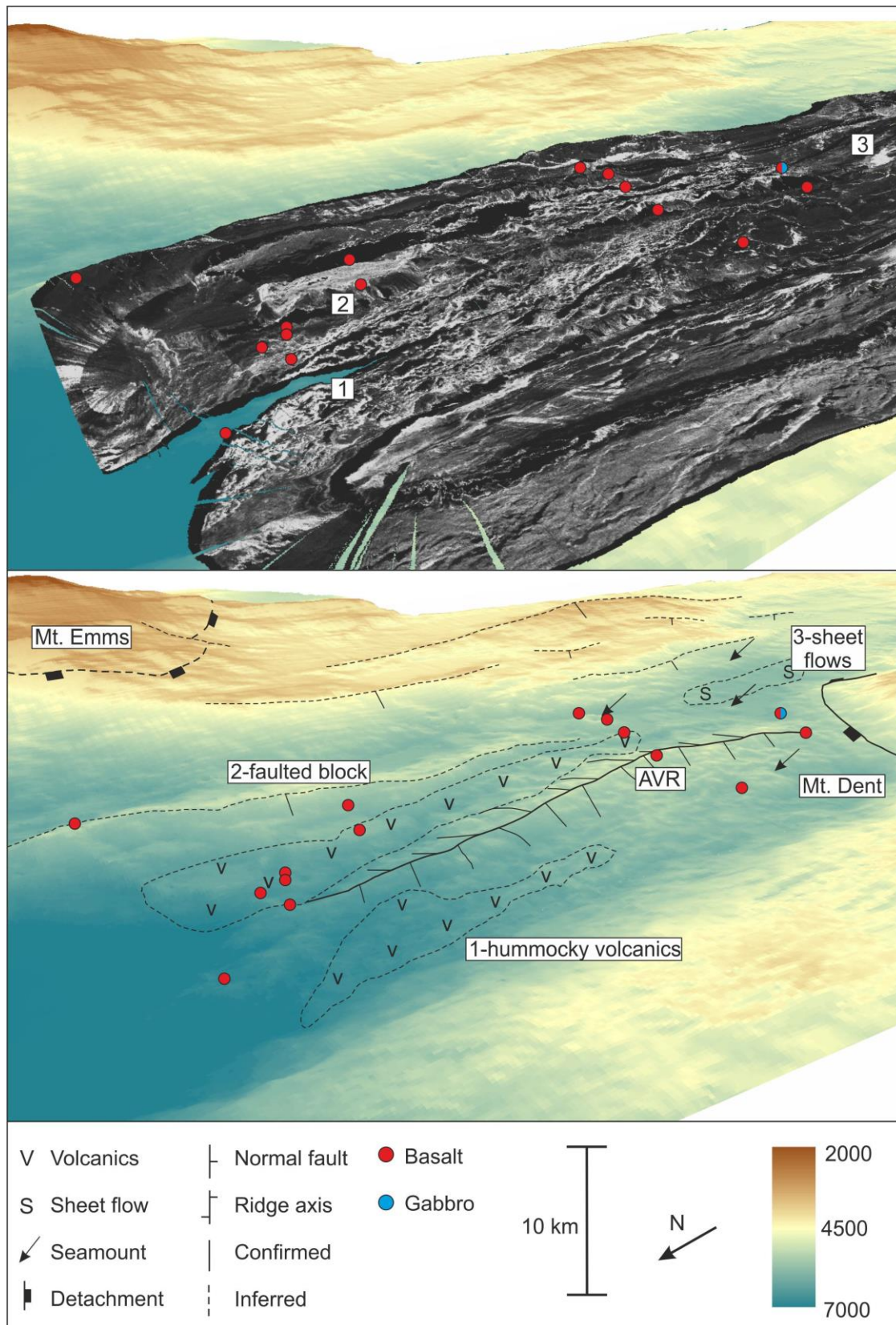


Figure 3.6: Sidescan sonar and interpretive tectonics of the northern segment of the MCR. Displays the detachment faults of the Mt. Emms and Mt. Dent OCC's, the AVR surrounding by hummocky volcanics, volcanic seamounts, and sheet flows within the axial valley. 1-hummocky texture of pillow basalts surrounding the AVR, 2-striations on faults surface of faulted block, 3-high reflectance smooth area depicting sheet flows.

The rift axis directly to the east of the base of Mt. Dent is characterised by slightly smoother topography and backscatter. Volcanic flows in this area are slightly less hummocky, indicating smaller amounts of basaltic pillows and more sheet-like flows with a lobate texture. Sediment cover is high in some places, indicated by the low backscatter. The Mt. Dent OCC is located on the western flank of the MCR and separates the northern and southern segments. The gabbro and peridotite basement of this tectonic feature is the host of the VDVF, and is discussed in more detail in section 3.4.

A few small seamounts occur along the northern segment of the MCR. The largest is located south of the central faulted block, and is ~2 km across and rises 350 m above the seafloor. The remainder of the seamounts range between 50 to 250 m high, and are between 0.5 and 1 km across.

3.3.3. Southern segment of the Mid Cayman Rise

Previous studies and samples recovered: Rocks recovered from the basins at the bottom of the axial valley trough main consist of variably altered aphyric basalts, some with thin glassy layers (Ballard et al., 1979). In one locality within the axial trough, serpentinite and gabbro were recovered along with dolerite and metamorphosed basalt (Figure 3.3; Ballard et al., 1979). The south east corner of the MCR features the extinct Mt. Hudson OCC (Cheadle et al., 2012), which peaks at a seawater depth of ~2500 m (Figure 3.8). The toe of the OCC has undergone normal and strike slip faulting since activity ceased. Submersible and dredge operations on the slopes reveal the dominant lithology is variably altered and metamorphosed gabbro, while serpentinised peridotite, including lherzolite, harzburgite and dunite, have also been recovered (Figure 3.3; Ballard et al., 1979).

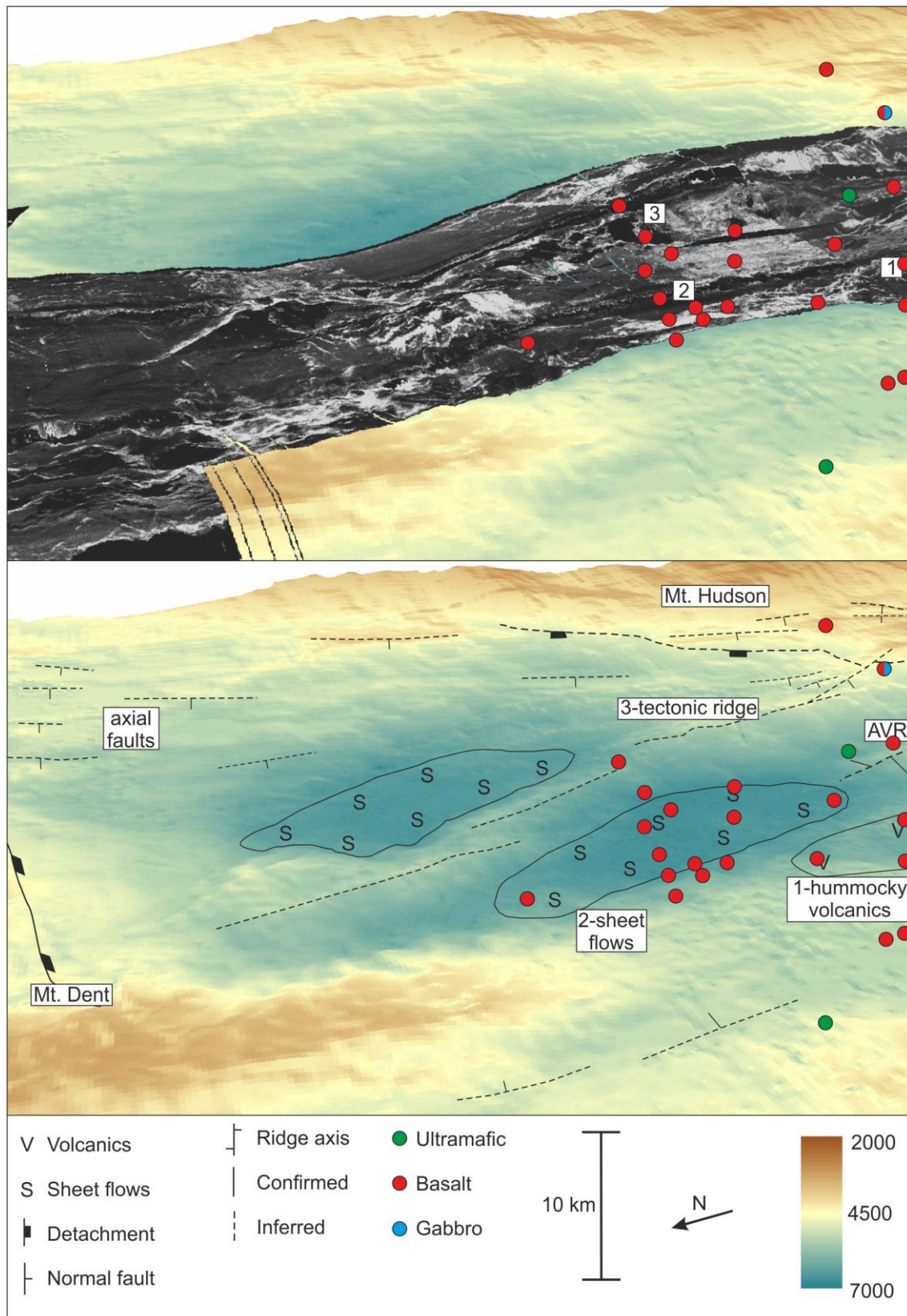


Figure 3.7: Sidescan sonar of the basin and tectonic ridge south of Mt. Dent on the southern segment of the MCR. Displays the Mt. Dent and Mt. Hudson OCC's, sheet flows, and northern part of the southern AVR. 1-hummocky volcanics on the west side of the AVR, 2-smooth, high reflectance (compared to sediment) areas depicting sheet flows, 3-tectonic ridge with little volcanic material and occasional striations.

Sidescan and bathymetric data of the southern segment: The northern half of the southern segment of the MCR is dominated by a NNW-SSE trending asymmetrical ridge within a large basin. Its northern end is terminated by the southern flank of Mt. Dent (Figure 3.7). The depth at the top of this ridge ranges between 5300 m to 4900 m. There is little volcanic terrain on top of the northern ridge and its flanks are not characterised by typical hummocky, pillow lavas. The backscatter data for this ridge show contrasting high and low reflectance areas due to changes in sediment cover thickness with little discernible texture. Occasional striations are visible (Figure 3.10), indicating that this ridge is most likely formed by tectonic processes as opposed to volcanic activity, but further sampling is required to confirm this assertion. Either side of the tectonic ridge are two bathymetrically flat, deep (up to 6000 m depth) areas with relatively low, but homogeneous backscatter. The acoustic reflectance here is greater than for the sediments, and the homogeneous nature of the backscatter is typical of volcanic sheet flows (Blondell and Murton, 1997). The sheet flow to the east of the ridge has an area of $\sim 60 \text{ km}^2$, while the western sheet flow is $\sim 45 \text{ km}^2$. The southern AVR is located to the south west of the asymmetric tectonic ridge and cuts across the Mt. Hudson OCC (Figure 3.8). The top of the AVR ranges between 5300 m and 5100 m deep and is relatively short in comparison to the northern AVR. There is little volcanic material to the east due to the intersection with Mt. Hudson, but the undulating topography and hummocky textures to the west, indicated by the sidescan sonar imagery, are similar to the volcanic seafloor surrounding the AVR at the northern segment of the MCR. The discontinuous AVRs and recovery of lower crust and upper mantle rocks indicates that volcanic layer across the length of the MCR is very thin, suggesting a low magma supply, characteristic of the ultra-slow spreading rate.

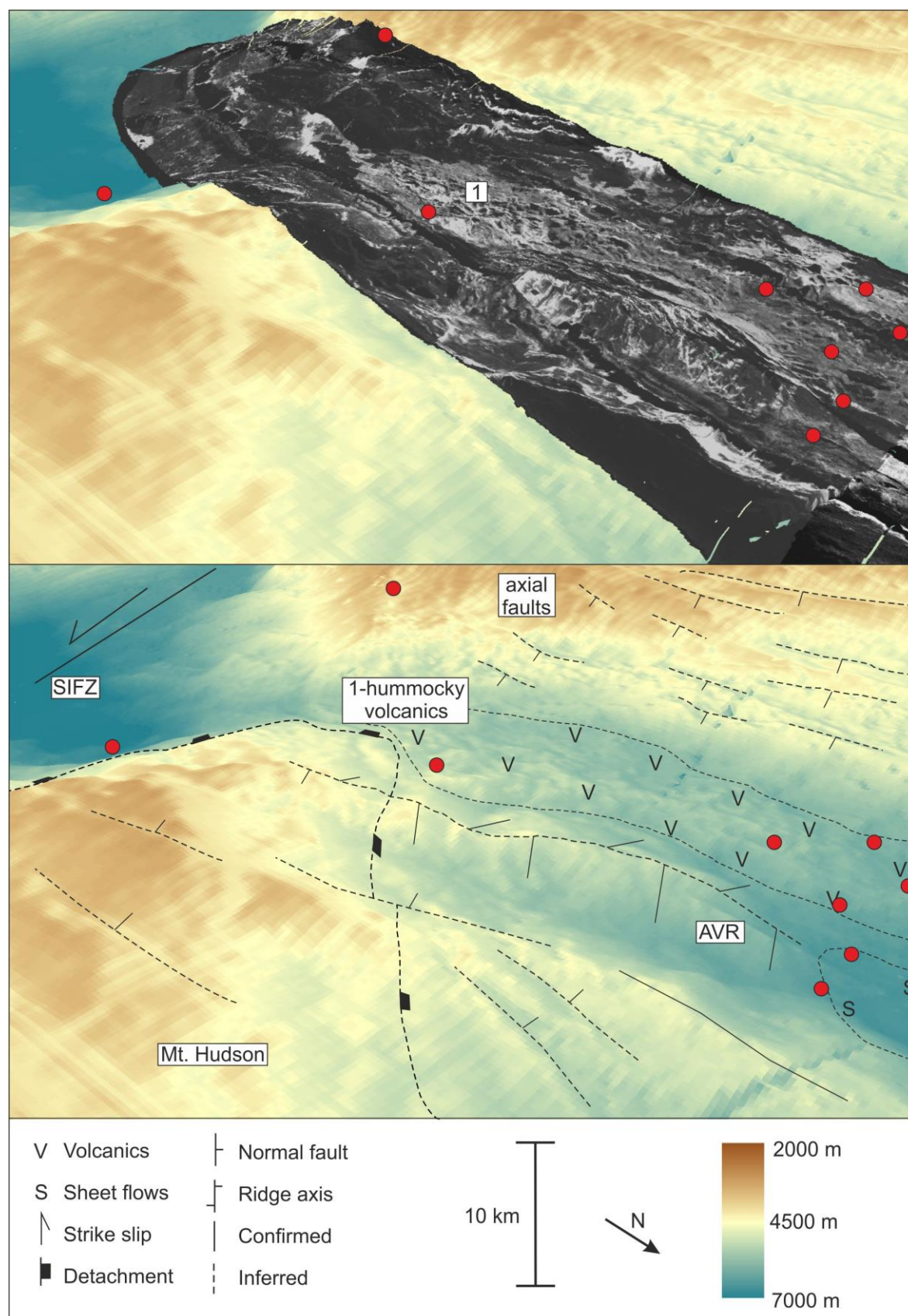


Figure 3.8: Sidescan sonar of the AVR and Mt. Hudson on the southern segment of the MCR. Displays the Mt. Hudson OCC, Swan Island Fracture Zone (SIFZ), southern AVR (displayed by the presence of hummocky volcanics) and axial faulting to the west of the AVR.

3.4. The Mount Dent oceanic core complex

This section will outline the regional geology of the Mt. Dent OCC, and describe the petrography of samples dredged during cruises *JC044* and *JC082*. Mt. Dent extends 21 km from its toe (termination zone) to the ridge defining its western extent (the breakaway zone), and is ~15 km across N-S at its widest point. The shallowest point of Mt. Dent is at 2000 m seawater depth, which is >3000 m shallower than the axial valley rift at the termination of the OCC (Figure 3.9). Usually, the fault surface forms a domed, convex-upward structure in between the termination of the core complex at the ridge axis, and the breakaway zone (Figure 3.9; Macleod et al., 2009). This surface commonly features corrugations on its surface, which form parallel to the spreading direction (Tucholke et al., 1998). Unfortunately there is a high proportion of sediment cover on Mt. Dent, indicated by the low degree of acoustic backscatter reflectance on the fault surface. Therefore, the characteristic features of detachment fault surfaces that are usually identifiable from backscatter data, (e.g. corrugations) are not widespread across the fault surface. However, rare, short corrugations occur sporadically, especially towards the southern flank of Mt Dent at the intersection with the axial rift (Figure 3.9). Axis-parallel extensional faults, with throws of ~10 m (estimated from bathymetric data) form towards the top of the domed structure of the OCC in response to the flexing of the cold lithosphere.

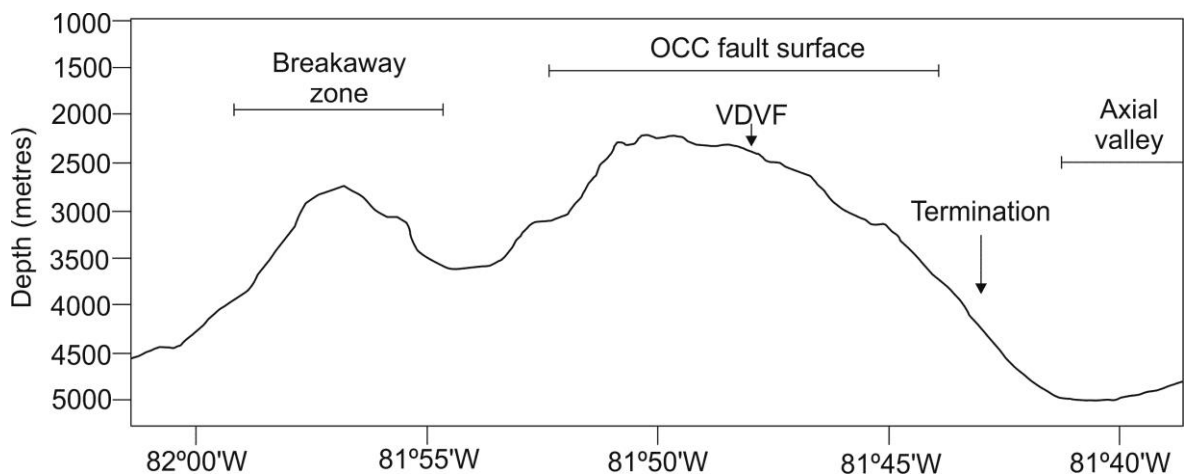


Figure 3.9: E-W cross section showing the topographic profile of Mt. Dent at a latitude of 18°22.5'N. Shows the location of the termination, the fault surface and the breakaway zone, which are outlined in the sidescan data in Figure 3.10.

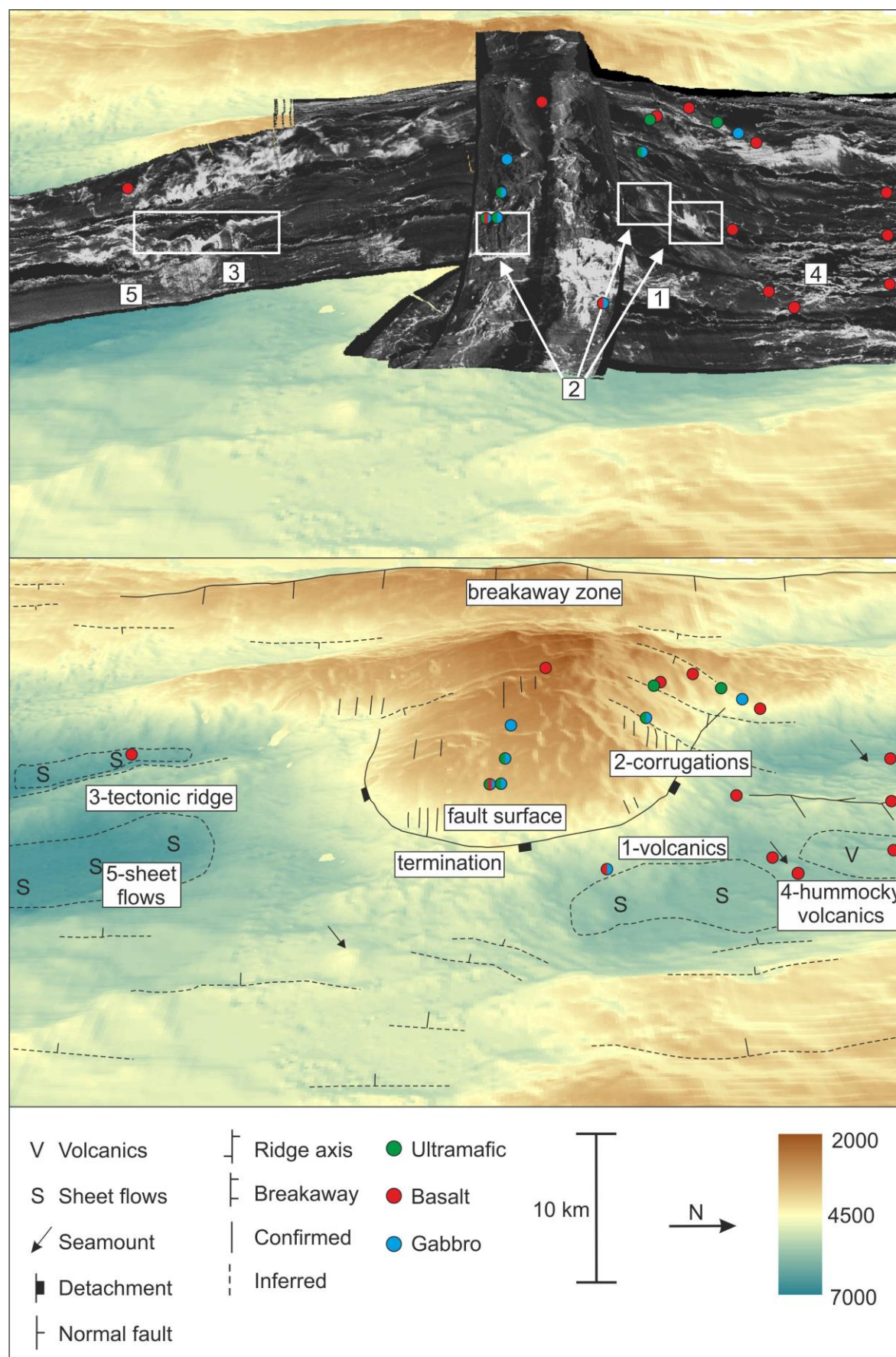


Figure 3.10: Sidescan sonar draped over bathymetry and viewed obliquely of the Mt. Dent OCC, showing corrugations and the fault surface. Displays the fault surface,

breakaway zone and termination of the OCC. 1-volcanic flows at the termination zone, indicating the intersection of the toe of the Mt. Dent OCC with the axial valley. 2-minor corrugations (labelled on the sidescan sonar data) on the fault surface of Mt. Dent. 3-tectonic ridge to the south of Mt. Dent; the rectangle outlines a few minor striations interpreted to occur from slip along the fault plane. 4-hummocky texture in pillow basalts to the east of the northern AVR. 5-deep basin either side of the tectonic ridge. Sidescan data here shows higher reflectance than would be expected from sediment cover, but a much smoother texture than either side of the two AVRs, suggesting the presence of basaltic sheet flows.

The morphology of the Mt. Dent OCC is similar to other studied oceanic detachment faults, such as those along the MAR (Smith et al., 2006). The lack of sediment cover of domed structures at 13°N on the MAR reveals extensive striations running perpendicular to the spreading direction (MacLeod et al., 2009), similar to the sporadic linear corrugations along the surface of Mt. Dent (Figure 3.10). Furthermore, the topography, dome shape, degree of dip and elevation to several hundreds of metres above the axial rift suggest similar processes of formation.

3.4.1. Submersible observations and samples from previous investigations to Mt. Dent

Outcrops of basement commonly show foliated surfaces, thin sediment cover and mass wasting of material from the top of fault scarps (Stroup and Fox, 1981). Mafic rocks recovered from the north side of Mt. Dent consist of fine-medium grained basalts and dolerites, with some plagioclase phenocrysts. They also form as relict clasts a few millimetres across within very fine grained, hydrothermally altered greenschists (Hayman et al., 2011). Gabbros recovered from along the north margin are highly deformed, and show mylonite and cataclastite textures (Hayman et al., 2011). Minerals present within them include clinopyroxene and plagioclase, replaced by sericite, amphibole and serpentine (Stroup and Fox, 1981). Submersible samples recovered from the central peak and slopes of the domed structure include gabbro, peridotite, fine grained mafic intrusives, and pillow basalts. In the gabbroic samples, olivine is magnesium rich ($>Fo_{72}$) and plagioclase composition ranges from An_{15} - An_{80} (Ito and Anderson, 1983). Calcium-bearing amphiboles, such as hornblende, are common and are either found as a corona enclosing clinopyroxene, or in veins and

fractures in gabbros. Alteration minerals include hornblende, talc, iddingsite and chlorite (Ito and Anderson, 1983). Ultramafic rocks are pervasively altered, with serpentine replacing much of the original mineralogy. The protoliths are inferred to be lherzolites, dunites and wehrlites (Stroup and Fox, 1981).

3.4.2. Dredged samples

Geophysical studies reveal that regionally Mt. Dent is of similar morphology and topography to OCC's elsewhere on the Mid-Atlantic and Southwest-Indian ridges e.g. (Cannat et al., 2006; Smith et al., 2006). Lithologies recovered from these localities include peridotite, serpentinites, troctolites, olivine gabbros and gabbros (Bach et al., 2004; Miranda and Dilek, 2010). The petrology of samples recovered from Mt. Dent (Figure 3.11) during cruises *JC044* and *JC082* are described in this section to determine the processes leading to the formation of the OCC.

Dredged rocks from the intersection of the Mt Dent detachment fault with the axial rift comprise small (<8 cm), angular fragments, with occasionally thin, ~1 mm manganese oxide coatings, or oxidised red-brown surfaces. Four fragments have a very smooth, soft (<2) outer surface with a greasy texture. In hand specimen, fresh, cut faces are grey, white and green in colour and range in grain size from fine to medium (Figure 3.11). These dredged fragments (total ~40) are dominantly greenschist facies altered mafic rocks, and include variably altered and mylonitised gabbro, and one sample each of peridotite and basalt.

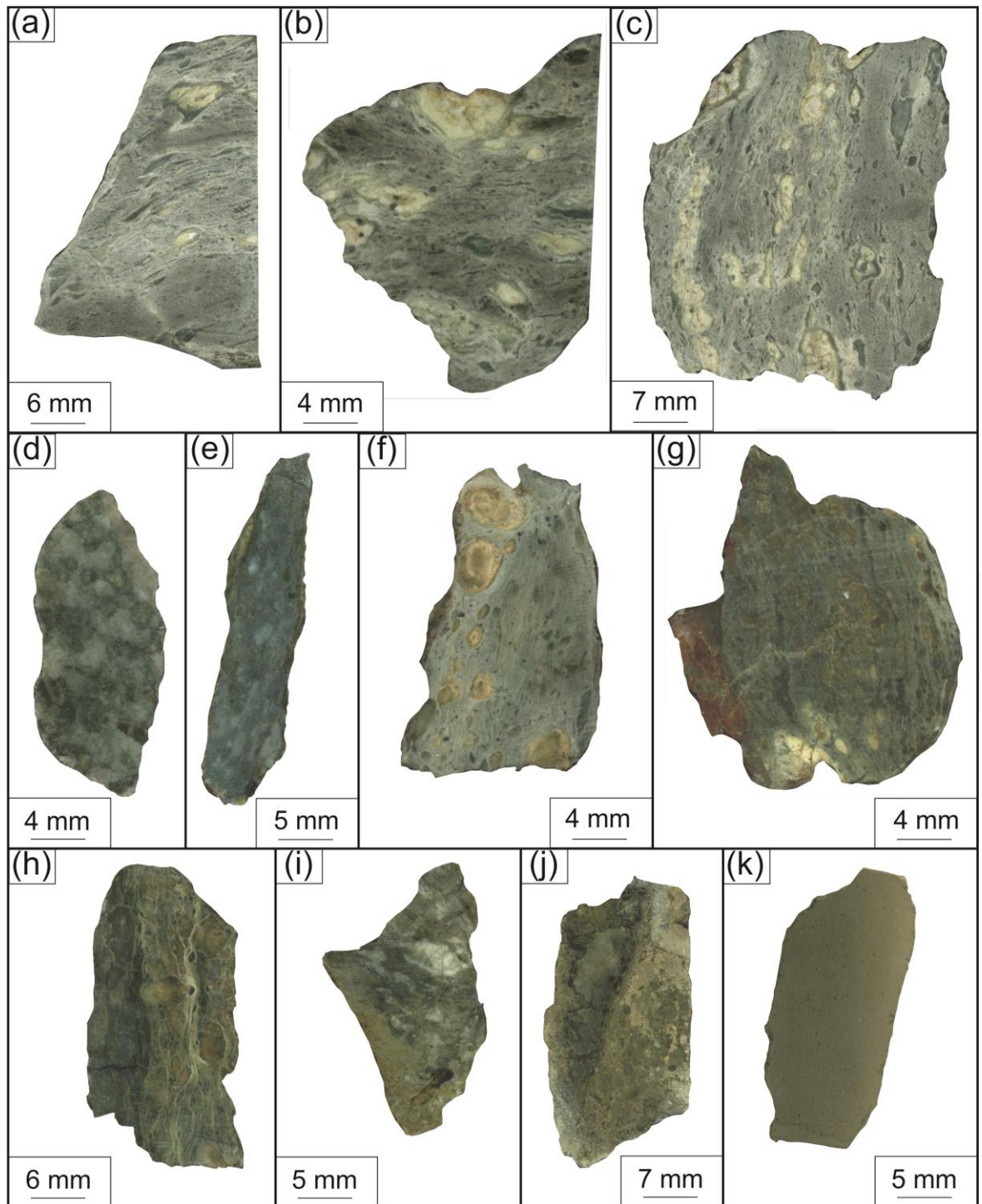


Figure 3.11: Scans of hand specimen fresh faces described in this study. Samples were recovered by dredging during JC082 from the toe of Mt. Dent. (a) JC082-D1-102: mylonitised gabbro (b) JC082-D1-102 : mylonitised gabbro (c) JC082-D1-104: mylonitised gabbro (d) JC082-D1-102: fresh gabbro with weak corona texture (e) JC082-D1-102: fresh gabbro (f) JC082-D1-106: weathered gabbro (g) JC082-D1-105: altered gabbro (h) JC082-D1-104: brecciated greenschist (i) JC082-D1-104: fresh gabbro with altered greenschist dyke (j) JC082-D1-104: brecciated dyke (k) JC082-D1-104: fine grained, altered dyke.

3.4.3. Primary phases and common alteration minerals in altered mafic rocks

Relict primary minerals include plagioclase and minor clinopyroxene (Figure 3.12; Figure 3.13; Figure 3.14). Plagioclase crystals are up to 4 mm across and twinning is commonly sheared and deformed. Interference colours are usually range from 1st order greys to yellows and twinsets are very narrow. The degree of internal deformation and alteration prevents Michel-Levy –based compositional estimates extinction angles, and the degree of alteration and lack of relict minerals leads to imprecise EDS analysis. However, some spectra were obtained. The composition of the plagioclases is more calcic in composition (An₆₀-An₇₀), but in most samples, plagioclase is completely replaced.

Clinopyroxene is extensively replaced and even less common than plagioclase. A few remnant phenocrysts show 2nd order interference colours and a subhedral, tabular habit (Figure 3.14). No completely fresh clinopyroxene grains were observed, and remnant phenocrysts feature clay-sized alteration along margins and fractures.

The most common minerals present in greenstones recovered from the toe of Mt. Dent are Mg-chlorite and amphiboles (Figure 3.12; Figure 3.13), which extensively replace primary igneous minerals. Chlorite regularly occurs as pseudomorphs of plagioclase up to 5 mm across, or reaction coronas on coarser grained feldspar crystals (e.g. ODP site 1309; Blackman et al., 2011), depending on the degree of alteration (Figure 3.15). Where replacement is incomplete, fine grained (<30 µm) chlorite occurs along fractures and veins of plagioclase and clinopyroxene. Fine grained aggregates of chlorite present as subhedral, colourless-pale green aggregates with dull grey interference colours. Individual grains are usually ~40 µm across, while coarser, more fibrous crystals can be up to 200 µm (Figure 3.16).

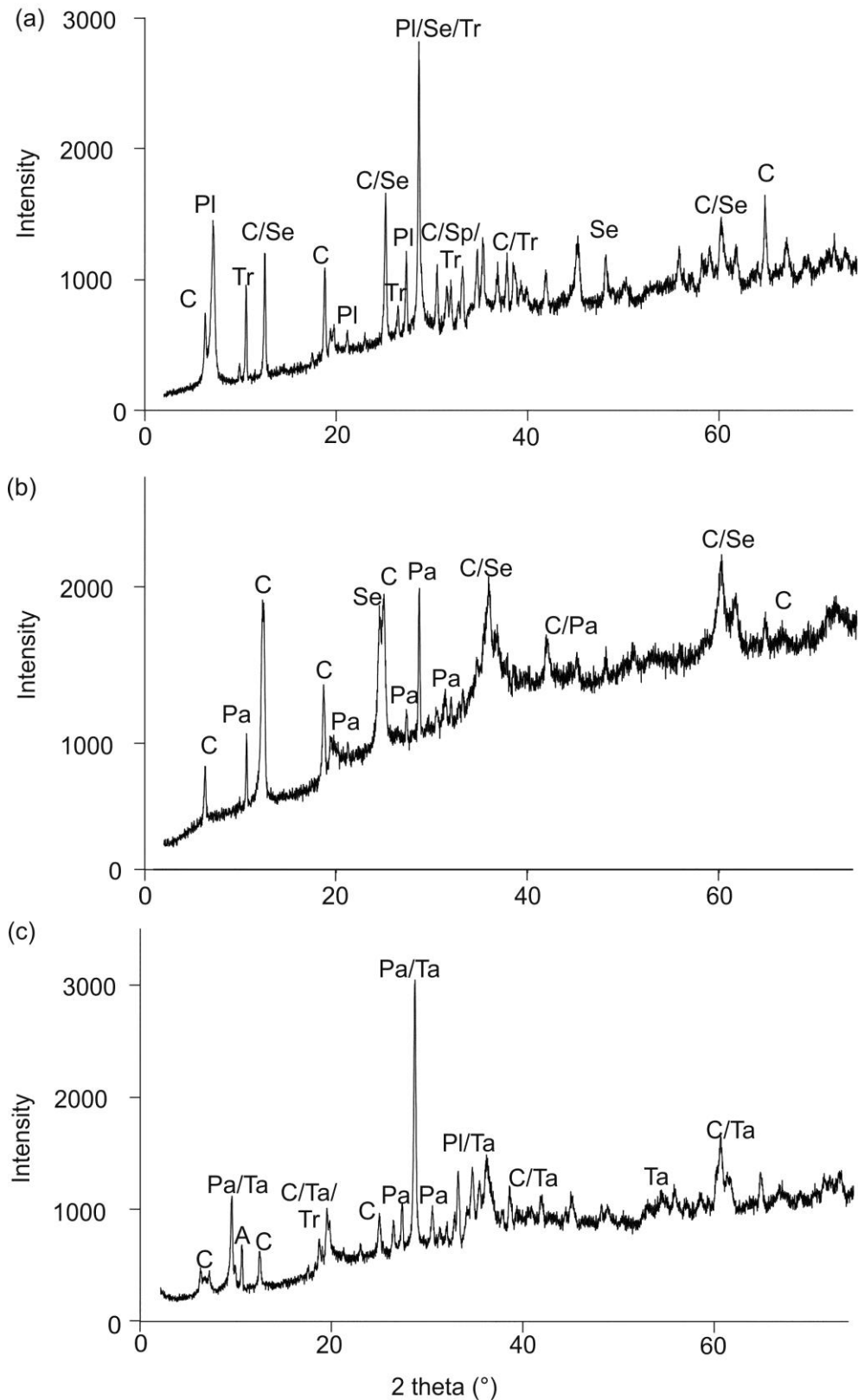


Figure 3.12: X-Ray diffraction (XRD) of dredged samples recovered from the toe of Mt. Dent. (a) JC082-D1-102: greenschist facies gabbro (b) JC082-D1-103: amphibolite facies gabbro (c) JC082-D1-104: altered greenstone inferred to be from the fault surface. Mineral abbreviations: a=actinolite; c=chlorite; pa=pargasite; pl=plagioclase; se=serpentine; ta=talc; tr=tremolite.

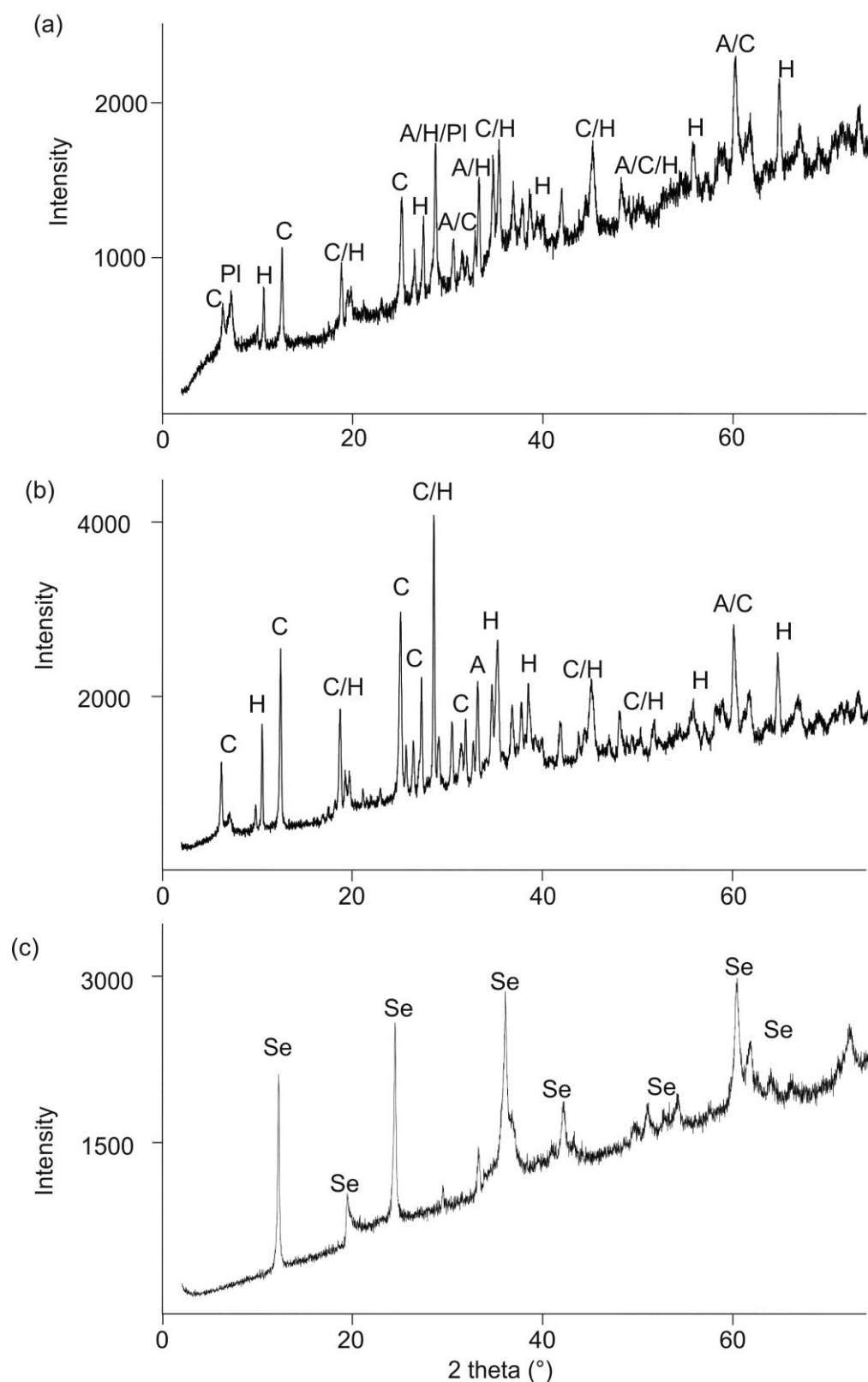


Figure 3.13: XRD of dredged samples from the toe of Mt. Dent. (a) JC082-D1-105: altered gabbro (b) JC082-D1-106: altered, hornblende-bearing gabbro (c) JC044-3A: serpentinised dunite. Mineral abbreviations: a=actinolite; c=chlorite; h=hornblende; pl=plagioclase; se=serpentine.

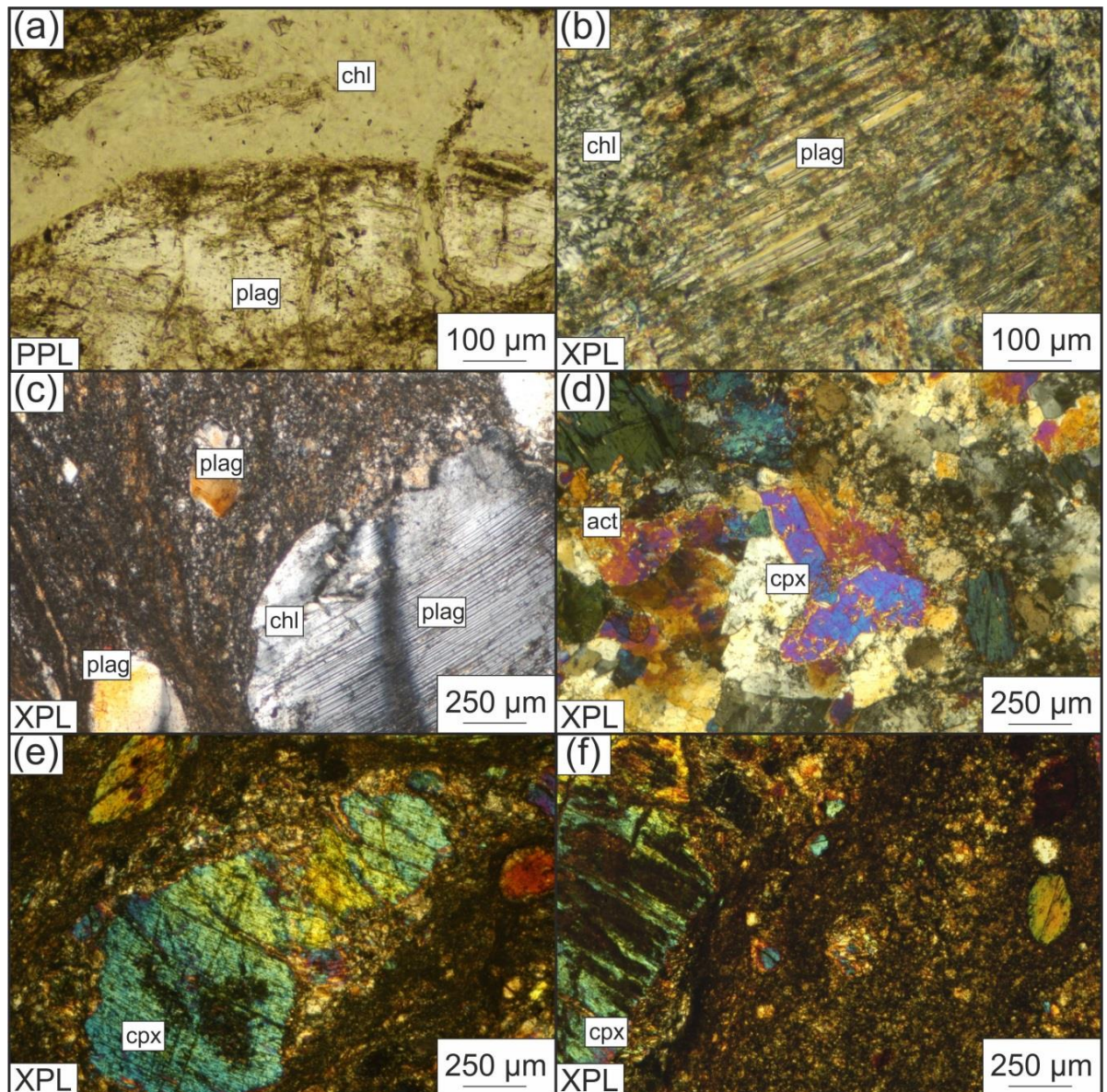


Figure 3.14: Photomicrographs of remnant plagioclase and clinopyroxene in dredged samples. The protolith of these samples is gabbro, and these show alteration to amphibole and chlorite. (a) JC082-D1-105: pale green chlorite along the edge of a plagioclase crystal (b) JC082-D1-106: fine grained chlorite alteration of plagioclase (c) JC082-D1-104: remnant plagioclase crystal in altered finer grained groundmass; chlorite can be seen along the fracture in the top left of the crystal (d) JC082-D1-106: replacement of clinopyroxene by amphibole along the margins of grains (e) JC082-D1-105: clinopyroxene within fine-grained groundmass (f) JC082-D1-105: alteration of clinopyroxene set in fine grained altered matrix of chlorite and amphibole. Mineral abbreviations: act = actinolite, chl = chlorite, cpx = clinopyroxene, plag = plagioclase. Abbreviations for type of image are PPL = plane polarised light, XPL = cross polarised light. These abbreviations are consistent throughout this chapter.

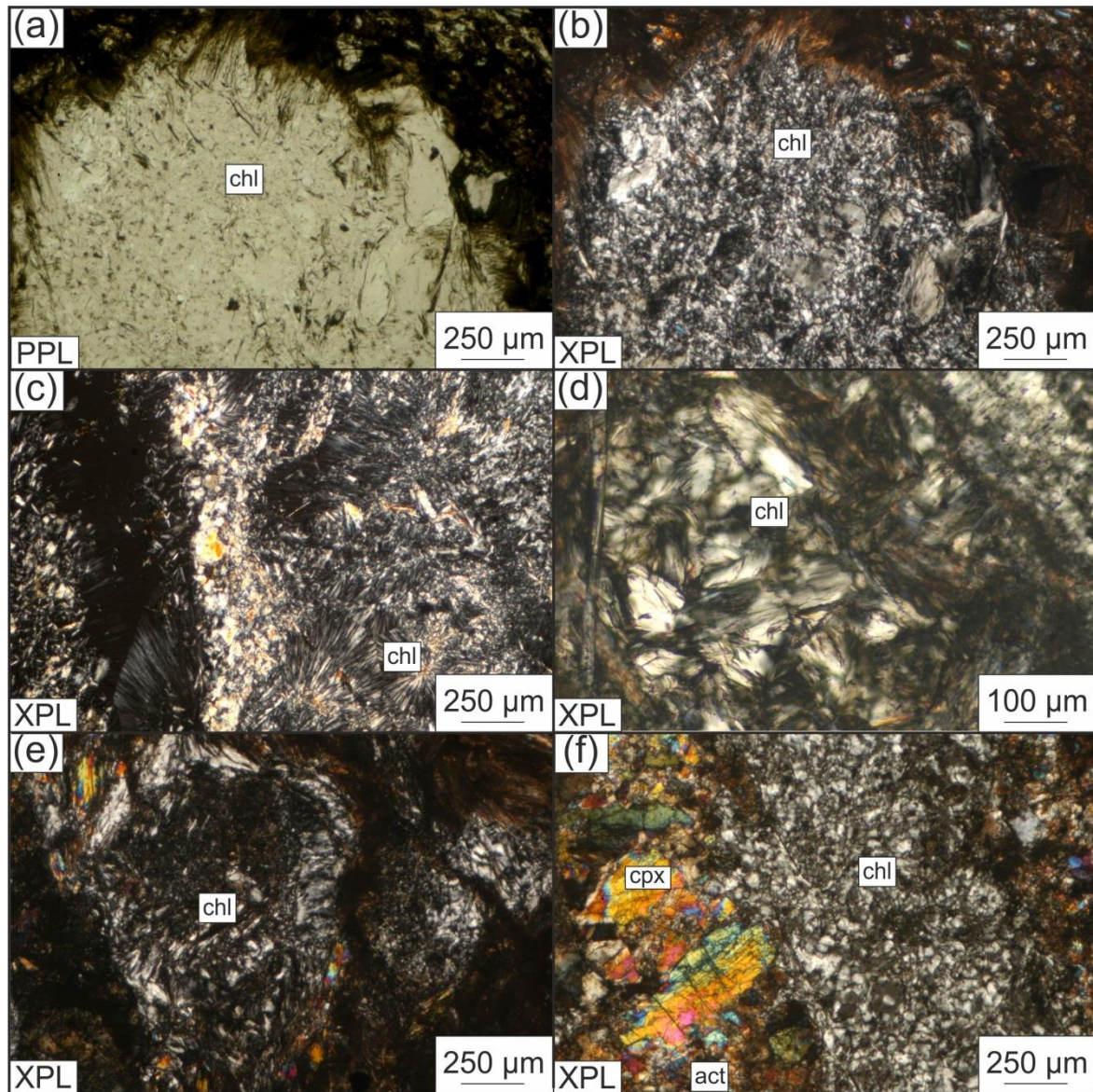


Figure 3.15: Photomicrographs of chlorite occurrences in dredged samples. Chlorite is observed to be the most common mineral after plagioclase and often shows complete replacement of individual crystals. (a) JC082-D1-102: and (b) chlorite pseudomorph after coarse grained plagioclase. Some acicular amphibole growth is visible at the top of the grain (c) JC082-D1-106: radial, fibrous chlorite within a fine grained groundmass (d) JC082-D1-104: interlocking, semi-fibrous chlorite in centre of an altered plagioclase crystal (e) JC082-D1-102: chlorite within a deformed plagioclase grain (f) JC082-D1-102: chlorite pseudomorph after plagioclase, with fine grained amphibole replacing partially recrystallised clinopyroxene on the left hand side. Mineral abbreviations: chl = chlorite, cpx = clinopyroxene

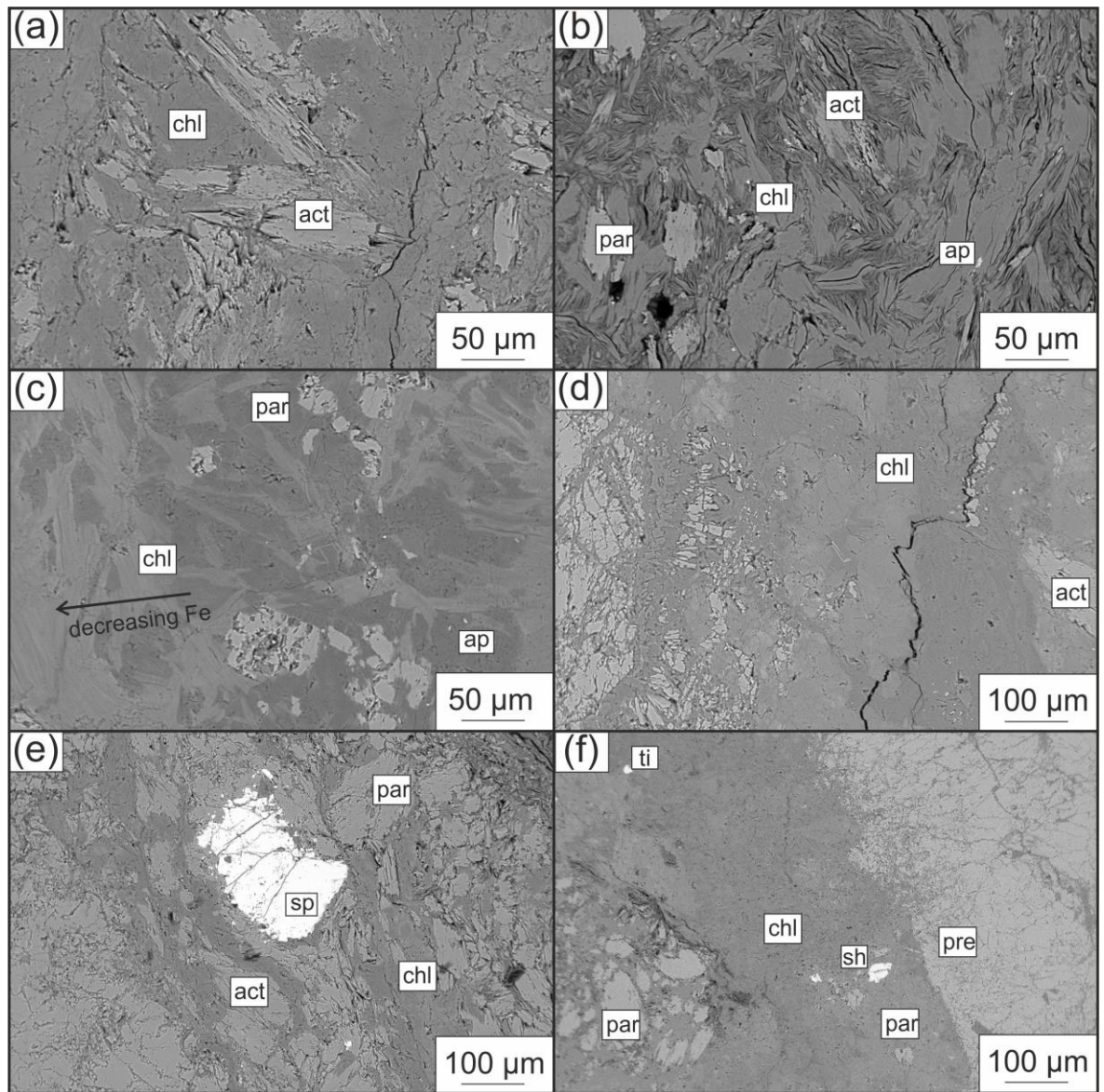


Figure 3.16: SEM images of common minerals within the groundmass. Images are taken where mineral identification was difficult in transmitted light due to the grain size. Groundmass is dominated by amphiboles and chlorite that have completely replaced plagioclase and clinopyroxene (a) JC082-D1-102: chlorite-actinolite groundmass (b) JC082-D1-102: fibrous amphibolite facies groundmass (c) JC082-D1-105: chlorite and pargasite groundmass (d) JC082-D1-102: chlorite and actinolite with remnant clinopyroxene (e) JC082-D1-102: Cr-spinel grain in amphibole and chlorite groundmass (f) JC082-D1-102: pargasite and chlorite, with accessory sphene; the right hand side of the image consists of a vein of prehnite. Mineral abbreviations: act=actinolite, ap=apatite, chl=chlorite, par=pargasite, pre=prehnite, sh = sphene, sp = spinel.

Amphibole phases present within altered mafics include actinolite, tremolite, pargasite and hornblende (Figure 3.12; Figure 3.13; Figure 3.17). Actinolite and tremolite form aggregates of fine grained (30-100 μm), colourless-pale green fibrous crystals completely replacing pyroxene. The actinolite crystals are slightly more acicular, pale green in PPL and show strong pleochroism. Individual crystals can be up to 0.5 mm long, and 50 μm wide. Tremolite occurs as interlocking crystals along with actinolite, and as prominent acicular growths within chlorite aggregates depending on the magnesium content of the protolith. Hornblende occurs as sub-rounded, euhedral/subhedral crystals in a fine grained matrix up to 0.5 mm across (Figure 3.17; Figure 3.18). Cleavage planes are occasionally offset, especially in mylonitised samples, indicating hornblende formed before brittle deformation. Pargasite occurs as 100-200 μm crystals within the groundmass and is light brown-green in PPL, with maximum 2nd order interference colours. It is usually associated with chlorite pseudomorphs, but is also seen along with actinolite in the groundmass (Figure 3.17; Figure 3.18). Compositions of hornblende and pargasite show a scattered trend in composition and a majority of crystals are in the Mg-hornblende are pargasitic hornblende fields (Figure 3.19).

Less common minerals that occur within the groundmass or replacing primary igneous minerals in mafic rocks include prehnite, serpentine and talc (Figure 3.19). Prehnite occurs as interlocking, sometimes radial, euhedral masses with grainsizes up to 300 μm across. It occurs either as interstitial grains within a finer matrix, or as veins up to 5 mm across. Serpentine occurs as mesh textured areas of up to 3 mm cross, and form from complete replacement of olivine (Figure 3.20).

The groundmass in a majority of samples is very fine grained (<20 μm), and ranges from colourless, pale green to light-dark brown (Figure 3.18). SEM analysis indicates that this groundmass consists of magnesium, calcium and iron bearing aluminosilicates such as chlorite, amphiboles and minor plagioclase (Figure 3.17).

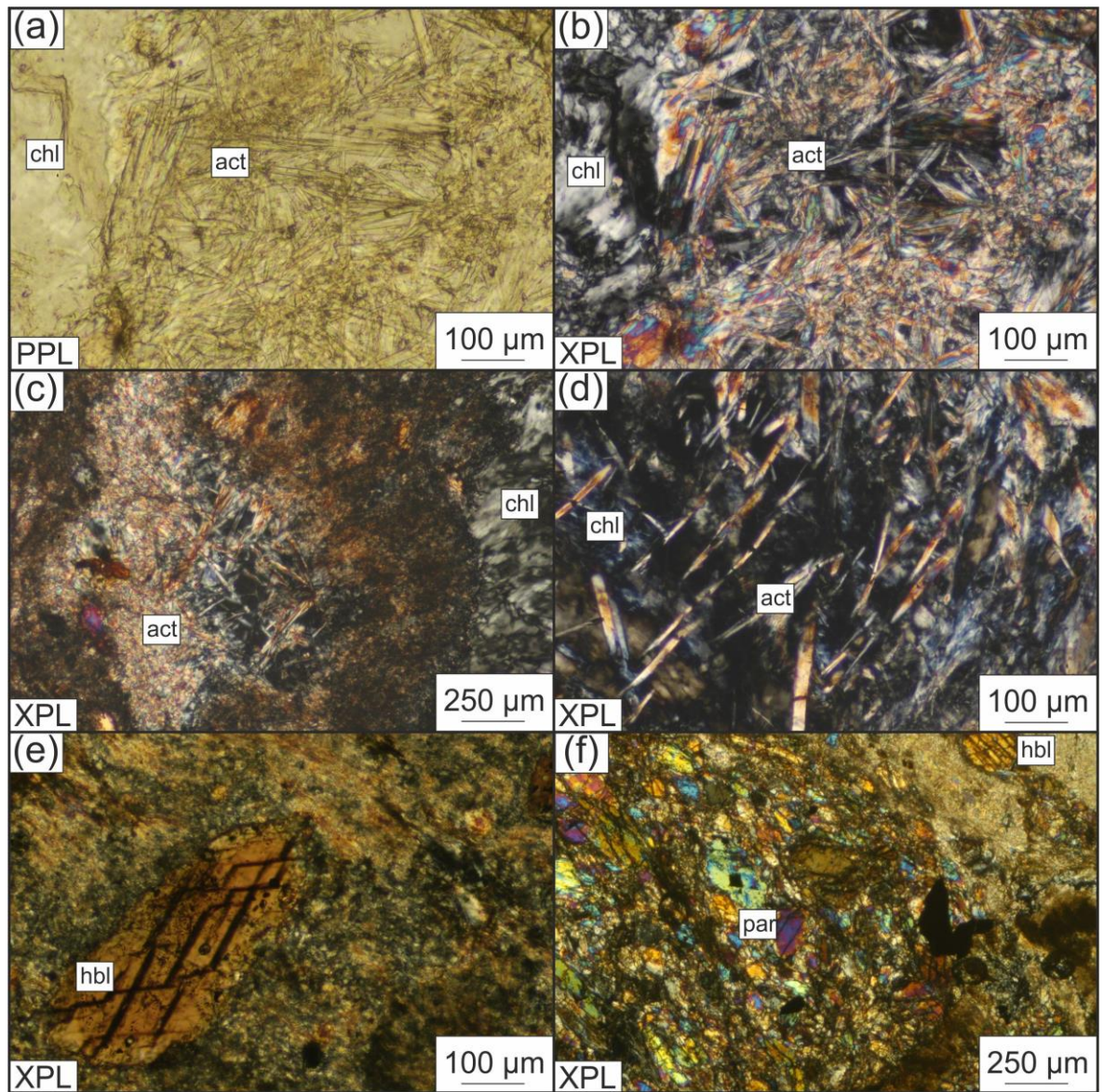


Figure 3.17: Photomicrographs of amphiboles present in dredged samples. The most common form of amphibole is pseudomorphic replacement of clinopyroxene by actinolite. Chlorite and actinolite regularly occur intergrown on the margins of primary plagioclase and clinopyroxene, indicative of amphibolite or upper greenschist facies metamorphism (a) JC082-D1-106: and (b), acicular, fine grained actinolite-tremolite pseudomorphs after clinopyroxene (c) JC082-D1-105: and (d) JC082-D1-104: actinolite occurring with chlorite and hornblende within the groundmass; the right side of image (d) shows chlorite (e) JC082-D1-106: hornblende crystal with offset cleavage planes within the altered groundmass (f) JC082-D1-105: pargasite (2nd order interference mineral) within the groundmass; a couple of grains of brown hornblende and fine grained chlorite replacing plagioclase also occur. Mineral abbreviations: act = actinolite, chl = chlorite, hbl = hornblende, par = pargasite

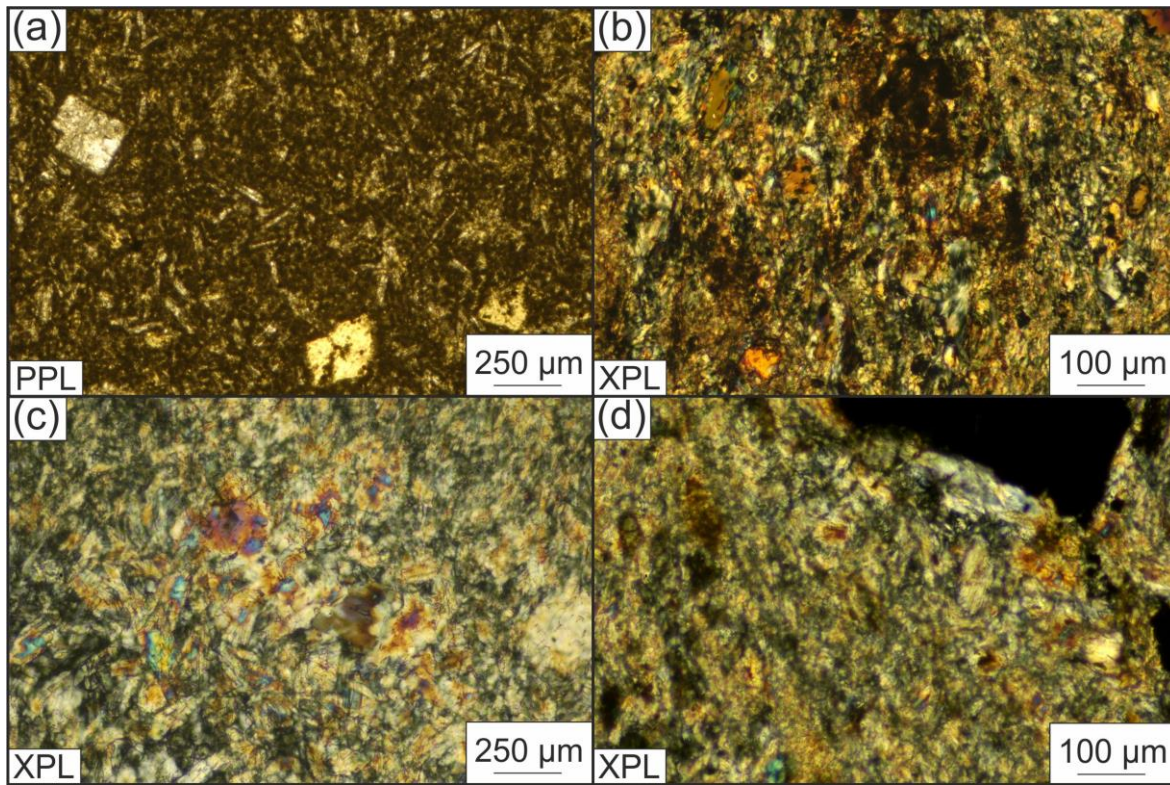


Figure 3.18: Groundmass within dredged samples. Images acquired using transmitted light microscopy (a) JC082-D1-104: plagioclase phenocrysts in a very fine grained matrix. This image is taken from the only sample of basalt, and is inferred to be a dyke (b) JC082-D1-104 and (c) JC082-D1-106: chlorite and actinolite groundmass, with some remnant clinopyroxene (d) JC082-D1-104: fine grained ($\sim 50 \mu\text{m}$) altered matrix containing chlorite and amphiboles (more detail is visible in SEM images in Figure 3.16).

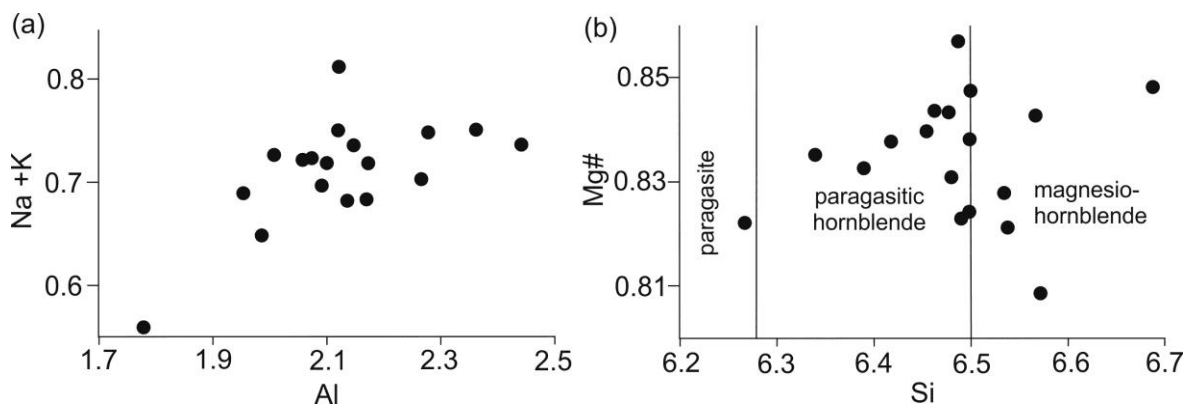


Figure 3.19: Chemistry of hornblende and pargasite. (a) Total Al vs Na+K (b) Si vs Mg# number indicating the composition of hornblende and paragenitic hornblende. All analyses are taken from gabbro lithologies and calculated using 23 oxygens in the formula.

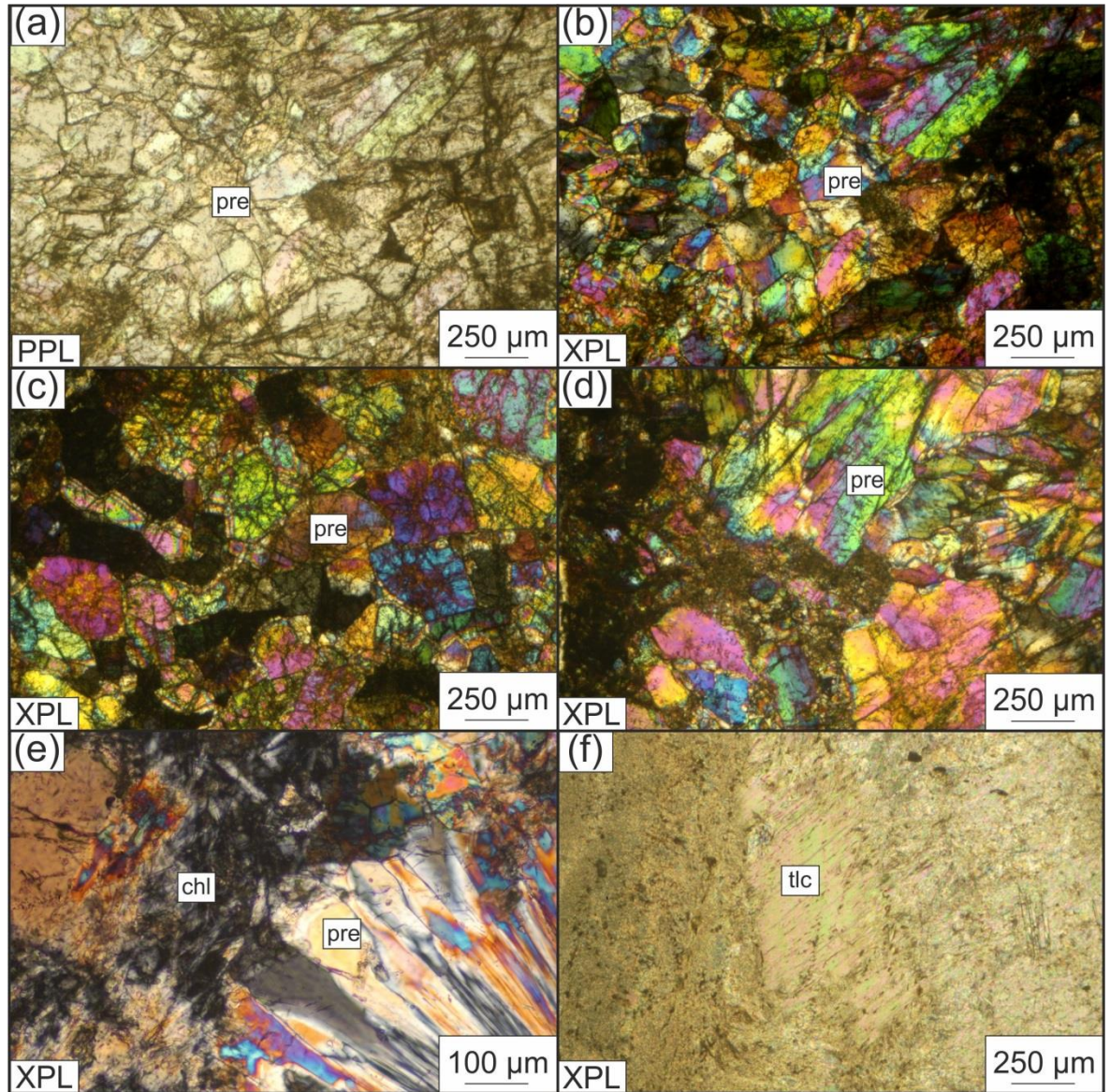


Figure 3.20: Photomicrographs of talc and prehnite forms within dredged samples. (a) JC082-D1-102: (b) JC082-D1-102: (c) JC082-D1-102: (d) JC082-D1-102: interlocking prehnite crystals within a late-stage vein. Vein cross-cuts previous amphibolite and greenschist facies minerals such as actinolite and chlorite (e) JC082-D1-106: radial crystals of prehnite within the groundmass; the left side of the image consists of fine grained chlorite; prehnite formation in the groundmass overprints previous chlorite alteration due to retrograde alteration at lower pressure and temperature conditions (f) JC082-D1-104: fibrous talc along with minor amounts of amphibole; the grain size of talc is much coarser in the centre of the image, meaning characteristic 3rd order interference colours are more visible. Mineral abbreviations: chl = chlorite, pre = prehnite, tlc = talc.

3.4.4. Altered ultramafics

There is one sample of serpentinised peridotite recovered during *JC044* that shows the characteristic mesh texture and complete replacement of olivine (Figure 3.21). The mineralogy consists dominantly of serpentine, with magnetite and accessory Cr-spinel and pentlandite. Serpentine is fine grained and divided by the presence of thin bands of magnetite. The edges of serpentine areas are colourless in PPL and gradually turn into dark brown towards the centre. SEM analysis indicates that the iron content of the core of serpentine areas is higher (2-4.5 wt. %) than the outer margins (1-2 wt. %; Figure 3.21), indicating a greater degree of serpentinisation towards the margin, (Bach et al., 2006), and an absence of brucite.

3.4.5. Accessory minerals

Altered mafics: accessory phases that are observed within the samples of altered mafics are magnetite, rutile, sphene and apatite, with minor Cr-spinel. Magnetite occurs as ~30 µm grains disseminated throughout the groundmass. Sphene, apatite and rutile were all confirmed using SEM analysis and are <25 µm across. Sphene is observed in one sample of altered mafics, and occurs with chlorite in the fine grained groundmass, whereas apatite is usually found on the margins of chlorite pseudomorphs (Figure 3.16). Rutile occurs on the margins between pargasite and chlorite intergrowths, and has a grain size of up to 10 µm. Cr-spinel forms subhedral, hexagonal and rounded crystals, which are up to 400 µm across. They are opaque in thin section and are generally disseminated throughout the fine grained groundmass matrix. Elemental concentrations in mafic spinels are 22-28 wt. % Cr, 16-21 wt. % Fe²⁺, 3-7 wt. % Mg and 12-17 wt. % Al, with a couple of grains showing up to 0.5 wt. % Zn (Table 3.1). Cr# (where $Cr\# = Cr/(Cr+Al)$) has values ranging from 0.58-0.69 (average of 0.64) and Mg# (where $Mg\# = Mg/(Fe^{2+}+Mg)$) values are 0.15-0.29 (Table 3.2).

Serpentinised peridotite: accessory minerals in the serpentinised peridotite are magnetite, Cr-spinel and pentlandite (Figure 3.16; Figure 3.21). Magnetite occurs on the margins of mesh textured serpentine areas in altered ultramafics at grain sizes of <30 µm (Figure 3.21). Cr-spinel occurs as hexagonal grains up to 1 mm across.

Pentlandite forms as small inclusions within Cr-spinel and has a grain size of $<10\ \mu\text{m}$. Elemental concentrations within the Cr-spinel are 22-25 wt. % Cr, 13-16 wt. % Fe^{2+} , 6-8 wt. % Mg, and 14-16 wt. % Al (Table 3.1). The Cr# in serpentinised peridotite is similar to the values observed in the altered mafics, and range from 0.60-0.64 (average of 0.61). The Mg# is slightly higher, and has values of 0.31-0.37 (Table 3.2). #Cr is high compared to other abyssal dunites, but is within the ranges observed (Dick and Bullen, 1984). The Mg numbers are unusually low for an ultramafic lithology located at a MOR, e.g. (Dick and Bullen, 1984), and this can arise from hydrothermal alteration e.g. (Kamenetsky et al. 2001; Ismail, 2009). This is because Mg and Al are mobilised by hydrothermal fluids, which results in the precipitation of secondary chlorite and amphibole, giving an increase of #Cr and a decrease in #Mg in spinel (Mellini et. al, 2005).

3.4.6. Textures and alteration at Mt. Dent

The most commonly observed relict primary minerals within samples from the toe of Mt. Dent are porphyroclasts of plagioclase and clinopyroxene. The alteration degree in most samples is $>80\%$, meaning that primary igneous textures are rarely observed, and no completely fresh plagioclase or clinopyroxene was observed. All the alignment and banding of mineral grains in samples recovered by dredging during *JC082* is metamorphic in origin and described below.

Mylonite textures are common in gabbroic samples. Coarser crystals are tapered out into lozenge shapes grains but the groundmass is deformed into alternate darker and lighter bands up to $300\ \mu\text{m}$ across that are generally discontinuous even at thin section scale (Figure 3.22). Lighter bands consist of fine grained, secondary quartz and feldspar at grainsizes up to $100\ \mu\text{m}$. The darker bands are generally thinner, and consist predominantly of very fine grained amphibole. The metamorphic fabric diverts around large, altered plagioclase crystals with deformed dislocations and kink banding in albite twinning (Figure 3.22). Recrystallisation of coarse plagioclase and occasionally clinopyroxene occurs on the margins of porphyroclasts, and occasionally, strain shadows of quartz and feldspar are observed.

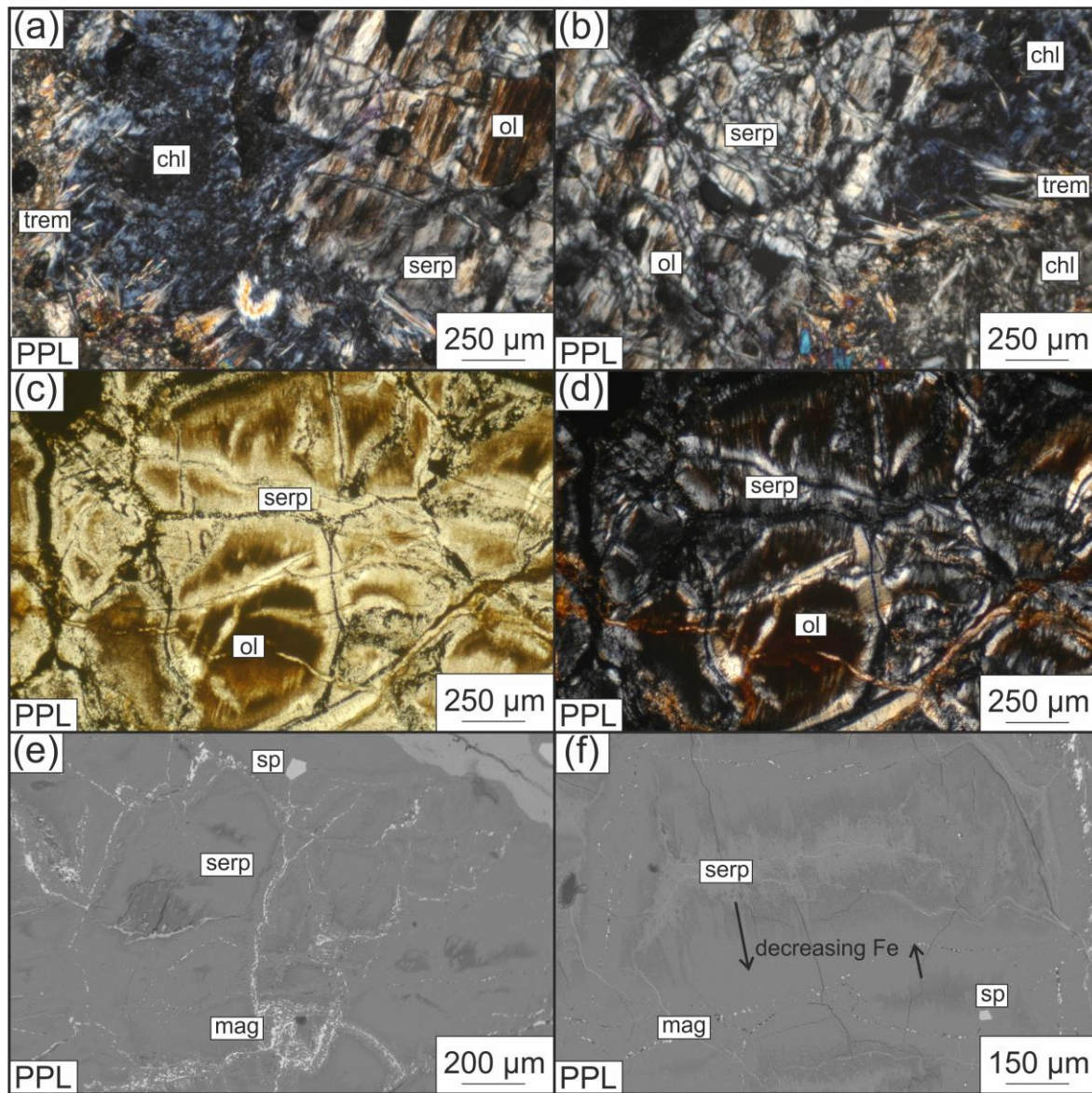


Figure 3.21: Photomicrographs and SEM images of serpentine occurrences within dredged samples (a) JC082-D1-106: and (b) JC082-D1-106: mesh textured serpentine after olivine within gabbros; the anomalous blue colours are from coarse grained chlorite replacing plagioclase (c) JC044-3A and (d) JC044-3A: mesh texture serpentine with magnetite (opaque bands) in serpentinised peridotite, with some remnant olivine (e) JC044-3A: serpentine with magnetite occurring on the margins of silicate areas. The top right hand corner shows a thin vein of calcite (f) JC044-3A : elemental iron concentrations changing within serpentine; the central areas contain 1-2 wt.% less Fe than the outer rim. Mineral abbreviations: chl = chlorite, mag = magnetite, ol = olivine, serp = serpentine, sp = Cr-spinel; trem = tremolite.

Sample	Analysis	Mineral	Lithology	O	Na	Mg	Al	Si	Ca	Fe ²⁺	Fe ³⁺	Ti	Cr	Zn	Total
JC082-D1-105	1	Actinolite	AG	44.64	0.67	12.96	1.48	25.75	9.04	3.76	-	-	-	-	98.30
JC082-D1-102	2	Actinolite	AG	44.96	0.88	12.91	2.72	24.56	8.28	3.77	-	0.52	1.05	-	99.65
JC082-D1-102	3	Actinolite	AG	45.16	0.62	12.81	2.20	25.56	9.13	4.18	-	-	-	-	99.66
JC082-D1-102	4	Actinolite	AG	43.72	-	12.61	-	26.01	9.24	4.89	-	-	-	-	96.47
JC082-D1-105	5	Chlorite	AG	39.35	-	17.19	9.30	15.24	-	5.57	-	-	-	-	86.65
JC082-D1-105	6	Chlorite	AG	38.77	-	15.45	8.79	14.49	-	9.86	-	-	-	-	87.36
JC082-D1-105	7	Chlorite	AG	39.09	-	15.79	8.93	14.65	-	9.38	-	-	-	-	87.84
JC082-D1-102	8	Chlorite	AG	40.43	-	18.43	7.92	15.95	-	7.21	-	-	-	-	89.94
JC082-D1-102	9	Chlorite	AG	39.96	-	15.50	11.07	13.62	-	10.25	-	-	-	-	90.40
JC082-D1-102	10	Chlorite	AG	38.93	-	16.11	9.92	14.47	-	7.03	-	-	-	-	86.46
JC082-D1-105	11	Cr-spinel	AG	34.83	-	5.97	16.45	-	-	17.05	3.00	-	22.80	-	100.10
JC082-D1-105	12	Cr-spinel	AG	36.08	-	5.85	13.10	-	-	16.04	4.81	-	25.18	-	101.06
JC082-D1-105	13	Cr-spinel	AG	34.51	-	6.50	14.23	-	-	16.14	3.17	0.49	25.38	-	100.42
JC082-D1-102	14	Cr-spinel	AG	32.74	-	3.74	12.17	-	-	20.47	3.89	-	27.03	-	100.04
JC082-D1-105	15	Cr-spinel	AG	37.09	-	6.10	14.40	-	-	15.66	2.11	-	25.55	-	100.91
JC082-D1-102	16	Cr-spinel	AG	36.15	-	6.05	14.28	-	-	15.88	3.01	0.27	23.97	0.46	100.07
JC082-D1-105	17	Cr-spinel	AG	36.41	-	5.84	13.19	-	-	16.98	4.39	0.74	23.91	0.49	101.95
JC082-D1-105	18	Hornblende	AG	42.15	1.88	10.70	6.28	20.77	8.09	-	5.11	-	-	-	94.98
JC082-D1-105	19	Pargasite	AG	42.91	1.93	10.63	7.54	20.13	8.20	4.75	-	0.44	-	-	96.53
JC082-D1-105	20	Pargasite	AG	43.34	2.17	11.22	6.65	21.06	8.26	4.43	-	-	0.23	-	97.36
JC082-D1-105	21	Pargasite	AG	43.64	1.95	11.73	6.57	21.39	8.26	4.05	-	-	-	-	97.59
JC082-D1-102	22	Pargasite	AG	43.87	1.75	11.39	6.30	21.69	7.63	5.57	-	-	-	-	98.20
JC082-D1-102	23	Pargasite	AG	42.86	1.80	10.88	6.63	21.00	8.00	4.79	-	-	-	-	95.96
JC082-D1-105	24	Plagioclase	AG	46.37	2.40	-	17.32	22.68	10.74	-	-	-	-	-	99.51
JC082-D1-102	25	Prehnite	AG	42.65	-	-	13.04	20.24	20.01	-	-	-	-	-	95.94
JC082-D1-102	26	Prehnite	AG	42.42	-	-	13.22	20.24	19.04	-	-	-	-	-	94.92
JC082-D1-102	27	Prehnite	AG	42.55	-	-	13.20	20.16	19.65	-	-	-	-	-	95.56
JC044-3A	28	Cr-spinel	SP	34.8	-	6.98	14.29	-	-	15.31	3.18	0.67	24.99	-	100.22
JC044-3A	29	Cr-spinel	SP	35.65	-	7.05	15.16	-	-	15.19	4.64	0.48	22.82	-	100.99
JC044-3A	30	Cr-spinel	SP	34.58	-	7.07	15.33	-	-	15.23	2.87	0.54	24.03	-	99.65
JC044-3A	31	Cr-spinel	SP	34.81	-	7.97	14.61	-	-	13.55	5.51	-	23.71	-	100.16
JC044-3A	32	Cr-spinel	SP	34.93	-	7.05	15.22	-	-	15.49	4.39	-	23.25	-	100.33

Table 3.1: Energy dispersive spectra (EDS) analysis of minerals from samples recovered during dredging. Oxygen was calculated stoichiometrically. Lithology abbreviations: AG = altered gabbro; SP = serpentinised peridotite

Sample	Analysis	Mineral	Cr#	Mg#	Emperical formula
JC082-D1-105	1	Actinolite	-	0.78	$\text{Na}_{0.24}\text{Ca}_{1.88}\text{Mg}_{4.45}\text{Fe}_{0.56}\text{Si}_{7.65}\text{Al}_{0.46}\text{O}_{22}(\text{OH})_2$
JC082-D1-102	2	Actinolite	-	0.77	$\text{Na}_{0.32}\text{Ca}_{1.75}\text{Mg}_{4.49}\text{Fe}_{0.57}\text{Si}_{7.38}\text{Al}_{0.85}\text{O}_{22}(\text{OH})_2$
JC082-D1-102	3	Actinolite	-	0.75	$\text{Na}_{0.22}\text{Ca}_{1.88}\text{Mg}_{4.35}\text{Fe}_{0.62}\text{Si}_{7.75}\text{Al}_{0.67}\text{O}_{22}(\text{OH})_2$
JC082-D1-102	4	Actinolite	-	0.72	$\text{Ca}_{1.98}\text{Mg}_{4.44}\text{Fe}_{0.75}\text{Si}_{7.92}\text{O}_{22}(\text{OH})_2$
JC082-D1-105	5	Chlorite	-	0.76	$\text{Mg}_{4.11}\text{Fe}_{0.58}\text{Si}_{3.15}\text{Al}_{2.00}\text{O}_{10}(\text{OH})_8$
JC082-D1-105	6	Chlorite	-	0.61	$\text{Mg}_{3.81}\text{Fe}_{1.06}\text{Si}_{3.10}\text{Al}_{1.95}\text{O}_{10}(\text{OH})_8$
JC082-D1-105	7	Chlorite	-	0.63	$\text{Mg}_{3.86}\text{Fe}_{1.00}\text{Si}_{3.10}\text{Al}_{1.96}\text{O}_{10}(\text{OH})_8$
JC082-D1-102	8	Chlorite	-	0.72	$\text{Mg}_{4.31}\text{Fe}_{0.73}\text{Si}_{3.23}\text{Al}_{1.67}\text{O}_{10}(\text{OH})_8$
JC082-D1-102	9	Chlorite	-	0.60	$\text{Mg}_{3.71}\text{Fe}_{1.07}\text{Si}_{2.82}\text{Al}_{2.38}\text{O}_{10}(\text{OH})_8$
JC082-D1-102	10	Chlorite	-	0.70	$\text{Mg}_{3.92}\text{Fe}_{0.74}\text{Si}_{3.04}\text{Al}_{2.17}\text{O}_{10}(\text{OH})_8$
JC082-D1-105	11	Cr-spinel	0.58	0.26	$\text{Mg}_{0.45}\text{Fe}^{2+}_{0.55}\text{Al}_{1.11}\text{Cr}_{0.80}\text{Fe}^{3+}_{0.10}\text{O}_4$
JC082-D1-105	12	Cr-spinel	0.66	0.27	$\text{Mg}_{0.46}\text{Fe}^{2+}_{0.55}\text{Al}_{0.92}\text{Cr}_{0.92}\text{Fe}^{3+}_{0.16}\text{O}_4$
JC082-D1-105	13	Cr-spinel	0.64	0.29	$\text{Mg}_{0.49}\text{Fe}^{2+}_{0.53}\text{Ti}_{0.02}\text{Al}_{0.96}\text{Cr}_{0.89}\text{Fe}^{3+}_{0.10}\text{O}_4$
JC082-D1-102	14	Cr-spinel	0.69	0.15	$\text{Mg}_{0.30}\text{Fe}^{2+}_{0.71}\text{Al}_{0.87}\text{Cr}_{1.00}\text{Fe}^{3+}_{0.13}\text{O}_4$
JC082-D1-105	15	Cr-spinel	0.64	0.28	$\text{Mg}_{0.47}\text{Fe}^{2+}_{0.53}\text{Al}_{1.00}\text{Cr}_{0.93}\text{Fe}^{3+}_{0.07}\text{O}_4$
JC082-D1-102	16	Cr-spinel	0.63	0.28	$\text{Mg}_{0.47}\text{Fe}^{2+}_{0.54}\text{Ti}_{0.01}\text{Zn}_{0.01}\text{Al}_{1.00}\text{Cr}_{0.87}\text{Fe}^{3+}_{0.10}\text{O}_4$
JC082-D1-105	17	Cr-spinel	0.64	0.26	$\text{Mg}_{0.45}\text{Fe}^{2+}_{0.58}\text{Ti}_{0.02}\text{Zn}_{0.01}\text{Al}_{0.92}\text{Cr}_{0.87}\text{Fe}^{3+}_{0.15}\text{O}_4$
JC082-D1-105	18	Hornblende	-	-	$\text{Na}_{0.72}\text{Ca}_{1.79}\text{Mg}_{3.87}\text{Fe}_{0.90}\text{Si}_{6.51}\text{Al}_{2.05}\text{O}_{22}(\text{OH})_2$
JC082-D1-105	19	Pargasite	-	0.69	$\text{Na}_{0.74}\text{Ca}_{1.80}\text{Mg}_{3.84}\text{Fe}_{0.73}\text{Ti}_{0.02}\text{Si}_{6.29}\text{Al}_{2.45}\text{O}_{22}(\text{OH})_2$
JC082-D1-105	20	Pargasite	-	0.72	$\text{Na}_{0.82}\text{Ca}_{1.78}\text{Mg}_{3.99}\text{Fe}_{0.68}\text{Cr}_{0.01}\text{Si}_{6.48}\text{Al}_{2.12}\text{O}_{22}(\text{OH})_2$
JC082-D1-105	21	Pargasite	-	0.74	$\text{Na}_{0.73}\text{Ca}_{1.76}\text{Mg}_{4.12}\text{Fe}_{0.62}\text{Si}_{6.51}\text{Al}_{2.08}\text{O}_{22}(\text{OH})_2$
JC082-D1-102	22	Pargasite	-	0.67	$\text{Na}_{0.65}\text{Ca}_{1.63}\text{Mg}_{4.01}\text{Fe}_{0.85}\text{Si}_{6.60}\text{Al}_{1.99}\text{O}_{22}(\text{OH})_2$
JC082-D1-102	23	Pargasite	-	0.68	$\text{Na}_{0.68}\text{Ca}_{1.74}\text{Mg}_{3.91}\text{Fe}_{0.75}\text{Si}_{6.53}\text{Al}_{2.14}\text{O}_{22}(\text{OH})_2$
JC082-D1-105	24	Plagioclase	-	-	$\text{Na}_{0.29}\text{Ca}_{0.74}\text{Al}_{1.76}\text{Si}_{2.2}\text{O}_8$
JC082-D1-102	25	Prehnite	-	-	$\text{Ca}_{2.06}\text{Al}_{1.99}\text{Si}_{2.97}\text{O}_{10}(\text{OH})$
JC082-D1-102	26	Prehnite	-	-	$\text{Ca}_{1.97}\text{Al}_{2.03}\text{Si}_{2.99}\text{O}_{10}(\text{OH})$
JC082-D1-102	27	Prehnite	-	-	$\text{Ca}_{2.03}\text{Al}_{2.02}\text{Si}_{2.97}\text{O}_{10}(\text{OH})$
JC044-3A	28	Cr-spinel	0.64	0.31	$\text{Mg}_{0.53}\text{Fe}^{2+}_{0.50}\text{Ti}_{0.03}\text{Al}_{0.97}\text{Cr}_{0.88}\text{Fe}^{3+}_{0.10}\text{O}_4$
JC044-3A	29	Cr-spinel	0.60	0.32	$\text{Mg}_{0.53}\text{Fe}^{2+}_{0.49}\text{Ti}_{0.02}\text{Al}_{1.02}\text{Cr}_{0.80}\text{Fe}^{3+}_{0.15}\text{O}_4$
JC044-3A	30	Cr-spinel	0.61	0.32	$\text{Mg}_{0.53}\text{Fe}^{2+}_{0.49}\text{Ti}_{0.02}\text{Al}_{1.03}\text{Cr}_{0.84}\text{Fe}^{3+}_{0.09}\text{O}_4$
JC044-3A	31	Cr-spinel	0.62	0.37	$\text{Mg}_{0.59}\text{Fe}^{2+}_{0.44}\text{Al}_{0.98}\text{Cr}_{0.82}\text{Fe}^{3+}_{0.18}\text{O}_4$
JC044-3A	32	Cr-spinel	0.60	0.31	$\text{Mg}_{0.53}\text{Fe}^{2+}_{0.50}\text{Al}_{1.02}\text{Cr}_{0.81}\text{Fe}^{3+}_{0.14}\text{O}_4$

Table 3.2: Cr#, Mg# and empirical mineral formulae calculated using EDS analysis.

Empirical formulae were calculated based on a charge balance between cations and O^{2-} and OH groups.

Alteration textures are most commonly observed to be pseudomorphic replacement of plagioclase by chlorite, and clinopyroxene by actinolite. Depending on the degree of alteration, this either occurs extensively on the margins or in fractures, or as complete replacement of the original gabbroic mineral assemblage. In samples where the groundmass was originally finer, chlorite and amphiboles (actinolite, tremolite, and pargasite) occur completely replacing primary minerals, and form a fibrous and interlocking texture.

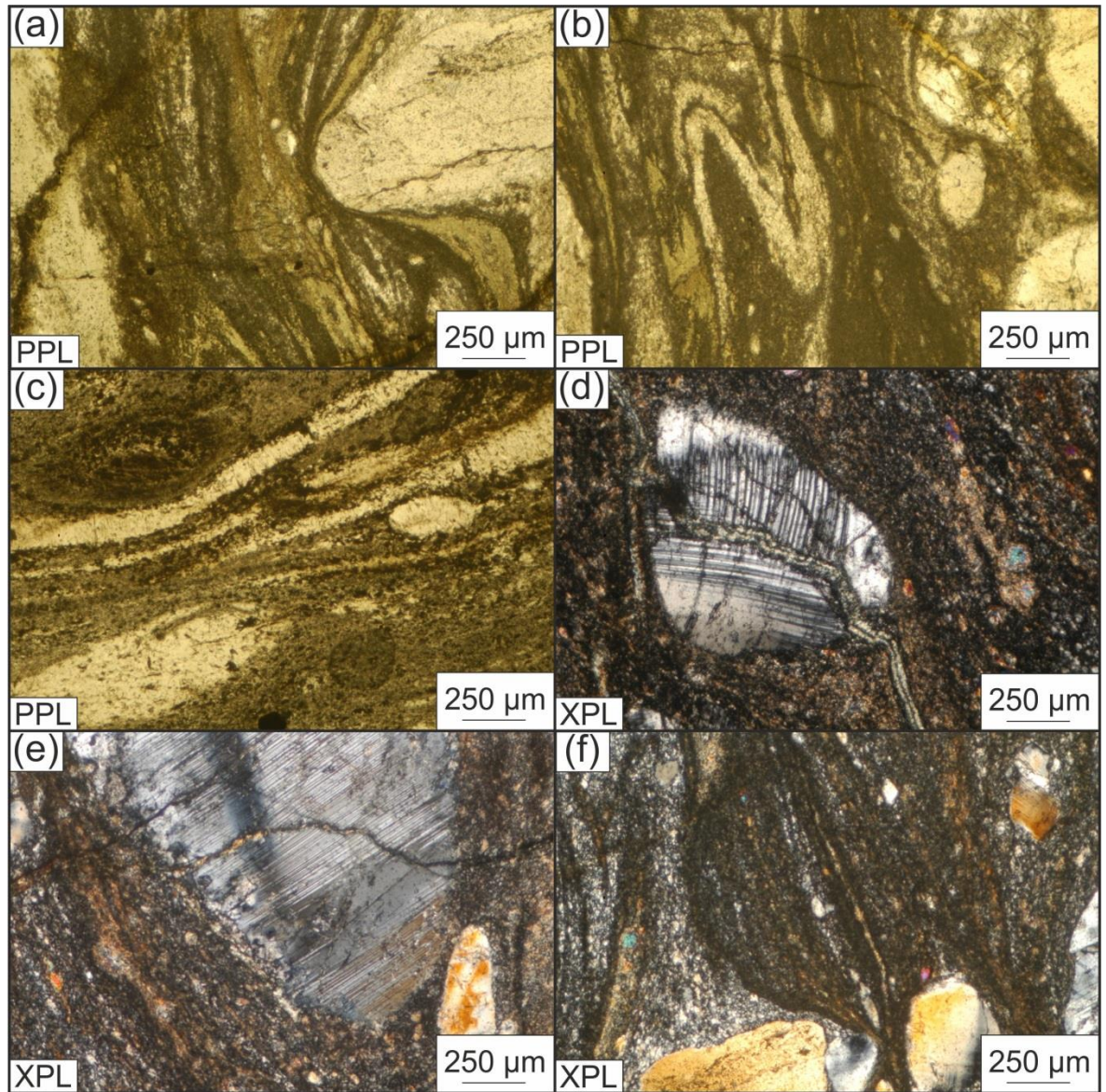


Figure 3.22: Photomicrographs of deformation textures in gabbros (a) JC082-D1-104: (b) JC082-D1- 104: (c) JC082-D1-104: ribbon textures and ductile deformation within mylonitised gabbro. Lighter coloured bands consist of quartz and feldspar, and the darker bands are hornblende (d) JC082-D1-104: and (e) JC082-D1-104: plagioclase crystals showing sheared twinning and minor amounts of recrystallisation on the margins (f) JC082-D1-104: strain shadow showing recrystallised quartz and plagioclase on the edges of a plagioclase crystal, indicating mylonitic deformation.

3.4.7. Origin of Mt. Dent: deformation and metamorphic history

The rock types recovered from Mt. Dent are primarily greenschist altered gabbros, and mylonites, with one sample of serpentinitised peridotite. The textures and mineralogies observed in dredge samples suggest that ductile deformation occurred at depth in the crust, which is then followed by retrograde hydrothermal alteration. Most samples have a peak in the upper greenschist or lower amphibolite facies, followed by subsequent retrograde alteration at prehnite-pumpellyite facies. The sample of serpentinitised peridotite had little original mineralogy remaining, while a lack of relict pyroxene suggests the protolith was dunite.

The first stage of deformation experienced at Mt. Dent is the development of mylonitic ribbon textures in ~30% of the samples. The dominance of plagioclase, quartz and hornblende in the mylonite mineral assemblages, and the recrystallisation of plagioclase suggest the recovered samples reached temperatures of 600-800°C (upper amphibolite or lower granulite facies). This plastic deformation is then post-dated by retrograde metamorphism in the form of brittle deformation and hydrothermal alteration.

The main phase of hydrothermal metamorphism is observed in all samples, and is inferred to postdate mylonitic deformation. This is because deformed plagioclase and clinopyroxene are replaced by amphibolite and greenschist facies minerals. Primary olivine was rarely observed in dredged samples, and is pervasively altered to serpentine in both mafic and ultramafic protoliths. Chlorite is the most common secondary mineral and replaces plagioclase and olivine. Clinopyroxene alters predominantly to amphiboles such as actinolite and tremolite, and occasionally talc and pargasite. Pargasite is a mineral that is commonly found in both contact and regional metamorphism at high temperatures, but can also occur as a secondary amphibole in hydrothermally altered mafics. The dominance of amphiboles such as high-T pargasite and actinolite-tremolite, with a lack of secondary plagioclase and quartz, suggest development of the main stage of hydrothermal alteration occurred at 500-600°C.

The precipitation of chlorite as pseudomorphic replacements of plagioclase indicates greenschist facies conditions and temperatures of 300-400°C. Continued tectonic exhumation leads to alteration at cooler temperatures (~200°C) of prehnite-pumpellyite facies, with precipitation of prehnite and further chlorite (Figure 3.23).

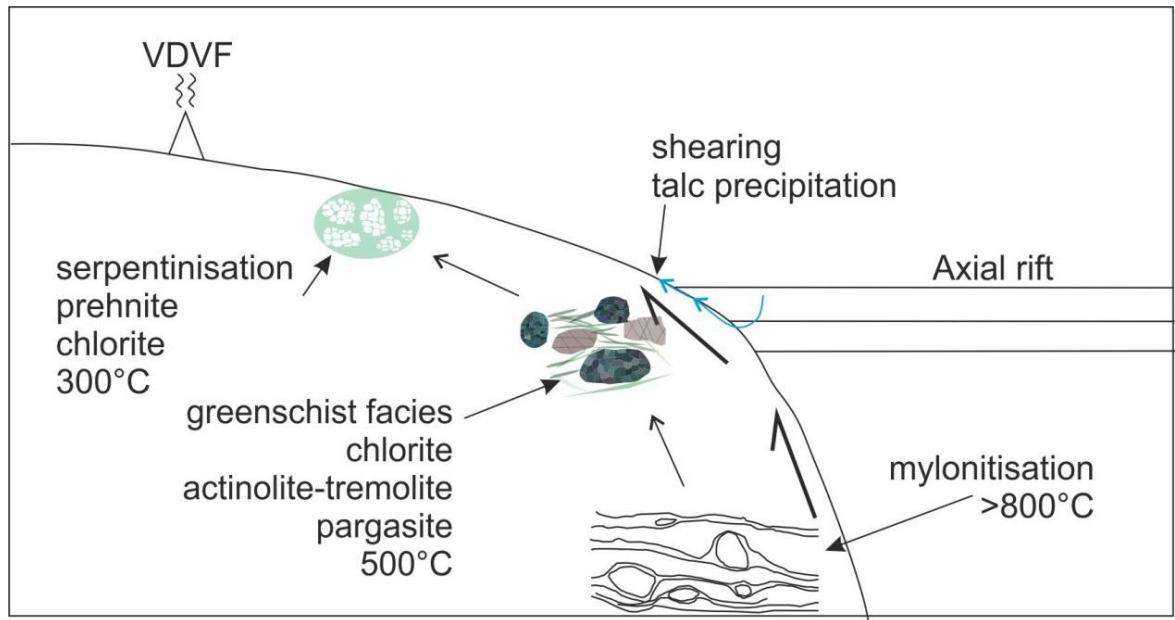


Figure 3.23: Schematic showing the evolution of the alteration assemblage within Mt. Dent. Some samples show evidence of mylonitic deformation and dynamic recrystallisation of plagioclase and quartz at depths. This is post-dated by retrograde alteration at upper greenschist and lower amphibolite facies, indicated by the dominance of chlorite and actinolite replacement of plagioclase and clinopyroxene. Further retrograde alteration at lower pressures and temperatures are indicated by precipitation of prehnite in the groundmass, and occasional veins.

The presence of talc in the rock samples recovered from Mt Dent, and especially as coating on the surfaces of a few specimens, is very important in aiding slip along fault surfaces. Talc reduces the frictional coupling in shear-related stress and allows strain to be focused on a single fault plane. This increases the extensional displacement along normal faults and is important in creating large, low angle detachment faults that expose the lower crust and upper mantle at the seafloor eg. (Moore and Lockner, 2011; Schroeder and John, 2004).

A combination of the morphology, recovered lithologies, sporadic striations along the fault surface and shallow average dip (~10°) of the fault surface suggest that Mt. Dent

is an OCC. The lithologies are lower crustal and upper mantle rocks, whilst the dome structure is similar to the morphologies of OCC's seen at the MAR and the SWIR e.g. (Dick et al., 2003; MacLeod et al., 2009; Miranda and Dilek, 2010).

Chapter Four – Local setting of the Von Damm Vent Field

This chapter describes the setting, basement rocks and hydrothermal precipitates of the Von Damm Vent Field (VDVF). The extent of current and historical hydrothermal activity at the top of the Mount Dent (Mt. Dent) oceanic core complex (OCC) is derived from bathymetric data and remotely operated vehicle (ROV) footage to create geological maps of the VDVF. In addition, petrographic and geochemical analysis from samples obtained during two *RRS James Cook* cruises to the Mid-Cayman Rise (MCR) are presented to determine the mineralogy and whole rock geochemistry of the basement rocks and hydrothermal material.

4.1. Situation on the flanks of the Mid-Cayman Rise

The VDVF is located at 18°22.5'N, 81°47.8'W, on the upper slopes of Mt. Dent, approximately 13 km away from the centre of the axial valley trough, and 10 km away from the intersection of the toe of the massif with the axial valley. The VDVF is situated at a water depth of 2280 metres (Figure 4.1), and towards the topographically highest (shallowest) point of Mt. Dent. The topography in this area of the OCC is generally smooth, with an average dip of ~10° to the south. There is an extensive amount of pelagic sediment cover (>1m thick) over the top of Mt. Dent and in the vicinity of the VDVF (Figure 4.2).

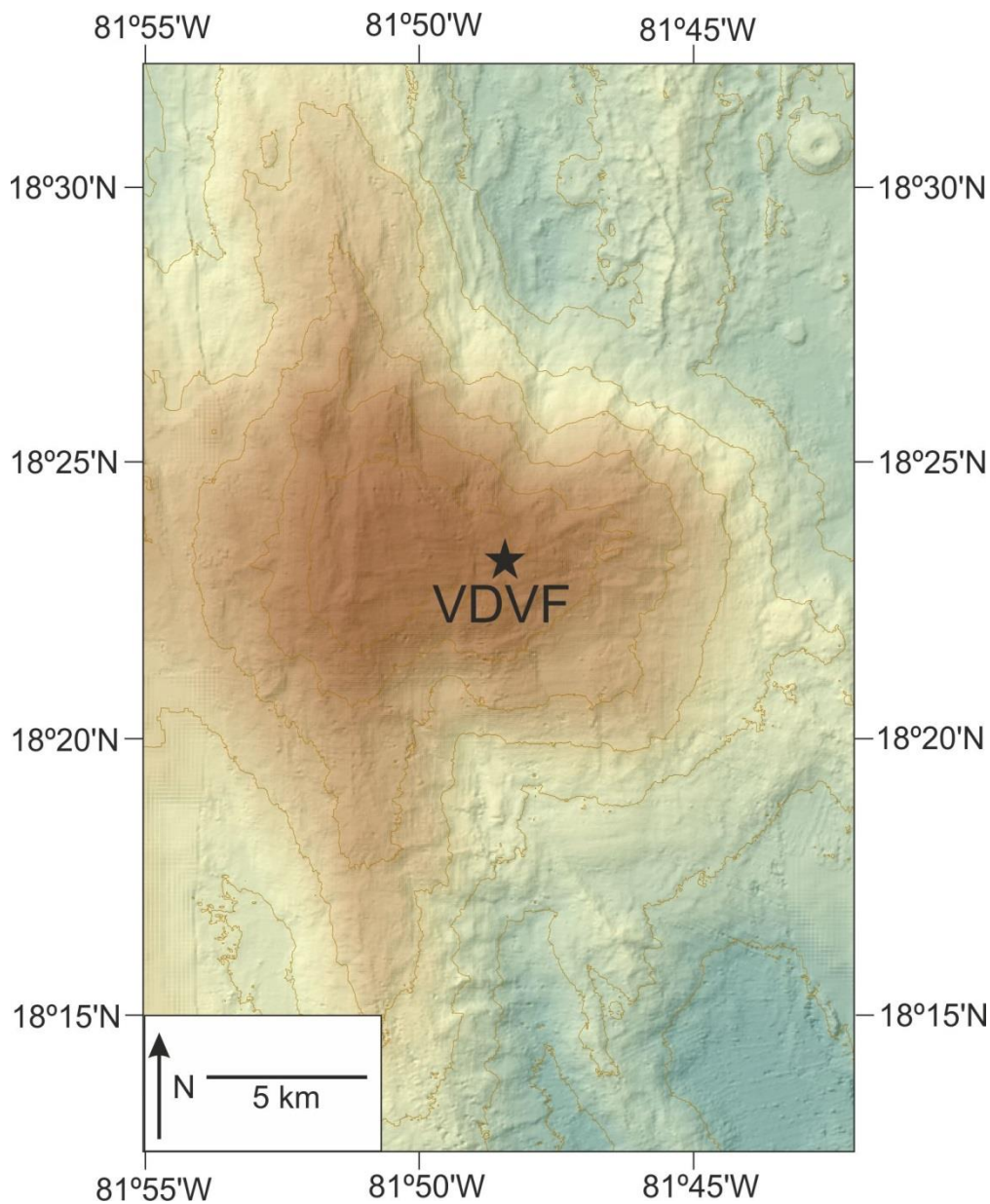


Figure 4.1: Map of Mt. Dent showing the location of the VDVf, indicated by the black star. The bathymetry and contour map of this bathymetric map is a composite of bathymetric data collected by the JC044 and JC082.

Figure 4.2: (On previous page) geological map of the region surrounding the VDVF. Areas that are solid in colour indicate outcrop whereas those that have a thin veneer of sediment cover are slightly faded. The total area shown in the regional geological map is $\sim 3 \text{ km}^2$, and the majority is sediment covered, as indicated by the faded cross hatch pattern. The margins of the extinct hydrothermal mounds are estimated from the major breaks in slope. Note: the areas assumed to be the sediment covered basement is shown as gabbro as this is the predominant recovered basement lithology at the VDVF. Background of the map is a combination of ROV bathymetry with a resolution of 25 cm, and Autosub bathymetry at a resolution of $\sim 1 \text{ m}$. Contours are from the Autosub bathymetry and are at a spacing of 10 m.

4.2. Setting of the VDVF

The active site consists of three conical mounds, aligned NNW-SSE (335° strike; Figure 4.3). Hydrothermal activity is generally concentrated towards the top of the largest active mound, referred to here as the “*main cone*”. The other two active mounds are located directly to the SSE and are not as high as the main cone. These form a NNW-SSE trending spur and are referred to as the “*north spur*” and the “*south spur*”. The main cone is up to 80 metres high, has an area of $\sim 30,000 \text{ m}^2$ and an estimated volume of $\sim 1,340,000 \text{ m}^3$. In contrast, the north spur is up to 50 metres high, covers an area of $12,000 \text{ m}^2$, with a volume of $\sim 420,000 \text{ m}^3$. The south spur is the smallest active mound, with a maximum height of 40 metres, an area extent of $10,000 \text{ m}^2$ and an estimated volume of $163,000 \text{ m}^3$ (Figure 4.3). These volumes were calculated within ArcMap. The base of the mounds was defined as the surface of the core complex, and triangular irregular networks (TINs) were calculated from the ROV bathymetry to represent their surface area. The volume of the mounds was then derived by ArcMap using the polygon volume tool.

Mass wasting is an important process on all sides of the VDVF but is most prominent on the eastern (downslope) side due to the gradient of $30^\circ - 40^\circ$. Very little in situ material is found exposed on the lower slopes of the main cone, and a lot of material observed here is scree formed from mass wasting. Far more in situ material occurs higher up the mounds, and there is a sharp boundary between scree dominated, and in situ dominated surface material (Figure 4.3). The boundaries of the mounds are

defined by abrupt rubble-sediment contacts with distinctive sediment – mound relationships. The rubble at the margins of the main cone onlaps onto the surrounding pelagic sediment, but with progression south, sediment cover gradually increases until the south spur, where a thin veneer of sediment covers the lower flanks of the mound (Figure 4.4). This sediment-rubble relationship suggests that the mounds young towards the north.

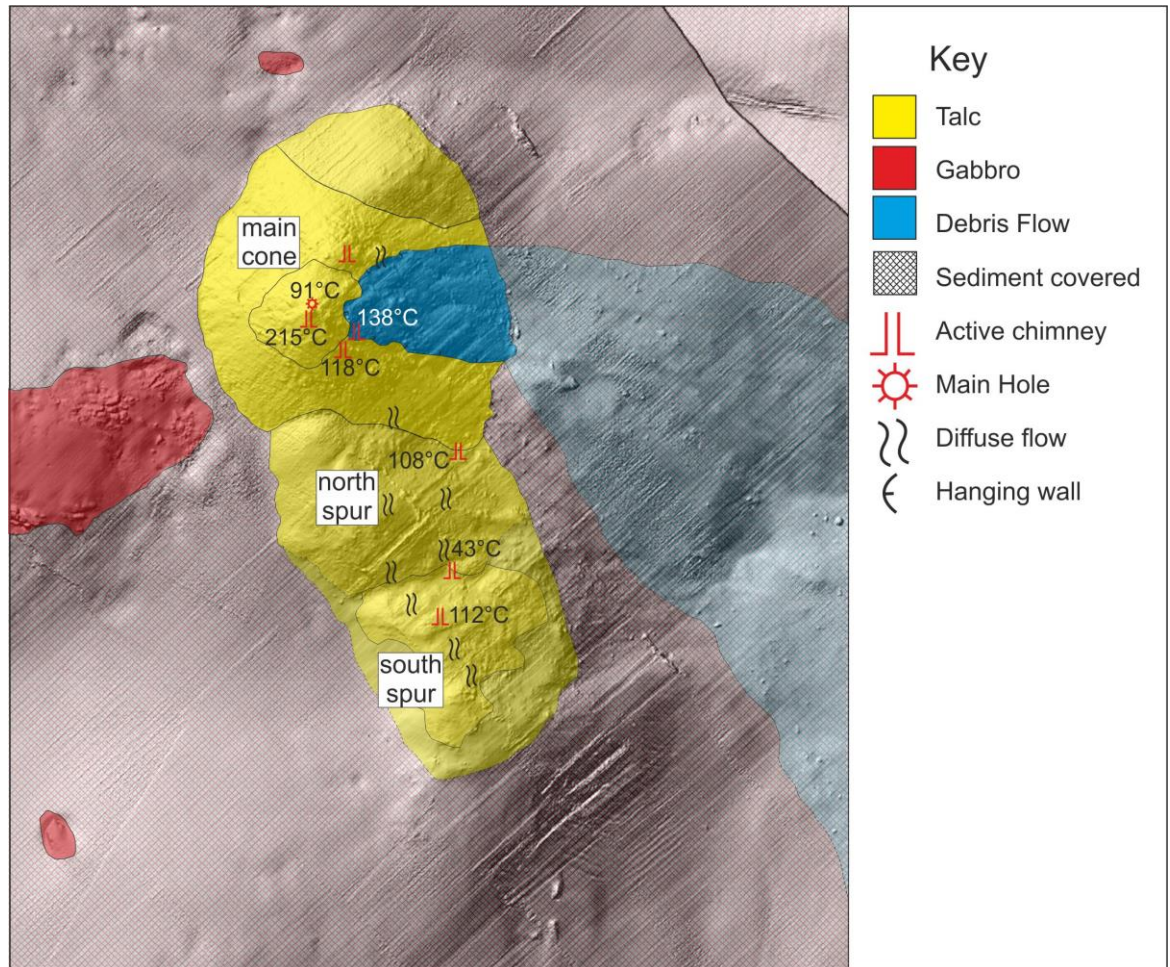


Figure 4.3: Geological map of the VDFV showing the location and temperature of active vents, and the distribution of diffuse flow across the site. Temperatures indicated are the highest measured on cruise JC082 by the ROV Isis high-temperature probe. The basemap is a shaded relief image of the Isis ROV bathymetry. Labels represent the three different mounds of the VDFV. Chimneys displayed: main hole - 91°C; spire - 215°C; hotter than hole - 138°C; chimlet 1 - 43°C; chimlet 2 - 108°C; X-15 - 112°C. Boundaries on the north and south spurs represent the margin between sediment-covered and fresh rubble. The hanging wall represents the exposed surface following multiple collapses of the main cone.

At the top of the main cone, a large, 4 metre high spire, defines the pinnacle of the VDVF. This pinnacle is divided into two small peaks, separated by a 2 metre saddle structure. The active vents are colonised by large numbers of *Rimicaris Hybisae* and vent clear shimmering fluid with low particulate content. The most active vent site is located at one of these peaks, with a maximum temperature recorded during cruise JC082 of 215°C, slightly lower than a previously reported temperature of 226°C (McDermott, 2015). The temperature of venting across the VDVF generally decreases towards the south, and the maximum temperature recorded on the south spur is 112°C.

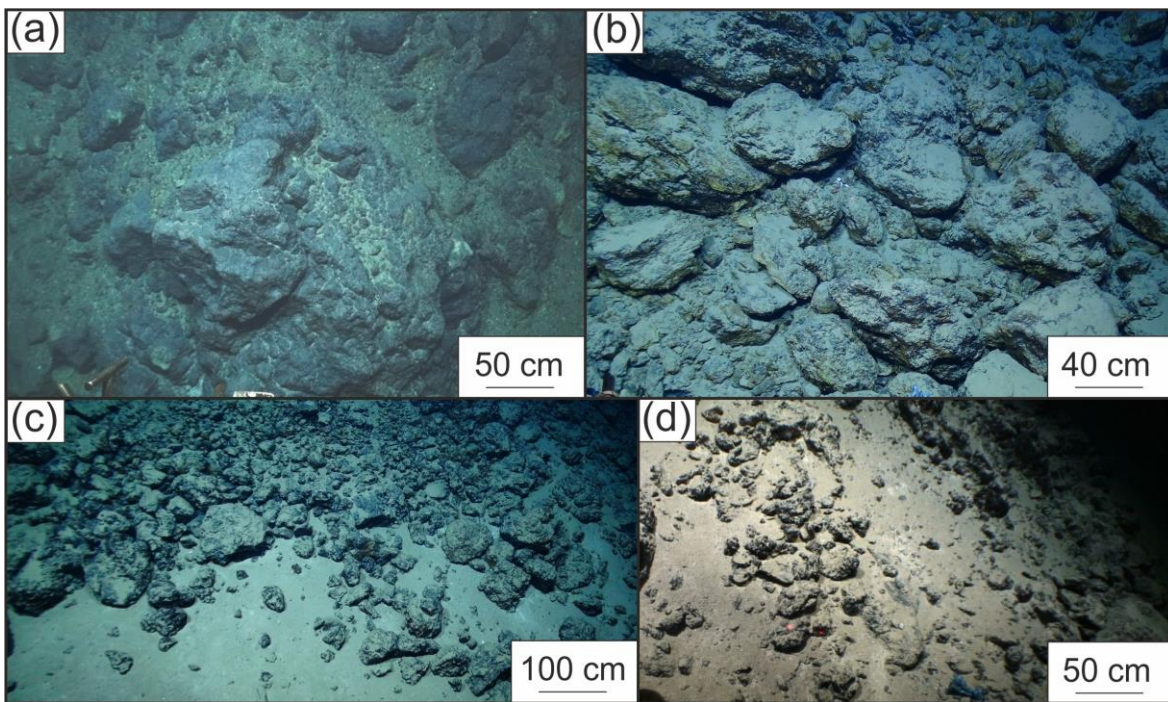


Figure 4.4: Rubble and sediment contacts. Images taken by the ISIS ROV (a) in situ material at the top of the main cone (b) scree slope on the lower sections of the main cone (c) rubble-sediment contact on the main cone, displaying light sediment cover (d) sediment covered rubble on the flanks of the south spur.

To the east and south of the VDVF lie several mounds, where no hydrothermal activity was detected using conductivity, temperature, depth (CTD) surveys, or E_h and light-scattering sensors on Autosub 6000. The inactive mounds located to the east range in size and volume. The largest is “*Mystic Mountain*”, which is up to 110 metres high and 240 metres across. This is around twice the size of the main cone at the VDVF. These mounds are between 500 to 1000 metres away from the VDVF (Figure 4.2) and define the extent of active and inactive hydrothermal activity discovered at

the top of Mt. Dent during cruises *JC044* and *JC082*, while the true extent of venting on the upper slopes of Mt. Dent remains unknown. These hydrothermally inactive areas are covered in sediment, suggesting a significant hiatus of hydrothermal activity. Using the estimated sedimentation rate of between 2 and 5 cm ka⁻¹ (Rosencrantz and Sclater, 1986), it is likely that hydrothermal activity at Mystic Mountain and the surrounding area ceased approximately 20,000 years ago.

A distinct partially sediment covered debris flow with an area of ~0.18 km² occurs downslope of the VDVF (Figure 4.2). The distance from the active site is not well constrained due to the sediment cover, but it extends at least 700 metres away from the main cone at the VDVF. As some of the largest blocks are closer to Mystic Mountain than the VDVF, this indicates the active mounds have undergone several cycles of growth, collapse and precipitation. This extensive, large scale mass wasting is supported by the presence of a hanging wall above a collapse structure towards the top of the main cone (Figure 4.3), and likely plays a part in the exposure of focussed hydrothermal venting.

“Pock marks” are observed in the sediment cover throughout the VDVF. These can be up to 2 metres across and 1 metre deep, but are generally closer to around 50 cm in diameter and a few tens of centimetres deep. Their density increases with proximity to the active vent field, and the majority of them are distributed in a W-NNW arc in relation to the VDVF (Figure 4.2). ROV obtained push cores from within the pock marks degassed on return to the sea surface and are saturated in methane (Mills pers comm., 2013). Small layers of detrital material, a few centimetres thick, were found at the bottom of some pock marks, however there is no correlation between the size or location of the pock mark and amount of detrital material (Figure 4.5). The resolution of the ROV bathymetry allows areas of significant pock marks to be mapped, even if they were not visited by ROV. One area, 100-200 metres to the west of the VDVF, features a row of pock marks aligned along the same ~345° orientation as the active mounds (Figure 4.2). However, the most significant observation associated with the pock marks is the detection of temperature anomalies up to 0.5°C above them, suggesting that they are contributing to the diffuse flow from the VDVF.

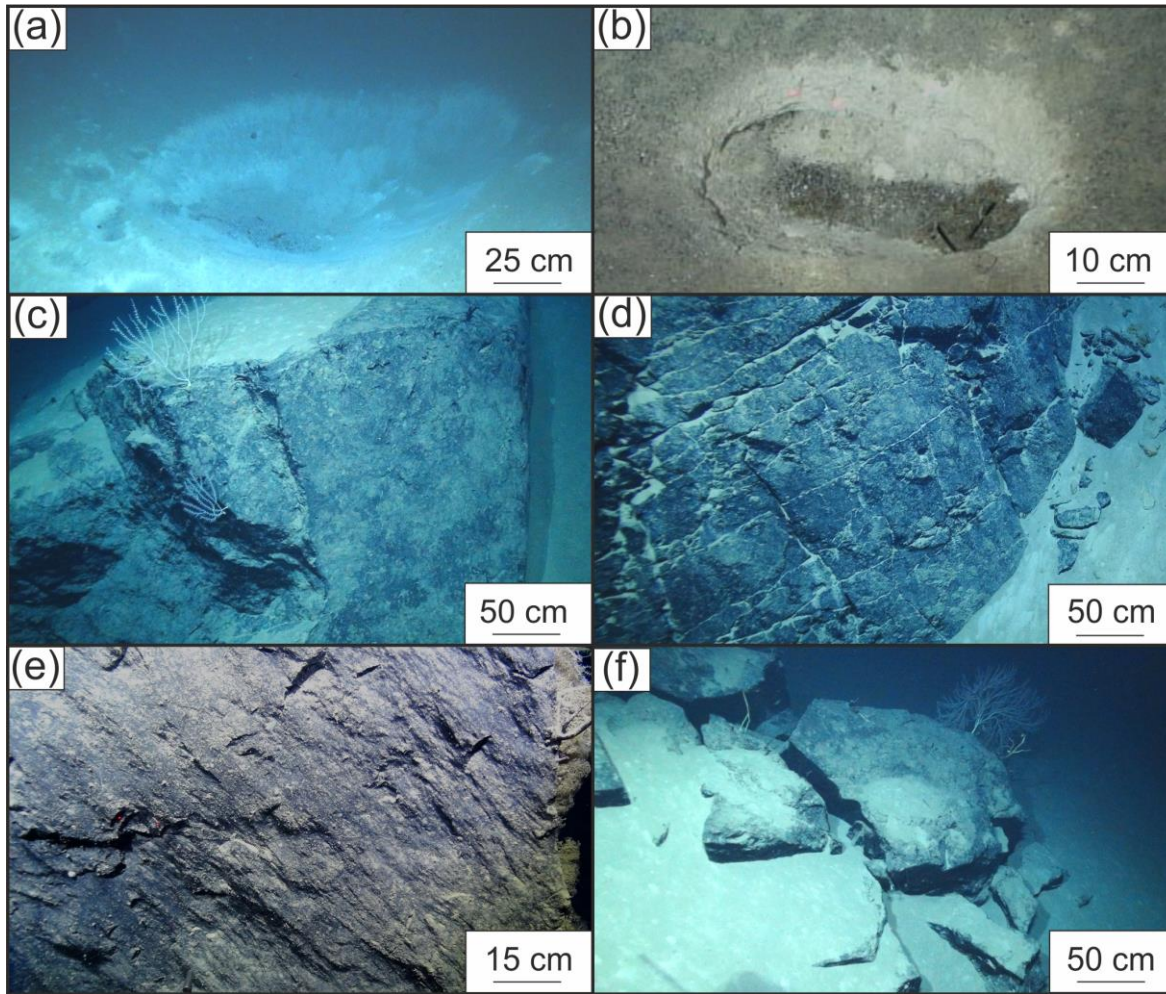


Figure 4.5: ROV images of the regional VDVF (a)-(b) pock marks located in pelagic sediment approximately 100 metres from the VDVF (c) along strike view of small fault face in gabbro outcrop (d) and (e) foliated, weathered faces on gabbro outcrops (f) sediment covered gabbro outcrop with small rubble blocks.

Faults up to 100 m long are located mainly to the west of the active site. Slickensides are apparent on the fault surfaces on gabbro outcrops indicating dip-slip. The fault strike ranges in orientation from 311° - 052° , but a majority are within the range of 330° - 015° (Figure 4.6). Fault throws estimated from individual outcrops are up to 5 m, however they may be greater in some localities where sediment cover obscures the base of the scarps. Along with the orientations of the pock marks and the hydrothermal mounds, the linear features at the VDVF are all aligned 311° - 052° , and a majority are within the range of 335° - 005° (Figure 4.6). This NNW-SSE structural trend is apparent in the alignment of the active and extinct hydrothermal mounds, the exposure of the host rock, and the linear clustering of the pock marks, indicative of underlying basement structural control. The NNW-SSE trend is parallel to the

extensional axis of the Mt Dent and may be related to normal faults that formed in response to flexural bending and fracturing of the detachment fault.

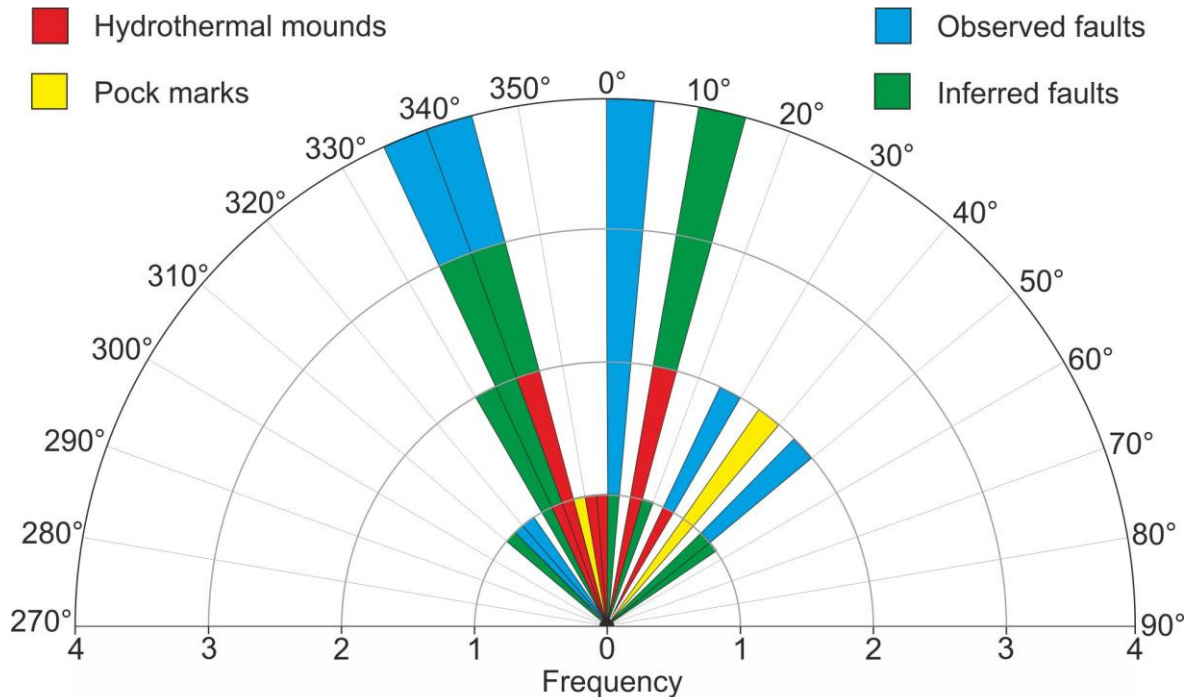


Figure 4.6: Rose diagram showing the orientations of linear features at the regional VDVF including fault strikes, pockmark patterns and hydrothermal mounds. Lengths of the spokes refer to the frequency.

4.3. Host rocks in the vicinity of the VDVF

Host material outcrops mainly to the west of the VDVF (Figure 4.2) and consists predominantly of variably altered gabbros, with a couple of fine-grained greenstone dykes, one fresher porphyritic dyke and one sample of partially serpentinised peridotite.

4.3.1. Appearance at outcrop scale

On the seafloor, the basement outcrops are usually black in colour and colonised by varying amounts of sessile fauna, such as soft corals and anemones. They have varying degrees of light-coloured (pelagic carbonate) sediment on the top of the exposures. Fallen blocks of basement (i.e. not *in situ* exposure) are often angular and up to 2 metres across (Figure 4.5). In hand specimen, many of the samples of basement rocks have a penetrative, metamorphic foliation. These are especially

apparent in gabbroic rocks to the NW of the VDVF. A particular area of host rock outcrop, situated between 15 and 150 m to the WSW of the main cone, features areas of diffuse fluid flow with near bottom (<1m) temperature anomalies of up to 2.5°C above ambient seawater.

4.3.2. Common primary igneous minerals

This section will describe the primary minerals that occur within the host rocks (Figures 4.7-4.9) recovered in the vicinity of the VDVF, divided into each observed rock type.

Gabbros: Within the gabbro samples plagioclase (Figures 4.8-4.10), clinopyroxene and olivine are preserved in varying amounts (Figure 4.11). Plagioclase shows varying degrees of alteration and fracturing (Figure 4.10). Plagioclase extinction angles are highly variable, and the highest measured in any sample was 43°, and the lowest was 13°. Each sample contains two distinctive groups of plagioclase composition, with a difference of 10-20° in extinction angle between each group. The two distinct groups have measured extinction angles either clustering at 30-40° or 15-20°, and are accompanied by a change in grain size. When combined with energy-dispersive spectra (EDS) scanning electron microscope (SEM) data, this indicates that the two groups of plagioclase within the gabbros have compositions of An₅-An₂₃ and An₄₀-An₈₀ (Tables 4.1 and 4.2).

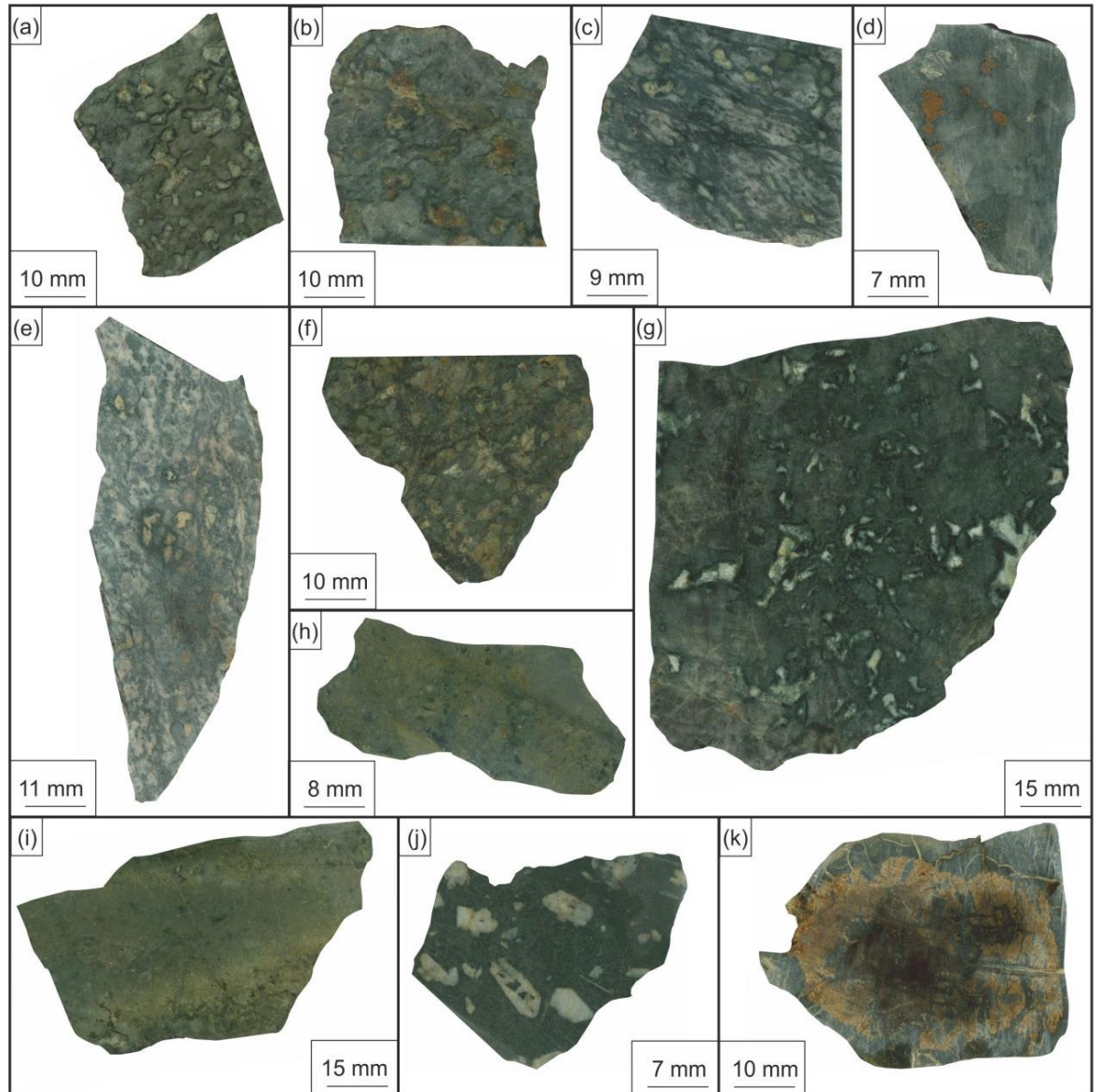


Figure 4.7: Scans of hand specimens from the vicinity of the VDVF (a) JC082-199-06: olivine gabbro showing olivine corona texture (b) JC082-199-07: altered and partially oxidised gabbro (c) JC082-199-12: mylonitised gabbro (d) JC082-199-19: partially weathered gabbro (e) JC082-199-13: fresh gabbro showing corona texture (f) JC082-199-14: altered and weathered gabbro (g) JC082-201-42: gabbro showing very coarse-grained plagioclase (h) JC082-199-15: amphibolite facies dolerite dyke and (i) JC082-199-16: fine grained, altered dolerite dyke (j) JC082-199-18: plagioclase-phyric basalt, within a fine grained, partially altered clinopyroxene and feldspar groundmass (k) JC082-199-17: partially serpentinised peridotite.

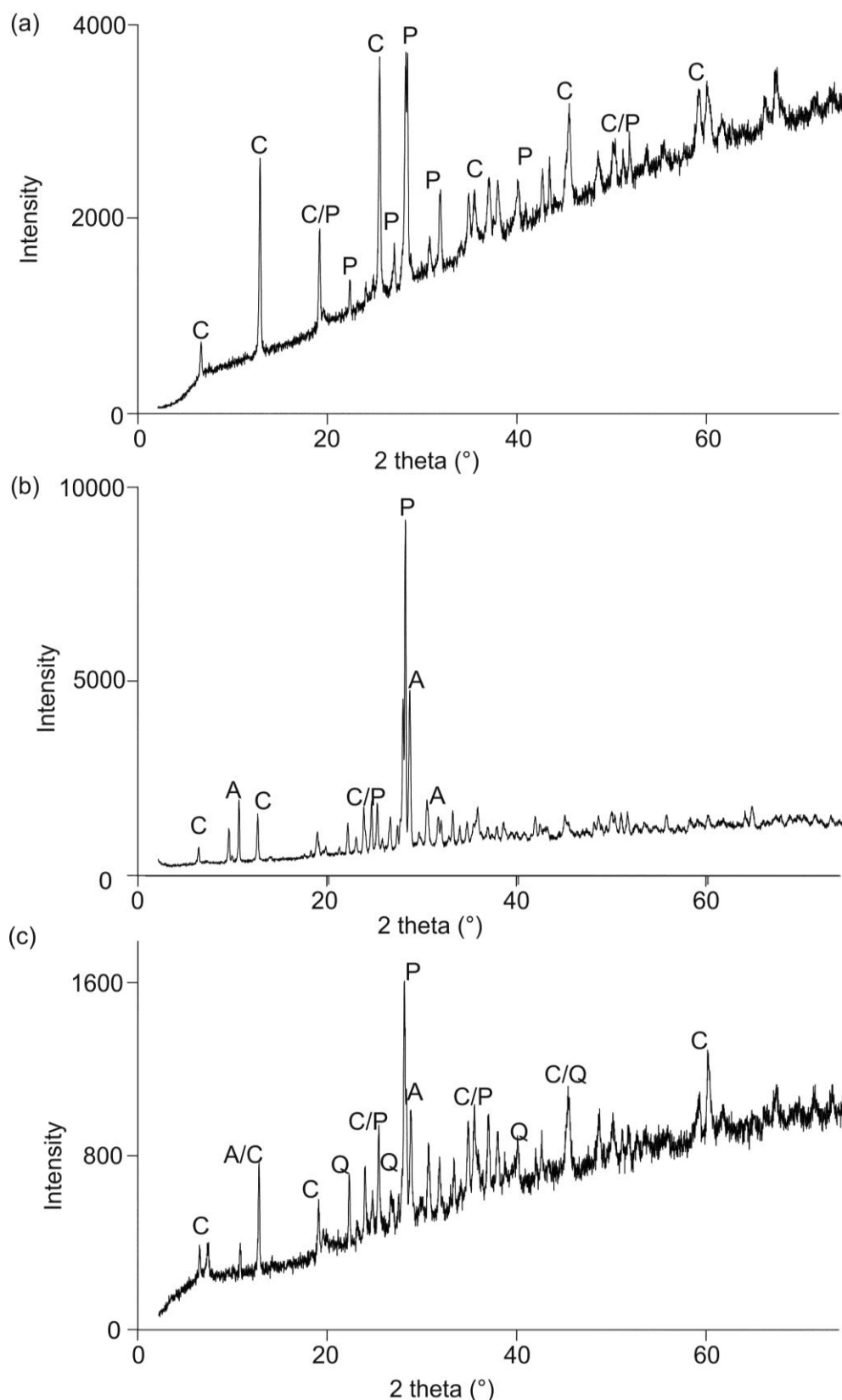


Figure 4.8: X-Ray diffraction (XRD) plots of VDFV host rocks (a) JC082-199-07: altered and oxidised gabbro (b) JC082-199-12: altered gabbro (c) JC082-199-15: altered dolerite dyke. Mineral abbreviations: A=actinolite, C=chlorite, P=plagioclase, Q=quartz. No clinopyroxene or olivine was detected in the XRD, but they are observed in minor concentrations in thin section.

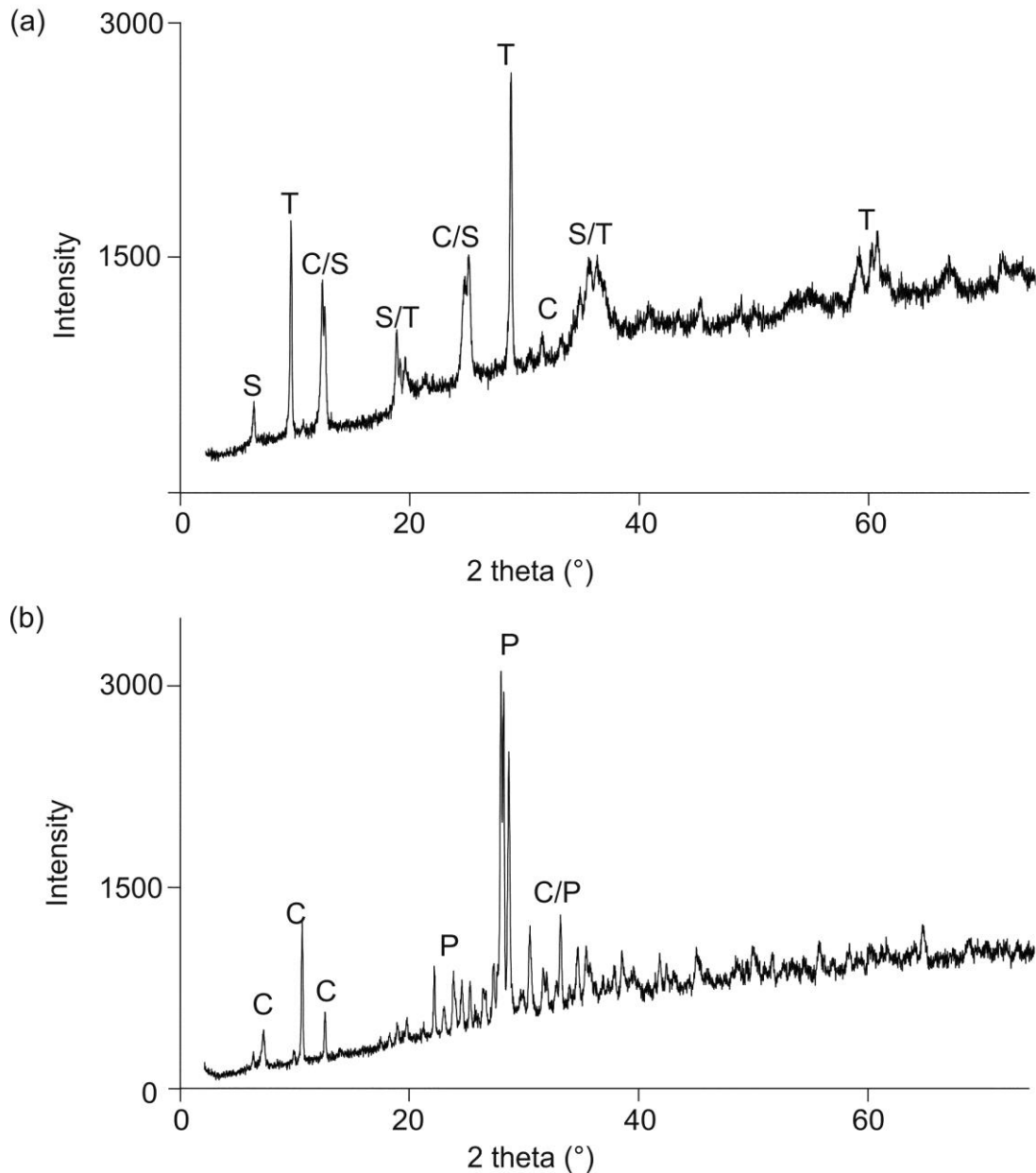


Figure 4.9: XRD plots of VDFV host rocks (a) JC082-199-17: serpentinitised peridotite (b) JC082-199-18: plagioclase-phyric basalt dyke with a partially altered groundmass.

Mineral abbreviations: C=chlorite, P=plagioclase, S=serpentine, T=talc.

Grain size of plagioclase with high anorthite content in the gabbroic samples is up to 6 mm across but is usually around 2-3 mm across. With increasing sodium content the grain size decreases, and ranges from 0.1 – 1 mm. Compositional changes also result in differences in twinning and observed interference colours. Plagioclase crystals that contain more calcium tend to show slightly higher interference colours of first order yellows, whereas those of oligoclase composition only show first order grey. Furthermore, in the anorthite plagioclase, each twin tends to be slightly wider at up to 0.5 mm across, whereas the Na-rich plagioclases have narrower twins. The

textural relationship of the two groups of plagioclase crystals indicate that anorthite in the highly altered gabbros has finer grained Na-rich plagioclase occurring on the margins and fractures. This Na-rich, secondary plagioclase has a more rounded and subhedral form and is an indication that the gabbros have undergone albitisation at 300-350°C.

The clinopyroxene in the gabbros is augite. The clinopyroxene grains are elongate, subhedral and rounded, and range from 1 mm to 10 mm in the gabbro samples. The colour ranges from colourless to very pale brown in plane polarised light (PPL), and a few grains display a pink tinge, indicative of elevated titanium contents (titanaugite). Interference colours are up to second order blues, along with yellows and oranges. Remnant clinopyroxene shows alteration along fractures and in the centre of crystals (Figure 4.11).

Olivine is as a remnant phase in some gabbros, but is completely absent in the pervasively altered samples. Pre-existing olivine is indicated by the crystal form of some amphibole pseudomorphs. Where present, olivine has a uniform grain size of 0.5-1 mm. It is colourless in PPL with interference colours up to third order, and no completely unaltered crystals are observed (Figure 4.11). The EDS spectra indicate magnesium content in the olivine is uniform, and has a value of Fo₇₇ in the gabbros (Table 4.2).

Sample	Analysis	Mineral	O	Na	Mg	Al	Si	Fe ²⁺	Fe ³⁺	Ca	Cr	Total
199-07	1	Act	43.40		10.31	1.75	24.33	9.39		8.29		97.47
199-15	2	Act	43.37		12.80	1.83	24.65	3.30		9.11		95.06
199-17	3	Act	45.20		14.45	1.60	26.00	3.09		7.71		98.05
201-42	4	Act	45.18		14.07	0.38	27.00	2.35		9.56		98.54
199-17	5	Act	45.64		14.91		27.40	2.03		9.37		99.35
201-42	6	Chl	39.30		15.44	9.68	14.08	10.27				88.77
201-42	7	Chl	39.79		14.76	10.72	13.64	11.64				90.55
199-07	8	Chl	38.24		13.49	8.98	13.72	13.36				87.79
199-15	9	Chl	38.60		12.78	9.27	13.79	14.13		0.41		88.98
199-15	10	Chl	38.07		12.31	9.85	12.96	14.87		0.13		88.19
201-42	11	Cpx	43.97		9.87	0.83	24.93	3.97		16.59		100.16
201-42	12	Cpx	44.39		10.18	1.11	25.02	3.72		16.56		100.98
199-15	13	Ho	43.72	1.70	10.20	5.34	21.17	6.13		8.97		97.23
199-17	14	Ol	44.81		30.07		18.88	6.70				100.46
199-17	15	Ol	44.71		29.08		18.93	8.80				101.52
201-42	16	Pl	48.87	7.63		12.13	30.31			2.25		101.19
201-42	17	Pl	46.88	3.39		16.32	24.13			9.24		99.96
201-42	18	Pl	46.97	3.32		16.18	24.32			9.30		100.09
201-42	19	Pl	47.00	2.67		17.13	23.38			10.53		100.71
199-15	20	Pl	46.89	3.00		16.61	23.86			9.73		100.09
199-15	21	Pl	46.67	2.48		17.00	23.21			10.64		100.00
199-15	22	Pl	49.38	8.61		10.76	32.31					101.06
199-15	23	Pl	49.36	8.55		10.71	32.27			0.25		101.14
199-15	24	Pl	46.80	3.91		15.80	24.50			8.44		99.45
199-15	25	Pl	47.24	4.89		14.74	25.97			6.87		99.71
199-17	26	Serp	40.91		24.09		21.04	2.54				88.58
199-17	27	Serp	39.62		23.46		20.36	2.28				85.72
199-17	28	Serp	39.94		22.28		20.81	3.64				86.67
199-17	29	Serp	39.44		21.72		20.85	3.24				85.25
199-15	30	Sp	35.14		3.99	10.94		20.30	6.20		23.89	100.46

Table 4.1: EDS analysis showing the wt. % of selected elements in minerals within VDVF host rocks. Mineral abbreviations: act = actinolite, chl = chlorite, cpx = clinopyroxene, fo = forsterite content, ho = hornblende, ol = olivine, pl = plagioclase, serp = serpentine, sp = Cr-spinel.

Sample	Analysis	An	Mg#	Fo	Cr#	Emperical formula
199-07	1		0.52			$\text{Ca}_{1.81}\text{Mg}_{3.71}\text{Fe}_{1.47}\text{Si}_{7.58}\text{Al}_{0.57}\text{O}_{22}(\text{OH})_2$
199-15	2		0.80			$\text{Ca}_{1.96}\text{Mg}_{4.54}\text{Fe}_{0.51}\text{Si}_{7.56}\text{Al}_{0.58}\text{O}_{22}(\text{OH})_2$
199-17	3		0.82			$\text{Ca}_{1.59}\text{Mg}_{4.91}\text{Fe}_{0.46}\text{Si}_{7.65}\text{Al}_{0.49}\text{O}_{22}(\text{OH})_2$
201-42	4		0.86			$\text{Ca}_{1.96}\text{Mg}_{4.75}\text{Fe}_{0.35}\text{Si}_{7.89}\text{Al}_{0.12}\text{O}_{22}(\text{OH})_2$
199-17	5		0.88			$\text{Ca}_{1.90}\text{Mg}_{4.98}\text{Fe}_{0.30}\text{Si}_{7.92}\text{O}_{22}(\text{OH})_2$
201-42	6		0.60			$\text{Mg}_{3.77}\text{Fe}_{1.09}\text{Si}_{2.98}\text{Al}_{2.12}\text{O}_{10}(\text{OH})_8$
201-42	7		0.56			$\text{Mg}_{3.56}\text{Fe}_{1.23}\text{Si}_{2.85}\text{Al}_{2.33}\text{O}_{10}(\text{OH})_8$
199-07	8		0.50			$\text{Mg}_{3.42}\text{Fe}_{1.48}\text{Si}_{3.01}\text{Al}_{2.05}\text{O}_{10}(\text{OH})_8$
199-15	9		0.47			$\text{Mg}_{3.22}\text{Ca}_{0.06}\text{Fe}_{1.55}\text{Si}_{3.01}\text{Al}_{2.10}\text{O}_{10}(\text{OH})_8$
199-15	10		0.45			$\text{Mg}_{3.16}\text{Ca}_{0.02}\text{Fe}_{1.66}\text{Si}_{2.88}\text{Al}_{2.27}\text{O}_{10}(\text{OH})_8$
201-42	11		0.71			$\text{Ca}_{0.92}\text{Mg}_{0.90}\text{Fe}_{0.15}\text{Al}_{0.07}\text{Si}_{1.96}\text{O}_6$
201-42	12		0.73			$\text{Ca}_{0.90}\text{Mg}_{0.92}\text{Fe}_{0.14}\text{Al}_{0.09}\text{Si}_{1.95}\text{O}_6$
199-15	13		0.62			$\text{Na}_{0.66}\text{Ca}_{1.98}\text{Mg}_{3.72}\text{Fe}_{0.97}\text{Si}_{6.68}\text{Al}_{1.75}\text{O}_{22}(\text{OH})_2$
199-17	14			0.82		$\text{Mg}_{1.83}\text{Fe}_{0.17}\text{Si}_{0.99}\text{O}_4$
199-17	15			0.77		$\text{Mg}_{1.77}\text{Fe}_{0.23}\text{Si}_{1.00}\text{O}_4$
201-42	16	0.23				$\text{Na}_{0.87}\text{Ca}_{0.15}\text{Al}_{1.17}\text{Si}_{2.82}\text{O}_8$
201-42	17	0.73				$\text{Na}_{0.40}\text{Ca}_{0.63}\text{Al}_{1.64}\text{Si}_{2.33}\text{O}_8$
201-42	18	0.74				$\text{Na}_{0.39}\text{Ca}_{0.63}\text{Al}_{1.63}\text{Si}_{2.35}\text{O}_8$
201-42	19	0.80				$\text{Na}_{0.32}\text{Ca}_{0.71}\text{Al}_{1.72}\text{Si}_{2.26}\text{O}_8$
199-15	20	0.76				$\text{Na}_{0.36}\text{Ca}_{0.66}\text{Al}_{1.67}\text{Si}_{2.31}\text{O}_8$
199-15	21	0.81				$\text{Na}_{0.30}\text{Ca}_{0.73}\text{Al}_{1.72}\text{Si}_{2.26}\text{O}_8$
199-15	22	0.00				$\text{Na}_{0.97}\text{Al}_{1.03}\text{Si}_{2.99}\text{O}_8$
199-15	23	0.03				$\text{Na}_{0.97}\text{Ca}_{0.02}\text{Al}_{1.03}\text{Si}_{2.99}\text{O}_8$
199-15	24	0.68				$\text{Na}_{0.46}\text{Ca}_{0.57}\text{Al}_{1.59}\text{Si}_{2.37}\text{O}_8$
199-15	25	0.58				$\text{Na}_{0.57}\text{Ca}_{0.46}\text{Al}_{1.47}\text{Si}_{2.49}\text{O}_8$
199-17	26		0.90			$\text{Mg}_{2.74}\text{Fe}_{0.13}\text{Si}_{2.07}\text{O}_5(\text{OH})_4$
199-17	27		0.91			$\text{Mg}_{2.75}\text{Fe}_{0.12}\text{Si}_{2.07}\text{O}_5(\text{OH})_4$
199-17	28		0.86			$\text{Mg}_{2.60}\text{Fe}_{0.19}\text{Si}_{2.11}\text{O}_5(\text{OH})_4$
199-17	29		0.87			$\text{Mg}_{2.57}\text{Fe}_{0.17}\text{Si}_{2.13}\text{O}_5(\text{OH})_4$
199-15	30		0.16		0.69	$\text{Mg}_{0.33}\text{Fe}^{2+}_{0.73}\text{Al}_{0.81}\text{Cr}_{0.92}\text{Fe}^{3+}_{0.22}\text{O}_4$

Table 4.2: anorthite content (An), Mg#, Cr#, forsterite (Fo) content and empirical formulae for analysis listed in table 4.1.

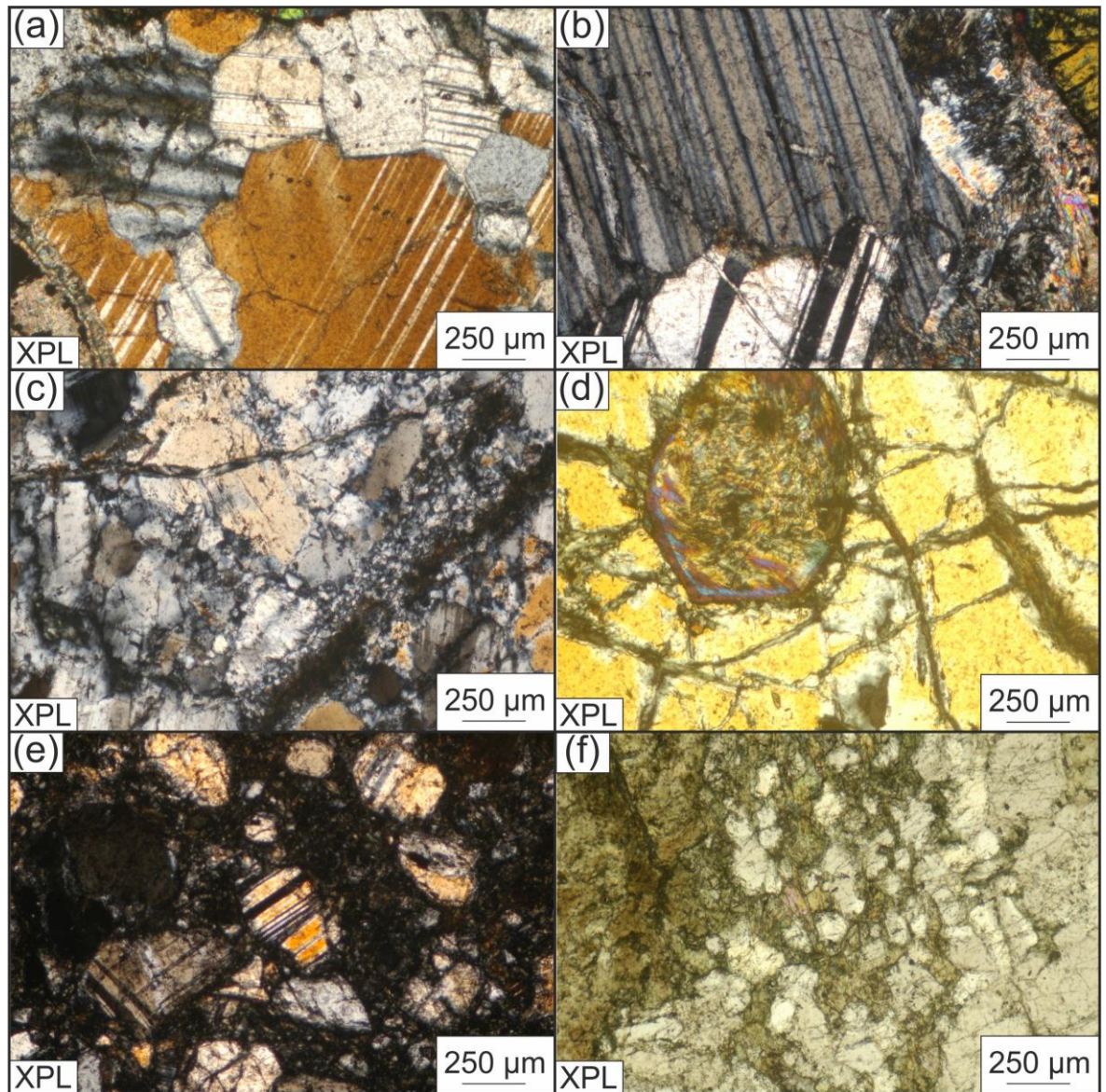


Figure 4.10: Feldspar habits in VDFV host rocks – images taken in transmitted light. Generally, secondary albite occurs on the margins of coarse grained anorthite (a) JC082-199-19: coarse grained plagioclase in gabbro (b) JC082-199-19: coarse grained plagioclase crystals, with some chlorite on the right of the image (c) JC082-199-07: plagioclase with fine-grained chlorite replacement in veins and on the margins of crystals (d) JC082-201-42: yellow crossed-polar interference colours in high-Ca plagioclase with thin fractures replaced by chlorite; in the top left of the image there is an actinolite pseudomorph after olivine (e) JC082-199-15: plagioclase phenocrysts in the very fine-grained matrix of a porphyritic dyke (f) JC082-199-11: the right of the image is slightly coarser plagioclase with some finer grained albite in the centre of the image; the left of the image is clinopyroxene altered to actinolite-tremolite. Abbreviations for type of image are PPL = plane polarised light, XPL = cross polarised light. These abbreviations are consistent throughout this chapter.

Dykes: Porphyritic dykes have plagioclase and rare clinopyroxene phenocrysts with grain sizes of up to 1 cm, and the groundmass is around 40 μm (Figures 4.10, 4.12). Variations in composition show a similar trend to the gabbros, with two different groups of plagioclase composition. The sodium rich group have compositions of An_0 - An_{10} , whereas the calcium rich group have compositions of An_{58} - An_{81} . The main primary mineral within the fine grained groundmass is plagioclase, and rare grains of clinopyroxene are observed. No olivine is observed in the dyke material.

Serpentinised peridotite: Olivine and rare clinopyroxene are the only primary minerals within the sample of peridotite. Olivine is almost entirely replaced but the remnant grains are up to 1.5 mm across and are colourless in PPL. Interference colours are up to lower 3rd order and the crystals are extensively fractured. Olivine composition measured by EDS analysis is Fo_{82} , lower than the value for depleted mantle (Table 4.2; Carter, 1970).

4.3.3. Common replacement minerals

The host rocks recovered from the VDVF have undergone peak metamorphism at up to amphibolite facies (except for the mylonites). This section describes the common replacement minerals observed in each lithology.

Gabbros: Chlorite replaces plagioclase to varying degrees, from fine-grained replacement along fractures and veins to complete replacement giving chlorite pseudomorphs after plagioclase (Figure 4.13). Chlorite generally takes the form of massive, fibrous and radial fine-grained masses up to 3 mm across, with individual grains being up to $\sim 100 \mu\text{m}$ across. Chlorite appears colourless to pale green in plane polarised light (PPL), and low first order greys are the highest interference colours seen. Mg numbers (where $\text{Mg\#} = \text{Mg}/(\text{Mg}+\text{Fe})$) in the chlorite range from 0.48 to 0.60, and have an average of 0.54, which is within the range of chlorites in greenschist facies rocks from other mid-ocean ridges (Table 4.2; Mottl 1983).

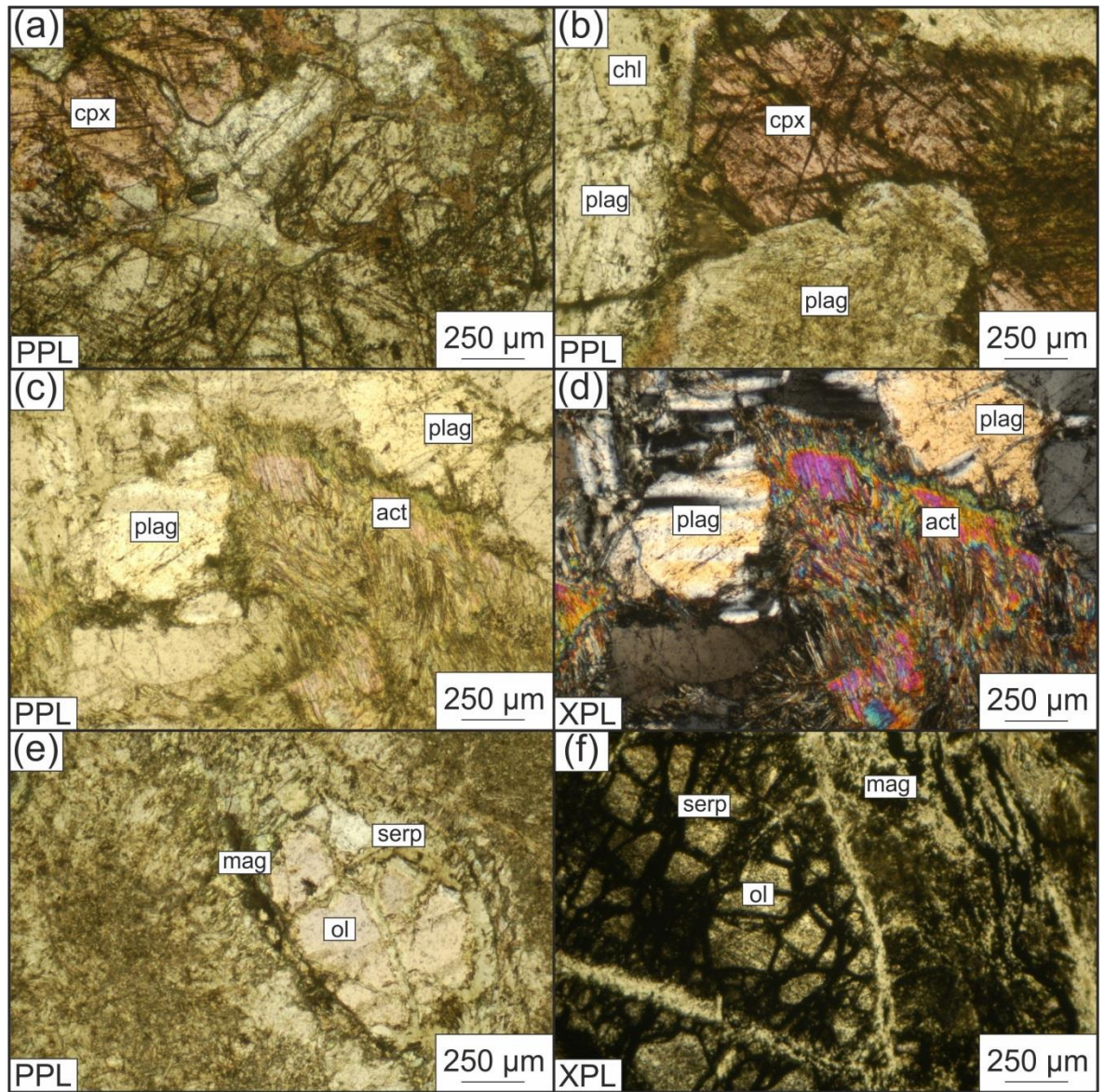


Figure 4.11: Remnant pyroxene and olivine in VDFV host rocks. Photomicrographs taken in transmitted light (a) JC082-199-19: augite in top left and bottom right of image (b) JC082-199-06: titanaugite surrounded by partially chloritised plagioclase on the left of the image, and some fine-grained actinolite-tremolite at the bottom (c) and (d) JC082-199-11: remnant titanaugite almost completely replaced by actinolite-tremolite; titanaugite is indicated by the slight pink tinge in PPL (e) JC082-199-06: remnant olivine partially replaced by serpentine along fractures and grain margins in gabbro (f) JC082-199-17: olivine replaced by very fine-grained, isotropic serpentine in serpentinised peridotite. Mineral abbreviations: act = actinolite, chl = chlorite, cpx = clinopyroxene, mag = magnetite, ol = olivine, plag = plagioclase, serp = serpentine.

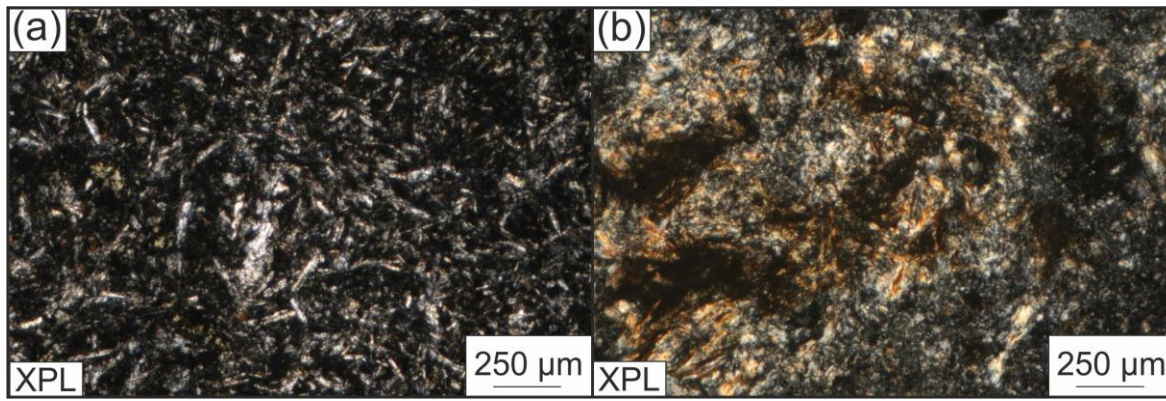


Figure 4.12: Groundmass in altered dykes. Photomicrographs taken in transmitted light (a) JC082-199-15: plagioclase dominated fine-grained groundmass (b) JC082-199-16: altered and oxidised groundmass.

Actinolite and tremolite are also common replacement minerals in metadolerite dykes but are not as abundant as in the dredged gabbro material. This is partly due to the slightly lower degree of alteration of the primary mineralogy observed in the dykes, but also due to the dominance of hornblende. In the gabbros, they form colourless-pale green fine-grained acicular and fibrous masses in the groundmass, and partially replace coarse grained clinopyroxene and olivine. The actinolite-tremolite masses are 1-4 mm across, and individual crystals are usually up to 0.5 mm across (Figure 4.14). Tremolite replacement of olivine occurs adjacent to secondary chlorite rims surrounding primary plagioclase. The actinolite-tremolite masses are not pure end-member compositions, but have varying concentrations of iron (2.0-9.4 wt.%), magnesium (10.3-15.0 wt.%) and calcium, (7.7-10.0 wt.%; Table 4.1).

Calcium-rich hornblende occurs within gabbro samples, and shows a range of forms and grain sizes. It is generally pleochroic pale brown-dark brown in PPL, and occurs either as medium grained, up to 1 mm across rounded grains or as finer grained, granular masses in the groundmass (Figure 4.15). Grains cut orthogonally to the 001 axis of the crystal show the characteristic $\sim 60^\circ$ and $\sim 120^\circ$ cleavage intersections. The calcium content of the amphibole, which ranges from 8.4-8.8 wt.% in hornblende, is indicative of secondary formation after clinopyroxene and plagioclase.

Serpentinised peridotite: Serpentine and actinolite-tremolite are observed as the dominant mineral replacing olivine and clinopyroxene in the samples of altered

peridotite. The replacement is not complete, as relict primary olivine is preserved in the groundmass. Where present, the serpentine forms fine-grained aggregates of lizardite and its opaque appearance means mesh textures are rare (Figure 4.16). Cross cutting veins up to 1 mm across consist of granular and fibrous antitaxial growths of fibrous chrysotile and antigorite. Tremolite grains are elongate and fibrous, and show 3rd order interference colours.

Dykes. Chlorite is the most common altered mineral within the altered dykes, and has a groundmass of around ~50 µm. Mg# chlorite ranges from 0.45 to 0.51, and averages 0.48, similar to the chlorite within the gabbros. Actinolite and tremolite are the other common phase within the altered groundmass of the dykes, and the grainsize is typically 40 µm. The elemental composition of actinolite masses falls within the ranges analysed for the gabbros. Quartz is found in a small proportion of samples that are hydrothermally altered. In the dyke material, small grains around 30-40 µm across are found disseminated within the groundmass. They are sub-rounded and generally subhedral.

4.3.4. Accessory minerals

Gabbro: Accessory minerals present in the VDVF gabbros include sphene, rutile, apatite and rare zircon. Most of these (except sphene) were identified using SEM analysis due to their small grain size (Figure 4.18). Sphene is the most common of these minerals and occurs either as blocky, very high relief, colourless crystals within the groundmass or as irregular, rounded inclusions enclosed by actinolite-tremolite masses. The grain size of the blocky crystals is up to 250 µm, but typically 50 µm, whereas the irregular inclusions in actinolite-tremolite are 10-20 µm. Rutile grains are 20-30 µm across and are usually found as irregular-shaped grains within the chlorite and actinolite-tremolite masses (Figure 4.18). Generally, rutile and sphene are found at different locations in the groundmass and are not associated with each other. Apatite has a grain size of <50 µm, and forms small rounded grains mainly within chlorite and occasionally within actinolite-tremolite. Rare grains of zircon, up to 30 µm across, are found associated with large plagioclase crystals, or as small inclusions within actinolite-tremolite masses.

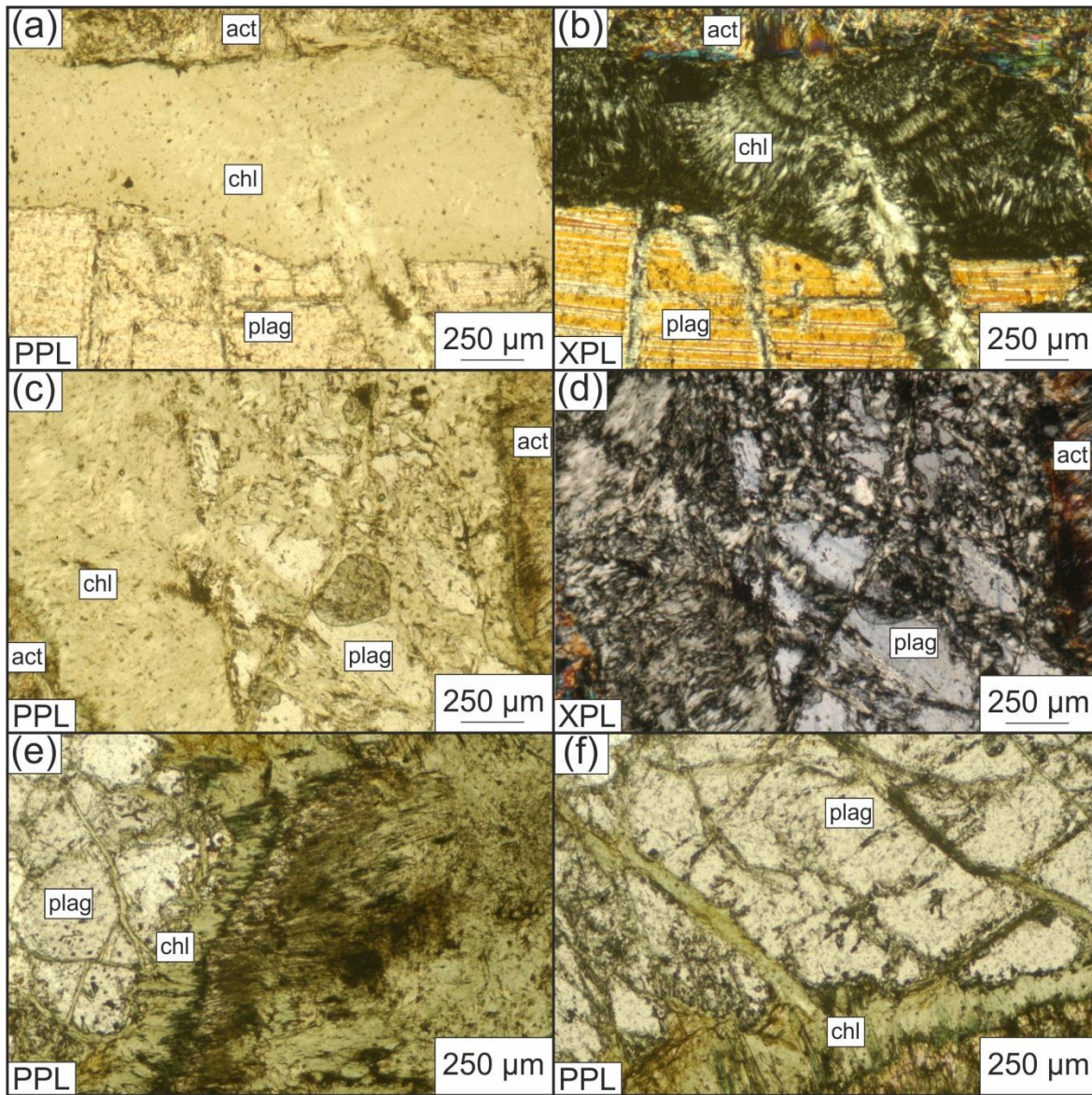


Figure 4.13: Chlorite replacement of plagioclase in VDFV host rocks. Photomicrographs taken by transmitted light microscopy; with actinolite-tremolite after olivine at the top of the images (a) JC082-199-06: and (b) radial chlorite replacing anorthite on grain margins (c) JC082-199-07: and (d) fine grained, almost complete replacement of plagioclase (e) JC082-199-14: remnant plagioclase on the left side of the image with chlorite replacement (f) JC082-199-14: green chlorite replacing plagioclase in veins and fractures. Mineral abbreviations: act=actinolite, chl = chlorite, plag=plagioclase.

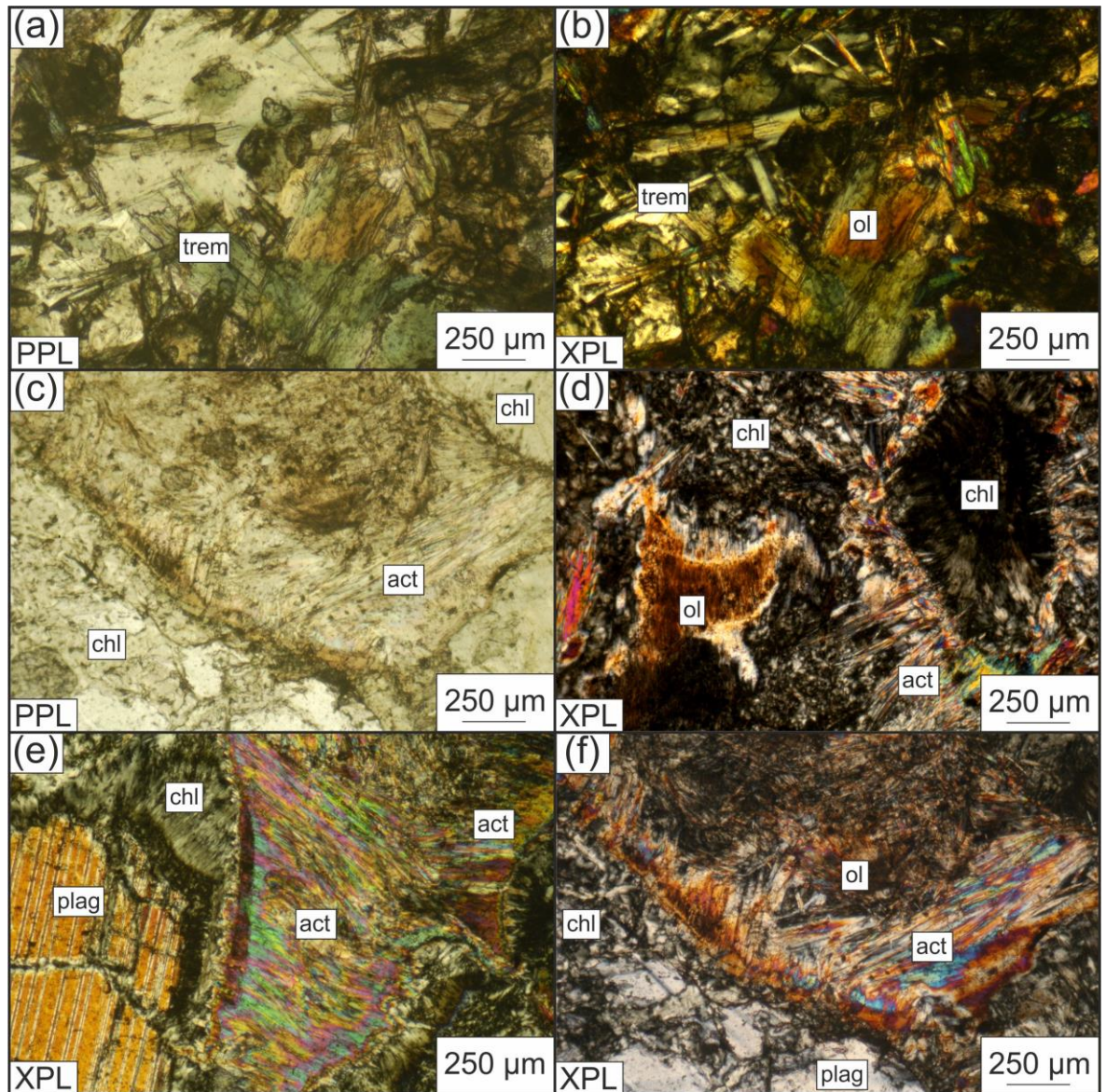


Figure 4.14: actinolite-tremolite forms in VDFV gabbros. Photomicrographs taken in transmitted light (a) JC082-199-07: and (b) actinolite-tremolite needles within altered gabbro replacing olivine (c) JC082-199-07: pseudomorph of actinolite after olivine with chlorite in the top right and bottom left (d) JC082-199-07: acicular actinolite with fine-grained chlorite and hornblende (e) JC082-199-06: fibrous actinolite-tremolite pseudomorphs after olivine occurring on the margins of plagioclase (f) JC082-199-07: actinolite-tremolite pseudomorphs with acicular growths of amphibole off the margins of relict olivine. Mineral abbreviations: act = actinolite, chl = chlorite, plag = plagioclase, ol=olivine, trem = tremolite.

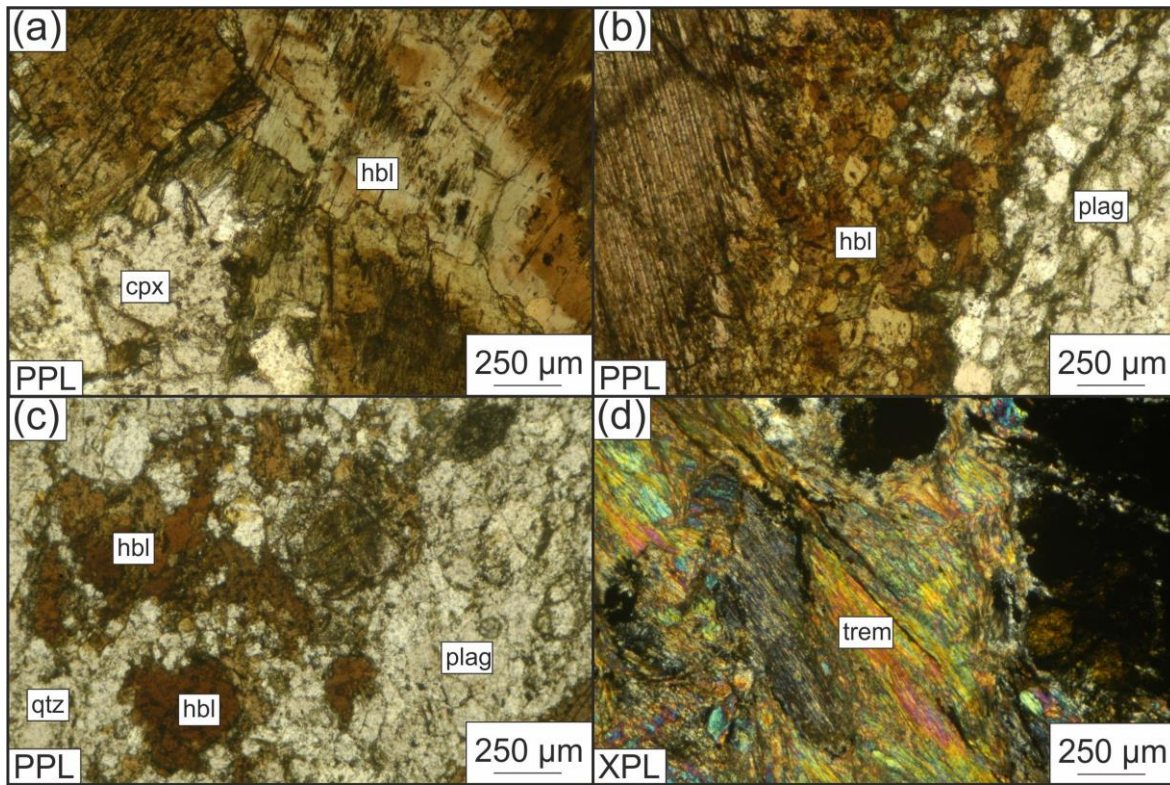


Figure 4.15: Hornblende in VDFV host rocks and amphibole occurrences in ultramafics. Images taken in transmitted light (a) JC082-199-07: coarser hornblende replacing clinopyroxene (b) JC082-199-13: hornblende grain with deformed, finer-grained margin due to mylonitisation (c) JC082-199-13: fine-grained, granular hornblende in the groundmass of plagioclase and minor quartz (d) JC082-199-17: tremolite replacing olivine in altered peridotite. Mineral abbreviations: cpx = clinopyroxene, hbl = hornblende, plag = plagioclase, qtz = quartz, trem = tremolite.

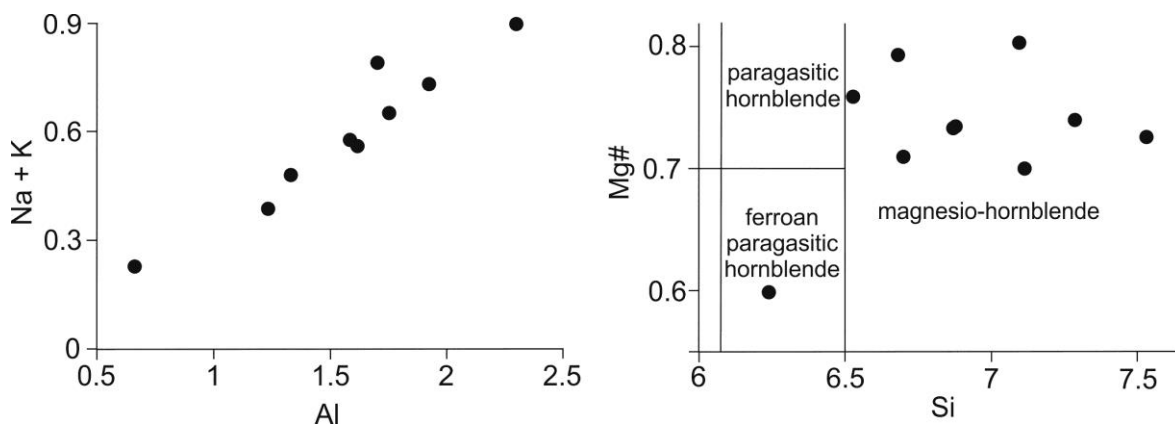


Figure 4.16: composition of hornblende in VDFV host rocks (a) Al vs. Na + K (b) Si vs. Mg# showing the classification of hornblende after Otten (1984).

Serpentinised peridotite: Magnetite, spinel and pyrrhotite, are found within the sample of serpentinised peridotite. Magnetite is only observed within serpentine and is generally concentrated in serpentine fractures along incompletely replaced olivine crystals, or as large, irregular shaped masses up to 300 μm across. Cr-spinel can be up to 1 mm across, but is generally around 2-300 μm (Figure 4.17).

4.3.5. Textures and summary of alteration

The gabbro samples that do not have a metamorphic foliation are isotropic and have a crystalline texture. Fresher gabbros occasionally show a sub-ophitic texture, where clinopyroxene is surrounded by coarser grains of plagioclase. In variably altered gabbros, plagioclase crystals are typically replaced by chlorite, while pyroxene is replaced by amphibole including actinolite-tremolite and hornblende, indicative of amphibolite facies alteration. Furthermore, albitisation of plagioclase leads to the development of fine-grained, Na-rich plagioclase on the margins of coarse grained anorthite, displayed by the occurrence of two groups of plagioclase composition within each sample. Olivine is replaced by tremolite in gabbros, and by tremolite and serpentine in altered ultramafics. Actinolite-tremolite masses regularly occur with chlorite, especially on the margins of replaced olivine and plagioclase in gabbros. Metadolerite dykes have a porphyritic texture, comprising of feldspar, quartz, chlorite and actinolite-tremolite groundmasses. One of the dyke samples displays a lower degree of alteration, indicating intrusion after the main phase of amphibolite facies metamorphism.

Two samples show strong mylonitic textures, indicative of ductile deformation. These textures are characterised by a ribbon texture of light bands consisting of secondary quartz and feldspar, and dark bands of fine-grained amphibole and pyroxene. Primary anorthite contains deformed twins and kink banding, and is partially recrystallised to neoblasts of secondary quartz and feldspar on its margins (Figure 4.19). One of the samples of dyke material shows rounded plagioclase within a fine-grained groundmass, and cataclastic textures indicative of brittle deformation.

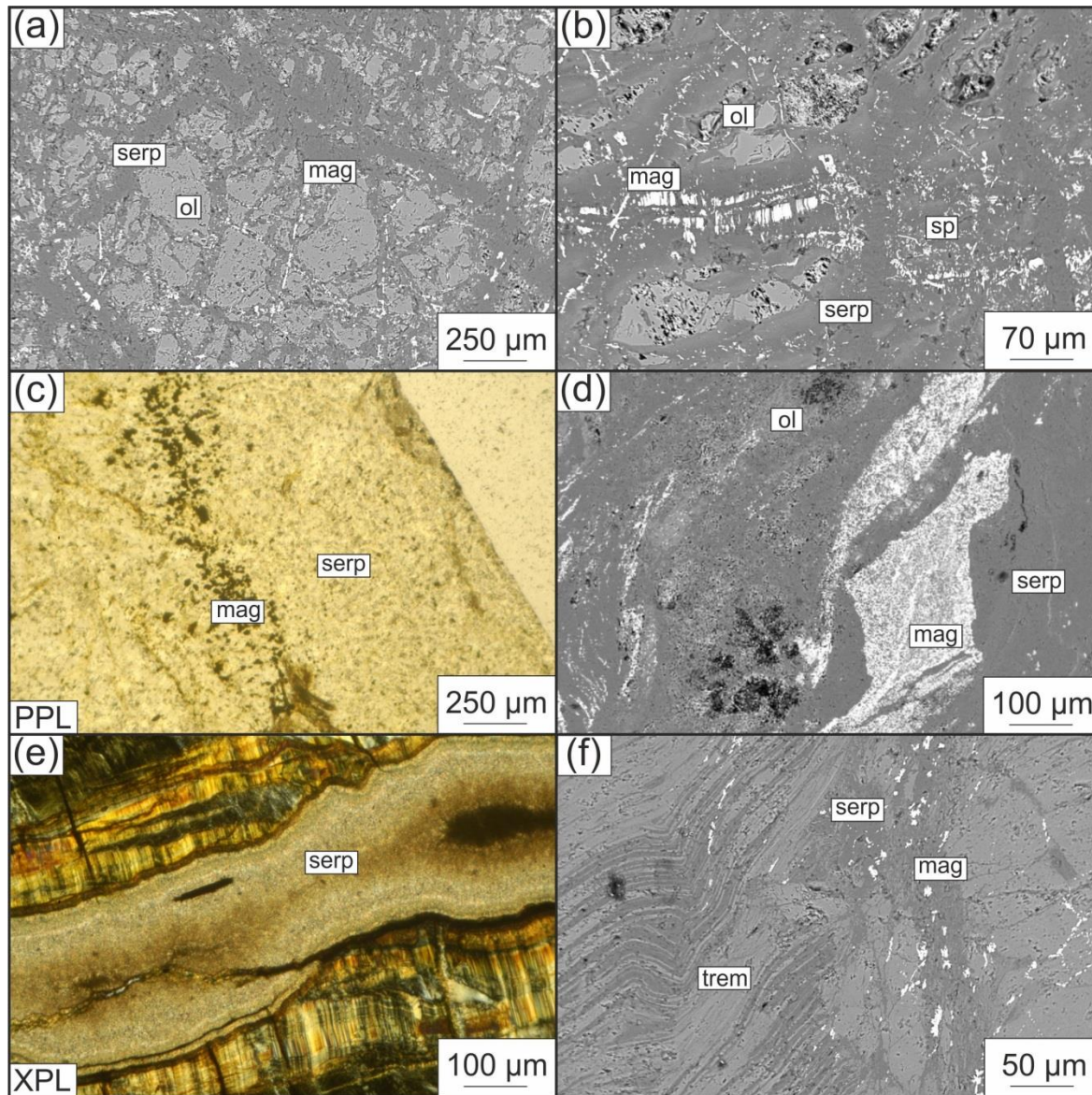


Figure 4.17: Mineralogy of serpentinised ultramafics. Images acquired using transmitted light microscopy and SEM. All images are of JC082- 199-17 (a) and (b) mesh-textured serpentine with magnetite, partially replacing olivine along fractures; occasional spinel (c) fine-grained serpentine with magnetite (d) irregular shaped accumulations of magnetite within serpentine (e) granular and fibrous serpentine vein (f) fibrous actinolite-tremolite intergrown with serpentine. Mineral abbreviations: mag = magnetite; ol = olivine, serp = serpentine, sp = spinel, trem = tremolite.

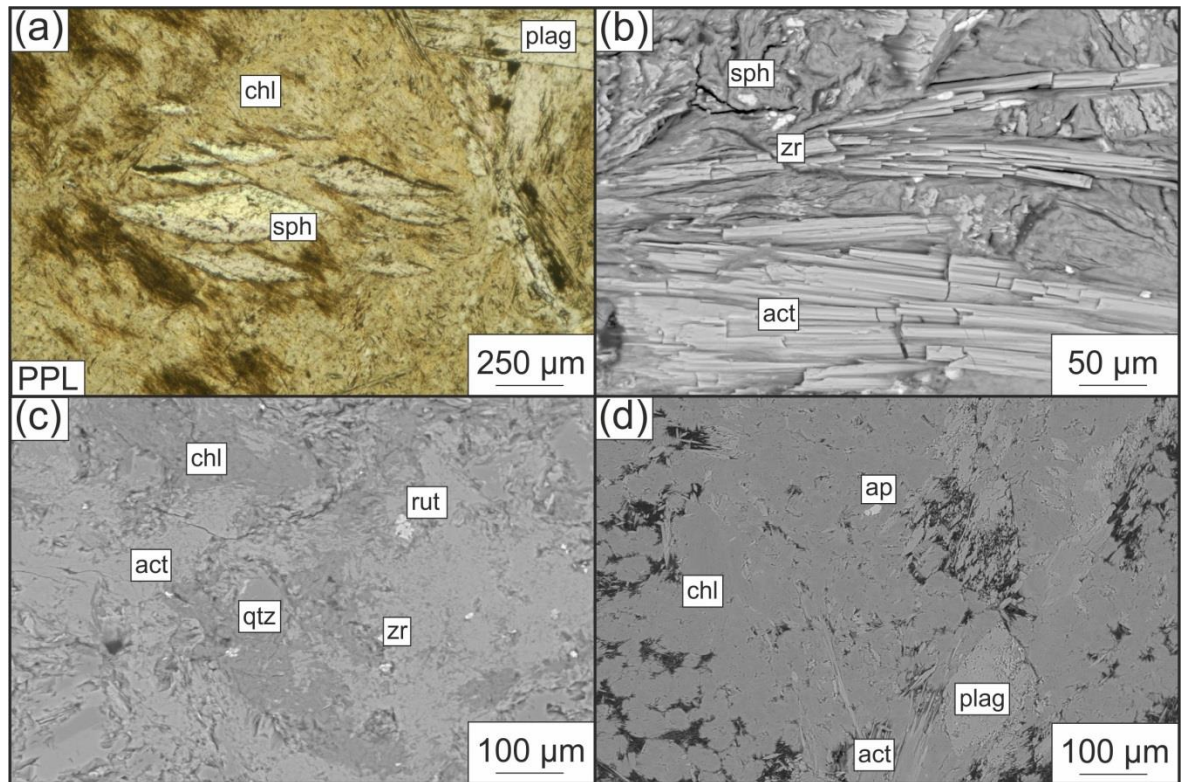


Figure 4.18: Accessory minerals in VDVF host rocks. Images taken in transmitted light and SEM (a) JC082-201-42: diamond shaped sphene within chlorite masses (b) JC082-199-07: acicular columns of actinolite with sphene and zircon (c) JC082-199-15: chlorite, actinolite and minor quartz groundmass with small accessory rutile and zircon (d) JC082-201-42: apatite within chlorite groundmass; minor plagioclase and acicular actinolite. Mineral abbreviations: act = actinolite, ap = apatite, chl= chlorite, plag = plagioclase, qtz = quartz, rut = rutile, sph = sphene, zr = zircon.

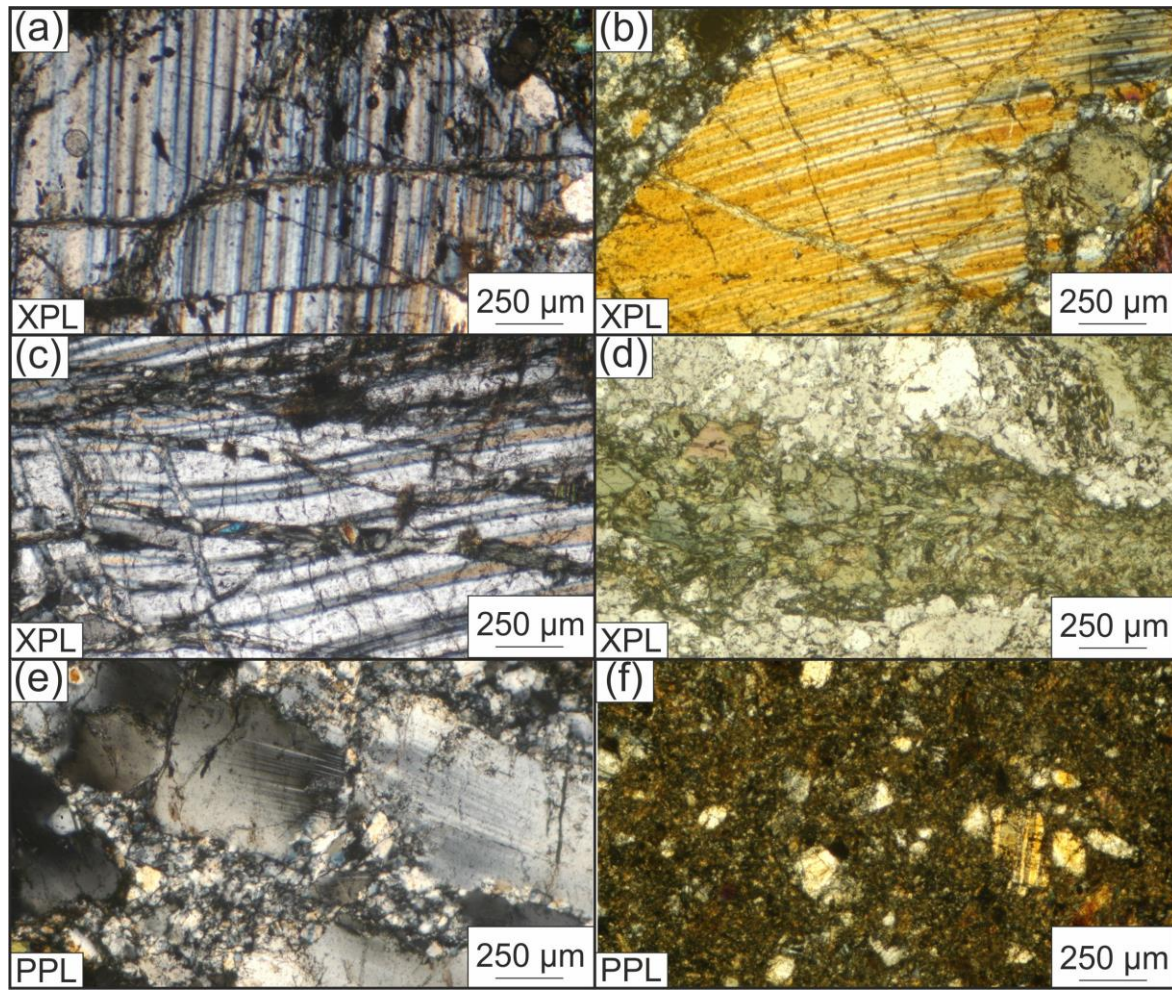


Figure 4.19: Deformation textures in VDFV host rocks. Photomicrographs taken in transmitted light (a) JC082-199-14: sheared and fractured coarse-grained plagioclase (b) JC082-199-13: deformed twins in anorthite, with recrystallisation on the margins (c) JC082-199-11: deformed twinning in plagioclase, with fine-grained chlorite veins (d) JC082-199-12: fine grained recrystallisation showing quartz and plagioclase (e) JC082-199-12: altered plagioclase with fine-grained neoblastic recrystallisation on grain margins from mylonitic deformation (f) JC082-199-16: cataclastic texture in fine-grained dyke material.

4.3.6. Whole rock geochemistry of basement rocks

Whole rock analysis of the host material indicates high concentrations of Al_2O_3 (16.3-20.2 wt. %), total Fe_2O_3 (5.1-9.4 wt. %), MgO (6.1-10.6 wt. %) and CaO (9.8-14.2 wt. %; Table 4.3). The least altered gabbro sample has the highest CaO content of 14.2 wt. %, and the second lowest Na_2O of 2.4 wt. %. This is keeping with the observation of a lack of albitisation, and the proportions of fresh augite, olivine and anorthite. The

porphyritic dyke contains higher proportions of fresher plagioclase, and lower proportions of chlorite and amphibole giving lower concentrations of MgO.

The calculation of the Na₂O content at 8 wt. % MgO basalts at mid-ocean ridges (MOR) is used as a method for the correction of low pressure fractionation in magma chambers (Klein and Langmuir, 1987). This is calculated using Equation 4.1, and is termed the Na_{8.0} value (Klein and Langmuir, 1987). The calculation of this number indicates a linear trend between depth and Na_{8.0}, and suggests basalts at deeper ridges undergo small degrees of partial melting. The porphyritic dyke plots below the range of MCR basalt glasses and has an Na_{8.0} value closer to that of basalts at ~4000 m seawater depth on the MAR, potentially implying a shallower, and thus more off-axis origin (Figure 4.20; Klein and Langmuir, 1987).

$$\text{Na}_{8.0} = \text{Na}_2\text{O} + (0.373 \times \text{MgO}) - 2.98 \quad (4.1)$$

The four samples of host rock (3 gabbro and one plagioclase-phyric dyke) from the vicinity of the VDVF, and the two samples of basalt glass from the neovolcanic axis have flat REE profiles (Figure 4.21). ΣREE in the gabbros and dykes is relatively uniform and similar to other samples in oceanic environments e.g. (Table 4.3; Humphris et al. 1998; Morishita et al., 2009; Hayman et al., 2011). Two gabbro samples have slight Eu/Eu* (where $\text{Eu}/\text{Eu}^* = \text{Eu}_{(\text{N})}/\sqrt{(\text{Sm}_{(\text{N})} \times \text{Gd}_{(\text{N})})}$) anomalies of 1.2-1.4, while the others show little or no anomaly (Table 4.4). One gabbro sample has a slight positive Ce anomaly of 1.5, and the dyke sample has a Ce/Ce* (where $\text{Ce}/\text{Ce}^* = \text{Ce}_{(\text{N})}/\sqrt{(\text{La}_{(\text{N})} \times \text{Pr}_{(\text{N})})}$) anomaly of 1.8 (Table 4.4). A positive Eu anomaly in oceanic gabbros is commonly associated with primitive gabbros and high plagioclase content, or an association with cumulate processes e.g. (Hayman et al. 2011). The lack of an Eu anomaly in the more heavily altered samples suggests that Eu is stripped from the host rock as it is mobilised by reducing hydrothermal fluids, resulting in no anomaly, or an Eu/Eu* value of slightly <1 (Humphris et al., 1998; Douville et al., 2002).

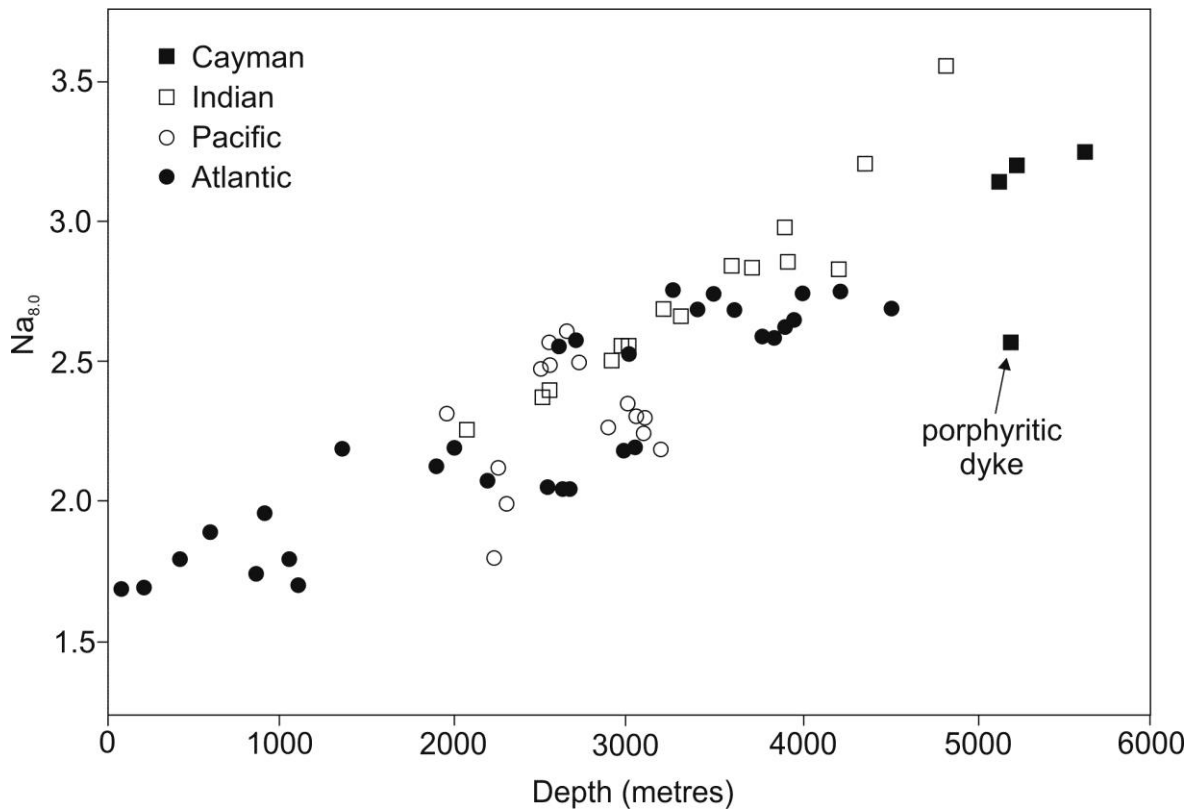


Figure 4.20: $Na_{8.0}$ values plotted against depth for the Atlantic, Pacific, Indian and Cayman regions, after Klein and Langmuir, (1987). The porphyritic dyke is plotted against the depth of the AVR.

Samples of basalt glass have very similar REE patterns to those recovered at other localities along the MCR by Elthon et al., (1995). MCR basalts have elevated ΣREE in comparison to the average N-MORB and D-MORB (normal- depleted- mid-ocean ridge basalt) and lower than the average E-MORB (enriched mid-ocean ridge basalt; Figure 4.21; Gale et al., 2013). The basalts from the axial volcanic ridge and the dyke have La_N/Sm_N ratios of 0.8 to 1.2. This ratio is higher than the ratios from the MAR, but lower than the ratios for E-MORB (>1.5 ; Gale et al., 2013). Nb and Zr concentrations of 4.4 ppm and 58.9 ppm in the basalt dyke are far greater than the ranges of 0.7-1.1 ppm and 11-26 ppm observed in the gabbros (Table 4.3). The elevated ΣREE , slight LREE enrichment of MCR basalts, and increased concentration of Nb and Zr in comparison to lower crustal rocks, suggest fractionation of incompatible elements due to the small melt fractions at the MCR (Sun et al., 1979; Klein and Langmuir, 1987). This degree of melting is consistent with ultraslow spreading rate, and tectonically dominated spreading at the Mt. Dent OCC (White et al., 2013).

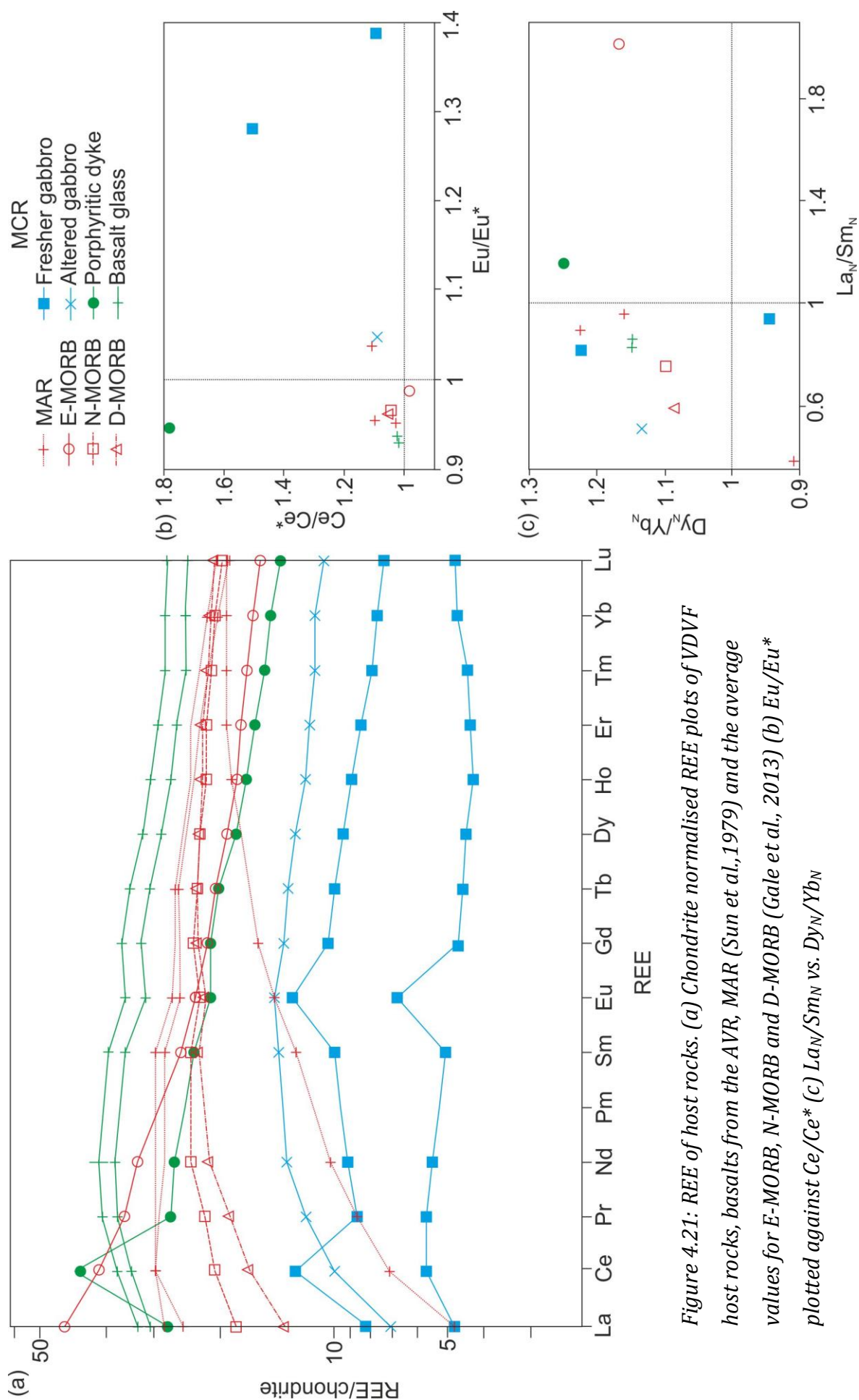


Figure 4.21: REE of host rocks. (a) Chondrite normalised REE plots of VDVF host rocks, basalts from the AVR, MAR (Sun et al., 1979) and the average values for E-MORB, N-MORB and D-MORB (Gale et al., 2013) (b) Eu/Eu^* plotted against Ce/Ce^* (c) La_N/Sm_N vs. Dy_N/Yb_N

Sample		199-11	199-14	199-18	199-19
Type		Gabbro	Gabbro	Dyke	Gabbro
SiO ₂	wt. %	48.56	46.80	49.33	50.72
TiO ₂	wt. %	0.18	0.26	1.26	0.68
Al ₂ O ₃	wt. %	19.74	17.68	20.16	16.39
Total FeO	wt. %	4.64	8.46	6.19	5.41
MgO	wt. %	10.32	10.57	6.10	9.38
CaO	wt. %	10.63	9.80	10.21	14.18
K ₂ O	wt. %	0.05	0.08	0.07	0.06
Na ₂ O	wt. %	2.51	2.22	3.25	2.36
P ₂ O ₅	wt. %	0.02	0.02	0.16	0.05
LOI	wt. %	2.09	3.50	2.30	1.76
Sum	wt. %	98.73	99.40	99.03	101.00
Cr	ppm	537	998	234	736
Mn	ppm	450	836	2076	802
Co	ppm	34.6	45.0	135	46.3
Ni	ppm	187	271	85.4	134
Cu	ppm	4.87	10.6	15.4	33.8
Zn	ppm	10.2	32.3	17.6	24.6
As	ppm	0.94	0.96	3.61	7.16
Rb	ppm	0.20	0.34	0.32	0.35
Sr	ppm	184	131	256	173
Y	ppm	7.0	18.2	25.6	13.3
Zr	ppm	11.8	20.7	58.8	25.9
Nb	ppm	0.77	1.20	4.42	0.81
Mo	ppm	0.15	0.12	1.76	0.62
Cd	ppm	0.02	0.04	0.05	0.07
Sb	ppm	0.02	0.03	0.14	0.38
Ba	ppm	0.03	0.01	0.02	0.01
La	ppm	1.15	1.70	6.57	1.95
Ce	ppm	3.55	6.22	30.2	7.87
Pr	ppm	0.54	1.12	2.56	0.82
Nd	ppm	2.54	6.19	12.3	4.27
Sm	ppm	0.76	2.10	3.55	1.50
Eu	ppm	0.39	0.83	1.21	0.74
Gd	ppm	0.95	2.75	4.29	2.09
Tb	ppm	0.17	0.49	0.74	0.37
Dy	ppm	1.12	3.16	4.57	2.36
Ho	ppm	0.24	0.66	0.95	0.50
Er	ppm	0.71	1.89	2.62	1.38
Tm	ppm	0.11	0.28	0.38	0.20
Yb	ppm	0.77	1.82	2.39	1.26
Lu	ppm	0.12	0.27	0.35	0.18
Hf	ppm	0.36	0.60	1.69	0.76
Ta	ppm	0.09	0.08	0.26	0.06
Pb	ppm	1.06	0.68	16.1	4.81
Th	ppm	0.11	0.07	1.38	0.32
U	ppm	0.03	0.04	0.19	0.15
ΣREE	ppm	0.01	0.03	0.07	0.03

Table 4.3: Major and trace elements in host rocks recovered from within 1 km of the VDVF. LOI is included in the total wt. %.

Sample	Type	Eu/Eu*	Ce/Ce*	La/Sm	Dy/Yb
199-11	Gabbro	1.4	1.1	0.9	0.9
199-14	Gabbro	1.0	1.1	0.5	1.1
199-18	Dyke	0.9	1.8	1.2	1.2
199-19	Gabbro	1.3	1.5	0.8	1.2
205-70	Basalt	0.9	1.0	0.8	1.1
207-86	Basalt	0.9	1.0	0.9	1.1

Table 4.4: Eu anomalies, Ce anomalies, La_N/Sm_N ratios and Dy_N/Yb_N ratios in host rock samples and basalt glass from the AVR.

4.3.7. Origin of basement lithologies

Gabbros recovered from within 1 km of the VDVF are less altered than those from the toe of Mt. Dent. Plagioclase is the dominant primary igneous mineral, and olivine and rare clinopyroxene occur in varying proportions (always <10%), although as the exact proportions are unknown due to alteration, the samples are described as gabbros. The lack of clinopyroxene and occurrences of corona textures in the plagioclase and olivine shows that cumulate processes occurred in the gabbros around the VDVF. This is also suggested by the REE chemistry of the fresh samples. The positive Eu/Eu* anomaly indicates an elevation in plagioclase content compared to isotropic gabbros, a process that has occurred from cumulate processes e.g. (Hayman, 2011). The serpentinised peridotite contains no orthopyroxene, and its assemblage consists mostly of olivine (Fo₇₇) and clinopyroxene. This assemblage and olivine composition indicates that this sample is not a peridotite of mantle origin, such as lherzolite or harzburgite, but is instead a lower crust/upper mantle cumulate.

Mylonite textures indicate ductile deformation at depth in the crust at amphibolite-granulite facies metamorphic conditions (600-800°C; Reynolds and Lister, 1987). This is post-dated by hydrothermal alteration that peaks at amphibolite facies conditions (400-600°C), replacing plagioclase and clinopyroxene with chlorite and actinolite, and then altering anorthite to albite. No pargasite was observed, unlike in the dredge samples. One of the dyke samples displays a lower degree of alteration, indicating intrusion after the main phase of amphibolite facies metamorphism, however some secondary chlorite and minor albitisation is observed.

4.4. Active chimneys

4.4.1. Venting styles at the VDVF

Focussed flow at the VDVF occurs across all three mounds at the active site (Table 4.5). The main mound features two vents which are responsible for a largest proportion of the focussed hydrothermal fluid discharge. The first of these, called the “Spire”, is located at the highest point of the VDVF, at the top of a 4 metre high, 2 metre diameter chimney structure that vents clear, shimmering fluid at 215°C.

The partial collapse of this structure reveals a large, 1 metre diameter orifice called the “Main Hole” (Figure 4.22). This vent is located 3 metres directly downslope of the Spire and has maximum measured temperatures from JC082 of 91°C, which is similar to previous measurements of 123°C (McDermott, 2015). Both of these chimneys are located along the same conduit at the top of the main cone. Other areas of focussed flow on the main cone include one large fissure 40 cm long, and up to 10 cm wide, venting at temperatures of up to 138°C (Hotter than Hole), and another small chimney that vents fluids at up to 118°C (Figure 4.23). Elsewhere across the active VDVF, hydrothermal discharge is focussed through small chimlets up to 30 cm tall, with a maximum temperature (recorded away from the main mound) of 112°C. Diffuse flow occurs all over the three active mounds at up to 20°C, and is easily identified by dense clusters of Rimicaris shrimp (Figure 4.23).

Vent	Mound	Latitude	Longitude	Depth	Max temp (°C)
Main Hole	MC	18°22.601'N	81°47.888'W	2294	91
Spire	MC	18°22.601'N	81°47.888'W	2291	215
Hotter than Hole	MC	18°22.599'N	81°47.881'W	2308	138
Fumerole	MC	18°22.593'N	81°47.884'W	2310	118
Chimlet 2	NS	18°22.561'N	81°47.844'W	2379	108
Chimlet 1	SS	18°22.516'N	81°47.845'W	2387	43
X-15	SS	18°22.498'N	81°47.848'W	2373	112

Table 4.5: List of active vent structures at the VDVF. Temperatures displayed are those measured by the ICL probe on ROV Isis.

4.4.2. Petrography of the active chimneys

In hand specimen, the active chimneys are white, cream, grey, blue and black, are exceptionally fragile, and have a very fine-grained texture (Figure 4.24). The structures and mineralogical zoning are not consistent between chimneys, but there are a few common mineral interactions. A large range of millimetre scale textures are seen in different samples and variations in mineralogy exist depending on the temperature of venting.

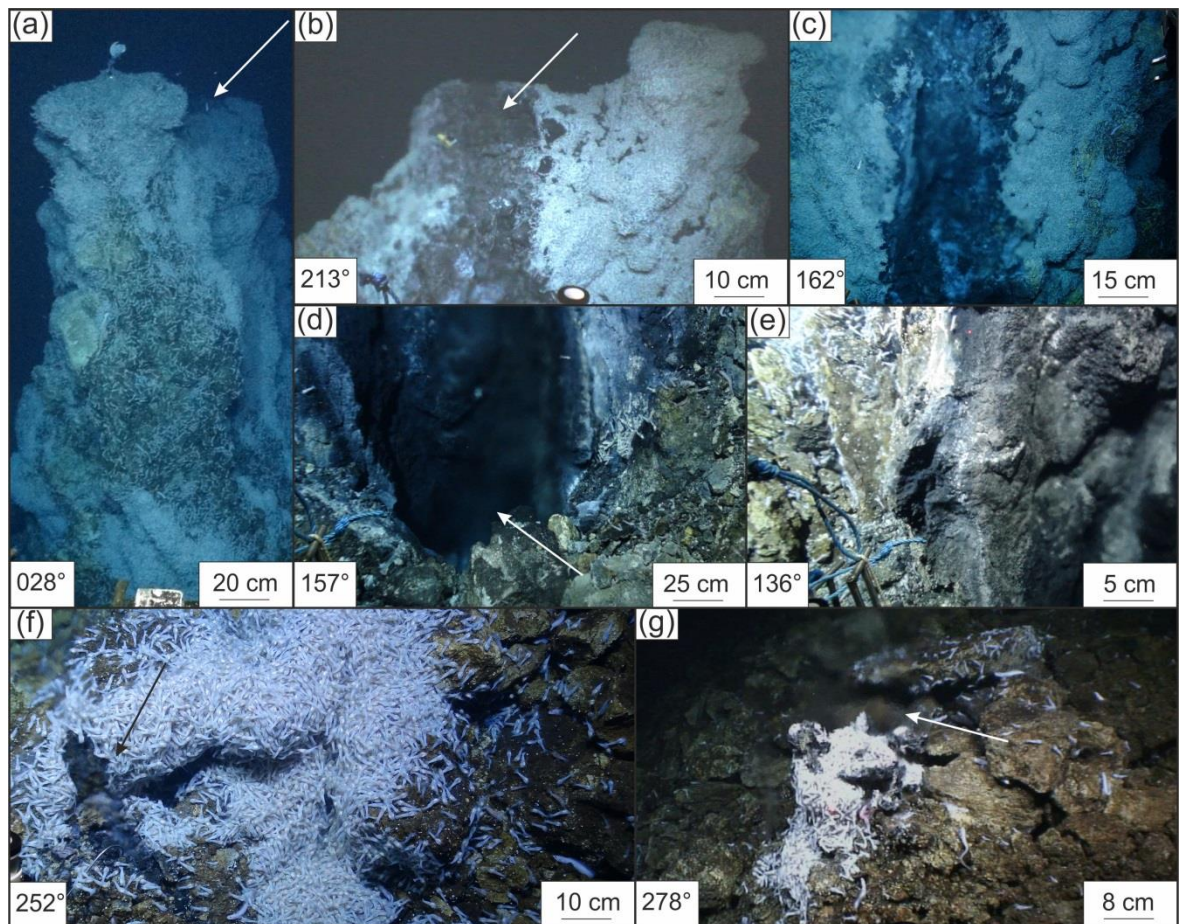


Figure 4.22: ROV images of venting styles at the main cone; images taken by ROVs Isis and HyBis (a) photomosaic of the Spire at the top of the main cone (b) 215°C vent at the top of the VDVF (c) top of the main cone between the Spire and the Main Hole (d) 1 metre diameter hole, located downslope of the Spire, venting at 91°C (e) black and white laminated layering on the edge of the Main Hole (f) large fissure venting fluids at 138°C downslope of the Spire (g) small chimney on the main cone venting fluids at 118°C. Where present, arrows identify the vent orifice in each image and the angle displayed shows the facing direction.

Chimney samples from the main cone consist of predominantly talc and smectite interlayers, with minor microcrystalline silica and sulphides (Figures 4.25-4.26). The talc shows a range of forms, but in thin section it is usually isotropic and pale to dark brown due to its very fine-grained habit, while characteristic interference colours and visible cleavage planes are rare.

The forms of talc in the chimneys include botryoidal, banded, massive, and clastic (note: clastic in this chapter is used as a term to describe the form of talc and is not related to its mode of genesis). Porosity is generally high, with voids and vugs a few millimetres across filled with botryoidal talc. This leads to the formation of a branching, dendritic and occasionally platy network of botryoidal talc. Individual dendrites are up to 300 μm across and botryoidal talc is usually around 50 μm across, but can be as small as 5 μm (Figure 4.27).

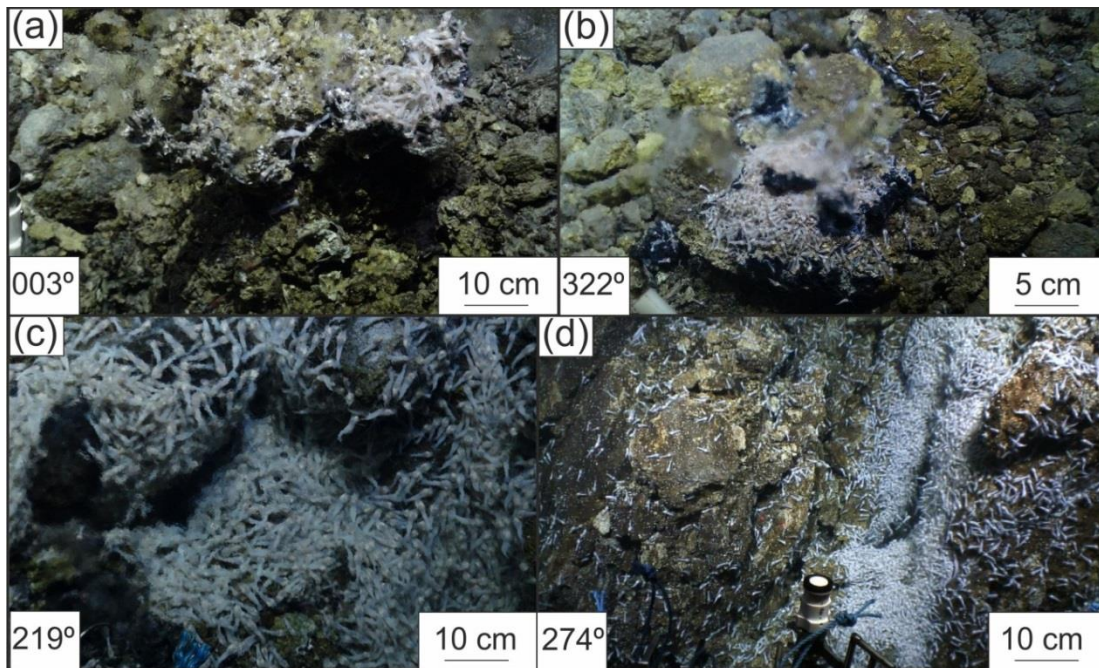


Figure 4.23: ROV images of venting styles on the north and south spurs of the VDVF; images taken by ROV Isis (a)-(b) small, up to 30 cm high chimlets on the spur to the south of the main cone (c) and (d) examples of diffuse flow occurring at the VDVF.

Areas of botryoidal talc are sometimes completely infilled with talc where they form white talc clasts indicative of continuing precipitation into pore space. Cross sections through these clasts, where they are not completely consolidated, reveal botryoidal talc precipitated into the voids in the centre of the masses. Acicular talc occurs rarely

in open pore spaces and is up to 0.5 mm long. Bands ranging in width from 50-200 μm occur in all talc forms (Figure 4.28).

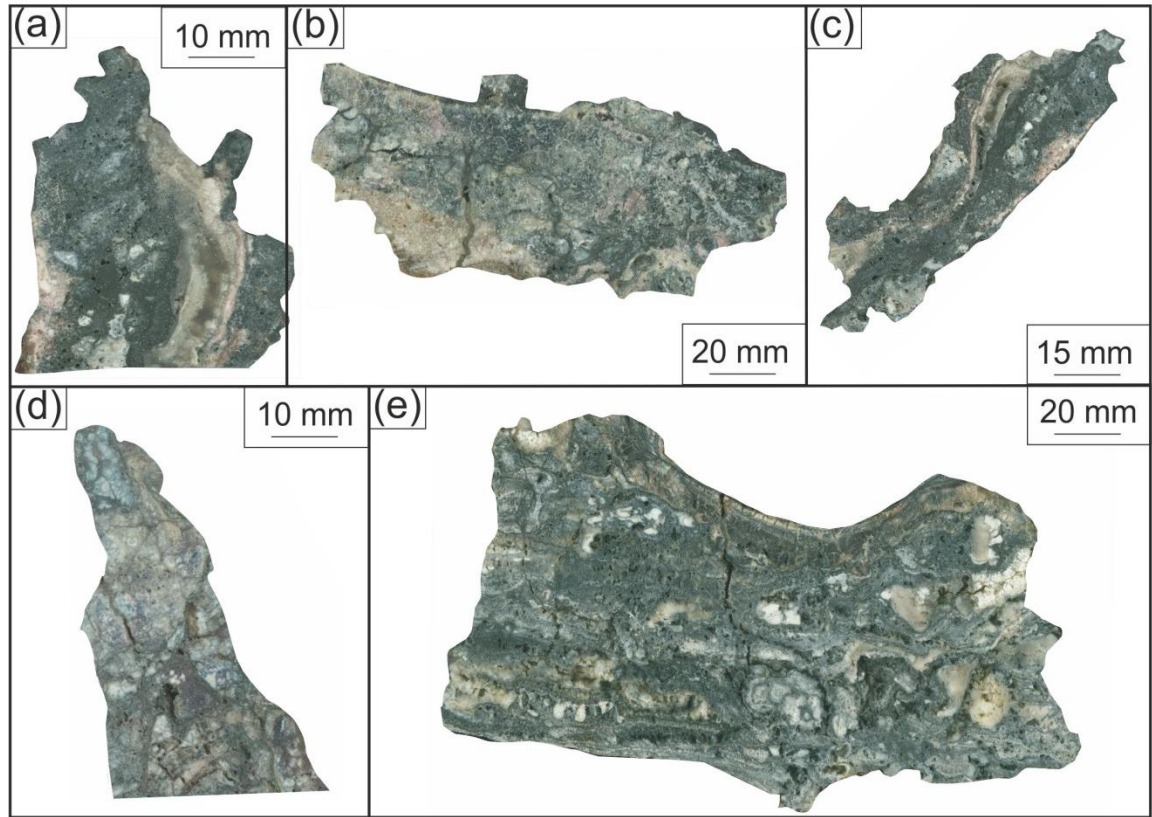


Figure 4.24: Scans of fresh faces of active chimneys. Black areas indicate a concentration of sulphides, whereas cream and white areas indicate talc (a) JC082-202-44 (b) JC082-202-46 (c) JC082-202-44(d) JC082-202-43 (e) JC082-200-24. Images a-d are of chimney hand specimens from the main cone, and image e is of the lower temperature chimney on the north spur.

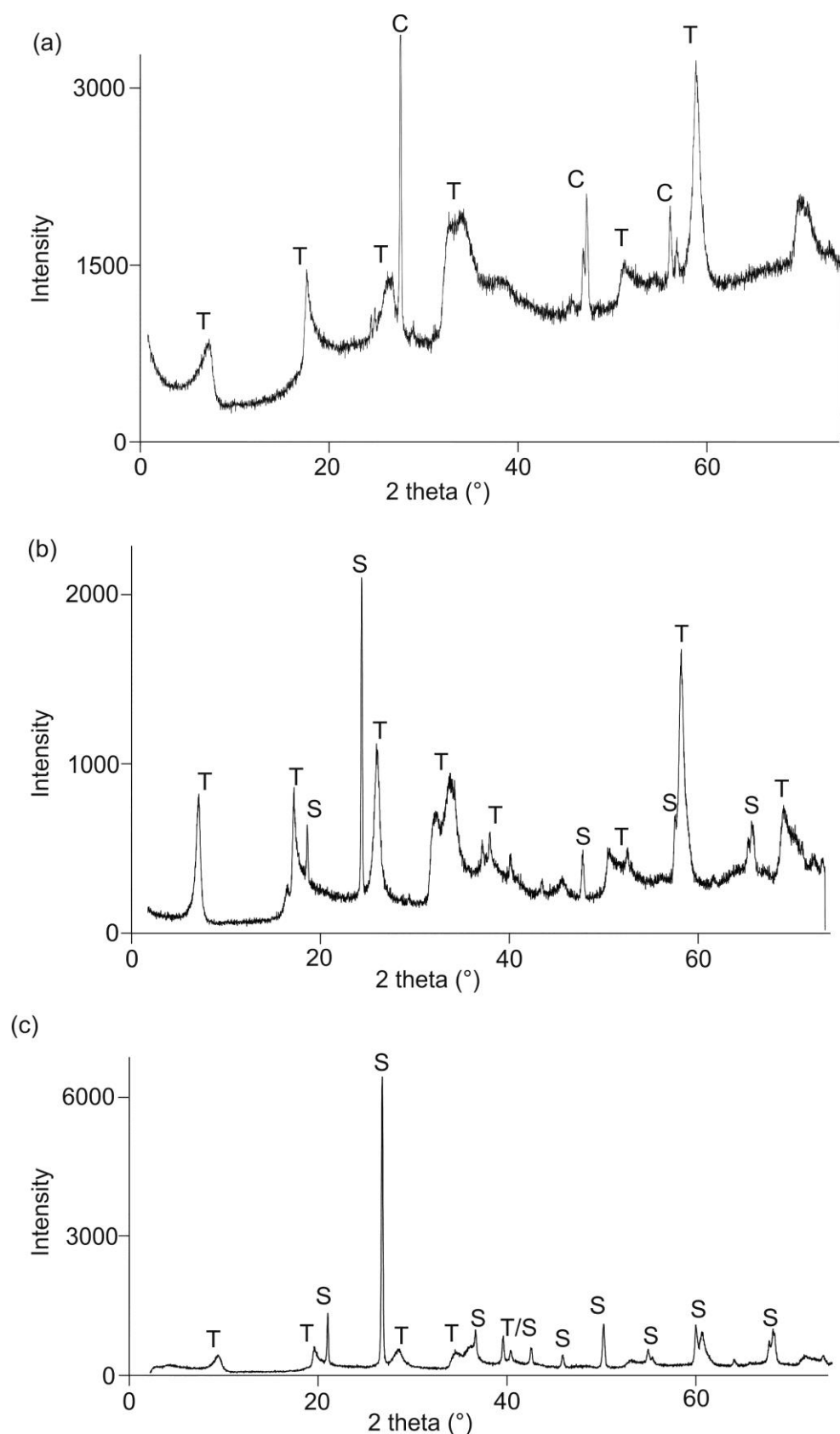


Figure 4.25: XRD of hydrothermal precipitates (a) JC082-202-44 active chimney from the main cone (b) JC082-199-10 mound material from the main cone (c) JC082-201-33 inactive mound to the south of the VDVF. Mineral abbreviations: C=chalcopyrite; S=microcrystalline silica; T=talc.

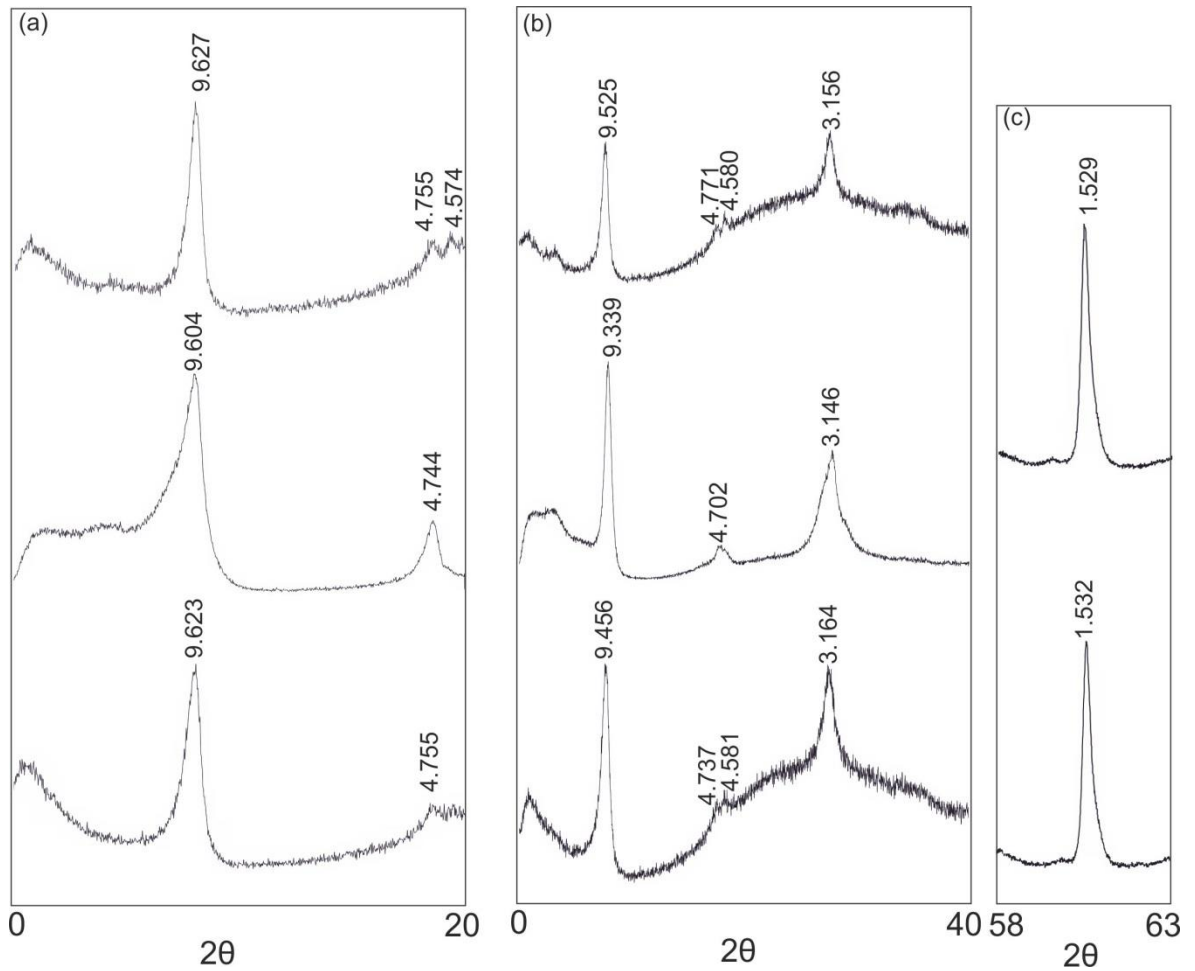


Figure 4.26: XRD of clay separates from the VDVF. Top row JC082- 198-03, middle JC082- 201-31, bottom JC082- 201-35 ; 060 peaks top JC082- 201-35, bottom JC082- 202-48 (a) Orientated air-dried mounts of talc separates. Peaks at $\sim 9.6 \text{ \AA}$ (001) and $\sim 4.7 \text{ \AA}$ indicate the main phyllosilicate mineral to be talc – the relatively narrow peaks (particularly for (001) peak) suggest that kerolite is absent. (b) Orientated glycolated mounts of talc separates. Glycolated mounts indicate a shift in the (001) peak from $9.604\text{--}9.627 \text{ \AA}$ to $9.339\text{--}9.525 \text{ \AA}$, suggesting the presence of a smectite-group clay. (c) Randomly orientated mounts of talc separates. (060) peak analysis indicate a d-spacing of 1.529 \AA and 1.532 \AA , which is close to the talc peak of 1.527 \AA but also falls in the range of the tri-octahedral structure (saponite) d-spacing of $1.52\text{--}1.54 \text{ \AA}$, but is outside of the di-octahedral (montmorillonite and beidellite) d-spacing range of $1.49\text{--}1.50 \text{ \AA}$.

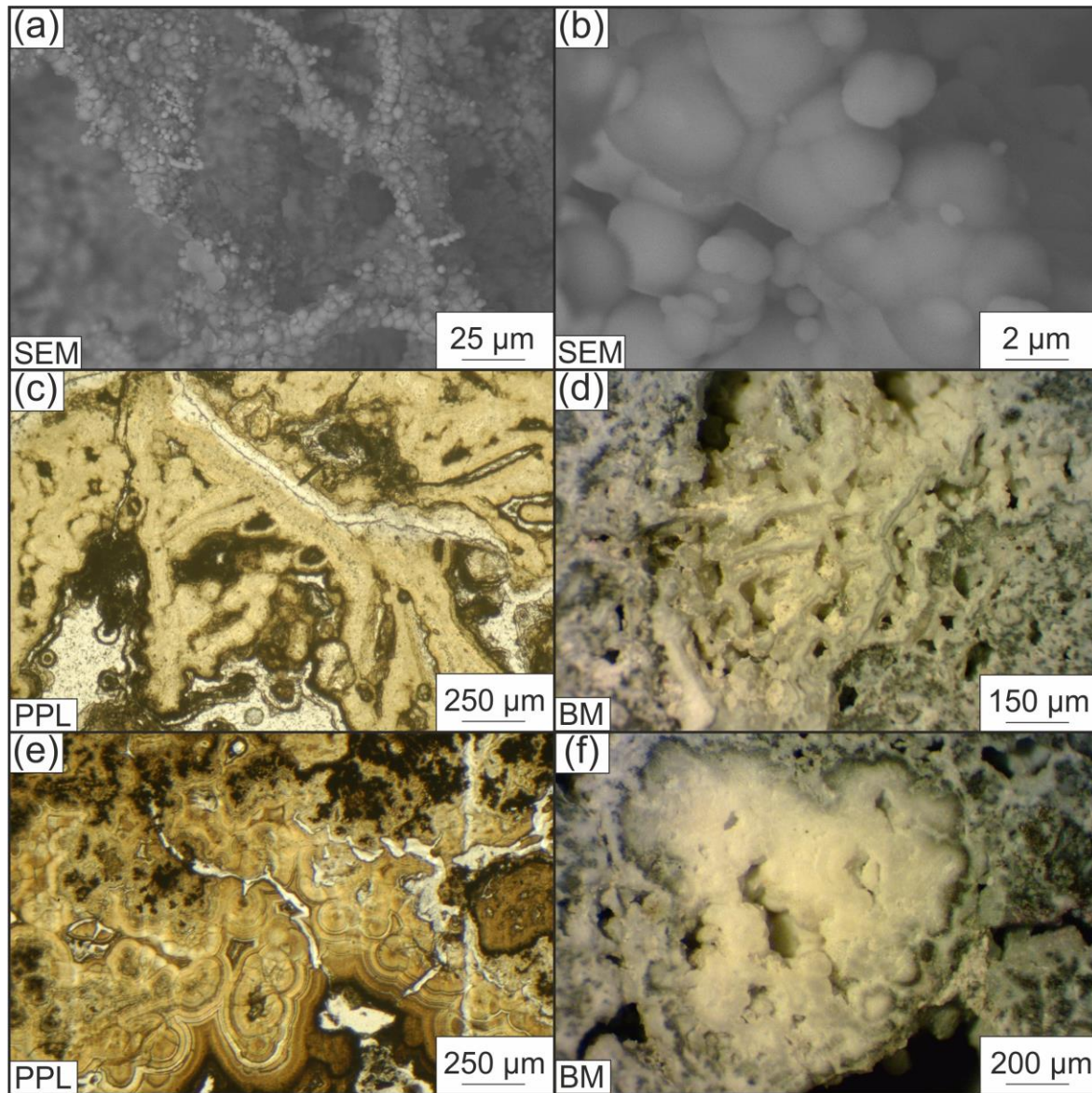


Figure 4.27: Precipitation textures observed in open pore spaces of active chimneys. Images acquired using SEM, binocular microscope and transmitted light microscopy (a) JC044-1E desktop SEM image of porous, branching network of talc (b) JC044-1E close up desktop SEM image of (a)-(c) JC082-202-44 dendritic talc surrounded by pore spaces (d) JC044-1E platy talc with fine-grained talc infilling the pore space; black areas are fine-grained sulphide (e) JC044-1C botryoidal talc with bands on the edges (f) JC044-1E botryoidal talc area with thin band of fine-grained sulphide on the margin.

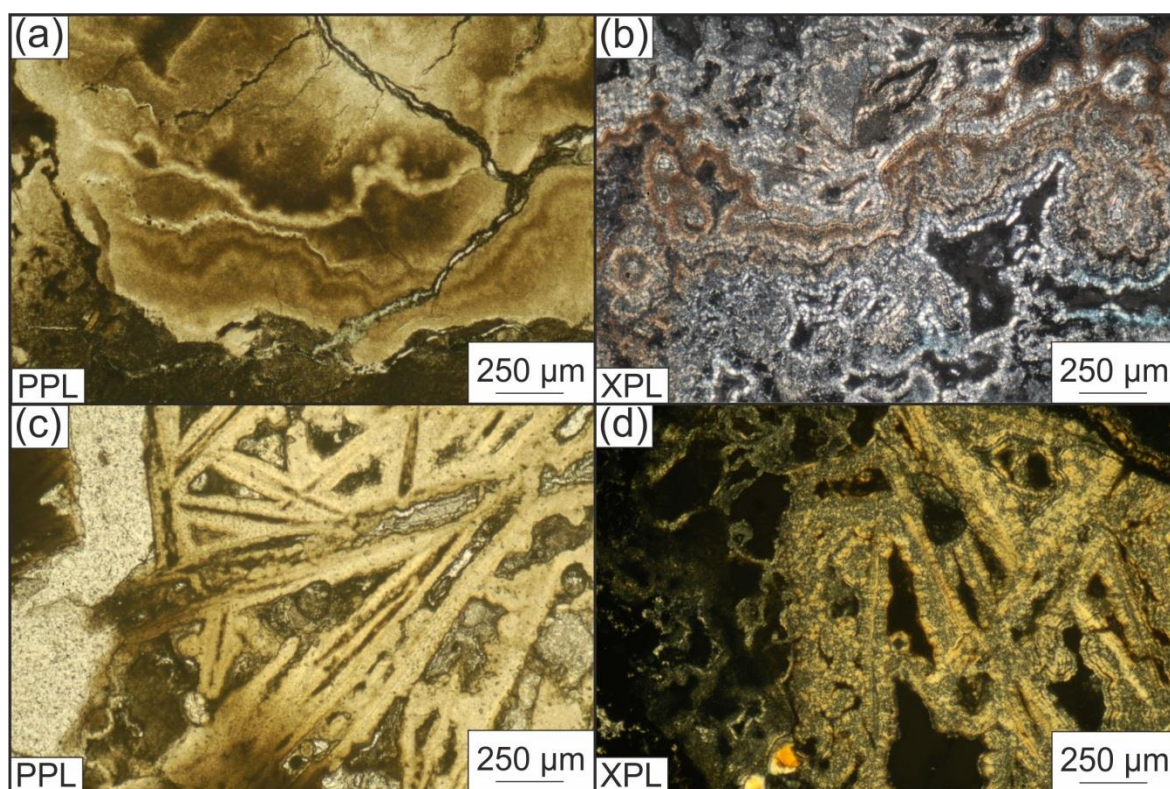


Figure 4.28: Common textures in less porous chimney areas. Photomicrographs taken in transmitted light (a) JC082-202-47 and (b) JC044-1B banded talc within more consolidated areas of chimney material, indicating different stages of precipitation (c) JC082-202-44 and (d) JC082-202-44 acicular talc masses with banded margins.

Sulphides in active chimneys consist of chalcopyrite, pyrite, sphalerite and galena. There is no macro-scale mineralogical zonation in samples recovered from actively venting chimneys, but areas within a few centimetres of the venting fluid contain a much greater proportion (up to 50%) of sulphides. Very fine-grained sulphide, with a massive texture, dominates within approximately 10 mm of the inner walls of the chimneys, and talc is generally a minor phase. In reflected light microscopy, the opaque sulphides do not show reflectance, due to their fine-grained nature. Occasionally, in areas of dense, slightly coarser-grained sulphide, faint grey and yellowish reflections are seen, but most sulphide petrography was conducted under SEM. Proportions of each sulphide phase vary between samples and localities on the active mounds, and the most common sulphides present in chimneys from the main mound are chalcopyrite (up to 70% of sulphide assemblage) and pyrite (between 20-40%), with sphalerite (<10%), bornite (<5%) and galena (<5%) also present. The smaller, lower temperature chimlets show a lower diversity of sulphide assemblages, where iron sulphide, dominantly marcasite, is common in the chimneys along the

south spur. Sphalerite, chalcopyrite and galena do occur, but are far less common than samples from the main cone. SEM EDS analysis was used to identify sulphides based on their composition, and differences in crystal form were used to distinguish between sulphides with the same composition (e.g. pyrite and marcasite). Chalcopyrite and rare bornite occur as irregular sub-rounded blebs up to 70 μm across, but grain size is usually 2-25 μm (Figure 4.29). Galena occurs as small, irregular grains most commonly on the margins of or as inclusions within chalcopyrite at grain sizes no more than 2 μm . Sphalerite is generally no more than 5 μm across, and occurs as small grains along with chalcopyrite, or as rounded skeletal grains disseminated in talc along with euhedral cubes of pyrite. Clusters of sulphides at chimneys from the main cone always contain chalcopyrite or pyrite, along with sphalerite or galena, i.e. galena and sphalerite grains are not observed by themselves. Marcasite crystals in the low-temperature chimlets (smaller chimneys) occur as acicular columns or as irregular, tabular prisms with triangular margins between 5 to 30 μm in size (Figure 4.29). Rarely, chalcopyrite occurs disseminated within botryoidal talc masses in the chimlets as grains <2 μm across.

The mineralogical interaction between talc and sulphide also shows many different textures. The most commonly observed habit is talc surrounding small, up to 200 μm across, areas of amorphous, opaque sulphide material. The bands of talc in these radial accumulations of sulphide are generally around 10-20 μm across. Talc and sulphide also occur as fine-grained intergrowths with grain sizes of ~ 40 μm . Sulphide and talc occurs as curved alternating bands a few tens of microns across, or as single bands on the margins of botryoidal/colloform talc masses. U-shaped concentric precipitates only occur in the lower temperature chimneys. These chimneys are more porous than the higher temperature chimneys and feature smaller vents orifices at 1-5 cm across. Concentric bands of marcasite found throughout the structures of low temperature chimneys could form from previous channelling of vent fluids and subsequent sealing (Figure 4.29).

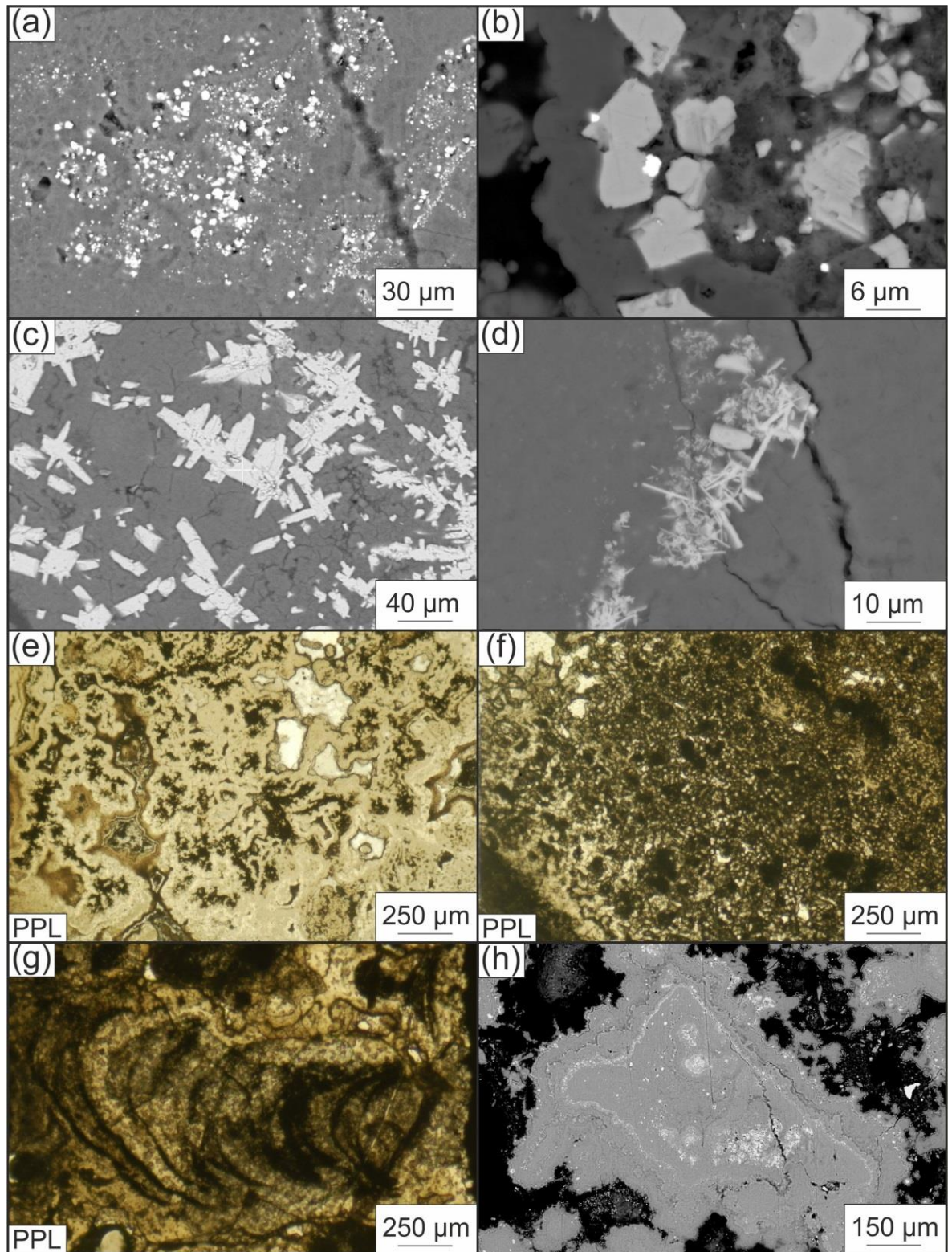


Figure 4.29: Sulphide textures in VDVF chimneys. Images acquired by transmitted light and SEM (a) JC044-1A SEM image of subhedral chalcopyrite bands (white areas) within the talc groundmass (b) JC044-1B talc groundmass with galena (bright) on the margins of chalcopyrite grains (c) JC082-200-24 and (d) JC082-200-24 hexagonal and acicular marcasite in the lower temperature chimneys within a talc groundmass (e) JC044-1B fine-grained opaque sulphide surrounded by talc (f) JC082-200-24 fine-grained talc and

sulphide intergrowths within high-temperature chimney (g) JC082-200-24 radial, u-shaped sulphide and talc bands in lower temperature chimneys (h) JC044-1A precipitation of thin bands of sulphide (dominantly chalcopyrite, minor pyrite) surrounding colloform talc masses.

Proportions of microcrystalline silica are variable in active chimneys. In some samples microcrystalline silica may contribute up to 25% of the total assemblage, but it generally makes up <10%, or is completely absent. Where present, it is intergrown with talc and commonly infills pore space and vugs between colloform, botryoidal or acicular networks of talc as a later stage precipitate in between a pre-existing talc network. Grain size of microcrystalline silica is up to 200 µm and it shows a subhedral, rounded form (Figure 4.30).

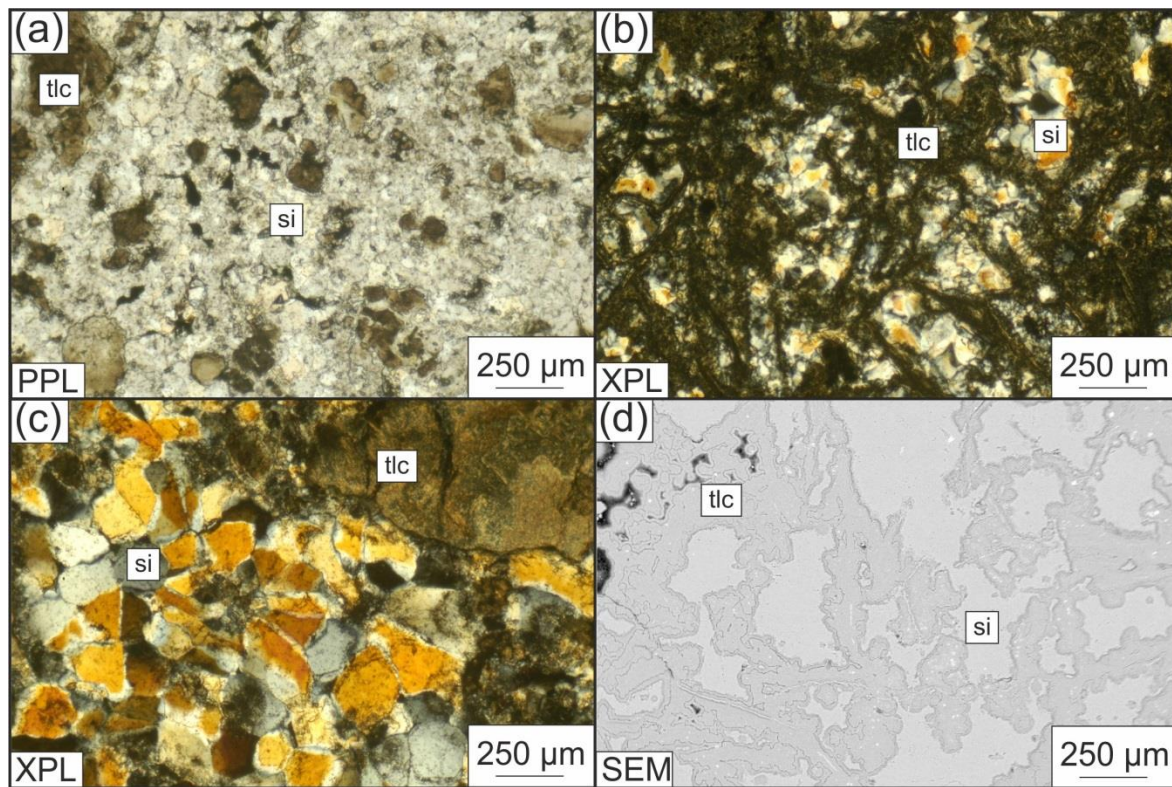


Figure 4. 30: Microcrystalline silica in VDFV chimneys. Images displayed acquired by transmitted light and SEM (a) JC082-202-47 and (b) JC044-1B microcrystalline silica intergrown with fine-grained talc (c) JC082-202-47 coarser silica on the margin of massive talc (d) JC044-1B SEM image of talc (darker grey) framework infilled with later stage microcrystalline silica (lighter grey). Mineral abbreviations = si= microcrystalline silica, tlc = talc.

Accessory anhydrite only occurs in two samples in close proximity to the vent margin, and does not appear to form an early-stage framework. Instead, subhedral grains up to 50 μm across, detectable only under SEM, are disseminated throughout the dominantly talc–sulphide groundmass.

4.5. Active mounds

4.5.1. Main cone

Rubble towards the base of the main cone is poorly consolidated and large boulders can be up to 2 metres across. These feature a thin covering of fine-grained material that is a combination of the pelagic sediment and broken up talc rubble from mass wasting further up the cone. With progression up the slope, talus size generally decreases to around 0.5 metres across, but large boulders of collapsed chimney from the Spire are common, and can be up to 1 metre across (Figure 4.31).

In hand specimen, the rubble has a brown weathered stain to the exterior, but fresh faces are white, cream, pale brown and black (Figure 4.32). Textures and structures from the chimneys are preserved in the talus, which is more consolidated than the active vent structures. Mineralogy is predominantly talc, with minor microcrystalline silica, sulphides and rare sulphate. Mound samples are dominantly massive, brecciated or locally banded. Porosity is generally absent, but can be up to 10% in some samples. Widespread veining is not apparent, instead reworking of original textures seems to be the dominant process within the active mound, and different textures are observed in the same samples even at thin section level.

Talc in samples of outcrop recovered from the main cone has very similar optical properties to the chimney talc. It has a fine-grained habit, ranging from colourless through to different shades of brown in PPL, with rare interference colours and no visible cleavage. Talc from talus and scree slopes at the main cone shows intricate banding and consolidated botryoidal or acicular talc clasts, which contain bands up to 250 μm across. Bands of talc defined by variations in grain size and colour in PPL occur in talc of all forms in mound and talus samples, and range between 10–300 μm across. These bands are not always visible in PPL, but differences in their orientations

allow their structure to be revealed in XPL. They do not always have a set pattern, but are usually radial or concentrically ringed precipitates with alternating bands occurring at very intricate, sub-millimetre scales (Figure 4.33).

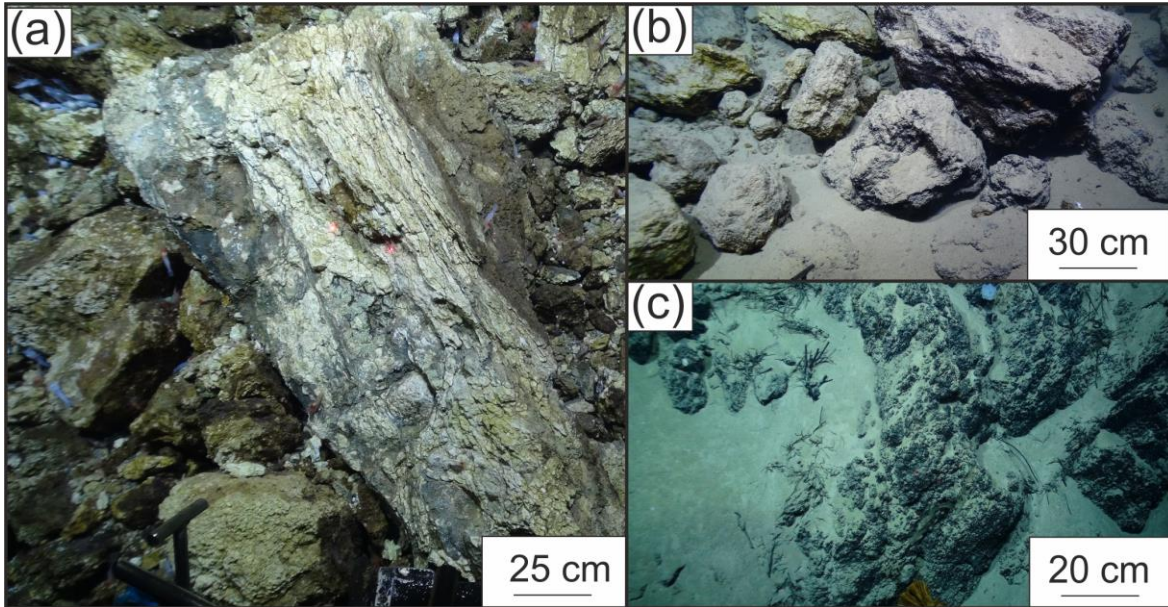


Figure 4.31: ROV Isis images of the active and inactive mounds (a) example of a collapsed chimney on the main cone that shows massive and banded talc (b) talus on the rubble-sediment contact on the main cone (c) outcrop towards the top of Mystic Mount.

Small clasts of fine-grained, massive talc, up to 200 μm across, precipitate and are consolidated by microcrystalline silica or later stage talc growth (Figure 4.34). Microcrystalline silica generally ranges between 50-200 μm , and is usually seen infilling pore spaces or as fine-grained intergrowths within a talc groundmass. Occasionally, rounded silica grains up to 50 μm across are observed surrounded by a thin band of talc 20 μm across. Later stage veins are not very common, however some samples do show small veins of quartz and occasionally gypsum, up to 200 μm across, which cross cut banded talc (Figure 4.35).

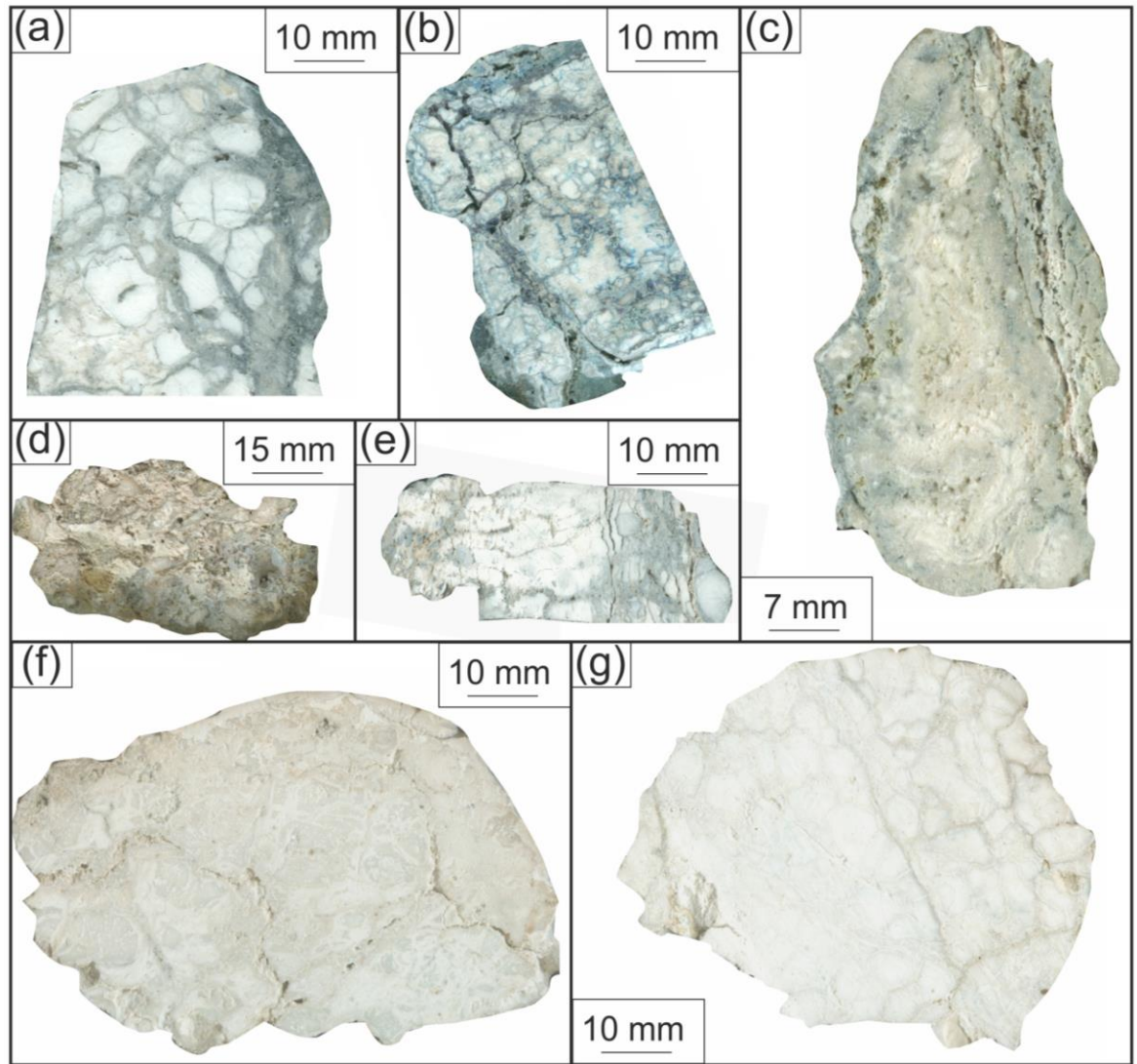


Figure 4.32: Scans of hand specimens of massive and brecciated talc with accessory silica and sulphides from the main cone (a) JC082-202-48 (b) JC082-199-10 (c) JC082-199-08 (d) JC082-201-39-(e JC082-201-40 (f) JC082-199-20 (g) JC082-198-02 and the two mounds that form the southern spur (f-g).

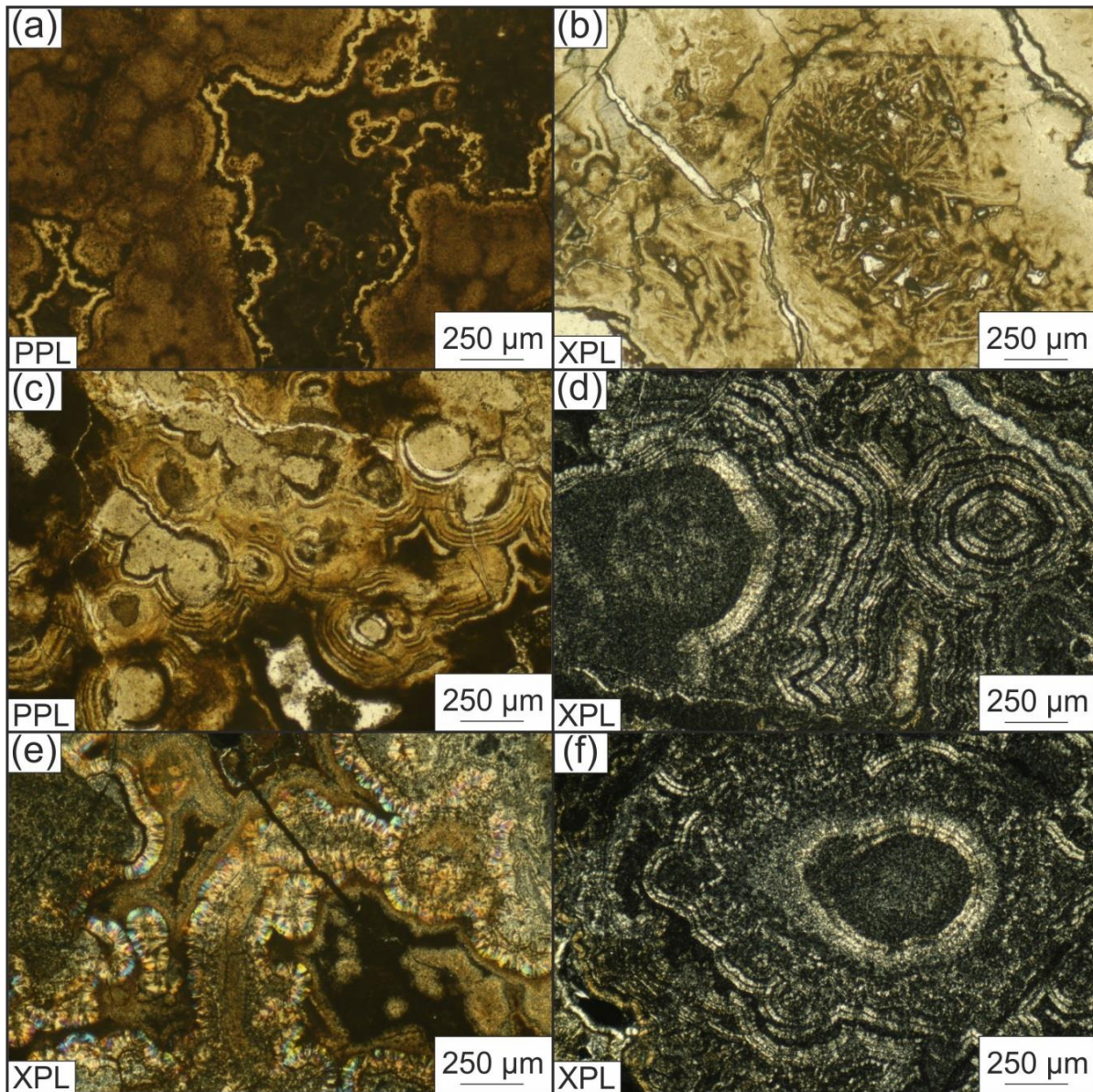


Figure 4.33: Textures observed in clastic talc. Photomicrographs taken in transmitted light (a) JC082-202-48 and (b) JC082-200-21 consolidated clasts of botryoidal and acicular talc clasts (c) JC082-201-34 (d) JC082-199-09 (e) JC082-201-35 (f) JC082-199-09 radial and concentric bands of talc showing different stages of precipitation into open pore spaces.

Sulphides in samples from the main cone occur as clusters within talc but also as thin bands. As with samples from the chimney, the very fine-grained nature of the sulphides means that almost all sulphide petrography was conducted under SEM. Sulphides do not occur as frequently throughout the main cone as they do in the active vents, but where they are present, they consist dominantly of subhedral chalcopyrite bands, with occasional bornite, pyrite and sphalerite. Grain size is very fine, as a majority of sulphides are <20 µm across. A few grains of native gold

approximately $\sim 0.5\text{--}2\text{ }\mu\text{m}$ across were observed in one sample in close proximity to a small chimney approximately 10 metres downslope of the Spire (Figure 4.36).

This sample also contained a few grains up to $10\text{ }\mu\text{m}$ across of antimony and arsenic bearing sulphides, although the precise phase could not be determined. Reworking of previous copper sulphides occurs and in samples towards the base of the main cone, secondary copper minerals such as atacamite and possibly idaite up to $5\text{ }\mu\text{m}$ across are found among chalcopyrite and bornite bands.

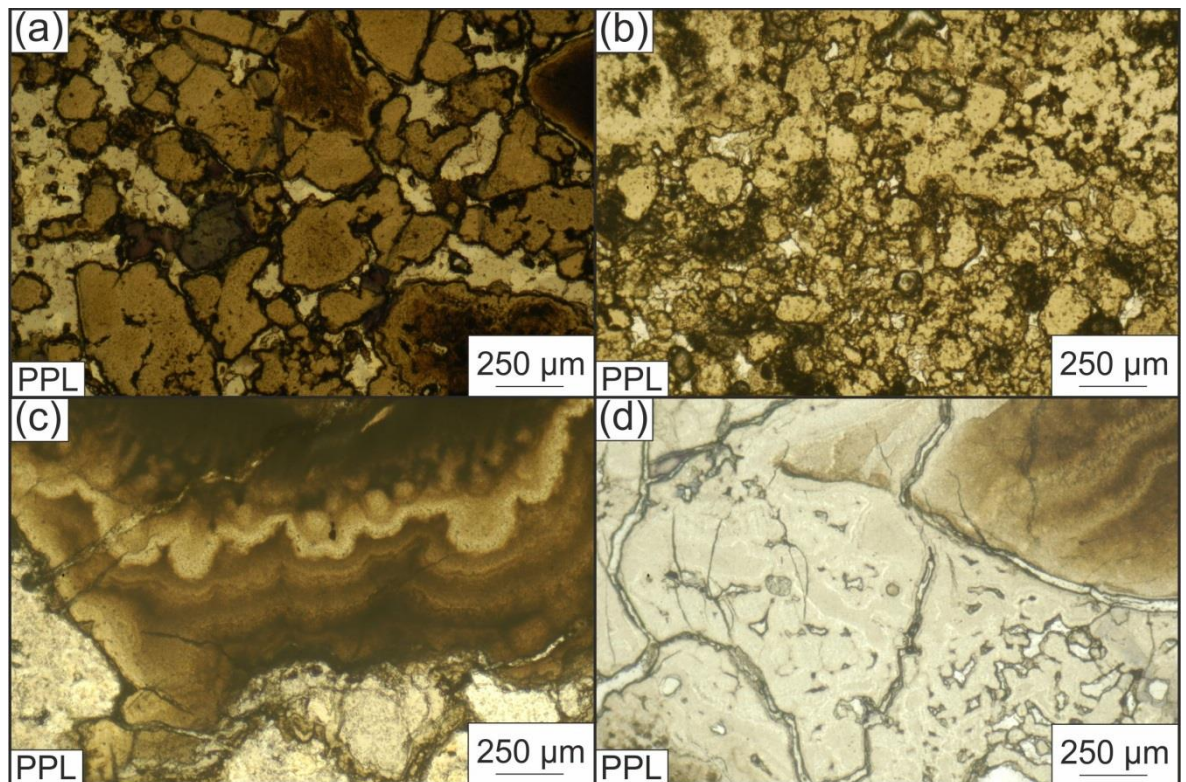


Figure 4.34: Fine grained and banded talc. Images taken in transmitted light (a) JC082-199-08 and (b) JC082-201-34 consolidated fine-grained talc (c) JC082-202-48 banded talc clast with microcrystalline silica infill at bottom of image (d) JC082-200-21 banded talc with a later stage, massive talc infill. Talc is the only mineral observed in all photomicrographs.

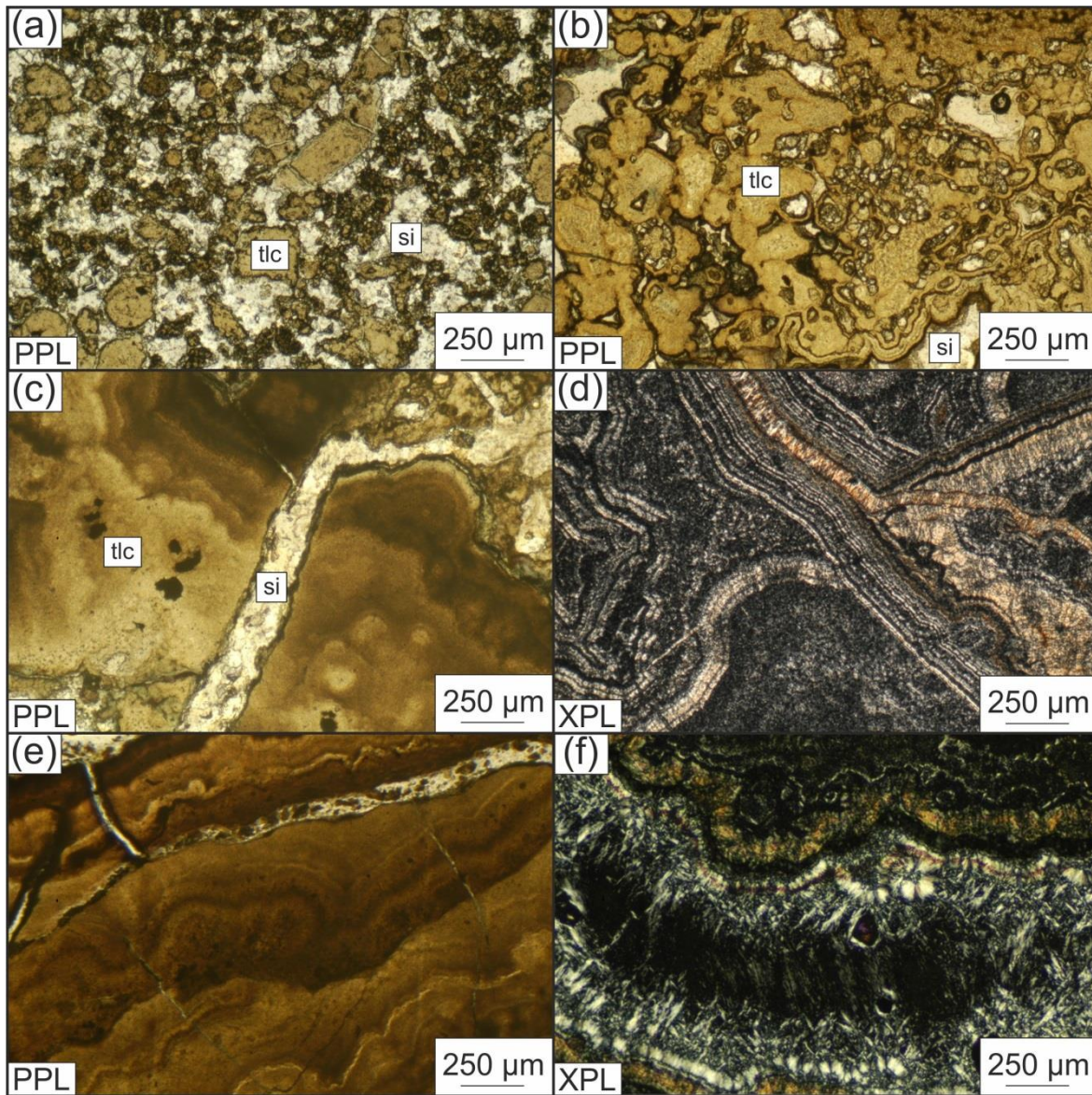


Figure 4.35: Microcrystalline silica in mound material and talc overprinting textures. Photomicrographs taken in transmitted light (a) JC082-199-08 intergrown talc and microcrystalline silica (b) JC082-199-08 talc surrounding individual grains of later-stage silica (c) JC082-202-48 banded talc cross cut by thin vein of silica (d) JC082-199-09 and (e) JC044-2C different stages of banded talc precipitation; individual bands are traceable only for a few millimetres across thin section (f) JC082-199-09 rare fibrous talc vein showing crystal growth on the edge of the fracture crosscutting banded talc groundmass. Mineral abbreviations: si = microcrystalline silica, tlc = talc

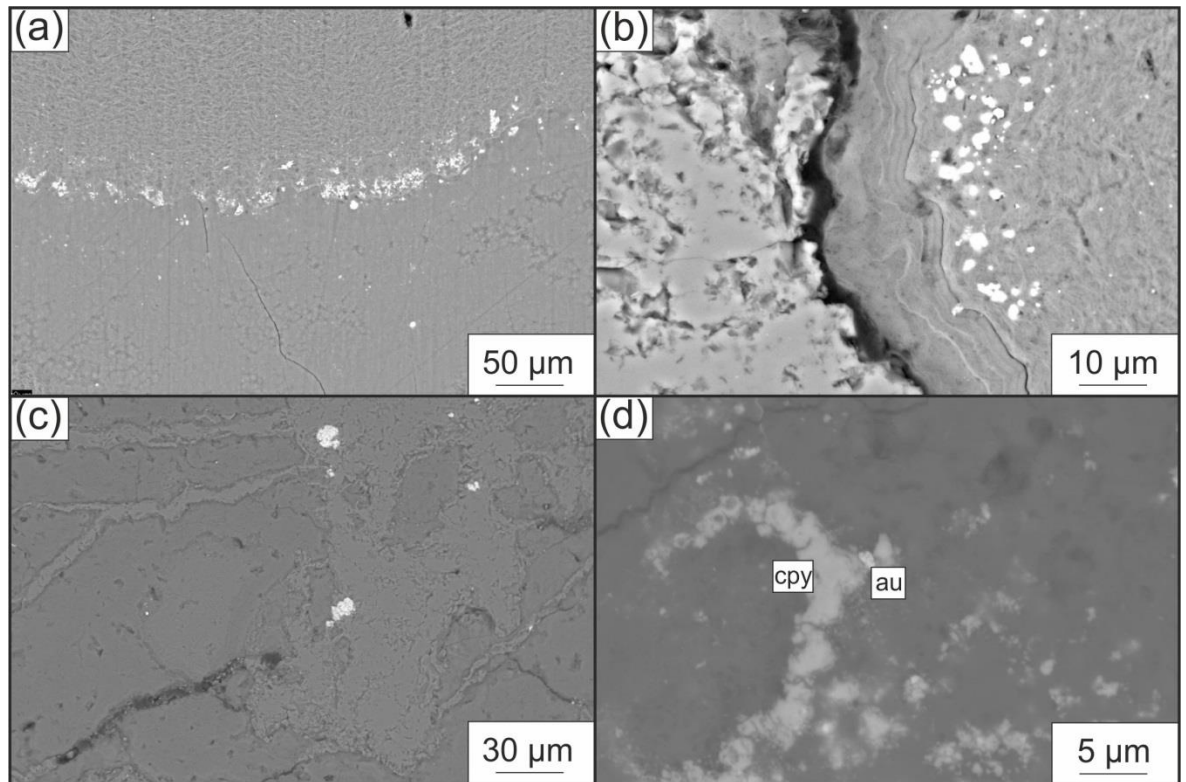


Figure 4.36: Sulphides in mound material from the main cone. Images acquired by SEM (a) JC082-199-10 and (b) JC082-199-10 fine-grained chalcopyrite bands in banded talc (c) JC082-202-48 large grains of disseminated chalcopyrite occurring in talc groundmass (d) JC082-202-48 clusters of chalcopyrite in talc with two $\sim 1\ \mu\text{m}$ across grains of native gold. Abbreviations: au = native gold, cpy = chalcopyrite.

4.5.2. North and south spurs

The two mounds to the south of the main cone are largely similar in appearance at outcrop scale to the main cone, although they do feature increasing sediment cover along the flanks. They have flatter summits and are less conical shaped than the main cone. Fallen scree is less common as the gradient is shallower but boulders up to 1 metre across lie along the flanks of the two mounds, and sediment cover is greater on the south spur than the north spur.

In hand specimen, the samples are white, cream, pale brown or translucent (Figure 4.32). Porosity generally makes up $<5\%$ of the assemblage, or is absent. Where it is present, talc has a botryoidal or dendritic form. The mineralogy consists predominantly of massive or banded talc, with occasional microcrystalline silica. Banding is far less pronounced, giving a more massive texture, although some

concentric bands on the margins of massive talc are 10-20 μm across (Figure 4.37). Clasts of talc are up to 3 mm across and have an isotropic centre, with alternating lighter and darker bands on the margins, and are overprinted by similar, dark brown talc. Sulphide phases are largely absent from these samples, due to oxidation by seawater. This occurs by infiltration of circulating seawater into the mounds in surface fractures, causing sulphide phases to be less stable under the more oxygenated conditions. The older mounds do not have an extensive sediment cover, meaning the sulphides have a more prolonged exposure to seawater, and are therefore prone to a greater degree of dissolution.

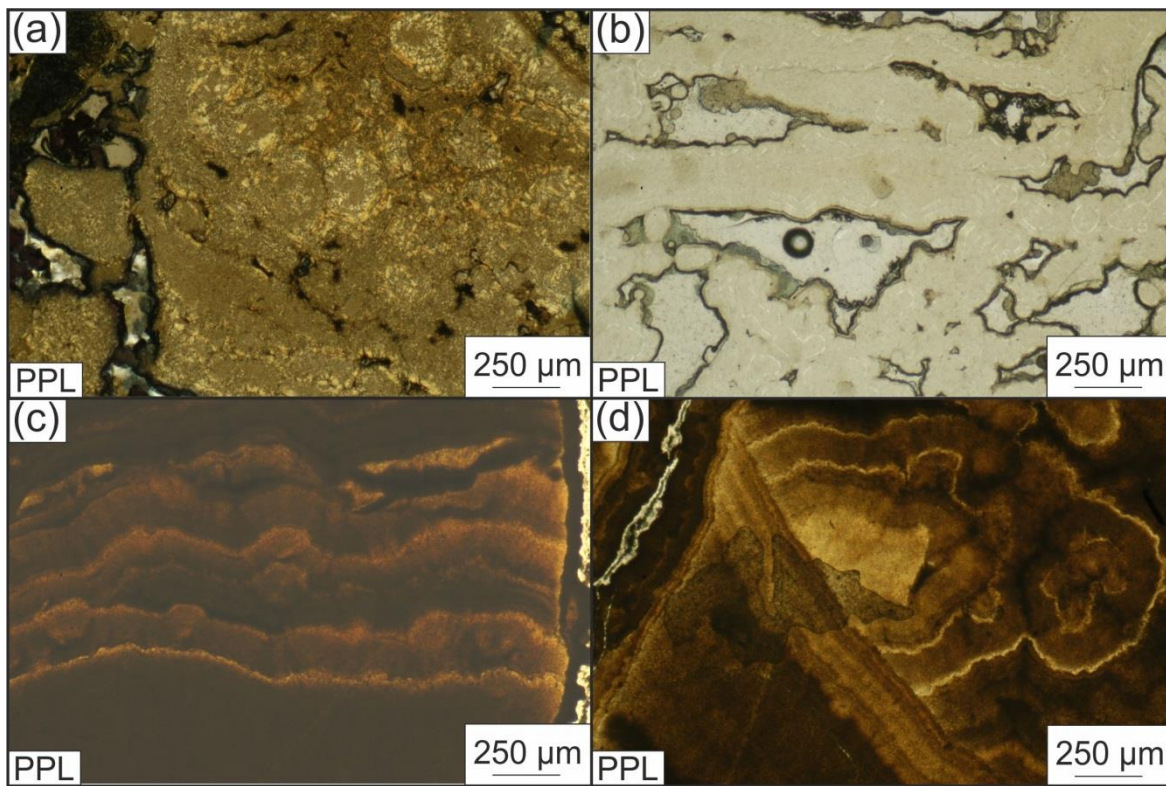


Figure 4.37: Talc textures in mound material from the north and south spurs.

Photomicrographs taken in transmitted light (a) JC082-200-23 massive, fine-grained talc (b) JC082-200-23 networks of botryoidal talc in pore spaces; occasionally show banding on the margins (c) JC082-199-03 bands on the margin of a talc clast (d) JC082-199-03 banded talc overprinting previous radial accumulations of fine-grained talc.

4.6. Inactive mounds

Inactive mounds of talc are located to the east and south of the active site. These mounds are largely sediment covered, but black outcrops of weathered, manganese oxide-coated talc are located towards the summit of the mounds. This section will describe the appearance and petrography of the inactive sites, and compare them to the VDVF.

4.6.1. Mystic Mountain area

Outcrop is sparse along the lower and middle slopes of the cones, and hydrothermal material is limited to a few small loose boulders no more than 0.5 metres across. In situ exposure is limited to the upper slopes and peaks of the mounds (Figure 4.31). The hand specimens have a massive and brecciated appearance (Figure 4.38). Manganese oxide coatings on the samples are usually around 5 millimetres thick, although one fragile sample of highly porous, acicular talc had a 5 centimetre thick coat.

Banded and dendritic textures occur in the samples recovered from these areas, with pale-dark brown clasts of talc featuring bands up to 300 μm thick on their margins. Botryoidal talc is largely absent, although some thick, dendritic networks with high pore spaces are rarely observed. A majority of talc is clastic or massive, and is dark brown and isotropic in PPL (Figure 4.39). Microcrystalline silica occurs intergrown within the groundmass talc, and occasionally forms small veins crosscutting banded talc.

4.6.2. Other hydrothermally inactive areas

Hydrothermal talc is also recovered in outcrops to the north east of the VDVF, a mound 500 metres to the south, and from the debris flow. At these localities, faces are also black due to manganese oxide coating, and have thin sediment covers. The peak of the mound to the south of the VDVF was not visited, although in the localities visited there is a greater degree of exposure observed towards the base of the cone compared to Mystic Mountain, but in both cases it remains <10%.

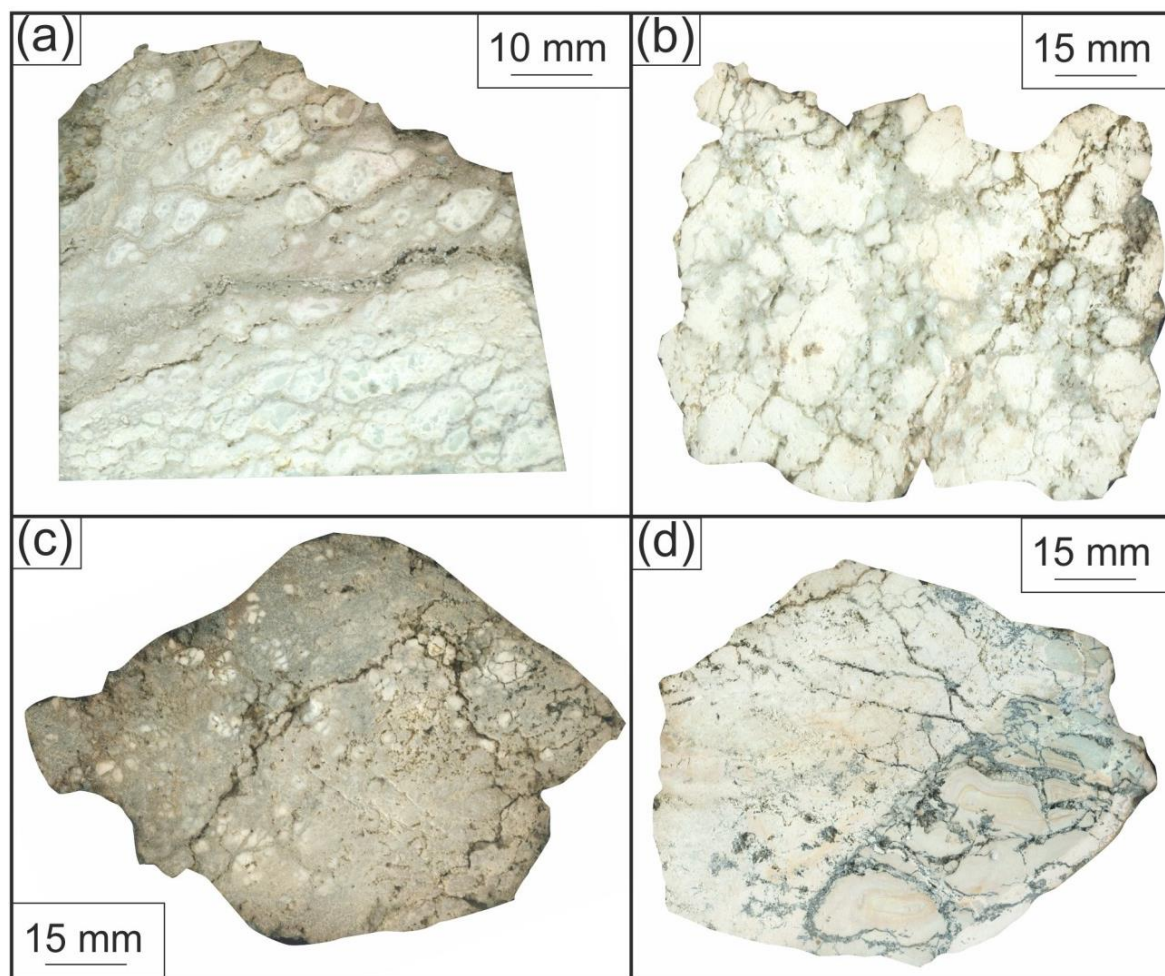


Figure 4.38: Scans of fresh faces of samples from inactive samples (a) JC082-201-30 (b) JC082-201-29 (c) JC082-201-28 hand specimen scans showing massive and brecciated talc breccia from inactive mounds to the east of the VDVF (d) JC082-201-32 hand specimen of the silicified massive talc from the debris flow.

The samples recovered from these areas are silicified talc breccias and massive talc (Figure 4.38). The observed textures are very homogenous across the samples, unlike the hydrothermal chimneys and active mounds (Figure 4.40). Surprisingly, a few fresh sulphides were observed in the sample from the debris flow. They consist of up to 30 μm across chalcopyrite and bornite, some of which have been weathered to atacamite (Figure 4.40).

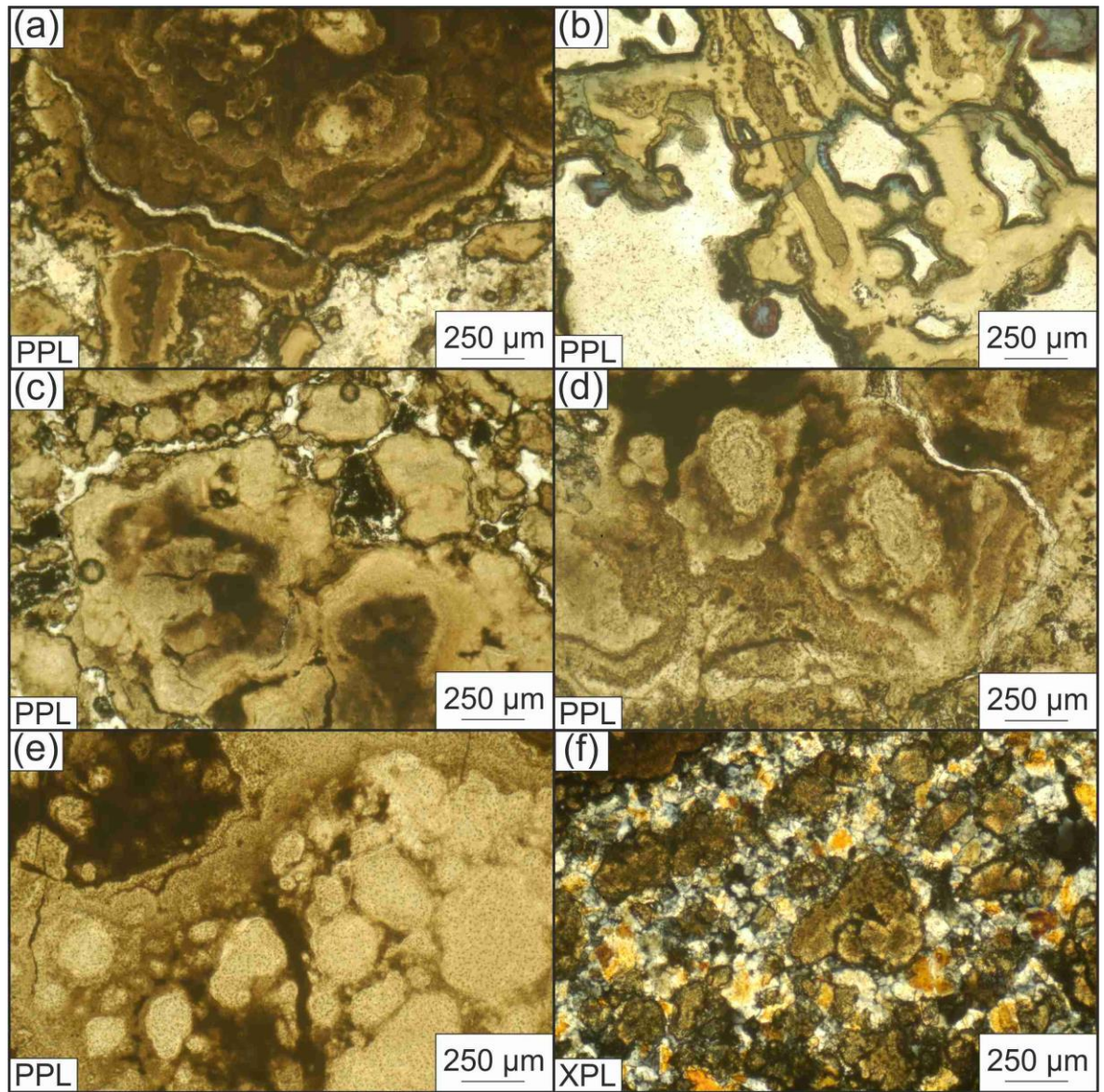


Figure 4.39: Textures and mineralogy of inactive precipitates from Mystic Mountain (a) JC082-201-30 radially banded talc with some microcrystalline silica (b) JC082-201-30 porous, dendritic and botryoidal talc within open pore space (c) JC082-201-26 (d) JC082-201-30 (e) JC082-201-30 clastic talc with occasional bands towards the margins of isotropic masses (f) JC082-201-30 talc and microcrystalline silica intergrowths

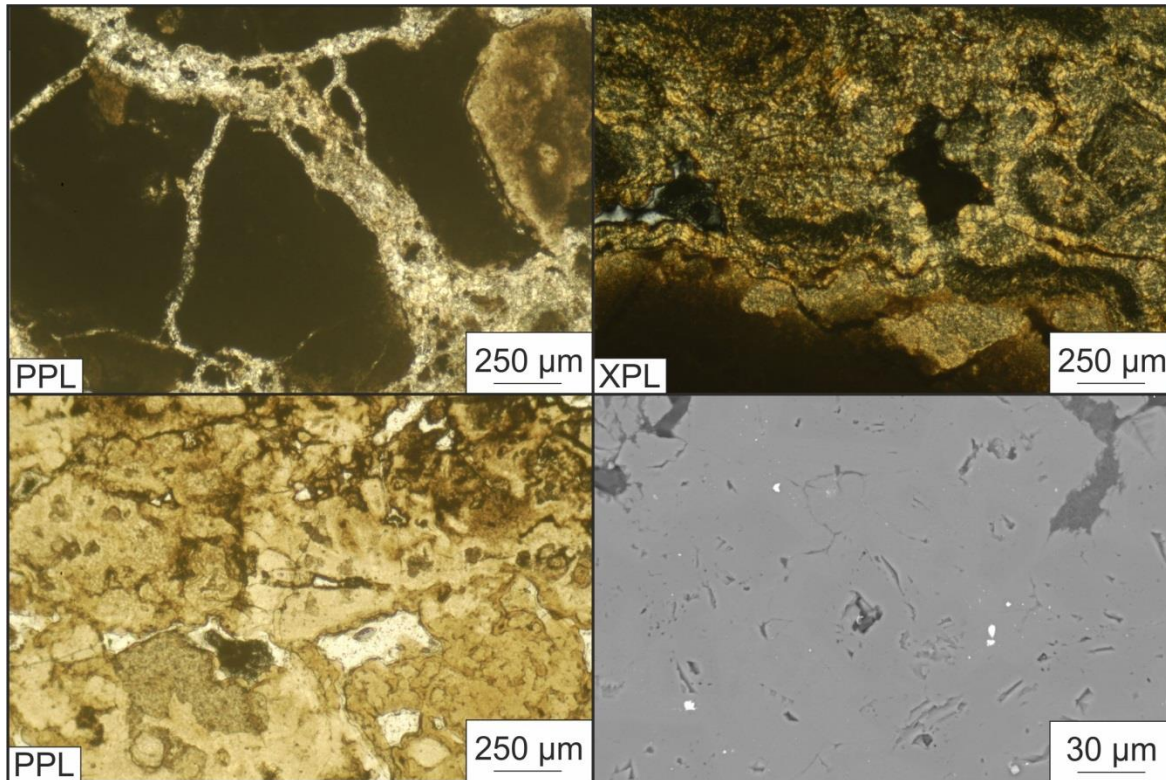


Figure 4.40: Mineralogy and textures of inactive samples (a) JC082-201-27 isotropic talc crosscut by thin veins of microcrystalline silica (b) JC082-201-27(c) JC082-201-27 massive and clastic talc groundmass (d) JC082-201-32 SEM image of disseminated chalcopyrite grains (white) in talc groundmass (grey).

4.7. Whole rock geochemistry of hydrothermal precipitates

The talc and microcrystalline silica dominated mineralogies of the VDVF and the inactive mounds are reflected in a combined SiO_2 and MgO of >79% for whole rock samples (which also exceeds 90% for 15 of 35 samples analyses; Table 4.6). Base-metal concentrations in the chimney structures are greater than in the active mounds: copper concentrations average 1900 ppm in the hydrothermal chimneys compared to 487 ppm in the flanks of the mounds. Zinc concentrations are 255 ppm for the chimneys compared with 77 ppm for the mounds, while the corresponding values for lead are 122 ppm and 24 ppm respectively (Table 4.6). These variations in concentrations are consistent with the observation of an increase in the degree of sulphide oxidation in the mounds compared to the chimney material, and the dominance of copper-bearing sulphides over iron and zinc-bearing sulphides at the VDVF.

4.8. Summary of the local setting of the Von Damm Vent Field

The key structural trend of the VDVF and the surrounding area is a NNW-SSE alignment of the exposed fault scarps, active and inactive hydrothermal mounds, outcrops and linearity of pock marks. This structural trend indicates an underlying basement control, and may be the result of the flexing of the lithosphere at the top of the Mt. Dent OCC. The flexural bending and accompanying faulting presents a major control on the location of hydrothermal venting and the exposure of host rock across the top of Mt. Dent.

The morphology of the mounds, observed textures and presence of active vent structures suggest that VDVF is a deposit formed from the direct precipitation of a hydrothermal fluid, and not from the alteration of an ultramafic protolith.

The active chimneys at the VDVF are dominated by talc with microcrystalline silica and sulphides. Talc forms botryoidal networks and clusters in open pore spaces and in more consolidated areas, shows a massive or clastic habit. Microcrystalline silica precipitates as a later stage growth into pre-existing frameworks of dendritic and acicular talc. Chimneys at the main cone generally vent higher temperature hydrothermal fluid and have a higher proportion of copper bearing minerals in their assemblage, whilst pyrite, sphalerite and galena are accessory grains. In the lower temperature chimlets located along the spur, marcasite is the dominant sulphide, with microcrystalline silica and lead, copper and zinc bearing sulphides rare or absent. The mounds of the active site consist predominantly of talc and microcrystalline silica, with the largest, most active site featuring copper, zinc, lead and iron sulphides, along with their secondary alteration products. Primary precipitation textures observed in the active chimneys are preserved in samples from the main cone, but are commonly locally overprinted by banded and massive talc.

The inactive mounds to the east and south of the VDVF consist of silicified massive and brecciated talc and have manganese oxide crusts on their exposed surfaces. Sulphide material is increasingly sparse in the older mounds, which typically has sediment cover > 1 metre thick.

The resemblance in mineralogical assemblages, textures and whole rock geochemistry between the VDVF and the hydrothermally extinct areas is indicative of extensive past and present hydrothermal activity at the top of Mt. Dent, and adds evidence to the importance of OCC's for locating hydrothermal circulation.

Table 4.6: Major and trace elements within hydrothermal precipitates from the VDVF and the surrounding inactive mounds. See Chapter 2 for map of sample locations.

Abbreviations: AM=active mount, C=chimney, IM=inactive mound. Major elements analysed by XRF, and traces using ICP-MS and ICP-AES.

Sample	Type	SiO ₂	TiO ₂	Al ₂ O ₃	Fe ₂ O ₃	MgO	CaO	K ₂ O	Na ₂ O	P ₂ O ₅	LOI	Sum
		wt.%	wt.%	wt.%	wt.%	wt.%	wt.%	wt.%	wt.%	wt.%	wt.%	wt.%
198-03	AM	62.12	0.01	0.27	0.16	31.26	0.08	0.04	0.18	0.01	5.70	99.81
198-04	AM	56.54	0.01	2.75	1.15	30.08	0.20	0.09	1.27	0.00	7.66	99.75
198-05	AM	57.88	0.02	0.70	0.68	29.51	1.81	0.10	0.43	0.02	8.50	99.65
199-09	AM	60.90	0.01	0.46	0.28	31.18	0.19	0.05	0.22	0.01	7.20	100.50
199-10	AM	66.11	0.01	0.18	0.27	28.10	0.08	0.03	0.13	0.00	5.50	100.41
200-21	AM	63.66	0.01	0.18	0.39	28.90	0.10	0.05	0.12	0.01	8.55	101.96
200-23	AM	59.91	0.01	0.17	0.28	31.41	0.27	0.09	0.22	0.02	7.30	99.68
200-24	C	57.61	0.01	0.02	0.81	28.33	0.41	0.14	0.68	0.02	11.60	99.63
201-26	IM	61.58	0.01	0.46	0.31	31.85	0.22	0.08	0.27	0.01	5.30	100.08
201-27	IM	58.51	0.02	1.19	1.39	29.53	0.65	0.07	0.39	0.02	7.11	98.87
201-29	IM	59.47	0.01	0.55	0.32	31.27	0.47	0.07	0.29	0.01	2.50	94.96
201-31	IM	61.60	0.02	1.14	0.98	31.46	0.19	0.07	0.36	0.01	2.30	98.12
201-32	IM	60.30	0.01	0.18	0.14	31.47	0.16	0.07	0.24	0.01	7.10	99.68
201-33	IM	61.42	0.01	0.42	0.39	31.28	0.09	0.04	0.21	0.01	6.09	99.95
201-34	AM	61.12	0.01	0.04	0.44	32.10	0.22	0.12	0.52	0.02	5.70	100.27
201-36	AM	58.51	0.01	1.00	0.71	30.53	0.15	0.07	0.44	0.01	7.70	99.13
201-37	C	53.51	0.01	0.24	0.57	30.71	0.06	0.07	0.24	0.02	9.63	95.04
201-38	AM	58.39	0.01	0.31	0.29	31.77	0.37	0.09	0.38	0.01	9.10	100.70
201-39	AM	54.26	0.09	2.04	0.90	34.19	0.06	0.02	0.22	0.12	8.79	100.68
201-40	AM	56.47	0.01	0.60	0.38	32.70	0.12	0.07	0.37	0.01	8.77	99.50
201-41	IM	54.33	0.04	1.02	0.88	27.98	0.26	0.13	0.38	0.04	11.10	96.16
202-43	C	57.99	0.01	0.19	0.33	31.81	0.18	0.10	0.43	0.01	8.30	99.33
202-45	C	51.85	0.01	0.05	0.41	31.04	0.32	0.07	0.35	0.06	15.10	99.25
202-46	C	60.05	0.01	0.07	0.34	30.58	0.18	0.06	0.25	0.02	12.17	103.73
202-48	C	66.22	0.01	0.71	0.37	25.51	0.15	0.06	0.43	0.01	6.26	99.71
202-49	C	54.83	0.01	0.05	0.49	30.79	0.32	0.07	0.31	0.03	12.76	99.65
199-107	C	58.31	0.01	0.65	0.64	30.92	0.15	0.07	0.40	0.01	8.78	99.94
199-110	C	57.05	0.01	0.19	0.19	30.73	0.21	0.08	0.41	0.02	11.02	99.91
44-1E	C	58.12	0.01	0.44	1.13	27.81	0.12	0.09	0.59	0.01	11.50	99.80
44-2G	AM	58.50	0.02	0.58	0.52	30.34	1.01	0.10	0.52	0.04	9.03	100.66

Sample	As	Ba	Cd	Co	Cs	Cu	Hf	Mn	Mo
	ppm	ppm	ppb	ppm	ppb	ppm	ppb	ppm	ppm
198-03	2.3	6.0	198	0.6	21	52	4	124	0.8
198-04	1.0	7.3	26	1.3	28	45	12	108	0.1
198-05	3.2	12.0	108	2.6	344	506	127	164	5.4
199-09	1.0	0.3	14	0.2	40	82	11	151	0.0
199-10	0.9	0.1	228	0.2	15	155	4	133	24
200-21	5.4	1.3	316	0.2	60	1293	<1	182	0.7
200-23	2.3	144	25	1.8	111	100	63	143	0.5
200-24	0.9	0.6	45	0.0	111	4	<1	2721	2.6
201-26	1.7	2.4	22	0.6	103	138	37	188	0.2
201-27	1.0	4.7	37	0.1	62	1047	80	89	0.1
201-29	1.7	1.8	44	4.0	76	1523	31	208	0.2
201-31	4.1	3.3	102	54	41	2218	53	806	4.7
201-32	4.0	1.9	65	3.8	55	614	292	130	0.2
201-33	1.2	2.1	24	1.3	27	100	27	87	1.3
201-34	2.8	1.0	34	0.2	90	32	3	1518	0.4
201-36	1.3	0.8	16	0.7	39	110	4	239	0.1
201-37	2.4	0.4	3249	0.5	71	4308	16	234	92
201-38	2.5	0.7	63	0.5	80	251	19	279	0.7
201-39	1.3	1.2	13	0.3	64	117	48	149	0.1
201-40	4.7	0.2	22	0.3	49	253	11	165	0.6
201-41	7.6	8.9	58	66	199	356	243	1233	1.7
202-43	8.1	0.8	2028	0.1	107	970	8	464	26.9
202-45	43.3	0.8	2807	0.2	47	1165	16	328	270
202-46	75.3	0.8	2791	0.1	51	1663	8	237	404
202-48	5.8	0.3	848	0.2	35	471	<1	175	23
202-49	65.8	1.7	2431	0.1	47	1949	4	278	253
199-107	2.6	2.0	134	0.6	63	1178	25	205	0.9
199-110	2.4	0.9	120	0.7	66	1416	62	240	0.5
44-1E	20.7	0.3	5975	0.3	83	5872	8	213	448
44-2G	5.4	5.2	63	13	134	589	87	552	1.2

Sample	Nb	Ni	Pb	Rb	Sb	Sc	Se	Sr
	ppb	ppm	ppm	ppb	ppb	ppb	ppm	ppm
198-03	14	3.1	12.8	434	292	39	0.2	2.9
198-04	16	1.2	7.4	710	44	28	0.1	17
198-05	269	7.2	22.8	2148	260	1100	0.8	48
199-09	22	2.6	1.2	636	44	73	0.1	8.9
199-10	4	1.2	35.4	270	325	53	0.4	2.4
200-21	4	1.5	66.1	569	1696	52	1.0	3.4
200-23	107	6.0	2.2	1589	87	530	0.3	26
200-24	4	0.6	0.2	1826	43	156	0.2	28
201-26	87	5.1	3.7	1336	109	352	0.1	11
201-27	819	8.0	32.2	912	107	303	0.7	48
201-29	129	3.6	4.5	1150	71	333	0.3	31
201-31	616	5.4	84.9	728	238	195	0.5	18
201-32	1276	10.2	56.1	591	217	2462	<0.1	52
201-33	78	3.2	2.4	495	129	241	<0.1	13
201-34	14	3.7	2.7	1500	136	83	0.1	13
201-36	20	0.6	12.6	771	40	47	0.5	12
201-37	12	3.1	325	794	2402	127	5.5	10
201-38	46	8.8	21.3	1305	328	159	1.0	26
201-39	76	6.5	2.2	1045	107	366	0.2	9.3
201-40	11	5.7	19.8	1047	454	19	0.1	14
201-41	1135	16.0	23.3	2596	219	1400	0.8	201
202-43	23	4.7	117	1216	3767	73	1.9	11
202-45	23	14.0	5.3	820	8229	160	7.4	172
202-46	16	5.7	25.7	767	25719	94	3.7	68
202-48	4	1.6	20.2	495	4703	58	1.4	7.2
202-49	4	6.5	31.6	839	20425	55	7.5	154
199-107	84	2.7	23.1	819	442	196	1.0	10
199-110	109	2.6	16.8	1154	257	505	1.3	14
44-1E	12	9.7	659	873	25042	802	19.4	8.4
44-2G	372	13.1	70.5	1938	798	575	0.5	59

Sample	Ta	Th	U	V	Y	Zn	Zr
	ppb	ppb	ppb	ppm	ppb	ppm	ppb
198-03	56	3.5	5.3	6.5	102	27	226
198-04	20	4.0	0.7	4.6	289	14	589
198-05	12	190	17	31.8	1052	73	6431
199-09	3.7	11	8.8	6.5	413	12	826
199-10	3.8	<1	20	4.6	84	47	266
200-21	<1	<1	13	7.3	82	162	168
200-23	7.4	74	16	10.5	978	20	3944
200-24	4.1	<1	9.5	2.8	439	2.6	86
201-26	8.3	62	8.9	10.4	281	58	2639
201-27	22	886	1.1	11.2	2212	97	3952
201-29	4.4	107	16	0.7	551	282	1870
201-31	19	781	1.1	6.4	1288	126	2586
201-32	98	1158	14	14.7	6934	236	11697
201-33	3.9	47	3.1	8.1	273	9.1	2072
201-34	<1	6.9	8.2	5.1	462	8.7	344
201-36	16	7.9	5.2	0.5	201	45	295
201-37	4.0	4.0	41	10.6	222	569	913
201-38	<1	27	28	33.2	558	63	1115
201-39	<1	24	20	7.1	567	30	3336
201-40	11	3.8	14	6.7	635	44	631
201-41	26	1219	16	7.7	2870	78	8677
202-43	12	3.8	73	15.3	418	235	445
202-45	105	3.9	136	22.8	762	53	965
202-46	7.8	3.9	127	14.8	309	123	544
202-48	3.8	<1	19	2.0	81	78	96
202-49	<1	<1	77	7.1	134	144	134
199-107	17	13	16	3.0	610	43	1491
199-110	7.8	35	20	4.6	820	33	3000
44-1E	3.9	3.9	120	10.8	220	1273	527
44-2G	17	363	17	5.6	1877	148	3741

Chapter Five – Talc precipitation at the Von Damm Vent Field

In this chapter the conditions of formation of the talc-dominated vents at the VDVF are investigated by consideration of: the major element chemistry of the hydrothermal fluids from three different localities on the VDVF; the rare earth element (REE) geochemistry of the talc; the strontium, oxygen and hydrogen isotope signatures of pure talc separates; and the results of thermodynamic modelling in the Geochemist's Workbench (GWB).

5.1. Von Damm Vent Field hydrothermal fluids

Shimmering fluids emanating at both focussed and diffuse structures at the VDVF are clear and low in particulate matter (Figure 5.1). Samples of hydrothermal fluids were collected from the Spire, Hotter than Hole, and Chimlet 2 sites at the VDVF (Table 5.1). Fluids were analysed by Jeff Hawkes, Matthew Cooper, and the *JC082* fluid chemistry team, both onboard and at the National Oceanography Centre, Southampton.

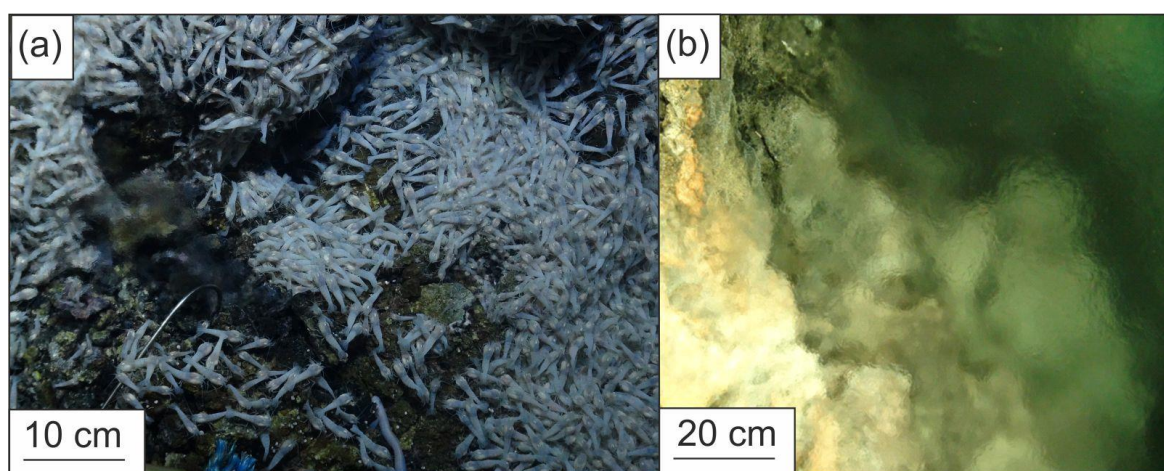


Figure 5.1: Shimmering fluid venting at the top of the VDVF. (a) diffuse venting on the main cone (b) close up of the main hole.

Sample number		198-GT1	198-GT2	200-GT1	200-GT3	200-GT4	202-GT3	202-GT4	End Member
Site		The Spire	The Spire	Hotter than Hole	Hotter than Hole	Hotter than Hole	Chimlet 2	Chimlet 2	VDVF
Depth	metres	2291	2291	2307	2308	2308	2379	2379	
Max temperature (in situ)	°C	215	215	138	138	138	108	108	215
pH (STP)		6	6.2	6.2	6.1	6.2	6.2	7	5.8
Cl	mmol kg ⁻¹	643	592	610	599	603	601	574	667
Si	mmol kg ⁻¹	12.3	7.48	5.83	5.91	5.83	5.26	5.11	13.6
Mg	mmol kg ⁻¹	14.7	31.4	27.3	26.3	29.5	22.7	40.6	0
Ca	mmol kg ⁻¹	15	13.4	12.9	13.1	13.2	13.4	11.6	16.4
Na	mmol kg ⁻¹	555	513	531	534	536	519	480	589
K	mmol kg ⁻¹	15.5	13.1	14.1	14.1	13.9	13.6	11.4	17.5
Fe	µmol kg ⁻¹	18.9	6.6	138	604	392	144	160	N.D.
Sr	µmol kg ⁻¹	92.8	91	90.9	90.6	90.1	88	86.8	N.D.
Mn	µmol kg ⁻¹	8	4.6	10.1	12.4	14.2	11.2	9.6	N.D.
Ba	µmol kg ⁻¹	5.55	2.61	3.23	5.11	5.4	5.43	2.52	8.4
Li	µmol kg ⁻¹	175	110	136	140	145	137	69.6	241
Cu	µmol kg ⁻¹	1.11	0.46	94.5	460	289	4.56	1.39	N.D.
H ₂ S	mmol kg ⁻¹	0.9	0.9	0.3	0.4	1.0	0.6	-	1.2
SO ₄	mmol kg ⁻¹	7.85	15.1	12.5	11.7	11.4	10.6	20.1	0
Br	µmol kg ⁻¹	N.D.	N.D.	943.8	891.0	908.3	920.6	857.7	N.D.
⁸⁷ Sr/ ⁸⁶ Sr		N.D.	0.706725	0.706174	0.705989	0.705958	0.705873	0.707801	0.702922
K/Cl		0.024	0.022	0.023	0.024	0.023	0.023	0.02	0.026
Br/Cl		N.D.	N.D.	0.00155	0.00149	0.00151	0.00153	0.00149	N.D.

Table 5.1: Measured concentrations in VDVF fluid samples with calculated end-members extrapolated to zero magnesium. STP = standard temperature and pressure

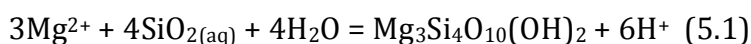
The concentration of Mg measured in the fluids ranges between 14.7 mmol kg⁻¹ to 40.6 mmol kg⁻¹ (Table 5.1), indicating significant entrainment of seawater during sample collection. Using a standard approach, the end-member fluid chemistry of the VDVF was derived by extrapolating measured concentrations in the samples to zero magnesium (Figure 5.2; e.g. Bischoff and Dickson, 1975; Von Damm, 1995). This is consistent with complete removal of Mg from seawater into alteration minerals in the

host lithologies, as observed in SO_4 concentrations in the fluids are 7.9-20.1 mmol kg^{-1} (Table 5.1), but trend towards zero when plotted against Mg (Figure 5.2).

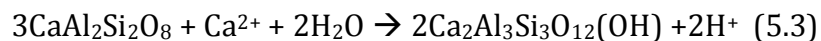
5.1.1. Vent fluid pH

The vent fluids range from 108°C to 215°C, with a pH of 6.1-7.0 at standard temperature and pressure (STP; Table 5.1). This measurement was obtained on ship at 25°C and 1 atmosphere of pressure, and is not an in situ measurement. Measurements of pH at STP give lower values than in situ analysis, as the precipitation of metal sulphides within sample bottles leads to an increase in acidity (Pester et al., 2012). This has potential issues when predicting the conditions of the reaction zones, but the pH measurements at the VDVF can still be discussed in comparison to other vent fields. The pH of the fluids at the VDVF is higher than values at mafic and ultramafic hosted high-temperature (black smoker) vent fields e.g. (Von Damm, 1995; Douville et al., 2002), and lower than the highly alkaline fluids emanating from the Lost City Hydrothermal Field (Table 5.2; Kelley et al., 2001).

Experiments have shown that hydrothermal fluids with an in situ pH in the range of 5-6 can be generated by <300°C seawater-basement reactions in mafic and ultramafic lithologies, providing the water/rock ratio progresses to low values (Seyfried Jr, 1987; Allen and Seyfried Jr, 2005). At these temperatures, the pH of the circulating fluid is controlled by the rate of Mg removal from seawater and silicate hydrolysis (Equations 5.1-5.2). At low water/rock ratios (<10), the rate of magnesium consumption is relatively low, and silicate hydrolysis acts as a pH buffer. At high water/rock ratios (>50), H^+ is produced at a rate greater than it is used up in silicate hydrolysis reactions, resulting in lower pH (Seyfried Jr, 1987).



In contrast, at temperatures of >350°C, the pH of the fluid is controlled more by the reactions involving the fixation of Ca and albitisation, and not by Mg removal (Seyfried Jr, 1987), with both reactions resulting in a lower fluid pH (Equations 5.3-5.4).



These reactions are based on the comparison between the shipboard pH measurements and those of in situ experimental results, which can differ by up to 1.5 (Pester et al., 2012). However, the discrepancy between shipboard and in situ values at the VDVF is likely to be lower than at black smoker fields, due to the far lower concentrations of dissolved metals. Furthermore, although the pH at the VDVF may be higher than the value measured on board, the reactions displayed in Equations 5.1-5.2 are more likely to occur than those of Equations 5.3-5.4, given the lower temperature. This would lead to a more alkaline fluid compared to those observed at black-smoker sites, indicating that the composition of the VDVF fluids is likely to be controlled by moderate temperature (<300°C) interactions with a gabbro ± peridotite reaction zone, at a low fluid-rock ratio.

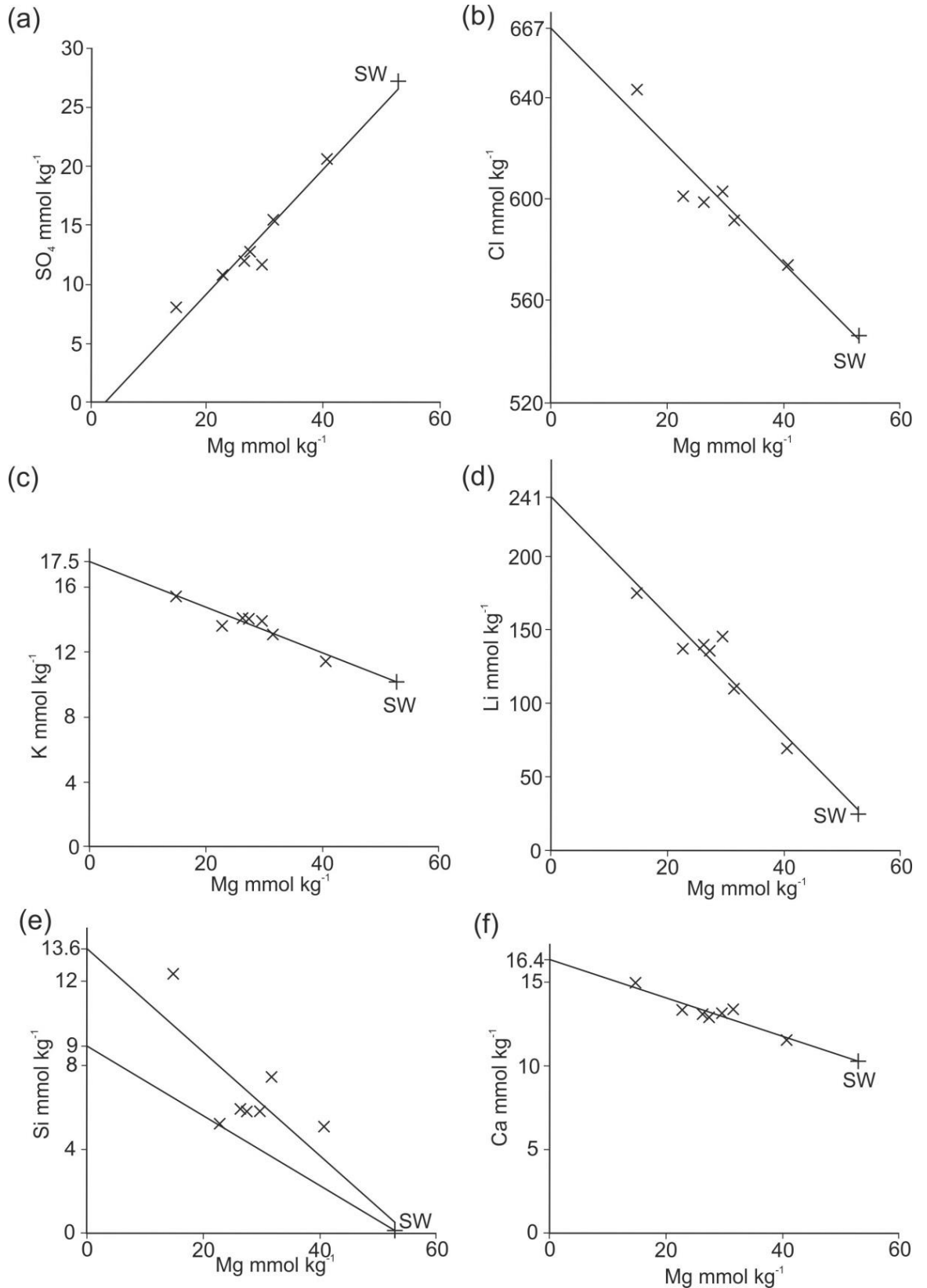


Figure 5.2: Plots of VDF fluid projected from seawater to zero magnesium, with the end-member labelled on the y axis (a) SO_4 (b) Cl (c) K (d) Li (e) Si (f) Ca. Abbreviation: SW=seawater.

5.1.2. Vent fluid chlorinity

Chlorinity concentrations of the samples and calculated end-member are elevated in comparison to seawater, with measured values of 574 to 643 mmol kg⁻¹ (Table 5.1). When projected to zero magnesium, this gives an end-member concentration of 667 mmol kg⁻¹, which is 22% greater than the background seawater concentration of 546 mmol kg⁻¹ (McDermott, 2015). In high-temperature black-smoker systems, chlorinity anomalies are considered to be a function of phase separation (Bischoff and Pitzer, 1985). Commonly, low chlorinity fluids are vented or, at the waning stage of hydrothermal circulation brine phases are occasionally sampled (Butterfield et al., 1997; Von Damm et al., 1997). Low chlorinity fluids can also be generated through water-rock interactions with peridotite lithologies, and/or residual brine or halite addition (Bischoff and Rosenbauer, 1984; Douville et al., 2002). At the depth of the VDVF, however, a venting temperature in excess of 360°C would be required to phase separate seawater (Figure 5.3), and even higher temperatures if phase separation was sub-surface in the hydrothermal reaction zone (i.e. several kilometres deeper; Bischoff and Rosenbauer, 1984; Bischoff and Rosenbauer, 1985). This temperature is at least 150°C greater than the maximum temperature recorded for fluids exiting the hydrothermally active orifices, and would require a cooling factor much greater than that predicted from the adiabatic cooling of the fluid on its rapid ascent from a reaction zone to the surface e.g. (Bischoff, 1980). Furthermore, experimental data shows that a moderate pH fluid cannot be generated if temperatures of >350°C were experienced in the sub-surface (Seyfried Jr and Bischoff, 1981; Seyfried Jr, 1987). Also, the venting fluids would have completely different geochemical signatures to those observed at the VDVF, and would bear more resemblance to those observed at black-smoker sites. For example, lower pH (~3-4) and higher concentrations of dissolved H₂S and base metals e.g. (Von Damm, 1995).

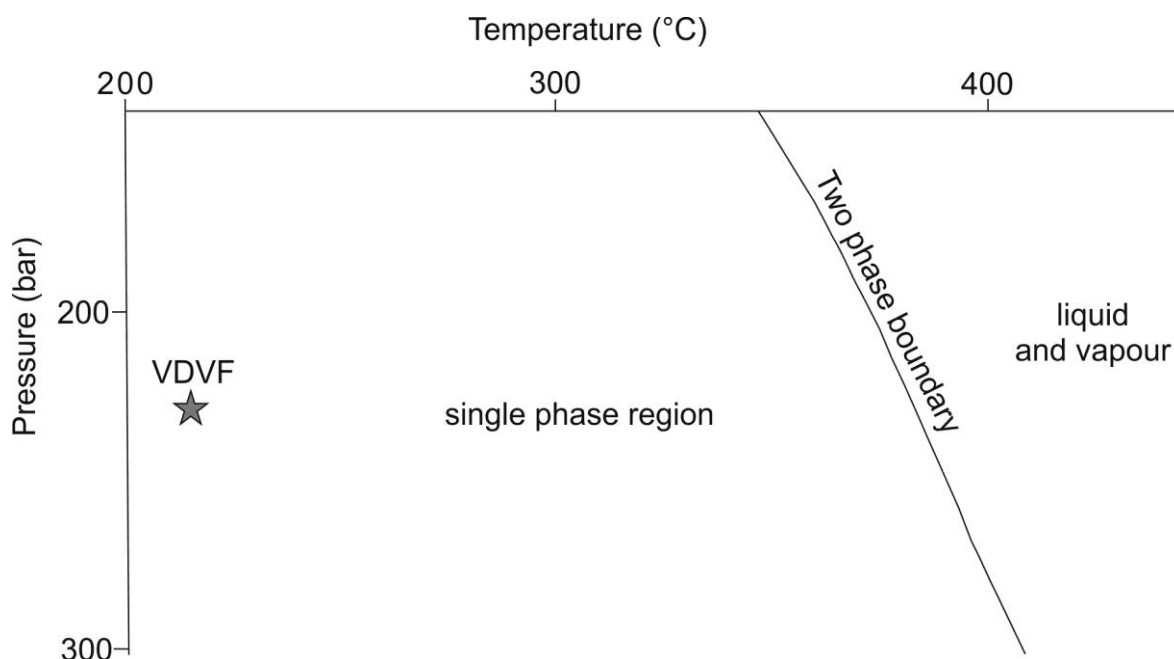
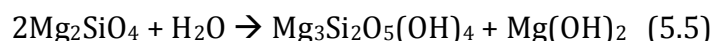


Figure 5.3: Phase diagram of seawater. The location of the two-phase boundary, the critical point and the physical conditions of venting at the VDVf are displayed. This indicates the considerable pressure and temperature increase required for the VDVf fluids to enter the two phase region. After Bischoff and Rosenbauer, (1985).

Alternatively, a residual reservoir of high-density brine could have developed in the lower crust from earlier episodes of hydrothermal circulation during which phase separation occurred. Mining of this residual brine in the sub-surface by fluids circulating below the VDVf could produce the observed elevated salinity. Similarly, the high-chlorinity of the VDVf fluid could also be a result of dissolution of residual halite from deep within the crust, again formed by magma-seawater interaction. However, the Br/Cl ratios of seawater and the end-member hydrothermal fluid are similar (Tables 5.1-5.2), indicating that chloride has not been preferentially added into the circulating hydrothermal fluids, as would be expected from dissolution of halite. Furthermore, a high-temperature hydrothermal circulation cell of sufficient magnitude to generate a substantial brine reservoir is likely to have formed a massive sulphide deposit in the locality of the VDVf, for which there is no evidence yet discovered. The only evidence for earlier hydrothermal activity in proximity to the active VDVf at the top of Mt. Dent is of similar mineralogy and composition to the VDVf, suggesting similar physical and chemical conditions during its formation. Another alternative explanation may lie in the interaction between seawater and the host rock beneath the VDVf. Recovery of serpentinised peridotite and gabbro from

the vicinity of the VDVF indicates a mixed basement lithology. Hydration of peridotite leads to serpentinisation and the addition of water into the host rock by the hydrolysis of olivine to serpentine e.g. (Barnes et al., 1967; Janecky and Seyfried Jr, 1986). This process can result in an increased chlorinity of the residual fluid without changing the Br/Cl ratio, and has been suggested to occur at other ultramafic hosted vent fields e.g. (Douville et al., 2002). It is difficult to quantify the degree or rate of serpentinisation required to generate the required chlorinity, but an estimate can be made based on the mass of pure forsterite and the equation for its reaction with water (Equation 5.5). The difference in chlorinity between seawater (546 mmol kg⁻¹) and the VDVF end-member (667 mmol kg⁻¹) requires that for every 1 kg of vent fluid, approximately 0.94 kg of pure forsterite is required to elevate the salinity of the VDVF fluids. Assuming a mass flux of 500 kg s⁻¹ of end-member vent fluid (using the temperature of each vent to derive the proportion of end-member hydrothermal fluid) this would require the complete serpentinisation of ~470 kg s⁻¹ of pure forsterite.



In summary, the elevated chlorinity in comparison to seawater in the VDVF end-member fluid could have been caused either by entrainment of brine during past hydrothermal circulation, or from water-ultramafic rock interaction. The entrainment of an early-formed brine or halite phase is consistent with a cooling hydrothermal system, while serpentinisation is compatible with the tectonic setting of the VDVF. However, few ultramafic samples have been recovered from Mt. Dent, despite the VDVF's situation on lower-crust and upper-mantle rocks, suggesting that entrainment of a brine solution is a more likely explanation. Ultimately, the chlorinity of the vent fluids are constrained by the degree of residual brine within the crust, or by the rate of serpentinisation and availability of fresh peridotite.

5.1.3. Cations

Potassium and lithium both show conservative mixing with seawater, and have concentrations ranging from 11.4 to 15.5 mmol kg⁻¹ and 69.6 to 175 µmol kg⁻¹, giving end-member concentrations of 17.5 mmol kg⁻¹ and 241 µmol kg⁻¹ respectively (Table 5.1, Figure 5.2). These values are much greater than the increase expected by phase separation of seawater alone (Von Damm, 1995), and indicates significant addition of these elements into the hydrothermal fluid by water-rock interactions. Fluid samples also have dissolved silica concentrations that range from 5.1 to 12.3 mmol kg⁻¹. While these form a less well constrained regression, a mean regression line through the data indicate an end-member concentration of 13.6 mmol kg⁻¹. However, as the fluid was not filtered and there remains a possibility of an entrained particulate silica-bearing phase adding to the analysis, the minimum silica concentration obtained by regression is 9 mmol kg⁻¹ (Table 5.1, Figure 5.2), comparable to the other reported end-member dissolved concentration of 7.5 mmol kg⁻¹ (McDermott, 2015). Calcium concentrations are better constrained across all the chimneys, ranging from 11.6 to 15.0 mmol kg⁻¹, and fall on a linear trend that gives an end-member fluid concentration of 16.4 mmol kg⁻¹ (Table 5.1, Figure 5.2).

The end-member dissolved silica concentration of 7.5 mmol kg⁻¹ obtained by McDermott, (2015) is lower than the concentrations of 21-22 mmol kg⁻¹ at the Trans-Atlantic Geotraverse (TAG) basalt-hosted system on the Mid-Atlantic Ridge (MAR), and within the ranges of the concentrations of 6.4-8.6 mmol kg⁻¹ for the Logatchev and Rainbow vent fields that are hosted by ultramafic dominated lithologies (Table 5.2). A higher concentration of dissolved Si would be expected at high-temperature hydrothermal systems hosted in a dominantly gabbro basement. However, lower venting temperatures at the VDVF result in a lower concentration of dissolved silica (Von Damm et al., 1991). The quartz geobarometer of Von Damm et al., (1991) indicates that the dissolved silica content of the VDVF fluids is higher than would be expected from quartz-fluid equilibrium, suggesting either that the fluids have cooled on ascent to the surface, or the elevated chlorinity of the fluids has increased the concentration of dissolved silica.

While the end-member fluid concentration of calcium of $16.4 \text{ mmol kg}^{-1}$ is comparatively low compared with other vent fields, calcium remains one of the dominant cations in the VDVF fluid. This would suggest that calcium sulphate would precipitate at the hydrothermal fluid-seawater mixing interface e.g. (Haymon, 1983). However, all but one of the chimneys at the VDVF have a venting temperature below the 150°C required for anhydrite stability, hence the lack of sulphate in most of the active VDVF vent structures is largely due to the lower temperature of venting here compared with black smoker systems (Bischoff and Seyfried, 1978). However, sulphate precipitation may occur in the subsurface where the end-member temperature is 215°C or greater and the fluid mixes with seawater.

Base metals, strontium and barium concentrations do not show conservative mixing with seawater. In the case of strontium, this is likely due to the similarity in concentration between the hydrothermal fluids and seawater, in which the concentrations are 86.8 to $92.8 \text{ mmol kg}^{-1}$ and $91.0 \text{ mmol kg}^{-1}$ respectively. Base metal concentrations in the samples from the Hotter than Hole vent are much higher than at the Spire or Chimlet 2 vents. Iron concentrations range from 138 to $604 \text{ } \mu\text{mol kg}^{-1}$ at the Hotter than Hole vent, compared to 6 and $19 \text{ } \mu\text{mol kg}^{-1}$ at the Spire, and 144 and 160 at the Chimlet 2 site (Table 5.1). Furthermore, Cu concentrations at the Hotter than Hole vent are 94.5 to $460.0 \text{ } \mu\text{mol kg}^{-1}$, compared to 0.4 and $1.2 \text{ } \mu\text{mol kg}^{-1}$ for the Spire, and 1.3 and $4.6 \text{ } \mu\text{mol kg}^{-1}$ at Chimlet 2 (Table 5.1). Manganese concentrations are low in all of the vents, with concentrations ranging from 4.6 to $14.2 \text{ } \mu\text{mol kg}^{-1}$ (Table 5.1). Despite base metals not showing conservative mixing across chimneys from the whole site, iron and copper plot on a mixing line with the chlorinity concentrations from the three samples taken from the Hotter than Hole vent. This is expected as copper and iron are transported as chloride complexes in hydrothermal vent fluids, and the differences between the two vents is due to small changes in redox conditions within the mounds (Seyfried Jr and Ding, 1993).

Vent field	VDVF	VDVF (McDermott)	TAG	Rainbow	Logatchev	Lost City	9-21°N	Guaymas Basin	Escanaba	Seawater
Temperature (in situ)	°C	215	226	362-365	350-353	91	273-405	264-315	108-218	4
pH (STP)		5.8	5.6	2.7-3.1	3.3-3.9	9	2.6-5.1	5.9	5.4	8.2
H ₂ S	mmol kg ⁻¹	1.2	3.2	1.2	2.5	0.06	2.9-26	3.95-6.00	1.1-5.98	0
Cl	mmol kg ⁻¹	667	651	745-756	515-551	541	41.6-760	580-637	632-668	545
Si	mmol kg ⁻¹	13.6	7.5	6.4-7.1	8.2-8.6	0.02-0.07	3.7-21.9	12-13.8	5.6-5.9	0.05
Mg	mmol kg ⁻¹	0	0	0	0	0-1.3	0			52.4
Ca	mmol kg ⁻¹	16.4	15.7	66.6	28-29	26.6-27.4	2.1-54.8	27.7-41.5	32-33.4	10.6
Na	mmol kg ⁻¹	589	603	553	438-455	49.4	242-449	472-513	536-560	466
K	mmol kg ⁻¹	17.5	16.5	20.2-20.4	22-24	10.5	1.56-25	40.1-49.2	33.2-40.4	10.2
Fe	μmol kg ⁻¹	N.D.	20	23600-25000	2400-2500	<0.01	687-12500	0.008-1.8	0.01-0.06	0
Mn	μmol kg ⁻¹	N.D.	10	2200-2350	330-340	N.D.	0.07-2.93	0.13-0.24	0.01-31.1	0
Ba	μmol kg ⁻¹	8.4	N.D.	59-79	n.d.	N.D.	0.27-95	15-54	4.4	0.07
Li	μmol kg ⁻¹	241	219	327-345	245-252	43-46	27-920	720-1076	1110-1286	26.6
Sr	μmol kg ⁻¹	N.D.	99	200	127-138	N.D.	8-387	158-226	192-209	89
Cu	μmol kg ⁻¹	N.D.	2.9	121-162	27-44	N.D.	45-162	0.02-1.1	3.2	0

Table 5.2: Extrapolated end-members for the VDVF compared to other hydrothermal vent fields and seawater. The concentrations obtained are largely similar to those of McDermott (2015). Data from the literature is taken from Edmond et al., 1982; Von Damm et al., 1985; Bowers et al., 1988; Campbell et al., 1988; Charlou and Donval, 1993; Campbell et al., 1994; Edmond et al., 1995; James et al., 1995; Edmonds et al., 1996; Gamo et al., 1996; James et al., 1999; Kelley et al., 2001; Charlou et al., 2002; Douville et al., 2002; Von Damm et al., 2003; Von Damm, 2004; Proskurowski et al., 2006; Schmidt et al., 2007; McDermott, 2015; Seyfried Jr et al., 2015. STP = standard temperature and pressure.

Base metal concentrations are much lower at the VDVf compared to other vent fields, especially high-temperature black smoker sites (Von Damm, 1995; Tivey, 2007). This is likely to be because the temperature at the VDVf is >150°C lower and the pH is more-neutral, meaning that the solubility of base metals such as Fe, Zn, Cu and Mn are greatly reduced (Seyfried Jr and Janecky, 1985).

5.2. Rare earth elements

REE are important indicators of sub-seafloor processes in geological environments due to their behaviour in hydrothermal systems. Hydrothermal vent fluids are characterised by light rare earth element (LREE) enrichment and positive europium anomalies (Douville et al., 1999), whereas seawater profiles are characterised by heavy rare earth element (HREE) enrichment, and negative cerium anomalies (Klinkhammer et al., 1983).

5.2.1. Hydrothermal precipitates

The sum total of the REEs (Σ REE) in pure talc separates from the VDVf ranges in concentration from 50 to 1291 ppb, and average 379 ppb (Table 5.3). Neodymium concentrations range from 2.9 to 205 ppb, and average 48 ppb (Table 5.). The Σ REE and Nd concentrations are similar to, or slightly lower than REE concentrations in seafloor talc occurrences at, for example, Red Seamount and the St. Paul Fracture Zone (D'Orazio et al., 2004; Dekov et al., 2008a). Chondrite normalised REE patterns in the pure talc separates have shallow, U-shaped profiles dominated by a positive europium anomaly that varies in magnitude between samples (Figures 5.4-5.6). The U-shaped profiles in the talc deposits reflect elevated LREE and HREE concentrations in comparison to middle rare earth's (MREE) concentrations.

Enrichment in the LREE in the VDVf samples is quantified here using $La_{(N)}/Sm_{(N)}$ (where (N)=chondrite normalised values). For the hydrothermally active chimneys and mounds $La_{(N)}/Sm_{(N)}$ ranges between 0.9 to 10.4 (Table 5.4), with an average of 3.2. $La_{(N)}/Sm_{(N)}$ ratios of 3.1 for the hydrothermally inactive mounds are slightly lower than samples from the active site (Table 5.4; Figure 5.7). The slight HREE enrichment in the VDVf talc samples from the VDVf is indicated by $Dy_{(N)}/Yb_{(N)}$

ranging from 0.5 to 1.3 for the chimney structures, and 0.3 to 2.1 for the active mounds (Table 5.4), averaging 0.9 for both sample sets. Two of the samples do not show HREE enrichment, and 19 out of 24 samples from the active site have a $Dy_{(N)}/Yb_{(N)}$ of <1 (Table 5.4). The hydrothermally inactive samples have variable $Dy_{(N)}/Yb_{(N)}$, with ratios ranging from 0.4 to 1.7, with only one sample of <1 , and an average of 1.2. The Eu anomaly as defined by Eu/Eu^* (where $Eu/Eu^* = Eu_{(N)}/\sqrt{(Sm_{(N)} \times Gd_{(N)})}$), ranges from 1.4 to 227.1 in all hydrothermal precipitates (Table 5.4; Figure 5.8).

The Eu anomaly for the chimney material ranges from 22.3 to 227.1, and averages 104.2. The Eu anomaly for samples from the hydrothermally active mounds ranges from 6.1 to 150.9 (Table 5.4), and averages 60.6. One of the samples from the hydrothermally inactive *Mystic Mountain* area does not have a positive Eu anomaly, but other samples from the hydrothermally inactive sites have Eu/Eu^* ranging from 4.4 to 99.4 (Table 5.4), with an average of 42.3. Positive and negative cerium anomalies, defined as Ce/Ce^* (where $Ce/Ce^* = Ce_{(N)}/\sqrt{(La_{(N)} \times Pr_{(N)})}$), are evident in a few samples. A majority of samples show little or no Ce anomaly, and have Ce/Ce^* values of 0.7-1.3 (Figure 5.8). Five samples have significant Ce anomalies and have Ce/Ce^* values of up to 2.2. One sample that is located on the rubble apron of the main cone has a Ce/Ce^* value of 0.5, indicating a negative cerium anomaly (Table 5.4).

Positive cerium anomalies in seafloor environments are generally only found in Fe-Mn crusts not associated with hydrothermal activity (Elderfield et al., 1981; Nath et al., 1992). In contrast, Fe-Mn crusts and sediments formed by particle fallout from neutrally buoyant plumes, or those associated with hydrothermal systems, either have a negative or no cerium anomaly (Elderfield and Greaves, 1981; Kuhn et al., 1998; Sun et al., 2011). REE profiles of talc in seafloor environments, including inactive hydrothermally precipitated talc, shear zone talc, or talc formed from serpentinisation reactions do not show positive cerium anomalies e.g. (Lonsdale et al., 1980; Dekov et al., 2008a). The positive cerium anomaly in a few of the talc samples could be explained by the oxidation of Ce^{3+} to Ce^{4+} in the water column above the VDFV. This is followed by subsequent fallout from the neutrally buoyant plume and sorption onto the talc samples, which could lead to a slight increase in the concentration of cerium within the talc. However, the oxidation of Ce^{3+} is kinetically

slow (Sholkovitz and Schneider, 1991), and would require long timescales for the development of a positive cerium anomaly in the talc through this process.

5.2.2. *Precipitation of talc from a hydrothermal fluid*

The LREE enrichment and positive Eu anomalies in the chimney and mound material indicate talc precipitation from a hydrothermal fluid. The concentration of REE in hydrothermal fluids is normally around 2 to 4 orders of magnitude higher than in seawater e.g. (Douville et al., 1999). As a result of this, REE patterns in primary precipitates from seafloor hydrothermal vent fields are dominated by the signature of the vent fluid, but are also influenced by the partition coefficients between the REE and the precipitate e.g. (Mitra et al., 1994). Both of these processes are evident in the REE patterns of talc from the VDVF. The reducing conditions in the VDVF vent fluid are indicated by the presence of sulphides, and lack of sulphate in the end-member fluids.

Eu mobility is enhanced by these reducing conditions and forms divalent Eu chloride complexes that are more stable in hydrothermal fluids than other REE chloride complexes, which have trivalent redox states. Furthermore, positive Eu anomalies occur in hydrothermal fluids from the dissolution of plagioclase from the host rock, which contains elevated, divalent Eu in the calcium site in its atomic structure.

Therefore, the interaction of a reducing hydrothermal fluid with plagioclase, which occurs in the sub-surface below the VDVF, results in large, positive Eu anomalies (Figure 5.8; Sverjensky, 1984; Douville et al., 2002). LREE are generally more stable in hydrothermal fluids, which is reflected in the patterns in the VDVF talc. However, while the Eu anomaly and the LREE enrichment are inherited from the vent fluid, the slight HREE enrichment is a result of the crystallographic effect of the talc structure. HREE substitute into talc more readily than the LREE and MREE as a result of their ionic radii being more similar in size to Mg^{2+} in the octahedral site (Shannon, 1976).

The patterns of REE in the VDVF hydrothermal talc have three characteristics: LREE enrichment, slight HREE enrichment, and large positive Eu anomalies. These characteristics are shown to be indicative of hydrothermal vent fluids, and the partitioning of REE between the fluid and the precipitate. This gives further evidence

towards the formation of talc at the VDFV being a direct result of primary precipitation from a hydrothermal vent fluid.

Sample	Type	La	Ce	Pr	Nd	Sm	Eu	Gd	Tb	Dy	Ho	Er	Tm	Yb	Lu	Sum
		ppb	ppb	ppb	ppb	ppb	ppb	ppb	ppb	ppb	ppb	ppb	ppb	ppb	ppb	ppb
198-03	AM	46.8	157.8	7.0	20.3	2.8	126.0	2.8	0.3	1.8	0.4	1.3	0.2	1.0	0.2	369
198-04	AM	4.0	9.8	1.4	6.5	2.3	16.6	4.5	0.8	5.7	1.3	3.9	0.6	4.3	0.6	62
198-05	AM	243.1	430.5	55.5	204.1	39.0	74.9	36.0	5.7	37.1	8.4	26.0	4.3	31.0	5.2	1201
199-09	AM	36.8	83.4	8.7	34.6	7.4	83.4	9.7	1.5	10.7	2.5	8.0	1.3	9.5	1.7	299
199-10	AM	19.7	68.1	4.8	17.8	2.6	109.6	3.0	0.4	2.4	0.7	2.3	0.3	2.3	0.3	234
200-23	AM	94.2	176.2	21.7	81.1	17.2	143.8	17.7	3.0	20.8	5.0	16.8	2.9	22.7	3.8	627
200-24	C	35.2	72.0	8.3	33.7	6.6	176.0	6.6	0.7	4.0	0.9	2.3	0.3	2.0	0.3	349
201-26	IM	24.8	75.8	5.7	20.0	4.6	25.8	4.7	0.7	4.1	0.8	2.1	0.3	1.8	0.3	171
201-27	IM	9.1	34.9	1.8	6.0	1.4	51.8	1.8	0.3	2.7	0.7	2.6	0.5	4.2	0.9	119
201-31	IM	116.5	388.5	48.6	194.0	32.9	12.9	23.4	2.1	8.5	1.3	3.2	0.5	3.3	0.5	836
201-33	IM	18.5	38.5	4.2	15.8	2.7	88.8	3.4	0.4	2.5	0.6	1.7	0.3	1.6	0.3	179
201-34	AM	63.7	173.6	17.9	68.5	9.7	372.5	10.7	1.2	7.6	1.7	5.5	0.8	5.3	0.8	739
201-35	AM	7.7	26.7	3.3	16.4	5.3	21.2	6.9	1.1	6.4	1.3	3.9	0.6	5.0	0.8	107
201-36	AM	23.5	52.1	5.6	22.1	4.5	75.2	5.1	0.6	3.3	0.7	1.5	0.2	1.1	0.2	196
201-38	AM	11.4	28.3	3.4	15.9	5.0	77.7	8.6	1.2	7.8	1.7	4.5	0.6	3.9	0.7	171
201-39	AM	12.5	25.5	3.0	12.2	1.9	102.9	2.3	0.2	1.9	0.4	1.3	0.2	1.3	0.2	166
201-40a	AM	5.9	11.0	1.7	7.2	1.7	94.8	3.3	0.5	4.0	1.1	3.7	0.5	3.6	0.5	139
201-40b	AM	2.6	4.5	0.6	2.9	0.8	38.9	1.4	0.2	1.5	0.4	1.3	0.2	1.0	0.1	56
201-41	AM	28.3	87.8	9.0	37.1	10.6	16.1	11.8	1.8	11.1	2.1	6.0	0.8	6.2	1.2	230
202-43b	C	21.0	30.3	4.3	16.8	3.4	275.3	4.4	0.6	4.6	1.2	3.6	0.6	3.3	0.6	370
202-47	C	8.5	19.5	1.7	6.1	1.0	84.2	1.2	0.2	1.7	0.4	1.3	0.2	2.2	0.4	128
199-107	C	19.8	49.5	6.1	25.5	6.6	77.7	9.2	1.2	7.7	1.6	4.3	0.6	4.2	0.7	214
199-108	C	7.3	17.6	2.0	9.0	2.4	20.9	3.4	0.5	3.6	0.8	2.6	0.4	2.8	0.5	74
202-48	AM	3.7	11.0	1.4	6.7	2.0	9.6	3.3	0.5	3.8	0.9	2.9	0.5	3.2	0.6	50
199-110	AM	12.1	28.2	3.6	15.0	3.5	58.2	5.0	0.8	5.3	1.3	4.1	0.7	6.2	1.2	145
1A	C	114.9	193.9	28.8	109.3	26.4	617.4	32.2	5.3	27.8	6.7	20.7	3.2	21.6	4.0	1212
1F	C	48.7	85.6	12.3	47.4	8.2	260.0	9.8	1.7	9.7	2.2	7.3	1.4	9.1	1.4	505
2C	AM	73.4	153.5	19.3	76.3	15.9	119.7	15.7	2.5	18.5	4.7	16.5	3.6	36.3	7.7	564
2O	AM	164.0	179.3	39.8	158.3	31.9	404.1	47.7	9.2	65.2	17.1	57.7	11.2	88.7	16.3	1290
Chondrite		237	613	93	457	148	56	199	36	246	55	160	25	161	25	2510

Table 5.3: REE concentrations in VDFV samples. Table includes pure talc separates from hydrothermally active and inactive sites. Concentrations in host rocks are presented in

Chapter 4. Abbreviations: AM = active mound, C=chimney, IM = inactive mound.

Chondrite values used to normalise the data for the REE plots are included and are taken from (McDonough and Sun, 1995).

Sample	Eu/Eu*	Ce/Ce*	La/Sm	Dy/Yb
198-03	135.9	2.1	10.4	1.1
198-04	15.5	1.0	1.1	0.9
198-05	6.1	0.9	3.9	0.8
199-09	30.1	1.1	3.1	0.7
199-10	119.8	1.7	4.8	0.7
200-23	25.2	0.9	3.4	0.6
200-24	81.5	1.0	3.3	1.3
201-26	16.8	1.5	3.3	1.5
201-27	99.4	2.1	4.1	0.4
201-31	1.4	1.2	2.2	1.7
201-33	89.5	1.1	4.2	1.0
201-34	111.6	1.2	4.1	0.9
201-35	10.7	1.3	0.9	0.8
201-36	47.8	1.1	3.3	2.0
201-38	36.2	1.1	1.4	1.3
201-39	150.8	1.0	4.1	1.0
201-40a	121.3	0.9	2.1	0.7
201-40b	111.5	0.9	2.0	1.0
201-41	4.4	1.3	1.7	1.2
202-43b	215.4	0.8	3.8	0.9
202-47	227.1	1.2	5.1	0.5
199-107	30.5	1.1	1.9	1.2
199-108	22.4	1.1	1.9	0.8
202-48	11.5	1.1	1.2	0.8
199-110	42.2	1.0	2.1	0.6
1A	64.5	0.8	2.7	0.8
1F	88.2	0.8	3.7	0.7
2C	23.1	1.0	2.9	0.3
2O	31.6	0.5	3.2	0.5

Table 5.4: Eu anomalies, Ce anomalies, $La_{(N)}/Sm_{(N)}$ and $Dy_{(N)}/Yb_{(N)}$ in VDVF precipitates.

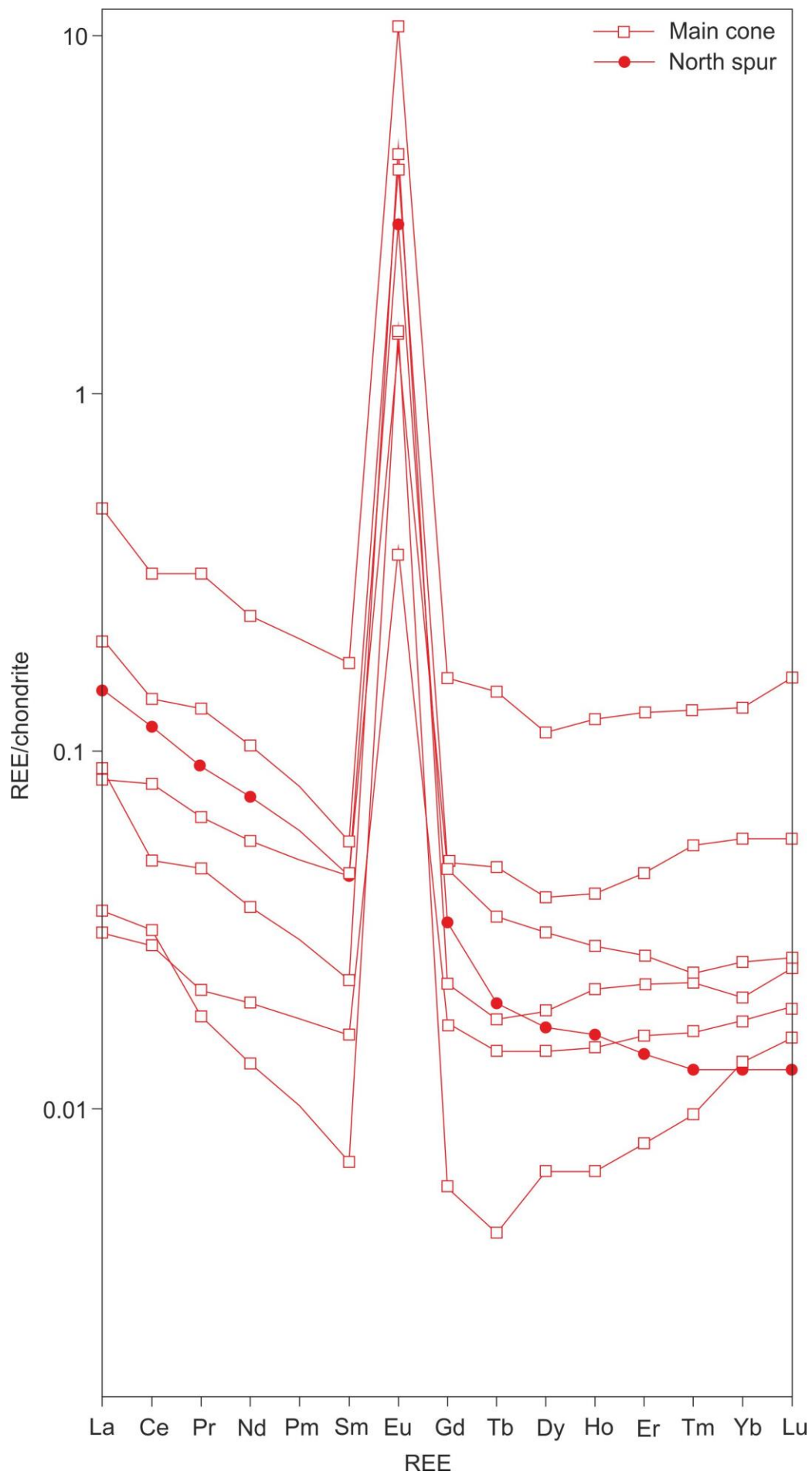


Figure 5.4: Chondrite normalised REE patterns for active chimneys at the VDF. Chondrite data is taken from (McDonough and Sun, 1995).

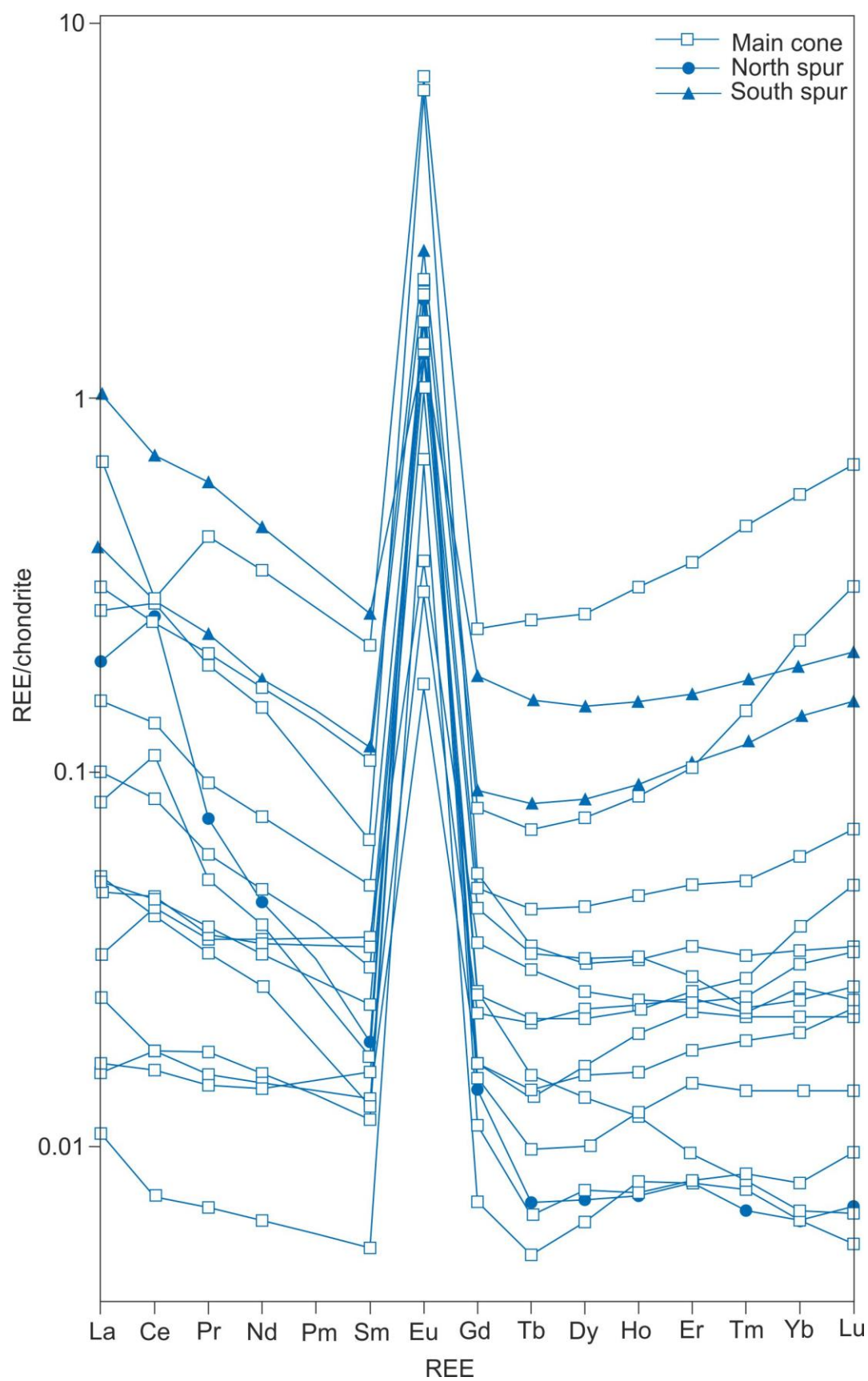


Figure 5.5: Chondrite normalised REE patterns for active mounds at the VDF. Chondrite data is taken from (McDonough and Sun, 1995).

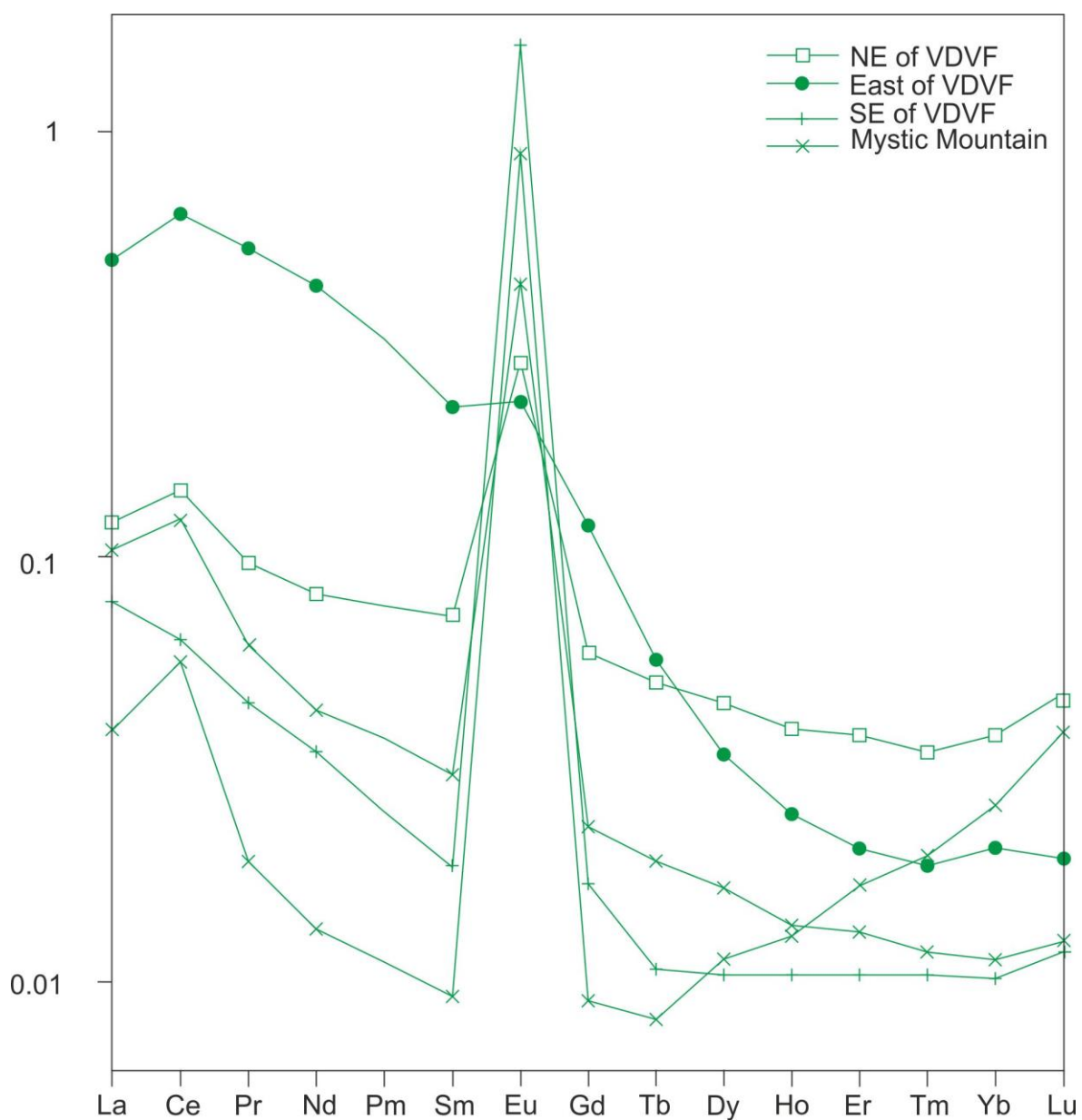


Figure 5.6: Chondrite normalised REE patterns for inactive mounds in the vicinity of the VDFV. Chondrite data is taken from (McDonough and Sun, 1995).

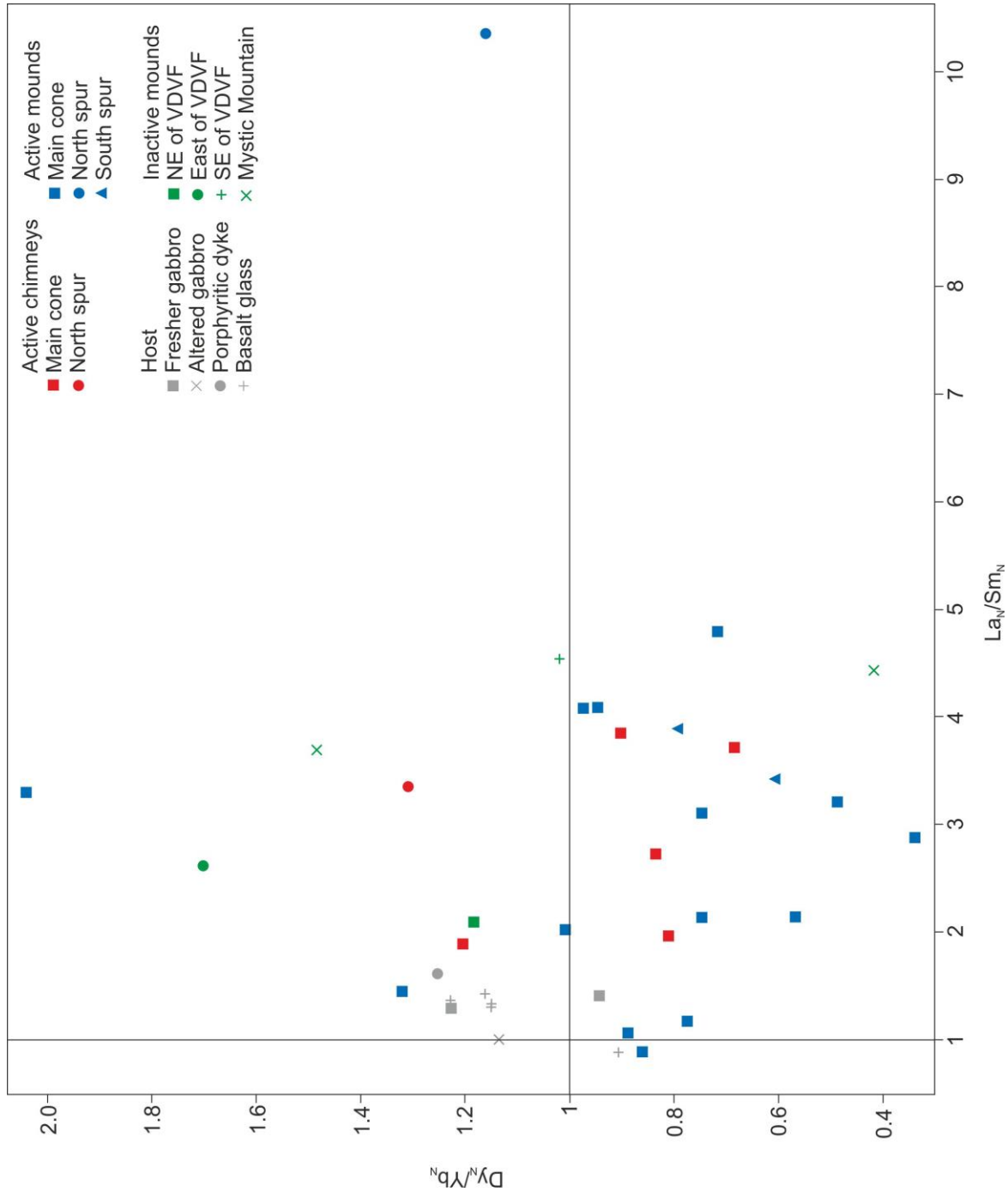


Figure 5.7: $La_{(N)}/Sm_{(N)}$ and $Dy_{(N)}/Yb_{(N)}$ ratios (where (N)=chondrite normalised) of hydrothermal precipitates. Values for host material displayed in Chapter 4 are added for comparison. Indicates the strong LREE and HREE enrichment in comparison to MREE in VDFV hydrothermal precipitations, displayed by the majority of samples displaying $Dy_{(N)}/Yb_{(N)}$ values of <1 , and $La_{(N)}/Sm_{(N)}$ values of >1 .

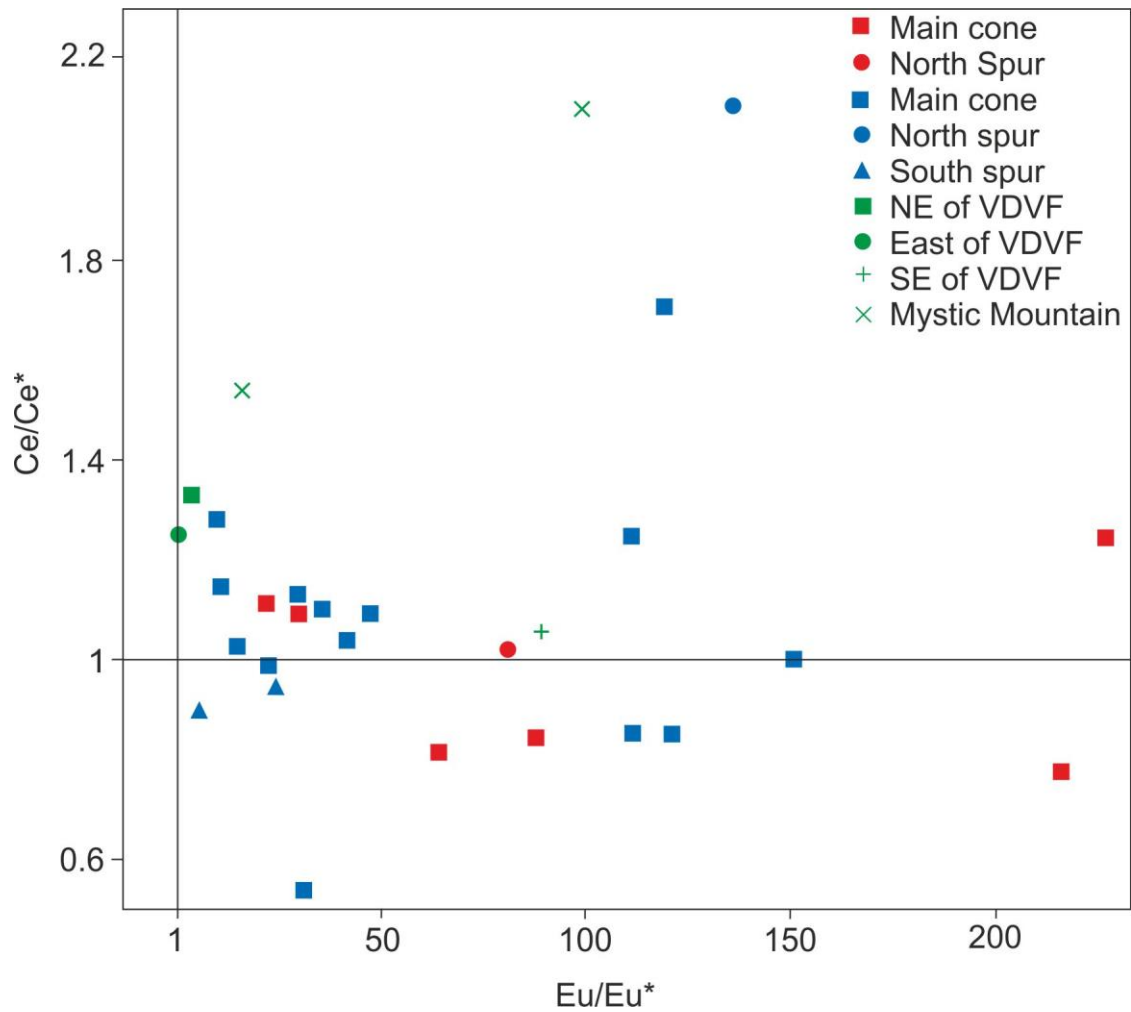


Figure 5.8: Eu/Eu^* and Ce/Ce^* anomalies of active and inactive hydrothermal precipitates. All samples show positive Eu/Eu^* anomalies of varying degrees, and varying Ce/Ce^* .

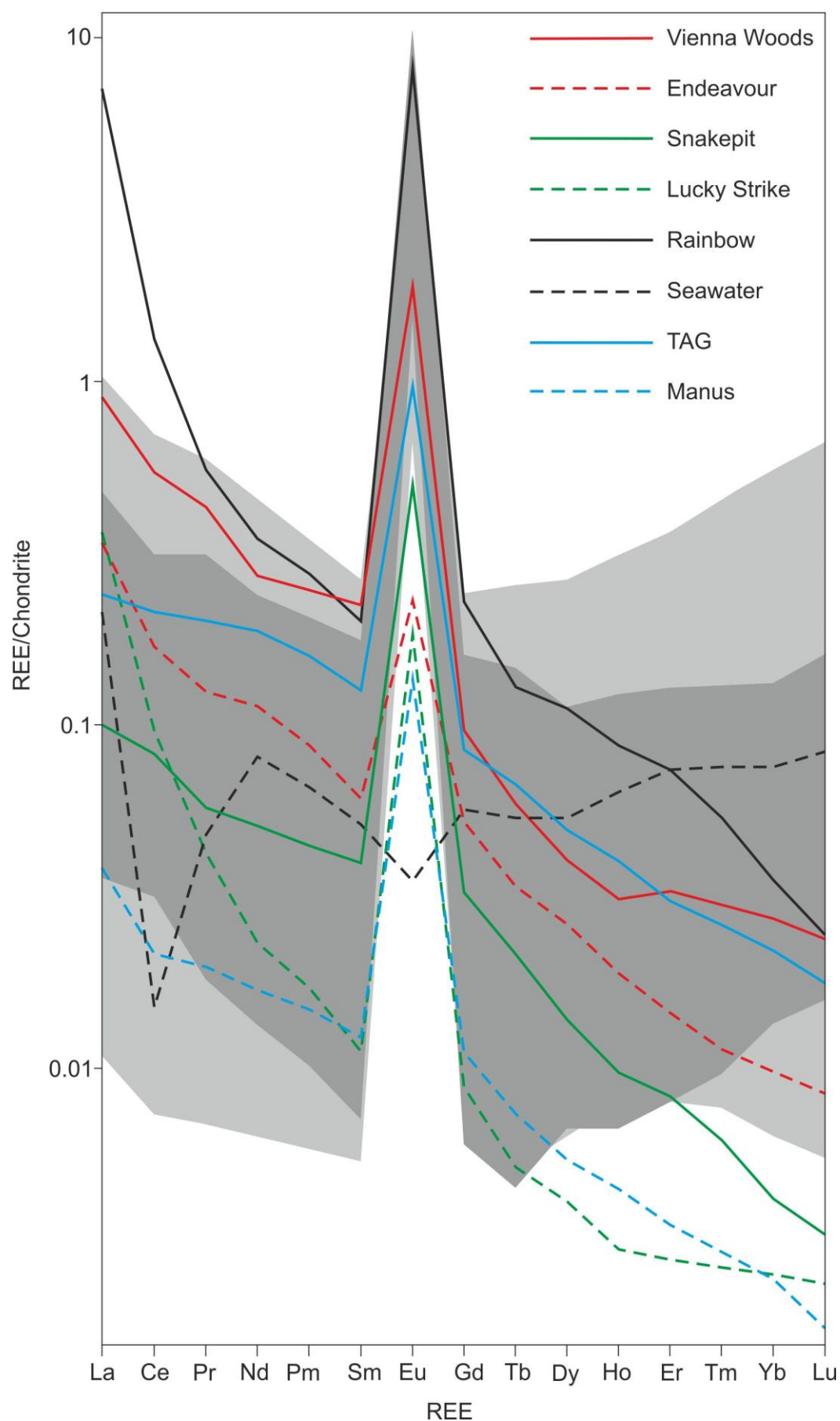


Figure 5.9: REE profiles of hydrothermal fluids from selected vent fields and seawater compared to the area for the chimneys and mounds from the VDVF.

5.3. Strontium isotopes

Strontium isotope ratios were determined for samples of hydrothermal fluid, talc separates and bulk host rocks.

5.3.1. Host rocks and dredged samples

Bulk rock $^{87}\text{Sr}/^{86}\text{Sr}$ ratios of for four host rocks sampled from the surrounding VDVF (three samples of gabbro and one dyke) range from 0.702902 to 0.703657 (Table 5.5 and Figure 5.10; please see Table 5.5 for the errors). Analyses of the glassy rims of unaltered basalt from the MCR ridge axis give values of 0.702824 and 0.703153, while two heavily altered samples recovered from the toe of Mt. Dent give values of 0.707544 (altered greenstone) and 0.709148 (serpentinite; Table 5.5 and Figure 5.10). This is a whole rock value for the serpentinite, and although no secondary carbonate was observed in thin section or by XRD, the presence of very minor concentrations may lead to an overall increase in the strontium isotope ratio of the sample.

The $^{87}\text{Sr}/^{86}\text{Sr}$ ratio of the host rocks and dredged material reflects the degree of seawater interaction. The two freshest gabbro show the lowest $^{87}\text{Sr}/^{86}\text{Sr}$ ratios whereas the serpentinitised peridotite from Mt. Dent that has very little primary mineralogy has a ratio of close to the seawater value of 0.70916 (Palmer and Edmond, 1989). The two samples of basalt glass were analysed for comparison to the host rocks at the VDVF, and they have ratios within the range for mid-ocean ridge basalt (Sun et al., 1979).

Sample	Type	Location	Concentration	Unit	$^{87}\text{Sr}/^{86}\text{Sr}$	Error (2 SE)	T (°C)
199-108	Chimney	MC	959	ppb	0.709032	0.000015	9.6
199-110	Chimney	MC	1046	ppb	0.709067	0.000015	8.0
202-43	Chimney	MC	6206	ppb	0.708824	0.000016	18.7
202-47	Chimney	MC	7628	ppb	0.708308	0.000017	41.2
200-24	Chimney	NS	3540	ppb	0.708375	0.000016	38.3
201-32	Mound	DF	7021	ppb	0.708714	0.000017	23.5
198-04	Mound	MC	3556	ppb	0.708937	0.000015	13.8
201-35	Mound	MC	891	ppb	0.708949	0.000014	13.2
201-36	Mound	MC	726	ppb	0.708770	0.000016	21.1
201-38	Mound	MC	1371	ppb	0.709083	0.000014	7.4
202-48	Mound	MC	770	ppb	0.706313	0.000014	128.0
201-26	Mound	MM	1599	ppb	0.709130	0.000013	5.3
201-27	Mound	MM	672	ppb	0.708550	0.000014	30.7
201-31	Mound	MM	1018	ppb	0.709066	0.000015	8.1
198-03	Mound	NS	720	ppb	0.708685	0.000014	24.8
200-23	Mound	SS	4895	ppb	0.707526	0.000015	75.3
199-11	Bulk gabbro	NWVDVF	184.1	ppm	0.702902	0.000015	-
199-14	Bulk gabbro	NWVDVF	130.5	ppm	0.703189	0.000015	-
199-18	Bulk dyke	NWVDVF	255.8	ppm	0.703657	0.000014	-
199-19	Bulk gabbro	NWVDVF	173.3	ppm	0.702997	0.000015	-
205-70	Basalt glass	AVR	190.5	ppm	0.703153	0.000014	-
207-86	Basalt glass	AVR	162.8	ppm	0.702824	0.000013	-
44-3A	Bulk serpentinite	TMD	11.8	ppm	0.709148	0.000017	-
D1-102	Bulk greenstone	TMD	237.6	ppm	0.707544	0.000015	-
FLU2	Fluid	MC	91.0	µmol/kg	0.706725	0.000014	-
FLU5	Fluid	MC	90.9	µmol/kg	0.706174	0.000012	-
FLU7	Fluid	MC	90.6	µmol/kg	0.705989	0.000015	-
FLU8	Fluid	MC	90.1	µmol/kg	0.705958	0.000016	-
FLU11	Fluid	NS	88.0	µmol/kg	0.705873	0.000014	-
FLU12	Fluid	NS	86.8	µmol/kg	0.707801	0.000017	-

Table 5.5: Strontium concentrations and $^{87}\text{Sr}/^{86}\text{Sr}$ isotope ratios in host rocks, fluids and hydrothermal precipitates. Precipitation temperatures listed are those calculated assuming linear mixing between vent fluid and seawater (Mills et al., 1998). Errors are internally calculated by obtaining up to 300 ratios for each sample. Abbreviations: AVR = axial volcanic ridge, DF = Debris Flow, MC = Main Cone, MM = Mystic Mountain, NS = North Spur, NVDVF = North of the Von Damm Vent Field, NWVDVF = North-west of the Von Damm Vent Field, SS = South Spur, TMD = Toe of Mt. Dent.

5.3.2. VDVF fluids

The $^{87}\text{Sr}/^{86}\text{Sr}$ ratio of the vent fluid ranges from 0.705873 to 0.707801 (Table 5.5 and Figure 5.10), indicating significant seawater entrainment, either during sampling, or prior to venting at the seafloor. These values lie between the ratios of the host rock and seawater, but when projected to zero magnesium, an end-member ratio of 0.702908 (Figure 5.10) is obtained. This is close to the ratio for the least altered host rocks and indicates the vent fluid Sr concentration and isotopic ratio is in equilibration with the host rocks in the sub-surface reaction zone.

Berndt et al., (1988) developed a method for estimating the water/rock ratio from the strontium isotope signatures and concentration of the unaltered host, the end-member fluid and seawater. This model allows for simultaneous dissolution and precipitation of strontium into and out of seawater and secondary alteration phases. The calculation (equations 9-11 in Berndt et al., 1988) gives a water/rock ratio of <1 for the end-member strontium concentrations and ratio, and for all Sr concentrations within the host rock. This water-rock ratio is in keeping with the intermediate pH of the vent fluids, which require reactions at low water-rock ratios at moderate temperatures.

The equations of Berndt et al., (1988) enable a step-by-step calculation of water-rock ratio. However water-rock ratios are also a function of the fluid mass flux propagating through the host lithologies, and the diffusion rate between the host rock and fluid (Bickle and Teagle, 1992). This means that chemical exchange between the host lithologies and hydrothermal fluid occurs at differing rates than changes to the isotopic signatures. The water-rock ratio is therefore dependent on the fluid's residence time in the crust, and the depth to the zone of chemical equilibrium between the fluid and the host rock. This is important for the reaction zone at the VDVF, as the concentrations and isotopic signatures of the basement material vary due to the differing elemental diffusion coefficients between ultramafics-fluid and gabbro-fluid. In order to calculate an accurate water-rock ratio, the proportions of gabbro and peridotite, and their strontium isotope signature and concentrations need to be better constrained.

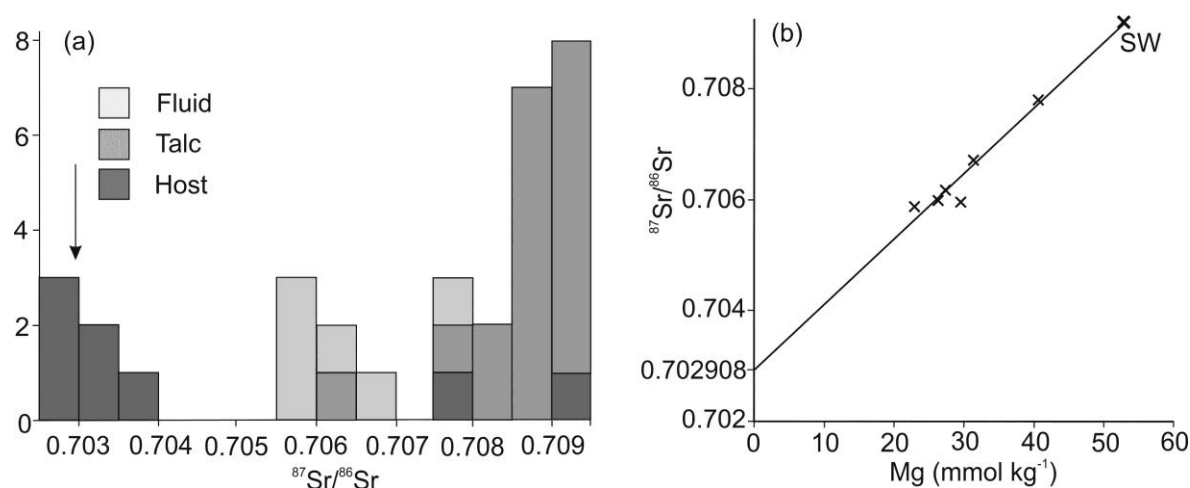


Figure 5.10: Distribution of $^{87}\text{Sr}/^{86}\text{Sr}$ and end-member fluid ratio (a) distribution of $^{87}\text{Sr}/^{86}\text{Sr}$ in samples from the VDVF; the position of the arrow indicates the ratio of the end-member fluid (b) samples of fluid $^{87}\text{Sr}/^{86}\text{Sr}$ plotted against Mg and projected to zero magnesium to give an end-member ratio.

5.3.3. Talc separates

The ratios of $^{87}\text{Sr}/^{86}\text{Sr}$ range between 0.708308 to 0.709067 for the chimney talc, and 0.706313 to 0.709130 for the mound talc, while all but two ratios are > 0.708 (Table 5.5 and Figure 5.10). This indicates a significant degree of seawater (0.70916) derived strontium occurring within the talc precipitates. Talc recovered from the hydrothermally inactive areas also has $^{87}\text{Sr}/^{86}\text{Sr}$ ratios that fall within the same range as samples recovered from the hydrothermally active site, suggesting similar mechanisms of precipitation from mixing between a hydrothermal fluid and seawater. A majority of the volume flux of fluid from the VDVF vents at the Main Hole with a temperature of 91°C . Given that the hottest temperature recorded at the VDVF is 226°C (McDermott, 2015), this lower venting temperature indicates significant mixing with seawater in the sub-surface prior to venting and talc precipitation. However, even this degree of sub-surface mixing is not enough to elevate the $^{87}\text{Sr}/^{86}\text{Sr}$ ratios to the values measured in the talc. This is because, assuming the temperature of the precipitated talc is defined by linear mixing between cold seawater and hot vent fluid (Equation 5.5; Mills et al., 1998), the strontium isotope ratios suggest nearly all of the samples precipitated at $<40^\circ\text{C}$. This is considered unlikely as a majority of the venting at the VDVF occurs at chimneys that have temperatures of $>90^\circ\text{C}$.

% end-member fluid = 100 *

$$\left[\frac{[^{87}\text{Sr}/^{86}\text{Sr}_{\text{SW}} * (\text{Sr})_{\text{SW}}] - [^{87}\text{Sr}/^{86}\text{Sr}_{\text{T}} * (\text{Sr})_{\text{SW}}]}{[^{87}\text{Sr}/^{86}\text{Sr}_{\text{SW}} * (\text{Sr})_{\text{SW}}] - [^{87}\text{Sr}/^{86}\text{Sr}_{\text{HT}} * (\text{Sr})_{\text{HT}}] + [^{87}\text{Sr}/^{86}\text{Sr}_{\text{T}} * [(\text{Sr})_{\text{HT}} - (\text{Sr})_{\text{SW}}]}} \right] \quad (5.5)$$

Where $^{87}\text{Sr}/^{86}\text{Sr}_x$ = strontium isotope ratio; $(\text{Sr})_x$ = strontium elemental concentration; HT=end-member fluid, SW=seawater, T=talc.

This discrepancy suggests a process occurring within the VDFV of elevating the $^{87}\text{Sr}/^{86}\text{Sr}$ ratio of the talc to a more seawater dominated strontium isotope signature. A likely scenario is that seawater percolating into the VDFV mound and surrounding basement is conductively heated, and the slight addition of dissolved silica from the hydrothermal fluid means talc becomes a stable phase and precipitates with seawater derived magnesium. This would allow the precipitation of talc within the mound with $^{87}\text{Sr}/^{86}\text{Sr}$ ratios close to that of seawater. Alternatively, there is a possibility that the ascending hydrothermal fluids interact with previously precipitated anhydrite in the sub-surface below the VDFV following mixing with seawater sulphate. Seawater dominated $^{87}\text{Sr}/^{86}\text{Sr}$ signatures in hydrothermal precipitates are observed in hydrothermal mounds up to 120 metres below the seafloor in other hydrothermal systems (Teagle et al., 1998). The interaction of hydrothermal fluid with seawater signatures of previous hydrothermally precipitated minerals has the potential to locally increase the $^{87}\text{Sr}/^{86}\text{Sr}$ ratio, but it is unlikely to cause a sufficient increase over the scale of the whole vent field.

5.4. Stable isotopes

In order to accurately derive temperatures and fluid isotope ratios, stable oxygen and hydrogen isotope analyses were conducted on pure talc and quartz separates from hydrothermal precipitates at the VDFV; reported here in per mil units (‰) relative to relative standard mean ocean water (SMOW; Equation 5.7). For a detailed method on how these were derived, please see the appendices.

$$\delta^{18}\text{O}(\text{‰}) = \left(\frac{(^{18}\text{O}/^{16}\text{O})_{\text{sample}} - (^{18}\text{O}/^{16}\text{O})_{\text{SMOW}}}{(^{18}\text{O}/^{16}\text{O})_{\text{SMOW}}} \right) \times 1000 \quad (5.7)$$

Hydrogen isotopes are reported using the same notation as the $\delta^{18}\text{O}$ values in relation to SMOW (Equation 5.8).

$$\delta D(\text{‰}) = \left(\frac{(D/H)_{\text{sample}} - (D/H)_{\text{SMOW}}}{(D/H)_{\text{SMOW}}} \right) \times 1000 \quad (5.8)$$

5.4.1. $\delta^{18}\text{O}$ results

$\delta^{18}\text{O}$ of the talc separates from all locations ranges from 3.2‰ to 11.7‰. The active vent structures has $\delta^{18}\text{O}_{\text{talc}}$ values ranging between 5.5‰ to 9.5‰, the VDVF mounds have values ranging between 5.9‰ to 11.7‰, and the inactive sites, including Mystic Mountain, have values of 3.2‰ to 9.5‰ (Table 5.6). Four results were obtained from quartz and the values obtained for $\delta^{18}\text{O}_{\text{quartz}}$ are 10.6‰ for the active chimney, 12.3‰ and 16.0‰ for the VDVF mounds and 7.7‰ for Mystic Mountain (Table 5.6).

Sample	Type	Location	$\delta^{18}\text{O}_{\text{talc}}$	$\delta^{18}\text{O}_{\text{quartz}}$	δD	T_{talc}	T_{quartz}
198-04	AM	MC	10.4	-	-43.1	131	-
199-08	AM	MC	-	16.0	-	-	144
199-09	AM	MC	9.8	-	-49.2	138	-
201-35	AM	MC	5.9	-	-26.7	202	-
201-38	AM	MC	7.9	-	-	165	-
201-40	AM	MC	8.6	-	-46.1	155	-
202-48	AM	MC	7.6	-	-51.8	170	-
44-2G	AM	MC	9.4	-	-67.0	143	-
44-2O	AM	MC	9.1	-	-58.7	148	-
198-02	AM	NS	7.4	12.3	-77.0	173	189
198-03	AM	NS	7.3	-	-	175	-
199-20	AM	NS	11.7	-	-	116	-
198-05	AM	SS	7.9	-	-49.6	165	-
199-107	C	MC	7.2	10.6	-37.6	177	-
199-108	C	MC	5.5	-	-	211	217
44-1A	C	MC	9.5	-	-64.6	142	-
44-1E	C	MC	9.1	-	-64.2	148	-
201-32	IM	DF	3.2	-	-	277	-
201-29	IM	MM	7.5	-	-	172	-
201-30	IM	MM	5.0	7.7	-76.3	223	280
201-33	IM	SEVDVF	9.5	-	-50.1	142	-
201-31	IM	SMM	5.3	-	-58.2	215	-

Table 5.6: $\delta^{18}\text{O}$ and δD of talc and $\delta^{18}\text{O}$ of quartz separates from the VDVF and surrounding inactive mounds. Calculated temperatures displayed for talc and quartz are made using fractionation factors from (Zheng, 1993b; Zheng, 1993a). Abbreviations: AM = active mound, C = chimney, DF = debris flow, IM = inactive mound, MC = Main Cone, MM = Mystic Mountain NS = North Spur, SEVDVF = south east of the Von Damm Vent Field, SMM = south of Mystic Mountain

5.4.2. Fractionation equations for talc and quartz

In order to accurately derive temperatures and fluid ratios from stable isotope studies, appropriate fractionation equations are required. Two models calculated the talc-water fractionation system based on theoretical methods using the bond strengths in hydroxyl-bearing silicates (Savin and Lee, 1988; Zheng, 1993b). The temperatures calculated in the range of $\delta^{18}\text{O}_{\text{talc}}$ using these two models vary by a maximum of 8°C as the fractionation factors vary by $\sim 0.3\text{‰}$ at the maximum venting temperatures of the VDFV (Figure 5.11; Savin and Lee, 1988; Zheng, 1993b). The only experimental study conducted to analyse the validity of these models was conducted by (Saccocia et al., 2009) using the partial exchange technique. According to (Saccocia et al., 2009), their experimentally-derived fractionation factors compare well to the empirical models at temperatures of 350°C but can vary by as much as 2‰ at 250°C (Figure 5.11). Considering the temperatures at the VDFV are $<215^\circ\text{C}$, this discrepancy is likely to be even greater. Also, unfortunately the range of temperatures in the experiment by Saccocia et al., (2009) is 250°C to 450°C , which is hotter than the highest temperature measured at the VDFV, and the experiment is also conducted at double the pressure conditions. The theoretically modelled fractionation factors of (Zheng, 1993b) lie within the measured temperature ranges, and are used for calculations using the $\delta^{18}\text{O}$ values of talc (Equation 5.9).

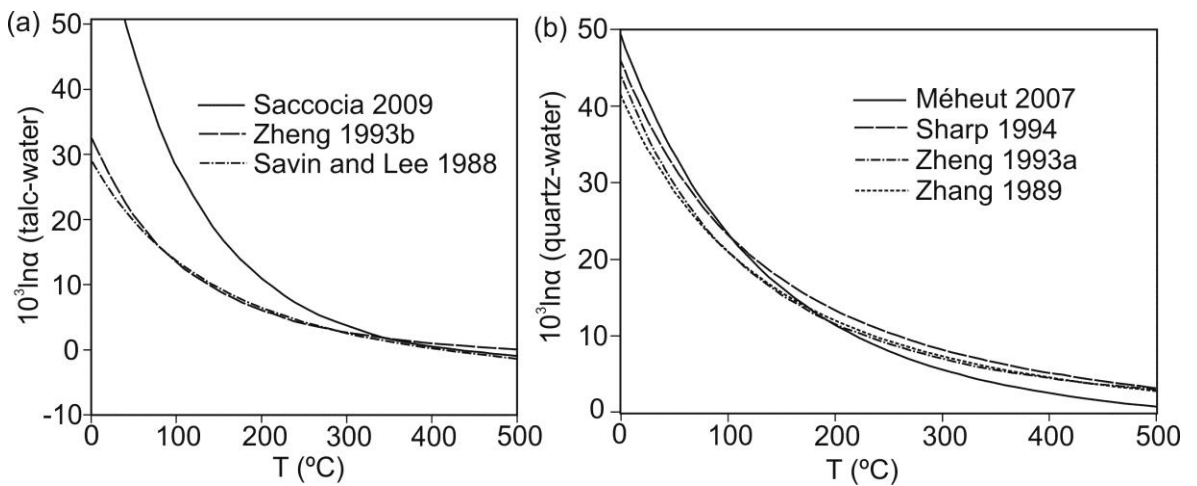


Figure 5.11: Stable isotope fractionation factors (a) talc and (b) quartz derived using both experimental and theoretical methods (Savin and Lee, 1988; Zhang et al., 1989; Zheng, 1993b; Zheng, 1993a; Sharp and Kirschner, 1994; Méheut et al., 2007; Saccocia et al., 2009).

$$1000\ln\alpha = 4.20 \left(\frac{10^6}{T^2} \right) - 7.04 \left(\frac{10^3}{T} \right) + 2.14 \quad (5.9)$$

ΔD fractionation factors between talc and water have been experimentally derived only by Saccocia et al., (2009), and there are no empirical or theoretical models based on the bond strengths. However, while the $\Delta^{18}\text{O}_{\text{talc-water}}$ varies considerably (-0.4‰ to 6.5‰) throughout the temperature range of the experiment by Saccocia et al., (2009), the $\Delta D_{\text{talc-water}}$ varies only by 3‰. This means that the error associated with extrapolating to the temperatures of the VDVF are reduced, thus the fractionation factors of (Saccocia et al., 2009) are used (Equation 5.10).

$$1000\ln\alpha = 11.70 \left(\frac{10^6}{T^2} \right) - 25.49 \left(\frac{10^3}{T} \right) + 12.48 \quad (5.10)$$

There are different methods published to derive isotopic fractionation in the quartz-water system including theoretical methods e.g. (Zheng, 1993a; Sharp and Kirschner, 1994; Méheut et al., 2007), and experimental methods e.g. (Zhang et al., 1989; Hu and Clayton, 2003). The examples calculated for the temperature range of the VDVF indicate ranges for $\Delta^{18}\text{O}_{\text{quartz-water}}$ varying by <2‰ (Figure 5.11). $\delta^{18}\text{O}$ fractionation calculations using the quartz-water system were conducted using the fractionation factors of (Equation 5.11; Zheng, 1993a), as these are in the temperature range of the VDVF, and similarly derived relationships were used for the talc-water calculations.

$$1000\ln\alpha = 4.48 \left(\frac{10^6}{T^2} \right) - 4.77 \left(\frac{10^3}{T} \right) + 1.71 \quad (5.11)$$

5.4.3. Temperatures of formation

Assuming $\delta^{18}\text{O}_{\text{fluid}}$ is 0‰, and using the fractionation factors of Zheng, (1993a) and Zheng, (1993b), the corresponding equilibrium fractionation temperatures for talc from the VDVF range between 116°C to 211°C, and the inactive talc ranges between 142°C to 277°C (Table 5.6). The three samples of quartz from the active site give a temperature range of 144°C to 217°C, and the sample from the inactive site has an equilibrium temperature of 280°C (Table 5.6).

The precipitation temperatures calculated at the active site are within the range of those measured at the seafloor during sampling. However, the temperatures calculated using talc geothermometry at the active chimney structures do not correlate well with measured temperatures from *JC082*. The samples from the Spire give calculated temperatures of 142°C and 148°C, compared to a measured temperature of 215°C, and talc sampled from the Main Hole has calculated temperatures of 177°C and 211°C, compared to a measured temperature of 91°C. The disparities between calculated and measured temperatures may simply be due to the dynamic mixing regime within the structure at the top of the main cone, as both the Spire and the Main Hole are thought to originate from the same fluid conduit at the centre of the main cone. Alternatively, it is possible that the stable isotope signature of the hydrothermal fluid is not equal to 0‰, although measurements from other hydrothermal systems typically show small ranges in $\delta^{18}\text{O}$, and have values of 0‰ to 2.5‰ (Shanks et al., 1995; Shanks, 2001). Applying these variations to the VDVF gives a maximum equilibrium temperature of 267°C.

The $^{87}\text{Sr}/^{86}\text{Sr}$ isotope ratios suggested precipitation temperatures of much lower than those observed from in situ probe measurements. This could suggest potential conductive heating of seawater, which is further supported by stable isotope equilibrium temperatures being closer to the venting temperatures.

The temperatures calculated at the inactive sites of talc precipitation are generally higher than at the VDVF. Assuming the $\delta^{18}\text{O}_{\text{fluid}}$ is 0‰, five measurements yielded a range of 142°C to 277°C, with three giving values of 215°C or more (Table 5.6). Extending the range of $\delta^{18}\text{O}_{\text{fluid}}$ to measured ratios from other hydrothermal vent fields gives a maximum temperature of 422°C (Zheng, 1993b; Shanks, 2001). This estimated temperature is unrealistic for a silicate dominated deposit on the seafloor, as venting temperatures this high would usually result in base metal mobilisation and the formation of massive sulphide deposits (Von Damm, 1995). It is also >200°C more than measured temperatures at the active site, although the VDVF could be in a waning stage. Given these constraints, the $\delta^{18}\text{O}$ of the fluid that precipitated the talc is considered to be closer to 0‰. This can be further explored using mineral pairs assuming isotopic equilibrium was reached.

5.4.4. Talc-quartz mineral pairs and calculation of fluid ratios

Using the combined $\delta^{18}\text{O}$ of co-existing talc and quartz mineral pairs, it is possible to estimate a temperature and oxygen isotope ratio for the fluid. $\delta^{18}\text{O}$ ratios for two out of the three quartz and talc pairs indicate equilibration with a hydrothermal fluid at 236°C and 252°C, with $\delta^{18}\text{O}_{\text{fluid}}$ of 1.0‰ and 3.4‰ (Figure 5.12). The third talc-quartz pair was found to be out of isotopic equilibrium and could not be used for this purpose. While these temperatures are slightly higher than those measured at the VDFV, they may indicate that the VDFV is in a cooler or waning phase.

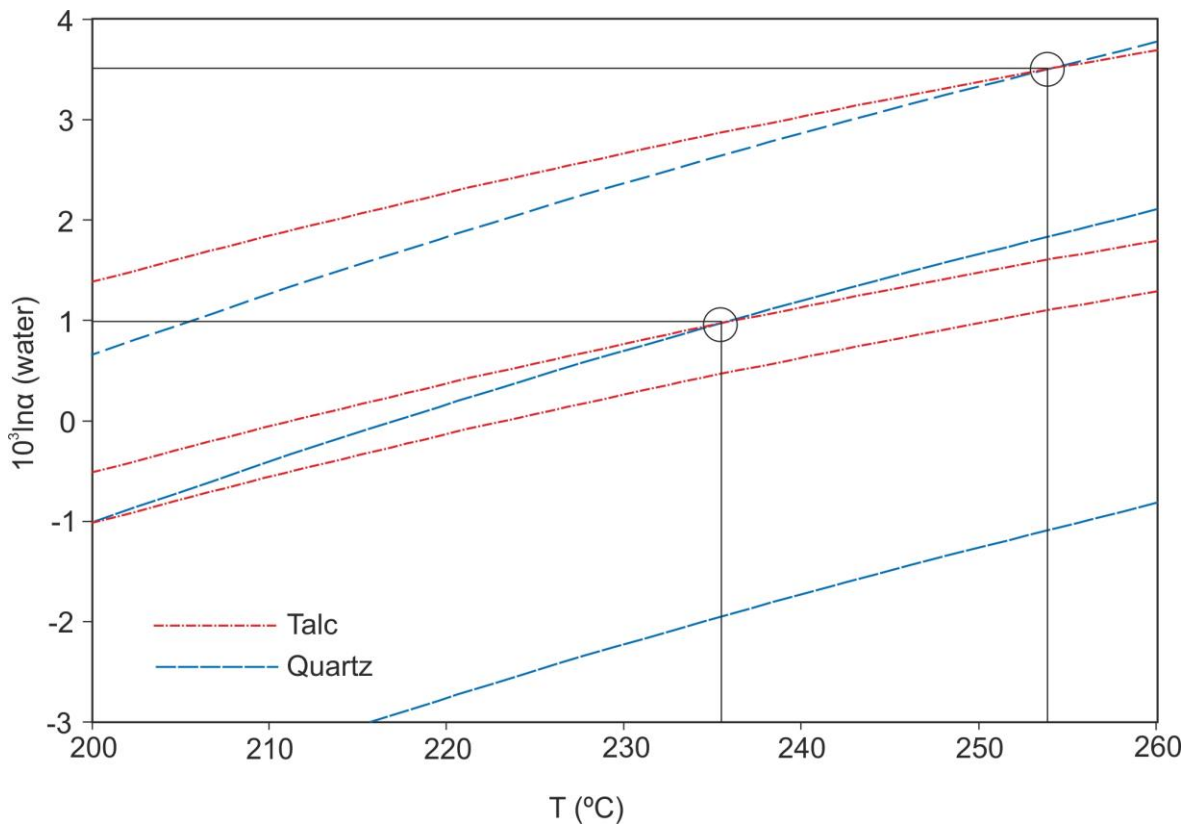


Figure 5.12: $\delta^{18}\text{O}_{\text{fluid}}$ of co-existing talc and quartz mineral pairs from three different samples calculated using the fractionation factors of Zheng, (1993a); Zheng, (1993b).

Using the temperatures calculated above, measurements of $\delta^{18}\text{O}_{\text{talc}}$ on the chimneys at the top of the main cone on the VDFV indicate a possible $\delta^{18}\text{O}_{\text{fluid}}$ composition ranging from 1‰ to 5.5‰ (Figure 5.13). These samples were used because they are collected from the hottest fluid conduit on the VDFV, and are the best estimate for an end-member fluid. The calculated $\delta^{18}\text{O}_{\text{fluid}}$ when using the maximum temperature measured at the VDFV ranges from -0.2‰ to 4.2‰ (Figure 5.13).

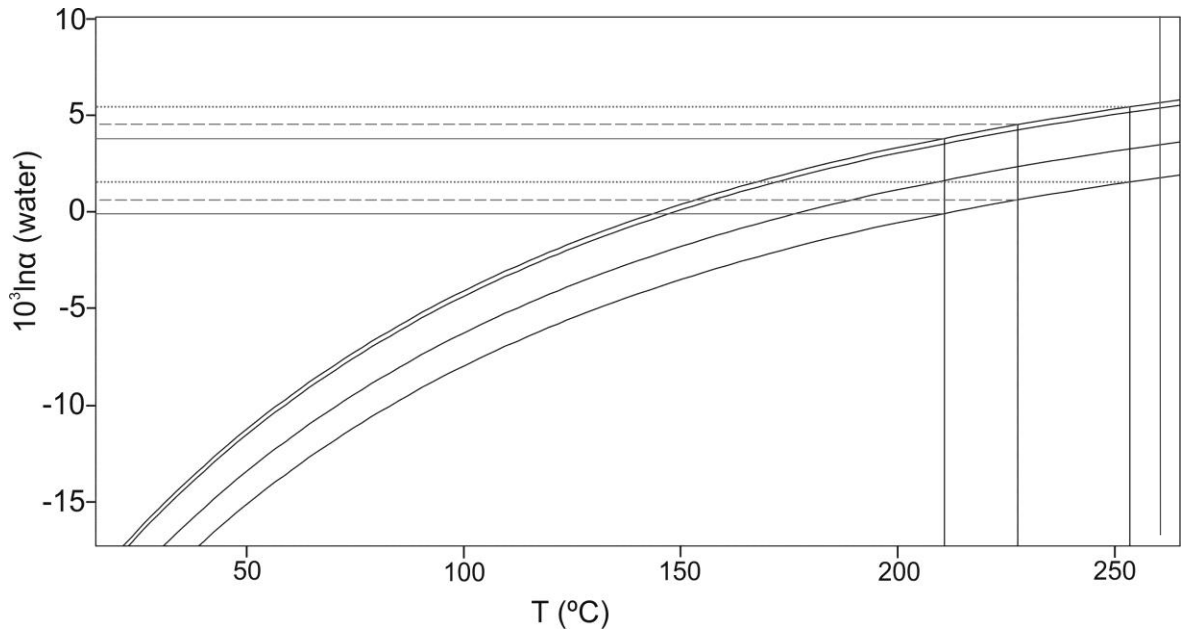


Figure 5.13: $\delta^{18}\text{O}_{\text{fluid}}$ versus temperature of 4 pure talc separates from the chimneys at the top of the main cone (Zheng, 1993b). The curves refer to the composition of a fluid in equilibrium with each sample. The temperatures used to calculate the fluid composition (215°C, 236°C, 252°C) refer to the hottest in situ temperature measured at the VDVF, and the two temperatures derived from talc-quartz mineral pairs.

Some of the end-member values calculated for $\delta^{18}\text{O}_{\text{fluid}}$ from the talc are within the range of those measured from other hydrothermal fluids (Shanks et al., 1995), potentially indicating equilibrium between the fluid and the precipitate is reached in some samples. Furthermore, the stable isotope signatures in all of the talc samples indicate a temperature up to 150°C greater than that assumed from $^{87}\text{Sr}/^{86}\text{Sr}$ ratios, suggesting a majority of talc precipitation at the VDVF occurs internally within the mound and involves conductive heating seawater. This is also indicated by the majority of the chimneys at the VDVF having measured venting temperatures of <140°C, which is well below the maximum recorded, and with only 3 of the $\delta^{18}\text{O}_{\text{talc}}$ signatures indicate calculated precipitation temperatures of <140°C.

5.4.5. Hydrogen isotopes

Hydrogen isotope analysis was conducted on pure talc separates as they can provide information concerning magmatic input into the hydrothermal system, the process of serpentinisation and the physical conditions of water-rock interactions. For details on the analysis and sample processing, please see the methods section and appendices.

Hydrogen isotopes, expressed as δD , for talc samples from the active VDVF chimneys ranges between -64.6‰ to -37.6‰ (Table 5.6). The hydrothermally active mounds show the full range of δD across the whole VDVF, with values ranging from -77.0‰ to -26.7‰, whilst the inactive sites have δD of -76.3‰ to -50.1‰ (Table 5.6). δD ratios from other talc samples on the seafloor are rare, but where reported the ratios of the VDVF talc are close to those observed in oceanic and ophiolite serpentinites (Figure 5.14).

Using the fractionation factors of (Saccocia et al., 2009) at the temperatures predicted by the talc-quartz mineral pairs, the fluids at the VDVF are strongly depleted in deuterium, and show a range of -43.0‰ to 7.3‰. This is a large range of >50‰ in δD , compared with other hydrothermal vent fields (e.g. PACMANUS, TAG), where stable isotope signatures at individual sites usually show variations of <5‰ (Shanks, 2001; Reeves et al., 2011; Yamanaka et al., 2013). Serpentinisation does have the potential to lower the δD of the fluid (Dubinina et al., 2007), but not to the extent predicted by δD_{talc} from the VDVF.

The low water/rock reaction indicated by the strontium isotope signature of the VDVF could indicate considerable equilibration with serpentine that has a δD value of <-40‰. However this is considered unlikely as the fluid chemistry suggests that there is a significant influence from mafic lithologies in the sub-surface, which have δD ratios approaching -80‰ e.g. (Agrinier et al., 1995; McCaig et al., 2010). None of the calculated ratios lie within established range of hydrothermal vent fluids (Von Damm 1995). However, while this may indicate unique conditions of formation for the VDVF, the large range of δD ratios indicate that it is likely that a majority of δD ratios obtained from the VDVF talc are at isotopic disequilibrium with the VDVF end-member fluid (Shanks et al., 1995; Shanks, 2001).

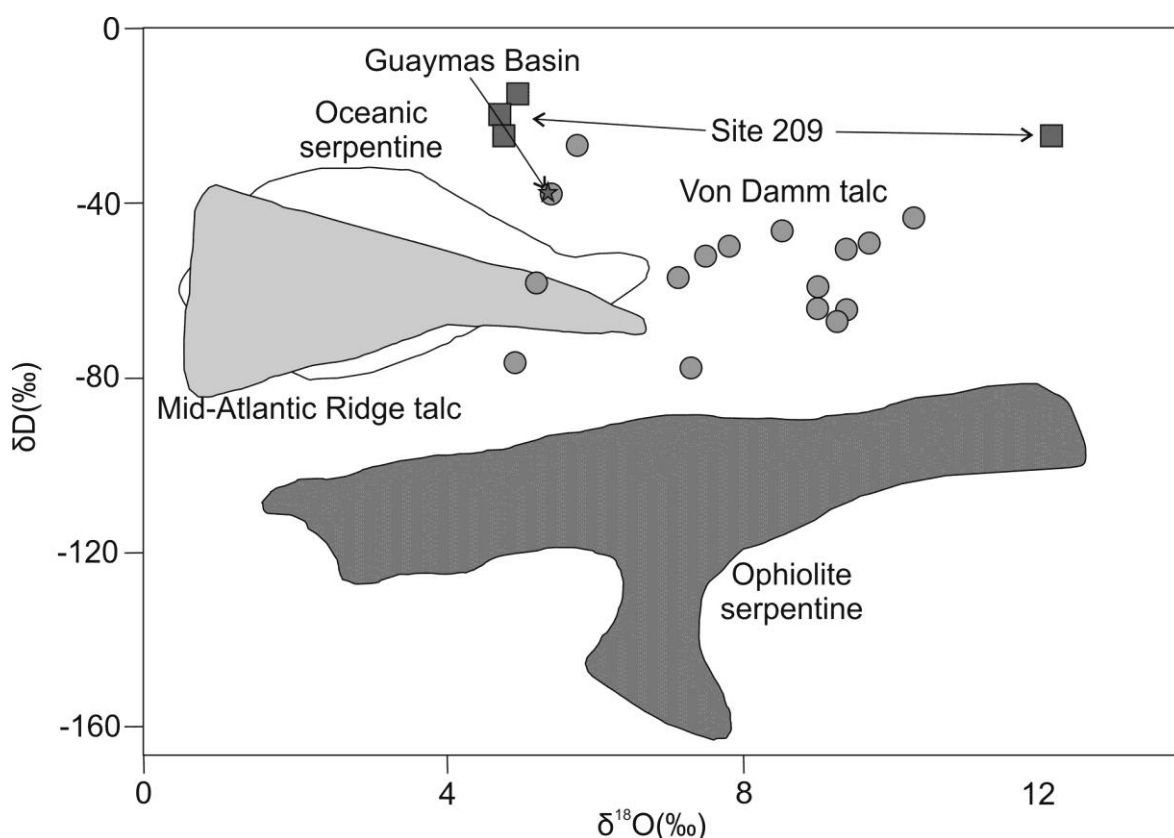


Figure 5.14: δD and $\delta^{18}O$ of talc and serpentine in oceanic environments; samples from the VDF are displayed as grey circles (Wenner and Taylor, 1973; Wenner and Taylor Jr, 1974; Lonsdale et al., 1980; Agrinier et al., 1988; Sakai et al., 1990; Agrinier et al., 1995; Barnes et al., 2009; McCaig et al., 2010).

5.5. Thermodynamic modelling

Thermodynamic modelling results are derived using GWB at the pressure and temperature conditions at the VDF, and the models described below aim to explain the dominance of silicate precipitation at the VDF. It should be noted before the results are presented that there are a few limitations associated with the thermodynamic models. The mineral saturation indices presented do not take into account the kinetics of mineral precipitation, and the indices are calculated at equilibrium conditions. It also requires the input of geochemical data derived from analytical methods that have errors associated with these results.

Mixing models do not account for the differences between the advective rate of heat transfer from the hydrothermal fluid to the ocean, and the rate of diffusion between the hydrothermal fluid and mineral during precipitation. The progress of the reaction in the mixing models is indicated as a linear relationship between the temperatures of the end-member fluid and seawater. However, as thermal and chemical exchanges do

not necessarily occur at the same rate, mineral saturation values may not be in equilibrium at stages in the reaction. There is not a single diffusion constant that can be applied to the mixing models, as there are multiple dissolved species within the fluid and different mineral phases precipitating. Therefore, a mineral saturation index at a given time in the reaction makes the assumption that equilibrium has been reached in terms of both temperature and chemical exchange.

As discussed in the fluid chemistry section, the end-member dissolved silica measured in samples collected during *JC082* is not as well constrained as the value obtained by McDermott, (2015), so their value of 7.5 mmol kg⁻¹ is used in thermodynamic calculations.

5.5.1. Simple mixing models

The end-member temperature at the VDVF is not well constrained by *in situ* thermistor probe measurements or the vent fluid data. Therefore, in developing simple mixing models between hydrothermal fluid and ambient seawater, three different starting temperatures are used: 215°C, 240°C, and 270°C. 215°C is the highest value measured on cruise *JC082*, 240°C, is close to the temperature measured previously (Seewald et al., 2012; McDermott, 2015), and 270°C is close to the highest temperature calculated from oxygen isotope thermometry. Mineral saturation indices were derived by using the thermodynamic database at the pressure and temperature conditions of the VDVF. The results were derived by inputting the chemical compositions of the end-member vent fluid, and mixing with seawater at 4°C over a period of 10 stages.

Thermodynamic models of mixing 215°C end-member fluid with seawater at 4°C indicates that talc is instantaneously stable on mixing with seawater (Figure 5.15). This trend is also seen in the models involving 240°C and 270°C starting temperatures, and in all three models talc remains stable until 25°C. Quartz remains saturated throughout the mixing regimes at all starting temperatures, however brucite never reaches stability in any of the three models. Anhydrite never becomes saturated in the mixing regime at a starting temperature of 215°C, despite being very close to the saturation threshold (Figure 5.15). However at starting temperatures of

240°C and 270°C, anhydrite just crosses the saturation threshold at temperatures above 140°C, after mixing with ~10% seawater (Figure 5.15).

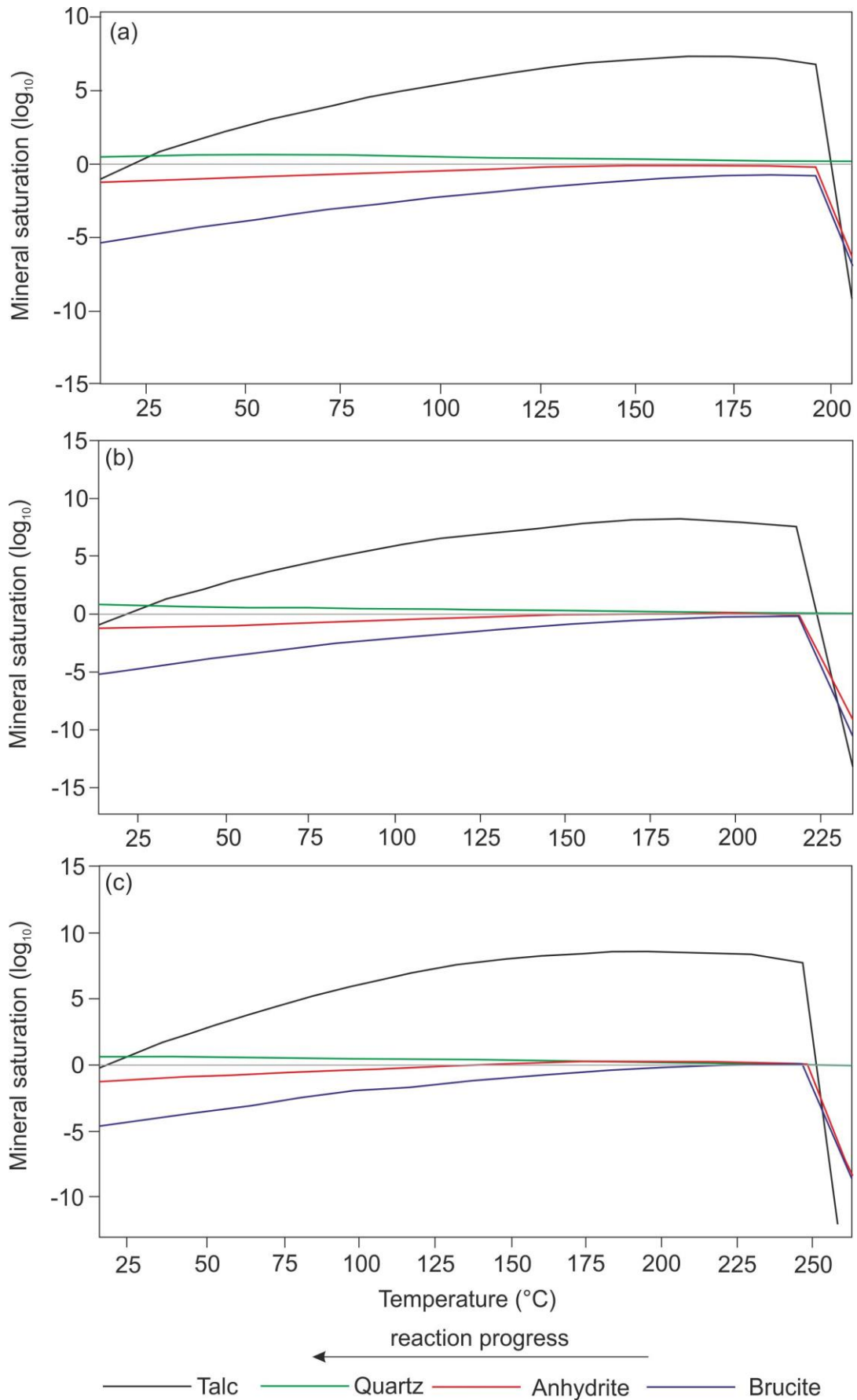


Figure 5.15: (On previous page). Saturation indices for talc, quartz, anhydrite and brucite on mixing with ambient seawater at 4°C. Starting temperatures for the end-member fluid are (a) 215°C (b) 240°C (c) 270°C.

5.5.2. Chimneys on the main cone

Although simple mixing models predict the precipitation of talc on instantaneous mixing with seawater, the chimneys at the VDVF vent fluids at least 70°C cooler than those emanating from the Spire. Mg concentrations of the fluids suggest that temperature differences are a result of seawater entrainment and heating of cooler seawater. Two models were run at the temperatures of the main hole (90°C) and another chimney on the main cone (140°C; Figure 5.16). The compositions of the venting fluids were derived from mixing the 215°C end-member with seawater to cool the fluid down to the observed vent temperatures. The resulting vent fluid compositions were then mixed with seawater. The temperatures of venting are below the temperature of precipitation for anhydrite, and brucite is also undersaturated (Figure 5.16). The addition of magnesium in the sub-surface from seawater means that talc is immediately saturated in the fluid along with quartz, and both phases remain stable throughout the mixing regime (Figure 5.16).

The mineral stability boundaries were calculated in the H_2O -MgO- SiO_2 system as a function of the temperatures measured at different vents, pH of the system, and Mg and SiO_2 activities (Figure 5.17). This approach illustrates the chemical conditions of the fluid as it mixes with end-member seawater, and to indicate the minerals present under equilibrium conditions.

The activity diagram indicates that the mixing line between hydrothermal fluid and seawater plots within the fields of talc and quartz stability, but outside of the field for brucite (Figure 5.17). This is consistent with the saturation indices of the minerals in the mixing models, and with petrographic observations from the minerals precipitated at the VDVF.

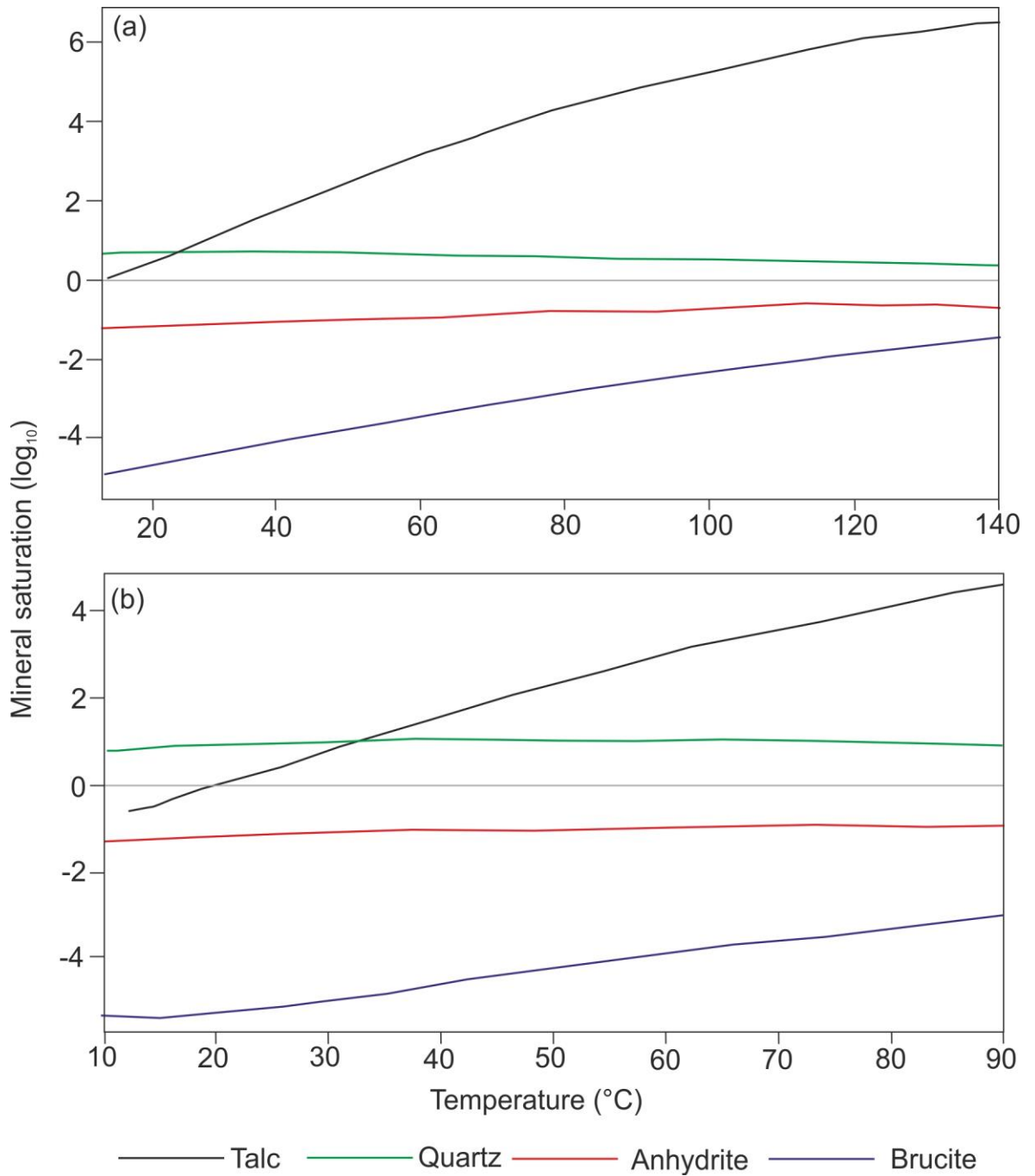


Figure 5.16: Mineral saturation indices in mixed fluids in chimneys from the main cone
(a) 140°C (b) 90°C

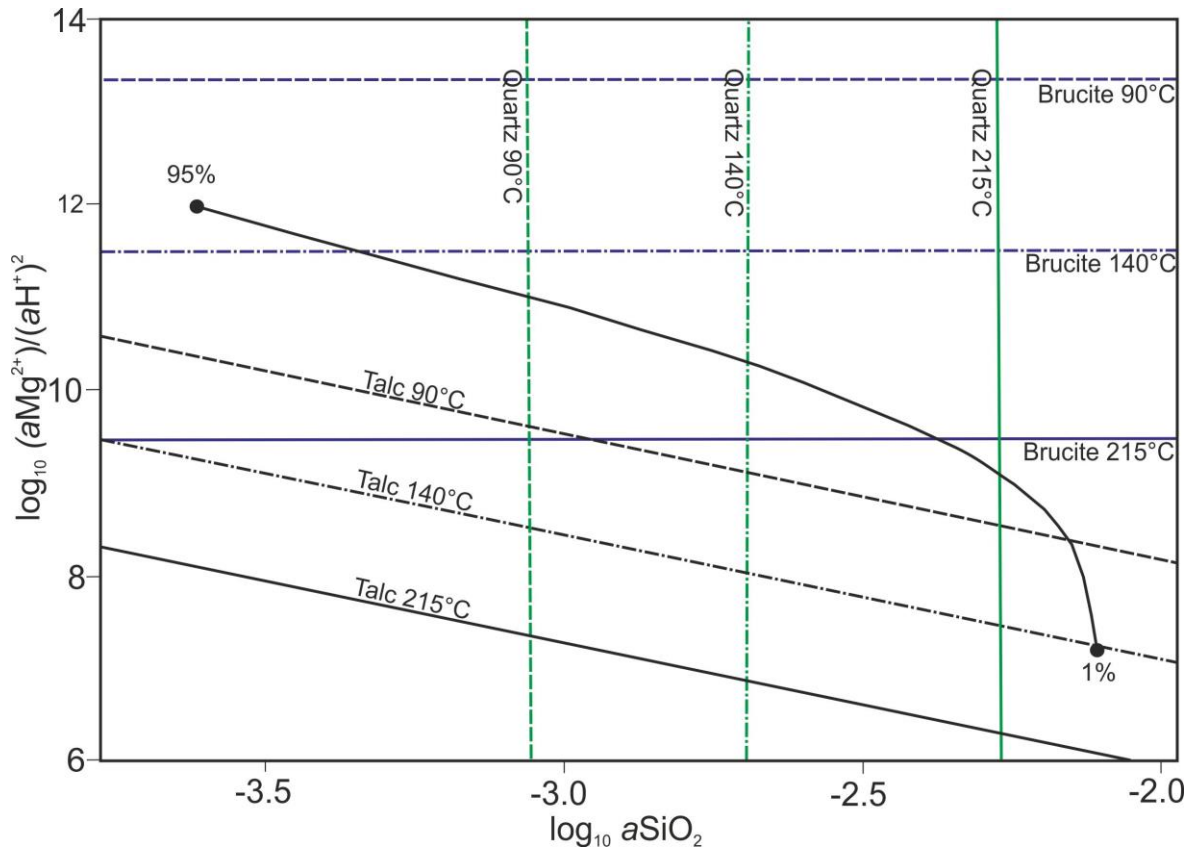


Figure 5.17: Stability boundaries of talc, quartz and brucite at varying temperatures in the $\text{H}_2\text{O-MgO-SiO}_2$ -system. Percentages indicate the proportion of seawater, and the progression along the reaction.

5.5.3. Conductive cooling

Strontium and stable isotope data indicates that some talc precipitation at the mounds of the VDFV occurs as a result of mixing between silica-rich hydrothermal fluid and conductively heated seawater. This is tested by mixing the chemical species of seawater that have been equilibrated at 100°C and 150°C with the end-member hydrothermal fluids at the temperatures of the simple mixing models.

All of the models show talc having the highest saturation indices (Figure 5.18). Brucite remains undersaturated, except when 270°C fluid is mixed with seawater that has been conductively heated to 150°C. Quartz remains saturated throughout the mixing regimes, while anhydrite just becomes saturated above 140°C (Figure 5.18).

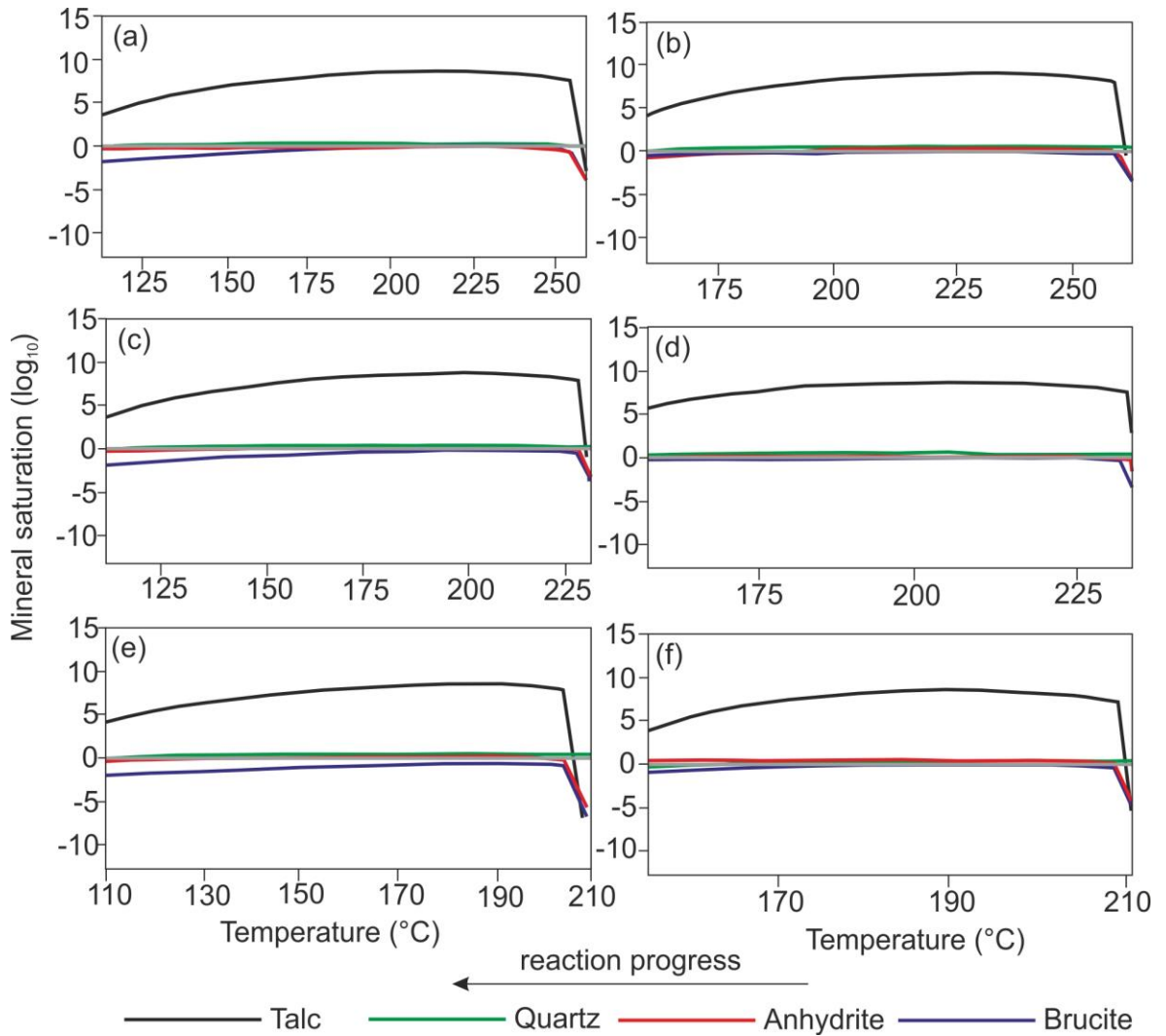


Figure 5.18: Conductive cooling mixing regimes for seawater heated up to 150°C and 100°C. Starting temperatures are (a) and (b) 270°C (c) and (d) 240°C and (e) and (f) 215°C.

5.5.4. pH at the VDVF

The moderate pH of 5.9 at the VDVF, which originates from the fluid interaction with the basement, plays an important role in talc stability at the VDVF. To test the saturation of talc on mixing hydrothermal fluid with seawater, models were calculated with pH ranging from 3 to 7. The results indicate that talc is stable at pH values of 5 to 7, but when pH is lowered to the values commonly associated with black smoker fluids (≤ 4), talc becomes undersaturated in the mixing regime and is therefore not precipitated (Figure 5.19).

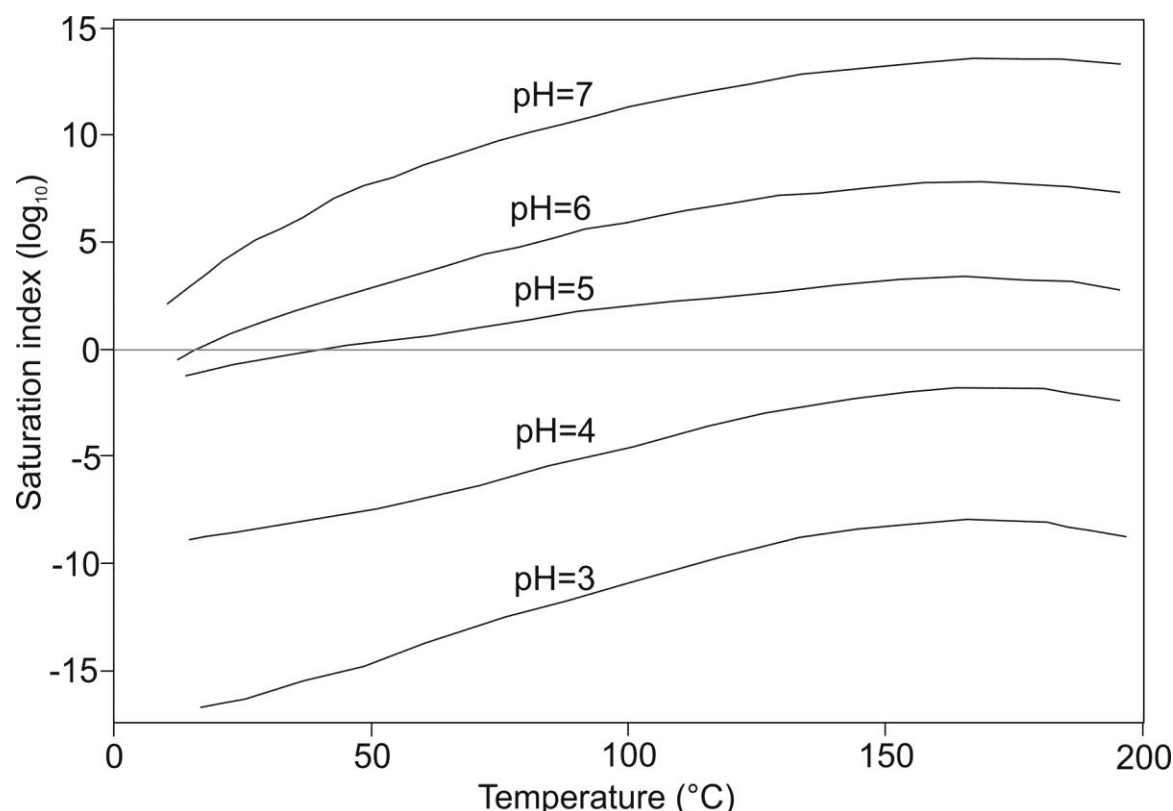


Figure 5.19: Talc saturation on mixing VDVF fluids with seawater ($pH=7.8$) at pH values ranging from 3 to 7.

5.6. Summary of talc precipitation processes at the VDVF

The hydrothermal fluid at the VDVF contains dissolved silica and calcium concentrations similar to those at black smoker vent fields, but contains very low concentrations of base metals and H_2S . This is mainly due to the moderate end-member pH of 5.9, and temperatures of venting of $\leq 215^\circ C$, which discourage the mobility of base metals. The pH of the vent fluids is derived from $<300^\circ C$ interaction with a mafic or mixed mafic and ultramafic basement at low water/rock ratios, as indicated by strontium isotope ratios for the hydrothermal fluid and host rocks. Stable isotope fractionation temperatures are generally within the ranges of in situ temperature probe measurements: talc-quartz pairs give temperature values of $236^\circ C$ and $252^\circ C$ and $\delta^{18}O_{fluid}$ of 1.0 and 3.4. Likewise, δD_{talc} is similar to the measurements on samples recovered from other core complexes in shear zones, and similar to $\delta D_{serpentine}$ on oceanic massifs and core complexes indicating a role for peridotite serpentinisation at VDVF.

All mixing models, including both ambient and conductively heated seawater, indicate that talc and quartz remain stable throughout the mixing regimes. Brucite rarely reaches saturation, and anhydrite just reaches saturation at temperatures above 140°C in some models requiring conductive heating of seawater. These results are in keeping with observations of recovered samples, that the VDVF hydrothermally precipitated material generally consist of >90% silicate, while sulphates are either accessory phases or absent altogether.

Chapter Six – Importance of the Von Damm Vent Field

Petrographic studies, geochemical analyses and thermodynamic modelling, indicate that the mounds of talc that form the Von Damm Vent Field (VDVF) result from primary precipitation after mixing a silica-rich hydrothermal fluid with seawater. This chapter highlights the unique nature and tectonic setting of the hydrothermal field, and compares it to previous discoveries of Mg-phyllosilicates on the seafloor, including extinct hydrothermal deposits with a similar tectonic setting to the VDVF. To do this, this chapter is split up into five different sections: the first three summarise the talc occurrences at seafloor spreading centres elsewhere, and extinct, off-axis silicate-rich hydrothermal venting which is compared to the VDVF deposits. The aim of this is to demonstrate that the processes leading to the formation of the types of hydrothermal activity and mineral deposition discovered at the VDVF are not unique, and may instead be widespread at mid-ocean ridges (MOR), particularly those with spreading rates that support the development of oceanic core complexes (OCC's). The second half of this chapter describes the calculation of the focused heat flux from the active site, and suggests that the VDVF-type hydrothermal systems may be of importance in terms of oceanic geochemical budgets and crustal heat loss.

6.1. Talc occurrences at seafloor spreading centres

The discovery of the VDVF is the first time that a talc-dominated seafloor hydrothermal system with actively venting chimneys, hosted in gabbro and peridotite and located on the flanks of a MOR has been found. Whilst it is a unique type of active hydrothermal system, talc and associated Mg-phyllosilicates (including kerolite and smectite) have been sampled on the seafloor in other locations (Figure 6.1; Dekov et al., 2008a). This section will briefly summarise these occurrences that have been described in the literature, and explain the key differences between these deposits and the VDVF. The most common occurrence of talc in seafloor environments is either as a constituent of hydrothermally altered sediments, or as an accessory mineral in massive sulphide deposits. This section describes the setting and petrography of these other seafloor deposits, to compare and contrast them to the VDVF.

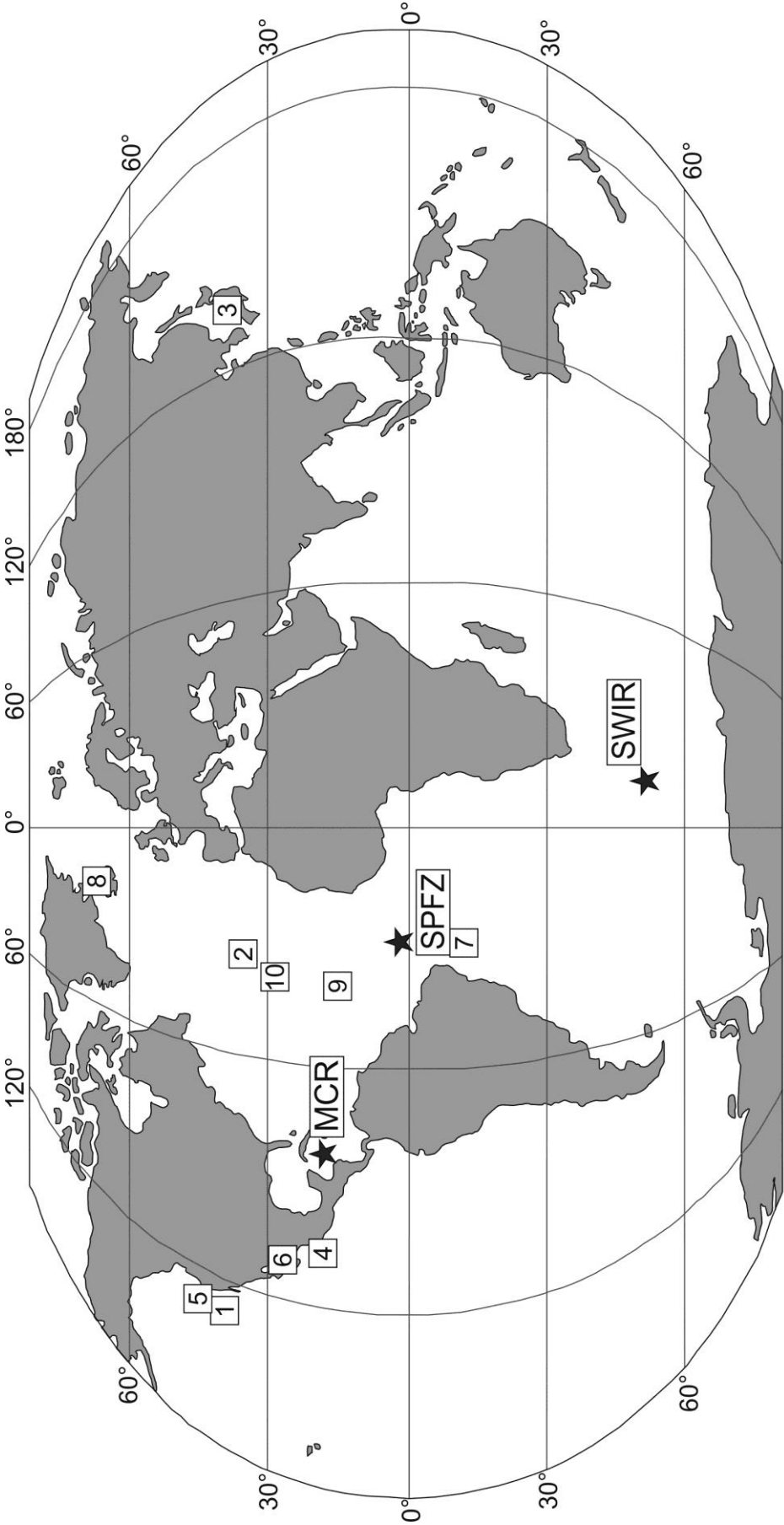


Figure 6.1: Map detailing the location of samples from other seafloor spreading centres. Numbers represent the location of vent field compared to the VDVF in Section 6.1, and stars the locations of samples recovered that are described in sections 6.2-6.3. 1 = NESCA, 2 = Saldanha, 3 = Jade, 4 = Red Seamount, 5 = Middle Valley, 6 = Guaymas Basin, 7 = Wakamiko, 8 = Grimsey, 9 = 15°20'N and 15°45'N core complexes, 10 = Atlantis Massif, MCR = Mid-Cayman Rise; SPFZ = St. Paul Fracture Zone; SWIR = Southwest Indian Ridge

6.1.1. Sediment-related talc

Talc is a more common accessory mineral in sedimentary-hosted hydrothermal deposits than at those where sediment cover is absent. Five examples of seafloor talc deposition within sediment hosted environments are summarised here:

- (i) The Escanaba Trough, Gorda Ridge is a slow spreading MOR with a ~500 m thickness of turbidite sediment cover. The NESCA vent field features fluids that vent at up to 217°C and precipitate mounds consisting predominantly of massive sulphide and sulphate (Koski et al., 1994a). Diffuse, lower temperature, silica rich fluids percolate through the surrounding sediments, which mix with Mg in pore fluids and precipitate platy and fibrous talc (Zierenberg and Shanks III, 1994).
- (ii) The Saldanha hydrothermal field is hosted within a basalt and serpentinite basement at the Mid-Atlantic Ridge (MAR) and hydrothermal fluids vent as low-temperature diffuse flow at temperatures of 7-9°C (Dias and Barriga, 2006; Dias et al., 2011). Massive talc precipitated during the earlier stages of venting, and it occurs within altered hydrothermal sediments along with sulphides. Stable isotope studies estimate that talc formed at up to 180°C (Dias et al., 2011).
- (iii) The Jade hydrothermal deposit is located at the Okinawa Trough back-arc basin in the Pacific, and is hosted in basalt and andesite (Marumo and Hattori, 1999). This metal-rich massive sulphide deposit is dominated by lead and zinc sulphides, with anhydrite and barite (Nakamura et al., 1990). The surrounding sediments are hydrothermally altered to Mg-clays and talc by fluids with temperatures of ~170°C (Marumo and Hattori, 1999).
- (iv) Talc is found within seamounts 20 to 30 km away from the volcanic axis on the East Pacific Rise (Alt et al., 1987). Active hydrothermal venting at this location is present as 10-15°C diffuse flow that precipitates Fe-oxyhydroxides (Alt et al., 1987). Minor amounts of iron-rich talc occurs as spherules in association with accessory amounts of nontronite, and is inferred to have formed from previous higher temperature hydrothermal circulation, due to the additional presence of sulphides (Alt et al., 1987; Dekov et al., 2008a).
- (v) The sedimented Middle Valley rift on the Juan de Fuca Ridge hosts an anhydrite and barite assemblage comprising kerolite and smectite clays that are similar in composition to talc (Dekov et al., 2008a). These clays form a major phase in the hydrothermal mounds and occur as an accessory phase in hydrothermally active

chimneys, occurring as radial, colloform and globular masses, formed from seawater and Mg-rich pore water entrainment into a hydrothermal fluid (Ames et al., 1993; Buatier et al., 1995).

Although talc is present within altered sediments at these different hydrothermal systems, the dominant minerals forming the hydrothermal mounds and chimneys are sulphides and sulphates. Talc is seen to constitute between 75-95% of the assemblage in samples recovered from the VDFV, which is in contrast to the five deposits described above. Instead, these deposits feature talc as accumulations in sediments. Furthermore, the tectonic setting of the deposits contrasts to the VDFV, except in the case of the Saldanha hydrothermal field, which features far lower (<10°C) temperatures of venting. However, the estimated precipitation temperatures of talc within these hydrothermal sediments are generally similar to those measured and estimated at the VDFV. Stable isotope ratios give equilibrium precipitation temperatures of around 170-180°C for sediment hosted talc (Marumo and Hattori, 1999; Dias et al., 2011), within the ranges determined from *in situ* measurements (42°C - 215°C) and stable isotope (116°C - 217°C) studies at the VDFV.

Map	Vent field/site	Location	Latitude	Longitude	Depth (m)	T estimated (°C)
1	NESCA	Gorda Ridge	41°00'N	127°25'W	3300	<217
2	Saldanha	MAR	36°34'N	109°27'W	2200	-
3	Jade	Okinawa Trough	27°16'N	127°05'E	1400	170
4	Red Seamount	EPR	20°48'N	109°27'W	1900	-
5	Middle Valley	JdF Ridge	48°27'N	128°42'W	2440	-
6	Southern Trough	Guaymas Basin	27°01'N	111°25'W	2460	280
6	Northern Trough	Guaymas Basin	27°18'N	111°30'W	2000	280
7	Wakamiko	Aira Caldera	31°40'N	130°49'E	200	200
8	Grimsey	Kolbeinsey Ridge	66°36'N	17°39'W	400	250
9	15°20'N OCC	MAR	14°51'N	45°05'W	3100	-
9	15°45'N OCC	MAR	15°44'N	46°56'W	2235	-
10	Atlantis Massif	MAR	30°07'N	42°07'W	1200	-

Table 6.1: Summary of other occurrences of talc at MOR's, detailing the situation, mid-ocean ridge and depth of deposit. Abbreviations: EPR = East Pacific Rise, JdF = Juan de Fuca, MAR = Mid-Atlantic Ridge, SWIR = Southwest Indian Ridge, T = temperature.

6.1.2. Talc and similar clays in other hydrothermally active hydrothermal deposits

Talc occurs as an accessory mineral within massive sulphides forming at active high-temperature hydrothermal sites such as the Escanaba Trough and in the Southern Trough of the Guaymas Basin. At the Escanaba Trough, talc occurs as rinds around massive sulphides, or as interstitial grains within a pyrrhotite dominated mineral assemblage (Zierenberg and Shanks III, 1994). Here, talc grains have a massive texture in the sulphide lenses, contrasting with the platy and fibrous textures observed in the hydrothermal sediments (Zierenberg and Shanks III, 1994). The massive sulphide deposits in the Southern Trough of the Guaymas Basin contain talc that occurs either as interstitial, fibrous grains within pyrrhotite-rich massive sulphide, or as platy aggregates surrounding disseminated sulphide (Koski et al., 1985). In both deposits, talc forms from the entrainment of bottom water and mixing with the end-member hydrothermal fluid at stable isotope equilibrium temperatures of 280°C (Koski et al., 1985). It is proposed that Mg is provided from seawater, and the Si from the hydrothermal fluid (Koski et al., 1985), which is a similar mechanism to that which occurs at the VDVF.

Two occurrences where talc and kerolite are observed in unusually shallow hydrothermal deposits are the Wakamiko Vent Site in the Aira Caldera, offshore Japan, and at the Grimsey Vent Field in the Tjornes Fracture Zone, 30 km north of Iceland (Hannington et al., 2001; Dekov et al., 2008b; Yamanaka et al., 2013). These two deposits are most comparable to the VDVF in terms of their venting temperature and petrological textures. Both deposits are situated at a depth of 200-400 m below sea level and vent fluids at temperatures of 200-270°C (Kuhn et al., 2003; Yamanaka et al., 2013). The dominant mineral at the Grimsey Vent Field is anhydrite, whereas carbonate minerals are prevalent at Wakamiko (Hannington et al., 2001; Yamanaka et al., 2013). At both vent fields, talc forms colloform masses in hydrothermally active chimneys and mounds, and precipitates as a result of silica rich fluids mixing with seawater (Kuhn et al., 2003; Yamanaka et al., 2013).

The conditions for the precipitation of talc and associated clay minerals in active hydrothermal fields require mixing of the hydrothermal fluid (providing silica) with either seawater or pore waters (providing magnesium). However, in contrast to the

VDVF, hydrothermal massive sulphide deposits contain talc as an accessory phase, and not a major mineral. The reason for this difference is principally because ‘black smoker’ vents have lower pH and are dominated by higher H₂S and base metal concentrations (Von Damm, 1995). With lower pH, talc becomes less saturated on mixing seawater with hydrothermal fluid such that, at pH values of <4, talc is unstable. Furthermore, as ‘black smoker’ fluids cool, any talc that is precipitated is diluted by the dominant precipitation of metal sulphides. Where there are similarities, the Middle Valley, Wakamiko and Grimsey deposits are closest to the VDVF example in terms of temperature and talc composition. However, talc remains in low abundance compared with the VDVF, and these other sites also differ in terms of their tectonic setting and host lithologies.

6.1.3. Extinct hydrothermal talc deposits

In other settings, larger abundances of precipitated talc have been recovered from the Northern Trough of the sediment covered rift at the Guaymas Basin in the Gulf of California (Lonsdale et al., 1980). Here, a stratiform and originally sub-surface accumulation of talc is exposed along the top of a fault scarp that extends for 200 m along strike (Lonsdale et al., 1980). This significant volume of exposed, tabular, platy and massive talc is interpreted as being a hydrothermal deposit that also contains smectite clays and microcrystalline silica within the assemblage (Lonsdale et al., 1980). This deposit is thought to have formed during the mixing of conductively-heated Mg-rich pore-water with ascending silica rich hydrothermal fluids (Lonsdale et al., 1980). A shallow volcanic sill, intruded into the sediments, is inferred to have been the thermal driver for the hydrothermal system, and talc precipitation temperatures are estimated from stable isotope studies to have been approximately 280°C (Lonsdale et al., 1980).

6.1.4. Hydrothermal talc at oceanic core complexes

Talc is commonly associated with detachment fault zones at oceanic core complexes, where it occurs as fault breccias or as the product of late stage serpentinisation e.g. (Escartin et al., 2003; Paulick et al., 2006). Three talc-rich samples from oceanic detachment faults on the Mid-Atlantic Ridge are included for comparison, and were

recovered from the 15°20'N and 15°45'N core complexes, and the Atlantis Massif. At the 15°20'N core complex, the infiltration of silica rich hydrothermal fluids lead to talc alteration of ultramafic protoliths, and overprints previous serpentinisation of the upper mantle (Paulick et al., 2006). The talc at the 15°45'N core complex generally occurs associated within brittle shear zones, and forms in schists along with minerals such as actinolite, tremolite and chlorite (Escartin et al., 2003). Alteration of the lower crustal gabbros and upper mantle peridotite within the ~100 m wide detachment fault zone of the Atlantis Massif forms talc, amphibole and chlorite bearing schists (Boschi et al., 2006). They are secondary phases after serpentine and orthopyroxene within gabbros and peridotites, and precipitate due to infiltration of hydrothermal fluids along the detachment fault zone (Boschi et al., 2006).

6.2. Extinct hydrothermal deposits located downslope of the VDVF

Downslope of the VDVF and Mystic Mountain, talc samples were recovered during earlier investigations of the Mid-Cayman Rise (MCR) in the 1970s and 1980s (Ballard et al., 1979; Stroup and Fox, 1981). The lithologies sampled are dominantly ultramafics, variably altered gabbros and basaltic rocks from two areas along the axis of the MCR (Stroup and Fox, 1981). Also recovered were a few talc-bearing samples that were classed as 'highly metasomatised', and were originally thought to have formed as the result of the serpentinisation of peridotite. The samples were recovered from approximately 2 km to the east of the VDVF. These samples are re-examined here, and following further petrographic analysis, two of the three samples analysed are found to have a very similar mineral assemblage and texture to those from Mystic Mountain (Figure 6.2).

In thin section, these talc samples present a brown colour in plane polarised light (PPL), and rarely show any interference colours. The talc generally shows a massive or fibrous habit, whilst the textures observed include radial aggregates up to 1 mm across, with individual grains approximately 100 µm across (Figure 6.3). Individual bands on the margins of massive talc are up to 200 µm across (Figure 6.3). As seen in some samples from the hydrothermally active site, massive, isotropic talc infills porous areas and consolidates previous precipitates of banded and botryoidal talc. Minor amounts of microcrystalline silica occur as massive aggregates up to 100 µm

across. A few grains of sulphide occur as bands in massive or fibrous talc, and the dominant sulphide phase is chalcopyrite (Figure 6.3).

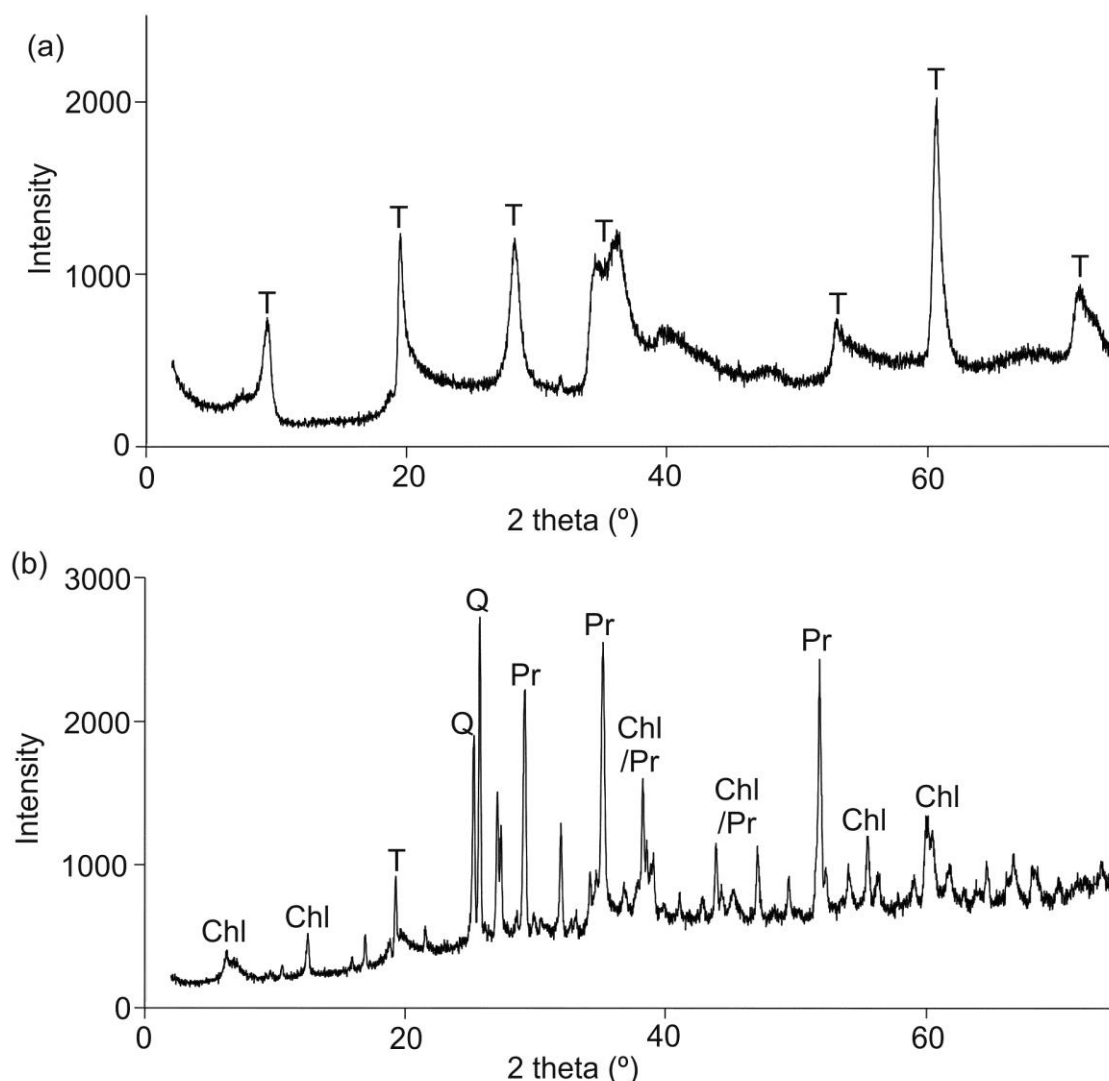


Figure 6.2. X-Ray diffraction (XRD) of bulk powders from east of the VDVF on Mt. Dent. (a) ALV-622-3-1 and (b) ALV-624-3-1. Mineral abbreviations: Chl= Chlorite, Pr = Prehnite, Q=Quartz, T=talc.

The Mg-silicate that forms the inactive deposits to the east of the VDVF also contains clay interlayers. The XRD peak positions in the unorientated air-dried mounts of clay separates have peak positions at 9.65 Å and 4.76 Å, suggesting that the main silicate mineral is talc (Figure 6.4a,b). Unorientated, glycolated mounts indicate a small shift in the peak positions from 9.65 Å to 9.34 Å, and 4.77 Å to 4.73 Å (Figure 6.4a,b), indicating the presence of a smectite clay in two out of three samples (Brindley, 1966). Trace amounts of kaolinite are indicated by the presence of very small peaks at 7.17 Å and 3.57 Å that do not shift in the glycolated mounts (Figure 6.4a,b).

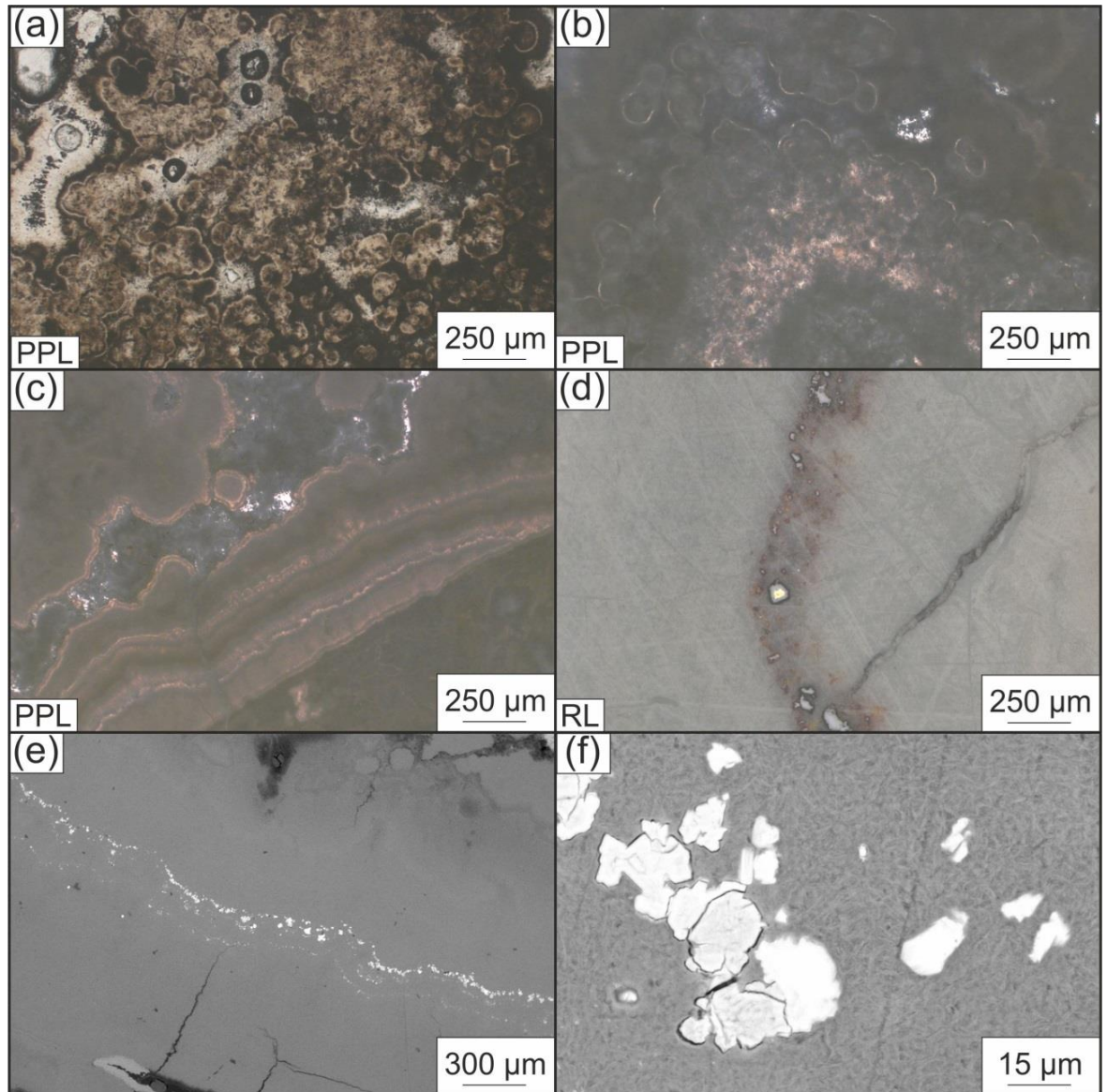


Figure 6.3: Transmitted light, reflected light and scanning electron microscope (SEM) images of samples from Mt. Dent, downslope of the VDVF. All images are from sample ALV-622-3-1. (a) and (b) radial, fine-grained and isotropic talc (c) banded, fine grained and isotropic talc (d) and (e) reflected light and SEM images of bands of chalcopyrite in massive talc groundmass (f) close up of subhedral chalcopyrite grains in talc groundmass.

The clay mineral in the other sample investigated is chlorite, with minor amounts of smectite and kaolinite. The presence of a small intensity peaks at 8.48 \AA in all the plots from sample 624-1 that do not decompose on heating (Figure 6.4c-f), and the

glycolated peak occurring at 16.70 Å (Figure 6.4d), indicate the presence of smectite clays (Srodon, 1980). The other large peaks in the clay separation plots are at 7.11 Å, ~4.7 Å and 3.54 Å (Figure 6.4c,d), which correspond to those of chlorite, but also overlap with kaolinite. The intensity of these peaks drops dramatically on heating to 550°C (Figure 6.4f), indicating these peaks are predominantly from chlorite, but are still just above background concentrations, therefore suggesting minor amounts of kaolinite are present.

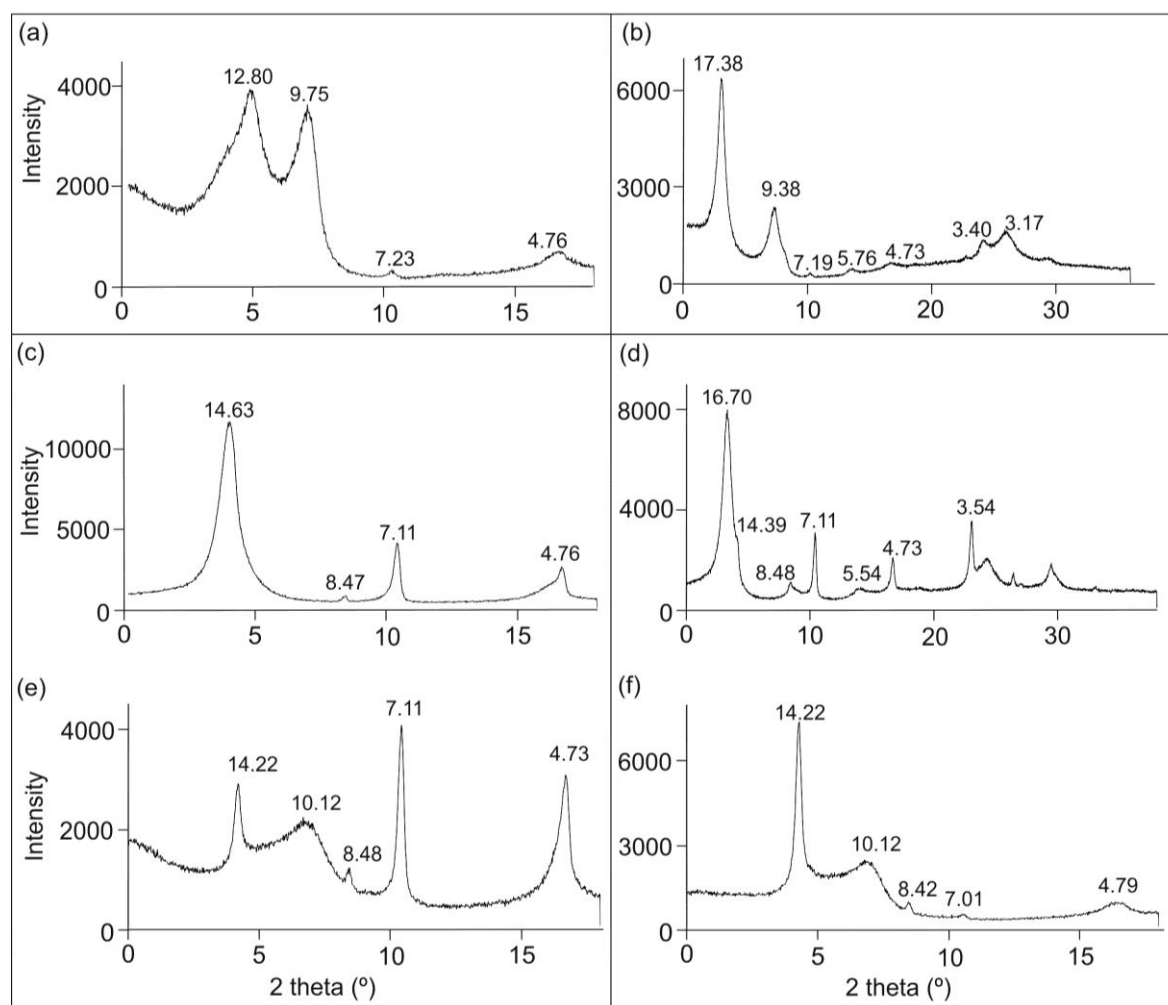


Figure 6.4: XRD of clay separates from the MCR (a) air-dried, unorientated mount of sample ALV-622-3-1 (b) glycolated mount of sample ALV-622-3-1 (c) air-dried, unorientated mount of sample ALV-624-3-1 (d) glycolated mount of sample ALV-624-3-1 (e) sample ALV-624-3-1 fired to 375°C (f) sample ALV-624-3-1 fired to 550°C. Peak positions are in angstroms.

Two of the samples from earlier investigations on the MCR have mineralogies and textures similar to those from the VDFV and Mystic Mountain regions. The dominance

of talc, with microcrystalline silica and chalcopyrite, are found in similar proportions to the Mystic Mountain deposits. Furthermore, these samples also indicate the presence of a smectite clay interlayer, the same mineralogical stratification that is present in minor amounts in the VDVF talc. The banded and botryoidal textures observed in fine grained talc from two of the samples downslope of the VDVF are indicative of precipitation from a hydrothermal fluid. This indicates that hydrothermal activity was not only restricted to the VDVF, but has occurred 2 km away from the active site.

6.3. Extinct hydrothermal deposits with similar tectonic settings to the VDVF

This section describes examples of other, silicate-dominated inactive hydrothermal deposits that have been discovered at tectonics settings similar to the VDVF. These samples were acquired from the Woods Hole Oceanographic Institute and the petrographic and geochemical analysis is used compared them here to the VDVF material. A sample map and table are shown in Chapter 2.

6.3.1. St Paul Fracture Zone

An extinct hydrothermal talc-bearing deposit was discovered at the St. Paul Fracture Zone (SPFZ) at the equatorial MAR (D'Orazio et al., 2004). One sample that was recovered from the site by (D'Orazio et al., 2004) consisted of botryoidal kerolite and smectite clays that have a banded texture very similar to those observed at the VDVF (D'Orazio et al., 2004; Dekov et al., 2008a). Other samples analysed from this site include some consolidated, fine-grained massive clays that have a manganese oxide coating, and some sepiolite-bearing consolidated sediments (Figure 6.5; Thompson, 1981).

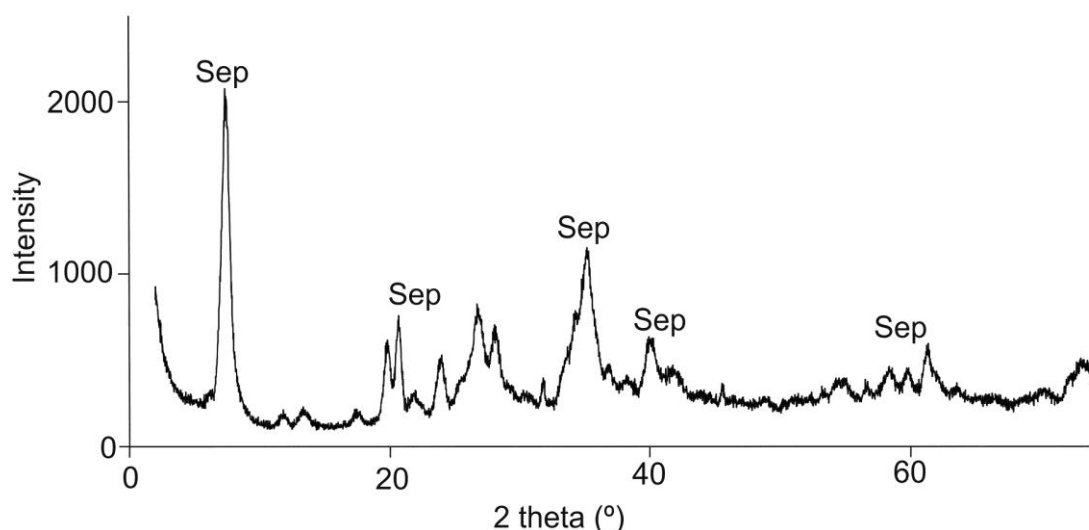


Figure 6.5: XRD of bulk powder from the SPFZ, showing the dominance of sepiolite.

Sample number CH35-11-4. Mineral abbreviations: sep=sepiolite.

In thin section, these consolidated sediments present as dark brown coloured (PPL), isotropic, and very fine grained, with individual grains not being visible. The sepiolite generally has a massive or fibrous habit (Figure 6.6), and contains a few small grains of microcrystalline silica up to 20 μm across. Accessory phases include oxidised sulphides, with rare grains of atacamite, chromite and native bismuth (Figure 6.6).

XRD of clay separates indicate the main peaks are at 12.17 \AA and 6.64 \AA , which are the two main peaks for sepiolite. The 011 peak expanded to 12.51 \AA after glycolation, which is unusual for sepiolite but has been observed in clay samples elsewhere (Argast, 1989). There are no other peaks in the plot above background intensities, suggesting a pure sepiolite with no inter-stratification from other clay phases (Figure 6.7).

The sepiolite-rich sediments bear little resemblance to the VDFV in terms of petrographic textures and mineralogy. High concentrations of bismuth are found in massive sulphide samples from the Escanaba Trough and inferred to be the result of interaction between a hydrothermal fluid and sediment (Törmänen and Koski, 2005). These sediments are likely to be hydrothermally derived and could potentially indicate extinct activity in the past (Thompson, 1981). Additionally, (D'Orazio et al., 2004) recovered a sample dominated by talc that has a similar botryoidal texture to the samples from the VDFV. Also recovered in their investigations were serpentinite

and gabbro samples, in crust that is ~ 0.6 Ma old (D'Orazio et al., 2004). This deposit is the most comparable to the VDVF in terms of both mineralogy and tectonic setting, and gives further evidence for off-axis, silicate-rich hydrothermal venting.

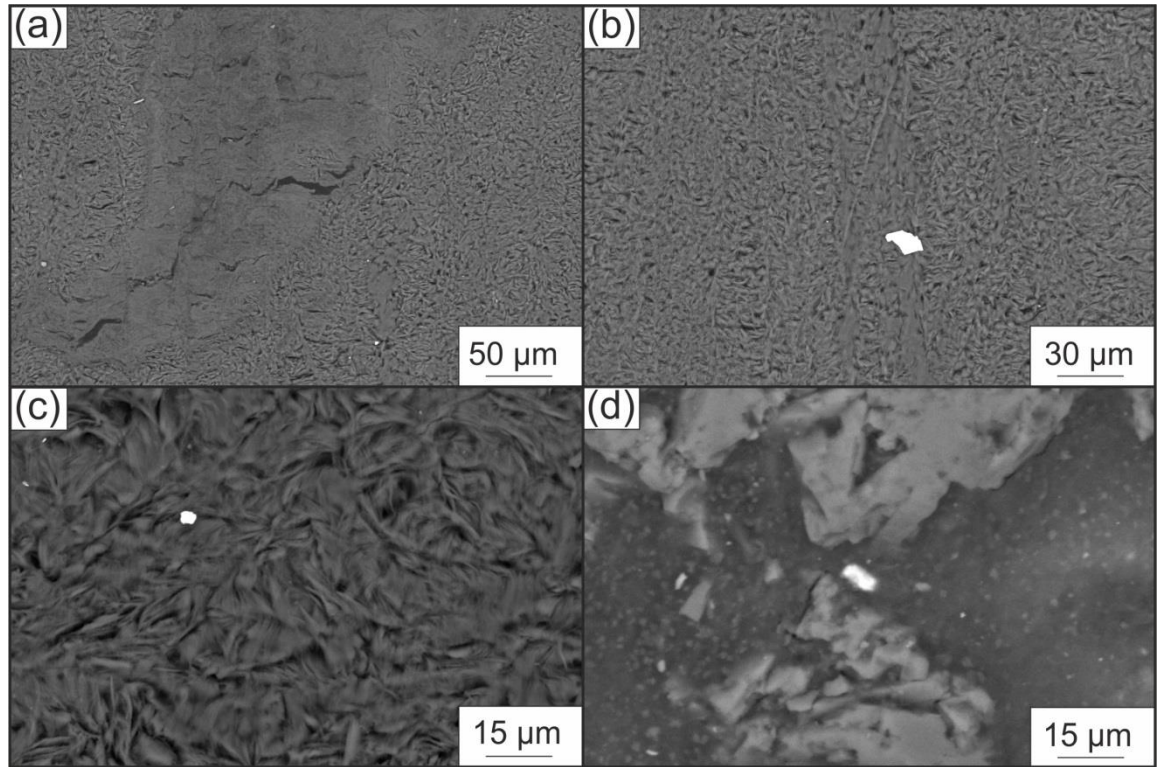


Figure 6:6: SEM images of accessory minerals and groundmass in samples from the SPFZ All images are from sample CH35-11-4 (a) fibrous and massive sepiolite (b) grain of native bismuth within sepiolite (c) chromite grain within fibrous sepiolite (d) atacamite (centre of image) within a sepiolite and microcrystalline silica (lighter grey) groundmass.

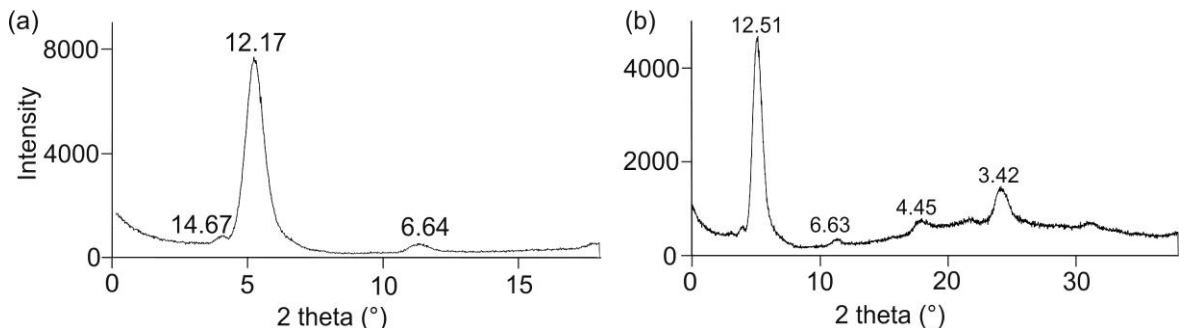


Figure 6.7: XRD of clay separates from the SPFZ, sample CH35-11-4 (a) air-dried, unorientated mounts, (b) glycolated, orientated mounts. Numbers represent peak positions in angstroms.

6.3.2. Southwest Indian Ridge

Extinct hydrothermal deposits discovered at the Southwest Indian Ridge (SWIR) are hosted in serpentinised peridotite on a large detachment fault surfaces in a similar tectonic setting to Mt. Dent (Bach et al., 2002). These samples consist mainly of microcrystalline silica and opal ($\text{SiO}_2 \cdot 1.5\text{H}_2\text{O}$), with accessory levels of clay minerals (Figure 6.8). Microcrystalline silica is the dominant SiO_2 polymorph but opal was identified by the presence of a very broad XRD peak at $\sim 22^\circ 2\theta$.

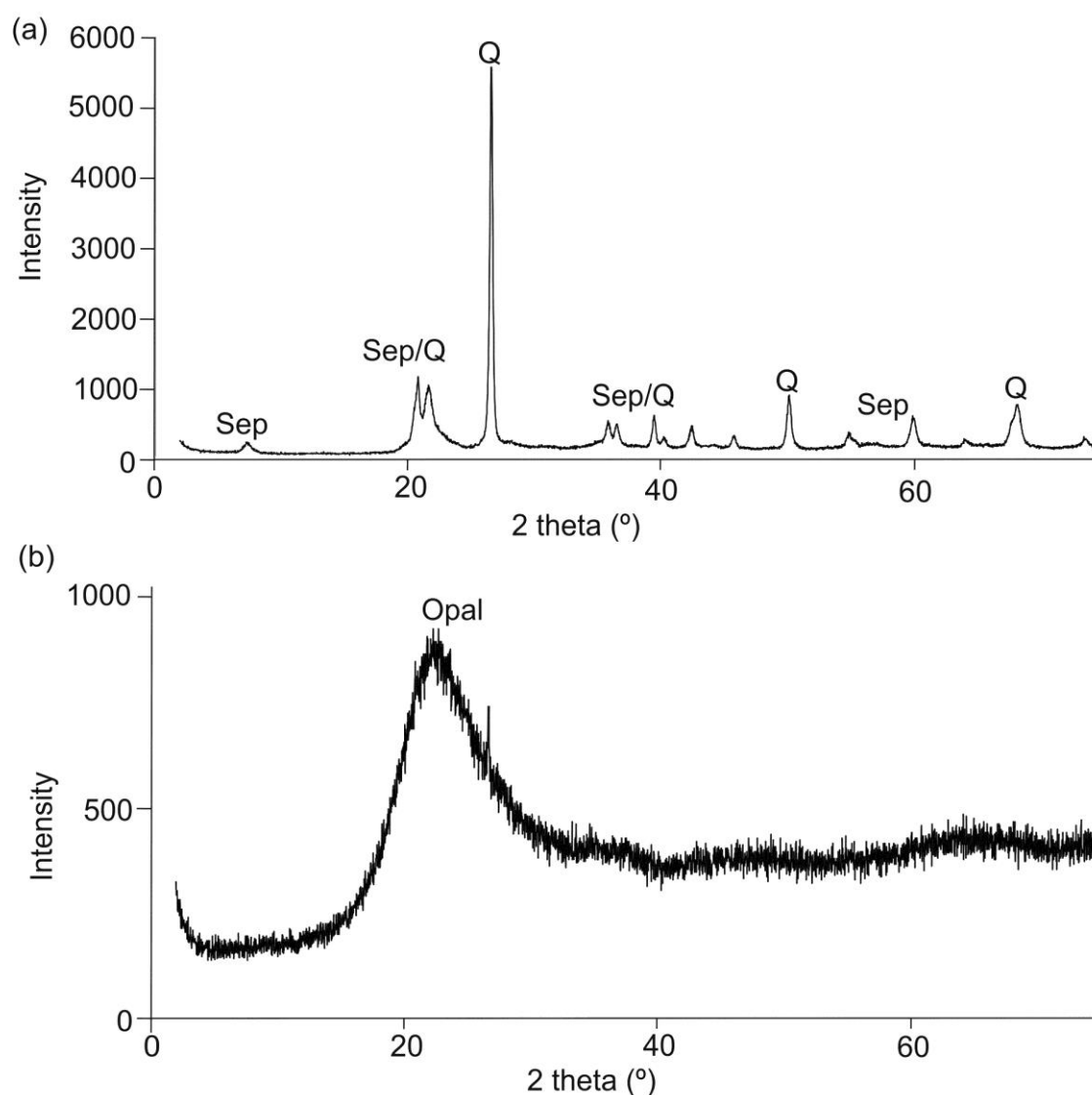


Figure 6.8: XRD of bulk powders from the SWIR (a) KN162-9-43-27 and (b) KN162-9-43-11. Mineral abbreviations: Q=quartz, Sep=sepiolite.

In thin section, the microcrystalline silica is fine grained and occurs intergrown with sepiolite. Microcrystalline silica has a massive texture, and individual grains are

usually around 20 μm across (Figure 6.9). Opal shows a radiating, fibrous habit, and clusters are up to 200 μm across (Figure 6.9). No sulphide material was observed, but a few grains of secondary iron and copper carbonates were detected in the SEM.

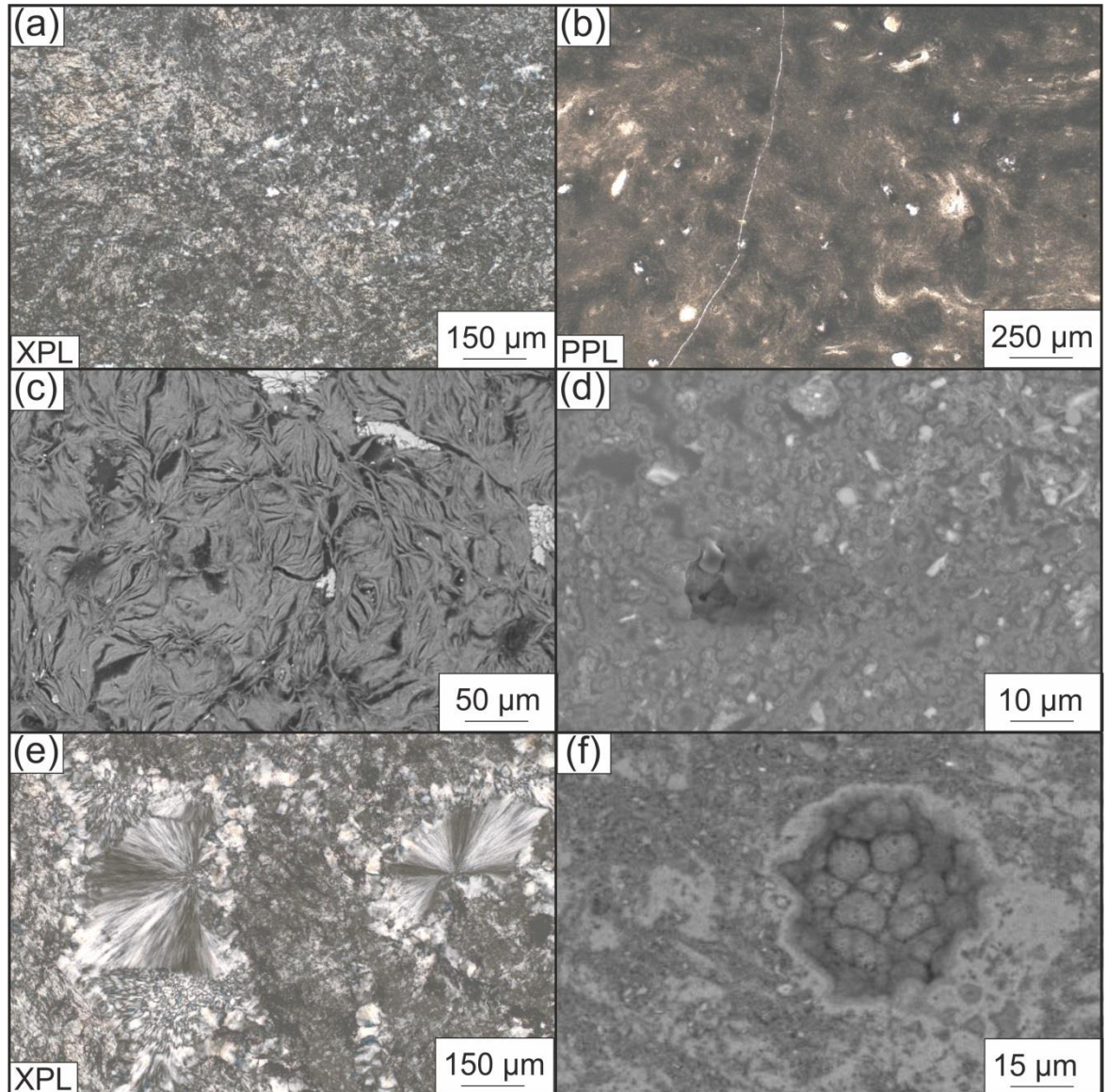


Figure 6.9: Transmitted light and SEM images of samples from the SWIR (a) KN162-9-43-4: intergrown microcrystalline silica and talc (b) KN162-9-43-3: very fine grained, isotropic clays within grains of microcrystalline silica (c) KN162-9-43-4: SEM image of fibrous sepiolite with light areas of microcrystalline silica (d) KN162-9-43-3: SEM image of intergrown Mg-clays and microcrystalline silica (e) KN162-9-43-4: radial opal, microcrystalline silica and clay groundmass (f) KN162-9-43-3: SEM image of broken surface showing botryoidal clay minerals with lighter areas representing microcrystalline silica.

Clays minerals are very fine grained and generally show a massive or fibrous form. One small, 50 μm across area consisting of sepiolite showed a broken surface in the SEM, where a botryoidal habit was observed (Figure 6.9). The XRD patterns of clay separates for samples from the SWIR show two different mineralogical groups. The clay minerals occur as two different phases, either illite-smectite or sepiolite. The illite-smectite component is indicated by the expansion of the 001 peak from 14.37 Å on the air-dried mounts to 16.86 Å on the glycolated mounts (Figure 6.10b,d; Brindley, 1966). The air-dried plots have similar peak positions to the plots of samples from the SPFZ, suggesting the presence of sepiolite, which also expands on glycolation from 12.31 Å to 12.51 Å (Figure 6.10a,c). The peaks at 4.27 Å and 3.34 Å on the glycolated plot are from slight contamination by microcrystalline silica (Figure 6.10a,c).

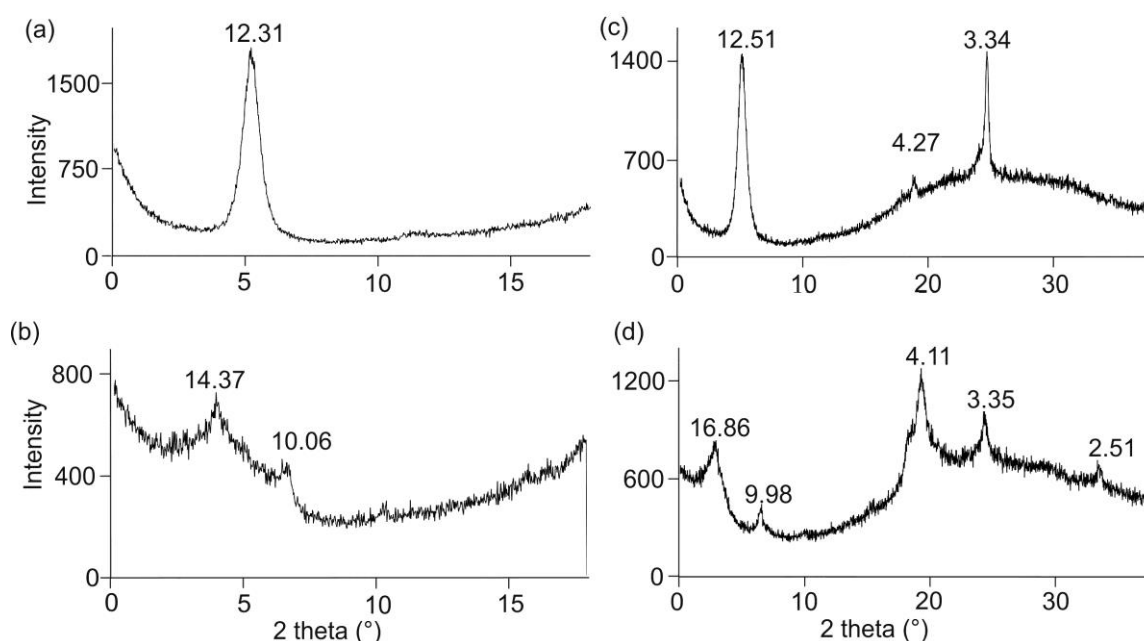


Figure 6.10: XRD of clay separates from the SWIR. Samples numbers: top: KN162-9-43-4, bottom: KN162-9-43-3 (a) and (b) air dried, unorientated mounts (c) and (d) glycolated orientated mounts. Numbers represent peak positions in angstroms.

These samples recovered by (Bach et al., 2002) from Knorr 162-9 are also recovered alongside oxidised massive sulphide deposits, indicating past high-temperature hydrothermal circulation. The silicates are formed due to hydrothermal alteration within the vicinity of past hydrothermal systems, and are inferred to be a few Ma old due to the distance from the ridge axis (Bach et al., 2002).

6.3.3. Whole rock geochemistry

SiO₂ has concentrations of 43.5 wt.% to 61.6 wt.% in the MCR samples, 57.2 wt.% and 58.9 wt. % in samples from the SPFZ, and 83.0 wt.% to 94.4 wt.% in the samples from the SWIR. MgO has concentrations of 9.3 wt.% to 30.2 wt.% in the MCR samples, 23.7 wt. % and 23.9 wt. % in the SPFZ samples and 0.1 wt.% to 6.7 wt.% in the SWIR samples (Table 6.2). Only one out of the SPFZ and MCR samples has a combined MgO and SiO₂ of <80 wt.%, indicative of the Mg-silicate and microcrystalline silica dominated mineralogies. Chlorite is the dominant clay in one of the samples from the MCR, meaning that Al₂O₃ is 20.1 wt.% in this sample, however the remainder range between 0.2 wt.% to 3.1 wt.%, indicative of small concentrations of smectite-group clays, with the lowest concentrations in sepiolite dominated samples.

	SiO ₂ wt.%	TiO ₂ wt.%	Al ₂ O ₃ wt.%	Fe ₂ O ₃ wt.%	MgO wt.%	CaO wt.%	K ₂ O wt.%	Na ₂ O wt.%	P ₂ O ₅ wt.%	LOI wt.%	Sum wt.%
ALV-622-1	58.57	0.01	1.51	1.23	30.15	0.14	0.08	0.63	0.01	7.65	99.97
ALV-622-1(a)	61.54	0.01	0.65	0.57	28.82	0.18	0.06	0.32	0.00	6.87	99.02
ALV-624-1	43.53	0.55	20.07	4.05	9.37	13.92	0.24	0.81	0.07	7.77	100.37
CH-4	57.17	0.03	1.38	0.28	23.89	0.29	0.13	0.83	0.02	15.23	99.24
CH-12	58.88	0.02	0.72	0.18	23.72	1.17	0.09	0.79	0.01	14.10	99.66
KN-3	90.18	0.10	1.99	0.87	0.79	0.15	0.54	0.47	0.01	2.71	97.82
KN-4	86.65	0.01	0.21	0.58	6.69	0.09	0.07	0.19	0.00	5.31	99.80
KN-11	91.75	0.04	0.42	0.29	0.18	0.13	0.13	0.24	0.01	3.88	97.06
KN-19	83.01	0.15	3.06	3.47	2.02	0.26	0.87	0.69	0.02	5.36	98.91
KN-27	92.45	0.03	0.56	0.21	2.51	0.10	0.13	0.19	0.00	3.29	99.46
KN-72	94.34	0.03	0.24	0.19	0.11	0.11	0.08	0.17	0.01	3.63	98.91
KN-79	92.57	0.05	0.82	0.36	0.95	0.11	0.23	0.29	0.01	2.66	98.05

Table 6.2: Major element concentrations derived by X-Ray fluorescence (XRF) for samples from the MCR, the SPFZ and the SWIR. Sample abbreviations ALV-622-1: ALV-622-3-1, ALV-622-1(a): ALV-622-3-1 (a), ALV-624-1: ALV-624-3-1, CH-4: CH35-11-4, CH-12: CH35-11-12, KN-3: KN162-9 43-3, KN-4: KN162-9 43-4, KN-11: KN162-9 43-11, KN-19: KN162-9 43-19, KN-27: KN162-9 43-27, KN-72: KN162-9 43-72, KN-79: KN162-9 43-79.

Base metal concentrations are low, with all but one sample having Cu concentrations of <125 ppm, Zn concentrations of <130 ppm, and Pb concentrations of <3 ppm. The sample from the MCR that contained sporadic chalcopyrite bands has Cu concentrations of ~650 ppm (Table 6.3). The Cr concentrations of sample 624-1 from

the MCR are ~ 7 times greater than the second highest concentration, indicating that this sample is probably an altered ultramafic, and not a hydrothermal precipitate.

Varying manganese concentrations are due to the contamination in the whole rock powders of the MnO coating on the samples.

6.3.4. Rare earth element geochemistry

The talc from the VDFV has rare earth element (REE) patterns that are similar to those from end-member hydrothermal fluids from other hydrothermal vent fields (see section 5.2; Douville et al., 1999). REE geochemistry of the talc at the VDFV is one of the key features that identify it as a primary hydrothermal mineral, and chondrite normalised patterns are useful proxies in indicating the processes that occur in seafloor hydrothermal deposits. REE concentrations and chondrite normalised patterns from other silicate-rich hydrothermal deposits are described in this section to compare them to the VDFV and investigate whether they have formed from similar methods (Figure 6.11). Also described are REE patterns in the samples of talc recovered from seafloor spreading centres elsewhere (Figure 6.12).

		ALV-622-1	ALV-622-1(a)	ALV-624-1	CH-4	CH-12	KN-3	KN-4	KN-11	KN-19	KN-27	KN-72	KN-79
As	ppm	1.9	0.8	0.4	0.7	0.3	0.1	0.3	0.3	0.3	0.1	0.1	0.4
Ba	ppm	0.3	2.5	3.5	3.2	1.9	52.9	1.0	467	516	142	140	411
Cd	ppb	19.0	15.7	25.7	148	246	4.0	24.1	82.1	15.9	22.1	16.7	59.3
Co	ppm	0.7	0.5	10.9	2.9	0.5	0.6	3.3	2.9	6.4	0.6	1.0	1.2
Cr	ppm	<0.1	0.8	139	2.8	4.3	<0.1	5.0	6.7	21.3	5.4	7.0	10.9
Cs	ppb	30.5	55.8	74.3	65.6	69.8	464	22.3	222	2172	210	322	108
Cu	ppm	652	52.1	11.0	101	125	4.2	111.5	66.6	41.8	17.1	17.2	46.8
Mn	ppm	135	95.4	1073	195	26.2	10.8	74.9	3446	129	8.7	31.3	3201
Mo	ppb	68.2	78.6	345	109	27.8	20.2	48.1	3011	71.6	44.1	45.8	3149
Ni	ppm	1.3	2.0	65.9	345	266	2.7	10.1	63.4	25.6	42.0	15.1	31.5
Pb	ppm	83.3	2.5	0.3	1.8	1.4	0.3	0.2	1.4	2.3	0.5	0.6	0.8
Rb	ppm	0.7	1.0	2.2	1.5	1.4	7.6	0.8	3.2	31.7	3.5	6.0	1.7
Sb	ppb	94.8	55.0	29.4	163	71.5	56.6	2287	508	275	1085	1112	454
Sr	ppm	9.2	11.5	13.5	12.5	21.0	3.9	1.9	24.2	27.4	5.7	7.7	18.7
Y	ppb	527	404	10764	1667	1077	1000	98.1	1202	5444	851	1429	940
Zn	ppm	114	20.5	17.7	113	128	6.3	44.5	27.8	35.8	34.3	7.6	17.7
Zr	ppm	0.4	2.0	40.3	20.1	7.1	7.6	14.1	7.6	45.2	8.4	12.5	4.4

Table 6.3: Trace element concentrations in samples from the MCR, the SPFZ zone and the SWIR. Sample abbreviations ALV-622-1: ALV-622-3-1, ALV-622-1(a): ALV-622-3-1 (a), ALV-624-1: ALV-624-3-1, CH-4: CH35-11-4, CH-12: CH35-11-12, KN-3: KN162-9 43-3, KN-4: KN162-9 43-4, KN-11: KN162-9 43-11, KN-19: KN162-9 43-19, KN-27: KN162-9 43-27, KN-72: KN162-9 43-72, KN-79: KN162-9 43-79.

REE analysis was conducted on whole rock powders in the samples described above from the MCR, the SWIR and the SPFZ. Σ REE in samples ranges from 0.3 ppm to 32.2 ppm and the Nd concentrations range from 54 ppb to 5526 ppb (Table 6.4).

$\text{La}_{(N)}/\text{Sm}_{(N)}$ ratios ranging from 0.8 to 3.5 indicate LREE enrichment in most of the samples. The $\text{Dy}_{(N)}/\text{Yb}_{(N)}$ values range from 0.2 to 1.3, which indicates little HREE enrichment compared to MREE (Figure 6.13). This is due to the analysis being conducted on whole rock powders, compared to the pure talc separates analysed in Chapter 5. This results in REE profiles that generally have a shallow gradient, with varying europium anomalies (Figure 6.11). Only two of the samples analysed show positive europium anomalies, with Eu/Eu^* values of 3.1 and 4.3. The remaining samples all have Eu/Eu^* values of <1 , and range from 0.5-0.9.

REE patterns in pure mineral separates of talc and associated Mg-silicates from other seafloor deposits are shown as chondrite normalised plots in Figure 6.12. REE patterns for average VDVF mound and chimney talc, average TAG anhydrite and three samples from terrestrial talc deposits are included on the figure for comparison. The terrestrial talc examples are the Hwanggangri deposits in South Korea, the Sivas Basin in Turkey, and the Atshan deposit in Egypt (Sharara, 1999; Shin and Lee, 2003; Yalçin and Bozkaya, 2006). These deposits were chosen as they represent common environments where talc forms in terrestrial environments under slightly different conditions. Talc deposits at Hwanggangri formed from the infiltration of silica rich metamorphic fluids derived from a granitic intrusion, which subsequently altered to dolomite and ultramafic host rocks (Shin and Lee, 2003). Two modes of talc formation are proposed to occur at the deposits of the Sivas Basin: the alteration of serpentine within an ophiolite sequence, and precipitation within siliciclastic sediments (Yalçin and Bozkaya, 2006). The Atshan deposit contains talc formed by the hydrothermal alteration of magnesium-bearing carbonates (Sharara, 1999).

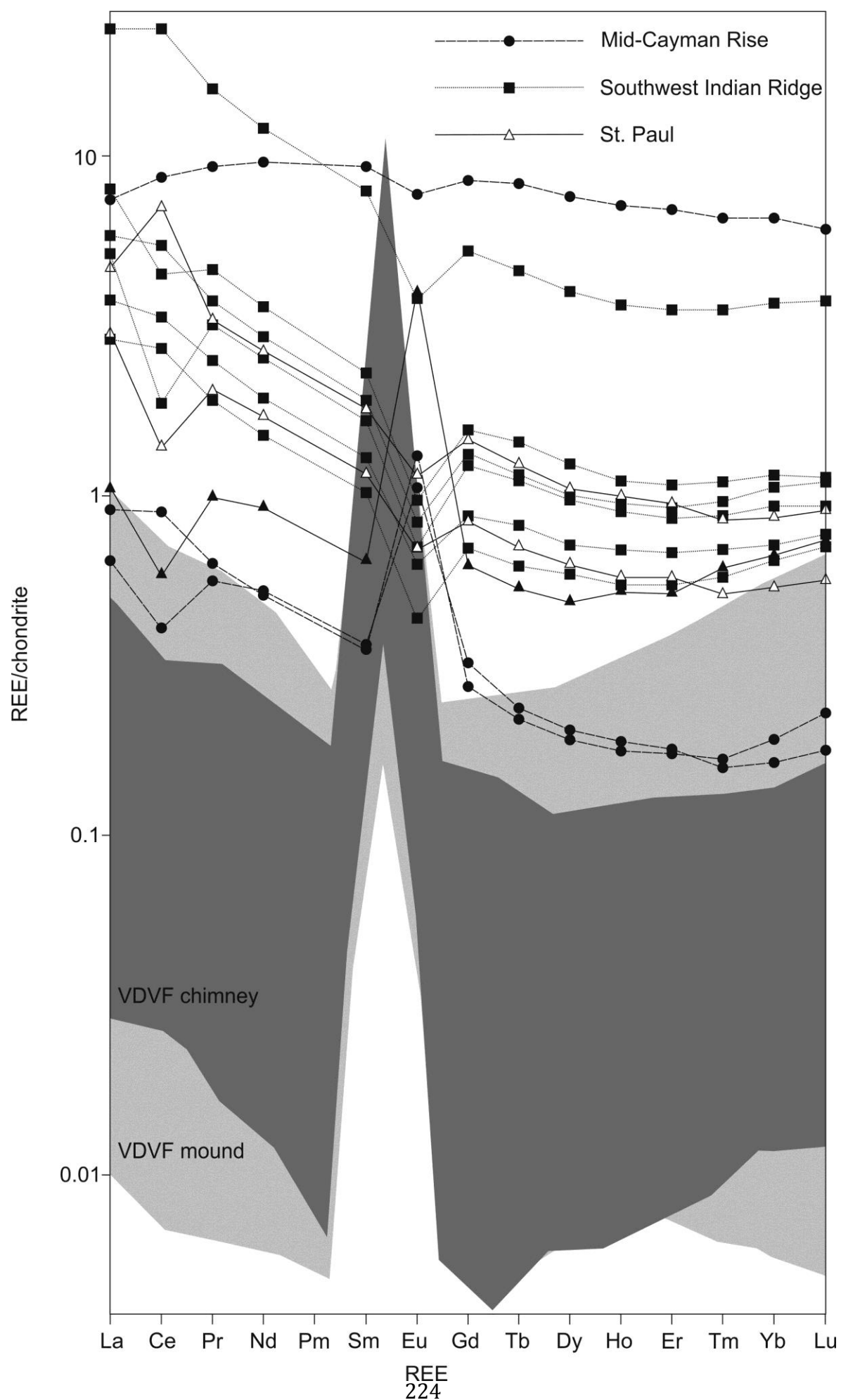


Figure 6.11: (On previous page) Chondrite normalised REE patterns in samples from the MCR, the SPFZ and the SWIR. The dark area indicates the area for active VDFV chimneys, and the light area is for the VDFV mound samples. The data at the SPFZ that shows a positive europium anomaly is taken from (D'Orazio et al., 2004), and chondrite data is from (McDonough and Sun, 1995). Colours and symbols are the same for Figure 6.13.

		ALV-622-1	ALV-622-1(a)	ALV-624-1	CH-4	CH-12	KN-3	KN-4	KN-11	KN-19	KN-27	KN-72	KN-79
La	ppb	153	217	1781	1102	718	903	49	1915	5641	686	1373	1229
Ce	ppb	249	553	5312	4359	851	2076	118	2752	14437	1662	3359	1150
Pr	ppb	53	59	869	302	190	232	13	432	1452	178	352	296
Nd	ppb	239	235	4372	1219	779	894	54	1655	5526	690	1338	1162
Sm	ppb	54	52	1377	270	171	193	13	342	1171	152	283	247
Eu	ppb	60	75	438	65	39	36	3	55	214	24	48	40
Gd	ppb	65	55	1693	290	167	175	13	312	1054	141	264	242
Tb	ppb	9	8	298	45	25	29	2	52	166	22	42	40
Dy	ppb	50	47	1866	259	153	177	15	304	983	145	248	243
Ho	ppb	10	10	394	54	32	38	3	60	199	30	51	49
Er	ppb	29	28	1113	152	92	109	11	173	563	87	146	138
Tm	ppb	4	4	163	21	13	17	3	27	87	14	24	22
Yb	ppb	26	31	1062	139	86	115	40	187	593	105	168	150
Lu	ppb	4	6	151	22	14	19	10	28	92	18	27	23
ΣREE	ppm	1.01	1.38	20.89	8.30	3.33	5.01	0.35	8.29	32.18	3.95	7.72	5.03
Eu/Eu*		3.1	4.3	0.9	0.7	0.7	0.6	0.7	0.5	0.6	0.5	0.5	0.5
Ce/Ce*		0.7	1.2	1.0	1.8	0.6	1.1	1.1	0.7	1.2	1.1	1.2	0.5
La/Sm		1.8	2.6	0.8	2.5	2.6	2.9	2.4	3.5	3.0	2.8	3.0	3.1
Dy/Yb		1.2	1.0	1.1	1.2	1.2	1.0	0.2	1.1	1.1	0.9	1.0	1.1

Table 6.4: REE concentrations in samples from the MCR, the SPFZ and the SWIR. Sample abbreviations ALV-622-1: ALV-622-3-1, ALV-622-1(a): ALV-622-3-1 (a), ALV-624-1: ALV-624-3-1, CH-4: CH35-11-4, CH-12: CH35-11-12, KN-3: KN162-9 43-3, KN-4: KN162-9 43-4, KN-11: KN162-9 43-11, KN-19: KN162-9 43-19, KN-27: KN162-9 43-27, KN-72: KN162-9 43-72, KN-79: KN162-9 43-79.

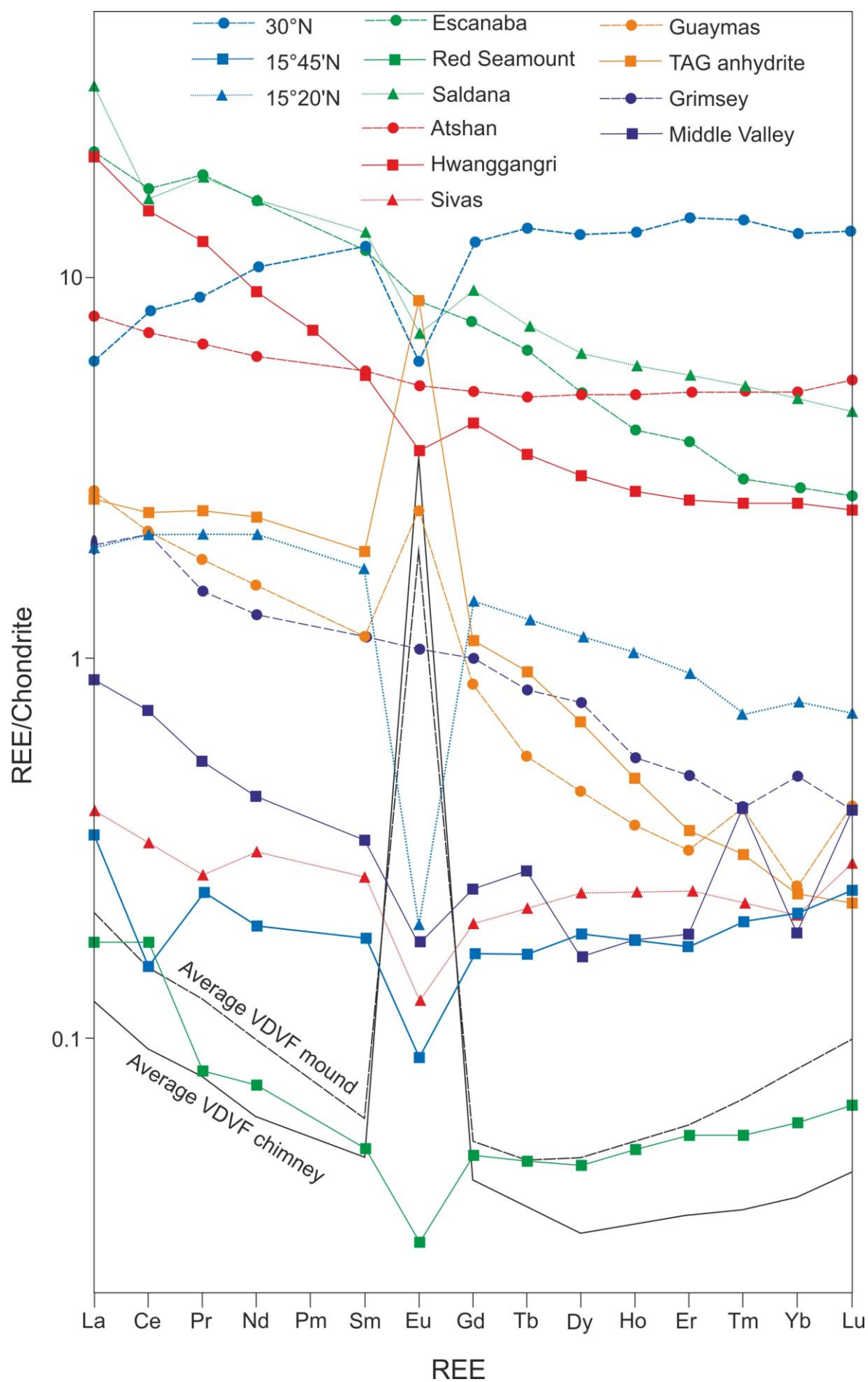


Figure 6.12: (on previous page) Chondrite normalised REE plots of available data from other talc and Mg-silicates recovered from the seafloor. Data is taken from (Alt et al., 1987; Humphris, 1998; Sharara, 1999; Escartin et al., 2003; Shin and Lee, 2003; Boschi et al., 2006; Dias and Barriga, 2006; Paulick et al., 2006; Yalçin and Bozkaya, 2006; Dekov et al., 2008a) and chondrite data from (McDonough and Sun, 1995). Colours and symbols are the same for Figure 6.13.

The REE plots in two of the three samples from the MCR are very similar to those acquired from the VDFV and the surrounding inactive mounds, indicating similar precipitation from a hydrothermal fluid. The other sample from this site has a lower $\text{La}_{(N)}/\text{Sm}_{(N)}$ ratios, and a slightly negative Eu anomaly. The positive Europium anomalies within hydrothermal fluids are generated either by reduction of Eu^{2+} to Eu^{3+} at temperatures $>250^{\circ}\text{C}$ in acidic solutions, or by the dissolution of plagioclase in mafic host rocks (Sverjensky, 1984; Wood, 1990; Bau, 1991; Klinkhammer et al., 1994). Generally, samples from the SPFZ and SWIR do not have the characteristic positive Eu anomalies seen in high temperature vent fluids, except for one sample analysed by (D'Orazio et al., 2004). Instead, the samples recovered from SPFZ and the SWIR have REE plots that closely resemble those of the altered sediments recovered from the Escanaba Trough, Red Seamount and the Saldanha hydrothermal fields (Figures 6.11-6.13; Alt et al., 1987; Zierenberg and Shanks III, 1994). Where diffuse hydrothermal fluid flow alters sediments the resulting precipitates of talc are found to have no Eu anomaly. The europium anomaly in high-temperature vent fluids is caused either by the reduction of Eu^{3+} to Eu^{2+} , or the dissolution of plagioclase in the sub-surface (Sverjensky, 1984). At areas of diffuse flow, the reduction of Eu^{3+} , or the dissolution of plagioclase does not occur as the temperatures ($<50^{\circ}\text{C}$) are too low (Sverjensky, 1984).

Two out of three of the samples analysed from downslope of the VDFV on the MCR are very similar in terms of their petrography and geochemistry to the inactive mounds in close proximity to the VDFV. Along with the discovery of the Mystic Mountain site, this suggests that widespread hydrothermal activity has occurred along the top Mt. Dent, and its true extent is currently unknown.

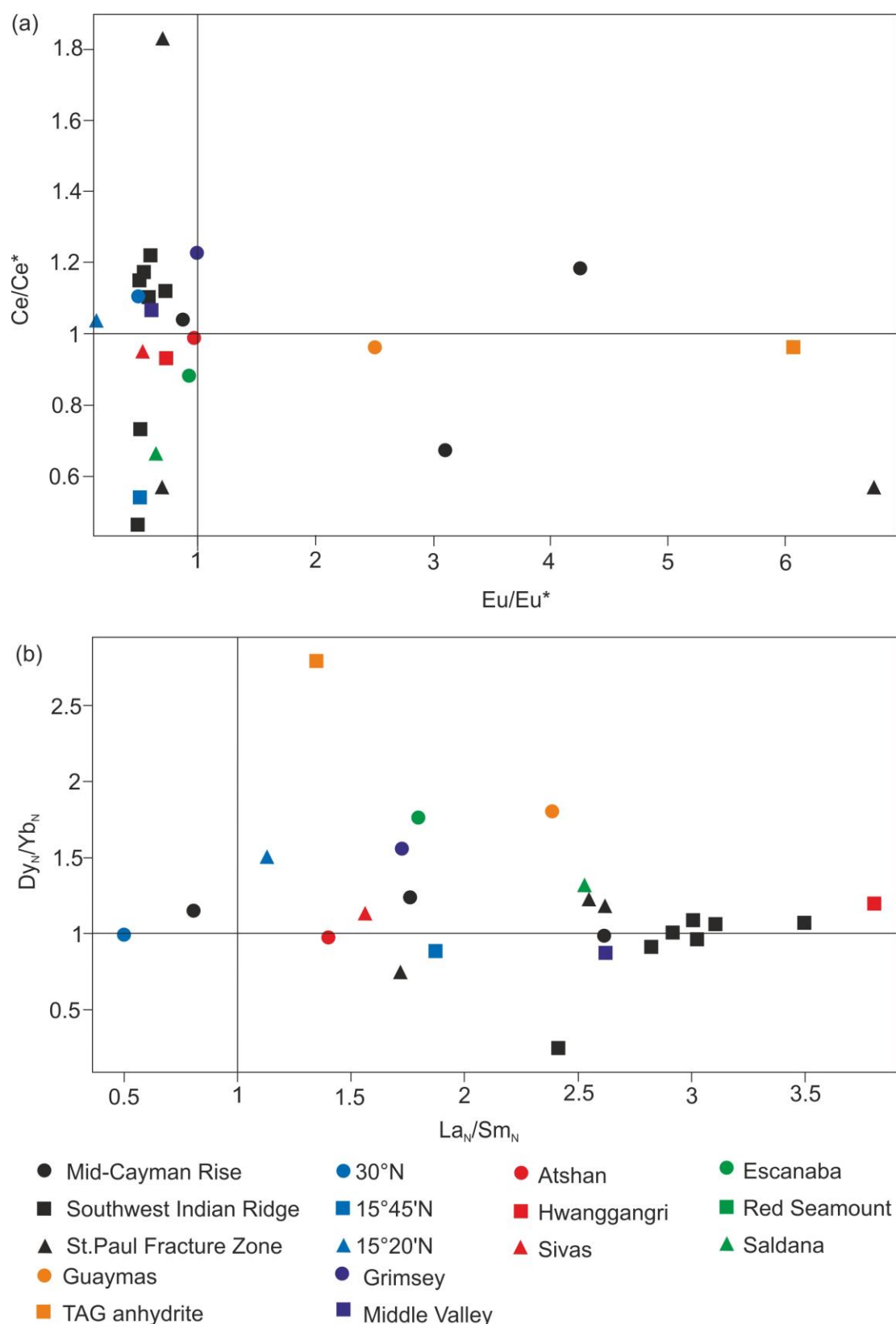


Figure 6.13: REE ratios and anomalies for other talc occurrences (a) Ce/Ce^* plotted against Eu/Eu^* . Indicates that the only samples to display large europium anomalies are mainly those associated direct precipitation from a hydrothermal fluid. (b) $La_{(N)}/Sm_{(N)}$ plotted against $Dy_{(N)}/Yb_{(N)}$. A majority of samples plot in the top right quadrant, indicating slight LREE and HREE enrichment, compared to MREE.

The samples analysed here from the SWIR and SPFZ do not have petrographic textures typical of primary precipitates from hydrothermal vent fluids. Furthermore, the samples show very similar REE plots to other hydrothermally derived sediments in the vicinity of hydrothermally active vent fields, suggesting extinct vent fields exist in close to where the samples were recovered. However, massive sulphide material was also recovered along with the silica and clay samples at the SWIR (Bach et al., 2002), suggesting high temperature venting has occurred nearby in the past.

6.4. Heat flux from the VDVF

The discovery of the VDVF in an off axis setting has implications for both oceanic chemical budgets, and the heat loss from the oceanic crust. It should be noted that the difficulty with quantifying the effect of more VDVF-type hydrothermal systems on the global ridge system is that the observation of an active vent field of this type is a unique discovery.

6.4.1. Assumptions and errors

The methods of estimating the heat and mass fluxes, along with the equations used in the calculations are described in Chapter 2. While this method provides our best estimate for quantifying the heat loss from the VDVF, it includes sources of errors and assumptions that are listed below.

The δT values at each individual chimney structure are calculated using the temperature of ambient seawater and the maximum measured temperature at each vent. This method makes the assumption that the measured vent temperature is uniform across the whole width of the vent orifice.

The area of the chimney was calculated by measuring the radius of each vent orifice using the calibrated lasers on the ROV that are 10 cm apart. While this is an accurate method of measuring the radius of each chimney, it does assume all the vent orifices are perfect circles.

The flow rate measurements were calculated from the upward motion of particles entrained in the upward flow of the vent fluid, and is assumed to be representative of the velocity of the discharging fluid. The particles analysed were those that were exiting as close to the centre of the orifice as possible, making the flow rate estimates the maximum possible.

6.4.2. Hydrothermal heat flux

The total focussed hydrothermal heat flux from the vents across the VDVF is 487 ± 101 MW (Table 6.5). This error is calculated from using the full range of flow rates measured at each vent. Of this heat flux, 82% comes from the Main Hole, which is a large proportion of the >90% of the total VDVF heat flux that comes from chimneys located on the Main Cone. Unfortunately, video data was not available for one small vent on the Main Cone, so it has had to be excluded from the calculation. The heat flux calculated here only takes into account the focussed flow from chimneys, and does not include any diffuse flow, for which we have no data. Estimates for the proportion of diffuse flow at hydrothermal vent fields is highly variable (Kadko et al., 1994; Veirs et al., 2006), and while there appears to be a significant amount at the VDVF at both the hydrothermally active mounds and emanating from the surrounding sediments, the amount is unconstrained. However, this would also contribute to the heat flux from the VDVF, but as it is difficult to quantify from flow measurements, it has been excluded from the calculation of the focussed flux, which is therefore reported here as a minimum estimate.

Mound	Vent orifice	δT (K)	Radius (m)	Vertical Flow rate (m/s)	Calculated heat flux (MW)	Mass flux (kg/s)	EM mass flux (kg/s)
Main Cone	Main Hole	87	0.5	1.5	401 ± 80	1025 ± 205	413 ± 85
Main Cone	Spire	211	0.1	1.5	39 ± 10	41 ± 11	39 ± 5
North spur	Chimlet 2	104	0.1	0.5	6 ± 3	14 ± 6	7 ± 2
North spur	Chimlet 1	39	0.15	1	11 ± 2	61 ± 12	11 ± 5
South spur	X-15	108	0.15	1	30 ± 6	61 ± 6	30 ± 2
Total					487 ± 101	1202 ± 240	500 ± 100

Table 6.5: Estimated heat flux at the VDVF. Errors listed are from variations in the particle velocities at each vent. Heat flux was calculated using the equation $Q = \delta T.C.M$, where Q = focused heat flux, δT = change in temperature, C = specific heat capacity of seawater, EM =end-member, and M = mass flux.

6.4.3. Comparison to other measurements

The assumptions and errors associated with calculating the heat fluxes at hydrothermal vent fields means that out of the >300 active sites known, only ~30 measurements have been recorded (Baker, 2007). These measurements carry large errors, which are occasionally larger than the calculated heat flux, and the same vent field often yields differing results depending on the method (Baker, 2007). For example, the lower and upper estimates for the heat flux at the TAG hydrothermal field are 86 MW and 2000 MW (James and Elderfield, 1996; Goto et al., 2003).

Heat fluxes calculated on vent fields in fast spreading ridges are lower than the flux at the VDVF as hydrothermal systems tend to have closer spacing along the ridge axis than at slow spreading ridges (Baker and German, 2004). The estimates based on other point source measurements for the Main Endeavour Field on the Juan de Fuca Ridge range from 240 MW to 364 MW (Bemis et al., 1993; Ginster et al., 1994), and the fluxes for the 21°N and 9°50'N fields on the East Pacific Rise (EPR) are 200 MW and 325 MW respectively (Converse et al., 1984; Ramondenc et al., 2006). The heat flux at the VDVF is lower than estimates from larger vent fields on slow spreading ridges. The mean estimates for the TAG and Rainbow hydrothermal fields are 758 MW and 1800 MW respectively (Baker, 2007). Although these estimates at slow-spreading ridges are higher than the value calculated for the VDVF, it is clear that there is a significant amount of heat dissipated by the VDVF.

6.4.4. Heat source at the VDVF

Mechanisms for heat extraction from the lower oceanic crust at slow-spreading ridges are not well constrained (Henstock et al., 1993; Phipps Morgan and Chen, 1993; Quick and Denlinger, 1993; Kelemen et al., 1997). Three different methods of driving hydrothermal circulation are magmatism, serpentinisation, and the residual heat of the oceanic crust. These three methods are described and investigated in this section to propose the potential heat source for the VDVF.

Magmatic heat sources on the ridge axis are the most common driver of hydrothermal circulation at seafloor spreading centres e.g. (Stein and Stein, 1994). This style of hydrothermal circulation usually results in metal-rich massive sulphide deposits that

vent fluids at up to $\sim 400^{\circ}\text{C}$ (Tivey, 2007). These hydrothermal systems usually vent fluids that have a much higher H_2S and base metal concentration, and precipitate lower amounts of silicates in comparison to the VDFV (Von Damm, 1995). A magmatic heat source would be unexpected due to the off-axis setting of the VDFV, and the differences in chemistry and precipitate listed above. However magmatic heat cannot be excluded purely on this basis, and the increased permeability generated by detachment faulting may enable deeper hydrothermal circulation and potential extraction of heat from close to the ridge axis (deMartin et al., 2007; McCaig et al., 2007). One method of evaluating whether magmatic heat is plausible at the VDFV is to calculate an estimate for the degree of magma replenishment required to sustain the heat flux using the single-pass model of (Lowell and Germanovich, 2004). This model follows the path of the hydrothermal fluid from downward percolating seawater through to venting at the seafloor at a high-temperature vent field, where circulation is modelled as a singular convection cell with a heat source at the bottom. The heat flux is based upon the conservation of mass throughout the hydrothermal system, and the flow rate of the hydrothermal circulation. The conservation of energy is expressed by the heat balance into the system between conduction from a crystallising magma chamber, and the output of heat from the venting hydrothermal system. This model makes the assumption that heat is transferred directly from a crystallising magma chamber into the base of the circulation cell through an impermeable thermal boundary layer. By using the heat flux from the VDFV, an approximation for the amount of magma that is required for the system can be calculated using Equation 6.1, (Lowell et al., 2013). This gives a result of 0.17 to $0.27 \text{ m}^3 \text{ s}^{-1}$ as a magma replenishment rate, when the errors in the heat flux are taken into consideration, and assumes a steady-state heat flux from the VDFV (using $2.2 \times 10^9 \text{ J m}^{-3}$ for the heat released per unit volume of magma). This value equates to over twice the volume of oceanic crust generated on average at the entire MCR per year (calculated using the full spreading rate of 15 mm yr^{-1} and a magmatic crustal thickness of 3 km). Furthermore it is also very high for an ultra-slow spreading ridge and is greater than the values for other point measurements at fast spreading ridges (Lowell et al., 2013). Hence, the magma replenishment rate at the VDFV, greater than that for a vent field located on the ridge axis at a faster spreading ridge, is considered to be unreasonable. Therefore, a purely magmatic source for the VDFV is unlikely due

to the volume of magma that is required to power it, and the tectonic setting of the vent field.

$$H = V_m H_m \quad (6.1)$$

where: H is the total heat flux out of the hydrothermal system, V_m is the magma replenishment rate, and H_m is the total heat released upon cooling per unit volume of magma. H_m is defined by the latent heat of crystallisation and the heat of cooling magma to the temperatures of hydrothermal circulation.

An alternative source of heat driving hydrothermal circulation in off-axis environments is the serpentinisation of the lower oceanic lithosphere for vent fields with an ultramafic host rock (Lowell and Rona, 2002). Hydrothermal fluids that originate from serpentinisation are much lower in dissolved silica (24-73 $\mu\text{mol kg}^{-1}$) and H_2S ($<0.3 \text{ mmol kg}^{-1}$), and have a much higher pH (~ 11). They result in the precipitation of tall chimneys of carbonate and brucite (Von Damm, 2001) instead of the talc and microcrystalline silica observed at the VDVF. These geochemical characteristics are different to the VDVF and suggest that serpentinisation reactions play little or no part in providing the heat source for the VDVF. Also, serpentinisation reactions are only likely to generate hydrothermal fluids at a few 10s of degrees (Lowell and Rona, 2002), much lower than the $>200^\circ\text{C}$ fluids that vent at the VDVF. Furthermore, the lithologies recovered from the top of the detachment fault thus far indicate that the core complex is dominantly gabbro e.g. (Stroup and Fox, 1981).

Magma chambers at faster spreading ridges tend to restrict hydrothermal circulation to the upper 2 km of the crustal section. However, magma chambers are largely absent at slow-spreading ridges, meaning that the volume of solid, hot crust available to provide heat for hydrothermal circulation is greatly increased compared to where an axial magma chamber is present. This is because the lack of an axial magma chamber allows hydrothermal fluids to percolate deeper into the crust, allowing a greater degree of residual heat extraction from the crust (Humphris and Cann, 2000; deMartin et al., 2007).

The residual heat of the tectonically exhumed lower crust can act as a driver for hydrothermal activity (Allen and Seyfried Jr, 2004). The lower crust and upper

mantle at the seafloor contains residual heat to power hydrothermal circulation, which is made available by continuously downward propagating faults e.g. (Lister, 1974). A simple energy mass balance based on the heat released by the cooling of the host rock down to the hydrothermal vent temperatures is calculated using Equation 6.2. Using the limits imposed by the errors of the heat flux, and adjusting the heat capacity for the temperature of the rock the energy mass balance means that the VDF requires all of the residual heat from 0.007-0.038 km³ of host rock per year. This calculation is based on the heat flux ranging from 386 MW to 588 MW, extracting all the heat from the rock in the temperature range of 400°C to 800°C to generate hydrothermal fluid temperatures of 215°C. The heat capacities are adjusted according to the temperature (1003-1077 J Kg⁻¹K⁻¹), and are the values for a rock of gabbro composition. However there is little variation in heat capacity between serpentinite and gabbro (Waples and Waples, 2004). The calculated volume is equivalent to a 10 km long fault zone, which is 10 m wide exposing and mining the heat from between 71 to 371 m of new crust exposed from faulting per year, or a 15 km long fault zone exposing between 47 and 247 m of new rock to hydrothermal circulation. While this indicates the amount of heat available per year simply from cooling the rock down to hydrothermal circulation temperatures, it is based purely on an energy balance.

$$\text{Total heat} = m \cdot \delta T \cdot C_p \quad (6.2)$$

where: m=mass of rock, δT =the change in temperature from cooling the host rock down from lower crustal temperatures the maximum measured at the VDF and C_p is the heat capacity of the host rock, taken from (Miao et al., 2014).

As described in Chapter 4, the axis-parallel extensional faulting that occurs at the top of Mt. Dent is a key structural control on the distribution of hydrothermal venting at Mt. Dent. The residual heat of the oceanic crust is proposed as a driver for hydrothermal circulation at other seafloor spreading centres (Allen and Seyfried Jr, 2004) and is likely to be the main driver of activity at the VDF. Although there are no time constraints on the active site, the presence of other talc mounds with sediment covers of >1 m suggest hydrothermal activity has been ongoing at the top of Mt. Dent for >20,000 years (Rosencrantz and Sclater, 1986). This episodic hydrothermal activity is in keeping with other vent fields, such as TAG and Lost City, that are

detachment fault controlled (Lalou et al., 1998; Mills et al., 1998; Fröh-Green et al., 2003).

6.5. Global implications of VDVF-type vents

6.5.1. Summary of current knowledge of mid-ocean ridge heat and chemical fluxes

The significant heat and volume flux from the VDVF indicate that if found to be widespread at OCC's, this style of moderate-temperature, silica-rich hydrothermal venting has implications for both the heat loss from OCC's and oceanic chemical fluxes. The methods for estimating the chemical and hydrothermal water fluxes outlined in Chapter 1 are based on mass balances between the inputs (hydrothermal fields, rivers) and sinks (oceanic crust). The discovery of a hydrothermally active vent field emanating moderate temperature fluids on the ridge flanks could potentially alter our understanding of off-axis chemical fluxes into the ocean. The balance of the strontium isotope and magnesium budgets of the ocean are still an unresolved problem (discussed in section 1.6.5), and it is proposed that ridge flank hydrothermal fluxes are of significant importance (Elderfield et al., 1999; Butterfield et al., 2001). One of the issues with the Mg and Sr isotopic budget of the oceans is the observed degrees and depths of hydrothermal alteration within Ocean Drilling Program (ODP) drill cores and ophiolites e.g. (Alt et al., 1986; Bickle and Teagle, 1992). In order to balance the ocean $^{87}\text{Sr}/^{86}\text{Sr}$ ratio and Mg budgets, the degree and depth of alteration observed thus far in the oceanic crust is required to be an underestimate (Alt et al., 1986; Staudigel et al., 1995; Bach et al., 2003). The constraints on the amount of heat available from the oceanic crust are well established by geophysical methods (Stein and Stein, 1994; Mottl, 2003). As a result of this, the flux of low-moderate temperature fluids is important (Davis et al., 2003).

6.5.2. Occurrence of oceanic core complexes and VDVF-type vents

The discovery of the VDVF is significant as it gives further evidence to the importance of OCC's as fluid pathways. The VDVF is the first moderate temperature hydrothermal field to be discovered hosted in gabbro and peridotite on a MOR flank. OCC's have the potential to be widespread at ultraslow-medium spreading ridges as they form at

spreading rates of less than 75 mm yr^{-1} (Cannat et al., 2006; Escartin et al., 2008; Tucholke et al., 2008). The global network of mid-ocean ridges is $\sim 60,000 \text{ km}$ in length (Parsons, 1981), and of this length, approximately 80% is classed as slow-spreading (full spreading rate of $<40 \text{ mm yr}^{-1}$; Murton and Rona, 2015). This is a significant portion of the global ridge system and detachment faulting has been reported at many different localities in the past two decades, including the MAR, SWIR, the Southeast Indian Ridge and the Central Indian Ridge (Cann et al., 1997; Christie et al., 1997; Dick et al., 2003; Cannat et al., 2006; Morishita et al., 2009; Sauter and Cannat, 2010). Furthermore, investigations into the MAR indicate that OCC's may represent up to 50% of the spreading at slow spreading MOR's (Escartin et al., 2008). The occurrence of silicate-rich hydrothermal venting at the SWIR and SPFZ suggests that the processes leading to the formation of the VDFV may not be unique, and have the potential to occur at OCC's along MOR's.

6.5.3. Heat loss at oceanic core complexes and VDFV-type vents

The energy required for the VDFV can be estimated from the flux of dissolved Si. Using the end-member concentration from McDermott (2015), which are better constrained than ours, and the volume of silica in the VDFV deposit, an estimate for the minimum energy required to precipitate it can be derived. Re-arranging Equation 6.2 allows the total mass of hydrothermal fluid that could have precipitated the assemblage within the VDFV. Using the specific heat capacity for seawater at the pressure and temperature conditions of the VDFV, the total heat for the deposit can be calculated (Bischoff and Rosenbauer, 1985; Waples and Waples, 2004). The concentration of dissolved silica in the end-member fluid is 7.5 mmol kg^{-1} (McDermott, 2015), and an estimate for the total Si in the active site is calculated from the average concentration in the whole rock analysis (in Chapter 4) ± 1 standard deviation. This estimate gives a range for the total silica precipitated of 1,290,000-1,620,000 tonnes, which is the equivalent to all the dissolved silica in $6.1\text{-}7.8 \times 10^{12} \text{ Kg}$ of end-member fluid. Substituting this mass of end-member fluid, the heat capacity of seawater at 215°C and 230 bar ($4250 \text{ J Kg}^{-1} \text{ K}^{-1}$) and the δT (211°C – the difference between cold seawater and the hydrothermal fluid) gives a total energy dissipated of between $5.5\text{-}6.9 \times 10^{18} \text{ J}$. This range represents the minimum amount of energy that could have precipitated the silica in the VDFV mounds, assuming that the end-

member concentration has been consistent throughout the formation of the active site. Using the total amount of energy to form the deposit and the residual heat of the oceanic crust, the volume of rock required can be determined as an energy mass balance. The specific heat capacity of the rock is taken from Waples and Waples, (2004) for a basement rock temperature in the range of 400-800°C, and the density of the rock is used is 2.7-3.0 g cm⁻³. The δT is the same as the difference between cold seawater and the hydrothermal fluid (211°C), while the total heat is 1.2-1.4*10¹⁸ J. Inputting these variables into Equation 6.2 gives a total volume of rock to cool the VDF of 1.8-2.2 km³, a small proportion of the total volume of 480 km³ estimated for Mt. Dent (calculated assuming a crustal depth of 3 km; ten Brink et al., 2002). When this total volume of rock is compared to the heat required by the VDF every year, it equates to between 47 and 315 years of steady-state venting. This indicates that venting towards the summit of Mt. Dent is either highly periodical, or the current heat flux from the VDF is not in steady-state.

Although these calculations are based only as an energy mass balance, and do not take into account mechanisms of mining the residual heat, the estimated volume of rock is realistic given the total amount of hot rock available within Mt. Dent, and the lack of other active hydrothermal fields in the vicinity. Furthermore, the periodic activity inferred at the top of Mt. Dent is similar to other hydrothermal fields that are associated with detachment faults, for example TAG.

Mottl, (2003) estimated the total hydrothermal heat loss to be 7.1 ± 2 TW, in crust that is 1-65 Ma. Currently, active hydrothermal venting in off-axis settings is restricted to low temperature, diffuse flow (Mottl et al., 1998; Cooper et al., 2000), or as 91°C, high pH fluids (Von Damm, 2001). Although the current heat flux from the VDF is up to 5 orders or magnitude lower than the global oceanic crustal off-axis heat budget, it is still greater than any other off-axis vent field discovered thus far (Baker, 2007).

6.5.4. Chemical fluxes from the VDVF

The magnesium and strontium isotope budgets are unresolved in terms of the mass balance between the sources and sinks of their oceanic cycles e.g. (Davis et al., 2003; Mottl, 2003). Two reasons why this occurs are that off-axis fluxes are poorly understood, and the currently observed depth of hydrothermal alteration is insufficient to balance the riverine fluxes (Drever, 1974; Palmer and Edmond, 1989).

The removal of Mg from Caribbean bottom water is equivalent to a loss of 52.4 mmol kg⁻¹ (McDermott, 2015). If the VDVF is venting 400-600 kg s⁻¹ of end-member, this is the equivalent to 20-32 mol s⁻¹, or 6.6-10.0*10⁸ mol yr⁻¹ of Mg sequestered into the oceanic crust from seawater. The total global hydrothermal sink of Mg required to balance the riverine input is 4.4-4.8*10¹³ mol yr⁻¹ (Drever, 1974), which is 33-70% that of the 1.6-3.1*10¹³ mol yr⁻¹ calculated by (Mottl, 2003). Understanding the flank fluxes of Mg is highly important due to the temperature dependence on sequestration into the crust (Elderfield and Shultz, 1996). Although there is a significant degree of sequestration of Mg by the fluids circulating at the VDVF, it is approximately five orders of magnitude lower than the amount required for balancing the river flux. This suggests that there are other hydrothermal sinks that must play a part in the oceanic geochemical cycle of Mg, such as off-axis, low temperature diffuse venting.

The end-member fluid has an ⁸⁷Sr/⁸⁶Sr ratio of 0.702908 and the concentrations of 86.8-91.0 µmol kg⁻¹ in the fluid samples show similar concentrations to the seawater value of 89 µmol kg⁻¹. Davis et al., (2003) calculate that the oceanic crust can contribute 3.1±0.8*10⁹ mol yr⁻¹ of strontium with a Mid-Ocean Ridge Basalt (MORB) signature, which is less than a third of the requirement towards maintaining the strontium isotope composition of the oceans. The end-member fluid volume flux from the VDVF is estimated from flow and temperature measurements to be 500±100 kg s⁻¹ (Table 6.5), which is equivalent to an annual mass flux of 1.2-1.9*10¹⁰ kg yr⁻¹. Using the end-member ratio of the VDVF fluid, this is equivalent to a flux of 1.0-1.7*10⁶ mol yr⁻¹ of basaltic strontium. Although this is several orders of magnitude lower than the required amount to balance the global river input of Sr, it is a significant annual input into the oceanic strontium cycle from a single vent field, and one that has thus far

been overlooked. It may also be much more significant if VDVF-types vents are widespread at slow spreading ridges.

The VDVF provides evidence for hydrothermal circulation on the ridge axis that is at significantly greater temperatures (ie. $>100^{\circ}\text{C}$) than that has been recognised thus far. Furthermore, if the VDVF is powered purely by residual heat, than this provides a mechanism for heat extraction at OCC's, and allows hydrothermal circulation to penetrate to greater depths in the crust. If further VDVF-type vents occurred, this would increase the supply of unradiogenic strontium to the ocean, and the degree of magnesium sequestration into the crust. If the processes forming the VDVF are widespread, they have the potential to help balance the oceanic Mg and Sr budgets.

Summary and conclusions

The Von Damm Vent Field (VDVF) was discovered in 2010 following the detection of a hydrothermal plume on the flanks of the Mid-Cayman Rise (MCR) in the Caribbean. It is a talc-dominated hydrothermal system hosted in a basement consisting of variably altered gabbros and serpentinised peridotite, covered by a thin layer of pelagic sediment.

This thesis had the aim of characterising the VDVF in terms of its geological and tectonic setting, and the mineralogy and geochemistry of the hydrothermal precipitates. The chemistry of the fluids was measured and modelled to confirm the stability of the mineral assemblage, and the potential implications of the VDVF were discussed in terms of oceanic geochemical budgets and crustal heat loss.

7.1. Summary of the VDVF

7.1.1. Mt. Dent

The VDVF is situated 13 km to the west of the rift axis of the MCR, and is hosted atop the Mt. Dent oceanic core complex (OCC). The domed surface of the detachment fault rises over 3 km above the rift axis of the MCR, and features axis parallel extensional faulting, which forms in response to the flexing of the brittle exhumed lithosphere. This tectonic extension controls likely controls the orientation of the hydrothermal mounds, and the exposure of the host rocks at both the VDVF and the inactive mounds located further downslope. Lithologies recovered from Mt. Dent include peridotite, serpentinised dunite, mylonite, greenschist, and gabbro.

7.1.2. Local geological setting

The host rocks recovered from within 1 km of the VDVF are mainly gabbros, greenschist facies dykes, one porphyritic dyke and one sample of serpentinised peridotite also sampled. The minerals present within the altered mafic rocks are plagioclase, clinopyroxene, chlorite, hornblende and actinolite, with minor quartz and

relict olivine. The three main mounds of the active site are situated at a seawater depth of approximately 2300 m, and are aligned NNW-SSE. Inactive mounds that are structurally, mineralogically and geochemically similar to the VDVF are found up to 2 km to the east on Mt. Dent, and feature a thin covering of pelagic sediment.

The chimneys and mounds of the VDVF consist predominantly of talc ($\text{Mg}_3\text{Si}_4\text{O}_{10}(\text{OH})_2$), with microcrystalline silica and sulphides. Branching networks of botryoidal talc form in open pore spaces in the active chimneys, whereas primary precipitation textures are reworked into massive and banded talc in the mounds. Microcrystalline silica is seen as a later stage phase infilling pore spaces in the more consolidated chimneys, and intergrown with talc in the active mounds. Sulphides are found either as thin bands precipitating on the margins of colloform talc, or as disseminated grains throughout the groundmass. Chalcopyrite is the dominant sulphide phase at the main cone, whilst at the smaller, lower-temperature chimneys, Fe-sulphides are dominant. Minor amounts of sphalerite and occasional galena are also present in the chimney structures.

7.1.3. Talc precipitation

The rare earth element (REE) profiles on pure talc separates indicate that the active and inactive mounds of talc at the top of Mt. Dent are primary precipitates from a hydrothermal fluid. The pronounced positive Eu anomaly and light rare earth element (LREE) enrichment are characteristic of high-temperature vent fields, whereas the heavy rare earth element enrichment (HREE) is due to the crystallographic controls imposed by talc.

The highest temperature measured at the active vent structures was 215°C and the end-member fluid has a pH of 6. The end-member hydrothermal fluid has elevated chlorinity in comparison to seawater, and less dissolved base metals ($<700 \mu\text{mol kg}^{-1}$) and H_2S ($<1 \text{ mmol kg}^{-1}$) relative to black smoker vent fields. These fluid characteristics are consistent with $<300^\circ\text{C}$ fluid-rock interactions with either a mafic or mafic-ultramafic basement at low water/rock ratios.

$^{87}\text{Sr}/^{86}\text{Sr}_{\text{taic}}$ is between 0.706313 and 0.709130, and plots between the values for seawater (0.70916) and the end-member hydrothermal fluid (0.702908). These ratios are consistent with mixing between conductively heated seawater and the VDVF end-member fluid, which has a $^{87}\text{Sr}/^{86}\text{Sr}$ ratio that suggests a low water/rock ratio.

7.2. Scope for further work

7.2.1. Understanding the processes of heat extraction at oceanic core complexes

The VDVF is the first discovery of a moderate temperature vent field hosted in a dominantly gabbro basement on the upper slopes of an OCC. The orientation of the active and inactive hydrothermal mounds, pock marks, and exposure at the top of Mt. Dent suggest that axis-parallel extensional faulting plays a role in forming the VDVF. The residual heat of the tectonically exhumed oceanic crust is the likely driver for hydrothermal activity up to 13 km away from the rift axis, but the mechanisms for cooling the lower crust are still poorly understood. If these processes were better constrained, then it would enhance our understanding for the processes that could generate hydrothermal circulation along the ridge flanks.

7.2.2. Discovery of VDVF-type vents

One of the issues with discovering further VDVF-type fields is the lack of a neutrally buoyant nephel plume immediately above the system, which only shows small anomalies in temperature and oxidation potential. This renders other VDVF-type fields difficult to detect using methods of plume detection such as CTD (conductivity, temperature, depth) and LSS (light scattering sensor). New developments, such as autonomous underwater vehicles (AUVs), mean that the potential for new discoveries in the past decade has greatly increased, although many parts of the global ridge system remain unexplored, particularly in off-axis settings. The VDVF is hosted atop an OCC, a tectonic feature that has the potential to form at ~80% of the global ridge system, but are poorly explored at the resolution for hydrothermal vent fields. The discovery of the VDVF further enhances the emergence of detachment faulting being important at mid-ocean ridges, in terms of the oceanic crustal heat loss, and the

controls on hydrothermal circulation. However, further discoveries of off-axis venting are required in order to characterise the heat and chemical fluxes along the ridge flanks.

7.2.3. Prediction of mineral assemblages

The unusual chemistry of the hydrothermal fluid that vents at the VDVF is inferred to result from moderate temperature interaction with a mafic-ultramafic basement, although the mineralogy is not constrained. In order to characterise the basement of the VDVF, further thermodynamic calculations using The Geochemists' Workbench could be conducted to predict the mineral assemblage that the end-member VDVF fluid is in equilibrium with. These calculations would enable the mineral assemblages in the underlying basement to be estimated, provide a greater understanding of the conditions required for VDVF-style vents, and increase the potential of future discoveries.

7.3. Concluding remarks

The VDVF singles itself out as a new class of hydrothermal system due to a combination of the hydrothermal precipitate, tectonic setting and fluid chemistry. It is the first silicate-rich active vent field to be discovered hosted in a dominantly gabbro basement, on the upper slopes of an OCC. Detachment faulting is a strong control on hydrothermal circulation at slow-spreading ridges as it enables heat extraction from depths in the crust. Furthermore, the diversity of host rock leads to a greater variety in the geochemistry of vent fluids and their hydrothermal precipitates.

The recovery of other talc samples from downslope of Mystic Mountain and the VDVF, along with silicate-rich extinct deposits at the Southwest Indian Ridge and the St. Paul Fracture Zone, suggest that moderate temperature, off-axis hydrothermal deposits are more widespread at medium-slow spreading ridges than originally thought. The VDVF therefore represents a previously unseen style of active hydrothermal venting on the flanks of a MOR, and deposits of this type could potentially play a role in controlling ocean chemistry and the heat loss from the oceanic crust.

Appendix A

Methods and analytical procedures

This section will describe in detail the methods for all geochemical procedures, including inductively coupled plasma mass spectroscopy (ICP-MS), inductively couple plasma atomic emission spectroscopy (ICP-AES), strontium isotopes, X-Ray fluorescence (XRF), X-Ray diffraction (XRD). The error calculation associated with the heat flux estimate is also included.

A.1. XRD

A.1.1. Bulk

Representative areas for bulk XRD analysis were chosen from hand specimens. These aliquots were crushed manually in an agate pestle and mortar to avoid damaging the crystal structures of the samples. The sample size normally used in analysis was between 80 to 100 μm .

A.1.2. Clays

Samples that showed the presence of clays in the bulk analysis were crushed further using an agate pestle and mortar, and the clay proportions were then separated using the following method. Approximately 5 grams of sample was added into a 100 ml solution of de-ionised water with an MgCl_2 concentration $\sim 2 \mu\text{mol kg}^{-1}$ and placed in an ultrasonic bath for 15 minutes. 5 ml of a dispersion agent (Calgon) was added to prevent the particles from flocculating and the solution was left to settle for 3 hours. The floating particles were then siphoned off and centrifuged at 3200 rpm for 6 minutes. The water was decanted off and a further 100 ml of $\sim 2 \mu\text{mol kg}^{-1}$ MgCl_2 solution was added and centrifuged for a further 3 minutes at 3200 rpm.

A.2. Preparation of whole rock samples for XRF

Representative areas for geochemistry were chosen after considering the hand specimens. Some of the chimney samples were fragile and were impregnated with resin before cutting. In the case of these samples, aliquots for geochemistry were taken beforehand to avoid contamination. Powders for whole rock analysis were crushed in agate mills using a Fritsch planetary ball mill rotating at 300 rpm for at least ten minutes, until the powders were completely homogeneous. These were then placed in an oven at 80°C overnight to dry the samples and then placed in a desiccator. Approximately one gram of sample was used to determine loss on ignition (LOI). The samples were weighed into ceramic crucibles and placed in a furnace at 1200°C for three hours, and then weighed afterwards to determine LOI. Fused glass beads were made using a Sigma Vulcan Fusion X-ray flux at a ratio of 10:1 lithium tetraborate flux to sample powder.

A.3. Preparation of talc separates and whole rock samples for trace element analysis

Talc was handpicked under an Olympus SZH binocular microscope and crushed using an agate pestle and mortar. The sample powders were then placed in clean beakers with clean dilute hydrochloric acid (~2 M; HCl). Samples were placed in an ultrasonic bath at 50°C for 40 minutes and the acid siphoned off afterwards. After drying in an oven overnight at 80°C, the process was repeated using de-ionised water (total organic carbon = 3 ppb; resistivity = 17.9-18.1 megohm cm⁻¹) instead of HCl. For the host rock and Woods Hole Oceanographic Institute (WHOI) samples, representative areas of the hand specimen were selected and crushed into powder using the same method as for preparing the XRF powders. The samples were then processed using the same method as the talc separates, except the powders were only treated in de-ionised water and not HCl. After the powders were dried, they were removed from the beakers and placed in clean, 7ml snap-lid glass vials. They were then digested in acid at 3 different stages, all under clean lab conditions. Firstly, ~400 mg of pure talc powder or ~100 mg of whole rock was weighed into 15 ml Teflon® vials.

Approximately 1 ml of concentrated nitric acid (HNO₃) was added to the Teflon, followed by 4 ml of concentrated hydrofluoric acid (HF). The vials were then placed

on a hot plate in a fume cupboard at 130°C and left overnight. This solution was then dried down on a hot plate in a fume cupboard and 5 ml of 6 M HCl were added and the samples were left overnight. After drying down again, a further 5 ml of 6 M HCl were added and the samples again placed on a hotplate at 130°C overnight. The solution was transferred from the Teflon into 30 ml plastic bottles that had been cleaned in 10% HNO₃ overnight and rinsed with de-ionised water. The sample was washed into the bottle from the Teflon by rinsing three times with 6 M HCl and then with de-ionised water to ensure no sample was left behind. Accurate dilution factors were derived by weighing the bottles empty, and after the samples were added. Aliquots of these mother solutions were taken for trace element analysis, dried down, and made up to ~10 ml at ~4000x dilution in 3% HNO₃.

A.4. Preparation and procedure of samples for strontium isotope analysis

Strontium isotopes were conducted from the same talc digested solutions as used in the ICP-MS sample preparation. The concentrations of strontium within the talc were low so only ~200 ng of strontium was available. For the host rock samples, 1 µg of strontium was run through columns made either of Teflon or plastic.

As described in Section 2.5.5, fluid samples were partitioned between a digested precipitate and the fluid phase. The total amount of strontium was calculated in both phases using ICP-MS analysis, which allowed the appropriate amount of each solution to be dried down to give 1 µg of total strontium. This was done to counter the effects of any fractionation between the water phase and solid phase that precipitated in the titanium syringes.

The talc samples were ran through cation resin AG50-X8 200-400 before running through Sr-spec, and the procedure is outlined below.

- 200 µm of each sample was dissolved in 200 µl of 1.75 M HCl.
- Columns were cleaned in de-ionised water, added to plastic racks and the resin was added to just below the top of the funnel.
- The samples were conditioned with 8 M of 1.75 M HCl (strength accurately measured by titration).

- 200 µl of sample in 1.75 M HCl loaded in, with a further 200 µl of 1.75 M HCl after for washing in.
- The columns were eluted with 6 ml of 1.75 M HCl and the waste pots were switched with 15 ml Teflon vials.
- 5 ml of 1.75 M HCl was added, and the samples collected in 15 ml Teflon pots
- The resin was then washed, firstly with 12 ml of 6 M HCl, and then with 12 ml of de-ionised water.

After running through the cation columns, the talc samples, along with the fluid and host rocks, were ran through Sr-spec columns through the following procedure:

- The sample was dried down in Teflon vials and 200 µl of 3 M HNO₃ acid was added.
- The columns, previously left soaking in ~10% HNO₃, were washed thoroughly in de-ionised water and placed in plastic racks with waste pots beneath.
- The columns were continually topped up with de-ionised water and Sr-spec resin was added to the top of the funnel and allowed to settle. Where present, any air bubbles were removed with a prewashed pipette.
- Resin was added into the columns until the level was just below the top part of the funnel.
- The resin was cleaned by running 1.5 ml of de-ionised water, 1.5 ml of 3 M HNO₃ (molar strength accurately determined by titration) and a further 1.5 ml of de-ionised water.
- A further 1.5 ml of HNO₃ was added to condition the resin.
- The 200 µl of sample was added and washed in with a further 200 µl of HNO₃. The columns were then eluted with 3 M of HNO₃, 2 ml for the Teflon funnels, and 2.5 ml for the plastic funnel. After elution, the waste bottles were replaced with Teflon vials, and 1.5 ml of de-ionised water was added and collected for loading onto filaments. The columns were then washed in de-ionised water and placed in ~10% HNO₃ to clean.

Filaments were cleaned by removing the previous filament using sandpaper and then placed in a clean beaker of de-ionised water with a small (<5%) fraction of hydrogen peroxide. The beaker was placed on a hotplate at 130°C for 2 hours to clean the filament holders. These were then placed in an oven at 80°C to dry. The filament

holders were then removed from the oven and allowed to cool. The rhenium/tantalum filaments were then welded to the holders outgassed under a vacuum using a ThermoScientific Bakeout Device and left overnight for sample loading the next day.

1.5 μl of H_2O that was collected after running through columns was dried down and 1 μl of 1M HCl was added to re-dissolved the sample before loading. While the sample was re-dissolving, the current of the filament was set to 1.6 A and two strips parafilm were added 3-4 mm apart on the outgassed filaments. The current was turned down to 0 and 1 μl of Sr loading solution with 1 M H_3PO_4 was added onto the centre of the filament in 0.25 μl steps, with the current turned up to 0.8 mA after the first aliquot was added. After the loading solution had dried down suitably, the 1 μl of sample was added slowly in 3-4 aliquots at a current of 0.8 mA. After the whole sample was added, the current was increased in 0.2 mA steps slowly to dry the sample down. When a current of 2.0 mA was reached, the filament was covered with a beaker and the current turned up until the filament glowed red and left for 5 seconds. Finally the current was turned off and the sample removed ready for analysis.

A.5. Preparation of samples for stable isotope analysis

1-2 mg samples of handpicked talc/quartz or standard were weighed into a nickel holder that could hold up to 12 samples at a time. After the sample had been added to the chamber and pumped down to a vacuum, a small amount of reagent (FCl_3) was introduced and the laser placed on the sample and gradually heated up. While reacting with the reagent, the sample glows brightly and usually takes up to 5 minutes to react completely. When the sample had stopped glowing, the laser was switched off and any unreacted reagent was frozen down. A mercury pump removes any contamination from fluoride compounds and the O_2 was converted to CO_2 by reaction with a heated carbon rod. The sample was then frozen down into glass bottles using liquid nitrogen ($\sim -195^\circ\text{C}$) and sealed for analysis. All 12 slots in the sample holder could be filled when analysing quartz and standards but unfortunately the talc powders reacted with the reagent without the laser and so had to be analysed individually along with a single standard. The standard was changed each time to allow plotting of a calibration line.

Samples of talc were handpicked under a binocular microscope and washed in acid and de-ionised water following the methods described above. Platinum crucibles were cleaned in HF and then ~30 mg of sample were added and left to outgas overnight at 110°C. The line was heated to evaporate any previous water lining the glass and pumped away to leave the line under vacuum. The samples were placed in a glass tube and within a radiofrequency induction coil. The voltage of the coil was increased gradually for 20 minutes until at 200 volts (giving a temperature in excess of 1000°C) and then left for 40 minutes. The sample is instantly frozen down using a liquid nitrogen trap. At the end of the heating cycle, the liquid nitrogen is replaced by slush trap (combined acetone and dry ice, at ~-80°C) to remove CO₂. Water was then released from the slush trap and passed through a chromium furnace at 800°C to reduce the water to pure H₂. The sample yield was then measured using a manometer and pumped into a glass tube for analysis.

A.6. Hydrothermal fluids

The fluid samples precipitated a small amount of material within the bottles, and this solid phase was acid digested as per the methods for the talc and the concentrations of each dissolved element were weighted accordingly. The tables displaying the concentrations in each phase are listed in Tables A.1-A.3.

Sample		198-GT1	198-GT2	200-GT1	200-GT3	200-GT4	202-GT3	202-GT4
Water fraction (g)		22.0523	21.1370	21.5756	20.6741	21.9043	21.3020	21.0807
Na	ppm	12865	11993	12265	12432	12547	12554	11444
Li	ppb	1226	777	946	981	1022	1003	504
B	ppb	2922	3761	3247	3180	3163	3278	4111
Mg	ppm	360	775	664	630	694	576	1020
Si	ppm	350	214	164	169	165	155	146
K	ppm	610	520	552	561	555	562	463
Ca	ppm	606	546	520	533	538	563	480
Fe	ppb	1070	374	7426	20200	19374	7772	9073
Sr	ppb	8183	8104	7995	8015	8014	8088	7868
Rb	ppb	381	244	329	349	351	353	186
Mn	ppb	444	258	555	672	758	638	544

Table A.1: Concentrations of dissolved elements within the water phase of hydrothermal fluid.

Sample		198-GT1	198-GT2	200-GT1	200-GT3	200-GT4	202-GT3	202-GT4
Solid weight (g)		0.2550	0.3429	0.1214	0.6397	0.7520	1.2902	0.8933
Na	ppm	3700	B.D.L.	3154	7070	5529	1726	1623
Li	ppb	266	B.D.L.	219	566	624	63	B.D.L.
B	ppb	B.D.L.	B.D.L.	410	934	712	170	272
Mg	ppm	91	B.D.L.	447	904	1405	134	178
Si	ppm	32	B.D.L.	59	74	117	29	76
K	ppm	139	B.D.L.	116	276	217	63	55
Ca	ppm	186	14	139	307	241	77	69
Fe	ppb	B.D.L.	B.D.L.	56907	470658	95752	12342	5672
Sr	ppb	3480	50	2792	5464	4522	1553	1363
Rb	ppb	108	B.D.L.	84	205	166	51	32
Mn	ppb	135	B.D.L.	434	1055	1468	248	171

Table A.2: Concentrations of elements within the solid phases that precipitated within the fluid sample bottles. B.D.L.=below detection limit

Sample		198-GT1	198-GT2	200-GT1	200-GT3	200-GT4	202-GT3	202-GT4
Total (g)		22.3073	21.4799	21.6970	21.3138	22.6563	22.5922	21.9740
Na	ppm	12760	11802	12214	12271	12314	11936	11045
Li	ppb	1215	764	941	968	1009	950	483
B	ppb	2889	3701	3231	3113	3082	3101	3955
Mg	ppm	357	763	663	638	717	551	986
Si	ppm	347	210	164	166	164	148	144
K	ppm	604	512	550	553	544	534	447
Ca	ppm	602	538	518	526	528	535	464
Fe	ppb	1057	368	7703	33719	21909	8033	8934
Sr	ppb	8129	7975	7966	7939	7898	7715	7604
Rb	ppb	378	240	327	345	345	336	180
Mn	ppb	441	254	554	684	782	616	529

Table A.3: Weighted concentrations of dissolved elements from both solid and water phases.

A.7. Heat flux calculations

The errors associated with the calculated heat flux were derived by variations in flow velocity measurements on particles entrained in the exhuming hydrothermal fluid. The variation in particle velocity for each vent is listed in Table A.4 and an image of the main hole is shown in Figure A.1. Also included as an electronic submission is a video of the main hole showing the section of video used in calculations.

Velocity (m/s)	Main Hole 91°C	Spire 215°C	North Spur 108°C	North Spur 43°C	South Spur 112°C
0.3			1		
0.4					
0.5			4		
0.6					
0.7			2		
0.8					2
0.9				4	
1.0					2
1.1		2		2	3
1.2	1			2	
1.3	2				
1.4	2	3			
1.5	4	4			
1.6	2	2			
1.7	2	3			
Average	1.5	1.5	0.5	1	1

Table A.4: Variations in the velocities of entrained particles.

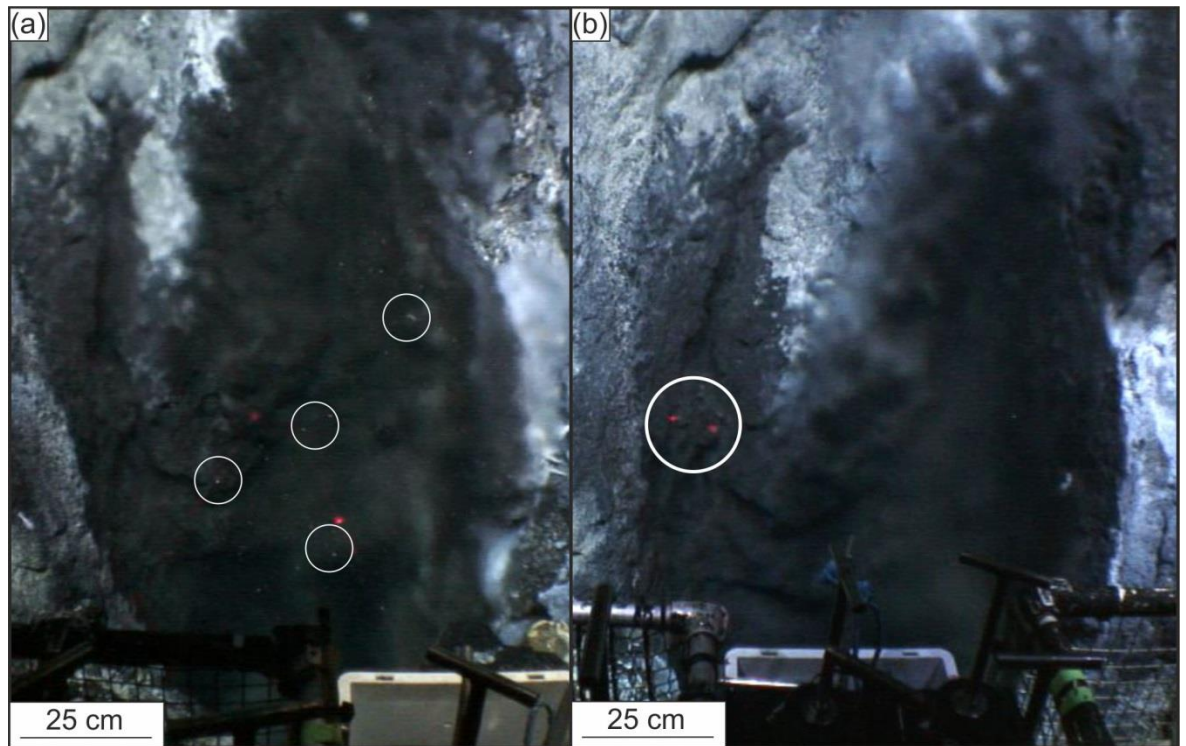


Figure A.1: velocity flow measurements at the main hole (a) particles entrained in the flow at the main hole (circled) (b) calibration of the distances was done using lasers 10 cm across directed onto the back of the vent structure.

Appendix B

Nature Communications manuscript

This section includes the uncorrected proofs of a manuscript submitted to *Nature Communications* submitted on the 10th June 2015, and accepted on the 9th November 2015.

ARTICLE

Received 10 Jun 2015 | Accepted 9 Nov 2015 | Published 22 Dec 2015

DOI: 10.1038/ncomms10150

OPEN

Talc-dominated seafloor deposits reveal a new class of hydrothermal system

Matthew R.S. Hodgkinson^{1,2}, Alexander P. Webber¹, Stephen Roberts², Rachel A. Mills², Douglas P. Connelly¹ & Bramley J. Murton¹

The Von Damm Vent Field (VDVF) is located on the flanks of the Mid-Cayman Spreading Centre, 13 km west of the axial rift, within a gabbro and peridotite basement. Unlike any other active vent field, hydrothermal precipitates at the VDVF comprise 85–90% by volume of the magnesium silicate mineral, talc. Hydrothermal fluids vent from a 3-m high, 1-m diameter chimney and other orifices at up to 215 °C with low metal concentrations, intermediate pH (5.8) and high concentrations (667 mmol kg^{-1}) of chloride relative to seawater. Here we show that the VDVF vent fluid is generated by interaction of seawater with a mafic and ultramafic basement which precipitates talc on mixing with seawater. The heat flux at the VDVF is measured at $487 \pm 101 \text{ MW}$, comparable to the most powerful magma-driven hydrothermal systems known, and may represent a significant mode of off-axis oceanic crustal cooling not previously recognized or accounted for in global models.

¹National Oceanography Centre, Waterfront Campus, Southampton SO14 3ZH, UK. ²Ocean and Earth Science, National Oceanography Centre Southampton, University of Southampton, Southampton SO14 3ZH, UK. Correspondence and requests for materials should be addressed to M.R.S.H. (email: matthew.hodgkinson@noc.soton.ac.uk).

Hydrothermal activity at mid-ocean ridges is dominated by basalt-hosted, high-temperature, metal-rich vent systems driven by magmatic activity¹. However, the discovery of ultramafic-hosted hydrothermal vent fields (for example, the high-temperature Rainbow and the low-temperature Lost City Vent Fields) demonstrates the diversity of hydrothermal activity associated with medium-slow spreading ridges^{2,3}. Tectonic exposure of upper mantle and lower crustal rocks gives rise to a more heterogeneous basement than at intermediate-fast spreading ridges, and detachment faulting provides pathways to enhance hydrothermal circulation^{4,5}.

A new class of hydrothermal system, the Von Damm Vent Field (VDVF), was discovered in the Caribbean during cruise JC044 of the RRS *James Cook* in April 2010, which hosts a community of hydrothermal vent fauna similar to those at the Mid-Atlantic Ridge⁶. The VDVF hydrothermal plume is rich in methane, has a significant Eh anomaly (indicative of reduced fluids) and is free of metallic particulates⁶. Here we describe how the unusual mineralogy of the VDVF results from mixing between moderate-temperature vent fluid and cold seawater. The processes leading to the formation of the VDVF may

be widespread throughout medium to ultraslow mid-ocean spreading ridges medium-ultraslow spreading mid-ocean ridges and could play a significant role in the cooling and chemical exchange between oceanic crust and seawater.

Results

Geological setting. The VDVF is located on the western flanks of the ultraslow spreading Mid-Cayman Spreading Centre, the deepest spreading centre on Earth (Fig. 1a). It is situated at a depth of 2,280 mbsl, 13 km to the west of the rift axis^{6,7} on the upper slopes of Mt Dent, an oceanic core complex (OCC) formed by detachment faulting (Fig. 1b). At this location, the basement age is estimated to be between 1 and 2 Ma (based on distance from spreading centre and spreading rate) and comprises meta-gabbro, dolerite dykes and serpentinized peridotites that are partially covered by calcareous pelagic sediment⁷. The hydrothermally active area of the VDVF comprises three overlapping conical-shaped talc mounds, up to 75 m high and 150 m in diameter, aligned north-northwest–south-southeast (NNW-SSE) (Fig. 1c). The summit of the largest mound (Main

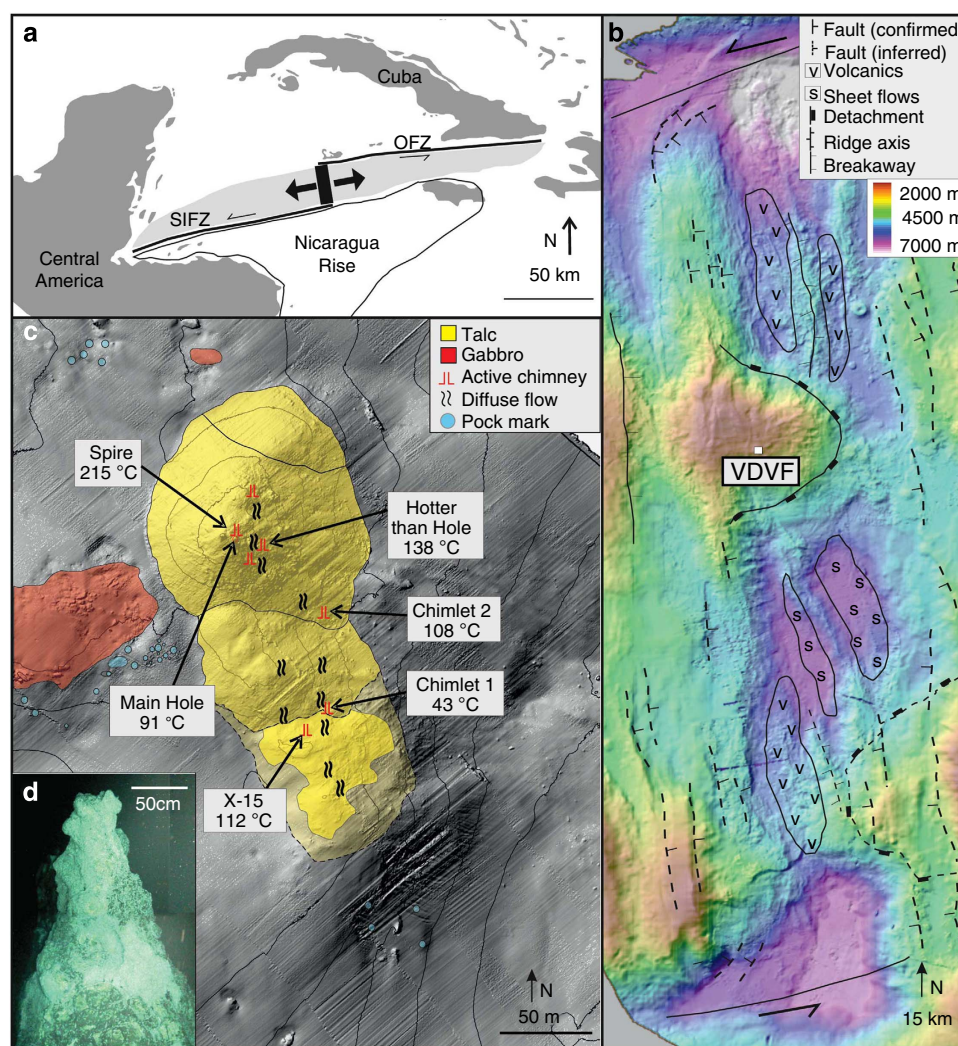


Figure 1 | Location and bathymetry of the VDVF. (a) map of the Caribbean showing the location of the Mid-Cayman Rise and the black rectangle represents the area of **b**; the lightly shaded area is the area occupied of the Cayman Trough; OFZ, Oriente Fracture Zone; SIFZ, Swan Island Fracture Zone. (b) Bathymetry and interpretative geology of the Mid-Cayman Rise showing regional tectonic structures. (c) Bathymetry of the active VDVF showing the location of hydrothermal activity across the vent field. Contours are at 20-m intervals. (d) Photomosaic of The Spire at the top of the main VDVF cone obtained from high-definition video.

Cone), which is the northern mound at the active site, hosts a 3-m tall, 1-m diameter chimney (The Spire, Fig. 1d). Hydrothermal fluid venting (215 °C) from The Spire has low concentrations of particles and a pH of 5.8 (determined at standard temperature and pressure (STP)). A 1-m diameter orifice (Main Hole) located at the base of The Spire vents fluids of up to 91 °C. Elsewhere across the VDVf, smaller orifices vent fluids of up to 138 °C (for example, Hotter than Hole, Chimlets 1 and Chimlets 2—Fig. 1c). Talc rubble at the base of the *Main Cone* onlaps the surrounding calcareous sediment—a relationship reversed at the base of the southern mound, indicating an increase in the age of the mounds towards the south (Fig. 1c). A further series of hydrothermally inactive, conical-shaped talc mounds is located 700 m to the south and east of the three active mounds. These include a 90-m high, sediment-covered cone (Mystic Mountain), which has twice the volume of the Main Cone. Samples from these extinct mounds are similar in composition, mineralogy and texture to the active mounds. With an estimated sedimentation rate of between 2 and 5 cm ka^{−1} (ref. 8), a thickness of 1 m or more of pelagic sediment covering most of Mystic Mountain indicates that its construction by hydrothermal activity ceased at least 20,000 years ago.

Petrology. Compared with hydrothermally active seafloor deposits elsewhere, the mounds and chimneys of the VDVf are highly unusual, constituting 85–90% talc by volume with up to 10% microcrystalline silica and 5% disseminated sulphides (Supplementary Fig. 1). In hand-specimen, the hydrothermally active chimneys show millimetric layers of laminated and botryoidal talc (Fig. 2a). These layers are parallel and have an internal colloform structure (Fig. 2a). Under scanning electron microscope (SEM), broken surfaces reveal dendritic networks and

botryoidal masses of talc, indicative of growth into open void spaces (Fig. 2b,c). Concentric bands of sulphide up to 50-μm thick are present as internal growth bands within the talc masses (Fig. 2d) and microcrystalline silica infills pore spaces (Fig. 2e). Talus forming the flanks of the mounds has a similar mineralogy to the venting chimneys, except that the botryoidal texture and open pore spaces are largely replaced by massive fine-grained talc, and the associated sulphides are mostly oxidized. Contrary to initial reports⁶, talc is the dominant mineralogy at the VDVf; only two of 50 samples recovered contain trace amounts of anhydrite and gypsum. Together with its botryoidal form, zoning, and layering. The talc deposits indicate precipitation from a hydrothermal fluid. The petrology of the hydrothermally active chimneys indicates a paragenetic sequence comprising initial talc growth into open space with co-precipitation of minor sulphide, followed by infilling of the pore space by later-stage microcrystalline silica. Loss of sulphides and a reduction in base-metal content in the flank talus indicate dissolution following exposure to cold and oxygenated seawater.

Mineralogy. Bulk X-ray diffraction analyses (Supplementary Fig. 1) and microscopy of the VDVf chimney and mound material confirm the dominant presence of talc, with microcrystalline silica and sulphide constituting up to 15%. Chalcopyrite is the dominant sulphide (70%), indicative of episodically higher vent temperatures⁹, with the remainder being 20% pyrite, 5% sphalerite and 5% galena. The presence of sulphides at the VDVf, and a lack of sulphate in the end-member fluids, confirms a reducing environment for the precipitation of the chimney and mound talc deposits¹⁰.

Other studies of talc, recovered from seafloor environments elsewhere, have revealed significant amounts of intracrystalline

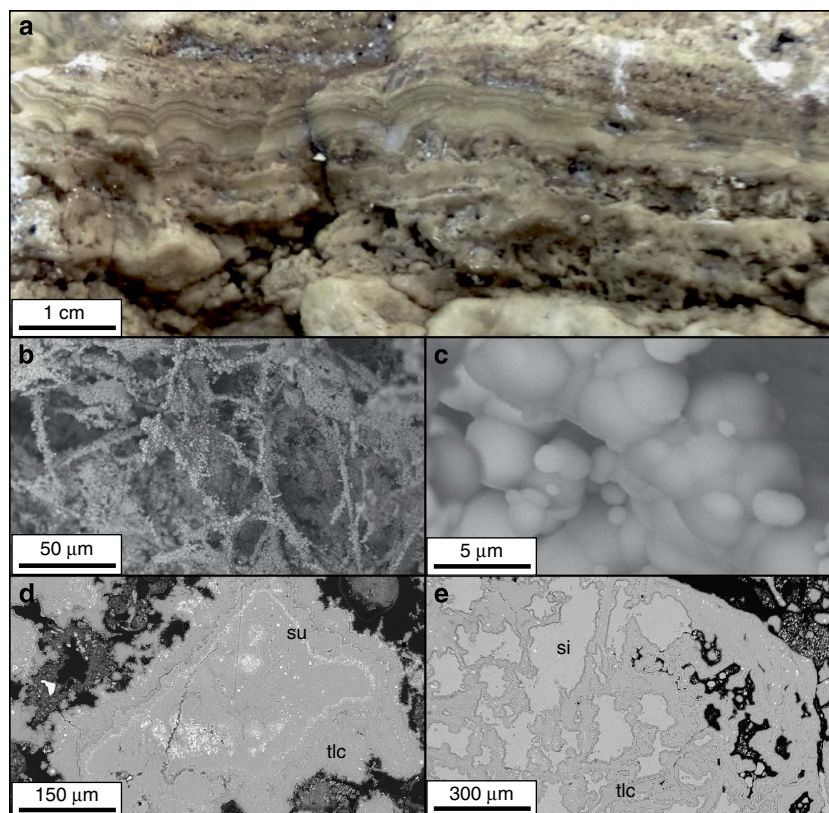


Figure 2 | Hand-specimen and SEM images of VDVf samples. (a) Collapsed chimney wall showing bands of massive talc. (b) and (c) SEM images of dendritic and botryoidal talc networks. (d) SEM image of a cross section through botryoidal talc with bands of sulphide. (e) SEM image showing microcrystalline silica precipitated into a talc framework with disseminated sulphides. Legend: tlc = talc, su = sulphide, si = microcrystalline silica.

layers of smectite clays reflecting the influence of sediment alteration and precipitation from Mg-rich pore waters¹¹. X-ray diffraction analyses of unorientated air-dried mounts of talc separates from the VDFV chimneys and talus deposits show peaks at ~ 9.6 Å (for the 001 plane) and ~ 4.7 Å (Supplementary Fig. 2) confirming talc ($\text{Mg}_3\text{Si}_4\text{O}_{10}(\text{OH})_2$) as the dominant phase. Shifts in peaks of the 001 plane from 9.604–9.627 Å for the air-dried mounts to 9.339–9.525 Å for the glycolated mounts show the presence of up to 10% of a smectite clay that is interlayered within the crystalline talc structure. The presence of peaks at 1.529 and 1.532 Å (for the 060 plane) indicate a tri-octahedral structure for the smectite clay interlayers (Supplementary Fig. 2). The dominance of talc (90%), with up to 10% clay interlayers, contrasts with previously reported, sediment-hosted seafloor talc deposits¹¹.

Deposit geochemistry. The high proportions of talc and microcrystalline silica are reflected in the whole-rock geochemistry (Table 1) by the high concentrations of SiO_2 (52–66 wt.%) and MgO , (25–34 wt.%). Average base-metal concentrations in the hydrothermal chimneys are 1,463 p.p.m. Cu, 239 p.p.m. Zn and 112 p.p.m. Pb. In contrast, concentrations in samples of mound talus are an order of magnitude lower with averages of 241 p.p.m. Cu, 48 p.p.m. Zn and 15 p.p.m. Pb, consistent with the observed oxidation and loss by dissolution of sulphides in the talus samples.

Rare earth element (REE) patterns for talc, separated from hydrothermally active chimneys and mound talus samples, have shallow U-shaped profiles dominated by a large and positive europium anomaly (Fig. 3). Enrichment in the light RREs (LREEs) is indicated by $\text{La}_{(N)}/\text{Sm}_{(N)}$ (where N = chondrite-normalized values) ratios ranging between 0.9 and 10.4, with an average of 3.3 for chimneys and 3.1 for mound talus (Table 2). The REE profiles also have slight enrichment in heavy RRE (HREE) with average $\text{Dy}_{(N)}/\text{Yb}_{(N)}$ ratios of 0.8 for chimney material and 0.9 for the mound talus. The magnitude of the positive Eu anomaly, defined as Eu/Eu^* (where $\text{Eu}/\text{Eu}^* = \text{Eu}_{(N)}/\sqrt{(\text{Sm}_{(N)} \times \text{Gd}_{(N)})}$), ranges between 6 and 228, with an average of 99 for the chimneys and 58 for the mounds (Fig. 3 and Table 2). The VDFV chimney and talus talc have $^{87}\text{Sr}/^{86}\text{Sr}$ ratios of between 0.706313 and 0.709168, respectively, which are similar to, but slightly less than, that of modern-day seawater (0.7092)¹². This contrasts with the surrounding meta-gabbros that have $^{87}\text{Sr}/^{86}\text{Sr}$ ratios of between 0.702902 and 0.703657 (Tables 2 and 3).

The U-shaped REE patterns and positive Eu anomalies in the chimney and mound material indicate talc precipitation from VDFV vent fluid that has some similarities to high-temperature ‘black smoker’ vent fluid REE chemistry¹³. Reducing conditions in the VDFV vent fluid, indicated by the presence of sulphides, enhance Eu mobility by the formation of divalent Eu chloride complexes, especially during the dissolution of plagioclase, resulting in large, positive Eu anomalies in fluids and precipitates¹⁴. Furthermore, the VDFV talc $^{87}\text{Sr}/^{86}\text{Sr}$ ratios indicate precipitation following mixing of the high-temperature VDFV vent fluid with a high proportion of seawater (of at least 10:1). Chlorinity in the end-member VDFV fluid of 667 mmol kg^{-1} is significantly elevated in comparison with seawater (546 mmol kg^{-1}), enhancing the complexation of LREEs in relation to mid-RREs (MREEs) and HREEs in hydrothermal solutions at high temperatures and pressures, resulting in elevated $\text{LREE}_{\text{talc}}/\text{MREE}_{\text{talc}}$ ratios¹⁵. In contrast, moderate HREE enrichment is largely a crystallographic effect of the talc mineralogy, where HREEs substitute in the octahedral Mg site as a result of the ionic radii being of a more similar size compared with the LREEs¹⁶.

Other examples of seafloor talc deposits, reported from the St Paul and Conrad fracture zones, are inferred to have precipitated from the interaction of hydrothermal fluid with either seawater or a mafic protolith¹⁷. These talc samples have positive Eu anomalies and flat HREE profiles (Fig. 3), closely resembling those for the VDFV chimney and mound talus¹⁷. Seafloor talc deposits from elsewhere lack a positive Eu anomaly and have flat HREE profiles, consistent with formation as alteration products of an ultramafic protolith or sediment (Fig. 3)^{17,18}. In contrast, the positive europium anomaly for the VDFV talc is consistent with primary precipitation from hydrothermal fluids. The radiogenic $^{87}\text{Sr}/^{86}\text{Sr}$ ratios for the talc further indicate that a significant component of seawater is mixed with the vent fluid during talc precipitation.

We conclude from the petrographic and geochemical evidence that the VDFV talc is a primary precipitate from a hydrothermal fluid mixed with seawater. To date, no other seafloor, talc-dominated, active hydrothermal vent field has been reported, making the discovery of the VDFV a new and unique class of hydrothermal system.

Vent fluid chemistry. To explore whether the VDFV is currently precipitating talc, we sampled and analysed the composition of the vent fluids escaping from three different chimneys with a maximum measured temperature range of 108–215 °C (Table 3). It should be noted that the vent temperatures and fluid chemistry samples are decoupled, which precludes the possibility of extrapolating to an end-member temperature using fluid chemistry. Instead, we use the highest measured temperature of 226 °C (ref. 19) and assume that this approaches the end-member temperature. We find that our vent fluid samples lie on a mixing line between seawater and zero Mg (Fig. 4). This is consistent with an end-member vent fluid from which Mg has been quantitatively removed in the subsurface²⁰. When extrapolated to zero Mg, the VDFV end-member fluid has a moderate pH of 5.8 (at STP; Table 3) and a dissolved Si concentration of 7.5 mmol kg^{-1} (ref. 21). End-member concentrations of K ($17.5 \text{ mmol kg}^{-1}$) and Li ($241 \mu\text{mol kg}^{-1}$) are much higher than those generated by phase separation of seawater alone (Fig. 4c and Table 3), indicating significant exchange with subsurface host rocks²⁰. Strontium isotopes for the VDFV fluid samples also lie on a mixing line against Mg/Sr with seawater indicating an end-member vent fluid $^{87}\text{Sr}/^{86}\text{Sr}$ of 0.702908, close to the basement rock values of 0.702902–0.703657 (Fig. 4d and Tables 2 and 3). Base-metal concentrations in the fluid samples range from 6.6 to $604 \mu\text{mol kg}^{-1}$ for Fe, 4.6 – $14.2 \mu\text{mol kg}^{-1}$ for Mn and 0.4 – $460.0 \mu\text{mol kg}^{-1}$ for Cu, but do not show conservative mixing with seawater and hence end-members cannot be derived (Table 3). Variation in base-metal concentrations and ratios between hydrothermal vents across the VDFV suggests subsurface processes of precipitation and/or zone refining within the talc mounds. Owing to highly variable concentrations, reliable end-member vent fluid Fe and Mn concentrations could not be determined. However, the range of concentrations of Fe and Mn are 10–1,000 times lower than those reported for the Rainbow ‘black smoker’ end-member vent fluid². In contrast, a chlorinity of 667 mmol kg^{-1} for the end-member fluid is 22% higher than ambient seawater (546 mmol kg^{-1}), indicating a process of brine concentration.

The low metal concentrations as well as the near-neutral pH of the fluids venting at VDFV are consistent with temperatures in the water–rock reaction zone, which are significantly cooler than the ~ 500 °C calculated for ‘black smoker’ vents²². It is also known that elevated hydrogen sulphide concentrations in ‘black smoker’ hydrothermal vents are related to magmatic input²³.

Table 1 Whole-rock geochemistry.												
Type	Sample	SiO ₂ (wt.%)	TiO ₂ (wt.%)	Al ₂ O ₃ (wt.%)	Fe ₂ O ₃ (wt.%)	MgO (wt.%)	CaO (wt.%)	K ₂ O (wt.%)	Na ₂ O (wt.%)	P ₂ O ₅ (wt.%)	LOI (wt.%)	Sum (wt.%)
Mound	198-03	62.12	0.01	0.27	0.16	31.26	0.08	0.04	0.18	0.01	5.70	99.81
Mound	198-04	56.54	0.01	2.75	1.15	30.08	0.20	0.09	1.27	0.00	7.66	99.75
Mound	198-05	57.88	0.02	0.70	0.68	29.51	1.81	0.10	0.43	0.02	8.50	99.65
Mound	199-09	60.90	0.01	0.46	0.28	31.18	0.19	0.05	0.22	0.01	7.20	100.50
Mound	199-10	66.11	0.01	0.18	0.27	28.10	0.08	0.03	0.13	0.00	5.50	100.41
Mound	200-21	63.66	0.01	0.18	0.39	28.90	0.10	0.05	0.12	0.01	8.55	101.96
Mound	200-23	59.91	0.01	0.17	0.28	31.41	0.27	0.09	0.22	0.02	7.30	99.68
Chimney	200-24	57.61	0.01	0.02	0.81	28.33	0.41	0.14	0.68	0.02	11.60	99.63
Mound	201-34	61.12	0.01	0.04	0.44	32.10	0.22	0.12	0.52	0.02	5.70	100.27
Mound	201-36	58.51	0.01	1.00	0.71	30.53	0.15	0.07	0.44	0.01	7.70	99.13
Chimney	201-37	53.51	0.01	0.24	0.57	30.71	0.06	0.07	0.24	0.02	9.63	95.04
Mound	201-38	58.39	0.01	0.31	0.29	31.77	0.37	0.09	0.38	0.01	9.10	100.70
Mound	201-39	54.26	0.09	2.04	0.90	34.19	0.06	0.02	0.22	0.12	8.79	100.68
Mound	201-40	56.47	0.01	0.60	0.38	32.70	0.12	0.07	0.37	0.01	8.77	99.50
Chimney	202-43	57.99	0.01	0.19	0.33	31.81	0.18	0.10	0.43	0.01	8.30	99.33
Chimney	202-45	51.85	0.01	0.05	0.41	31.04	0.32	0.07	0.35	0.06	15.10	99.25
Chimney	202-46	60.05	0.01	0.07	0.34	30.58	0.18	0.06	0.25	0.02	12.17	103.73
Chimney	202-48	66.22	0.01	0.71	0.37	25.51	0.15	0.06	0.43	0.01	6.26	99.71
Chimney	202-49	54.83	0.01	0.05	0.49	30.79	0.32	0.07	0.31	0.03	12.76	99.65
Chimney	199-107	58.31	0.01	0.65	0.64	30.92	0.15	0.07	0.40	0.01	8.78	99.94
Chimney	199-110	57.05	0.01	0.19	0.19	30.73	0.21	0.08	0.41	0.02	11.02	99.91
Chimney	44-1E	58.12	0.01	0.44	1.13	27.81	0.12	0.09	0.59	0.01	11.50	99.80
Mound	44-2G	58.50	0.02	0.58	0.52	30.34	1.01	0.10	0.52	0.04	9.03	100.66
As (p.p.m.)	Ba (p.p.m.)	Cd (p.p.b.)	Cs (p.p.b.)	Cu (p.p.m.)	Mn (p.p.m.)	Nb (p.p.b.)	Ni (p.p.m.)	Pb (p.p.m.)	Rb (p.p.b.)	Sb (p.p.b.)	Sr (p.p.m.)	Zn (p.p.m.)
2.3	6.0	198	21	51.7	124.3	14	3.1	12.8	434	292	2.9	26.9
1.0	7.3	26	28	44.8	107.6	16	1.2	7.4	710	44	16.8	14.4
3.2	12.0	108	344	506.5	163.9	269	7.2	22.8	2,148	260	47.9	72.7
1.0	0.3	14	40	82.5	151.2	22	2.6	1.2	636	44	8.9	12.3
0.9	0.1	228	15	154.8	133.4	4	1.2	35.4	270	325	2.4	47.3
5.4	1.3	316	60	1,292.7	182.1	4	1.5	66.1	569	1,696	3.4	161.8
2.3	143.6	25	111	100.2	143.5	107	6.0	2.2	1,589	87	26.2	19.9
0.9	0.6	45	111	4.2	2,721.0	4	0.6	0.2	1,826	43	28.2	2.6
2.8	1.0	34	90	31.7	1,518.5	14	3.7	2.7	1,500	136	13.0	8.7
1.3	0.8	16	39	110.0	239.3	20	0.6	12.6	771	40	11.6	44.5
2.4	0.4	3,249	71	4,307.7	233.6	12	3.1	324.5	794	2,402	10.4	569.4
2.5	0.7	63	80	250.9	279.3	46	8.8	21.3	1,305	328	25.7	62.9
1.3	1.2	13	64	117.1	148.9	76	6.5	2.2	1,045	107	9.3	29.7
4.7	0.2	22	49	253.0	165.3	11	5.7	19.8	1,047	454	14.5	43.9
8.1	0.8	2,028	107	970.2	463.9	23	4.7	116.6	1,216	3,767	11.0	234.7
43.3	0.8	2,807	47	1,165.3	328.4	23	14.0	5.3	820	8,229	171.9	52.9
75.3	0.8	2,791	51	1,663.4	237.1	16	5.7	25.7	767	25,719	68.0	123.3
5.8	0.3	848	35	471.1	175.2	4	1.6	20.2	495	4,703	7.2	77.9
65.8	1.7	2,431	47	1,948.8	277.6	4	6.5	31.6	839	20,425	154.3	144.2
2.6	2.0	134	63	1,178.4	205.0	84	2.7	23.1	819	442	9.8	43.3
2.4	0.9	120	66	1,416.4	240.5	109	2.6	16.8	1,154	257	14.1	33.1
20.7	0.3	5,975	83	5,871.7	212.9	12	9.7	658.9	873	25,042	8.4	1,272.7
5.4	5.2	63	134	588.9	551.5	372	13.1	70.5	1,938	798	59.1	148.2

ICP-AES, inductively couple plasma atomic emission spectroscopy; ICP-MS, inductively coupled plasma mass spectrometry; VDFV, Von Damm Vent Field; XRF, X-ray fluorescence. Major and trace elements within hydrothermal active samples from the VDFV. Major elements were derived by XRF and trace elements derived by ICP-AES and ICP-MS.

Hence, we suggest the low H₂S concentrations at the VDFV are indicative of minimal magmatic contribution, consistent with the lower temperature of the end-member vent fluid and the ridge-flank setting of the vent field.

Increases in chlorinity for hydrothermal fluids interacting with an ultramafic basement have been suggested to occur in a number of ways: rock alteration, phase separation and brine and halite addition^{2,24}. Temperatures in excess of 360 °C are required to phase-separate seawater at 200 bar (that is, at the depth of the VDFV) and even higher for deep subsurface reactions²⁵. This is considerably hotter than the maximum temperature recorded at the VDFV²¹ and would require substantial subsurface cooling by

seawater circulating deep within the talc mounds for which there is no evidence. The dissolution of residual halite, or the mixing with residual brine formed during an earlier and higher-temperature period of hydrothermal circulation and phase separation deep in the crust, could increase the end-member chlorinity^{26,27}; however, the VDFV and surrounding area lacks any mineralogical evidence for a ‘black smoker’-like phase of venting. The process of serpentinization also has the potential to increase fluid chlorinity by the removal of water from the fluid^{2,21}. Using the equation for the serpentinization of pure forsterite to serpentine and brucite (equation (1)), we calculate that the increase in chlorinity for the VDFV end-member fluid

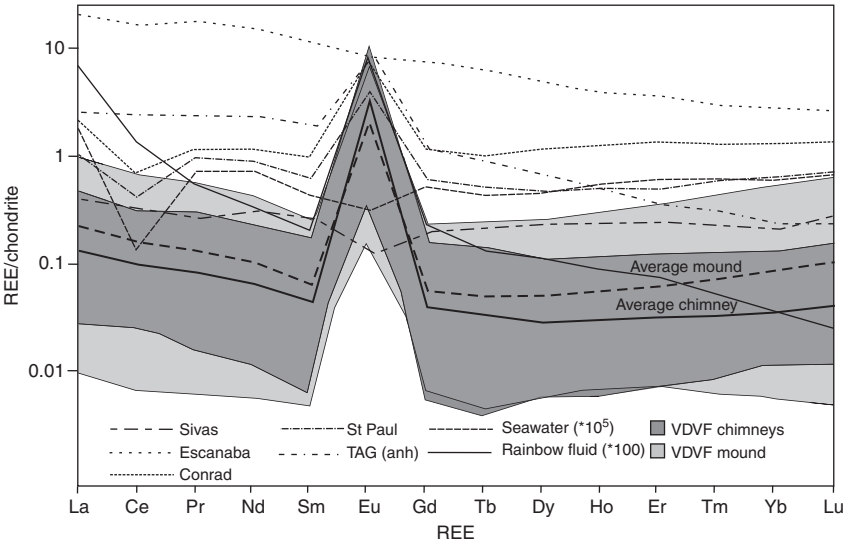
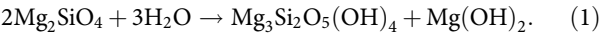


Figure 3 | REE plots. Chondrite-normalized REE patterns showing the range and average concentrations of the VDFV mound ($n = 15$) and chimney ($n = 9$) materials. The patterns are characterized by light and heavy REE enrichment and large positive Eu/Eu^* anomalies. Also shown for comparison are samples from the St Paul Fracture Zone, Conrad Fracture Zone, Escanaba Trough, ($n = 5$), Sivas Basin ($n = 2$), TAG anhydrite ($n = 24$), Rainbow hydrothermal vent fluids ($n = 2$) and seawater^{2,17,54–56}.

Table 2 REE geochemistry.																
Type	Sample number	La (p.p.b.)	Ce (p.p.b.)	Pr (p.p.b.)	Nd (p.p.b.)	Sm (p.p.b.)	Eu (p.p.b.)	Gd (p.p.b.)	Tb (p.p.b.)	Dy (p.p.b.)	Ho (p.p.b.)	Er (p.p.b.)	Em (p.p.b.)	Yb (p.p.b.)	Lu (p.p.b.)	⁸⁷ Sr/ ⁸⁶ Sr
Mound	198-03	46.8	157.8	7.0	20.3	2.8	126.0	2.8	0.3	1.8	0.4	1.3	0.2	1.0	0.2	0.708685
Mound	198-04	4.0	9.8	1.4	6.5	2.3	16.6	4.5	0.8	5.7	1.3	3.9	0.6	4.3	0.6	0.708937
Mound	198-05	243.1	430.5	55.5	204.1	39.0	74.9	36.0	5.7	37.1	8.4	26.0	4.3	31.0	5.2	N.D.
Mound	199-09	36.8	83.4	8.7	34.6	7.4	83.4	9.7	1.5	10.7	2.5	8.0	1.3	9.5	1.7	N.D.
Chimney	199-10	19.7	68.1	4.8	17.8	2.6	109.6	3.0	0.4	2.4	0.7	2.3	0.3	2.3	0.3	N.D.
Chimney	199-107	19.8	49.5	6.1	25.5	6.6	77.7	9.2	1.2	7.7	1.6	4.3	0.6	4.2	0.7	N.D.
Chimney	199-108	7.3	17.6	2.0	9.0	2.4	20.9	3.4	0.5	3.6	0.8	2.6	0.4	2.8	0.5	0.709032
Chimney	199-110	12.1	28.2	3.6	15.0	3.5	58.2	5.0	0.8	5.3	1.3	4.1	0.7	6.2	1.2	0.709067
Mound	200-23	94.2	176.2	21.7	81.1	17.2	143.8	17.7	3.0	20.8	5.0	16.8	2.9	22.7	3.8	0.707526
Chimney	200-24	35.2	72.0	8.3	33.7	6.6	176.0	6.6	0.7	4.0	0.9	2.3	0.3	2.0	0.3	0.708375
Mound	201-34	63.7	173.6	17.9	68.5	9.7	372.5	10.7	1.2	7.6	1.7	5.5	0.8	5.3	0.8	N.D.
Mound	201-35	7.7	26.7	3.3	16.4	5.3	21.2	6.9	1.1	6.4	1.3	3.9	0.6	5.0	0.8	0.708949
Mound	201-36	23.5	52.1	5.6	22.1	4.5	75.2	5.1	0.6	3.3	0.7	1.5	0.2	1.1	0.2	0.708770
Mound	201-38	11.4	28.3	3.4	15.9	5.0	77.7	8.6	1.2	7.8	1.7	4.5	0.6	3.9	0.7	0.709083
Mound	201-39	12.5	25.5	3.0	12.2	1.9	102.9	2.3	0.2	1.9	0.4	1.3	0.2	1.3	0.2	N.D.
Mound	201-40a	5.9	11.0	1.7	7.2	1.7	94.8	3.3	0.5	4.0	1.1	3.7	0.5	3.6	0.5	0.709168
Mound	201-40b	2.6	4.5	0.6	2.9	0.8	38.9	1.4	0.2	1.5	0.4	1.3	0.2	1.0	0.1	N.D.
Chimney	202-43	21.0	30.3	4.3	16.8	3.4	275.3	4.4	0.6	4.6	1.2	3.6	0.6	3.3	0.6	0.708824
Chimney	202-47	8.5	19.5	1.7	6.1	1.0	84.2	1.2	0.2	1.7	0.4	1.3	0.2	2.2	0.4	0.708308
Mound	202-48	3.7	11.0	1.4	6.7	2.0	9.6	3.3	0.5	3.8	0.9	2.9	0.5	3.2	0.6	0.706313
Chimney	44-1A	114.9	193.9	28.8	109.3	26.4	617.4	32.2	5.3	27.8	6.7	20.7	3.2	21.6	4.0	N.D.
Chimney	44-1F	48.7	85.6	12.3	47.4	8.2	260.0	9.8	1.7	9.7	2.2	7.3	1.4	9.1	1.4	N.D.
Mound	44-2C	73.4	153.5	19.3	76.3	15.9	119.7	15.7	2.5	18.5	4.7	16.5	3.6	36.3	7.7	N.D.
Mound	44-2O	164.0	179.3	39.8	158.3	31.9	404.1	47.7	9.2	65.2	17.1	57.7	11.2	88.7	16.3	N.D.
Host	199-11	1,149.7	3,549.6	535.8	2,545.0	762.8	387.0	948.8	167.4	1,116.2	238.1	710.7	111.6	773.9	119.1	0.702902
Host	199-14	1,702.2	6,215.1	1,121.0	6,194.4	2,104.9	826.2	2,748.4	485.8	3,155.3	660.1	1,893.2	282.3	1,822.6	265.7	0.703189
Host	199-18	6,570.5	30,208.5	2,562.0	12,293.1	3,551.1	1,212.2	4,294.8	736.2	4,569.9	948.2	2,621.5	383.0	2,394.7	345.8	0.703657
Host	199-19	1,951.4	7,873.6	821.3	4,272.1	1,495.6	742.1	2,087.1	365.4	2,358.3	501.0	1,378.8	199.7	1,262.0	184.6	0.702997

N.D., not determined; REE, rare earth element; VDFV, Von Damm Vent Field.
REE concentrations and ⁸⁷Sr/⁸⁶Sr in pure talc and host rock from the hydrothermally active VDFV. Samples were all recovered during cruises JC044 and JC082 (refs 57,58). Please refer to the Methods section for analytical precision and errors.

could result from serpentinization at a ratio of 944 g of forsterite to 1 kg seawater. The presence of any mineralogical Cl in serpentine makes this estimate a minimum.



We have calculated a mass flux of end-member hydrothermal fluid at VDFV of $\sim 500 \text{ kg s}^{-1}$ (see below) for which the increase in chlorinity requires brine expulsion following serpentinization of pure forsterite at a rate of at least 470 kg s^{-1} . Alternatively, the entrainment of an early-formed brine or halite phase is consistent with a cooling hydrothermal system, while serpentinization is

compatible with the tectonic setting of the VDFV on slowly exhumed lower-crust and upper-mantle rocks. Both processes are ultimately constrained by the availability of residual brine, halite or fresh peridotite.

Fluid pH. A measured pH of 5.8 (at STP) for the VDFV end-member fluid is significantly higher than the observed range (pH 2.5–3.5) for sulphide-rich, high-temperature ‘black smoker’ vent fluids. It is also lower than the alkaline, low-temperature fluids vented at the ultramafic-hosted Lost City Vent Field^{3,20}.

Table 3 | Fluid data.

Sample number		198-GT1	198-GT2	200-GT1	200-GT3	200-GT4	202-GT3	202-GT4	End-members			Seawater
Site		The Spire	The Spire	Hotter than Hole	Hotter than Hole	Hotter than Hole	Chimlet 2	Chimlet 2	VDVF	Rainbow	Lost City	
Depth	m	2,291	2,291	2,307	2,308	2,308	2,379	2,379	2,379-2,291	2,300	700-800	
Max temperature	°C	215	215	138	138	138	108	108	215	365	91	4
pH		6	6.2	6.2	6.1	6.2	6.2	7	5.8	2.7	9	8.2
Cl	mmol kg ⁻¹	643	592	610	599	603	601	574	667	745-756	541	546
Mg	mmol kg ⁻¹	14.7	31.4	27.3	26.3	29.5	22.7	40.6	0	0	0-1.3	52.8
Ca	mmol kg ⁻¹	15	13.4	12.9	13.1	13.2	13.4	11.6	16.4	66.6	26.6-27.4	10.3
Na	mmol kg ⁻¹	555	513	531	534	536	519	480	589	553	49.4	469
K	mmol kg ⁻¹	15.5	13.1	14.1	14.1	13.9	13.6	11.4	17.5	20.2-20.4	10.5	10.2
Fe	μmol kg ⁻¹	18.9	6.6	138	604	392	144	160	N.D.	23,600-25,000	<0.01	0.001
Sr	μmol kg ⁻¹	92.8	91.0	90.9	90.6	90.1	88.0	86.8	N.D.	200	N.D.	91
Mn	μmol kg ⁻¹	8	4.6	10.1	12.4	14.2	11.2	9.6	N.D.	2,200-2,350	N.D.	0
Ba	μmol kg ⁻¹	5.55	2.61	3.23	5.11	5.4	5.43	2.52	8.4	59-79	N.D.	0.07
Li	μmol kg ⁻¹	175	110	136	140	145	137	69.6	241	327-345	43-46	24.5
Cu	μmol kg ⁻¹	1.11	0.46	94.5	460	289	4.56	1.39	N.D.	121-162	N.D.	<0.001
H ₂ S	mmol kg ⁻¹	0.927	0.898	0.332	0.439	0.967	0.635	n.d.	N.D.	1.2	0.06	<0.001
SO ₄	mmol kg ⁻¹	7.85	15.1	12.5	11.7	11.4	10.6	20.1	0	0	0	28.2
⁸⁷ Sr/ ⁸⁶ Sr		N.D.	0.706725	0.706174	0.705989	0.705958	0.705873	0.707801	0.702908	N.D.	N.D.	0.7092
K/Cl		0.024	0.022	0.023	0.024	0.023	0.023	0.02	0.026	0.027	0.019	0.019

N.D., not determined; VDVF, Von Damm Vent Field.
VDVF fluid dissolved elemental concentrations from three hydrothermal vents around the active VDVF, with the end-member vent fluid obtained by extrapolation to zero Mg concentration. End-member hydrothermal vent fluid data from the Lost City and Rainbow hydrothermal fields are included for comparison^{2,3,38,59}.

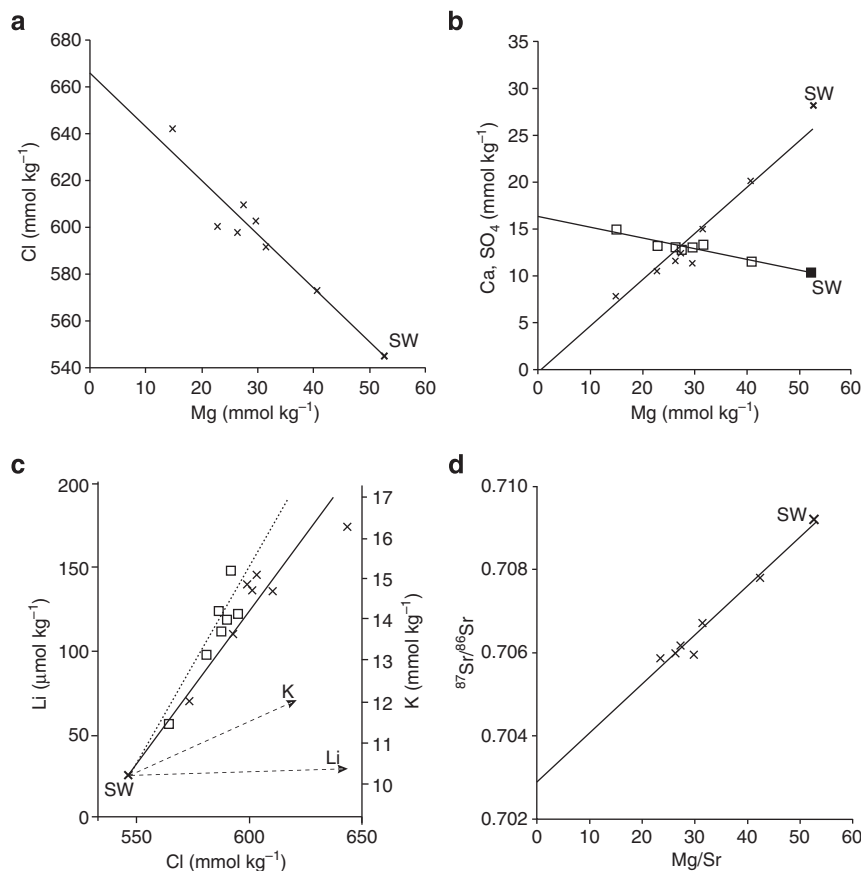
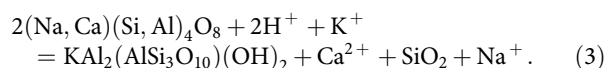
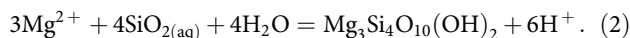


Figure 4 | VDVF fluid plots. (a,b) The top diagrams show Cl, SO₄ (crosses) and Ca (squares) with best fit lines extrapolated to zero Mg concentration. (c) Plots of Cl versus Li and K. The solid line and crosses indicate the linear trend of Li towards seawater (SW); the dashed line and squares indicate the linear trend of K towards SW. The arrows indicate the expected increase in Li, K and Cl concentration resulting from phase separation of seawater alone. (d) Ratios of ⁸⁷Sr/⁸⁶Sr plotted against Mg concentration in fluid samples and extrapolated to zero Mg/Sr to determine the VDVF end-member vent fluid ratio.

Hydrothermal fluids with intermediate pH (5–6) can result from the interaction of seawater with mafic and/or ultramafic lithologies at temperatures <300 °C (refs 28,29). Under these conditions, pH is controlled by the balance between Mg removal from seawater and silicate hydrolysis (equation (2)). At low water/rock ratios (<10), the rate of magnesium consumption is relatively low, and silicate hydrolysis acts as a pH buffer (equation (3)). At high water/rock ratios (>50), H⁺ is produced at a rate greater than it is used up in hydrolysis reactions, resulting in lower pH²⁸.



With its intermediate pH, 215 °C temperature and setting on lower-crustal and upper-mantle rocks, the fluids venting at the VDFV are consistent with moderate-temperature interaction within a gabbro/peridotite basement (equation (3)).

Talc precipitation. Thermodynamic modelling using the Geochemist's Workbench and SUPCRT92 (refs 30–32), under the ambient pressure and temperature conditions of the VDFV, predicts instantaneous precipitation of talc and silica as the primary phases on mixing the 215 °C VDFV end-member vent fluid with cold seawater (Fig. 5a). Both phases remain supersaturated throughout the mixing regime until seawater makes up ~90%, and the fluid reaches ~25 °C (Fig. 5b). Below this temperature, talc remains undersaturated that, together with the kinetics of the reaction, may explain why talc was not visibly precipitating in the hydrothermal plume. Oscillatory zoning of talc and silica within active chimneys indicates a fluid composition at the VDFV that fluctuates around the intersection of the talc–silica saturation limits in the H₂O–HCl–(Al₂O₃)–MgO–SiO₂ system. A fluid composition around the eutectic between talc and amorphous silica would be influenced by slight changes in Mg or Si activity, brought about either by precipitation of one or the other phase, or by fluctuating seawater proportions within the mound. Silica is saturated in the end-member fluid, therefore would precipitate when no seawater is available to provide Mg for talc precipitation. Such dynamic conditions, which are well documented at other sites^{33–35}, could lead to alternating layers of mineral phases. Bands of chalcopyrite also indicate episodically higher temperatures. The prediction that talc precipitates directly as a result of mixing between the VDFV vent fluid and seawater is further supported by the range of ⁸⁷Sr/⁸⁶Sr ratios for the talc (0.706313–0.709168), which lie between the value of modern seawater (0.7092) and the VDFV end-member hydrothermal fluid (0.702908; Tables 2 and 3 and Fig. 4).

The dissolved silica concentrations in the VDFV end-member fluids are similar to those reported from 'black smoker' vents²⁰, where talc is also theoretically stable on mixing with cold seawater. However, the large quantity of sulphides precipitated at these vent sites results in talc and other silicates only occurring as accessory minerals (for example, Middle Valley)³⁶. At the VDFV, the low metal content of the fluid results in only accessory amounts of metal sulphides, allowing talc and silica to become the dominant phases. By comparison, the higher pH of the Lost City vent fluids results in calcium carbonate and brucite precipitation instead of talc³.

In summary, the geochemistry of the solid and fluid phases and thermodynamic modelling are consistent with the observed texture of the talc, its growth into pore spaces, the presence of actively venting talc chimneys and the precipitation of significant volumes of talc-forming large conical mounds on the seafloor.

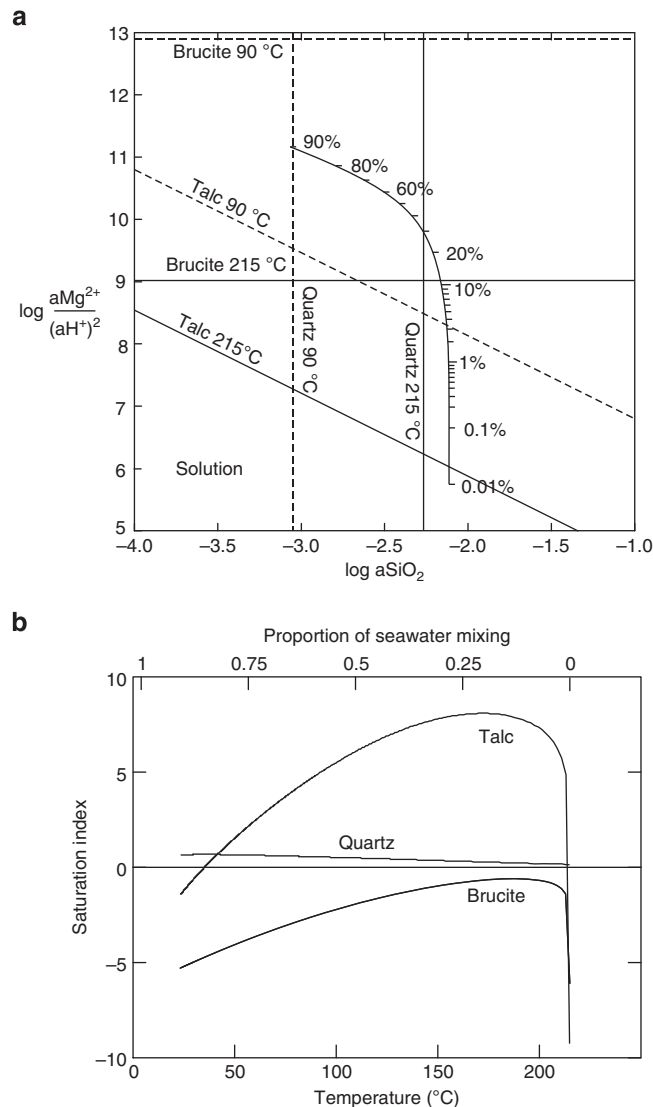


Figure 5 | Thermodynamic phase diagram. (a) Stability boundaries of talc, quartz and brucite at 215 and 90 °C, calculated in Geochemist's Workbench (GWB) at the ambient pressure conditions of the seafloor at the VDFV. The percentages indicate the proportion of seawater mixing with the end-member VDFV fluid. (b) Saturation indices for talc, quartz and brucite during modelled mixing of VDFV end-member fluid with seawater from 0.01 to 99%. This indicates that talc becomes saturated on mixing end-member VDFV vent fluid with seawater, and remains stable throughout the mixing regime. Brucite, which is the dominant magnesium phase at the higher pH Lost City vent field, never reaches stability at the VDFV.

We suggest that similar conditions prevailed during the formation of the other, now hydrothermally extinct, talc mounds (for example, Mystic Mountain) located ~700 m to the east of the currently active site. The current VDFV represents the latest stage in talc precipitation and hydrothermal circulation in the mafic and ultramafic basements beneath the Mt Dent OCC over tens of thousands of years.

Discussion

Hydrothermal venting on ocean crust more than 1 Ma in age has only been observed previously as either low-temperature (<10 °C) diffuse flow of reduced fluids³⁷ or as medium-temperature (91 °C) venting of high pH fluids (for example, at

the Lost City hydrothermal field^{3,38}) forming brucite and carbonate chimneys. In contrast, the VDVF vents fluid in excess of 200 °C, from seafloor mounds and chimneys of predominantly talc, developed on a 1–2-Ma basement of lower-crust and upper-mantle rocks that were tectonically exhumed. This discovery, of an active hydrothermal system depositing predominantly talc as chimneys and forming large mounds on the seafloor, is unique.

While talc-rich deposits of postulated hydrothermal origin have been reported before¹¹, these were mainly precipitated as accessory phases associated with massive sulphides, either where Si-rich low-pH hydrothermal fluids mixed with seawater, or as a result of conductive heating of Mg-rich sedimentary pore waters. Only two seafloor talc deposits, from the St Paul’s and Conrad fracture zones in the Atlantic Ocean¹⁷, appear directly comparable to the VDVF in terms of mineralogy, texture and geological setting.

At both sites, botryoidal talc, with similar REE patterns to the VDVF talc, was recovered from a tectonically exhumed gabbro–peridotite basement¹⁷. The presence of similar material to the active VDVF deposits at two different sites suggests that talc-dominated seafloor hydrothermal mineralization may be a widespread process at other slow spreading ridges, where tectonic uplift exposes lower-crustal and upper-mantle rocks to alteration by moderate-temperature hydrothermal circulation.

By measuring vertical velocities of vent fluid as it exits the seafloor, *in situ* fluid temperatures and the diameters of vent orifices at the VDVF, we have calculated a focused hydrothermal heat flux of 487 ± 101 MW, produced from the venting of ~500 kg s^{−1} of end-member fluid (Table 4). Despite being dissipated from crust of 1–2 Ma, this heat flux is comparable to that reported for focused heat flux dissipated by magma-driven ‘black smoker’ vent fields on zero-age ridge axes such as the Endeavour Ridge (302 MW), the East Pacific Rise at 21°N (200 MW) and the TAG vent field (758 MW) on the Mid-Atlantic Ridge³⁹. When compared with other ridge-flank hydrothermal systems³⁷, the heat flux at the VDVF is exceptionally high. It is also greater than the estimate for the Lost City hydrothermal field, which is thought to derive heat from the exothermic reaction of serpentinization^{40,41} in addition to residual crustal heat⁴².

While hydrothermal activity is effective at extracting heat from the magmatic ridge axis^{43,44}, processes of residual heat extraction from ridge flanks remain unclear. The intermediate temperature, near-neutral pH, low H₂S and low concentration of dissolved metals in the VDVF vent fluid are all features consistent with hydrothermal circulation driven by residual heat within the tectonically uplifted lower crust and upper mantle⁴⁵. Despite a high heat flux, the neutrally buoyant VDVF hydrothermal plume contains very little particulate matter⁶ and, as a result, is difficult to detect using conventional optical sensors. Given the widespread occurrence of OCC’s exhuming lower-crustal and

upper-mantle rocks at ultraslow-medium spreading ridges, and the presence of similar talc deposits at the St Paul’s and Conrad fracture zones¹⁷, we suggest that the processes leading to the formation of the VDVF could be widespread at slow-ultraslow spreading. In that case, the VDVF class of hydrothermal activity could contribute significantly to the cooling of the oceanic crust, but are not yet included in current estimates of global hydrothermal activity based on plume incidence⁴⁶.

Methods

Sample collection. Sonar data, photographic and video imagery and samples of rocks, minerals, fluids and temperatures were acquired using remotely operated vehicles (*Isis* and *HyBIS*) during RRS *James Cook* cruises JC44 and JC82.

Vent fluids. High-temperature fluids were sampled using titanium gas-tight syringes at three different high-temperature chimneys (Table 3). Fluid exit temperatures were determined separately from the fluid sampling using a laboratory-calibrated, high-temperature thermal probe that was inserted deep into each vent orifice. Hence, the fluid samples and temperatures are decoupled. The highest measured value for each vent is reported in Table 3. Subsamples of vent fluids were taken for geochemical analyses, with pH, halides, sulphate and H₂S being determined at STP (25 °C) immediately after recovery of the titanium syringes on the surface. Anions were determined using ion chromatography, and cations using inductively coupled plasma atomic emission spectroscopy and inductively coupled plasma mass spectrometry (ICP-MS) at NOCS. Data quality was assessed using the ‘Mottl Vent Fluid Database’ protocols⁴⁷. This included analysis of all solid precipitates from within the sampling syringes following total dissolution and weighted volumetric addition of concentrations to the clear fluid samples. Hence, any precipitates after the fluid samples were taken were re-dissolved and accounted for in final concentrations. Quality control included screening for samples with excessive Mg on a regression of elements such as Si, Ca, K and Li to zero Mg. Samples that were found to be contaminated with Mg concentrations more than those of seawater were subsequently excluded from the database. Our end-member concentration for dissolved silica is not as well constrained as that obtained in ref. 21, and thus their concentration is cited and used in our thermodynamic modelling.

Petrography. Petrographic analyses were conducted using transmitted and reflected light microscopy on polished thin sections. SEM was conducted using two different systems: one using a low-resolution Hitachi TM1000 Desktop SEM operating at 15 kV, imaging 1-cm² blocks of untreated broken surfaces; the second was a high-resolution LEO 1450-VP SEM operating at 20 kV and imaging carbon-coated polished thin sections. Crystallographic analysis was made using X-ray diffraction with Cu Kα radiation 2θ ranging between 2° and 76°, at steps of 0.02° and at rates of 0.02° per s. Unorientated air-dried mounts and glycolated mounts were scanned in the ranges 0–20° and 0–40°. Randomly orientated mounts were prepared and scanned in the range 57–62° to identify the peak signifying the (060) crystallographic plane.

Geochemistry. X-ray fluorescence (XRF) analysis was conducted on fused beads in a 10:1 ratio of sample powder to lithium tetraborate flux. Precision was determined from repeat analysis of standards UB-N, BRR-1 and OPY-1, and gives errors of <10%. Talc mineral separates were handpicked and washed in a weak acid solution and rinsed in de-ionized water. Following hydrofluoric and nitric acid digestion, the samples were analysed for trace element and REE analyses using ICP-MS. Standards included international reference materials: BIR-1, JB1a, JGB1, JB-3 and BHVO-2. Precision was determined from repeat analysis and gives errors in the range of 0.21–5.71%. Whole-rock analysis was conducted using both ICP-MS and inductively couple plasma atomic emission spectroscopy, and calibration was made using synthetic multielement standards. ⁸⁷Sr/⁸⁶Sr ratios were

Table 4 Heat flux calculation.						
Mound	Vent orifice	ΔT (K)	Radius (m)	Vertical flow rate (m s ^{−1})	Calculated flux	Units
Main Cone	Main Hole	87	0.5	1.5	401 ± 80	MW
Main Cone	Spire	211	0.1	1.5	39 ± 10	MW
North spur	Chimlet 2	104	0.1	0.5	6 ± 3	MW
North spur	Chimlet 1	39	0.15	1	11 ± 2	MW
South spur	X-15	108	0.15	1	30 ± 6	MW
Total					487 ± 101	MW

The equation used to calculate the heat flux is $Q = \Delta T \times C \times M$, where: Q , heat flux (Watts); ΔT , difference in temperature (°C) between the mean temperature of venting hydrothermal fluid and ambient bottom water (4 °C); C , specific thermal capacity of seawater at 200 bar and 215 °C (that is, 4,500 J kg^{−1} K^{−1})⁵³; M , mass flux (kg s^{−1}) = $A \times V \times \rho$, where A , area of vent orifice (m²); V , mean vertical flow rate (m s^{−1}); ρ , density of seawater at 215 °C.

obtained using a thermal ionization mass spectrometer. Fluid and host rock samples were analysed by running through Sr-specTM resin to obtain 1 µg of strontium. Samples of strontium (200 µg) were obtained from pure talc by running through cation resin AG50-X8 200–400 and then through Sr-specTM resin. External reproducibility of analysis was checked by analysing standard NBS987 every 11 samples and is reported here with an average of 0.710250 ($1\sigma = 0.0000053$), which is within an error of the accepted value of 0.710254.

Thermodynamic modelling. Modelling was carried out using Geochemist's Workbench³⁰ at pressure and temperature conditions appropriate for the depth of the VDFV. A thermodynamic database for the composition of the vent fluid and seawater, at 250 bar and 4–215 °C, with logK values calculated through this range of temperatures, was generated using DBCreate³¹, which in turn uses SUPCRT92 (ref. 32). Thermodynamic properties for aqueous species and phases were taken from the 2006 revision of the SUPCRT database³².

Heat flux calculation. Focused hydrothermal flow rates were calculated from high-definition video footage of the vertical velocity of particles entrained within venting hydrothermal fluid.

Individual particles entrained in the exiting vent fluid were filmed over a rise height of ~1 m and their velocity calculated from frame to frame. The distance travelled by the particles was measured against two parallel laser beams separated by a constant distance of 10 cm and shone through the rising vent fluid. The fluid exit velocities at each vent orifice were determined by measuring multiple particles in the upflowing fluid across the entire dimensions of the vent orifices. Different particles entrained in the up-flow zone from each orifice displayed only slight variation in their velocities, indicating that the flow rates are relatively uniform for fluids exiting each vent orifice (Supplementary Table 1). The velocity of a number of particles was thus calculated over a period of several minutes and a mean velocity derived for vent fluid as it escaped the vent orifice. The calculated error in the velocities is derived from the variation in particle velocity. These data were then integrated for each orifice as per established methods^{48–52}.

This method models the vent orifices as circles, and makes the assumptions that the fluid is emanating from the vent at a constant velocity across its diameter, the temperature is uniform across the vent orifice and the particle velocities recorded were representative of the flow velocity. Specific heat capacity of the venting fluids was calculated using specific densities and thermal capacities for seawater⁵³ at the temperature and pressure conditions recorded at the VDFV.

References

1. Tivey, M. K. Generation of seafloor hydrothermal vent fluids and associated mineral deposits. *Oceanography* **20**, 50–65 (2007).
2. Douville, E. *et al.* The Rainbow vent fluids (36°14'N, MAR): the influence of ultramafic rocks and phase separation on trace metal content in Mid-Atlantic Ridge hydrothermal fluids. *Chem. Geol.* **184**, 37–48 (2002).
3. Kelley, D. S. *et al.* An off-axis hydrothermal vent field near the Mid-Atlantic Ridge at 30°N. *Nature* **412**, 145–149 (2001).
4. Pedersen, R. B., Thorseth, I. H., Nygård, T. E., Lilley, M. D. & Kelley, D. S. in *Diversity Of Hydrothermal Systems On Slow Spreading Ocean Ridges* Vol. 188 (eds Rona, P., Dewey, C. F., Dymont, J. & Murton, B. J.) 67–89 (American Geophysical Union, 2010).
5. McCaig, A. M., Delacour, A., Fallick, A. E., Castelain, T. & Frueh-Green, G. L. in *Diversity of Hydrothermal Systems on Slow Spreading Ocean Ridges*, *Geophysical Monograph Series* Vol. 188 (eds Rona, P., Dewey, C. F., Dymont, J. & Murton, B. J.) 207–239 (American Geophysical Union, 2010).
6. Connelly, D. P. *et al.* Hydrothermal vent fields and chemosynthetic biota on the world's deepest seafloor spreading centre. *Nat. Commun.* **3**, 620 (2012).
7. Hayman, N. W. *et al.* Oceanic core complex development at the ultraslow spreading Mid-Cayman Spreading Center. *Geochem. Geophys. Geosyst.* **12**, Q0AG02 (2011).
8. Rosencrantz, E. & Sclater, J. G. Depth and age in the Cayman trough. *Earth Planet. Sci. Lett.* **79**, 133–144 (1986).
9. Seyfried, Jr W. E. & Ding, K. The effect of redox on the relative solubilities of copper and iron in Cl-bearing aqueous fluids at elevated temperatures and pressures: an experimental study with application to seafloor hydrothermal systems. *Geochem. Cosmochim. Acta* **57**, 1905–1917 (1993).
10. Shanks, III W. C., Bischoff, J. L. & Rosenbauer, R. J. Seawater sulfate reduction and sulfur isotope fractionation in basaltic systems: interaction of seawater with fayalite and magnetite at 200–350 °C. *Geochem. Cosmochim. Acta* **45**, 1977–1995 (1981).
11. Dekov, V. M., Cuadros, J., Shanks, W. C. & Koski, R. A. Deposition of talc-kerolite-smectite at seafloor hydrothermal vent fields: evidence from mineralogical, geochemical and oxygen isotope studies. *Chem. Geol.* **247**, 171–194 (2008).
12. Palmer, M. R. & Edmond, J. M. The strontium isotope budget of the modern ocean. *Earth Planet. Sci. Lett.* **92**, 11–26 (1989).
13. Douville, E. *et al.* Yttrium and rare earth elements in fluids from various deep-sea hydrothermal systems. *Geochem. Cosmochim. Acta* **63**, 627–643 (1999).
14. Sverjensky, D. A. Europium redox equilibria in aqueous solution. *Earth Planet. Sci. Lett.* **67**, 70–78 (1984).
15. Bao, S.-X., Zhou, H.-Y., Peng, X.-T., Ji, F.-W. & Yao, H.-Q. Geochemistry of REE and yttrium in hydrothermal fluids from the Endeavour segment, Juan de Fuca Ridge. *Geochem. J.* **42**, 359–370 (2008).
16. Shannon, R. Revised effective ionic radii and systematic studies of interatomic distances in halides and chalcogenides. *Acta Crystallogr.* **32**, 751–767 (1976).
17. D'Orazio, M., Boschi, C. & Brunelli, D. Talc-rich hydrothermal rocks from the St Paul and Conrad fracture zones in the Atlantic Ocean. *Eur. J. Mineral.* **16**, 73–83 (2004).
18. Bach, W., Garrido, C. J., Paulick, H., Harvey, J. & Rosner, M. Seawater-peridotite interactions: first insights from ODP Leg 209, MAR 15°N. *Geochem. Geophys. Geosyst.* **5**, Q09F26 (2004).
19. McDermott, J. M., Seewald, J. S., German, C. R. & Sylva, S. P. Pathways for abiotic organic synthesis at submarine hydrothermal fields. *Proc. Natl Acad. Sci. USA* **112**, 7668–7672 (2015).
20. Von Damm, K. L. in *Physical, Chemical, Biological, and Geological Interactions within Hydrothermal Systems*, *Geophysical Monograph Series* Vol. 91 (ed. Humphris, S.) 222–247 (American Geophysical Union, 1995).
21. McDermott, J. M. *Geochemistry of Deep-Sea Hydrothermal Vent Fluids from the Mid-Cayman Rise, Caribbean Sea*. Doctor of Philosophy thesis, Massachusetts Institute of Technology and Woods Hole Oceanographic Institute (2015).
22. Alt, J. C. in *Seafloor Hydrothermal Systems: Physical, Chemical, Biological, and Geological Interactions*, *Geophysical Monograph Series* Vol. 91 (eds Humphris, S., Zierenberg, R. A., Mullineaux, L. S. & Thomson, R. E.) 85–114 (AGU, 1995).
23. Von Damm, K. *et al.* Evolution of East Pacific Rise hydrothermal vent fluids following a volcanic eruption. *Nature* **375**, 47–50 (1995).
24. Von Damm, K. L. Seafloor hydrothermal activity: black smoker chemistry and chimneys. *Annu. Rev. Earth Planet. Sci.* **18**, 173–204 (1990).
25. Bischoff, J. L. & Rosenbauer, R. J. The critical point and two-phase boundary of seawater, 200–500 °C. *Earth Planet. Sci. Lett.* **68**, 172–180 (1984).
26. Kelley, D. S., Robinson, P. T. & Malpas, J. G. Processes of brine generation and circulation in the oceanic crust: fluid inclusion evidence from the Troodos Ophiolite, Cyprus. *J. Geophys. Res.* **97**, 9307–9322 (1992).
27. Berndt, M. E. & Seyfried, W. E. Calibration of BrCl fractionation during subcritical phase separation of seawater: possible halite at 9 to 10° N East Pacific Rise. *Geochem. Cosmochim. Acta* **61**, 2849–2854 (1997).
28. Seyfried, Jr W. Experimental and theoretical constraints on hydrothermal alteration processes at mid-ocean ridges. *Annu. Rev. Earth Planet. Sci.* **15**, 317 (1987).
29. Allen, D. E. & Seyfried, Jr W. E. Compositional controls on vent fluids from ultramafic-hosted hydrothermal systems at mid-ocean ridges: an experimental study at 400 °C, 500 bars. *Geochem. Cosmochim. Acta* **67**, 1531–1542 (2003).
30. Bethke, C. M. Geochemical reaction modelling: concepts and applications. *Forensic Sci. Int.* **198**, 126–133 (1996).
31. Kong, X.-Z., Tutolo, B. M. & Saar, M. O. DBCreate: a SUPCRT92-based program for producing EQ3/6, TOUGHREACT, and GWB thermodynamic databases at user-defined T and P. *Comput. Geosci.* **51**, 415–417 (2013).
32. Johnson, J. W., Oelkers, E. H. & Helgeson, H. C. SUPCRT92: a software package for calculating the standard molal thermodynamic properties of minerals, gases, aqueous species, and reactions from 1 to 5000 bar and 0 to 1000 °C. *Comput. Geosci.* **18**, 899–947 (1992).
33. Petersen, S., Herzig, P. M. & Hannington, M. D. in *Proceedings of the Ocean Drilling Program: Scientific Results*, Vol. 158, (eds P. Herzig, S. Humphris, D. J. Miller, & R. A. Zierenberg) 163–178 (Ocean Drilling Program, 1998).
34. Vanko, D. A., Bach, W., Roberts, S., Yeats, C. J. & Scott, S. D. Fluid inclusion evidence for subsurface phase separation and variable fluid mixing regimes beneath the deep-sea PACMANUS hydrothermal field, Manus Basin back arc rift, Papua New Guinea. *J. Geophys. Res.* **109**, B03201 (2004).
35. Webber, A. P., Roberts, S., Burgess, R. & Boyce, A. J. Fluid mixing and thermal regimes beneath the PACMANUS hydrothermal field, Papua New Guinea: helium and oxygen isotope data. *Earth Planet. Sci. Lett.* **304**, 93–102 (2011).
36. Ames, D. E., Franklin, J. M. & Hannington, M. Mineralogy and geochemistry of active and inactive chimneys and massive sulphide, middle valley, northern Juan de Fuca ridge: an evolving hydrothermal system. *Can. Mineral.* **31**, 997–1024 (1993).
37. Bemis, K., Lowell, R. P. & Farough, A. Diffuse flow on and around hydrothermal vents at mid-ocean ridges. *Oceanography* **25**, 182 (2012).
38. Seyfried, Jr W. E., Pester, N. J., Tutolo, B. M. & Ding, K. The Lost City hydrothermal system: constraints imposed by vent fluid chemistry and reaction path models on seafloor heat and mass transfer processes. *Geochem. Cosmochim. Acta* **163**, 59–79 (2015).
39. Baker, E. T. Hydrothermal cooling of midocean ridge axes: do measured and modeled heat fluxes agree? *Earth Planet. Sci. Lett.* **263**, 140–150 (2007).
40. Lowell, R. & Rona, P. Seafloor hydrothermal systems driven by the serpentinization of peridotite. *Geophys. Res. Lett.* **29**, 26-1–26-4 (2002).

41. Lowell, R. P. in *Diversity Of Hydrothermal Systems On Slow Spreading Ocean Ridges* Vol. 188 (eds Rona, P., Dewey, C. F., Dymont, J. & Murton, B. J.) 11–26 (American Geophysical Union, 2010).
42. Allen, D. E. & Seyfried, Jr W. E. Serpentinization and heat generation: constraints from Lost City and Rainbow hydrothermal systems. *Geochem. Cosmochim. Acta* **68**, 1347–1354 (2004).
43. Henstock, T. J., Woods, A. W. & White, R. S. The accretion of oceanic crust by episodic sill intrusion. *J. Geophys. Res.* **98**, 4143–4161 (1993).
44. Quick, J. E. & Denlinger, R. P. Ductile deformation and the origin of layered gabbro in ophiolites. *J. Geophys. Res.* **98**, 14015–14027 (1993).
45. McCaig, A. M., Cliff, R. A., Escartin, J., Fallick, A. E. & MacLeod, C. J. Oceanic detachment faults focus very large volumes of black smoker fluids. *Geology* **35**, 935–938 (2007).
46. Baker, E. T. & German, C. R. in *Mid-Ocean Ridges: Hydrothermal Interactions between the Lithosphere and Oceans, Geophysical Monograph Series* Vol. 148 (eds Lin, C. R., Parson, J. & German, L. M.) 245–266 (AGU, 2004).
47. Mottl, M. J. Explanatory notes and master chemical item. Spreadsheet for the VentDB data collections housed in the EarthChem Library. *EarthChem Library*. doi:10.1594/IEDA/100213 (2012).
48. Rona, P. A. & Trivett, D. A. Discrete and diffuse heat transfer atashes vent field, Axial Volcano, Juan de Fuca Ridge. *Earth Planet. Sci. Lett.* **109**, 57–71 (1992).
49. Converse, D. R., Holland, H. D. & Edmond, J. M. Flow rates in the axial hot springs of the East Pacific Rise (21°N): implications for the heat budget and the formation of massive sulfide deposits. *Earth Planet. Sci. Lett.* **69**, 159–175 (1984).
50. Ramondenc, P., Germanovich, L. N., Von Damm, K. L. & Lowell, R. P. The first measurements of hydrothermal heat output at 9° 50' N, East Pacific Rise. *Earth Planet. Sci. Lett.* **245**, 487–497 (2006).
51. Ginster, U., Mottl, M. J. & Von Herzen, R. P. Heat flux from black smokers on the Endeavour and Cleft segments, Juan de Fuca Ridge. *J. Geophys. Res.* **99**, 4937–4950 (1994).
52. Macdonald, K. C., Becker, K., Spiess, F. N. & Ballard, R. D. Hydrothermal heat flux of the 'black smoker' vents on the East Pacific Rise. *Earth Planet. Sci. Lett.* **48**, 1–7 (1980).
53. Bischoff, J. L. & Rosenbauer, R. J. An empirical equation of state for hydrothermal seawater (3.2 percent NaCl). *Am. J. Sci.* **285**, 725–763 (1985).
54. Humphris, S. E. & Bach, W. On the Sr isotope and REE compositions of anhydrites from the TAG seafloor hydrothermal system. *Geochem. Cosmochim. Acta* **69**, 1511–1525 (2005).
55. Yalçın, H. & Bozkaya, Ö. Mineralogy and geochemistry of Paleocene ultramafic- and sedimentary-hosted talc deposits in the southern part of the Sivas Basin, Turkey. *Clay Clay Miner.* **54**, 333–350 (2006).
56. Zierenberg, R. A. & Shanks, III W. in *Geologic, Hydrothermal, and Biologic Studies at Escanaba Trough, Gorda Ridge, Offshore Northern California* (eds J. Morton, R. A. Zierenberg, & C. A. Reiss) 257–277 (U.S. G.P.O., 1994).
57. Connelly, D. P. *et al.* *Hydrothermal Activity and Deep-Ocean Biology of the Mid-Cayman Rise*. 100 (National Oceanography Centre Southampton, 2012).
58. Copley, J. T. *et al.* *Montego Bay to Antigua, Hydrothermal Activity and Deep-Ocean Biology of the Mid-Cayman Rise* (National Oceanography Centre Southampton, 2013).
59. Charlou, J. L., Donval, J. P., Fouquet, Y., Jean-Baptiste, P. & Holm, N. Geochemistry of high H₂ and CH₄ vent fluids issuing from ultramafic rocks at the Rainbow hydrothermal field (36°14'N, MAR). *Chem. Geol.* **191**, 345–359 (2002).

Acknowledgements

The work published in this study was funded using NERC grants NE/F017758/1 and NE/I012613/1 to B.J.M. and S.R. at the National Oceanography Centre. We thank the JC44 and JC82 shipboard parties for data collection and sample acquisition. We thank R. Williams and R. Pearce for their help with the X-ray diffraction and M. Cooper, J. Hawkes and V. Chavagnac for analysing the vent fluids. We are grateful to two anonymous reviewers and M. Palmer for comments on the manuscript.

Author contributions

M.R.S.H. conducted the petrographic, geochemical and mineral analyses, and heat flux calculations; A.P.W. made the thermodynamic modelling; R.A.M. conducted vent fluid analysis. B.J.M. and S.R. conceived and directed the research; M.R.S.H., A.P.W., B.J.M., S.R., D.P.C. and R.A.M. wrote the manuscript, and all contributed to collection of the data on cruises JC44 and JC82.

Additional information

Supplementary Information accompanies this paper at <http://www.nature.com/naturecommunications>

Competing financial interests: The authors declare no competing financial interests.

Reprints and permission information is available online at <http://npg.nature.com/reprintsandpermissions/>

How to cite this article: Hodgkinson, M. R. S. *et al.* Talc-dominated seafloor deposits reveal a new class of hydrothermal system. *Nat. Commun.* 6:10150 doi: 10.1038/ncomms10150 (2015).



This work is licensed under a Creative Commons Attribution 4.0 International License. The images or other third party material in this article are included in the article's Creative Commons license, unless indicated otherwise in the credit line; if the material is not included under the Creative Commons license, users will need to obtain permission from the license holder to reproduce the material. To view a copy of this license, visit <http://creativecommons.org/licenses/by/4.0/>

List of References

- Adamson, A. 1985. Basement lithostratigraphy, Deep Sea Drilling Project Hole 504B. *Initial Reports of the Deep Sea Drilling Project*, 83, 121-127.
- Agrinier, P., Hékinian, R., Bideau, D. & Javoy, M. 1995. O and H stable isotope compositions of oceanic crust and upper mantle rocks exposed in the Hess Deep near the Galapagos Triple Junction. *Earth and Planetary Science Letters*, 136, 183-196.
- Agrinier, P., Javoy, M. & Girardeau, J. 1988. Hydrothermal activity in a peculiar oceanic ridge: Oxygen and hydrogen isotope evidence in the Xigaze ophiolite (Tibet, China). *Chemical Geology*, 71, 313-335.
- Allen, D. E. & Seyfried Jr, W. E. 2004. Serpentinization and heat generation: constraints from Lost City and Rainbow hydrothermal systems. *Geochimica et Cosmochimica Acta*, 68, 1347-1354.
- Allen, D. E. & Seyfried Jr, W. E. 2005. REE controls in ultramafic hosted MOR hydrothermal systems: An experimental study at elevated temperature and pressure. *Geochimica et Cosmochimica Acta*, 69, 675-683.
- Alt, J. C. 1995. Seafloor processes in mid-ocean ridge hydrothermal systems. In: Humphris, S., Zierenberg, R. A., Mullineaux, L. S. & Thomson, R. E. (eds.) *Seafloor Hydrothermal Systems: Physical, Chemical, Biological, and Geological Interactions*. Washington, DC: American Geophysical Union.
- Alt, J. C., France-Lanord, C., Floyd, P., Castillo, P. & Galy, A. 1992. Low-temperature hydrothermal alteration of Jurassic ocean crust, site 801. In: Larson, R. L. & Lancelot, Y. (eds.) *Proceedings of the Ocean Drilling Program, Scientific Results*. College Station, TX: Ocean Drilling Program.
- Alt, J. C. & Honnorez, J. 1984. Alteration of the upper oceanic crust, DSDP site 417: mineralogy and chemistry. *Contributions to Mineralogy and Petrology*, 87, 149-169.

- Alt, J. C., Honnorez, J., Laverne, C. & Emmermann, R. 1986. Hydrothermal alteration of a 1 km section through the upper oceanic crust, Deep Sea Drilling Project Hole 504B: Mineralogy, chemistry and evolution of seawater-basalt interactions. *Journal of Geophysical Research: Solid Earth*, 91, 10309-10335.
- Alt, J. C., Laverne, C., Coggon, R. M., Teagle, D. A. H., Banerjee, N. R., Morgan, S., Smith-Duque, C. E., Harris, M. & Galli, L. 2010. Subsurface structure of a submarine hydrothermal system in ocean crust formed at the East Pacific Rise, ODP/IODP Site 1256. *Geochemistry, Geophysics, Geosystems*, 11, Q10010.
- Alt, J. C., Lonsdale, P., Haymon, R. & Muehlenbachs, K. 1987. Hydrothermal sulfide and oxide deposits on seamounts near 21°N, East Pacific Rise. *Geological Society of America Bulletin*, 98, 157-168.
- Alt, J. C., Zuleger, E. & Erzinger, J. 1995. Mineralogy and stable isotopic compositions of the hydrothermally altered lower sheeted dike complex, ODP Hole 504B. In: Dick, H. J. B., Erzinger, J. & Stokking, L. (eds.) *Proceedings of the Ocean Drilling Program, Scientific Results*. College Station, TX: Ocean Drilling Program.
- Ames, D. E., Franklin, J. M. & Hannington, M. 1993. Mineralogy and geochemistry of active and inactive chimneys and massive sulphide, Middle Valley, northern Juan de Fuca Ridge: an evolving hydrothermal system. *The Canadian Mineralogist*, 31, 997-1024.
- Anderson, R., Honnorez, J., Becker, K., Adamson, A., Alt, J., Emmermann, R., Kempton, P., Kinoshita, H., Laverne, C. & Mottl, M. 1982. DSDP Hole 504B, the first reference section over 1 km through Layer 2 of the oceanic crust. *Nature*, 300, 589-594.
- Andrews, A. J. 1977. Low temperature fluid alteration of oceanic layer 2 basalts, DSDP Leg 37. *Canadian Journal of Earth Sciences*, 14, 911-926.
- Argast, S. 1989. Expandable sepiolite from Ninetyeast Ridge, Indian Ocean. *Clays and Clay Minerals*, 37, 371-376.
- Audemard, F. A. 2009. Key issues on the post-Mesozoic Southern Caribbean Plate boundary. *Geological Society, London, Special Publications*, 328, 569-586.

- Audemard, F. A., Romero, G., Rendon, H. & Cano, V. 2005. Quaternary fault kinematics and stress tensors along the southern Caribbean from fault-slip data and focal mechanism solutions. *Earth-Science Reviews*, 69, 181-233.
- Authemayou, C., Brocard, G., Teyssier, C., Simon-Labric, T., Gutiérrez, A., Chiquín, E. & Morán, S. 2011. The Caribbean–North America–Cocos Triple Junction and the dynamics of the Polochic–Motagua fault systems: Pull-up and zipper models. *Tectonics*, 30, TC3010.
- Bach, W., Banerjee, N. R., Dick, H. J. B. & Baker, E. T. 2002. Discovery of ancient and active hydrothermal systems along the ultra-slow spreading Southwest Indian Ridge 10°-16°E. *Geochemistry Geophysics Geosystems*, 3, 293-324.
- Bach, W., Garrido, C. J., Paulick, H., Harvey, J. & Rosner, M. 2004. Seawater-peridotite interactions: First insights from ODP Leg 209, MAR 15°N. *Geochemistry Geophysics Geosystems*, 5.
- Bach, W., Paulick, H., Garrido, C. J., Ildefonse, B., Meurer, W. P. & Humphris, S. E. 2006. Unraveling the sequence of serpentinization reactions: petrography, mineral chemistry, and petrophysics of serpentinites from MAR 15°N (ODP Leg 209, Site 1274). *Geophysical Research Letters*, 33.
- Bach, W., Peuker-Ehrenbrink, B., Hart, S. R. & Blusztajn, J. S. 2003. Geochemistry of hydrothermally altered oceanic crust: DSDP/ODP Hole 504B - Implications for seawater-crust exchange budgets and Sr- and Pb-isotopic evolution of the mantle (vol 4, art no 8904, 2003). *Geochemistry Geophysics Geosystems*, 4.
- Baker, E. T. 2007. Hydrothermal cooling of midocean ridge axes: Do measured and modeled heat fluxes agree? *Earth and Planetary Science Letters*, 263, 140-150.
- Baker, E. T., Chen, Y. J. & Phipps Morgan, J. 1996. The relationship between near-axis hydrothermal cooling and the spreading rate of mid-ocean ridges. *Earth and Planetary Science Letters*, 142, 137-145.
- Baker, E. T. & German, C. R. 2004. On the global distribution of hydrothermal vent fields. In: German, C. R., J., L. & M., P. L. (eds.) *Mid-Ocean Ridges: Hydrothermal Interactions between the Lithosphere and Oceans*. Washington, DC: AGU.

- Ballard, R., Bryan, W., Dick, H., Emery, K., Thompson, G., Uchupi, E., Davis, K. E., De Boer, J., Delong, S. E. & Fox, P. J. 1979. Geological and geophysical investigation of the Mid Cayman Rise Spreading Center: initial results and observations. *In*: Talwani, M., Harrison, G. G. & Hays, D. E. (eds.) *Deep Drilling Results in the Atlantic Ocean: Oceanic Crust*. Washington, D.C.: American Geophysical Union.
- Barnes, I., LaMarche, V. C. & Himmelberg, G. 1967. Geochemical Evidence of Present-Day Serpentinization. *Science*, 156, 830-832.
- Barnes, J. D., Paulick, H., Sharp, Z. D., Bach, W. & Beaudoin, G. 2009. Stable isotope ($\delta^{18}\text{O}$, δD , $\delta^{37}\text{Cl}$) evidence for multiple fluid histories in mid-Atlantic abyssal peridotites (ODP Leg 209). *Lithos*, 110, 83-94.
- Bau, M. 1991. Rare-earth element mobility during hydrothermal and metamorphic fluid-rock interaction and the significance of the oxidation state of europium. *Chemical Geology*, 93, 219-230.
- Beaulieu, S. 2010. InterRidge Global Database of Active Submarine Hydrothermal Vent Fields. 2.0 ed.
- Beaulieu, S. E., Baker, E. T. & German, C. R. 2012. On the global distribution of hydrothermal vent fields: One decade later. *AGU Fall Meeting*. San Francisco, CA, USA: American Geophysical Union.
- Bemis, K. G., Von Herzen, R. P. & Mottl, M. J. 1993. Geothermal heat flux from hydrothermal plumes on the Juan de Fuca Ridge. *Journal of Geophysical Research: Solid Earth*, 98, 6351-6365.
- Berkenbosch, H. A., de Ronde, C. E. J., Gemmell, J. B., McNeill, A. W. & Goemann, K. 2012. Mineralogy and Formation of Black Smoker Chimneys from Brothers Submarine Volcano, Kermadec Arc. *Economic Geology*, 107, 1613-1633.
- Berndt, M. E., Allen, D. E. & Seyfried, W. E. 1996. Reduction of CO_2 during serpentinization of olivine at 300 °C and 500 bar. *Geology*, 24, 351-354.
- Berndt, M. E., Seyfried, W. E. & Beck, J. W. 1988. Hydrothermal alteration processes at midocean ridges: Experimental and theoretical constraints from Ca and Sr

- exchange reactions and Sr isotopic ratios. *Journal of Geophysical Research: Solid Earth*, 93, 4573-4583.
- Bethke, C. M. 1996. Geochemical reaction modelling: concepts and applications. *Forensic Science International*, 198, 126-133.
- Bickle, M. J. & Teagle, D. A. H. 1992. Strontium alteration in the Troodos ophiolite: implications for fluid fluxes and geochemical transport in mid-ocean ridge hydrothermal systems. *Earth and Planetary Science Letters*, 113, 219-237.
- Bischoff, J. L. 1980. Geothermal System at 21°N, East Pacific Rise: Physical Limits on Geothermal Fluid and Role of Adiabatic Expansion. *Science*, 207, 1465-1469.
- Bischoff, J. L. & Dickson, F. W. 1975. Seawater-basalt interaction at 200°C and 500 bars: Implications for origin of sea-floor heavy-metal deposits and regulation of seawater chemistry. *Earth and Planetary Science Letters*, 25, 385-397.
- Bischoff, J. L. & Pitzer, K. S. 1985. Phase relations and adiabat in boiling seafloor geothermal systems. *Earth and Planetary Science Letters*, 75, 327-338.
- Bischoff, J. L. & Rosenbauer, R. J. 1984. The critical point and two-phase boundary of seawater, 200–500°C. *Earth and Planetary Science Letters*, 68, 172-180.
- Bischoff, J. L. & Rosenbauer, R. J. 1985. An empirical equation of state for hydrothermal seawater (3.2 percent NaCl). *American Journal of Science*, 285, 725-763.
- Bischoff, J. L. & Rosenbauer, R. J. 1988. Liquid-vapor relations in the critical region of the system NaCl-H₂O from 380 to 415°C: A refined determination of the critical point and two-phase boundary of seawater. *Geochimica et Cosmochimica Acta*, 52, 2121-2126.
- Bischoff, J. L. & Seyfried, W. E. 1978. Hydrothermal chemistry of seawater from 25°C to 350°C. *American Journal of Science*, 278, 838-860.
- Blackman, D. K., Cann, J. R., Janssen, B. & Smith, D. K. 1998. Origin of extensional core complexes: Evidence from the Mid-Atlantic Ridge at Atlantis fracture zone. *Journal of Geophysical Research: Solid Earth*, 103, 21315-21333.

- Blackman, D. K., Karson, J. A., Kelley, D. S., Cann, J. R., Früh-Green, G. L., Gee, J. S., Hurst, S. D., John, B. E., Morgan, J. & Nooner, S. L. 2002. Geology of the Atlantis Massif (Mid-Atlantic Ridge, 30°N): Implications for the evolution of an ultramafic oceanic core complex. *Marine Geophysical Researches*, 23, 443-469.
- Blackman, D. K., Ildefonse, B., John, B. E., Ohara, Y., Miller, D. J., Abe, N., Abratis, M., Andal, E. S., Andreani, M., Awaji, S., Beard, J. S., Brunelli, D., Charney, A. B., Christie, D. M., Collins, J. A., Delacour, A., Delius, H., Drouin, M., Einaudi, F., Escartin, J., Frost, B. R., Früh-Green, G. L., Fryer, P., Gee, J. S., Godard, M., Grimes, C. B., Halfpenny, A., Hansen, H. E., Harris, A. C., Tamura, A., Hayman, N., Hellebrand, E., Hirose, T., Hirth, J. G., Ishimaru, J., Johnson, K. T. M., Karner, G. D., Linek, M., MacLeod, C. J., Maeda, J., Mason, O. U., Mccaig, A. M., Michibayashi, K., Morris, A., Nakagawa, T., Nozaka, T., Rosner, M., Searle, R. C., Suhr, G., Tominaga, M., von der Handt, A., Yamasaki, T. & Zhao, X. 2011. Drilling constraints on lithospheric accretion and evolution at Atlantis Massif, Mid-Atlantic Ridge 30°N. *Journal of Geophysical Research: Solid Earth (1978–2012)*, 116.
- Blondel, P. & Murton, B. J. 1997. *Handbook of Seafloor Sonar Imagery*, Wiley-Praxis Series in Remote Sensing, 314 pp., John Wiley, New York.
- Böhlke, J., Honnorez, J. & Honnorez-Guerstein, B.-M. 1980. Alteration of basalts from site 396 B, DSDP: Petrographic and mineralogic studies. *Contributions to Mineralogy and Petrology*, 73, 341-364.
- Böhlke, J. K., Honnorez, J., Honnorez-Guerstein, B. M., Muehlenbachs, K. & Petersen, N. 1981. Heterogeneous alteration of the upper oceanic crust: Correlation of rock chemistry, magnetic properties, and O isotope ratios with alteration patterns in basalts from site 396B, DSDP. *Journal of Geophysical Research: Solid Earth*, 86, 7935-7950.
- Bonatti, E. & Harrison, C. 1988. Eruption styles of basalt in oceanic spreading ridges and seamounts: Effect of magma temperature and viscosity. *Journal of Geophysical Research: Solid Earth*, 93, 2967-2980.

- Boschi, C., Früh-Green, G. L., Delacour, A., Karson, J. A. & Kelley, D. S. 2006. Mass transfer and fluid flow during detachment faulting and development of an oceanic core complex, Atlantis Massif (MAR 30°N). *Geochemistry, Geophysics, Geosystems*, 7.
- Boschman, L. M., van Hinsbergen, D. J., Torsvik, T. H., Spakman, W. & Pindell, J. L. 2014. Kinematic reconstruction of the Caribbean region since the Early Jurassic. *Earth-Science Reviews*, 138, 102-136.
- Boudier, F., Nicolas, A. & Ildefonse, B. t. 1996. Magma chambers in the Oman ophiolite: fed from the top and the bottom. *Earth and Planetary Science Letters*, 144, 239-250.
- Bowers, T. S., Campbell, A. C., Measures, C. I., Spivack, A. J., Khadem, M. & Edmond, J. M. 1988. Chemical Controls on the Composition of Vent Fluids at 13°–11°N and 21°N, East Pacific Rise. *Journal of Geophysical Research*, 93, 4522-4536.
- Bowland, C. L. 1993. Depositional history of the western Colombian Basin, Caribbean Sea, revealed by seismic stratigraphy. *Geological Society of America Bulletin*, 105, 1321-1345.
- Briden, J. C., Rex, D. C., Faller, A. M. & Tomblin, J. F. 1979. *K-Ar Geochronology and Palaeomagnetism of Volcanic Rocks in the Lesser Antilles Island Arc*.
- Brindley, G. 1966. Invited review: ethylene glycol and glycerol complexes of smectites and vermiculite. *Clay minerals*, 6, 273.
- Buatier, M. D., Früh-Green, G. L. & Karpoff, A. M. 1995. Mechanisms of Mg-phyllosilicate formation in a hydrothermal system at a sedimented ridge (Middle Valley, Juan de Fuca). *Contributions to Mineralogy and Petrology*, 122, 134-151.
- Buck, W. R., Lavier, L. L. & Poliakov, A. N. 2005. Modes of faulting at mid-ocean ridges. *Nature*, 434, 719-723.
- Burke, K. 1988. Tectonic evolution of the Caribbean. *Annual Review of Earth and Planetary Sciences*, 16, 201-230.

- Burke, K., Fox, P. & Şengör, A. 1978. Buoyant ocean floor and the evolution of the Caribbean. *Journal of Geophysical Research: Solid Earth*, 83, 3949-3954.
- Butterfield, D. A., Jonasson, I. R., Massoth, G. J., Feely, R. A., Roe, K. K., Embley, R. E., Holden, J. F., McDuff, R. E., Lilley, M. D., Delaney, J. R. & Pyle, D. 1997. Seafloor Eruptions and Evolution of Hydrothermal Fluid Chemistry. *Philosophical Transactions: Mathematical, Physical and Engineering Sciences*, 355, 369-386.
- Butterfield, D. A., Nelson, B. K., Wheat, C. G., Mottl, M. J. & Roe, K. K. 2001. Evidence for basaltic Sr in midocean ridge-flank hydrothermal systems and implications for the global oceanic Sr isotope balance. *Geochimica et Cosmochimica Acta*, 65, 4141-4153.
- Campbell, A. C., Bowers, T. S., Measures, C. I., Falkner, K. K., Khadem, M. & Edmond, J. M. 1988a. A Time Series of Vent Fluid Compositions From 21°N, East Pacific Rise (1979, 1981, 1985), and the Guaymas Basin, Gulf of California (1982, 1985). *Journal of Geophysical Research*, 93, 4537-4549.
- Campbell, A. C., German, C., Palmer, M., Gamo, T. & Edmond, J. 1994. Chemistry of hydrothermal fluids from the Escanaba Trough, Gorda Ridge. *US Geological Survey Bulletin*, 2022, 201-221.
- Campbell, A. C., Palmer, M. R., Klinkhammer, G. P., Bowers, T. S., Edmond, J. M., Lawrence, J. R., Casey, J. F., Thompson, G., Humphris, S., Rona, P. & Karson, J. A. 1988b. Chemistry of hot springs on the Mid-Atlantic Ridge. *Nature*, 335, 514-519.
- Canales, J. P., Sohn, R. A. & deMartin, B. J. 2007. Crustal structure of the Trans-Atlantic Geotraverse (TAG) segment (Mid-Atlantic Ridge, 26°10'N): Implications for the nature of hydrothermal circulation and detachment faulting at slow spreading ridges. *Geochemistry, Geophysics, Geosystems*, 8, Q08004.
- Cann, J., Blackman, D., Smith, D., McAllister, E., Janssen, B., Mello, S., Avgerinos, E., Pascoe, A. & Escartin, J. 1997. Corrugated slip surfaces formed at ridge-transform intersections on the Mid-Atlantic Ridge. *Nature*, 385, 329-332.
- Cannat, M. 1996. How thick is the magmatic crust at slow spreading oceanic ridges? *Journal of Geophysical Research: Solid Earth*, 101, 2847-2857.

- Cannat, M., Bideau, D. & Bougault, H. 1992. Serpentinized peridotites and gabbros in the Mid-Atlantic Ridge axial valley at 15°37'N and 16°52'N. *Earth and Planetary Science Letters*, 109, 87-106.
- Cannat, M., Sauter, D., Mendel, V., Ruellan, E., Okino, K., Escartin, J., Combier, V. & Baala, M. 2006. Modes of seafloor generation at a melt-poor ultraslow-spreading ridge. *Geology*, 34, 605-608.
- Carbotte, S. M. & Macdonald, K. C. 1990. Causes of variation in fault-facing direction on the ocean floor. *Geology*, 18, 749-752.
- Carter, J. L. 1970. Mineralogy and Chemistry of the Earth's Upper Mantle Based on the Partial Fusion-Partial Crystallization Model. *Geological Society of America Bulletin*, 81, 2021-2034.
- Chan, L.-H., Alt, J. C. & Teagle, D. A. H. 2002. Lithium and lithium isotope profiles through the upper oceanic crust: a study of seawater–basalt exchange at ODP Sites 504B and 896A. *Earth and Planetary Science Letters*, 201, 187-201.
- Chan, L. H., Edmond, J. M. & Thompson, G. 1993. A lithium isotope study of hot springs and metabasalts from mid-ocean ridge hydrothermal systems. *Journal of Geophysical Research: Solid Earth*, 98, 9653-9659.
- Charlou, J.-L. & Donval, J.-P. 1993. Hydrothermal methane venting between 12°N and 26°N along the Mid-Atlantic Ridge. *Journal of Geophysical Research: Solid Earth*, 98, 9625-9642.
- Charlou, J., Donval, J., Fouquet, Y., Erzinger, J. & Von Stackelberg, U. Year. Hydrothermal activity in the Lau Basin: plumes and hot fluids chemistry. In: Terra Abstract, 1991. 466.
- Charlou, J. L., Donval, J. P., Fouquet, Y., Jean-Baptiste, P. & Holm, N. 2002. Geochemistry of high H₂ and CH₄ vent fluids issuing from ultramafic rocks at the Rainbow hydrothermal field (36°14'N, MAR). *Chemical Geology*, 191, 345-359.
- Charlou, J. L., Fouquet, Y., Donval, J. P., Auzende, J. M., Jean-Baptiste, P., Stievenard, M. & Michel, S. 1996. Mineral and gas chemistry of hydrothermal fluids on an

- ultrafast spreading ridge: East Pacific Rise, 17° to 19°S (Naudur cruise, 1993)
phase separation processes controlled by volcanic and tectonic activity.
Journal of Geophysical Research, 101, 15899-15919.
- Cheadle, M. J., John, B. E., German, C. R. & Kusznir, N. J. 2012. The Death Throes of
Ocean Core Complexes: Examples from the Mid-Cayman Spreading Centre.
AGU Fall Meeting. San Francisco, CA: American Geophysical Union.
- Chen, Y. J. & Phipps Morgan, J. 1996. The effects of spreading rate, the magma budget,
and the geometry of magma emplacement on the axial heat flux at mid-ocean
ridges. *Journal of Geophysical Research: Solid Earth*, 101, 11475-11482.
- Christie, D. M., West, B. P. & Pyle, D. Year. Extreme morphologic and petrologic
diversity within the southeastern Indian Ocean. *In: EOS Transactions of the*
American Geophysical Union, 1997. American Geophysical Union, F673.
- Christie, D. M., West, B. P., Pyle, D. G. & Hanan, B. B. 1998. Chaotic topography, mantle
flow and mantle migration in the Australian-Antarctic discordance. *Nature*,
394, 637-644.
- Collier, J. & Sinha, M. 1990. Seismic images of a magma chamber beneath the Lau
Basin back-arc spreading centre. *Nature*, 346, 646-648.
- Connelly, D. P., Copley, J. T., Murton, B. J., Stansfield, K., Tyler, P. A., German, C. R., Van
Dover, C. L., Amon, D., Furlong, M., Grindlay, N., Hayman, N., Huhnerbach, V.,
Judge, M., Le Bas, T., McPhail, S., Meier, A., Nakamura, K.-i., Nye, V., Pebody, M.,
Pedersen, R. B., Plouviez, S., Sands, C., Searle, R. C., Stevenson, P., Taws, S. &
Wilcox, S. 2012. Hydrothermal vent fields and chemosynthetic biota on the
world's deepest seafloor spreading centre. *Nature Communications*, 3, 620.
- Converse, D. R., Holland, H. D. & Edmond, J. M. 1984. Flow rates in the axial hot
springs of the East Pacific Rise (21°N): Implications for the heat budget and
the formation of massive sulfide deposits. *Earth and Planetary Science Letters*,
69, 159-175.
- Coogan, L. A. 2007. The Lower Oceanic Crust. *In: Heinrich, D. H. & Karl, K. T. (eds.)*
Treatise on Geochemistry. Oxford: Pergamon.

- Coogan, L. A., Jenkin, G. R. T. & Wilson, R. N. 2002. Constraining the cooling rate of the lower oceanic crust: a new approach applied to the Oman ophiolite. *Earth and Planetary Science Letters*, 199, 127-146.
- Cooper, M., Elderfield, H. & Schultz, A. 2000. Diffuse hydrothermal fluids from Lucky Strike hydrothermal vent field: Evidence for a shallow conductively heated system. *Journal of Geophysical Research: Solid Earth*, 105, 19369-19375.
- Corliss, J. B., Dymond, J., Gordon, L. I., Edmond, J. M., Richard, P. v. H., Ballard, R. D., Green, K., Williams, D., Bainbridge, A., Crane, K. & Andel, T. H. v. 1979. Submarine Thermal Springs on the Galápagos Rift. *Science*, 203, 1073-1083.
- Craddock, P. R., Bach, W., Seewald, J. S., Rouxel, O. J., Reeves, E. & Tivey, M. K. 2010. Rare earth element abundances in hydrothermal fluids from the Manus Basin, Papua New Guinea: Indicators of sub-seafloor hydrothermal processes in back-arc basins. *Geochimica et Cosmochimica Acta*, 74, 5494-5513.
- Craig, H. 1961. Standard for Reporting Concentrations of Deuterium and Oxygen-18 in Natural Waters. *Science*, 133, 1833-1834.
- Craig, H. & Lupton, J. 1981. 11. Helium-3 and mantle volatiles in the ocean and the oceanic crust. *The Sea, ideas and observations on progress in the study of the seas*, 7, 391.
- D'Orazio, M., Boschi, C. & Brunelli, D. 2004. Talc-rich hydrothermal rocks from the St. Paul and Conrad fracture zones in the Atlantic Ocean. *European Journal of Mineralogy*, 16, 73-83.
- Davis, A. C., Bickle, M. J. & Teagle, D. A. H. 2003. Imbalance in the oceanic strontium budget. *Earth and Planetary Science Letters*, 211, 173-187.
- Davis, E. & Villinger, H. 1992. Tectonic and thermal structure of the Middle Valley sedimented rift, northern Juan de Fuca Ridge. In: Herzig, P., Humphris, S., Miller, D. J. & Zierenberg, R. A. (eds.) *Proceedings of the Ocean Drilling Program, Initial Reports*. College Station, TX: Ocean Drilling Program.
- de Wit, M. J. & Stern, C. R. 1976. A model for ocean-floor metamorphism, seismic layering and magnetism. *Nature*, 264, 615-619.

- Dekov, V. M., Cuadros, J., Shanks, W. C. & Koski, R. A. 2008a. Deposition of talc-kerolite-smectite at seafloor hydrothermal vent fields: Evidence from mineralogical, geochemical and oxygen isotope studies. *Chemical Geology*, 247, 171-194.
- Dekov, V., Scholten, J., Garbe-Schönberg, C. D., Botz, R., Cuadros, J., Schmidt, M. & Stoffers, P. 2008b. Hydrothermal sediment alteration at a seafloor vent field: Grimsey Graben, Tjörnes Fracture Zone, north of Iceland. *Journal of Geophysical Research: Solid Earth*, 113.
- deMartin, B. J. R., Sohn, R. A., Canales, J. P. & Humphris, S. E. 2007. Kinematics and geometry of active detachment faulting beneath the Trans-Atlantic Geotraverse (TAG) hydrothermal field on the Mid-Atlantic Ridge. *Geology*, 35, 711-714.
- DeMets, C. 2001. A new estimate for present-day Cocos-Caribbean plate motion: Implications for slip along the Central American volcanic arc. *Geophysical Research Letters*, 28, 4043-4046.
- DeMets, C., Mattioli, G., Jansma, P., Rogers, R. D., Tenorio, C. & Turner, H. L. 2007. Present motion and deformation of the Caribbean plate: Constraints from new GPS geodetic measurements from Honduras and Nicaragua. *Geological Society of America Special Papers*, 428, 21-36.
- DeMets, C. & Wiggins-Grandison, M. 2007. Deformation of Jamaica and motion of the Gonâve microplate from GPS and seismic data. *Geophysical Journal International*, 168, 362-378.
- Detrick, R. S., Buhl, P., Vera, E., Mutter, J., Orcutt, J., Madsen, J. & Brocher, T. 1987. Multi-channel seismic imaging of a crustal magma chamber along the East Pacific Rise. *Nature*, 326, 35-41.
- Dewey, J. F. 1988. Extensional collapse of orogens. *Tectonics*, 7, 1123-1139.
- Dias, Á. S. & Barriga, F. J. A. S. 2006. Mineralogy and geochemistry of hydrothermal sediments from the serpentinite-hosted Saldanha hydrothermal field (36°34'N; 33°26'W) at MAR. *Marine Geology*, 225, 157-175.

- Dias, Á. S., Früh-Green, G. L., Bernasconi, S. M. & Barriga, F. J. A. S. 2011. Geochemistry and stable isotope constraints on high-temperature activity from sediment cores of the Saldanha hydrothermal field. *Marine Geology*, 279, 128-140.
- Dick, H. B. & Bullen, T. 1984. Chromian spinel as a petrogenetic indicator in abyssal and alpine-type peridotites and spatially associated lavas. *Contributions to Mineralogy and Petrology*, 86, 54-76.
- Dick, H. J., Lin, J. & Schouten, H. 2003. An ultraslow-spreading class of ocean ridge. *Nature*, 426, 405-412.
- Donnelly, T., Melson, W., Kay, R. & Rogers, J. 1973. Basalts and dolerites of Late Cretaceous age from the central Caribbean. *Initial Reports of the Deep Sea Drilling Project*, 15, 989-1004.
- Donnelly, T., Waldron, S., Tait, A., Dougans, J. & Bearhop, S. 2001. Hydrogen isotope analysis of natural abundance and deuterium-enriched waters by reduction over chromium on-line to a dynamic dual inlet isotope-ratio mass spectrometer. *Rapid Communications in Mass Spectrometry*, 15, 1297-1303.
- Donnelly, T. W., Horne, G. S., Finch, R. C. & López-Ramos, E. 1990. Northern Central America; the Maya and chortis blocks. In: Dengo, G. & Case, J. E. (eds.) *The Caribbean Region. The Geology of North America*. Boulder, CO: Geological Society of America.
- Douville, E., Bienvenu, P., Charlou, J. L., Donval, J. P., Fouquet, Y., Appriou, P. & Gamo, T. 1999. Yttrium and rare earth elements in fluids from various deep-sea hydrothermal systems. *Geochimica et Cosmochimica Acta*, 63, 627-643.
- Douville, E., Charlou, J. L., Oelkers, E. H., Bienvenu, P., Jove Colon, C. F., Donval, J. P., Fouquet, Y., Prieur, D. & Appriou, P. 2002. The Rainbow vent fluids (36°14'N, MAR): the influence of ultramafic rocks and phase separation on trace metal content in Mid-Atlantic Ridge hydrothermal fluids. *Chemical Geology*, 184, 37-48.
- Drever, J. 1974. The magnesium question. *The Sea, Marine Chemistry*, 5, 337-358.

- Dubinina, E., Chernyshev, I., Bortnikov, N., Lein, A. Y., Sagalevich, A., Gol'tsman, Y. V., Bairova, E. & Mokhov, A. 2007. Isotopic-geochemical characteristics of the Lost City hydrothermal field. *Geochemistry International*, 45, 1131-1143.
- Edmond, J. M. 1981. Hydrothermal activity at mid-ocean ridge axes. *Nature*, 290.
- Edmond, J. M., Campbell, A. C., Palmer, M. R., Klinkhammer, G. P., German, C. R., Edmonds, H. N., Elderfield, H., Thompson, G. & Rona, P. 1995. Time series studies of vent fluids from the TAG and MARK sites (1986, 1990) Mid-Atlantic Ridge: a new solution chemistry model and a mechanism for Cu/Zn zonation in massive sulphide orebodies. *Geological Society, London, Special Publications*, 87, 77-86.
- Edmond, J. M., Measures, C., Mangum, B., Grant, B., Sclater, F. R., Collier, R., Hudson, A., Gordon, L. I. & Corliss, J. B. 1979a. On the formation of metal-rich deposits at ridge crests. *Earth and Planetary Science Letters*, 46, 19-30.
- Edmond, J. M., Measures, C., McDuff, R. E., Chan, L. H., Collier, R., Grant, B., Gordon, L. I. & Corliss, J. B. 1979b. Ridge crest hydrothermal activity and the balances of the major and minor elements in the ocean: The Galapagos data. *Earth and Planetary Science Letters*, 46, 1-18.
- Edmond, J. M., Von Damm, K. L., McDuff, R. E. & Measures, C. I. 1982. Chemistry of hot springs on the East Pacific Rise and their effluent dispersal. *Nature*, 297, 187-191.
- Edmonds, H. N., German, C. R., Green, D. R. H., Huh, Y., Gamo, T. & Edmond, J. M. 1996. Continuation of the hydrothermal fluid chemistry time series at TAG, and the effects of ODP drilling. *Geophysical Research Letters*, 23, 3487-3489.
- Edmonds, H. N., Michael, P. J., Baker, E. T., Connelly, D. P., Snow, J. E., Langmuir, C. H., Dick, H. J. B., Muhe, R., German, C. R. & Graham, D. W. 2003. Discovery of abundant hydrothermal venting on the ultraslow-spreading Gakkel ridge in the Arctic Ocean. *Nature*, 421, 252-256.
- Eggler, D. H., Fahlquist, D. A., Pequegnat, W. E. & Herndon, J. M. 1973. Ultrabasic Rocks from the Cayman Trough, Caribbean Sea. *Geological Society of America Bulletin*, 84, 2133-2138.

- Elderfield, H. & Greaves, M. J. 1981. Negative cerium anomalies in the rare earth element patterns of oceanic ferromanganese nodules. *Earth and Planetary Science Letters*, 55, 163-170.
- Elderfield, H., Hawkesworth, C., Greaves, M. & Calvert, S. 1981. Rare earth element geochemistry of oceanic ferromanganese nodules and associated sediments. *Geochimica et Cosmochimica Acta*, 45, 513-528.
- Elderfield, H. & Shultz, A. 1996. Mid-ocean ridge hydrothermal fluxes and the chemical composition of the ocean. *Annual Review of Earth and Planetary Sciences*, 24, 191-224.
- Elderfield, H., Wheat, C. G., Mottl, M. J., Monnin, C. & Spiro, B. 1999. Fluid and geochemical transport through oceanic crust: a transect across the eastern flank of the Juan de Fuca Ridge. *Earth and Planetary Science Letters*, 172, 151-165.
- Elthon, D. 1987. Petrology of Gabbroic Rocks from the Mid-Cayman Rise Spreading Center. *Journal of Geophysical Research*, 92, 658-682.
- Elthon, D., Ross, D. K. & Meen, J. K. 1995. Compositional variations of basaltic glasses from the Mid-Cayman Rise spreading center. *Journal of Geophysical Research*, 100, 12497-12512.
- Escalona, A. & Mann, P. 2011. Tectonics, basin subsidence mechanisms, and paleogeography of the Caribbean-South American plate boundary zone. *Marine and Petroleum Geology*, 28, 8-39.
- Escartin, J., Hirth, G. & Evans, B. 2001. Strength of slightly serpentized peridotites: Implications for the tectonics of oceanic lithosphere. *Geology*, 29, 1023-1026.
- Escartín, J., Mével, C., MacLeod, C. & McCaig, A. 2003. Constraints on deformation conditions and the origin of oceanic detachments: The Mid-Atlantic Ridge core complex at 15°45' N. *Geochemistry, Geophysics, Geosystems*, 4.
- Escartin, J., Smith, D. K., Cann, J., Schouten, H., Langmuir, C. H. & Escrig, S. 2008. Central role of detachment faults in accretion of slow-spreading oceanic lithosphere. *Nature*, 455, 790-794.

- Fouquet, Y., Stackelberg, U. V., Charlou, J. L., Donval, J. P., Erzinger, J., Foucher, J. P., Herzig, P., Muhe, R., Soakai, S., Wiedicke, M. & Whitechurch, H. 1991. Hydrothermal activity and metallogenesis in the Lau back-arc basin. *Nature*, 349, 778-781.
- Fouquet, Y., von Stackelberg, U., Charlou, J. L., Erzinger, J., Herzig, P. M., Muehe, R. & Wiedicke, M. 1993. Metallogenesis in back-arc environments; the Lau Basin example. *Economic Geology*, 88, 2154-2181.
- Fourcade, E., Mendez, J., Azema, J., Cros, P., Dewever, P., Duthou, J. L., Romero, J. E. & Michaud, F. 1994. Pre-Santonian Campanian age for the obduction of the Guatemalan ophiolites. *Comptes Rendus de l'academie des Sciences Serie II*, 318, 527-533.
- Francheteau, J., Needham, H., Choukroune, P., Juteau, T., Seguret, M., Ballard, R., Fox, P., Normark, W., Carranza, X. & Cordoba, D. 1979. Massive deep-sea sulphide ore deposits discovered on the East Pacific Rise. *Nature*, 277, 523-528.
- Früh-Green, G. L., Kelley, D. S., Bernasconi, S. M., Karson, J. A., Ludwig, K. A., Butterfield, D. A., Boschi, C. & Proskurowski, G. 2003. 30,000 Years of Hydrothermal Activity at the Lost City Vent Field. *Science*, 301, 495-498.
- Gale, A., Dalton, C. A., Langmuir, C. H., Su, Y. & Schilling, J.-G. 2013. The mean composition of ocean ridge basalts. *Geochemistry, Geophysics, Geosystems*, 14, 489-518.
- Gamo, T., Chiba, H., Masuda, H., Edmonds, H. N., Fujioka, K., Kodama, Y., Nanba, H. & Sano, Y. 1996. Chemical characteristics of hydrothermal fluids from the TAG Mound of the Mid-Atlantic Ridge in August 1994: Implications for spatial and temporal variability of hydrothermal activity. *Geophysical Research Letters*, 23, 3483-3486.
- Gamo, T., Okamura, K., Charlou, J.-L., Urabe, T., Auzende, J.-M., Ishibashi, J., Shitashima, K. & Chiba, H. 1997. Acidic and sulfate-rich hydrothermal fluids from the Manus back-arc basin, Papua New Guinea. *Geology*, 25, 139-142.
- German, C. R., Baker, E. T., Mevel, C., Tamaki, K. & Team, F. S. 1998. Hydrothermal activity along the southwest Indian ridge. *Nature*, 395, 490-493.

- German, C. R., Bowen, A., Coleman, M. L., Honig, D. L., Huber, J. A., Jakuba, M. V., Kinsey, J. C., Kurz, M. D., Leroy, S., McDermott, J. M., de Lépinay, B. M., Nakamura, K., Seewald, J. S., Smith, J. L., Sylva, S. P., Van Dover, C. L., Whitcomb, L. L. & Yoerger, D. R. 2010a. Diverse styles of submarine venting on the ultraslow spreading Mid-Cayman Rise. *Proceedings of the National Academy of Sciences*, 107, 14020-14025.
- German, C. R., Thurnherr, A. M., Knoery, J., Charlou, J. L., Jean-Baptiste, P. & Edmonds, H. N. 2010b. Heat, volume and chemical fluxes from submarine venting: A synthesis of results from the Rainbow hydrothermal field, 36°N MAR. *Deep Sea Research Part I: Oceanographic Research Papers*, 57, 518-527.
- Gillis, K. M. 1995. Controls on hydrothermal alteration in a section of fast-spreading oceanic crust. *Earth and Planetary Science Letters*, 134, 473-489.
- Ginster, U., Mottl, M. J. & Von Herzen, R. P. 1994. Heat flux from black smokers on the Endeavour and Cleft segments, Juan de Fuca Ridge. *Journal of Geophysical Research: Solid Earth*, 99, 4937-4950.
- Giunta, G. & Beccaluva, L. 2006. Caribbean Plate margin evolution: constraints and current problems. *Geologica Acta*, 4, 265.
- Goncalves, P., Guillot, S., Lardeaux, J.-M., Nicollet, C. & de Lépinay, B. M. 2000. Thrusting and sinistral wrenching in a pre-Eocene HP-LT Caribbean accretionary wedge (Samaná Peninsula, Dominican Republic). *Geodinamica Acta*, 13, 119-132.
- Gordon, M. B., Mann, P., Cáceres, D. & Flores, R. 1997. Cenozoic tectonic history of the North America-Caribbean plate boundary zone in western Cuba. *Journal of Geophysical Research: Solid Earth*, 102, 10055-10082.
- Goto, S., Kinoshita, M., Schultz, A. & Von Herzen, R. P. 2003. Estimate of heat flux and its temporal variation at the TAG hydrothermal mound, Mid-Atlantic Ridge 26° N. *Journal of Geophysical Research: Solid Earth*, 108.
- Gràcia, E. & Escartín, J. 1999. Crustal accretion at mid-ocean ridges and backarc spreading centers: insights from the Mid-Atlantic Ridge, the Bransfield Basin and the North Fiji Basin. *Contributions to Science*, 1, 175-192.

- Hannington, M., Herzig, P., Stoffers, P., Scholten, J., Botz, R., Garbe-Schönberg, D., Jonasson, I. R. & Roest, W. 2001. First observations of high-temperature submarine hydrothermal vents and massive anhydrite deposits off the north coast of Iceland. *Marine Geology*, 177, 199-220.
- Hannington, M., Jamieson, J., Monecke, T., Petersen, S. & Beaulieu, S. 2011. The abundance of seafloor massive sulfide deposits. *Geology*, 39, 1155-1158.
- Hannington, M. D., de Ronde, C. D. J. & Petersen, S. 2005. Sea-floor tectonics and submarine hydrothermal systems. In: Hedenquist, J. W., Thompson, J. F. H., Goldfarb, R. J. & Richards, J. P. (eds.) *Economic Geology 100th Anniversary Volume* Littleton, Colorado, U.S.: Society of Economic Geologists.
- Harper, G. D. 1985. Tectonics of slow spreading mid-ocean ridges and consequences of a variable depth to the brittle/ductile transition. *Tectonics*, 4, 395-409.
- Hauff, F., Hoernle, K., van den Bogaard, P., Alvarado, G. & Garbe-Schönberg, D. 2000. Age and geochemistry of basaltic complexes in western Costa Rica: Contributions to the geotectonic evolution of Central America. *Geochemistry, Geophysics, Geosystems*, 1.
- Hayman, N. W., Grindlay, N. R., Perfit, M. R., Mann, P., Leroy, S. & de Lépinay, B. M. 2011. Oceanic core complex development at the ultraslow spreading Mid-Cayman Spreading Center. *Geochemistry Geophysics Geosystems*, 12, Q0AG02.
- Haymon, R. M. 1983. Growth history of hydrothermal black smoker chimneys. *Nature*, 301, 695-698.
- Haymon, R. M., Fornari, D. J., Edwards, M. H., Carbotte, S., Wright, D. & Macdonald, K. C. 1991. Hydrothermal vent distribution along the East Pacific Rise crest (9°09' – 54'N) and its relationship to magmatic and tectonic processes on fast-spreading mid-ocean ridges. *Earth and Planetary Science Letters*, 104, 513-534.
- Henstock, T. J., Woods, A. W. & White, R. S. 1993. The accretion of oceanic crust by episodic sill intrusion. *Journal of Geophysical Research: Solid Earth*, 98, 4143-4161.

- Hoernle, K., van den Bogaard, P., Werner, R., Lissinna, B., Hauff, F., Alvarado, G. & Garbe-Schönberg, D. 2002. Missing history (16–71 Ma) of the Galápagos hotspot: Implications for the tectonic and biological evolution of the Americas. *Geology*, 30, 795-798.
- Holcombe, T. L., Vogt, P. R., Matthews, J. E. & Murchison, R. R. 1973. Evidence for sea-floor spreading in the Cayman Trough. *Earth and Planetary Science Letters*, 20, 357-371.
- Honnorez, J., Laverne, C., Hubberten, H., Emmermann, R. & Muehlenbachs, K. 1983. Alteration process of layer 2 basalts from, DSDP Hole 504, Costa Rica Rift. *In*: Cann, J., Honnorez, J., Langseth, M. & Von Herzen, R. (eds.) *Initial Reports of the Deep Sea Drilling Project*. Washington, USA: DSDP.
- Honnorez, J. J., Alt, J. C. & Humphris, S. E. 1998. Vivisection and autopsy of active and fossil hydrothermal alterations of basalt beneath and within the TAG hydrothermal mound. *In*: Herzig, P., Humphris, S., Miller, D. J. & Zierenberg, R. A. (eds.) *Proceedings of the Ocean Drilling Program Scientific Results*. College Station, TX: Ocean Drilling Program.
- Hu, G. & Clayton, R. N. 2003. Oxygen isotope salt effects at high pressure and high temperature and the calibration of oxygen isotope geothermometers. *Geochimica et Cosmochimica Acta*, 67, 3227-3246.
- Humphris, S. E. 1998. Rare earth element composition of anhydrite: implications for deposition and mobility within the active TAG hydrothermal mound. *In*: Herzig, P., Humphris, S., Miller, D. J. & Zierenberg, R. A. (eds.) *Proceedings of the Ocean Drilling Program: Scientific results*. College Station, TX: Ocean Drilling Program.
- Humphris, S. E., Alt, J. C., Teagle, D. A. & Honnorez, J. J. 1998. Geochemical changes during hydrothermal alteration of basement in the stockwork beneath the active TAG hydrothermal mound. *In*: Herzig, P., Humphris, S., Miller, D. J. & Zierenberg, R. A. (eds.) *Proceedings of the Ocean Drilling Program: Scientific results*. College Station, TX: Ocean Drilling Program.

- Humphris, S. E. & Cann, J. R. 2000. Constraints on the energy and chemical balances of the modern TAG and ancient Cyprus seafloor sulfide deposits. *Journal of Geophysical Research: Solid Earth*, 105, 28477-28488.
- Humphris, S. E., Herzig, P. M., Miller, D. J., Alt, J. C., Becker, K., Brown, D., Brugmann, G., Chiba, H., Fouquet, Y., Gemmell, J. B., Guerin, G., Hannington, M. D., Holm, N. G., Honnorez, J. J., Iturrino, G. J., Knott, R., Ludwig, R., Nakamura, K., Petersen, S., Reysenbach, A. L., Rona, P. A., Smith, S., Sturz, A. A., Tivey, M. K. & Zhao, X. 1995. The internal structure of an active sea-floor massive sulphide deposit. *Nature*, 377, 713-716.
- Humphris, S. E. & Thompson, G. 1978. Hydrothermal alteration of oceanic basalts by seawater. *Geochimica et Cosmochimica Acta*, 42, 107-125.
- Ishibashi, J.-i., Sato, M., Sano, Y., Wakita, H., Gamo, T. & Shanks Iii, W. C. 2002. Helium and carbon gas geochemistry of pore fluids from the sediment-rich hydrothermal system in Escanaba Trough. *Applied Geochemistry*, 17, 1457-1466.
- Ishibashi, J.-i. & Urabe, T. 1995. Hydrothermal Activity Related to Arc-Backarc Magmatism in the Western Pacific. In: Taylor, B. (ed.) *Backarc Basins*. New York, US: Springer US.
- Ismail, S. A. 2009. Chemistry of accessory chromian spinel in serpentinites from the Penjwen ophiolite rocks, Zagros thrust zone, northeastern Iraq. *Journal of Kirkuk University–Scientific Studies*, 4.
- Ito, E. & Anderson, A. T. 1983. Submarine metamorphism of gabbros from the Mid-Cayman Rise: Petrographic and mineralogic constraints on hydrothermal processes at slow-spreading ridges. *Contributions to Mineralogy and Petrology*, 82, 371-388.
- Jacobs, C. L., Edgar, N. T., Parson, L. M., Dillon, W. P., Scanlon, K. M. & Holcombe, T. L. 1989. A revised bathymetry of the Mid-Cayman Rise and central Cayman Trough using long range side-scan sonar. *Institute of Oceanographic Sciences Deacon Laboratory*, 272, 11.

- James, K. Year. Arguments for and against the Pacific origin of the Caribbean Plate: discussion, finding for an inter-American origin. *In: Geologica Acta*, 2006. 0279-302.
- James, K. H. 2009. In situ origin of the Caribbean: discussion of data. *Geological Society, London, Special Publications*, 328, 77-125.
- James, R. H. & Elderfield, H. 1996. Chemistry of ore-forming fluids and mineral formation rates in an active hydrothermal sulfide deposit on the Mid-Atlantic Ridge. *Geology*, 24, 1147-1150.
- James, R. H., Elderfield, H. & Palmer, M. R. 1995. The chemistry of hydrothermal fluids from the Broken Spur site, 29°N Mid-Atlantic ridge. *Geochimica et Cosmochimica Acta*, 59, 651-659.
- James, R. H., Rudnicki, M. D. & Palmer, M. R. 1999. The alkali element and boron geochemistry of the Escanaba Trough sediment-hosted hydrothermal system. *Earth and Planetary Science Letters*, 171, 157-169.
- Janecky, D. R. & Seyfried Jr, W. E. 1986. Hydrothermal serpentinization of peridotite within the oceanic crust: Experimental investigations of mineralogy and major element chemistry. *Geochimica et Cosmochimica Acta*, 50, 1357-1378.
- Johnson, J. W., Oelkers, E. H. & Helgeson, H. C. 1992. SUPCRT92: A software package for calculating the standard molal thermodynamic properties of minerals, gases, aqueous species, and reactions from 1 to 5000 bar and 0 to 1000 C. *Computers & Geosciences*, 18, 899-947.
- Jordan, T. H. 1975. The Present-Day Motions of the Caribbean Plate. *Journal of Geophysical Research*, 80, 4433-4439.
- Kadko, D., Baker, E. T., Alt, J. C. & Baross, J. A. 1994. RIDGE/VENTS Workshop Final Report on "Global Impact of Submarine Hydrothermal Processes". Ridge office publication.
- Kadko, D., Baross, J. & Alt, J. 1995. The magnitude and global implications of hydrothermal flux. *In: Humphris, S., Zierenberg, R. A., Mullineaux, L. S. & Thomson, R. E. (eds.) Seafloor Hydrothermal Systems: Physical, Chemical,*

- Biological, and Geological Interactions*. Washington, DC: American Geophysical Union.
- Kadko, D., Koski, R., Tatsumoto, M. & Bouse, R. 1985. An estimate of hydrothermal fluid residence times and vent chimney growth rates based on $^{210}\text{Pb}/\text{Pb}$ ratios and mineralogic studies of sulfides dredged from the Juan de Fuca Ridge. *Earth and Planetary Science Letters*, 76, 35-44.
- Kamenetsky, V. S., Crawford, A. J. & Meffre, S. 2001. Factors Controlling Chemistry of Magmatic Spinel: an Empirical Study of Associated Olivine, Cr-spinel and Melt Inclusions from Primitive Rocks. *Journal of Petrology*, 42, 655-671.
- Kelemen, P. B., Koga, K. & Shimizu, N. 1997. Geochemistry of gabbro sills in the crust-mantle transition zone of the Oman ophiolite: implications for the origin of the oceanic lower crust. *Earth and Planetary Science Letters*, 146, 475-488.
- Kelley, D. S., Karson, J. A., Blackman, D. K., Fruh-Green, G. L., Butterfield, D. A., Lilley, M. D., Olson, E. J., Schrenk, M. O., Roe, K. K., Lebon, G. T., Rivizzigno, P. & the, A. T. S. P. 2001. An off-axis hydrothermal vent field near the Mid-Atlantic Ridge at 30°N . *Nature*, 412, 145-149.
- Kelley, D. S., Karson, J. A., Früh-Green, G. L., Yoerger, D. R., Shank, T. M., Butterfield, D. A., Hayes, J. M., Schrenk, M. O., Olson, E. J. & Proskurowski, G. 2005. A serpentinite-hosted ecosystem: the Lost City hydrothermal field. *Science*, 307, 1428-1434.
- Kennan, L. & Pindell, J. L. 2009. Dextral shear, terrane accretion and basin formation in the Northern Andes: best explained by interaction with a Pacific-derived Caribbean Plate? *Geological Society, London, Special Publications*, 328, 487-531.
- Kerr, A. C. & Tarney, J. 2005. Tectonic evolution of the Caribbean and northwestern South America: The case for accretion of two Late Cretaceous oceanic plateaus. *Geology*, 33, 269-272.
- Kerr, A. C., Tarney, J., Marriner, G. F., Nivia, A. & Saunders, A. D. 1997. The Caribbean-Colombian Cretaceous igneous province: the internal anatomy of an oceanic plateau. *Large igneous provinces: Continental, oceanic, and planetary flood volcanism*, 123-144.

- Klein, E. M. & Langmuir, C. H. 1987. Global correlations of ocean ridge basalt chemistry with axial depth and crustal thickness. *Journal of Geophysical Research: Solid Earth*, 92, 8089-8115.
- Klein, F. & Bach, W. 2009. Fe-Ni-Co-O-S Phase Relations in Peridotite-Seawater Interactions. *Journal of Petrology*, 50, 37-59.
- Klinkhammer, G., Elderfield, H., Edmond, J. & Mitra, A. 1994. Geochemical implications of rare earth element patterns in hydrothermal fluids from mid-ocean ridges. *Geochimica et Cosmochimica Acta*, 58, 5105-5113.
- Klinkhammer, G., Elderfield, H. & Hudson, A. 1983. Rare earth elements in seawater near hydrothermal vents. *Nature*, 305, 185-188.
- Knott, R., Fouquet, Y., Honnorez, J., Petersen, S. & Bohn, M. 1998. Petrology of hydrothermal mineralization: a vertical section through the TAG mound. In: Herzig, P., Humphris, S., Miller, D. J. & Zierenberg, R. A. (eds.) *Proceedings of the Ocean Drilling Program. Scientific Results*. College Station, TX: Ocean Drilling Program.
- Kong, X.-Z., Tutolo, B. M. & Saar, M. O. 2013. DBCreate: A SUPCRT92-based program for producing EQ3/6, TOUGHREACT, and GWB thermodynamic databases at user-defined T and P. *Computers & Geosciences*, 51, 415-417.
- Koschinsky, A., Garbe-Schönberg, D., Sander, S., Schmidt, K., Gennerich, H.-H. & Strauss, H. 2008. Hydrothermal venting at pressure-temperature conditions above the critical point of seawater, 5°S on the Mid-Atlantic Ridge. *Geology*, 36, 615-618.
- Koski, R. A., Lonsdale, P. F., Shanks, W. C., Berndt, M. E. & Howe, S. S. 1985. Mineralogy and Geochemistry of a Sediment-Hosted Hydrothermal Sulfide Deposit From the Southern Trough of Guaymas Basin, Gulf of California. *Journal of Geophysical Research*, 90, 6695-6707.
- Koski, R. A., Jonasson, I. R., Kadko, D. C., Smith, V. K. & Wong, F. L. 1994a. Compositions, growth mechanisms, and temporal relations of hydrothermal sulfide-sulfate-silica chimneys at the northern Cleft segment, Juan de Fuca Ridge. *Journal of Geophysical Research: Solid Earth*, 99, 4813-4832.

- Koski, R. A., Benninger, L. M., Zierenberg, R. A. & Jonasson, I. R. 1994b. Composition and Growth History of Hydrothermal Deposits in Escanaba Trough, Southern Gorda Ridge. In: Morton, J., Zierenberg, R. A. & Reiss, C. A. (eds.) *Geologic, Hydrothermal, and Biologic Studies at Escanaba Trough, Gorda Ridge, Offshore Northern California*. US Geological Survey.
- Kuhn, T., Bau, M., Blum, N. & Halbach, P. 1998. Origin of negative Ce anomalies in mixed hydrothermal–hydrogenetic Fe–Mn crusts from the Central Indian Ridge. *Earth and Planetary Science Letters*, 163, 207-220.
- Kuhn, T., Herzig, P. M., Hannington, M. D., Garbe-Schönberg, D. & Stoffers, P. 2003. Origin of fluids and anhydrite precipitation in the sediment-hosted Grimsey hydrothermal field north of Iceland. *Chemical Geology*, 202, 5-21.
- Lalou, C., Reyss, J. L. & Brichet, E. 1998. 9. Age of sub-bottom sulfide samples at the TAG active mound. In: Herzig, P. (ed.) *Proceedings of the Ocean Drilling Program, Scientific Results*.
- Langmuir, C. H., Klein, E. M. & Plank, T. 1992. Petrological Systematics of Mid-Ocean Ridge Basalts: Constraints on Melt Generation Beneath Ocean Ridges. In: Phipps Morgan, J., Blackman, D. K. & Sinton, J. M. (eds.) *Mantle Flow and Melt Generation at Mid-Ocean Ridges*. Washington D.C.: American Geophysical Union.
- Leroy, S., Mauffret, A., Patriat, P. & Mercier de Lépinay, B. 2000. An alternative interpretation of the Cayman trough evolution from a reidentification of magnetic anomalies. *Geophysical Journal International*, 141, 539-557.
- Leroy, S., Mauffret, A. & Pubellier, M. 1996. Structural and tectonic evolution of the eastern Cayman Trough (Caribbean Sea) from seismic reflection data. *AAPG bulletin*, 80, 222-247.
- Levander, A., Schmitz, M., Avé Lallemant, H. G., Zelt, C. A., Sawyer, D. S., Magnani, M. B., Mann, P., Christeson, G., Wright, J. E. & Pavlis, G. L. 2006. Evolution of the southern Caribbean plate boundary. *Eos, Transactions American Geophysical Union*, 87, 97-100.

- Lewis, J., Mattiotti, G. K., Perfit, M. & Kamenov, G. 2011. Geochemistry and petrology of three granitoid rock cores from the Nicaraguan Rise, Caribbean Sea: implications for its composition, structure and tectonic evolution. *Geologica Acta*, 9, 467-479.
- Lewis, J. F., Draper, G., Bourdon, C., Bowin, C., Mattson, P., Maurrasse, F., Nagle, F. & Pardo, G. 1990. Geology and tectonic evolution of the northern Caribbean margin. In: Dengo, G. & Case, J. E. (eds.) *The Caribbean Region: The Geology of North America*. Boulder, CO: Geological Society of America.
- Lilley, M. D., Baross, J. A. & Gordon, L. I. 1983. Reduced gases and bacteria in hydrothermal fluids: the Galapagos spreading center and 21 N East Pacific Rise. *Hydrothermal processes at seafloor spreading centers*, 411-449.
- Lin, J. & Morgan, J. P. 1992. The spreading rate dependence of three-dimensional mid-ocean ridge gravity structure. *Geophysical Research Letters*, 19, 13-16.
- Lister, C. R. B. 1974. On the Penetration of Water into Hot Rock. *Geophysical Journal of the Royal Astronomical Society*, 39, 465-509.
- Lister, C. R. B. 1982. "Active" and "passive" hydrothermal systems in the oceanic crust: predicted physical conditions. In: Fanning, K. A. & Manheim, F. T. (eds.) *The Dynamic Evolution of the Ocean Floor*. Coral Gables, FL: Lexington.
- Lonsdale, P. F., Bischoff, J. L., Burns, V. M., Kastner, M. & Sweeney, R. E. 1980. A high-temperature hydrothermal deposit on the seabed at a gulf of California spreading center. *Earth and Planetary Science Letters*, 49, 8-20.
- Lowell, R. & Rona, P. 2002. Seafloor hydrothermal systems driven by the serpentinization of peridotite. *Geophysical Research Letters*, 29, 26-1-26-4.
- Lowell, R. P. 2010. Hydrothermal Circulation at Slow Spreading Ridges: Analysis of Heat Sources and Heat Transfer Processes. In: Rona, P., Dewey, C. F., Dymant, J. & Murton, B. J. (eds.) *Diversity of Hydrothermal Systems on Slow Spreading Ocean Ridges*. Washington D.C.: American Geophysical Union.

- Lowell, R. P., Farough, A., Hoover, J. & Cummings, K. 2013. Characteristics of magma-driven hydrothermal systems at oceanic spreading centers. *Geochemistry, Geophysics, Geosystems*, 14, 1756-1770.
- Lowell, R. P. & Germanovich, L. N. 2004. Hydrothermal Processes at Mid-Ocean Ridges: Results from Scale Analysis and Single-Pass Models. In: German, C. R., Lin, J. & Parson, L. M. (eds.) *Mid-Ocean Ridges: Hydrothermal Interactions between the Lithosphere and Oceans*. Washington, D.C.: American Geophysical Union.
- Ludwig, K. A., Kelley, D. S., Butterfield, D. A., Nelson, B. K. & Fröh-Green, G. 2006. Formation and evolution of carbonate chimneys at the Lost City Hydrothermal Field. *Geochimica et Cosmochimica Acta*, 70, 3625-3645.
- Lupton, J., Klinkhammer, G., Normark, W., Haymon, R., Macdonald, K., Weiss, R. & Craig, H. 1980. Helium-3 and manganese at the 21 N East Pacific Rise hydrothermal site. *Earth and Planetary Science Letters*, 50, 115-127.
- Lupton, J. E., Baker, E. T. & Massoth, G. J. 1989. Variable ^3He /heat ratios in submarine hydrothermal systems: evidence from two plumes over the Juan de Fuca ridge. *Nature*, 337, 161-164.
- Lydon, J. W. 1989. Volcanogenic Massive Sulphides Part 2: Genetic Models. In: Roberts, R. G. & Sheahan, P. A. (eds.) *Ore Deposit Models*. Newfoundland: Geological Association of Canada.
- Macdonald, K. C. 1982. Mid-ocean ridges: Fine scale tectonic, volcanic and hydrothermal processes within the plate boundary zone. *Annual Review of Earth and Planetary Sciences*, 10, 155.
- Macdonald, K. C., Fox, P., Perram, L., Eisen, M., Haymon, R., Miller, S., Carbotte, S. M., Cormier, M. & Shor, A. 1988. A new view of the mid-ocean ridge from the behaviour of ridge-axis discontinuities. *Nature*, 335, 217-225.
- Macdonald, K. C. & Holcombe, T. L. 1978. Inversion of magnetic anomalies and sea-floor spreading in the Cayman Trough. *Earth and Planetary Science Letters*, 40, 407-414.

- MacLennan, J., Hulme, T. & Singh, S. C. 2005. Cooling of the lower oceanic crust. *Geology*, 33, 357-366.
- MacLeod, C. J., Searle, R. C., Murton, B. J., Casey, J. F., Mallows, C., Unsworth, S. C., Achenbach, K. L. & Harris, M. 2009. Life cycle of oceanic core complexes. *Earth and Planetary Science Letters*, 287, 333-344.
- MacLeod, C. J. & Yaouancq, G. 2000. A fossil melt lens in the Oman ophiolite: Implications for magma chamber processes at fast spreading ridges. *Earth and Planetary Science Letters*, 176, 357-373.
- Magde, L. S. & Sparks, D. W. 1997. Three-dimensional mantle upwelling, melt generation, and melt migration beneath segment slow spreading ridges. *Journal of Geophysical Research: Solid Earth*, 102, 20571-20583.
- Mann, P., Burke, K. & Matumoto, T. 1984. Neotectonics of Hispaniola: plate motion, sedimentation, and seismicity at a restraining bend. *Earth and Planetary Science Letters*, 70, 311-324.
- Mann, P., DeMets, C. & Wiggins-Grandison, M. 2007a. Toward a better understanding of the Late Neogene strike-slip restraining bend in Jamaica: geodetic, geological, and seismic constraints. *Geological Society, London, Special Publications*, 290, 239-253.
- Mann, P., Rogers, R. D. & Gahagan, L. 2007b. Overview of plate tectonic history and its unresolved tectonic problems. *Central America: Geology, resources and hazards*, 1, 201-237.
- Mann, P., Taylor, F., Edwards, R. L. & Ku, T.-L. 1995. Actively evolving microplate formation by oblique collision and sideways motion along strike-slip faults: An example from the northeastern Caribbean plate margin. *Tectonophysics*, 246, 1-69.
- Marjanovic, M., Carbotte, S. M., Carton, H., Nedimovic, M. R., Mutter, J. C. & Canales, J. P. 2014. A multi-sill magma plumbing system beneath the axis of the East Pacific Rise. *Nature Geoscience*, 7, 825-829.

- Marr, C., John, B. E., Cheadle, M. J. & German, C. R. L. J. P. L. M. 2014. Character of High Temperature Mylonitic Shear Zones Associated with Oceanic Detachment Faults at the Ultra-Slow Mid-Cayman Rise. *AGU Fall Meeting*. San Francisco, CA: American Geophysical Union.
- Marshall, J. S., Fisher, D. M. & Gardner, T. W. 2000. Central Costa Rica deformed belt: Kinematics of diffuse faulting across the western Panama block. *Tectonics*, 19, 468-492.
- Marumo, K. & Hattori, K. H. 1999. Seafloor hydrothermal clay alteration at Jade in the back-arc Okinawa Trough: mineralogy, geochemistry and isotope characteristics. *Geochimica et Cosmochimica Acta*, 63, 2785-2804.
- Mattinson, J. M., Pessagno, E. A., Montgomery, H. & Hopson, C. A. 2008. Late Jurassic age of oceanic basement at La Désirade Island, Lesser Antilles arc. In: Wright, J. E. & Shervais, J. W. (eds.) *Ophiolites, Arcs, and Batholiths: A Tribute to Cliff Hopson*. Geological Society of America.
- Mauffret, A. & Leroy, S. 1997. Seismic stratigraphy and structure of the Caribbean igneous province. *Tectonophysics*, 283, 61-104.
- McCaig, A. M., Cliff, R. A., Escartin, J., Fallick, A. E. & MacLeod, C. J. 2007. Oceanic detachment faults focus very large volumes of black smoker fluids. *Geology*, 35, 935-938.
- McCaig, A. M., Delacour, A., Fallick, A. E., Castelain, T. & Frueh-Green, G. L. 2010. Detachment fault control on hydrothermal circulation systems: Interpreting the subsurface beneath the TAG hydrothermal field using the isotopic and geological evolution of oceanic core complexes in the Atlantic. In: Rona, P., Dewey, C. F., Dymet, J. & Murton, B. J. (eds.) *Diversity of Hydrothermal Systems on Slow Spreading Ocean Ridges*. Washington, DC: American Geophysical Union.
- McDermott, J. M. 2015. *Geochemistry of deep-sea hydrothermal vent fluids from the Mid-Cayman Rise, Caribbean Sea*. Doctor of Philosophy, Massachusetts Institute of Technology and Woods Hole Oceanographic Institute.

- McDonough, W. F. & Sun, S.-S. 1995. The composition of the Earth. *Chemical Geology*, 120, 223-253.
- McDougall, T. J. 1990. Bulk properties of “hot smoker” plumes. *Earth and Planetary Science Letters*, 99, 185-194.
- McKenzie, D. P. 1967. Some remarks on heat flow and gravity anomalies. *Journal of Geophysical Research*, 72, 6261-6273.
- Méheut, M., Lazzeri, M., Balan, E. & Mauri, F. 2007. Equilibrium isotopic fractionation in the kaolinite, quartz, water system: Prediction from first-principles density-functional theory. *Geochimica et Cosmochimica Acta*, 71, 3170-3181.
- Mellini, M., Rumori, C. & Viti, C. 2005. Hydrothermally reset magmatic spinels in retrograde serpentinites: formation of “ferritchromit” rims and chlorite aureoles. *Contributions to Mineralogy and Petrology*, 149, 266-275.
- Meschede, M. & Frisch, W. 1998. A plate-tectonic model for the Mesozoic and Early Cenozoic history of the Caribbean plate. *Tectonophysics*, 296, 269-291.
- Miao, S., Li, H. & Chen, G. 2014. Temperature dependence of thermal diffusivity, specific heat capacity, and thermal conductivity for several types of rocks. *Journal of Thermal Analysis and Calorimetry*, 115, 1057-1063.
- Mills, R. A., Teagle, D. A. & Tivey, M. K. 1998. Fluid mixing and anhydrite precipitation within the TAG mound. In: Herzig, P., Humphris, S., Miller, D. J. & Zierenberg, R. A. (eds.) *Proceedings of the Ocean Drilling Program: Scientific results*. College Station, TX: Ocean Drilling Program.
- Miranda, Elena A. & Dilek, Y. 2010. Oceanic Core Complex Development in Modern and Ancient Oceanic Lithosphere: Gabbro-Localized versus Peridotite-Localized Detachment Models. *The Journal of Geology*, 118, 95-109.
- Mitra, A., Elderfield, H. & Greaves, M. 1994. Rare earth elements in submarine hydrothermal fluids and plumes from the Mid-Atlantic Ridge. *Marine Chemistry*, 46, 217-235.

- Miyashiro, A., Shido, F. & Ewing, M. 1969. Composition and origin of serpentinites from the Mid-Atlantic Ridge near 24 and 30 north latitude. *Contributions to Mineralogy and Petrology*, 23, 117-127.
- Molnar, P. & Sykes, L. R. 1969. Tectonics of the Caribbean and Middle America regions from focal mechanisms and seismicity. *Geological Society of America Bulletin*, 80, 1639-1684.
- Montes, C., Bayona, G., Cardona, A., Buchs, D. M., Silva, C., Morón, S., Hoyos, N., Ramírez, D., Jaramillo, C. & Valencia, V. 2012. Arc-continent collision and orocline formation: Closing of the Central American seaway. *Journal of Geophysical Research: Solid Earth*, 117.
- Moore, D. E. & Lockner, D. A. 2011. Frictional strengths of talc-serpentine and talc-quartz mixtures. *Journal of Geophysical Research: Solid Earth*, 116.
- Morishita, T., Hara, K., Nakamura, K., Sawaguchi, T., Tamura, A., Arai, S., Okino, K., Takai, K. & Kumagai, H. 2009. Igneous, Alteration and Exhumation Processes Recorded in Abyssal Peridotites and Related Fault Rocks from an Oceanic Core Complex along the Central Indian Ridge. *Journal of Petrology*, 50, 1299-1325.
- Mottl, M. J. 1983. Metabasalts, axial hot springs, and the structure of hydrothermal systems at mid-ocean ridges. *Geological Society of America Bulletin*, 94, 161-180.
- Mottl, M. 2003. Partitioning of energy and mass fluxes between mid-ocean ridge axes and flanks at high and low temperature. *Energy and mass transfer in marine hydrothermal systems*.
- Mottl, M. J. 2012. Explanatory Notes and Master Chemical Item. Spreadsheet for the VentDB Data Collections housed in the EarthChem Library. EarthChem Library.
- Mottl, M. J. & Holland, H. D. 1978. Chemical exchange during hydrothermal alteration of basalt by seawater—I. Experimental results for major and minor components of seawater. *Geochimica et Cosmochimica Acta*, 42, 1103-1115.

- Mottl, M. J. & Wheat, C. G. 1994. Hydrothermal circulation through mid-ocean ridge flanks: Fluxes of heat and magnesium. *Geochimica et Cosmochimica Acta*, 58, 2225-2237.
- Mottl, M. J., Wheat, G., Baker, E., Becker, N., Davis, E., Feely, R., Grehan, A., Kadko, D., Lilley, M., Massoth, G., Moyer, C. & Sansone, F. 1998. Warm springs discovered on 3.5 Ma oceanic crust, eastern flank of the Juan de Fuca Ridge. *Geology*, 26, 51-54.
- Murton, B. J., Copley, J. T., Connelly, D. P. & Party, J. S. S. Year. Hydrothermal vents at 5000m on the Mid-Cayman Rise: Where basement lithology and depth of venting controls sulphide deposit composition. *In: Oceans 11 MTS/IEEE Conference and Exhibition*, 2011 Kona, HI, USA.
- Murton, B. J., Redbourn, L. J., German, C. R. & Baker, E. T. 1999. Sources and fluxes of hydrothermal heat, chemicals and biology within a segment of the Mid-Atlantic Ridge. *Earth and Planetary Science Letters*, 171, 301-317.
- Murton, B. J. & Rona, P. A. 2015. Carlsberg Ridge and Mid-Atlantic Ridge: Comparison of slow spreading centre analogues. *Deep Sea Research Part II: Topical Studies in Oceanography*, In Press.
- Nakamura, K., Marumo, K. & Aoki, M. 1990. Discovery of a black smoker vent and a pockmark emitting CO₂-rich fluid on the seafloor hydrothermal mineralization field at the Izena Cauldron in the Okinawa Trough. *6th Symposium on Deep-sea Research using the Submersible "SHINKAI 2000" System* 33-50.
- Nath, B., Balaram, V., Sudhakar, M. & Plüger, W. L. 1992. Rare earth element geochemistry of ferromanganese deposits from the Indian Ocean. *Marine Chemistry*, 38, 185-208.
- Neill, I., Kerr, A. C., Hastie, A. R., Stanek, K.-P. & Millar, I. L. 2011. Origin of the Aves Ridge and Dutch–Venezuelan Antilles: interaction of the Cretaceous 'Great Arc' and Caribbean–Colombian Oceanic Plateau? *Journal of the Geological Society*, 168, 333-348.

- Nerlich, R., Clark, S. R. & Bunge, H.-P. 2014. Reconstructing the link between the Galapagos hotspot and the Caribbean Plateau. *Geophysical Research Journal*, 1-2, 1-7.
- Nielsen, S. G., Rehkämper, M., Teagle, D. A. H., Butterfield, D. A., Alt, J. C. & Halliday, A. N. 2006. Hydrothermal fluid fluxes calculated from the isotopic mass balance of thallium in the ocean crust. *Earth and Planetary Science Letters*, 251, 120-133.
- O'Hanley, D. S. 1992. Solution to the volume problem in serpentinization. *Geology*, 20, 705-708.
- Ohmoto, H. 1996. Formation of volcanogenic massive sulfide deposits: the Kuroko perspective. *Ore Geology Reviews*, 10, 135-177.
- Otten, M. T. 1984. The origin of brown hornblende in the Artfjället gabbro and dolerites. *Contributions to Mineralogy and Petrology*, 86, 189-199.
- Oudin, E. & Constantinou, G. 1984. Black smoker chimney fragments in Cyprus sulphide deposits. *Nature*, 308, 349-353.
- Palmer, M. R. & Edmond, J. M. 1989. The strontium isotope budget of the modern ocean. *Earth and Planetary Science Letters*, 92, 11-26.
- Parsons, B. 1981. The rates of plate creation and consumption. *Geophysical Journal International*, 67, 437-448.
- Paulick, H., Bach, W., Godard, M., De Hoog, J. C. M., Suhr, G. & Harvey, J. 2006. Geochemistry of abyssal peridotites (Mid-Atlantic Ridge, 15°20'N, ODP Leg 209): Implications for fluid/rock interaction in slow spreading environments. *Chemical Geology*, 234, 179-210.
- Perfit, M. R. 1977. Petrology and geochemistry of mafic rocks from Cayman Trench - evidence for spreading. *Geology*, 5, 105-110.
- Perfit, M. R. & Chadwick, W. W. 1998. Magmatism at Mid-Ocean Ridges: Constraints from Volcanological and Geochemical Investigations. *Faulting and Magmatism at Mid-Ocean Ridges*. American Geophysical Union.

- Perfit, M. R. & Heezen, B. C. 1978. The geology and evolution of the Cayman Trench. *Geological Society of America Bulletin*, 89, 1155-1174.
- Pester, N. J., Reeves, E. P., Rough, M. E., Ding, K., Seewald, J. S. & Seyfried, W. E. 2012. Subseafloor phase equilibria in high-temperature hydrothermal fluids of the Lucky Strike Seamount (Mid-Atlantic Ridge, 37°17' N). *Geochimica et Cosmochimica Acta*, 90, 303-322.
- Phipps Morgan, J. & Chen, Y. J. 1993. The genesis of oceanic crust: Magma injection, hydrothermal circulation, and crustal flow. *Journal of Geophysical Research: Solid Earth*, 98, 6283-6297.
- Phipps Morgan, J., Parmentier, E. & Lin, J. 1987. Mechanisms for the origin of mid-ocean ridge axial topography: Implications for the thermal and mechanical structure of accreting plate boundaries. *Journal of Geophysical Research: Solid Earth*, 92, 12823-12836.
- Pindell, J., Kennan, L., Draper, G., Maresch, W. & Stanek, K. 2006. Foundations of Gulf of Mexico and Caribbean evolution: eight controversies resolved. *Geologica Acta: an international earth science journal*, 4, 303-341.
- Pindell, J., Maresch, W. V., Martens, U. & Stanek, K. 2012. The Greater Antillean Arc: Early Cretaceous origin and proposed relationship to Central American subduction mélanges: implications for models of Caribbean evolution. *International Geology Review*, 54, 131-143.
- Pindell, J. L. & Barrett, S. F. 1990. Geological evolution of the Caribbean region: a plate tectonic perspective. In: Dengo, G. & Case, J. E. (eds.) *The Caribbean Region. The Geology of North America*. Boulder, CO: Geological Society of American.
- Pindell, J. L. & Kennan, L. 2009. Tectonic evolution of the Gulf of Mexico, Caribbean and northern South America in the mantle reference frame: an update. *Geological Society, London, Special Publications*, 328, 1-55.
- Pollack, H. N., Hurter, S. J. & Johnson, J. R. 1993. Heat flow from the Earth's interior: analysis of the global data set. *Reviews of Geophysics*, 31, 267-280.

- Proskurowski, G., Lilley, M. D., Kelley, D. S. & Olson, E. J. 2006. Low temperature volatile production at the Lost City Hydrothermal Field, evidence from a hydrogen stable isotope geothermometer. *Chemical Geology*, 229, 331-343.
- Quick, J. E. & Denlinger, R. P. 1993. Ductile deformation and the origin of layered gabbro in ophiolites. *Journal of Geophysical Research: Solid Earth*, 98, 14015-14027.
- Ramana, M., Ramprasad, T., Grahm, B., Welsh, R. & Pathak, M. 1995. Magnetic studies in the Cayman Trough, Caribbean Sea. *Caribbean Marine Studies*, 30, 38p.
- Ramondenc, P., Germanovich, L. N., Von Damm, K. L. & Lowell, R. P. 2006. The first measurements of hydrothermal heat output at 9 50' N, East Pacific Rise. *Earth and Planetary Science Letters*, 245, 487-497.
- Ratschbacher, L., Franz, L., Min, M., Bachmann, R., Martens, U., Stanek, K., Stübner, K., Nelson, B. K., Herrmann, U. & Weber, B. 2009. The North American-Caribbean plate boundary in Mexico-Guatemala-Honduras. In: James, K. H., Lorente, M. A. & Pindell, J. (eds.) *The Origin and Evolution of the Caribbean Plate*. London: Geological Society.
- Reeves, E. P., Seewald, J. S., Saccocia, P., Bach, W., Craddock, P. R., Shanks, W. C., Sylva, S. P., Walsh, E., Pichler, T. & Rosner, M. 2011. Geochemistry of hydrothermal fluids from the PACMANUS, Northeast Pual and Vienna Woods hydrothermal fields, Manus Basin, Papua New Guinea. *Geochimica et Cosmochimica Acta*, 75, 1088-1123.
- Reynolds, S. J. & Lister, G. S. 1987. Structural aspects of fluid-rock interactions in detachment zones. *Geology*, 15, 362-366.
- Rogers, R. D. & Mann, P. 2007. Transtensional deformation of the western Caribbean-North America plate boundary zone. *Special Papers-Geological Society of America*, 428, 37.
- Rogers, R. D., Mann, P. & Emmet, P. A. 2007. Tectonic terranes of the Chortis block based on integration of regional aeromagnetic and geologic data. *Special Papers-Geological Society of America*, 428, 65.

- Rona, P. A. 2010. Emerging Diversity of Hydrothermal Systems on Slow Spreading Ocean Ridges. *In: Rona, P., Dewey, C. F., Dymont, J. & Murton, B. J. (eds.) Diversity of Hydrothermal Systems on Slow Spreading Ocean Ridges.* Washington DC: American Geophysical Union.
- Rona, P. A., Klinkhammer, G., Nelsen, T. A., Trefry, J. H. & Elderfield, H. 1986. Black smokers, massive sulphides and vent biota at the Mid-Atlantic Ridge. *Nature*, 321, 33-37.
- Rosencrantz, E. 1990. Structure and tectonics of the Yucatan Basin, Caribbean Sea, as determined from seismic reflection studies. *Tectonics*, 9, 1037-1059.
- Rosencrantz, E. 1995. Opening of the Cayman Trough and the evolution of the northern Caribbean Plate boundary. *In: Geological Society of America Abstracts with Programs*, 1994. 153.
- Rosencrantz, E. & Mann, P. 1991. SeaMARC II mapping of transform faults in the Cayman Trough, Caribbean Sea. *Geology*, 19, 690-693.
- Rosencrantz, E., Ross, M. I. & Sclater, J. G. 1988. Age and spreading history of the Cayman Trough as determined from depth, heat flow, and magnetic anomalies. *Journal of Geophysical Research*, 93, 2141-2157.
- Rosencrantz, E. & Sclater, J. G. 1986. Depth and age in the Cayman Trough. *Earth and Planetary Science Letters*, 79, 133-144.
- Ryabchikov, I. D. 1981. Mobilization of ore metals by supercritical fluids from crystallizing magmas. *Physics and Chemistry of The Earth*, 13-14, 529-536.
- Saccocia, P. J., Seewald, J. S. & Shanks Iii, W. C. 2009. Oxygen and hydrogen isotope fractionation in serpentine–water and talc–water systems from 250 to 450°C, 500MPa. *Geochimica et Cosmochimica Acta*, 73, 6789-6804.
- Sakai, R., Kusakabe, M., Noto, M. & Ishii, T. 1990. Origin of waters responsible for serpentinization of the Izu-Ogasawara-Mariana forearc seamounts in view of hydrogen and oxygen isotope ratios. *Earth and Planetary Science Letters*, 100, 291-303.

- Sauter, D. & Cannat, M. 2010. The Ultraslow Spreading Southwest Indian Ridge. *In*: Rona, P., Dewey, C. F., Dymant, J. & Murton, B. J. (eds.) *Diversity of Hydrothermal Systems on Slow Spreading Ocean Ridges*. Washington D.C.: American Geophysical Union.
- Sauter, D., Cannat, M., Roumejon, S., Andreani, M., Birot, D., Bronner, A., Brunelli, D., Carlut, J., Delacour, A., Guyader, V., MacLeod, C. J., Manatschal, G., Mendel, V., Menez, B., Pasini, V., Ruellan, E. & Searle, R. 2013. Continuous exhumation of mantle-derived rocks at the Southwest Indian Ridge for 11 million years. *Nature Geoscience*, 6, 314-320.
- Savin, S. M. & Lee, M. 1988. Isotopic studies of phyllosilicates. *Reviews in Mineralogy and Geochemistry*, 19, 189-223.
- Schmidt, K., Koschinsky, A., Garbe-Schönberg, D., de Carvalho, L. M. & Seifert, R. 2007. Geochemistry of hydrothermal fluids from the ultramafic-hosted Logatchev hydrothermal field, 15°N on the Mid-Atlantic Ridge: Temporal and spatial investigation. *Chemical Geology*, 242, 1-21.
- Schroeder, T. & John, B. E. 2004. Strain localization on an oceanic detachment fault system, Atlantis Massif, 30 N, Mid-Atlantic Ridge. *Geochemistry, Geophysics, Geosystems*, 5.
- Searle, R. C. 2012. Multiple seafloor spreading modes in the Mid-Cayman Spreading Centre. *AGU Fall Meeting*. San Francisco, CA: American Geophysical Union.
- Seewald, J. S., Doherty, K. W., Hammar, T. R. & Liberatore, S. P. 2002. A new gas-tight isobaric sampler for hydrothermal fluids. *Deep Sea Research Part I: Oceanographic Research Papers*, 49, 189-196.
- Seewald, J. S., McDermott, J. M., German, C. R., Sylva, S. P., Reeves, E. & Klein, F. Year. Geochemistry of hydrothermal fluids from the ultra-slow spreading Mid-Cayman Rise. *In*: AGU Fall Meeting, 2012 San Francisco, CA, USA.
- Seewald, J. S. & Seyfried Jr, W. E. 1990. The effect of temperature on metal mobility in subseafloor hydrothermal systems: constraints from basalt alteration experiments. *Earth and Planetary Science Letters*, 101, 388-403.

- Seyfried Jr, W. & Bischoff, J. 1981. Experimental seawater-basalt interaction at 300 C, 500 bars, chemical exchange, secondary mineral formation and implications for the transport of heavy metals. *Geochimica et Cosmochimica Acta*, 45, 135-147.
- Seyfried Jr, W. 1987. Experimental and theoretical constraints on hydrothermal alteration processes at mid-ocean ridges. *Annual Review of Earth and Planetary Sciences*, 15, 317.
- Seyfried Jr, W. E. & Ding, K. 1993. The effect of redox on the relative solubilities of copper and iron in Cl-bearing aqueous fluids at elevated temperatures and pressures: An experimental study with application to seafloor hydrothermal systems. *Geochimica et Cosmochimica Acta*, 57, 1905-1917.
- Seyfried Jr, W. E., Foustoukos, D. I. & Fu, Q. 2007. Redox evolution and mass transfer during serpentinization: An experimental and theoretical study at 200°C, 500;bar with implications for ultramafic-hosted hydrothermal systems at Mid-Ocean Ridges. *Geochimica et Cosmochimica Acta*, 71, 3872-3886.
- Seyfried Jr, W. E. & Janecky, D. R. 1985. Heavy metal and sulfur transport during subcritical and supercritical hydrothermal alteration of basalt: Influence of fluid pressure and basalt composition and crystallinity. *Geochimica et Cosmochimica Acta*, 49, 2545-2560.
- Seyfried Jr, W. E., Pester, N. J., Tutolo, B. M. & Ding, K. 2015. The Lost City hydrothermal system: Constraints imposed by vent fluid chemistry and reaction path models on seafloor heat and mass transfer processes. *Geochimica et Cosmochimica Acta*, 163, 59-79.
- Seyfried, W. & Bischoff, J. 1979. Low temperature basalt alteration by sea water: an experimental study at 70 C and 150 C. *Geochimica et Cosmochimica Acta*, 43, 1937-1947.
- Seyfried, W., Foustoukos, D. & Allen, D. 2004. Ultramafic-Hosted Hydrothermal Systems at Mid-Ocean Ridges: Chemical and Physical Controls on pH, Redox and Carbon Reduction Reactions. In: German, C. R., Lin, J. & Parson, L. M. (eds.)

Mid-Ocean Ridges: Hydrothermal Interactions between the Lithosphere and Oceans. Washington, DC: AGU.

Seyfried, W., Janecky, D. & Mottl, M. 1984. Alteration of the oceanic crust: implications for geochemical cycles of lithium and boron. *Geochimica et Cosmochimica Acta*, 48, 557-569.

Shanks, W. C. 2001. Stable Isotopes in Seafloor Hydrothermal Systems: Vent fluids, hydrothermal deposits, hydrothermal alteration, and microbial processes. In: Valley, J. W. & Cole, D. R. (eds.) *Reviews in Mineralogy and Geochemistry*. Mineralogical Society of America.

Shanks, W. C., Bohlke, J. K. & Seal, R. R. 1995. Stable isotopes in mid-ocean ridge hydrothermal systems: Interactions between fluids, minerals, and organisms. In: Humphris, S., Zierenberg, R. A., Mullineaux, L. S. & Thomson, R. E. (eds.) *Seafloor Hydrothermal Systems: Physical, Chemical, Biological, and Geological Interactions*. Washington, DC: American Geophysical Union.

Shannon, R. 1976. Revised effective ionic radii and systematic studies of interatomic distances in halides and chalcogenides. *Acta Crystallographica Section A*, 32, 751-767.

Sharara, N. A. 1999. The origin of the Atshan talc deposit in the Hamata area, eastern desert, Egypt: a geochemical and mineralogical study. *The Canadian Mineralogist*, 37, 1211-1227.

Sharp, Z. D. 1990. A laser-based microanalytical method for the in situ determination of oxygen isotope ratios of silicates and oxides. *Geochimica et Cosmochimica Acta*, 54, 1353-1357.

Sharp, Z. D. & Kirschner, D. L. 1994. Quartz-calcite oxygen isotope thermometry: A calibration based on natural isotopic variations. *Geochimica et Cosmochimica Acta*, 58, 4491-4501.

Shaw, W. J. & Lin, J. 1996. Models of ocean ridge lithospheric deformation: Dependence on crustal thickness, spreading rate, and segmentation. *Journal of Geophysical Research: Solid Earth*, 101, 17977-17993.

- Shin, D. & Lee, I. 2003. Carbonate-hosted talc deposits in the contact aureole of an igneous intrusion (Hwanggangri mineralized zone, South Korea): geochemistry, phase relationships, and stable isotope studies. *Ore Geology Reviews*, 22, 17-39.
- Sholkovitz, E. R. & Schneider, D. L. 1991. Cerium redox cycles and rare earth elements in the Sargasso Sea. *Geochimica et Cosmochimica Acta*, 55, 2737-2743.
- Singh, S. C., Crawford, W. C., Carton, H., Seher, T., Combier, V., Cannat, M., Canales, J. P., Dusunur, D., Escartin, J. & Miranda, J. M. 2006. Discovery of a magma chamber and faults beneath a Mid-Atlantic Ridge hydrothermal field. *Nature*, 442, 1029-1032.
- Sinton, C. W., Duncan, R. A., Storey, M., Lewis, J. & Estrada, J. J. 1998. An oceanic flood basalt province within the Caribbean plate. *Earth and Planetary Science Letters*, 155, 221-235.
- Smith, D. K. & Cann, J. R. 1993. Building the crust at the Mid-Atlantic Ridge. *Nature*, 365, 707-715.
- Smith, D. K., Cann, J. R. & Escartin, J. 2006. Widespread active detachment faulting and core complex formation near 13[deg][thinsp]N on the Mid-Atlantic Ridge. *Nature*, 442, 440-443.
- Spivack, A. J. & Edmond, J. M. 1987. Boron isotope exchange between seawater and the oceanic crust. *Geochimica et Cosmochimica Acta*, 51, 1033-1043.
- Srodon, J. 1980. Precise identification of illite/smectite interstratifications by X-ray powder diffraction. *Clays and Clay Minerals*, 28, 401.
- Stakes, D. & Moore, W. S. 1991. Evolution of hydrothermal activity on the Juan de Fuca Ridge: Observations, mineral ages, and Ra isotope ratios. *Journal of Geophysical Research: Solid Earth*, 96, 21739-21752.
- Staudigel, H., Davies, G., Hart, S. R., Marchant, K. & Smith, B. M. 1995. Large scale isotopic Sr, Nd and O isotopic anatomy of altered oceanic crust: DSDP/ODP sites 417/418. *Earth and Planetary Science Letters*, 130, 169-185.

- Staudigel, H. & Hart, S. 1985. Dating of ocean crust hydrothermal alteration: strontium isotope ratios from 504B carbonates and reinterpretation of Sr-isotope data from DSDP sites 105, 332, 417 and 418. *Initial Reports of the Deep Sea Drilling Project*.
- Steiger, R. H. & Jäger, E. 1977. Subcommittee on geochronology: Convention on the use of decay constants in geo- and cosmochemistry. *Earth and Planetary Science Letters*, 36, 359-362.
- Stein, C. A. & Stein, S. 1994. Constraints on hydrothermal heat flux through the oceanic lithosphere from global heat flow. *Journal of Geophysical Research: Solid Earth*, 99, 3081-3095.
- Stein, C. A., Stein, S. & Pelayo, A. M. 1995. Heat flow and hydrothermal circulation. In: Humphris, S., Zierenberg, R. A., Mullineaux, L. S. & Thomson, R. E. (eds.) *Seafloor Hydrothermal Systems: Physical, Chemical, Biological, and Geological Interactions*. Washington, DC: American Geophysical Union.
- Stroup, J. B. & Fox, P. J. 1981. Geologic investigations in the Cayman Trough: Evidence for thin oceanic crust along the Mid-Cayman Rise. *The Journal of Geology*, 89, 395-420.
- Sun, S.-S., Nesbitt, R. W. & Sharaskin, A. Y. 1979. Geochemical characteristics of mid-ocean ridge basalts. *Earth and Planetary Science Letters*, 44, 119-138.
- Sun, Z., Zhou, H., Yang, Q., Sun, Z., Bao, S. & Yao, H. 2011. Hydrothermal Fe–Si–Mn oxide deposits from the Central and South Valu Fa Ridge, Lau Basin. *Applied Geochemistry*, 26, 1192-1204.
- Sverjensky, D. A. 1984. Europium redox equilibria in aqueous solution. *Earth and Planetary Science Letters*, 67, 70-78.
- Tao, C., Lin, J., Guo, S., Chen, Y. J., Wu, G., Han, X., German, C. R., Yoerger, D. R., Zhou, N., Li, H., Su, X., Zhu, J., DY115-19, a. t. & Parties, D.-S. 2012. First active hydrothermal vents on an ultraslow-spreading center: Southwest Indian Ridge. *Geology*, 40, 47-50.

- Teagle, D. A., Alt, J. C., Bach, W., Halliday, A. N. & Erzinger, J. 1996. Alteration of upper ocean crust in a ridge-flank hydrothermal upflow zone: mineral, chemical, and isotopic constraints from Hole 896A. *Proceedings of the Ocean Drilling Program: Scientific results*. College Station, TX: Ocean Drilling Program.
- Teagle, D. A., Alt, J. C., Humphris, S. E. & Halliday, A. N. 1998a. Dissecting an active hydrothermal deposit the strontium and oxygen isotopic anatomy of the TAG hydrothermal mound whole rock and silicate minerals. *In*: Herzig, P., Humphris, S., Miller, D. J. & Zierenberg, R. A. (eds.) *Proceedings of the Ocean Drilling Program: Scientific results*. College Station, TX: Ocean Drilling Program.
- Teagle, D. A. H. & Alt, J. C. 2004. Hydrothermal Alteration of Basalts beneath the Bent Hill Massive Sulfide Deposit, Middle Valley, Juan de Fuca Ridge. *Economic Geology*, 99, 561-584.
- Teagle, D. A. H., Alt, J. C., Chiba, H. & Halliday, A. N. 1998b. Dissecting an active hydrothermal deposit the strontium and oxygen isotopic anatomy of the TAG hydrothermal mound-anhydrite. *In*: Herzig, P., Humphris, S., Miller, D. J. & Zierenberg, R. A. (eds.) *Proceedings of the Ocean Drilling Program, Scientific Results*. College Station, TX: Ocean Drilling Program.
- Teagle, D. A. H., Alt, J. C. & Halliday, A. N. 1998c. Tracing the chemical evolution of fluids during hydrothermal recharge: Constraints from anhydrite recovered in ODP Hole 504B. *Earth and Planetary Science Letters*, 155, 167-182.
- ten Brink, U. S., Coleman, D. F. & Dillon, W. P. 2002. The nature of the crust under Cayman Trough from gravity. *Marine and Petroleum Geology*, 19, 971-987.
- Thompson, G. 1981. St Peter and St Pauls' rocks (Equatorial Atlantic) and the surrounding sea floor. Woods Hole Oceanographic Institute.
- Tivey, M. K. 1995. The influence of hydrothermal fluid composition and advection rates on black smoker chimney mineralogy: Insights from modeling transport and reaction. *Geochimica et Cosmochimica Acta*, 59, 1933-1949.
- Tivey, M. K. 2007. Generation of Seafloor Hydrothermal Vent Fluids and Associated Mineral Deposits. *Oceanography*, 20, 50-65.

- Törmänen, T. O. & Koski, R. A. 2005. Gold Enrichment and the Bi-Au Association in Pyrrhotite-Rich Massive Sulfide Deposits, Escanaba Trough, Southern Gorda Ridge. *Economic Geology*, 100, 1135-1150.
- Tucholke, B. E., Behn, M. D., Buck, W. R. & Lin, J. 2008. Role of melt supply in oceanic detachment faulting and formation of megamullions. *Geology*, 36, 455-458.
- Tucholke, B. E., Lin, J. & Kleinrock, M. C. 1998. Megamullions and mullion structure defining oceanic metamorphic core complexes on the Mid-Atlantic Ridge. *Journal of Geophysical Research: Solid Earth*, 103, 9857-9866.
- Turner, J. S. & Campbell, I. H. 1987. A laboratory and theoretical study of the growth of “black smoker” chimneys. *Earth and Planetary Science Letters*, 82, 36-48.
- van Benthem, S., Govers, R., Spakman, W. & Wortel, R. 2013. Tectonic evolution and mantle structure of the Caribbean. *Journal of Geophysical Research: Solid Earth*, 118, 3019-3036.
- Vance, D., Teagle, D. A. & Foster, G. L. 2009. Variable Quaternary chemical weathering fluxes and imbalances in marine geochemical budgets. *Nature*, 458, 493-496.
- VanTongeren, J. A., Kelemen, P. B. & Hanghøj, K. 2008. Cooling rates in the lower crust of the Oman ophiolite: Ca in olivine, revisited. *Earth and Planetary Science Letters*, 267, 69-82.
- Veirs, S. R., McDuff, R. E. & Stahr, F. R. 2006. Magnitude and variance of near-bottom horizontal heat flux at the Main Endeavour hydrothermal vent field. *Geochemistry, Geophysics, Geosystems*, 7, Q02004.
- Venable, M. E. 1994. *A geologic, tectonic and metallogenic evaluation of the Siuna terrane*. Ph.D University of Arizona.
- Vogt, P. R., Taylor, P. T., Kovacs, L. C. & Johnson, G. L. 1979. Detailed aeromagnetic investigation of the Arctic Basin. *Journal of Geophysical Research*, 84, 1071-1089.
- Von Damm, K., Oosting, S., Kozlowski, R., Buttermore, L., Colodner, D., Edmonds, H., Edmond, J. & Grebmeier, J. 1995. Evolution of East Pacific Rise hydrothermal vent fluids following a volcanic eruption. *Nature*, 375, 47-50.

- Von Damm, K. L. 1990. Seafloor Hydrothermal Activity: Black Smoker Chemistry and Chimneys. *Annual Review of Earth and Planetary Sciences*, 18, 173-204.
- Von Damm, K. L. 1995. Controls on the chemistry and temporal variability of seafloor hydrothermal fluids. In: Humphris, S. (ed.) *Physical, Chemical, Biological, and Geological Interactions within Hydrothermal Systems*. American Geophysical Union.
- Von Damm, K. L. 2001. Lost City found. *Nature*, 412, 127-128.
- Von Damm, K. L. 2004. Evolution of the hydrothermal system at East Pacific Rise 9°50'N: Geochemical evidence for changes in the upper oceanic crust. In: German, C. R., Lin, J. & Parson, L. M. (eds.) *Mid-Ocean Ridges: Hydrothermal Interactions between the Lithosphere and Oceans*. Washington, DC: AGU.
- Von Damm, K. L., Buttermore, L. G., Oosting, S. E., Bray, A. M., Fornari, D. J., Lilley, M. D. & Shanks III, W. C. 1997. Direct observation of the evolution of a seafloor 'black smoker' from vapor to brine. *Earth and Planetary Science Letters*, 149, 101-111.
- Von Damm, K. L., Edmond, J. M., Measures, C. I. & Grant, B. 1985. Chemistry of submarine hydrothermal solutions at Guaymas Basin, Gulf of California. *Geochimica et Cosmochimica Acta*, 49, 2221-2237.
- Von Damm, K. L., Bischoff, J. L. & Rosenbauer, R. J. 1991. Quartz solubility in hydrothermal seawater; an experimental study and equation describing quartz solubility for up to 0.5 M NaCl solutions. *American Journal of Science*, 291, 977-1007.
- Von Damm, K. L., Lilley, M. D., Shanks Iii, W. C., Brockington, M., Bray, A. M., O'Grady, K. M., Olson, E., Graham, A. & Proskurowski, G. 2003. Extraordinary phase separation and segregation in vent fluids from the southern East Pacific Rise. *Earth and Planetary Science Letters*, 206, 365-378.
- Von Damm, K. L., Parker, C. M., Zierenberg, R. A., Lilley, M. D., Olson, E. J., Clague, D. A. & McClain, J. S. 2005. The Escanaba Trough, Gorda Ridge hydrothermal system: Temporal stability and subseafloor complexity. *Geochimica et Cosmochimica Acta*, 69, 4971-4984.

- Wadge, G., Draper, G. & Lewis, J. F. 1984. Ophiolites of the northern Caribbean: A reappraisal of their roles in the evolution of the Caribbean plate boundary. *Geological Society, London, Special Publications*, 13, 367-380.
- Wanless, V. D. & Shaw, A. M. 2012. Lower crustal crystallization and melt evolution at mid-ocean ridges. *Nature Geoscience*, 5, 651-655.
- Waples, D. W. & Waples, J. S. 2004. A review and evaluation of specific heat capacities of rocks, minerals, and subsurface fluids. Part 1: Minerals and nonporous rocks. *Natural resources research*, 13, 97-122.
- Webber, A. P., Roberts, S., Murton, B. J. & Hodgkinson, M. R. S. 2015. Geology, sulfide geochemistry and supercritical venting at the Beebe Hydrothermal Vent Field, Cayman Trough. *Geochemistry, Geophysics, Geosystems*, 16, 2661-2678.
- Welhan, J. & Lupton, J. 1987. Light hydrocarbon gases in Guaymas Basin hydrothermal fluids: thermogenic versus abiogenic origin. *AAPG Bulletin*, 71, 215-223.
- Welhan, J. A. 1988. Origins of methane in hydrothermal systems. *Chemical Geology*, 71, 183-198.
- Wenner, D. B. & Taylor, H. P. 1973. Oxygen and hydrogen isotope studies of the serpentinization of ultramafic rocks in oceanic environments and continental ophiolite complexes. *American Journal of Science*, 273, 207-239.
- Wenner, D. B. & Taylor Jr, H. P. 1974. D/H and O¹⁸/O¹⁶ studies of serpentinization of ultramafic rocks. *Geochimica et Cosmochimica Acta*, 38, 1255-1286.
- Wetzel, L. R. & Shock, E. L. 2000. Distinguishing ultramafic-from basalt-hosted submarine hydrothermal systems by comparing calculated vent fluid compositions. *Journal of Geophysical Research*, 105, 8319-8340.
- Whattam, S. A. & Stern, R. J. 2015. Late Cretaceous plume-induced subduction initiation along the southern margin of the Caribbean and NW South America: The first documented example with implications for the onset of plate tectonics. *Gondwana Research*, 27, 38-63.

- White, G. W. & Stroup, J. B. 1979. Distribution of rock types in the Mid-Cayman Rise, Caribbean Sea, as evidence for conjugate normal faulting in slowly spreading ridges. *Geology*, 7, 32-36.
- White, R. S., McKenzie, D. & O'Nions, R. K. 1992. Oceanic crustal thickness from seismic measurements and rare earth element inversions. *Journal of Geophysical Research: Solid Earth*, 97, 19683-19715.
- White, R., Minshull, T., Bickle, M. & Robinson, C. 2001. Melt generation at very slow-spreading oceanic ridges: Constraints from geochemical and geophysical data. *Journal of Petrology*, 42, 1171-1196.
- Wilson, S., Murton, B. & Taylor, R. 2013. Mantle composition controls the development of an Oceanic Core Complex. *Geochemistry, Geophysics, Geosystems*, 14, 979-995.
- Wolery, T. J. & Sleep, N. H. 1976. Hydrothermal Circulation and Geochemical Flux at Mid-Ocean Ridges. *The Journal of Geology*, 84, 249-275.
- Wood, S. A. 1990. The aqueous geochemistry of the rare-earth elements and yttrium: 2. Theoretical predictions of speciation in hydrothermal solutions to 350°C at saturation water vapor pressure. *Chemical Geology*, 88, 99-125.
- Yalçin, H. & Bozkaya, Ö. 2006. Mineralogy and geochemistry of Paleocene ultramafic- and sedimentary-hosted talc deposits in the southern part of the Sivas Basin, Turkey. *Clays and Clay Minerals*, 54, 333-350.
- Yamanaka, T., Maeto, K., Akashi, H., Ishibashi, J.-I., Miyoshi, Y., Okamura, K., Noguchi, T., Kuwahara, Y., Toki, T., Tsunogai, U., Ura, T., Nakatani, T., Maki, T., Kubokawa, K. & Chiba, H. 2013. Shallow submarine hydrothermal activity with significant contribution of magmatic water producing talc chimneys in the Wakamiko Crater of Kagoshima Bay, southern Kyushu, Japan. *Journal of Volcanology and Geothermal Research*, 258, 74-84.
- You, C. F. & Bickle, M. J. 1998. Evolution of an active sea-floor massive sulphide deposit. *Nature*, 394, 668-671.

- Zhang, L., Liu, J., Zhou, H. & Chen, Z. 1989. Oxygen isotope fractionation in the quartz-water-salt system. *Economic Geology*, 84, 1643-1650.
- Zheng, Y.-F. 1993a. Calculation of oxygen isotope fractionation in anhydrous silicate minerals. *Geochimica et Cosmochimica Acta*, 57, 1079-1091.
- Zheng, Y.-F. 1993b. Calculation of oxygen isotope fractionation in hydroxyl-bearing silicates. *Earth and Planetary Science Letters*, 120, 247-263.
- Zierenberg, R. A., Fouquet, Y., Miller, D., Bahr, J., Baker, P., Bjerkgaard, T., Brunner, C., Duckworth, R., Gable, R. & Gieskes, J. 1998. The deep structure of a sea-floor hydrothermal deposit. *Nature*, 392, 485-488.
- Zierenberg, R. A. & Shanks III, W. 1994. Sediment alteration associated with massive sulfide formation in Escanaba Trough, Gorda Ridge: The importance of seawater mixing and magnesium metasomatism. In: Morton, J., Zierenberg, R. A. & Reiss, C. A. (eds.) *Geologic, Hydrothermal, and Biologic Studies at Escanaba Trough, Gorda Ridge, Offshore Northern California*.